PRESSURE FLUCTUATIONS ON STATIONARY AND OSCILLATING SQUARE SECTION CYLINDERS

by

Emmanuel Dupe Obasaju
Department of Aeronautics
Imperial College of Science and Technology
London SW7
England

Thesis submitted for the degree of Doctor of Philosophy in the Faculty of Engineering, University of London and for the Diploma of Imperial College.

SUMMARY

A study has been made of the pressure fluctuations on a stationary and oscillating square section cylinder. Among the measurements taken are - mean and fluctuating pressures, chordwise and spanwise lift correlations, the phase angle between the fluctuating lift and cylinder's displacement, vortex shedding frequency, vortex convection velocity, spectra of fluctuating pressures and the variation in the phase angle at the shedding frequency around a section of the cylinder. Also investigated are the effects of end plates on the stationary model mean pressures. To compliment these measurements, a film of the vortex shedding phenomenon was made using smoke as the flow indicator. Of particular interest are the changes in the flow during wake synchronisation or lock-in. Under this condition, it is shown that the sectional mean drag is always lower than the stationary cylinder value and that, due largely to a decrease in amplitude modulation, there is an increase in RMS pressure fluctuations. The spanwise correlation is shown to be greatly increased especially around $\frac{U_\infty}{f_N d} = 7.8$ (the reduced windspeed at which the lift pressure fluctuations are maximum) where the correlation is practically unity over the whole span. Both the measured values of $\frac{1 - C_{Pb}}{2\pi S}$ (the non-dimensional vorticity shed by each shear layer into the wake per cycle of vortex shedding) and the values of $\frac{\Gamma_o}{\pi U_\infty d}$ obtained using a potential vortex wake drag formula are shown to indicate that the lock-in value of non-dimensional vortex strength is less than the stationary cylinder value. An important result, as far as flow-induced vibration is concerned, is the variation in the lift phase angle ϕ. The measured values of ϕ are shown to indicate trends that are consistent with the observations of previous workers on square section cylinders undergoing flow-induced lateral oscillations.

The potential flow model of vortex-induced fluctuating pressures

proposed by McGregor (1957) is improved to include the effects of the wake vortex street and applied to an oscillating as well as a stationary circular cylinder. For the stationary cylinder, it is shown that the improved model can predict reasonable values of vortex strength. The model is also shown to be useful in studying the fluctuating pressures and, particularly for the oscillating model, the harmonic content of velocity fluctuations.

With a different choice of forcing function, it is shown that the lift oscillator model proposed by Hartlen & Currie (1970) can be used to model the fluctuating lift on a forced square section cylinder.

ACKNOWLEDGMENTS

I would like to express my thanks to all those who have helped me during the course of this work particularly the following:

a) My supervisor, Dr P.W. Bearman, who was very patient and understanding throughout.

b) The Imperial College Aeronautics Department's academic, technical and secretarial staff including the photographer - Mr J. O'Leary and the Librarian - Mrs A. Barrack. All were friendly and co-operative.

c) My friends particularly Mr Jide Maiye, Mr Olupomi A. Medaiyedu, Femi & Christine Kolade, Mr Paul B. Fadunmiyo and, more importantly, Miss Martina Karpe. This work would never have been completed without them.

d) The members of the OBASAJU family - for their love and encouragement.

The experimental phase of this work was supported by the Commonwealth Scholarship Commission in the United Kingdom. The writing-up phase was supported by loans and/or grants from various organisations and friends and I thank all these. I am greatly indebted - to Professor P.R. Owen for allowing me this opportunity, to the Old Centralians and to Mrs P. Mumford of the British Council's Commonwealth Education Awards Department.

CONTENTS

CHAPTER I

INTRODUCTION

1.1 THE PROBLEM

Despite more than one hundred years of systematic study there is still no doubt that we do not fully understand the problem of fluid flow past a long obstacle of bluff cross-section. A very important feature of such flow is the instability of the two shear layers separating from the body and the subsequent non-linear interaction of these shear layers to form vortices that are shed alternately from each side of the body. This shedding of vortices is approximately periodic and it causes the generation on the obstacle of periodic forces which can, under suitable conditions of damping etc., cause structural oscillations. Thus apart from adding to fundamental knowledge a study of the phenomenon of vortex shedding has many useful engineering applications.

Although the motion of fluid around a bluff obstacle is governed by the Navier Stokes equations, a full analytic solution of the equations are unknown. Because of the enormous amount of computer time and space required a numerical solution of the equations for cases of engineering importance is still out of reach of modern day computers. Our basic understanding of the flow and the predictions of important flow characteristics, like fluid dynamics loadings, must therfore come mainly from wind-tunnel experiments. This is why wind-tunnel investigations, such as the one presented in this thesis are necessary.

1.2 ENGINEERING APPLICATIONS.

Modern design techniques often result in structure and buildings which are light in weight, tall and have low mechanical damping. These structures invariably have a bluff cross-section and are therefore susceptible to vortex

induced oscillation. The designers of stuctures like chimney stacks, piles, electric power transmission lines, tall buildings, suspension bridges etc. must therefore take into consideration the possibility of vortex-induced structural oscillations. Structural oscillations, even when they are not by themselves immediately catastrophic, can lead to fatigue failure.

It is not only the possibility of failure due to oscillations that worry designers. There are applications, such as in the missile and radio-telescope fields for example, where minor movements make systems inoperative without actually destroying them. Even when oscillation does not occur, the periodicity introduced into the flow by vortex shedding can create problems by, for example, producing undesirable aerodynamic noise or by, as in heat exchanger tubes (see Wilkinson (1974)), downgrading the performance of pumps located downstream of the vortex source.

The above examples show that the phenomenon of vortex shedding is of interest to engineers of various disciplines. Most of the past research work on bluff body flows (particularly those on oscillating bluff bodies) were stimulated primarily by the needs of engineers rather than the need for a basic understanding of the flow. Although the title of this thesis suggests only force measurements, considerable attention is also given to the basic flow mechanisms involved.

1.3 A BRIEF REVIEW OF PREVIOUS WORK

1.3.1 Before 1940

Strouhal, 1878, and Rayleigh, 1896, started the quantitative study of periodic flow past bluff bodies. They investigated the aeolian tones generated by the relative motion of a wire (or circular cylinder) and the air. Their findings as reported in Bishop & Hassan (1964A) are:

1) The frequency, f_s, of the aeolian tone varies with the diameter, d, and with the speed, U, of the relative motion such that:

$$f_s = f\left(\frac{Ud}{\nu}\right) \quad \text{or} \quad \left[\frac{f_s d}{U} = f\left(\frac{Ud}{\nu}\right)\right]$$

(The dimensionless group $\frac{f_s d}{U_\infty}$ is now known as Strouhal number)

2) When the speed is such that the aeolian tone coincides with one of the natural frequencies of the wire, which is supported so as to be capable of performing free vibration, the sound is greatly reinforced.

3) It is not essential that the wire should vibrate for a fluctuating force to be applied to it by the flowing fluid.

4) Vibrations of the wire are performed in a plane perpendicular to the direction of the wind.

5) The production of these vibrations is doubtless connected with the instability of vortex sheets.

According to Birkhoff & Zarantonello (1957), it was Benard who in 1908 first correlated the aeolian tones of Strouhal and Reyleigh with a wake vortex street.

In 1911 - 1912 Karman and later Karman & Rubach investigated the stability of an infinite vortex street. They found, see Rosenhead (1953), that if all the vortices were given a two-dimensional disturbance according to a stated general law, first order analysis showed instability unless the spacing ratio was 0.281 . The above works of Karman, Karman & Rubach and subsequent works concerning the stability of idealised vortex streets are reviewed by Rosenhead (1953). Rosenhead stresses in his review that Karman conclusions regarding stability apply only to disturbances of the kind specified and not to the more general types of disturbance which probably occur in normal experimental conditions.

Early attempts to determine the fluctuating lift on bluff bodies are reviewed by Bishop & Hassan (1964A). Only three of the investigations (Thom 1931, Schwabe 1935 and Ruedy 1935) reviewed took place before 1940. Probably due to the lack of suitable instrumentation none of these three attempts involved direct measurements of either surface pressure or total force. Thom (1931) suspended his circular cylinder as a pendulum free to

swing across the stream. He then estimated the fluctuating lift from the semi-angular amplitude of the cylinder's swing during vortex-excited oscillation. Schwabe is said, see Wilkinson (1974), to have calculated pressures from the velocity field obtained by time lapse photography. Ruedy (1935) assumed that a true Karman vortex street existed in the wake of his circular cylinder and estimated the fluctuating lift by considering momentum balance far downstream of the cylinder. Ruedy's results are certainly incorrect because he did not consider the rate of change of the momentum of that part of the wake where the vortices are formed. It is interesting to note that Ruedy's investigation was conducted to solve the engineering problem of vibration of power lines in a steady wind.

The failure of the Tacoma Narrow bridge in 1940 demonstrated that despite the practical significance of the above works of Thom and Ruedy, most engineers and designers of long flexible structures were not giving enough consideration to dynamic wind loading. Karman who was involved in the post-mortem is said, see Davenport (1975), to have written:

> " I hadn't reckoned on the depth and long standing of the prejudices of the bridge designers. Their thinking was still largely influenced by consideration of 'static forces' like weight and pressures which create no motion instead of "dynamic forces" which produces motion or changes motion. Bridges had been observed to oscillate in the wind before, but nobody had thought such motion is important. Bridge failures were usually blamed on other things."

The above extract sums up the attitude adopted, before 1940, by most engineers and designers of structures to dynamic wind loadings such as those due to vortex shedding.

1.3.2 After 1940

The need to predict the dynamic wind loading on structures stimulated an extensive amount of research into bluff body flows. No attempt will be made to discuss references in chronological order, instead the major findings that

are relevant to vortex induced vibrations will be discussed. The interested reader is referred to the works of Bisphop & Hassan (1964 A & B), Markovin (1964), Berger & Wille (1972) and Mair & Maull (1971) for references. Other sources of references are the proceedings of international conferences See for example Naudascher (1974) and Eaton (1977).

1.3.2.1 Characteristics of the body-wake interaction during resonant vibrations

The characteristics of the body-wake interaction presented in this section are collected from the works of various workers on bluff bodies undergoing either forced or vortex-induced resonant vibrations. All the characteristics are dependent on after-body shape, and experimental conditions such as frequency ratio f_N/f_s, amplitude to diameter ratio A/D, and in some cases Reynolds number. (f_N is the frequency of body oscillation, f_s is the natural vortex shedding frequency that would occur if the body were stationary).

a) Synchronisation or "Lock-in"

Vibrations of an elastic cylinder due to the periodic force resulting from vortex shedding do not occur at one particular flow velocity. Instead vibration starts when the frequency of vortex shedding is near the natural frequency of the cylinder and continues over a range of windspeed called the "synchronisation" or "lock-in" range. In the "lock-in" range vortices are shed at the body oscillation frequency in violation of the strouhal relationship

$$S = \frac{f_s d}{U_\infty} = \text{constant.}$$

References and further discussion on the "lock-in" phenomenon can be found in Berger & Wille (1972).

b) Hysterisis

The characteristic properties of the cylinder-wake interaction (i.e. extent of "lock-in" range, cylinder amplitude, fluid forces etc.) can be different depending on whether windspeed or f_N/f_s is increasing or decreasing.

It appears that whether or not hysterisis is observed depends on whether

oscillation is forced or vortex-induced. Lightly-damped, spring-mounted cylinders undergoing vortex-induced vibrations have been reported by various workers, see for example Feng (1968) and Landl (1975), to display hysterisis effects. Hysterisis is **rarely** reported in forced oscillation experiments except on a circular cylinder as in Bishop & Hassan (1964B).

c) Phase Angle variation in the "lock-in" range

All investigators have reported that within the "lock-in" range very large variations exist in the phase angle between the fluctuating lift and displacement. Some workers like Bishop & Hassan (1964B) have pointed out that the phase angle changes in a manner comparable with the response of a simple oscillator.

Typical values of the phase angle observed on various bluff body shapes can be found in the works of Protos et al (1968), Nakamura & Mizota (1975) and Feng (1968) . All except Feng used externally forced bluff cylinders.

The phase angle between lift and displacement is very important because it shows whether or not energy can be transferred from the fluid to the body to promote instability.

d) Force Amplification at "lock-in"

In addition to the above phase angle changes within "lock-in" , large variations in the amplitudes of the total fluctuating lift and drag forces have been reported. The nature of the fluid force variations is best shown by experiments on externally forced cylinders. For constant amplitude of forcing it has been shown by workers like Bishop & Hassan (1964B) and Protos et al (1968) that within the "lock-in" range, the amplitudes of the fluctuating lift and drag forces increase and decrease in a manner comparable with the response of a non-linear oscillator. Generally the maximum total dynamic force measured at "lock-in" on an oscillating body has been found to be larger than that on the stationary body at the same Reynolds number.

It must however be pointed out that total dynamic force amplification does not necessarily imply amplifications of the sectional dynamic forces.

Experiments (see Berger & Wille (1972) for references) have shown that body oscillations align the axes of the wake vortices parallel to the axis of the cylinder. The alignment of the wake vortices greatly increases the spanswise correlation of the dynamic forces. It is therefore possible that the increased total dynamic forces measured on some bluff bodies during resonant vibration are due solely to increased spanwise correlations. It is in particular even possible that the increases in total dynamic forces reported by some workers at "lock-in" are accompanied by decreases in sectional dynamic forces.

Some workers like Tanida et al (1973) have reported that within the "lock-in" range, the mean drag force can have a response pattern similar to those of the dynamic forces.

e) Frequency demultiplication or frequency division

This is the phenomenon whereby wake synchronisation or "lock-in" is produced when the wake is forced at hormonics and subharmonics of the natural shedding frequency f_s . Wake synchronisation is reported by Bishop & Hassan (1964B) at a forcing frequency $f = f_{s/3}$, $f_{s/2}$, f_s , $2f_s$ and $3f_s$, and by Stansby (1976) at $f = f_s$, $2f_s$ and $3f_s$. Other references concerning this phenomenon can be found in Berger & Wille (1972).

1.3.2.2 The wake as a non-linear oscillator.

The characteristics of the body wake interaction discussed in the preceeding section led Bishop & Hassan (1964B) to suggest that the wake behaves like a non-linear self-excited fluid oscillator. Hartlen & Currie (1970) took this suggestion further by showing that when the fluid oscillator is modelled with the Van der Pol equation, the predicted and observed characteristics of fluctuating lift on a circular cylinder are in good qualitative agreement. Other workers like Landl (1975) and Skop & Griffin (1973) have modelled fluctuating lift forces on oscillating circular cylinders with different versions of the Van der Pol equation that are more complicated than the basic equation of Hartlen & Currie. The difficulty in this field is in relating the parameters of a proposed oscillator to the physical characteristics of

the flow. The dependence of the fluctuating lift characteristics on body shape also makes it unlikely that a single non-linear oscillator, which can generate the lift characteristics on all bluff body shapes, can be found. Nevertheless modelling vortex-induced vibration by a non-linear oscillator is still very attractive because the analytical alternative is the formidable task of solving the full Navier-Stokes equation for separated flow around an oscillating boundary.

1.3.2.3 After-body effects.

It was reported in sections 1.3.2.1 and 1.3.2.2 that for a bluff body undergoing resonant vibration the characteristics of the body-wake interaction (i.e. dynamic forces, lift phase angles etc) are dependent on body shape. The most important part of the body is that part downstream of the flow separation lines called the afterbody. Workers like Parkinson et al (1968) and Parkinson (1972) have pointed out that the aeroelastic behaviour of bluff cylinders is dominated by the shape of their afterbodies. Consideration of afterbody effects makes it incorrect to generalise results obtained from a particular bluff body. The investigator is thus compelled, in the absence of a unifying bluff-body theory, to determine the aerodynamic and aeroelastic characteristics of each bluff body shape from separate experiments.

Rectangular cylinders having various side ratios provide a vivid demonstration of afterbody effects. Fig 1.1A , which has been taken from Parkinson (1972), summarises the results of several workers. The mean drag coefficient , C_D , is seen to be very sensitive to changes in the side ratio, d/h , (where d is section depth and h is section width normal to the wind direction) particularly when d/h is close to a critical value of 0.62 for which C_D is maximum. Experiments, see for example Fig 1.1B , have shown that the variation of C_D with d/h is due solely to variation in the base pressure, C_{pb} , which according to Bearman & Trueman (1971)is in turn due to variation in the distance, l_f , between the back face of the model and the position of the fully formed vortex. In an earlier work, which can also be viewed as

a subtle demonstration of afterbody effects, Bearman (1965) has already shown using splitter plates that an inverse relationship exists between the base suction, $-C_{pb}$, and the distance l_f. The interested reader is referred to Bearman & Trueman (1971) where a more detailed discussion of the variation of C_D with d/h is presented.

From the discussion of Bearman & Trueman (1971) on afterbody effects on stationary rectangular cylinders, one can make some deductions about afterbody effects under dynamic conditions. If $d/h < 0.62$ the afterbody is such that oscillation can cause the vortex formation region length, l_f, and base pressure C_{pb}, to assume values that are either higher or lower or equal to the stationary cylinder values. For $0.62 < d/h < 2.5$ oscillation will either increase l_f and C_{pb} (either by causing flow reattachment or by causing the flow to readjust to give less shear layer curvature) or cause them to stay the same. For $d/h > 2.5$ flow reattachment has occured, oscillation would again cause l_f and C_{pb} to behave as in the case $d/h < 0.62$. (However the higher values of C_{pb} and strouhal number S for the sections with $d/h > 2.5$ easily distinguish them under dynamic conditions from the sections with $d/h < 0.62$.) Thus under dynamic conditions the behaviour of l_f and C_{pb} will again be dependent on the afterbody. The works of Wilkinson (1974) and Davies (1975) confirm this view. Davies (1975) investigated bluff cylinders of three different cross-sectional shapes including a flat plate for which he reported that synchronised oscillation caused large reductions in l_f and C_{pb}. By contrast Wilkinson (1974) reported that for a square section cylinder $(d/h = 1)$, undergoing synchronised oscillation C_{pb}, when compared to the stationary cylinder value, was either increased or unaltered but never decreased. Now the base pressure will, by determining the total amount of vorticity shed by the body into the wake, also determine the strength of the wake vortices. It therefore follows that the afterbody will affect the aerodynamic and aeroelastic characteristics of an oscillating bluff body - particularly those characteristics (like aerodynamic forces, lift

phase angles etc.) that result from vortex shedding. This view is supported by the measurements of Nakamura & Mizota (1975) on rectangular cylinders with d/h of 1.0 , 2.0 and 4.0 - See Figs 1.2 and 1.3 .

1.4 PREVIOUS WORK ON SQUARE-SECTION CYLINDERS

The present dissertation is on the aerodynamic and aeroelastic characteristics of square-section cylinders in a uniform approach flow. It is known, however, that natural wind is highly turbulent. If wind tunnel results are to be used to predict wind effects on engineering structures, it is important to know how the interactions between the wind and the structure are affected by turbulence. It is for this reason that the effects of turbulence are considered briefly in this review.

1.4.1 Stationary square-section cylinders

1.4.1.1 Variation of C_D , C_L , C_{pb} and S with incidence α

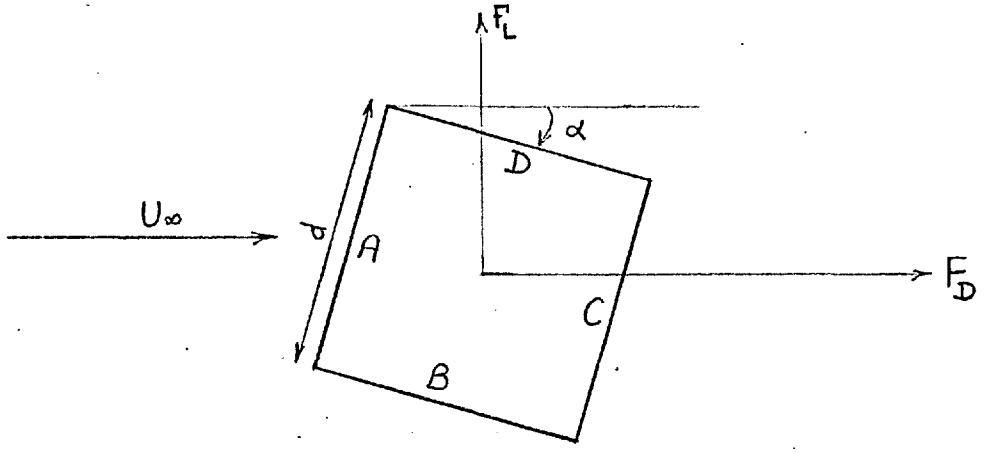

C_{pb} = average mean pressure on face C . Sketch (1.1)

$S = \frac{f_s d}{U_\infty}$ where f_s is the frequency of vortex shedding.

F_L = steady sectional lift force.

F_D = steady sectional drag force.

$$C_D = \frac{F_D}{\frac{1}{2}\rho U_\infty^2 d} \quad ; \quad C_L = \frac{F_L}{\frac{1}{2}\rho U_\infty^2 d} \qquad \text{(1.1)}$$

Many workers including Cowdrey & Lawes (1959), Vickery (1966), Pocha (1971)

and Lee (1974) have measured the variations of C_D , C_L , C_{pb} and S with α The works of Vickery and Lee, particularly thelatter, also include force measurements in turbulent flow. Fig 1.4 taken from Lee shows the important features of the variations of C_D , C_L , C_{pb} and S with α .

Perhaps the most interesting feature of Fig 1.4 is the sharp minimum in both C_L and C_D at a critical α , henceforth denoted by α_{crit} , which for a smooth flow has a value of 13.5^o . Flow visualisation (see for example Mulhearn (1973), Pocha (1971) and Laneville et al (1975)) has shown that α_{crit} corresponds very closely to the incidence at which flow first reattaches steadily to corner B/C - see sketch (1.1) . With increasing free stream turbulence intensity, Fig 1.4 shows that α_{crit} becomes smaller suggesting, as confirmed by the flow visualisations of Mulhearn (1973) and Laneville et al (1975), that turbulence causes earlier flow reattachment. For a given rectangular cylinder in smooth flow, it is known (see for example Laneville (1975)) that increasing the depth of the section parallel to the wind direction decreases the value of α_{crit} . This has lead investigators like Parkinson (1971) and Laneville et al (1975) to suggest that turbulence makes a section behave like a longer section in smooth flow.

The overall behaviour of C_D , C_L , C_{pb} and S will now be discussed.

$0 \leq \alpha \leq \alpha_{crit}$

From flow visualisation Pocha (1971) reported that the vortex formation region length increases with increasing incidence. This, according to the works of Bearman (1965) and Bearman & Trueman (1971) already discussed in section 1.3 , should increase C_{pb} and decrease C_D . The same mechanism is suggested by Lee (1974) for the minimum value of C_D at α_{crit} .

The increase in the magnitude of C_L with increasing α has been attributed to the increase shear layers asymmetry observed by many workers including Pocha (1971) . As α increases the lower shear layer (see sketch (1.1)) moves nearer to side B than the upper one does to side D . Side B

therefore experiences a higher suction than side D so that there is a net downward side force which increases with α. The maximum in $|C_L|$ at $\alpha = \alpha_{crit}$ is attributed, see Lee (1974), to the maximum in the length of the separation bubble caused by flow reattachment at corner B/C .

Lee (1974) suggests that the increase in the strouhal Number , S , is due to decreases in wake width with increases in α. He argues that the minimum value of C_D at α_{crit} is associated with a minimum wake width and hence with a minimum longitudinal vortex spacing if a constant ratio of vortex spacing to wake width is maintained. This, he further suggests, leads to an increase in the frequency of vortex shedding frequency and an increase in S .

Fig. 1.4 confirms the observation by Vickery (1966) that the influence of turbulence is most marked at low angles of incidence. In the present range of α Lee (1974) explains the decreases in C_D and $-C_{pb}$ (negative base pressure) with increase in free stream turbulence intensity in terms of a thickening of the shear layers and their subsequent deflection by the ends of the prism which causes weaker vortices to form further downstream of the body thus reducing $-C_{pb}$ and C_D .

Measurements of the mean pressure distribution around a section by Lee (1974) are presented in Fig 1.5 . They show that, for $\alpha = 0$ and 5° , increase in the level of free stream turbulence intensity leads to more complete pressure recovery towards the rear of the side faces. This supports the remark by Mulhearn (1973) that even at low angles of incidence where flow reattachment does not occur, turbulence brings the separated shear layers closer to the body.

The lowering of the value of α_{crit} by increased free stream turbulence intensity has already been discussed.

$\alpha_{crit} < \alpha < 45^\circ$

The lower shear layer reattaches to the side face B of sketch (1.1) and finally separates from corner B/C . As α increases the reattachment

position on the side face B moves near corner A/B (see for example Mulhearn (1973)) thus decreasing both the size of the separation bubble and the net suction on that face (see ESDU (1971)). The negative C_L thus falls.

Another effect of increasing α is to cause the shear layers from either side of the body to diverge and thus decrease S . In the present range of α , $-C_{pb}$ and C_D are shown, see Fig 1.4 , to increase with α. These increases are usually attributed, see for example Lee (1974), to corresponding decreases in the vortex formation region length, l_f , shown, for example, in the flow visualisation of Pocha (1971) .

Fig. 1.4 shows the influence of turbulence in the present range of α to be small and not to follow an obvious consistent trend. For α close to α_{crit} , Mulhearn (1973) has shown that turbulence moves the position of flow reattachment nearer corner A/B thus decreasing the length of the separation bubble on face B . This, according to Lee (1974), is the reason why turbulence decreases the magnitude of C_L when $13.5 < \alpha \lesssim 25^\circ$.

1.4.1.2 Fluctuating Lift and Drag forces

A. Flow at 0° incidence

(i) The distribution of fluctuating pressure

Vickery (1966), Chaplin & Shaw (1971), Pocha (1971), Lee (1974) and Wilkinson (1974) have measured the sectional distribution of surface fluctuating pressures. The works of Vickery (1966) and Lee (1974), particular the latter, include pressure measurements in turbulent flow. Fig 1.6A shows the smooth flow results of these workers in a range of Reynolds number 10^4 to 1.76×10^5 . The scatter is seen to be very large. Examination of the fluctuating pressure at the centre of the side face, see Fig 1.6B, shows that it does not follow a consistent trend with Reynolds number. Since all the measurements are said to have been made in nominally smooth flows, the spread of results may therefore be due, at least in part, to instrumentation problems thus showing that fluctuating pressures are difficult to measure.

The sectional RMS lift coefficient, C_{Lrms}, measured by the above workers range, with the exception of that of Chaplin & Shaw, between 1.2 and 1.4. Chaplin & Shaw reported that their C_{Lrms} increased from 0.90 to 1.2 (without any correction for blockage)with increasing Reynolds number Re, over the range $5.15 \times 10^3 < Re < 1.3 \times 10^4$. When the free stream velocity is corrected for blockage, this gives C_{Lrms} ranging from 0.739 to 0.985 which is much lower than those of other workers. It is worth noting that Chaplin & Shaw used a model which has an aspect ratio of only 2.95 and produced a blockage ratio of 11.1% and that their results are likely to be greatly influenced by the tunnel wall boundary layer.

The sectional RMS drag coefficient, C_{Drms}, is much less than C_{Lrms}. Vickery (1966), Pocha (1971) and Lee (1974) have reported C_{Drms} of 0.17, 0.175 and 0.23 respectively in smooth flow.

(ii) Spanwise correlation of fluctuating pressure.

Measurements of spanwise correlations in smooth flow by Vickery (1966), Pocha (1971), Lee (1974) and Wilkinson (1974) are presented in Fig 1.7. All the measurements, except those of Wilkinson (1974), indicate, as reported in Vickery (1966), a smooth flow spanwise correlation length of 5.6 body diameters.

Wilkinson (1974) reported a spanwise correlation length of 2.5 body diameters in his smooth flow. Although his experimental set-up (blockage free stream turbulence, aspect ratio, end conditions etc) appears comparable with those of other workers, he still suggested that his low value of correlation may be due to these same factors. It is however interesting to note that for circular cylinders measurements, see for example Novak & Tanaka (1975), indicate a smooth flow spanwise correlation length of 3.5 diameters at subcritical Reynolds number. Generally one expects bluff cylinders with fixed flow separation lines (like the square-section cylinder) to produce straighter wake vortex filaments and hence have higher spanwise correlations than circular cylinders for which the flow separation positions

are free to oscillate.

(iii) Effects of turbulence.

It has been reported in section 1.4.1.1 that for small angles of incidence ($0 < \alpha < \alpha_{crit}$) the base pressure, C_{pb} , increases with increasing free stream turbulence intensity. Vickery (1966) has observed that the reduction in the oscillating lift and the change in base pressure are closely related. This notion is also supported by the measurements of Lee (1974), see Fig 1.8, where an approximately inverse relation between C_{pb} and C_{Lrms} , for flow at 0^{o} incidence, is seen. Thus C_{Lrms} decreases with increasing free stream turbulence intensity - a behaviour similar to those of $-C_{pb}$ and C_{D} already discussed in section 1.4.1.1 . Typically Vickery (1966) reported a 50% decrease in C_{Lrms} with a turbulence intensity of 10% in the free stream.

The measurements of Lee (1974) indicate that spanwise correlation measured along the centerline of a side face is very little affected by free stream turbulence when the intensity of the turbulence is less than 8% . With a free stream turbulence intensity of 12% , Lee's (1974) measurements indicate a marked reduction in the spanwise correlation length. Vickery (1966) has also reported that a free stream turbulence intensity of 10% reduced the spanwise correlation length, λ , from the smooth flow value of 5.6 diameters to only 3.3 diameters. In view of these results, the already discussed low value of λ (i.e. 2.5 diameters) reported by Wilkinson (1974) is all the more surprising as the turbulence intensity in his nominally smooth free stream is reported to be only 1.5%.

The existing measurements, see for example Vickery (1966) and Lee (1974) indicate that the fluctuating drag coefficient is little affected by free stream turbulence when the intensity is not higher than 12%.

B. Flow at an angle to the cylinder

Comparison of Figs 1.4 and 1.8 shows that the trends in the sectional fluctuating force coefficients C_{xrms} and C_{Yrms} (see sketch 1.2 for notation) are identical to the trend in $-C_{pb}$. The overall level of the surface pressure fluctuations around a section (see Fig 1.9), particularly in the separated flow region, also follow the trend in $-C_{pb}$. Thus at $\alpha = \alpha_{crit}$ where $-C_{pb}$ is minimum, surface pressure fluctuations are also minimum so that C_{xrms} and C_{Yrms} are minimum.

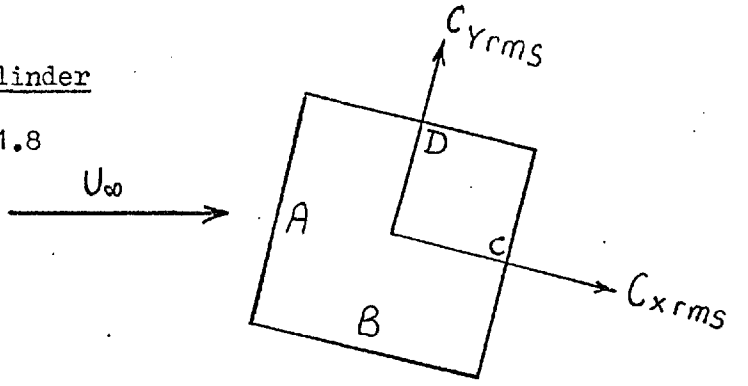

sketch (1.2)

The effects of free stream turbulence is shown in Fig 1.8. C_{xrms} is seen to be little affected by turbulence. C_{Yrms}, with the exception of the results for Grid A4 which produces free stream turbulence of intensity 12.5% and $L_{x/D}$ of 0.94 - see Lee (1974), follows broadly the qualitative trend in $-C_{pb}$. It is interesting to note that on face A where flow is always attached, the level of pressure fluctuations, see Fig 1.9, increases with increasing free stream turbulence intensity.

1.4.1.3 The effects of turbulence length scale

Laneville et al (1975) have demonstrated that turbulence need only be present along the front stagnation streamline to produce the major effects of free stream turbulence on the flow around rectangular cylinders. They argued that because the effects of free-stream turbulence cannot be produced simply by increasing Reynolds number, the mechanism responsible for the observed effects is the modifications to the turbulence structure of the shear layers rather than earlier transition. Furthermore they suggested that the distortion of the turbulence (by the mean flow field) as it approaches the stagnation region of the cylinder is a very important feature of the turbulence mechanism as it determines the amount of turbulence actually fed into the

separated shear layers. Now measurements, see for example Bearman (1972), have shown that the distortion of turbulence approaching the stagnation region of a two-dimensional bluff body depends on the scale, L_x, of the turbulence relative to the body diameter D. For $L_x/D \gg 1$ Bearman (1972) reported that along the mean stagnation streamline the turbulence fluctuation, $(\overline{u^2})^{\frac{1}{2}}$ attenuates like the mean flow whereas if $L_x/D \ll 1$ the turbulence is distorted by the mean flow field and $(\overline{u^2})^{\frac{1}{2}}$ will amplify because of vortex stretching. One therefore expects, from these works, that the influence of turbulence on the square section cylinder will depend on the scale as well as the intensity of the turbulence.

Surprisingly Laneville et al (1975) reported that, for $L_x/D \leqslant 5$, they detected little turbulence scale effect in their measurements of C_D. In direct contrast Mclaren et al (1969) and Lee (1975/1976) reported that C_D is sensitive to L_x/D, particularly for L_x/D around unity. Mclaren et al reported that at incidence, α, of 0°, C_D has a distinct maximum when L_x/D is in the range 1.2 to 1.6 and that for large L_x/D, C_D appears to level off rather than decrease continuously - see Fig 1.10. They also reported that when α is 45°, all the C_D results, regardless of the free stream turbulence intensity, collapse onto one curve similar in shape to the curves for $\alpha = 0$ with maximum C_D occuring when L_x/D is approximately equal to 1.4 and C_D again tending to become constant at large values of L_x/D. Lee (1975/1976) made measurements at $\alpha = 0^\circ$ only and reported that they broadly substantiate the trends outlined by Mclaren et al for the variation of C_D with L_x/D. Lee reported that C_D and $-C_{pb}$ show a distinct maximum at L_x/D of approximately unity, followed by a munimum at L_x/D of between 1.5 and 2.0 and that for high values of L_x/D, both C_D and $-C_{pb}$ tends to a constant value greater than that at low values. The results of Mclaren et al and C_{pb} measurements by Lee are presented in Fig 1.10.

Mclaren et al and Lee did not provide any explanation for the maximum they observed in C_D when L_x/D is around unity. Examination of the

report by Lee shows that his results for $L_{x/D} < 1.5$ where obtained using cylinders with aspect ratios of 9.27 and 10 whereas those for $L_{x/D} > 1.5$ were obtained using cylinders with aspect ratios of 24.4 and 30 . The sharp maximum and minimum reported by Lee at $L_{x/D}$ of around unity - (see Fig 1.10C) occur at the position of transition from low aspect ratio cylinders to high aspect ratio ones. It is known, see for example EDSU (1971), that for square section cylinders, C_D is sensitive to changes in aspect ratio particularly when aspect ratio is low (below 30)and when as in Lee (1975/1976) no end plates are used. Other factors that may have influenced Lee's results are the changes in blockage and the variations in the distance between the turbulence grid and the model; The work of Mclaren et al similarly suffer from aspect ratio and blockage variations as they used cylinders with five different diameters and aspect ratios.

The situation, therefore, is still generally very confusing. Further work is needed in this field to identify more clearly the effects of turbulence scale.

1.4.2 Oscillating square-section cylinders

We are concerned in this section with transverse oscillations perpendicular to the free stream direction. Self-excited oscillations of this type can be caused either by the periodic shedding of vortices (vortex-induced oscillations) or by the steady lift and drag forces following an initial transverse disturbance motion (transverse galloping). Parkinson (1971) has remarked that "an observer of an oscillating cylinder susceptible to both vortex-induced and galloping oscillations would be unable to determine which form was present unless the amplitude $\bar{y}$ was appreciable greater than the transverse cylinder dimension h ." Thus small amplitude self-excited transverse oscillations of a square section cylinder are difficult to classify when they occur at f_N/f_S of around unity. It is for this reason that both transverse galloping and vortex-induced oscillations are reviewed here.

1.4.2.1 Galloping Oscillations

Consider a stationary square section cylinder in a free stream of

velocity U_∞ at 0° incidence. Impressing a downward motion with velocity $\dot{y}$ on the cylinder induces a relative wind, U_{REL}, at an incidence $\alpha_{rel} = \tan^{-1}\left(\dot{y}/U_\infty\right)$ to the cylinder. The steady

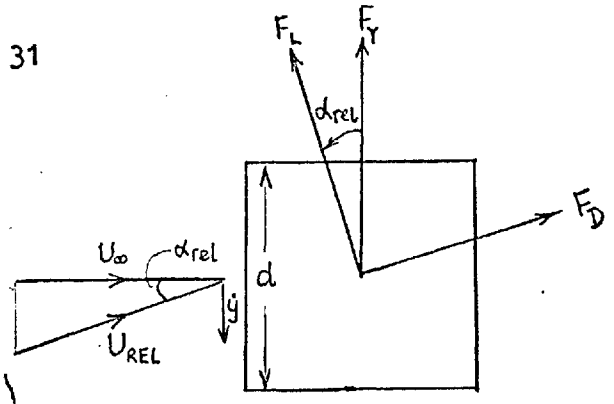

sketch (1.3)

sectional lift and drag forces F_L and F_D respectively will have a resultant, $-F_Y$, in the direction of the motion. Let us assume that at every instant during the motion, the aerodynamic forces (F_D and F_L) on the cylinder are the same as those on a stationary body at the instantaneous angle of incidence $\alpha = \alpha_{rel}$ (this is the quasi-steady assumption). Then the resultant force, $-F_Y$, in the direction of motion can be expressed as

$$\frac{-F_Y}{\frac{1}{2}\rho U_\infty^2 d} = C_{FY} = -\sec\alpha\left(C_L + C_D \tan\alpha\right) \quad \text{- - - - (1.2)}$$

Where C_L and C_D are defined as in equation (1.1) and are obtained from measurements on the stationary cylinder at the instantaneous incidence $\alpha = \alpha_{rel}$.

Fig 1.11 shows that in smooth flow, the excitation, C_{FY}, is positive (i.e. in the direction of the disturbance velocity) and increases with α when $0 < \alpha \lesssim 13^\circ$. C_{FY} will therefore promote instability by assisting the initial small transverse disturbance motion.

If the cylinder of sketch (1.3) is elastically mounted transverse oscillations called transverse galloping can occur when C_{FY} is large enough to overcome the structural damping. This oscillation will grow in amplitude until a limit set by either the flow or the structural damping is reached. Since the excitation, $-F_Y$, increases with windspeed, U_∞, the steady state oscillation amplitude will also increase with U_∞ so that oscillation amplitudes many times the cylinder diameter, d, can occur. These are the main features of transverse galloping.

Transverse galloping of a square section cylinder has been investigated

experimentally and theoretically by many workers including Parkinson & Brooks (1961), and Parkinson & Smith (1962, 1964). Theoretically the structure is idealised as an elastic cylinder with both linear spring and damping forces. The curve of the excitation, C_{FY}, versus α, see Fig 1.11, is next approximated by a polynomial in $\left(\dot{y}/U_\infty\right)$ or $\tan^{-1}(\alpha)$ over the relevant range of α. The resulting equation is then solved for motion characteristics such as steady-state amplitude and build-up time.

The above theory is called the quasi-steady theory because of the quasi-steady assumption employed in the derivation of the excitation C_{FY}. It has been reported, see for example Parkinson & Smith (1964), that the theory predicts instability for all values of U_∞ greater than a critical value defined as

$$U_o = \frac{2\beta}{\eta A} \qquad \text{(1.3)}$$

where $A = \left.\frac{dC_{FY}}{d\alpha}\right|_{\alpha=0}$ (A is positive for a square section cylinder see Fig 1.12)

β = damping parameter .

η = dimensionless mass parameter .

Thus when structural damping is negligible, the quasi-steady theory predicts instability on a square section cylinder at all values of wind speed U_∞. Contrary to theoretical prediction self-excited oscillations have never been observed on elastic square section cylinders when f_s/f_N is below unity even when the damping parameter, β, is made so small that instability should, according to the quasi-steady theory, occur - see Otsuki et al (1974)

It has been reported, see for example Parkinson & Brooks (1961) and Parkinson & Smith (1962,1964), that the quasi-steady theory predicts accurate values of steady-state amplitude and build up time when $f_s/f_N \gtrsim 2.0$. Otsuki et al (1974) and Nakamura & Mizota (1975) have also reported that the measured aerodynamic force at the body's frequency on forced square section

cylinders are in good agreement with the quasi-steady predictions when $f_s/f_N \gtrsim 2.0$. Nakamura & Mizota (1975) also measured the phase angle, ϕ, between the force and the displacement and reported that it tends to the quasi-steady theoretical values at large values of f_s/f_N.

At f_s/f_N of around unity, the agreement between the theory and experiment is poor. This is usually attributed, see for example Parkinson & Smith (1964), to the dominance of the vortex shedding effect.

Effects of turbulence on Galloping

It has been reported, see for example Laneville et al (1975) that the quasi-steady theory is still valid for rectangular cylinders in turbulent flow. To determine the effects of turbulence on galloping one therefore only has to examine how the C_{FY} versus α curve is affected by the turbulence. In other words one only need to examine how C_L and C_D (or infact the mean pressure distribution) on the stationary cylinder changes with turbulence. This has already been considered in section (1.4.1.1).

Fig 1.11 shows the variation of C_{FY} with α in turbulent flow calculated by the author from Lee (1974) values of C_L and C_D. It is seen that:

a) Turbulence reduces the range of α for which $dC_{FY}/d\alpha$ is positive (i.e. range of instability)

b) The maximum value of C_{FY}, C_{FYmax}, occurs at a lower value of incidence in turbulent flow

c) C_{FYmax} in turbulent flow is less than the value in smooth flow.

Thus for a square-section cylinder, turbulence will not only reduce the range of incidence for which transverse galloping can occur, the steady-state amplitude of oscillation at a given windspeed, U_∞, will also be reduced. This is confirmed by the measurements of Novak reported in Parkinson (1971). The reduction of galloping amplitude by turbulence was so marked that Parkinson (1971) suggested that a sufficient intensity of turbulence would suppress galloping.

It is, perhaps, interesting to note that the incidence, α, for which

C_{FY} has a maximum value of C_{FYmax} corresponds very closely to the α at which flow reattachment first occur - this α has been denoted by α_{crit} in section (1.4.1.1). Thus the reduction of galloping amplitude by turbulence is due to the way in which turbulence causes earlier flow reattachment.

1.4.2.2 Vortex-dominated cross-wind oscillations

We are concerned in this section with cross-wind oscillations of square-section cylinders in the frequency range $0.5 < f_S/f_N < 2.0$. In this range of f_S/f_N the oscillating square section cylinder is still likely to experience fluctuating pressures caused by the aerodynamic lift and drag forces as a result of the cyclic variation in the instantaneous angle of incidence although the magnitude of such excitations may be different from the prediction of the quasi-steady theory of section 1.4.2.1 . Thus the aerodynamic and aeroelastic characteristics observed on square section cylinders oscillating in the present range of f_S/f_N cannot be attributed solely to vortex shedding. It is for this reason that the term 'vortex-dominated' rather than 'vortex-induced' is used in the heading of this section.

We have remarked in the preceeding section that self-excited cross-wind oscillations have never been observed on spring-mounted square section sylinders at f_S/f_N below unity. A full investigation of the square section cylinder in the range $0.5 < f_S/f_N < 2.0$ therefore requires external forcing. This is the method of experimentation in the three works (Wilkinson (1974), Otsuki et al (1974) and Nakamura & Mizota (1975)) so far published. All three publications only became available during the course of the present investigation.

Otsuki et al (1974) and Nakamura & Mizota (1975) measured $L_m(t)$ which is the component of the total force $L(t) - V(t)$ (See footnote 1.1 for definition) at the body's frequency and the phase angle , ϕ , between $L_m(t)$ and the cylinder's displacement.

Wilkinson (1974) measured mean and fluctuating surface pressures around a section, lift phase angle ϕ , and correlations - particularly spanwise

ones. He complimented these measurements with a smoke flow visualisation of the vortex shedding phenomenon. The range and scope of his measurements are similar to those presented in this dissertation.

Before assessing Wilkinson results it must be pointed out that he mounted his pressure transducer outside the wind tunnel. His pressure tappings were therefore connected to the transducer by very long plastic tubing which he himself showed , see Fig 1.12, to suffer from resonance effects and phase distortion in his declared frequency range of interest of around 50Hz . Quite apart from the distortion produced by the long length of tubing, cyclic distortion (i.e. 'flappings') of the long tubings during model oscillation is bound to create spurious pressure signals particularly at high values of f_N/f_S . Thus Wilkinson's measurements of dynamic pressures and phase angles, particularly during model oscillations, can at best indicate only broad qualitative trends.

The main findings of the three workers are discussed below.

A. Effects of oscillation on vortex shedding frequency

The results of Otsuki et al (1974) indicate that oscillation at amplitude to diameter ratios, A/D , of 0.013 and 0.033 do not affect vortex shedding frequency (i.e. vortices are shed at the frequency, f_s , that would exist if body were stationary). For A/D of 0.067 , 0.1 and 0.133 he reported wake synchronisation or 'lock-in' when f_s/f_N is around

---

Footnote (1.1)

L(t) is the total fluctuating lift on the oscillating cylinder.

V(t) is the total fluctuating lift on the cylinder during oscillation in still air.

Lm(t) is the component of L(t) - V(t) at the frequency of oscillation

$C_{Lm} = \dfrac{|L_m(t)|}{\frac{1}{2}\rho U_\infty^2 d l}$, $|L_m(t)|$ is the amplitude of Lm(t) .

"d" and "l" are cylinders diameter and span respectively.

unity with the lock-in range increasing with increasing A/D . His measurements outside the lock-in range indicate that vortex shedding frequency is either less than or equal to the stationary cylinder value, f_s , depanding on whether f_s/f_N is less or greater than unity - see Fig 1.13 .

Wilkinson (1974) reported that at the high f_s/f_N extremity of the 'lock-in' range, lock-in was intermittent with the amount of time spent in the lock-in position increasing with decreasing f_s/f_N . He also reported that for large values of A/D (his maximum value of A/D was 0.134) there appeared to be no lower limit to the lock-in region and that there was no sign of any appreciable energy at the strouhal frequency.

B. Hysterisis

Wilkinson reported that tests conducted to detect hysterisis indicated that there was none. The other two workers did not report hysterisis.

C. Phase angle variation in the lock-in range

The measurements of the three workers indicate that within the lock-in range, the phase angle, ϕ , between the fluctuating lift and displacement rises very sharply with increasing f_s/f_N . The approximate values of ϕ reported by each worker at the lower (i.e. low f_s/f_N) and the upper (i.e. high f_s/f_N) extremes of the lock-in range are respectively -80° and 110° - Otsuki et al (1974) see Fig 1.14B, -105° and 150° - Wilkinson (1974) see Fig 1.16A, and -120° and 60° - Nakamura & Mizota (1975) see Fig 1.3A . The three works are best compared by examining the values of f_s/f_N and A/D at which ϕ becomes zero. These zero crossings are plotted in Fig 1.15 .

Now when $0^\circ < \phi < 180^\circ$, the oscillating cylinder experiences an exciting force in phase with the velocity (i.e. negative damping). When the cylinder is spring-mounted, this negative damping will input energy into the system so that the oscillation amplitude increases either until this energy input per cycle is balanced by the energy dissipated per cycle by structural damping or, when structural damping forces are very small, until the phase

angle, ϕ, becomes 0° or 180° so that the flow itself cuts off the excitation energy. A small damping force can be the result of either small damping parameter or small amplitude of oscillation. The zero crossing in forced oscillation experiments therefore indicate both the steady state oscillation amplitude and the corresponding value of f_S/f_N or windspeed that a lightly-damped spring-mounted cylinder will experience when undergoing small amplitude self-excited lateral oscillations. This view is confirmed by the work of Nakamura & Mizota (1975) where values of A/D and f_S/f_N measured on three different spring-mounted rectangular cylinders (including a square section cylinder) undergoing self-excited oscillations are shown, see Fig 1.2A **,to be in** good agreement with the values deduced from the zero crossings in forced oscillation experiments.

Returning to Fig 1.15 the ϕ values of Otsuki et al (1974) and Nakamura & Mizota (1975) indicate that the spring-mounted square section cylinder will experience self-excited oscillation at f_S/f_N above unity with the steady-state amplitude of lateral oscillations increasing with increasing windspeed or f_S/f_N (note that $\frac{U_\infty}{f_N d} = \frac{1}{S} \cdot f_S/f_N$ where S is the stationary cylinder strouhal number). In direct contrast Wilkinson values indicate self-excited oscillation with amplitude that decreases sharply with increasing windspeed. Wilkinson's results are odd because all known observations of steady-state self-excited oscillation amplitude on spring mounted square section cylinders, see for example Parkinson & Smith (1966), support the trend indicated by the measurements of Otsuki et al and Nakamura & Mizota.

After comparing his square section cylinder ϕ values with those measured on an oscillating circular cylinder by Hassan in 1962, see Fig 1.16B, Wilkinson remarked that the difference between the two results are "mainly the result of differences in amplitude ratio and are more or less independent of body shape". In other words at same values of A/D and f_N/f_S, ϕ values on a forced circular cylinder should be identical to those on a forced

square section cylinder. This is most unlikely. We have already remarked in the preceeding paragraph that the phase angle, ϕ , determines the mode of energy transfer between the flow and the oscillating cylinder. Experiments, see for example Feng (1969), have shown that the lightly damped spring-mounted circular cylinder will undergo vortex-induced oscillations only within a DISCRETE range of f_s/f_N starting approximately from $f_s/f_N = 1.0$. In direct contrast the lightly damped spring-mounted square section cylinder will undergo, see the preceeding paragraph, self-excited oscillation at ALL values of f_s/f_N above a critical value $\left(f_s/f_N\right)_{crit}$ ($\left(f_s/f_N\right)_{crit}$ has never been found to be less than unity) with the amplitude of oscillation increasing with increasing f_s/f_N . These results show that the mode of energy transfer between the flow and the body is different for the two cylinders, ϕ values obtained on a forced square section cylinder at given values of A/D and f_s/f_N will therefore generally be different from those obtained on a forced circular cylinder under identical conditions. This casts further **suspicion on the accuracy of Wilkinson's measurements .**

D. Force Amplification at lock-in

(i) Mean drag forces. Wilkinson (1974) compared the mean drag coefficient $C_{D(f)}$ during oscillation with that of the stationary cylinder, C_{DO} - see Fig 1.17A , Except at f_s/f_N of around 1.2 where $C_{D(f)}/C_{DO}$ is approximately unity, oscillation is shown to decrease the mean drag throughout the lock-in range. Wilkinson attributed the drop in the mean drag to a rise in base pressure.

Wilkinson also reported that his flow visualisation indicated that at lock-in, the vortex formation region length was decreased below the stationary cylinder value. This, from work on oscillating cylinders, see for example Davies (1975), and on stationary cylinders, see for example Bearman (1965), leads one to expect increases in the mean drag and base suction. Surprisingly Wilkinson measurements, see Fig 1.17A and the preceeding paragraph, indicated decreases in mean

drag and base suction.

(ii) Spanwise correlation

Only Wilkinson measured spanwise correlation. His results indicate that oscillation produces very large increases in the spanwise correlation length particularly at lock-in - see Fig 1.18 . He reported that maximum spanwise correlation occured at f_N/f_S of about 0.85 to 0.90 . He expressed the maximum correlation length , λ/D, at lock-in approximately by:

$$\lambda/D = 2.50 + 250\, A/D$$

where A is the amplitude of oscillation and D is the diameter of the cylinder.

(iii) Sectional fluctuating lift coefficient, C_{Lrms}

Measurements by Wilkinson (1974) indicate that at lock-in, oscillation greatly increases C_{Lrms} - see Fig 1.19 . He reported that C_{Lrms} was maximum, in the lock-in range, at f_N/f_S of about 0.90 . He compared this maximum value of C_{Lrms} with that on a stationary cylinder and reported, see Fig 1.19B , lift amplifications of 1.45 , 1.92 and 2.2 for A/D of 0.022 , 0.067 and 0.134 respectively.

Otsuki et al (1974) and Nakamura & Mizota (1975) measured the coefficient, C_{Lm} , of the amplitude of the total force Lm(t) where Lm(t) is the component of L(t) - V(t) at the body's frequency (see footnote 1.1 for definition). Experimental measurements, see for example Fig 1.17B , suggest that V(t) is much less than L(t) even when A/D is as high as 0.134 and f_S/f_N is around unity. Now for a stationary square section cylinder in a smooth stream at 0° incidence Vickery (1966) has reported that 95% of the total energy of the fluctuating lift is contained in a 2% band width centered on the strouhal frequency. It is known that at lock-in lateral oscillation makes vortex shedding frequency even more regular (i.e. more nearly periodic) than on the stationary body so that

almost all the fluctuating lift energy will be contained in a narrow band width centered on the common frequency of oscillation and vortex shedding. Furthermore the measurements of Wilkinson already discussed indicate excellent spanwise correlation at lock-in. The C_{Lm} values of Otsuki et al and Nakamura & Mizota will therefore correspond very closely to the amplitude of the sectional lift coefficient (i.e. $C_{Lm} = C_{Lrms} \times \sqrt{2}$) particularly when A/D is large. The result of Otsuki et al therefore indicate, see Fig 1.14A a maximum C_{Lrms} of 1.06 at A/D of 0.133 and $f_S/f_N = 0.92$. Those of Nakamura & Mizota indicate, see Fig 1.2B , a maximum C_{Lrms} of 1.50 at A/D = 0.15 and $f_S/f_N = 0.9$. As the stationary cylinder value of C_{Lrms} has been reported in section 1.4.1.2 to range between 1.2 and 1.4 , the two works indicate that when $A/D < 0.15$, the maximum value of C_{Lrms} at lock-in is approximately equal to the stationary cylinder value. This does not agree with the measurements of Wilkinson, see Fig 1.19B , where amplifications of over 220% is reported at lock-in in the same range of A/D .

E. Magnification of surface dynamic pressures at high values of f_N/f_S

Wilkinson measurements, see Fig 1.17B , show that the magnification, $\frac{\tilde{C}_{p(f=f)}}{\tilde{C}_{p(f=0)}}$ (see Footnote 1.2), of the fluctuating pressure at the centre of the side face is very large at high values of oscillation frequency f_N/f_S . For example his results for A/D = 0.134 for which he also presented measurements of the virtual mass pressures (see Footnote (1,2)) show that for $f_N/f_S > 1.2$ the magnification, even after virtual mass pressures have been substracted, increases with increasing f_N/f_S so

FOOTNOTE (1.2)

a) $\frac{\tilde{C}_{p(f=f)}}{\tilde{C}_{p(f=0)}}$ = RMS pressure coefficient on the oscillating model divided by RMS pressure coefficient on the stationary model.

b) Virtual mass pressure - The dynamic pressure on the model during oscillation in still air

that at f_N/f_S of about 1.8 the value of the magnification less the contribution of the virtual mass pressures is already more than the maximum magnification in the lock-in range. Wilkinson suggested that this may be due to a first harmonic locking range. Even then his results are still rather unusual because his measurements of mean drag amplification, see Fig 1.17A , indicate large reductions at high values of f_N/f_S . Usually one expects large drag reductions to indicate reduced vortex activities so that at large values of f_N/f_S one expects Wilkinson's values of $\frac{\tilde{C}_{p(f=f)}}{\tilde{C}_{p(f=o)}}$ to tend to his virtual mass pressure values, as the total force measurements of Nakamura & Mizota (1975) indicate, rather than diverge even more from them as Wilkinson's measurements of Fig 1.17B show.

1.5 PURPOSES AND SCOPE OF PRESENT INVESTIGATION

The present investigation is aimed primarily at improving our understanding of the body-wake interaction that takes place during vortex-induced and forced vibrations. There is also generally insufficient data on the fluctuating surface pressures experienced by bluff bodies - particularly stationary and oscillating non-circular bluff bodies. The secondary aim of this investigation is therefore to add to existing sparse fluctuating surface pressure data.

In the present investigation, the characteristics of surface fluctuating pressures (particularly those contributing to fluctuating lift) have been examined on a stationary and oscillating square section cylinder. Observations on the oscillating cylinder were conducted at forcing frequencies at and around resonance. Other flow characteristics observed include surface mean pressures, pressure correlations, vortex longitudinal spacings and the phase angle between the fluctuating C_{lift} and the displacement of the oscillating cylinder. Finally a smoke visualisation of the vortex shedding phenomenon was conducted to complement the above observations and to provide more insight into the complex body-wake interaction that takes during body oscillation.

CHAPTER 2

EXPERIMENTAL APPARATUS

2.1 WIND TUNNEL

All experiments were performed in the 3' x 3' wind tunnel of the Department of Aeronautics, Imperial College of Science and Technology, London. The wind tunnel is a low speed, low turbulence closed-return type. Details of the wind tunnel can be found in the work of Clements & Unwin (1973) where it is reported that the turbulence level in the tunnel working section is less than 0.04% .

2.2 THE OSCILLATING MECHANISM

Mounted underneath the floor of the tunnel working section is the oscillating mechanism. This device is capable of producing simple harmonic oscillations at a continuously variable frequency and peak-to-peak amplitude up to a maximum value of 40Hz and 30mm respectively. The detailed design is due to Mr. Gasson of the Department of Aeronautics, Imperial College, London. The operating principles are outlined in Davies (1975).

Body amplitude and frequency were detected with a D.C Linear Variable Differential Transformer (24V, Voltage Electro Mechanisms , type 500 DC) mounted on one arm of the oscillating mechanism. This produced a voltage output of 5V for 12.5mm displacement and the output signal was fed to a Muirhead Wave Analyser (Model K-134-A) for body displacement frequency measurement.

2.3 THE PRESSURE TRANSDUCERS

Two capacitive pressure transducers were used. The majority of the fluctuating pressure measurements on the stationary model were conducted with the B & K $\frac{1}{4}$" microphone. A $\frac{1}{2}$" Setra Pressure Transducer which was more sensitive and almost drift-free was used for measurements of mean and fluctuating pressures, correlations and lift phase angles on the

oscillating models. Details of the transducers and the associated mounting systems are summarised below.

B & K ½" Condenser Microphone Type 4136

This was used in a resonant circuit consisting of a Disa Oscillator 51 E32 and a Disa Reactance Converter type 51E01 . The same circuitry was used earlier by Fackrell (1973) and the operating principle and description of the system can be found in his Ph.D Thesis. The sensitivity of the system was adjustable. Under the present experimental conditions the most appropiate value of sensitivity was found to be 7.5 millivolts/mm of water gauge pressure.

½" Setra Low Range Pressure Transducer Model 237

The setra systems transducer has built-in electronics and only requires external D.C. excitation voltage in the range 15 to 30 volts The excitation voltage was kept at the nominal value of 24 volts throughout the experiments. The sensitivity was found to be 35.4 Millivolt/mm of water gauge pressure.

The Mountings for the Pressure Transducers'

The setra pressure transducer as supplied by the manufacturer is sketched in Fig. (2.1A) . For the purpose of the experiment, which is surface pressure measurement, the mounting technique described below was employed.

A cap terminating in a short tube of bore 0.078" was fitted above the diaphragm. The cap which rested on an 'O' ring placed on the transducer's mounting flange, was held in place by a nut - See Fig. (2.1B) . The 'O' ring seals the diaphragm from the external air so that pressure can only be applied to the diaphragm either through the tube on the cap or through the equalisation tube. When the cap is properly tightened the clearance between the transducer's diaphragm and the inside of the cap is as small as 0.03" . More details of the transducer and cap system are provided in Figs. (2.1A) and(2.1B).

The setra transducer/cap system was clamped firmly to the inside of the model by two insulating holders. The first holder grips the transducer's cap unit very firmly while the second gently supports the tail of the transducer. Details of the holders are given in Fig. (2.1C).

The above cap and nut principle was also used to mount the B & K $\frac{1}{4}$" microphone inside the model. Due to the small size of the B & K microphone, only one insulating holder was required to fix the microphone/cap unit to the inside of the model.

2.4 THE MODELS

2.4.1 General Details

Four 2-inch square section cylinders with sharp edges were tested. All spanned the 3' x 3' low speed wind tunnel horizontally at mid-height. During the experiments three of the models to be referred to as the oscillating models, were subjected to oscillations. The remaining model, was kept stationary throughout. Important details about the models are outlined below.

2.4.2 The Stationary Model.

This model was mounted on turntables located on the side walls of the wind tunnel as sketched in Fig. (2.2) . It has two types of pressure tapping labelled type (A) and type (B) . More details about the model and pressure tappings are provided below.

Type (A) Pressure tappings

They were manufactured from brass tubing of external diameter 5/64" and were used exclusively for mean pressure measurements. Narrow-bore plastic tubing running through the model connected these pressure tappings to two inclined Alcohol Multitube Manometers.

Forty type (A) pressure tappings are provided on the stationary model. The locations of these tappings are given in Fig. (2.3).

Type (B) Pressure Tappings

Nine type (B) pressure tappings are positioned on one of the side

faces of the stationary model as indicated in Fig. (2.4). The tappings are provided by brass tubing of internal and external diameters of 1/16" and 3/32" respectively. During pressure measurement each tapping was connected in turn to the Pressure transducer inside the model by plastic tubings of internal diameter 3/32" . From consideration of frequency response (see Chapter 3 for more details) the total length of brass and plastic tubing between the surface of the model (where fluctuating pressure is to be measured) and the transducer's diaphragm was kept below 3" .

End Plates

Five sets of sharp-edged end plates with rounded corners were tested on the stationary model. The end plates of each set were located seventeen model diameters (34") apart. More details including the dimensions of the end plates are provided in Fig. (2.5).

2.4.3 The Oscillating Models

These rigid models were mounted externally on the arms of the oscillating mechanism through two circular slots, each of diameter 6.5", on the side walls of the wind tunnel. (To obtain the circular slots, the turntables, see Fig. (2.2) used to mount the stationary model on the wind tunnel side walls were simply removed). The mounting procedure of the models is sketched in Fig (2.6). Each oscillating model carried a set of end plates of the type labelled No.2 in Fig. (2.5).

More details about each model are provided below.

Oscillating Model 1

This model was used first for mean pressure measurement during body oscillations and later for flow visualisation. Eight of the type (A) pressure tappings described in section 2.4.2 were positioned along the span on the centerline of the model's back face as indicated in Fig. (2.7),

Oscillating Model 2

Eight type (B) pressure tappings were distributed around the mid-section of the model as indicated in Fig. (2.7) . These tappings

were used for fluctuating and mean pressure measurements. Tapping details are given in Section 2.4.2.

Oscillating Model 3

This model was built primarily for pressure correlation measurements. Type (B) pressure tappings were distributed on this model as indicated in Fig. (2.7).

2.5 MAGNETIC TAPE RECORDING

The fluctuating signals related to wake velocities, model surface pressures and body displacements were recorded on an Ampex FR 1300 analogue tape recorder. These recorded signals were later digitised on the Imperial College Aeronautics Department Data Logging System. A description of the analogue tape recorder and the associated data logging system can be found in Davies (1975) and Bradshaw (1972).

2.6 OTHER ELECTRONIC EQUIPMENT

These were standard instruments normally employed in turbulence research. A hot-wire probe with a 5-micron platinum wire as sensor was used with a Disa D01 Anemometer to detect vortex shedding. Other instruments used in the experiments are listed below.

Voltmeters Disa 55 D35 R.M.S. voltmeters, Disa 55 D30 Digital D.C. Voltmeters, Datron R.M.S. Voltmeter Model 1030a , Solatron digital voltmeters.

Filters Rockland Dual Filter Model 452-01 , Kemo Dual Variable Filter Type VBF/1 .

Oscilloscope Tecktronix Type 549 Storage Oscilloscope.

Sum and Difference Units Disa Test Sum & diff. (PHI Module); Op. Amps. (PHI Analogue Module 16).

Amplifiers Fixed Gain Amplifier ; Data Amplifier (PHI Analogue modules 19 and 17 respectively) .

Power Supply Units 30V Power Supply, Startronic Ltd. Model 119.6 .

Footnote P.H.I. - Patchable Hybrid Instrumentation .

CHAPTER 3

EXPERIMENTAL TECHNIQUES AND DATA REDUCTION

3.1 WIND TUNNEL CALIBRATION

Below is a sketch of the contraction and working section of the wind tunnel. $\bar{C}_p$ is the desired mean pressure coefficient on the model. With the notation in the sketch

$$\bar{C}_p = \frac{P_m - P_\infty}{\frac{1}{2}\rho U_\infty^2} \qquad \text{----------(3.1)}$$

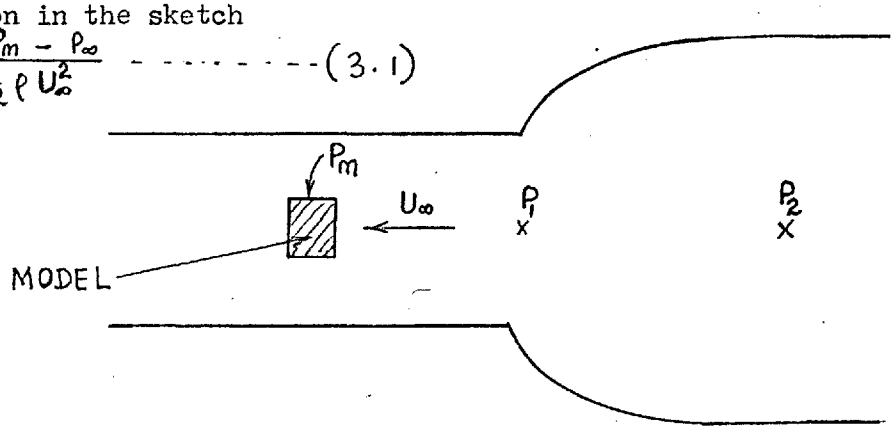

Equation (3.1) can be written as

$$\bar{C}_p = \left[\frac{P_m - P_1}{P_2 - P_1} + \frac{P_1 - P_\infty}{P_2 - P_1}\right] \cdot \frac{P_2 - P_1}{\frac{1}{2}\rho U_\infty^2}$$

With the definition

$$k_1 = \frac{P_\infty - P_1}{P_2 - P_1}, \qquad K_2 = \frac{P_2 - P_1}{\frac{1}{2}\rho U_\infty^2} \qquad \text{----------(3.2)}$$

$$\bar{C}_p = \left(\frac{P_m - P_1}{P_2 - P_1} - K_1\right) K_2 \qquad \text{----------(3.3)}$$

where P_∞ and $\frac{1}{2}\rho U_\infty^2$ are the static and the dynamic pressures at the location of the center section of the model in the empty wind tunnel.

P_2 and P_1 are static pressures at the begining and the end of the wind tunnel contraction respectively.

P_m - mean pressure at the surface of the model.

With the tunnel empty a pitot-static tube was located at the position to

be occupied by the model center section. Variation of $(P_2 - P_1)$ and $(P_1 - P_\infty)$ with $\frac{1}{2}\rho U_\infty^2$ were observed. In the Reynolds number range of interest, K_1 was found to be constant at 1.006 (see Fig (3.1)). K_1 varied with $\frac{1}{2}\rho U_\infty^2$ but was found to be never higher than 0.02 [see Table (3.1)].

Betz Manometer reading in mm of H_2O	K_1
8.08	0.020
11.40	0.018
19.12	0.011
20.70	0.011
51.65	0.010
57.85	0.011
71.90	0.015

FOR X LESS THAN 5 MM ; $K_1 = 0$

TABLE (3.1)

3.2 PRESSURE TRANSDUCERS - CALIBRATION PROCEDURE.

3.2.1 Effect of tube length on the transducers' frequency response.

It is known that any connecting tubing or cavity above the diaphragm will degrade the frequency response of a diaphragm pressure transducer. The connecting tubing and cavity have their own frequency response characteristics so that the joint response of the transducer/tubing or volume may be radically different from the flat frequency response of the transducer on its own. Analytical treatment of this problem can be found in textbooks such as Doebelin (1966).

Doebelin (1966) treats the transducer/tubing system as a second order mechanical system. He presents the equivalent natural frequency and damping

parameter of the system as [see footnote (3.1)]

$$\omega_N = \frac{\sqrt{\gamma P/\rho}}{L\sqrt{\frac{1}{2} + V/V_t}} = \frac{C}{L\sqrt{\frac{1}{2} + V/V_t}} \qquad \text{----------(3.4)}$$

$$\zeta = \frac{64\mu L^2}{\pi d_t^4 \sqrt{\gamma P \rho}} \sqrt{\frac{1}{2} + \frac{V}{V_t}} \qquad \text{----------(3.5)}$$

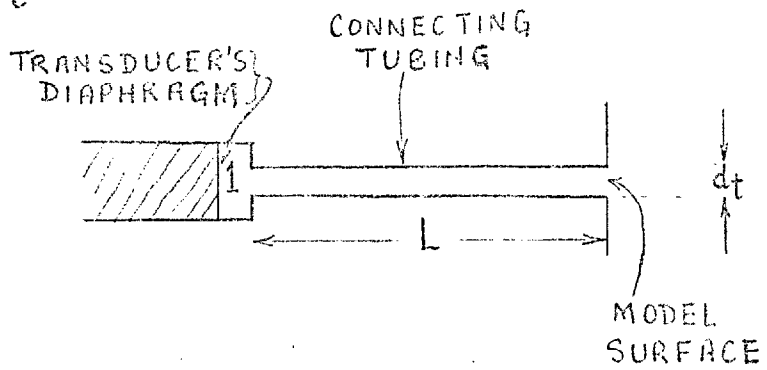

where

V = Volume of the cavity labelled 1

V_t = Internal volume of tubing of length L

d_t = Internal diameter of tubing

C = Velocity of sound

Thus if the resonant frequency f_N is to be removed far above the maximum frequency of interest, L must be made small. To minimise damping and the attendant attenuation it is necessary to make d_t as large as possible.

FOOTNOTE (3.1) Equations (3.4) and (3.5) hold only when the tube volume, V_T, becomes a significant part of the total volume of the system - see Doebelin (1966) page 401 .

In the experiments V was 0.006128 cub. in., d_t was 3/32" so that for a tubing of length 3" $V_t/V = 3.38$. Equations (3.4) and (3.5) then suggests $\zeta \approx 0.003$ and $f_N \approx 803$ HZ .

The effect of the connecting tubing was measured experimentally by observing the dynamic response of the transducer with various lengths of tubing attached to the end. A B & K pistonphone type 4220 gave a constant amplitude pressure signal with frequency , f , variable in the range $12 < f < 600$ cps . Typical transducer/connecting tubing response curves are shown in Fig (3.2).

Fig (3.2) shows that when the tube length , L , is less than 3" , the microphone response is flat up to at least 300 HZ and that resonance occur far above 500 HZ . This flat response suggests that the phase shift between the pressure source and the transducer is negligible. It is interesting to note that when $L = 5\frac{1}{4}$" equation (3.4) predicts a resonant frequency of about 460 HZ which is, see Fig (3.2) , in good agreement with the experimentally observed trend.

No means of producing a constant amplitude pressure signal at frequencies below 12 HZ was available. There was therefore no direct way of determining whether or not the pressure transducers used in the experiments suffer from sensitivity changes at low frequencies. From private communication with the manufacturers, it was learnt that the static sensitivity of the B & K $\frac{1}{4}$" Type 4136 microphone was 0.25 dB (3%) higher than the dynamic sensitivity and that the transformation from the static to the dynamic sensitivity factor occurs between 0.5 and 5 HZ . The $\frac{1}{2}$" Setra pressure transducer is not expected to suffer significantly from sensitivity changes at low frequencies as measurements of fluctuating pressures at such frequencies display no features that are attributable to sensitivity variation.

For fluctuating pressure measurement the total length of tubing between the pressure source and the transducer's diaphragm was kept below 2.75" . A low pass filter was then employed to give a sharp cut-off at a frequency of 300 HZ which was by far higher than both the vortex shedding frequency f_s , and the body oscillation frequency , f_N . On the stationary model f_s was always below 46 HZ except on one occasion when, in order to investigate the effects of Reynolds number, f_s was increased up to 91 HZ.

On the oscillating model f_s and f_N varied between 3 and 25 HZ .

3.2.2 Static Calibration of Pressure Transducer

The static calibration of the transducer (with the mounting system and connecting tubing in place) was conducted by comparing its response to pressure with that of a Betz manometer. The static pressure difference across the wind tunnel contraction (labelled $P_2 - P_1$ in section 3.1) was used for the calibration.

Fig (3.3) shows the results obtained with the $\frac{1}{2}$" Setra pressure transducer over a period of six months. That the points all lie on a straight line indicates the stability of the transducer's static sensitivity to changes in environmental conditions. Typically the static sensitivity of the transducer calculated from the best fit straight line (least square method) was found to be 35.4 millivolt/mm which is in good agreement with the value of 35 millivolt/mm specified by the manufacturers.

A similar procedure was used to determine the static sensitivity of the B & K $\frac{1}{4}$" microphone system of section 2.3 . Great care was however required as the system suffers severely from output voltage drift. The static sensitivity of the B & K microphone system depended on the adjustments of the Disa Oscillator and the Reactance Converter (see section 2.3). The most appropriate value of the static sensitivity was found to be 7.6 millivolt/mm . This value was also found to be stable to environmental conditions - see Fig (3.4) .

3.3 EVALUATION OF MEAN AND FLUCTUATING PRESSURE

3.3.1 Mean Pressure

In agreement with Fackrell (1973) , the B & K $\frac{1}{4}$" microphone system described in section 2.3 was found to suffer severely from output voltage drift. This system was therefore unsuitable for measuring mean pressure.

The $\frac{1}{2}$" Setra pressure transducer was in contrast found to be drift-free after a warm up period of about six hours. To measure mean pressure on the

models, the reference side of the transducer was connected to the wind tunnel static pressure tapping at the end of the contraction (this tapping is labelled P_1 in section 3.1). By using the transducer's static sensitivity, changes in the transducer's mean voltage output due to the flow were converted to the differential pressures labelled $P_m - P_1$ in section 3.1. Equation (3.3) was then used to calculate the mean pressure coefficient $\bar{C}_p$.

3.3.2 Fluctuating Pressure

The R.M.S. component of output voltage of each transducer was converted to R.M.S. pressure P'_{rms} by using the transducer's static sensitivity - see Footnotes(3.2). The R.M.S. pressure coefficient $C_{PRMS} = P'_{rms} / \frac{1}{2}\rho U_\infty^2$ was then determined by non-dimensionalising with the dynamic head $\frac{1}{2}\rho U_\infty^2$.

Measurements of C_{PRMS} on the oscillating model were found to require special care. The procedure adopted is described in the section below.

FOOTNOTES (3.2) This in effect means that all the RMS pressure coefficients measured with the B & K ¼" microphone system are 3% too low. (It was reported under section 3.2.1 that the manufacturers of the B & K ¼" microphone expect the static sensitivity to be about 0.25 dB (3%) higher than the dynamic sensitivity). This applies only to the stationary model measurements as the B & K system was not used in body oscillation experiments.

3.3.2.1 Determination of C_{prms} on the oscillating model.

When a long flexible tube was attached to the equalisation tube of the ½" Setra pressure transducer, it was found that cyclic distortions of the flexible tube with model oscillation affected the transducers RMS voltage output. After some investigation it was found that it was necessary to seal off the equalisation tube when RMS pressure is to be measured during model oscillation. Pressure measurements to be presented later confirm that sealing off the equalisation tube does not affect the transducers dynamic response. Mean pressure coefficient $\bar{C}_p$ cannot however be measured with the equalisation tube sealed because as equation (3.3) demonstrates every $\bar{C}_p$ is measured relative to the static pressure, P_1, at the end of the wind tunnel contraction (i.e. with the equalisation tube connected by plastic tubing to tapping P_1).

3.4 PRESSURE CORRELATION MEASUREMENTS

The correlation coefficients of two signals, P_1 and P_2 is defined as

$$R_{P12} = \frac{\overline{P_1 P_2}}{P_{1rms} P_{2rms}} \qquad \text{(3.6)}$$

As reported by Pendergast (1958) equation (3.6) can be written as:

$$R_{P12} = \frac{1}{4}\left[\frac{\overline{(P_1+P_2)^2} - \overline{(P_1-P_2)^2}}{P_{1rms} \cdot P_{2rms}}\right] \qquad \text{(3.7)}$$

Patchable Hybrid Instrumentation (PHI) module see section 2.6, provided $P_1 + P_2$ and $P_1 - P_2$. The squaring and averaging facilities on two Disa 55D35 RMS voltmeters then gave simultaneous values of $\overline{(P_1 + P_2)^2}$ and $\overline{(P_1 - P_2)^2}$. These were then combined with P_{1rms} and P_{2rms} as in equation (3.7) to obtain R_{P12}. ½" Setra pressure transducers were used in all pressure correlation measurements.

3.5 SUMMARY OF EXPERIMENTS

3.5.1 STATIONARY MODEL EXPERIMENTS

A description of this model and its pressure tappings has been given in section 2.4.2.

3.5.1.1 General Details of the Experiments

Reynolds Number Range: $1.0 \times 10^4 < Re < 1.2 \times 10^5$

Incidence Range: $0^\circ \leq \alpha \leq 45^\circ$

End Conditions: Five sets of end plates described in section 2.4.2 were tested on the model.

The particular Reynolds Number, incidence and end-plates used in each experiment are indicated where necessary on the appropriate graph of results.

3.5.1.2 Brief description of the Experiments.

a) Measurement of Mean pressure coefficients, $\overline{C}_p$

Mean pressure coefficients, $\overline{C}_p$, were measured around the mid-section of the model and along the span on the centerline of the back face (face c) using an inclined alcohol multi-tube manometer.

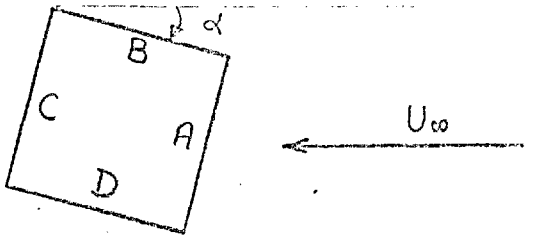

Detailed distribution of C_p around the mid-section of the model was obtained by making observations under identical conditions at incidences $\alpha = \theta^\circ$ and $(\theta + 90)^\circ$ and presenting the results under a single incidence $\alpha = \theta^\circ$. (This was necessary because there are fewer mean pressure tappings on faces B & D than on faces A & C).

b) Fluctuating Pressure Measurement

All measurements of pressure fluctuations on this model were made with the B & K $\frac{1}{4}$" microphone system described in section 2.3. The microphone was connected in turn to each of the Type (B) pressure tapping described in section 2.4.2. All type (B) pressure tappings on this model are positioned on face B. For each tapping, setting the model at incidences

of α° , $(\alpha + 90)^{\circ}$, $(\alpha + 180)^{\circ}$ and $(\alpha + 270)^{\circ}$ gave the fluctuating pressures on faces B , C , D and A respectively.

c) Shedding Frequency Measurement

Vortex shedding was detected both with the pressure transducer system and with a hot-wire suitably located downstream of the model outside the wake. The shedding frequency was either counted on a storage Oscilloscope or obtained digitally from spectral analysis (see sections 2.5 and 3.6.1) of the tape-recorded vortex shedding signal.

d) Measurement of the longitudinal spacing of the vortex street

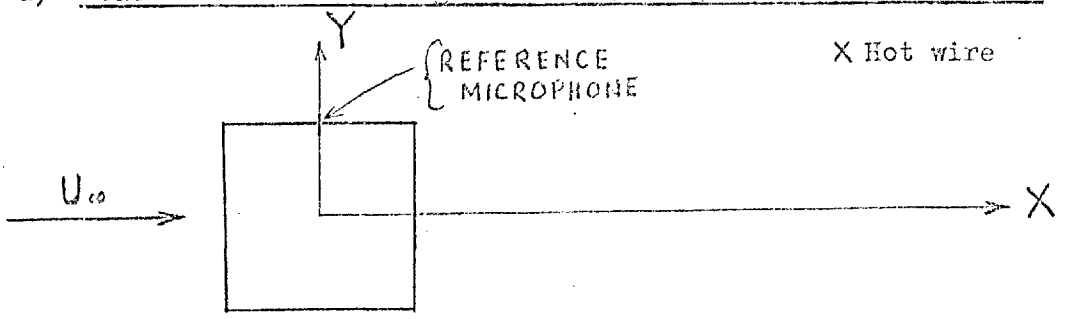

The surface pressure signal from the tapping at the center of the top side face was used as reference. A hot-wire was transversed streamwise in the same spanwise plane as that containing the reference pressure transducer. At each streamwise location, X , of the hot-wire simultaneous tape recording of the hot-wire and pressure signals were made. Subsequent digital analysis of the recorded signals (see sections 2.5 and 3.6) then yielded the phase difference, $\phi_{\omega}(f_s)$, between the hot-wire and the microphone signals. The average longitudinal vortex spacing was determined from the change in X required to produce a 360° degree change in $\phi_{\omega}(f_s)$.

e) Other Information obtained from Spectral Analysis

(i) Spectral distribution of fluctuating pressures at various location around the mid-section of the model.

(ii) Variation of phase angle at the shedding frequency around the mid-section of the model. (A fixed hot-wire located down-stream of the model outside the wake produced the reference signal).

3.5.2 OSCILLATING MODEL EXPERIMENTS

These models have been described in section 2.4.3 .

3.5.2.1 General Details of the Experiments

Reynolds Number Range: $4 \times 10^3 < Re < 1.2 \times 10^5$.

Incidence : $\alpha = 0^o$ only

Amplitude to diameter ratios : A/D = 0.05 , 0.1 and 0.25 .

Reduced Windspeed Range : $3.0 < \frac{U_\infty}{f_N d} < 15.00$.

$\frac{U_\infty}{f_N d}$ was varied either by varying U_∞ or by varying f_N .

End Conditions : No. 2 sets of end plates (see section 2.4.2 for details) were used throughout.

The particular condition prevailing in each experiment is indicated in the appropiate graph of results.

3.5.2.2 List of Oscillating Model Experiments

a) Measurement of mean pressure coefficients, $\bar{C}_p$.

$\bar{C}_p$ were measured either with a Betz manometer or with the $\frac{1}{2}$" Setra pressure transducer.

b) Fluctuating Pressure Measurement

The $\frac{1}{2}$" Setra pressure transducer was used .

c) Shedding Frequency Measurements

Performed as in section 3.5.1.2 (c).

c) Measurement of longitudinal vortex street spacing

Performed as in section 3.5.1.2 (d). At lock-in the displacement signal was sometimes used as the reference signal.

e) Pressure Correlation Measurements

Obtained with two $\frac{1}{2}$" Setra pressure transducer as described in section 3.4.

f) Phase Angle between fluctuating Lift and Displacement

Obtained digitally from simultaneous tape recording of the fluctuating lift and displacement signals (see section 2.5 and 3.6 for relevant digital instrumentation and references).

g) Flow Visualisation

See Chapter 5 for details.

3.6 DATA REDUCTION

3.6.1 Digital Analysis: Spectral Measurements

Analogue recordings of unsteady pressures and velocities (see section 2.5) were digitised on the Imperial College Aeronautics Department Data-Logging System. The resulting computer-compatible digital magnetic tapes were processed on the Imperial College CDC 6400 computer using either the 'Powspec' or 'Cophase' described in Davies (1974) and (1975). The 'Powspec' computes the power spectral density for a single channel of input data. The 'Cophase' computes the complex cross-spectral density function for two simultaneous input channels. The output of'Cophase' include the power spectral density of each channel of input data, coherence and phase angle. Detailed discussion of the Spectral Analysis Programs, Powspec and Cophase, are provided by Davies (1974) and (1975).

3.6.2 Blockage Correction

Stationary Model

The blockage correction method proposed by Maskell (1963) was used. The appropiate equations are:

$$\frac{K^2}{K_c^2} = 1 + \frac{C_D}{K_c^2 - 1}\left(\frac{S}{C}\right) \qquad (3.8)$$

$$\frac{1 - C_p}{1 - C_{pc}} = \frac{C_D}{C_{Dc}} = \frac{U_c^2}{U^2} = \frac{K^2}{K_c^2} \qquad (3.9)$$

The suffix C refers to corrected quantities

C_p - mean pressure coefficient

C_D - mean drag coefficient

S/C - blockage ratio

$K^2 = 1 - C_{pb}$ where C_{pb} is the base-pressure coefficient.

From measured values of C_D and C_{pb} and known values of S/C , K_c

was calculated from equation (3.8) using the expression :

$$K_c^2 = \frac{1 + K^2 - C_D S/C \pm \sqrt{[C_D S/C - (1+K^2)]^2 - 4K^2}}{2} \quad \ldots (3.10)$$

Equation (3.9) was then used to correct the measured values of C_p, C_{pb} and C_D.

The velocity, U_∞, used to formulate the fluctuating pressure coefficient $C_{p_{rms}} = p'_{rms}/\frac{1}{2}\rho U_\infty^2$ and the Strouhal number $S = \frac{f_s d}{U_\infty}$ was corrected for blockage using equation (3.9).

Table (3.2) gives the values of the correction ratio, K^2/K_c^2, that obtained at each angle of incidence. K^2/K_c^2 was found to be independent of Reynolds number.

Angle of Incidence	0°	5°	10°	13.5°	15°	20°	25°	30°	35°	40°	45°
Maskell correction factor, K^2/K_c^2	1.090	1.093	1.102	1.102	1.095	1.099	1.102	1.105	1.107	1.106	1.106

TABLE (3.2)

Oscillating body

No blockage correction method has been proposed for oscillating bluff bodies

During body oscillation the values of C_D and C_{pb} were observed to vary continuously with amplitude to diameter ratio A/D and reduced windspeed $\frac{U_\infty}{f_N d}$. As a result of flow reattachment to the side faces the values of C_{pb} became so high at low values of $\frac{U_\infty}{f_N d}$, see Fig. 7.3, that K_c could no longer be determined from equation (3.10) because the quantity $\{[C_D S/C - (1+K^2)]^2 - 4K^2\}$ became negative. Thus rather than use a dubious correction method, it was decided not to correct the data for the oscillating body.

3.6.3 Calculation of the RMS sectional lift coefficient on the side face of the square section cylinder.

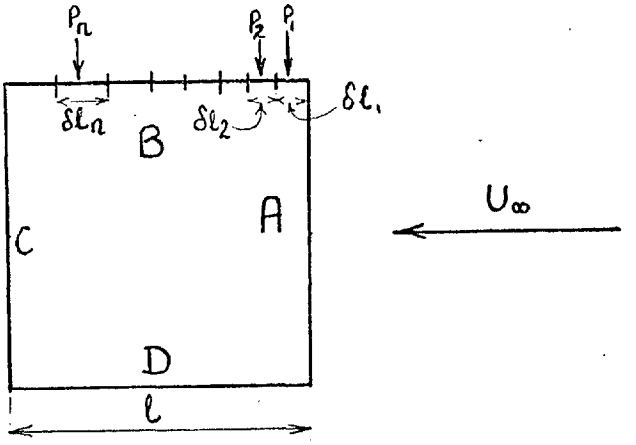

Consider a section of small depth δy into the paper. The instantaneous fluctuating side force F_B on face B is given by:

$$F_B = (P_1 \delta l_1 + P_2 \delta l_2 + P_3 \delta l_3 + \cdots\cdots\cdots P_n \delta l_n)\delta y$$

where P_1, P_2 ..... P_n are the instantaneous values of the fluctuating pressures on elements δl_2 ---------- δl_n respectively.

$$\overline{F_B^2} = \{ \overline{P_1^2 \delta l_1^2} + \overline{P_2^2 \delta l_2^2} + \overline{P_3^2 \delta l_3^2} - - - - - \overline{P_n^2 \delta l_n^2} + 2\overline{P_1 P_2 \delta l_1 \delta l_2} + 2\overline{P_1 P_3 \delta l_1 \delta l_3} + 2\overline{P_1 P_n \delta l_1 \delta l_n} \cdots\cdots \} \delta y^2$$

This can be written as

$$\overline{F_B^2} = \delta y^2 \sum_{\substack{i=1 \\ j=1}}^{I,J} \overline{P_i P_j \delta l_i \delta l_j} \qquad \cdots\cdots\cdots\cdots (3.11)$$

choosing $\delta l_1 = \delta l_2 = \delta l_3 \cdots\cdots = \delta l_n = \delta l$.

$$\overline{F_B^2} = \delta y^2 \delta l^2 \sum_{\substack{i=1 \\ j=1}}^{I,J} \overline{P_i P_j} \qquad \cdots\cdots\cdots\cdots (3.12)$$

From the definition of pressure correlation coefficient

$$\overline{P_1 P_2} = R_{P12} \times P_{1rms} \times P_{2rms}$$

where R_{p12} is the correlation coefficient of the fluctuating pressures P_1 and P_2.

Equation (3.12) then becomes

$$F_B^2 = \delta\ell^2 \delta y^2 \sum_{\substack{i=1 \\ j=1}}^{I,J} R_{P_{ij}} P_{irms} P_{jrms} \qquad (3.13)$$

In this investigation the side BC of the 2-inch square section cylinder was divided into eight equal parts so that $\delta\ell = \frac{1}{2}$". Because the fluctuating pressures on face B are 180° out of phase with those on face D, the sectional RMS lift coefficient, C_{Lrms}, was estimated from the expression

$$C_{Lrms} = 2 \left[\frac{\sqrt{F_B^2}}{\ell \delta y \left(\frac{1}{2} \rho U_\infty^2\right)} \right] \qquad (3.14)$$

CHAPTER 4

4.0 MATHEMATICAL MODELS OF VORTEX-INDUCED LIFT FORCES

4.1 INTRODUCTION

It is impossible to solve analytically the full Navier-Stokes equations for unsteady separated flow around a bluff body. The complexity and the large amounts of computer time required has so far limited numerical solutions of the equations to low Reynolds Number. For cases of Engineering importance it is therefore necessary to abandon the full Navier-Stokes equations and resort to simpler flow models.

Two basic types of models will be discussed in this chapter. The first, the potential flow model, represents the real wake vortex system by potential vortices. Two potential flow models will be discussed. The second basic model, the Lift-Oscillator model, has its origin in Electrical Engineering and is based on the notion that the fluctuating lift due to vortex shedding may be considered to be generated by a non-linear oscillator in the wake. The models are incomplete in the sense that they require experimentally determined inputs.

It must be remembered that models are crude, two-dimensional approximations of the complicated three-dimensional real flow situation. The models cannot therefore be expected to predict all the observed characteristics of the unsteady lift in flow around bluff bodies.

4.2 POTENTIAL FLOW MODELS

4.2.1 MODEL I : The von Karman-type wake model.

This assumes that an ideal von Karman vortex street is formed in the wake of a bluff body. The usual assumptions made in vortex drag calculation apply here. They are listed in Milne-Thomson (1968) as :

(i) The wake vortices can be represented by point vortices .

(ii) The origin being taken in the midst of the regular portion of the wake, the complex potential will be nearly the same as that for an infinite vortex street.

(iii) If we surround the cylinder by a contour which advances with the same velocity as the wake and whose dimensions are large compared with the cylinder and distances between successive vortices and the rows, the motion on the boundaries of the contour will be steady.

(iv) That the formation of the vortices is truly periodic.

The cylinder in sketch (4.1) moves with velocity U along the x-axis. The vortices which are shed from the body at a frequency f_s form a vortex street which advances along the x-axis with velocity V shown in Milne-Thomson (1968) to be $V = \frac{\Gamma}{2a} \tanh \frac{\pi b}{a}$. The large contour ABCD moves with the wake velocity V so that the x-directed velocity of the cylinder relative both to the contour and to the wake is $U - V$ given by $f_s a$.

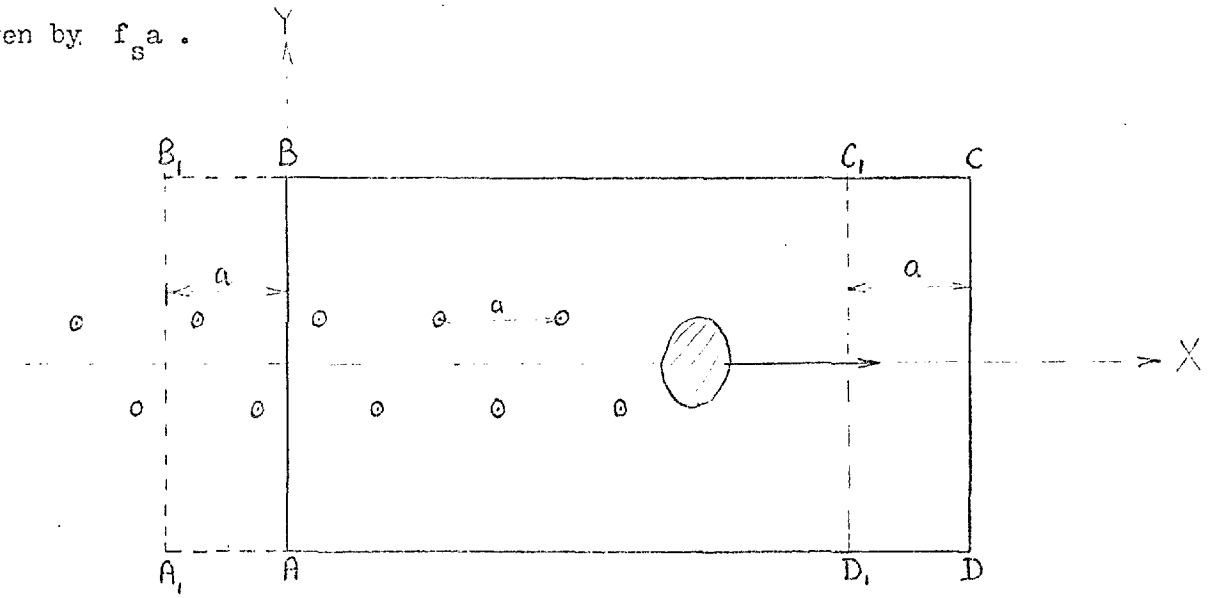

SKETCH (4.1)

At the end of one cycle of shedding, the cylinder has moved forward along the x-axis by a distance 'a'. Two more vortices are now included in the contour whose new boundary is $A_1B_1C_1D_1$ - see sketch (4.1). The picture in ABC_1D_1 which is common to contours ABCD and $A_1B_1C_1D_1$ is the same. The increase in the Y-momentum, J_y, of the control volume is then the difference in Y-momentum enclosed by contours A_1B_1BA and D_1C_1CD - which can be shown in this case to be zero.

When half a cycle of shedding is considered the situation is different.

The new contour $A^1B^1C^1D^1$ is shown in sketch (4.2)

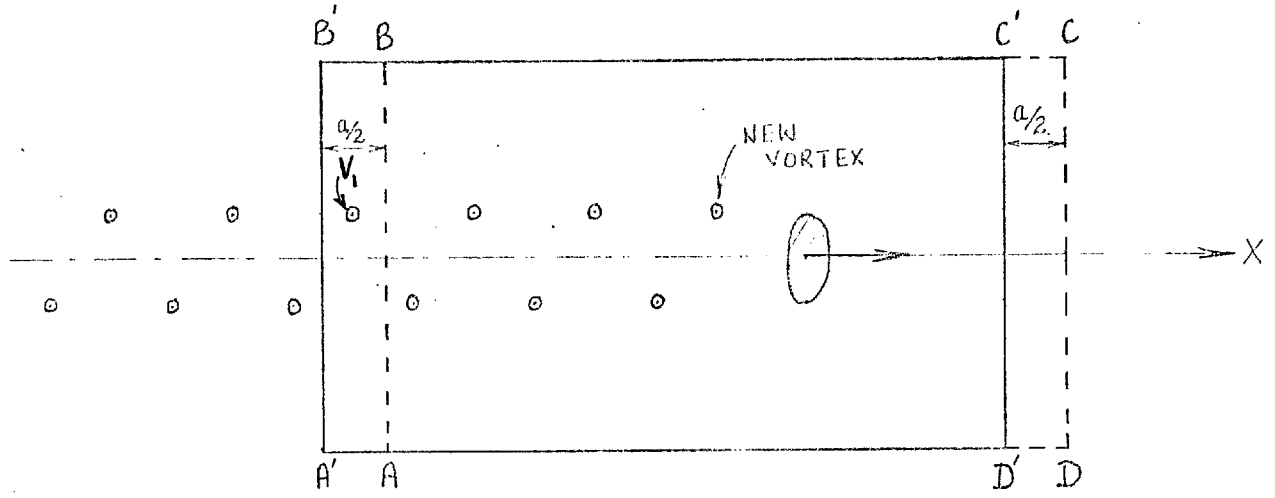

SKETCH (4.2)

Let $J_{Y_{ABB'A'}}$ and $J_{Y_{DCC'D'}}$ be the Y momenta of the fluid inside rectangles ABB^1A^1 and DCC^1D^1 respectively. It is shown by Ruedy (1935) that

$$\Delta J_Y = J_{Y_{ABB'A'}} - J_{Y_{DCC'D'}} = \pm \frac{\rho}{4} \Gamma a \quad \text{- - - - - - (4.2.1)}$$

The time interval Δt for half a cycle of shedding is

$$\Delta t = \frac{a}{2(U-V)} \quad \text{- - - - - - - - - (4.2.2)}$$

$$F_Y = \frac{\Delta J_Y}{\Delta t} = \pm \frac{\rho}{2}(U-V)\Gamma \quad \text{- - - - - - - - - (4.2.3)}$$

[The actual signs of ΔJ_Y and F_Y depends on the sign of the vortex V_1 (i.e. depends on whether the V_1 vortex appears above or below the x-axis in sketch (4.2)]

Ruedy (1935) equates F_Y to the instantaneous lift on the bluff body.

From consideration of rate of change of momentum in a control volume bounded by ABCD in sketch (4.3), the instantaneous lift $L(t)$ on the bluff body is given by :

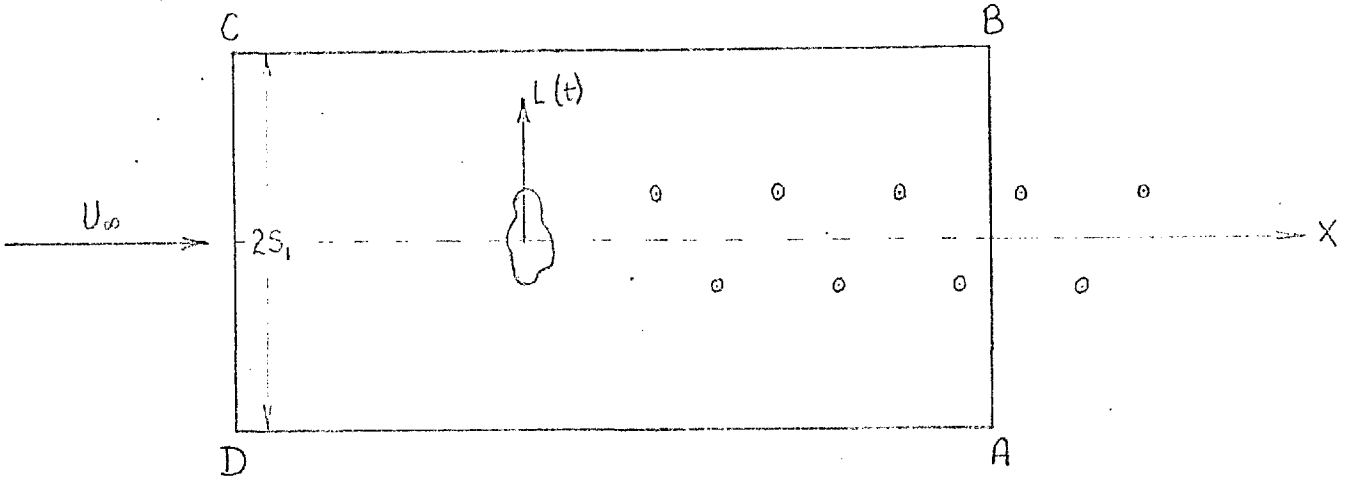

SKETCH (4.3)

$$-L(t) = -\int_c P\,dx + \rho \int_c V(U\,dy - V\,dx) + \rho \iint_S \frac{dv}{dt}\,dx\,dy \quad \cdots (4.2.4)$$

$L_1(t)$ $L_2(t)$ $L_3(t)$

In the limit as S_1 approaches infinity :

$$L_1(t) = 0 .$$

$L_2(t)$ is the flow of momentum out of AB and CD . This is the expression represented by equation (4.2.3). When, as in Ruedy (1935), $L_2(t)$ is taken as the instantaneous lift, $L(t)$, the assumption is that $L_3(t)$ is zero. This is incorrect because the continuous formation and discharge of vortices from the near wake region of the body ensures that $L_3(t)$ does not vanish.

Recently Chen (1972) using essentially the above principle (equating $L_3(t)$ in equation (4.2.4) to zero and therefore neglecting Y-momentum changes in the near wake region of the body) reported a value for $F_Y = \pm \rho V \Gamma$. He claims "that the curve of the calculated fluctuating lift coefficient plotted over the Reynolds number practically goes just through the points of maximum values measured." He concluded "that

the ideal vortex street model is adequate not only for the determination of the steady drag force as done by Karman, but also for the calculation of the fluctuating lift force as well."

The validity of equation (4.2.3) is strengthened by the argument: that the circulation, Γ_c , in a formation region which includes the body must change by Γ_o each time a vortex of strength Γ_o is shed. From consideration of symmetry it is seen that the only possibility is for Γ_c to oscillate between $\pm \Gamma_o/2$. Taking into account the convection velocity, $U - V$, of the vortices then gives a lift force oscillating between $\pm \rho \frac{\Gamma_o}{2}(U-V)$ as in equation (4.2.3) . However $\pm \rho \frac{\Gamma_o}{2}(U-V)$ in this argument is the lift force on a formation region that includes the body. To extract the lift force on the body itself from $\pm \rho \frac{\Gamma_o}{2}(U-V)$ one requires an understanding of the flow in the vortex formation region close to the body.

Finally let us consider the example of a very thin flat plate quoted in Belvins & Burton (1976). A very thin flat plate held perpendicular to a free stream produces a regular vortex street which has a measureable circulation, Γ , and a measureable convection velocity, $U - V$. By equation (4.2.3) the lift force on the very thin flat plate should be comparable to the lift force on say a circular cylinder. But because the plate has no projected area on which pressures can act, the lift force on the plate must by negligibly small even though its vortex street may be comparable to that of a circular cylinder. We therefore conclude that it is extremely difficult, if not impossible, to directly relate the transverse momentum of the vortex street to the fluid forces on the tripping cylinder because of the uncertainty in the magnitude of the transverse momentum of the flow in the near wake.

4.2.2 MODEL II : Potential Flow Model of Flow around an oscillating circular cylinder.

4.2.2.1 Derivation of Φ

In this section the potential flow model used by McGregor (1957) is extended to include both the effects of the wake vortex street and of cylinder oscillations.

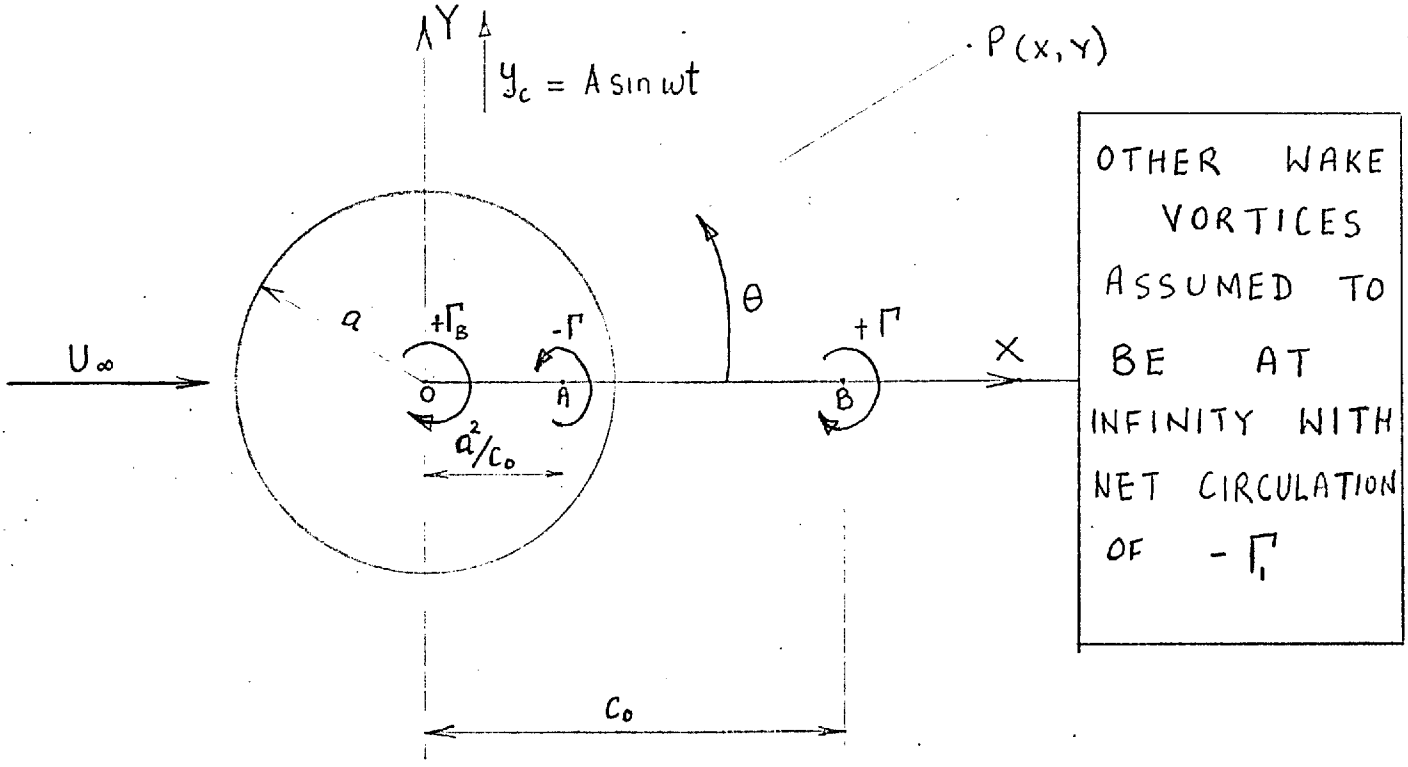

SKETCH (4.4)

The circular cylinder of sketch (4.4) is produced by a uniform flow and a doublet at the origin. The circulation in the vortex formation region of the cylinder is assumed to be concentrated at position B . The bound vortex $+\Gamma_B$ at the origin O is the image of all the shed vortices that have drifted to infinity (strictly infinity in this case means $x > c_o$).

The arguments of Davies (1975) will now be used to determine Γ_B .

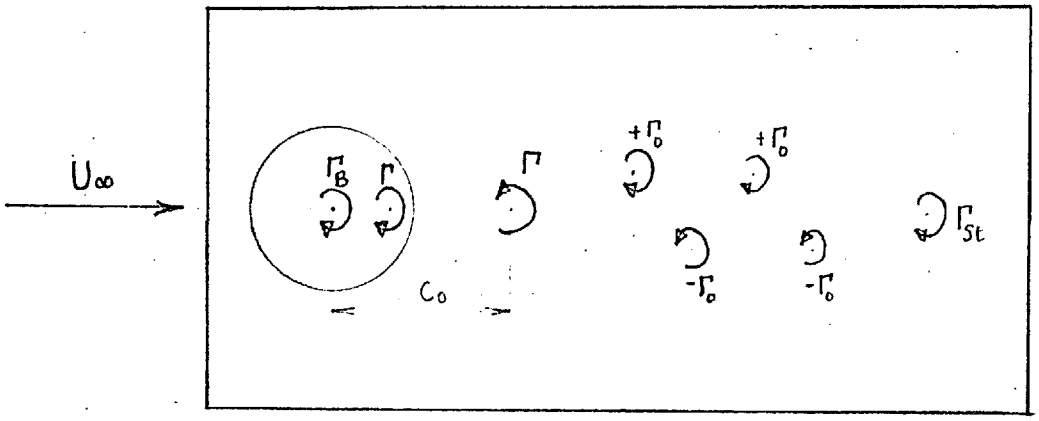

SKETCH (4.5)

Allow Γ_{St} to represent the net circulation produced in the starting-up of the flow i.e. before the steady state production of alternating vortices of strength $\pm \Gamma_0$. If Γ_{St} is positive, the first full vortex should be negative and thus $+\Gamma_0$ completes a cycle. Proceeding from the right of sketch (4.5), at the end of the first half cycle the net circulation in the wake (i.e. at $X > C_0$) is $(\Gamma_{St} - \Gamma_0)$ so that Γ_B is $-(\Gamma_{St} - \Gamma_0)$. At the end of the first complete cycle the wake has net circulation $+\Gamma_{St}$ so that Γ_B is $-\Gamma_{St}$. Thus Γ_B oscillates between $(\Gamma_0 - \Gamma_{St})$ and $(-\Gamma_{St})$. Since the vortex shedding process is symmetrical, we have: $\Gamma_0 - \Gamma_{St} = -(-\Gamma_{St})$ or $\Gamma_{St} = \Gamma_0/2$.
Γ_B therefore oscillate between $\pm \frac{\Gamma_0}{2}$ - where $|\Gamma_0|$ is the magnitude of the circulation of a fully formed vortex. In this simple analysis Γ_B will be approximated by :

$$\Gamma_B = \frac{\Gamma_0}{2} \sin \beta t \quad \text{- - - - - - - - - -} \quad (4.3.5a)$$

Following McGregor (1957) the wake vortex at B and its image at A will be ascribed a harmonically varying circulation so that

$$\Gamma = \Gamma_0 \sin \beta t \quad \text{- - - - - - - - -} \quad (4.2.5b)$$

The complex potential, ω_1 , of a circular cylinder moving with velocity $\dot{V}$ along the positive direction of the y-axis is:

$$\omega_1 = -\frac{i \dot{V} a^2}{Z} \quad \text{- - - - - - - - -} \quad (4.2.6)$$

In equation (4.2.6) the origin is at the center of the moving cylinder. For an oscillating cylinder with motion described by equation (4.2.7),

$$\left.\begin{aligned} y_c &= A \sin \omega t \\ \dot{y}_c &= \dot{V} = A\omega \cos \omega t \end{aligned}\right\} \quad \text{- - - - - -} \quad (4.2.7)$$

substituting for $\dot{V}$ in equation (4.2.6) gives

$$w_1 = -i a^2 \frac{A\omega \cos \omega t}{Z} \qquad (4.2.8)$$

From equations (4.2.5) to (4.2.8) the complex potential function, $W(Z)$, of the combined system in sketch (4.4) is

$$W(Z) = U_\infty \left(Z + \frac{a^2}{Z}\right) - i a^2 \frac{A\omega \cos \omega t}{Z} + i \frac{\Gamma_0 \sin \beta t}{2\pi} \left[\log_e \frac{Z - Z_B}{Z - Z_A} + \frac{1}{2} \log_e \frac{Z}{Z_\infty}\right] \qquad (4.2.9)$$

The origin in equation (4.2.9) is fixed at the displaced center of the oscillating cylinder at the time t considered so that although the wake vortex at B in sketch (4.4) is fixed in space, its coordinates and those of its image at A relative to the displaced center of the oscillating cylinder are given at time t when the amplitude of oscillation, A, is small by

$$\left.\begin{aligned} Z_B &= C_0 - i A \sin \omega t \\ Z_A &= \frac{a^2}{C_0} \left(1 - i \frac{A}{C_0} \sin \omega t\right) \end{aligned}\right\} \qquad (4.2.10)$$

In equation (4.2.9) Z_∞, which is the representative distance of all the wake vortices that are downstream of the formation region, is taken as

$$Z_\infty = X_\infty \qquad (4.2.11)$$

where X_∞ means very large X.

Substituting for Z_A, Z_B and Z_∞ in equation (4.2.9) and noting that $W(Z) = \phi + i\psi$ and $Z = x + iy$ gives:

$$\phi = U_\infty \left(x + \frac{a^2 x}{x^2 + y^2}\right) - \frac{a^2 y A\omega \cos \omega t}{x^2 + y^2} - \frac{\Gamma_0 \sin \beta t}{2\pi} \left[\tan^{-1}\left(\frac{y + A \sin \omega t}{x - C_0}\right) - \tan^{-1}\left(\frac{y C_0^2 + a^2 A \sin \omega t}{x C_0^2 - a^2 C_0}\right) - \frac{\pi}{2} + \frac{1}{2} \tan^{-1} \frac{y}{x}\right] \qquad (4.2.12)$$

4.2.2.2 Pressure equation referred to the moving axes

From the unsteady Bernoulli's equation for incompressible flow we have:

$$\frac{P}{\rho} = \frac{P_\infty}{\rho} + \frac{1}{2}U_\infty^2 - \frac{\partial \phi}{\partial t} - \frac{1}{2} q^2 \quad \ldots\ldots (4.2.13)$$

According to Milne-Thomson (1968) the rate of change of ϕ at a fixed point as measured by an observer in a frame of reference moving with velocity vector $\underset{\sim}{V}$ is :

$$\frac{\partial \phi}{\partial t} - \underset{\sim}{V} \nabla \phi \quad \ldots\ldots\ldots\ldots (4.2.14)$$

In this particular example the motion of the cylinder is given by :

$$u_c = 0 \;, \quad v_c = A\omega \cos \omega t$$

The pressure equation referred to the moving axes therefore becomes

$$\frac{P}{\rho} = \frac{P_\infty}{\rho} + \frac{1}{2}U_\infty^2 - \frac{\partial \phi}{\partial t} + A\omega \cos \omega t \cdot \frac{\partial \phi}{\partial y} - \frac{1}{2} q^2 \quad \ldots (4.2.15)$$

where ϕ is the velocity potential given by equation (4.2.12)

q is the velocity determined from the velocity potential

U_∞ and P_∞ are velocity and pressure respectively at infinity.

ρ is the fluid density

with

$$\left.\begin{aligned} q^2 &= (U + u')^2 + (V + v_i)^2 \\ \frac{\partial \phi}{\partial t} &= \overline{\frac{\partial \phi}{\partial t}} + \left(\frac{\partial \phi}{\partial t}\right)' \\ P &= \bar{P} + P' \end{aligned}\right\} \quad \ldots\ldots (4.2.16)$$

Using equation (4.2.16) in equation (4.2.15) and taking time averages gives :

$$\frac{\bar{P}}{\rho} = \frac{P_\infty}{\rho} + \frac{1}{2}U_\infty^2 - \left(\frac{\overline{\partial\phi}}{\partial t}\right) - \frac{1}{2}\left(U^2 + V^2 + \overline{u'^2} + \overline{v'^2}\right) \qquad (4.2.17)$$

$$\frac{P'}{\frac{1}{2}\rho U_\infty^2} = C_p' = -\frac{2}{U_\infty^2}\left(\frac{\partial\phi'}{\partial t}\right) - \left[\frac{2Uu'}{U_\infty^2} + \frac{2Vv'}{U_\infty^2} + \frac{u'^2 - \overline{u'^2}}{U_\infty^2} + \frac{v'^2 - \overline{v'^2}}{U_\infty^2}\right] \qquad (4.2.18)$$

It can be seen from equations (4.2.17) and (4.2.18) that the evaluation of $\frac{\bar{P}}{\rho}$ and $\frac{P'}{\frac{1}{2}\rho U_\infty^2}$ requires knowledge of the values of $\left(\frac{\overline{\partial\phi}}{\partial t}\right)$, U and V on the oscillating cylinder. These quantities can be obtained from equations (4.2.12) by using the equations

$$\left.\begin{aligned} U &= \frac{\partial\phi}{\partial x} \\ V &= \frac{\partial\phi}{\partial y} \end{aligned}\right\} \qquad (4.2.19)$$

With the definitions

$$C_{p_1}' = -\frac{2}{U_\infty^2}\left(\frac{\partial\phi}{\partial t}\right)', \quad \bar{C}_{p_1} = -\frac{2}{U_\infty^2}\left(\frac{\overline{\partial\phi}}{\partial t}\right) \qquad (4.2.20a)$$

$$C_{p_2}' = -\left[\frac{2Uu'}{U_\infty^2} + \frac{u'^2 - \overline{u'^2}}{U_\infty^2}\right], \quad \bar{C}_{p_2} = -\left[\frac{U^2 + \overline{u'^2}}{U_\infty^2}\right] \qquad (4.2.20b)$$

$$C_{p_3}' = -\left[\frac{2Vv'}{U_\infty^2} + \frac{v'^2 - \overline{v'^2}}{U_\infty^2}\right], \quad \bar{C}_{p_3} = \left[\frac{V^2 + \overline{v'^2}}{U_\infty^2}\right] \qquad (4.2.20c)$$

Equation (4.2.18) becomes

$$C_p' = C_{p_1}' + C_{p_2}' + C_{p_3}' \qquad (4.2.21)$$

SYNCHRONIZATION OR 'LOCK-IN' CASE

When the frequency of body oscillation, ω, is synchronized to the vortex shedding frequency, β, we have

$$\beta t = \omega t + \phi_1 \qquad (4.2.22)$$

where ϕ_1 is the phase angle between the circulation Γ and the displacement

$\bar{C}_p$ and C_p' can be evaluated from equations (4.2.20) and (4.2.21) by first evaluating $\left(\frac{\partial \phi}{\partial t}\right)$, U and V using equations (4.2.12) and (4.2.19) The result after all terms of higher order than unity in A (except for the terms of order A^2 that are required in latter analysis where $\Gamma_0 = U_\infty = 0$) have been neglected are as follows.

$$\left.\begin{aligned}
\bar{C}_{p_1} &= -\frac{A^2\omega^2}{U_\infty^2}\cos 2\theta - \frac{A\omega\Gamma_0}{2\pi U_\infty^2}\sin\phi_1 \cdot B_1 \\
C_{p_1}' &= -\frac{2A\omega}{U_\infty}\sin 2\theta\cos\omega t - \frac{2A\omega^2 y}{U_\infty^2}\sin\omega t \\
&\quad - \frac{A^2\omega^2}{U_\infty^2}\cos 2\theta\cos 2\omega t - \frac{A\omega\Gamma_0}{2\pi U_\infty^2} B_1 \sin(2\omega t + \phi_1) \\
&\quad + \frac{\beta\Gamma_0}{\pi U_\infty^2}\cos(\omega t + \phi_1)\left[\frac{1}{2}\tan^{-1}\left(\frac{y}{x}\right) + \tan^{-1}\left(\frac{y + A\sin\omega t}{x - c_0}\right)\right. \\
&\quad \left. - \tan^{-1}\left(\frac{yc_0^2 + Aa^2\sin\omega t}{xc_0^2 - a^2 c_0}\right) - \frac{\pi}{2}\right]
\end{aligned}\right\} \quad (4.2.23)$$

$$\left.\begin{aligned}
\bar{C}_{p_2} &= -\frac{1}{U_\infty^2}\left[\left(U_\infty(1-\cos 2\theta) - B_6 A\cos\phi_1\right)^2 + \frac{A^2\omega^2}{2}\sin^2 2\theta + \frac{B_5^2}{2}\right. \\
&\quad \left. + \frac{B_6^2 A^2}{2} - B_5 A\omega\sin 2\theta\sin\phi_1\right] \\
C_{p_2}' &= -\frac{2(1-\cos 2\theta)}{U_\infty} A\omega\sin 2\theta\cos\omega t + \frac{2(1-\cos 2\theta)}{U_\infty} B_5\sin(\omega t + \phi_1) \\
&\quad - \frac{2B_6 B_5}{U_\infty^2} A\cos\phi_1\sin(\omega t + \phi_1) - \frac{B_5 B_6}{U_\infty^2} A\sin\omega t \\
&\quad - \frac{B_5}{2U_\infty^2}\cos(2\omega t + 2\phi_1) + \frac{B_5 A\omega}{U_\infty^2}\sin 2\theta\sin(2\omega t + \phi_1) \\
&\quad + A B_5 B_6\sin(3\omega t + \phi_1) - \frac{A^2\omega^2}{2U_\infty^2}\sin^2 2\theta\cos 2\omega t
\end{aligned}\right\} \quad (4.2.24)$$

$$\bar{C}_{P_3} = -\frac{1}{U_\infty^2}\left[\left(U_\infty \sin 2\theta + B_3 A \cos\phi_1\right)^2 + \frac{A^2\omega^2\cos^2 2\theta}{2} + \frac{B_2^2}{2} + \frac{B_3^2 A^2}{2} + B_2 A\omega \cos 2\theta \sin\phi_1\right]$$

$$C'_{P_3} = \frac{B_2^2}{2U_\infty^2}\cos(2\omega t + 2\phi_1) - \frac{A\omega}{U_\infty^2}\cos 2\theta\, B_2 \sin(2\omega t + \phi_1)$$
$$+ B_2 B_3 A\left[\sin(3\omega t + \phi_1) - \sin\omega t\right]$$
$$- \frac{A\omega}{U_\infty}\sin 4\theta \cos\omega t - \frac{2}{U_\infty} B_2 \sin 2\theta \sin(\omega t + \phi_1)$$
$$+ \frac{2\sin 2\theta}{U_\infty} B_3 A \cos(2\omega t + \phi_1) - \frac{2B_3 B_2}{U_\infty^2} A\cos\phi_1 \sin(\omega t + \phi_1)$$
$$- \frac{A^2\omega^2}{2U_\infty^2}\cos^2 2\theta \cos 2\omega t \qquad (4.2.25)$$

where

$$B_1 = \left[\frac{x(3a^2 - c_0^2 - 2xc_0)}{2a^2(a^2 + c_0^2 - 2xc_0)} - \frac{(a^2 - c_0^2)}{c_0(a^2 + c_0^2 - 2xc_0)}\right]$$

$$B_2 = \frac{\Gamma_0}{4\pi a^2}\,\frac{(3a^2 - c_0^2 - 2xc_0)\,x}{a^2 + c_0^2 - 2xc_0}$$

$$B_3 = \frac{\Gamma_0}{4\pi}\,\frac{(c_0^2 - a^2)\sin 2\theta}{(a^2 + c_0^2 - 2xc_0)^2}$$

$$B_5 = \frac{\Gamma_0\, y}{4\pi a^2}\,\frac{2xc_0 + c_0^2 - 3a^2}{c_0^2 + a^2 - 2xc_0}$$

$$B_6 = \frac{\Gamma_0 y^2}{2\pi a^2}\,\frac{a^2 - c_0^2}{(c_0^2 + a^2 - 2xc_0)^2} \qquad (4.2.26)$$

4.2.2.3 Model Predictions

A. Stationary Cylinder

A.(i) Prediction of C'_{prms}

For a stationary cylinder $A = 0$. Noting that $\omega t + \phi_1 = \beta t$, see equation (4.2.22), and considering only the fundamental (i.e. βt) component, $C_{P_{FUN}}$, of pressure fluctuations, equations (4.2.23) to (4.2.25) give :

$$\left.\begin{aligned} C'_{PFUN} &= C'_{p_1} + C'_{p_2} + C'_{p_3} \\ &= \frac{\beta \Gamma_0}{\pi U_\infty^2} \cos \beta t \left[\tfrac{1}{2} \tan^{-1}\left(\tfrac{y}{x}\right) + \tan^{-1}\left(\frac{y}{x - c_0}\right) \right. \\ &\qquad \left. - \tan^{-1}\left(\frac{y c_0^2}{x c_0^2 - a^2 c_0}\right) - \pi/2 \right] \\ &+ \frac{2(1 - \cos 2\theta)}{U_\infty} B_5 \sin \beta t \\ &- \frac{2}{U_\infty} B_2 \sin 2\theta \sin \beta t \end{aligned}\right\} \quad (4.2.27)$$

The quantity $\frac{\beta}{\pi U_\infty}$ can be expressed as

$$\frac{\beta}{\pi U_\infty} = \frac{2 f_s}{U_\infty} = \frac{S}{a} \qquad \text{-----(4.2.28)}$$

where f_s = vortex shedding frequency.

S = strouhal Number.

By substituting for B_2 and B_5 in equation (4.2.27), the fluctuating pressure, C'_{PFUN}, at a given position θ on the stationary cylinder is seen to be dependent on the parameters $\frac{\Gamma_0}{U_\infty a}$ and c_0. The non-dimensional vortex strength, $\frac{\Gamma_0}{2\pi U_\infty a}$, will now be estimated following a method due to Roshko (1954a). Roshko (1954A) has shown that the

rate of shedding of circulation from the body, $\frac{1}{2} K^2 U_\infty^2$, can be related to the rate at which circulation passes downstream as discrete vortices by :

$$f_s \Gamma_0' = \frac{\epsilon K^2 U_\infty^2}{2} \qquad \text{(4.2.29)}$$

which can be expressed as

$$\frac{\Gamma_0'}{2\pi U_\infty a} = \frac{\epsilon K^2}{2\pi S} \qquad \text{(4.2.30)}$$

where $K = \sqrt{1 - C_{pb}}$ and C_{pb} is the mean base pressure coefficient.

S = strouhal number

ϵ = the fraction of the vorticity of the shear layers that is present in the discrete vortices of the wake.

To calculate ϵ , Roshko (1954A) assumed that :

a) the vortex spacing ratio, h/l , has the Karman theoretical value of 0.281

b) the lateral spacing h of the vortex street is equal to d' where d' , the distance between the free streamlines (or vortex streets) when parallel, is obtained from the free-streamline theory presented in Roshko (1954B)

He then expressed equation (4.2.29) as

$$\left(1 - \frac{u}{U_\infty}\right) \frac{\Gamma_0'}{U_\infty l} = \frac{\epsilon K^2}{2} \qquad \text{(4.2.31)}$$

where u is the induced velocity of the vortex street.

l is the distance between consecutive vortices in a row.

From the assumption that h/l = 0.281 we have

$$\Gamma_0' = 2\sqrt{2}\, u l \qquad \text{(4.2.32)}$$

Substituting this value in equation (4.2.31) gives

$$\frac{u}{U_\infty} = \frac{1}{2}\left(1 \pm \sqrt{1 - \frac{\epsilon K^2}{2}}\right) \qquad (4.2.33)$$

With $h/l = 0.281$ the Karman drag formula can be written as :

$$C_D \, d/h = 5.65 \frac{u}{U_\infty} - 2.25 \left(\frac{u}{U_\infty}\right)^2 \qquad (4.2.34)$$

Using equations (4.2.33) and 4.2.34) Roshko plotted $C_D \, d/h$ as a function of K with ϵ appearing as a parameter - see Fig 4.1 . On the same graph Roshko also plotted the variation of $C_D \, d/d'$ with K where $C_D \, d/d'$ was calculated from his free-streamline theory, see Roshko (1954B) . When K is known (from measurement of C_{pb} for example), ϵ can be determined from the intersection of the curves $C_D \, d/h$ and $C_D \, d/d'$

Bloor & Gerrard (1966) have reported that although Roshko's assumptions that $h/l = 0.281$ and $h = d'$ are incorrect (see Footnote 4.1), Roshko's method still yield values of $\frac{\Gamma_o}{2\pi U_\infty a}$ that are in excellent agreement with their experimental measurements. The values of $\frac{\Gamma_o}{2\pi U_\infty a}$ calculated by Roshko's (1954A) method using Roshko's (1954A) and Bloor & Gerrard (1966) values of K will be denoted by $\left(\frac{\Gamma_o}{2\pi U_\infty a}\right)_R$ and $\left(\frac{\Gamma_o}{2\pi U_\infty a}\right)_{BG}$ respectively. Bloor & Gerrard (1966) have shown, see Fig 4.4, that $\left(\frac{\Gamma_o}{2\pi U_\infty a}\right)_{BG}$ is less than $\left(\frac{\Gamma_o}{2\pi U_\infty a}\right)_R$ and also that $\left(\frac{\Gamma_o}{2\pi U_\infty a}\right)_{BG}$ agrees with their measured value of vortex strength at 10 diameters downstream of the cylinder. In the present analysis $\frac{\Gamma_o}{2\pi U_\infty a}$ is assumed to be initial strength of a fully formed vortex. As it is known that the strength of a vortex diminishes with downstream distance, the intitial strength of the fully formed vortex

---

FOOTNOTE 4.1 Bloor & Gerrard (1966) reported that h/l was 0.14 at 10 diameters downstream and they also suggested that d'/h was 2.4 .

will be higher than the value measured at 10 diameters downstream. It is for this reason that $\frac{\Gamma_o}{2\pi U_\infty a}$ will be represented by $\left(\frac{\Gamma_o}{2\pi U_\infty a}\right)_R$ in the present analysis.

Fig 8 of Gerrard (1965) suggests that Roshko's (1954A) value of K at McGregor's (1957) Reynolds number of 4.3×10^4 is 1.46 . Using this value of K in Fig 4.1 gives $\epsilon = 0.454$ which when substituted into equation (4.2.30) gives $\frac{\Gamma_o}{2\pi U_\infty a}$ of 0.83 when, as in Keefe (1961) for example, the strouhal number , S , at Re of 4.3×10^4 is taken as 0.185 . The length C_o is assumed to be vortex formation region length. At his Reynolds Number of 4.3×10^4 , McGregor (1957) suggested that C_o was 2a where "a" is cylinder radius. This value of C_o is in good agreement with the measurement of Bloor & Gerrard (1966) and will also be used in the present calculation.

With $C_o = 2a$, and $\frac{\Gamma_o}{2\pi U_\infty a} = 0.83$ the predictions of RMS pressure coefficients at the fundamental frequency by the present model and that of McGregor are compared in Fig 4.2 with the experimental measurements of McGregor (1957) and Gerrard (1961). The predictions of the present model are seen to agree better with experimental measurements than those of McGregor.

Generally the predictions of the potential flow models are seen, see Fig 4.2, to be better at the front, $90^\circ < \theta < 180^\circ$, of the cylinder. Good agreement between model predictions and experimental measurements is not expected at the back of the cylinder because in the potential flow model flow is always attached whereas there is separation in the real flow.

A(ii) Prediction of the non-dimensionalised vortex strength, $\Gamma_o / \pi U_\infty d$

When C'_{PFUN} and C_o are known, the potential flow model can predict $\frac{\Gamma_o}{\pi U_\infty d}$. On the cylinder at $\theta = \pi/2$ the predictions of $\left(\frac{\Gamma}{\pi U_\infty d}\right)^{-1}\left(C'_{PFUN}\right)$ by equation (4.2.27) of the present model are presented in Fig 4.3 together with the predictions of McGregor's (1957) model.

For example at a Reynolds number of 1.45×10^4 the measurements of Roshko (1954A) on a circular cylinder suggests that C_o is 2.26a . It

has already been reported that at McGregor's (1957) Reynolds number of 4.3×10^4, an appropiate value of C_o is $2a$. Using the above values of C_o and the values of C'_{PFUN} on the cylinder at $\theta = \pi/2$ observed by McGregor (1957) and Gerrard (1961), the predicted values of $\frac{\Gamma_o}{\pi U_\infty d}$ were obtained from Fig 4.3 and tabulated in Table 4.1 .

Reynolds number	C_o/a	Col.3 $(C_{PFUN})_{\theta=\pi/2}$ GERRARD (1961)	Col.4 $(C_{PFUN})_{\theta=\pi/2}$ McGREGOR (1957)	Prediction of $\Gamma_o/\pi U_\infty d$			
				present model		McGregor(1957)model	
				From Col.3	From Col.4	From Col.3	From Col.4
1.5×10^4	2.26	0.15		0.306		0.075	
4.3×10^4	2	0.465	0.254	1.501	0.820	0.260	0.142

TABLE 4.1

The predictions of $\frac{\Gamma_o}{\pi U_\infty d}$ by the potential flow models are compared with values obtained by the other workers in Fig 4.4. The present model is seen to predict values of $\frac{\Gamma_o}{\pi U_\infty d}$ that are compatible with the measurement of Bloor & Gerrard (1966) and also in good agreement with the values of $\frac{\Gamma_o}{\pi U_\infty d}$ calculated by the already described Roshko (1954A) method particularly when McGregor's value of $(C'_{PFUN})_{\theta=\pi/2}$ is used. McGregor'S model on the other hand predicts values of $\frac{\Gamma_o}{\pi U_\infty d}$ that are much too small.

Fig. 4.3 also shows that even when $\frac{\Gamma_o}{\pi U_\infty d}$ is constant, changes in C_o can still produce increases in C_{PFUN} .(The real flow situation is, of course, more complicated as $\Gamma_o/\pi U_\infty d$ will generally be a function of C_o). According to the potential flow model it is even possible for a decrease in $\Gamma_o/\pi U_\infty d$ to produce an increase in C'_{PFUN} if it is accompanied by a sufficiently large increase in C_o . The potential flow model thus shows that unless the formation region length, C_o , is known to be unchanged, changes in fluctuating pressures cannot be attributed solely to changes in

the non-dimensional vortex strength, $\frac{\Gamma_o}{\pi U_\infty d}$.

B. Cylinder Oscillating in still air

It is now more convenient to work with fluctuating pressure $p' = C_p' \cdot \frac{1}{2}\rho U_\infty^2$. Multiplying both sides of equations (4.2.23) to (4.2.26) by $\frac{1}{2}\rho U_\infty^2$ and then equating Γ_o and U_∞ to zero gives:

$$\left(\bar{p}\right)_{\Gamma_o = U_\infty = 0} = -\frac{\rho}{4} A^2 \omega^2 (1 + 2\cos 2\theta) \quad \text{- - - - - -(4.2.35)}$$

$$\left(p'\right)_{\Gamma_o = U_\infty = 0} = -\rho A\omega^2 a \sin\theta \sin\omega t - \rho \frac{A^2\omega^2}{4}(1 + 2\cos 2\theta)\cos 2\omega t \quad \text{- - - - - -(4.2.36)}$$

Considering only the fundamental (i.e. wt) component of p' gives :

$$\left(p'_{FUN}\right)_{\Gamma_o = U_\infty = 0} = -\rho A\omega a \sin\theta \sin\omega t \quad \text{- - - - - -(4.2.37)}$$

Equation (4.2.37) indicates that for a cylinder performing simple harmonic oscillation in still air, the components of the fluctuating lift at the oscillation frequency are everywhere in phase with the cylinders displacement .

C. Circular Cylinder Oscillating at lock-in a uniform flow with circulation as in sketch (4.4)

For this case $\beta t = \omega t + \phi_1$ - see equation (4.2.22). For small amplitudes of oscillation, the fundamental (i.e. wt) component of the coefficient of fluctuating pressure on the oscillating cylinder is given by equations (4.2.23) to (4.2.26) as:

$$
\begin{aligned}
C_p' = {} & \frac{\left(P'_{FUN}\right)_{\Gamma_0 = U_\infty = 0}}{\frac{1}{2}\rho U_\infty^2} + \left(C'_{P\,FUN}\right)_{A=0} \\
& + \frac{\beta \Gamma_0 \cos \beta t}{\pi U_\infty^2}\left[\tan^{-1}\left(\frac{y + A\sin\omega t}{x - c_0}\right) - \tan^{-1}\left(\frac{y}{x - c_0}\right)\right. \\
& \left. - \tan^{-1}\left(\frac{y c_0^2 + A a^2 \sin\omega t}{x c_0^2 - a^2 c_0}\right) + \tan^{-1}\left(\frac{y c_0^2}{x c_0^2 - a^2 c_0}\right)\right] \\
& - \frac{2 A\omega}{U_\infty}\sin 2\theta \cos \omega t - \frac{2(1 - \cos 2\theta) A\omega \sin 2\theta \cos \omega t}{U_\infty} \\
& - \frac{2 B_6 B_5}{U_\infty^2} A \cos\phi_1 \sin(\omega t + \phi_1) - \frac{B_5 B_6}{U_\infty^2} A \sin \omega t \\
& - \frac{B_2 B_3}{U_\infty^2} A \sin \omega t - \frac{A\omega}{U_\infty}\sin 4\theta \cos \omega t \\
& - \frac{2 B_2 B_3}{U_\infty^2} A \cos\phi_1 \sin(\omega t + \phi_1)
\end{aligned}
\qquad (4.2.38)
$$

where $\left(C'_{P\,FUN}\right)_{A=0}$ is the fundamental component of C_p' experienced by the stationary cylinder with $\frac{\Gamma_0}{U_\infty a}$ and c_0 having the same values as on the oscillating model. $\left(C'_{P\,FUN}\right)_{A=0}$ is defined by equation (4.2.27). $\left(P'_{FUN}\right)_{\Gamma_0 = U_\infty = 0}$ is wt - component of the fluctuating pressure experienced by model during oscillation in still air. $\left(P'_{FUN}\right)_{\Gamma_0 = U_\infty = 0}$ is defined by equation (4.2.37).

At lock-in the potential flow model shows, see equations (4.2.23) to (4.2.26), that in addition to terms at the common angular frequency of body oscillation and vortex shedding, ω, the fluctuating pressure on the oscillating model, P'_{osc}, also contain terms in 2ω, 3ω.....etc. Furthermore equation (4.2.38) shows that P'_{osc} cannot be obtained simply by adding vectorially the fluctuating pressures $(P')_{A=0}$ and $(P')_{\Gamma_0 = U_\infty = 0}$ where $(P')_{A=0}$ is the fluctuating pressure on the stationary model and $(P')_{\Gamma_0 = U_\infty = 0}$ is the fluctuating pressure on the model during vibration is

still air.

An important implication of equation (4.2.38) is that even when $\frac{\Gamma_o}{U_\infty a}$ and C_o are unaffected by model oscillation, the fluctuating pressure on the oscillating model can still be larger than that on the stationary cylinder even after inertia pressure, $(p')_{\Gamma_o = U_\infty = 0}$, has been taken into account. Thus, even after inertia affects have been considered, amplification of surface fluctuating pressures during model oscillation cannot always be attributed solely to changes in non-dimensionalised vortex strength, $\frac{\Gamma_o}{U_\infty a}$, and the formation region length C_o.

D. Off-locked flow case.

To demonstrate the usefulness of the potential flow model consideration will be given to the instantaneous velocities at two fixed points, P and P' located on either side of the cylinder having co-ordinates (0 , Y) and (0 , -Y), see sketch (4.5), relative to the MEAN position of the center of the oscillating cylinder.

To further simplify the analysis it will be assumed that $Z_B = C_o$ (i.e. that the wake vortex at B in sketch (4.4) also oscillates with the circular cylinder).

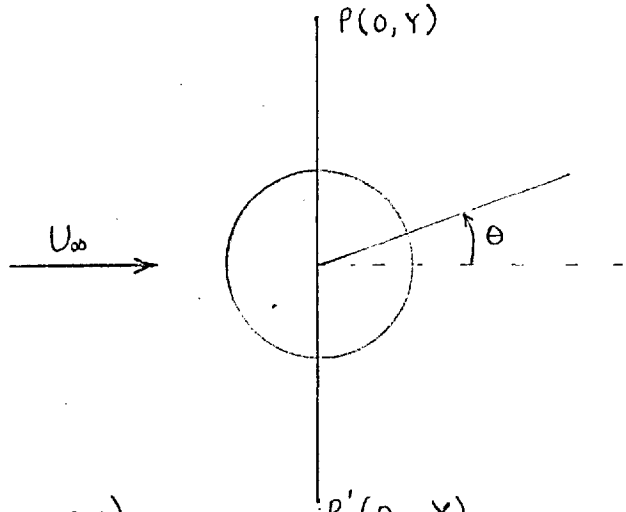

sketch (4.5)

Equation (4.2.10) then becomes

$$\left.\begin{aligned} Z_B &= C_o \\ Z_A &= a^2/C_o \end{aligned}\right\} \quad - - - - - - - (4.2.39)$$

Substituting these values of Z_A and Z_B in equation (4.2.9) and differentiating ϕ with respect to X gives:

$$\left.\begin{aligned} \frac{\partial \phi}{\partial x} = U_\infty + \frac{U_\infty a^2}{x^2+y^2} - \frac{2U_\infty a^2 x^2}{x^2+y^2} + \frac{2a^2 y x}{x^2+y^2} A\omega \cos \omega t \\ - \frac{\Gamma_o \sin \beta t}{2\pi} \left[- \frac{y}{y^2+(x-C_o)^2} + \frac{y C_o^2}{y^2 C_o^2 + (xC_o - a^2)^2} - \frac{y}{2(y^2+x^2)} \right] \end{aligned}\right\} (4.2.40)$$

The co-ordinates of P relative to the displaced center of the oscillating cylinder is

$$\left.\begin{aligned} x &= 0 \\ y &= Y - A\sin\omega t \end{aligned}\right\} \qquad (4.2.41)$$

Now $\dfrac{\partial\phi}{\partial x} = \overline{\dfrac{\partial\phi}{\partial x}} + \left(\dfrac{\partial\phi}{\partial x}\right)'$

where $\overline{\dfrac{\partial\phi}{\partial x}} = u$ and $\left(\dfrac{\partial\phi}{\partial x}\right)' = u'$ with overbar denoting time mean.

Substituting equation (4.2.41) into equation (4.2.40) and then separating the resulting u' into its frequency components we have, after terms of higher order than A^2 have been neglected, that:

$$\left.\begin{aligned} (u')_p = {} & 2U_\infty a^2 A\sin\omega t + \frac{\Gamma_0}{2\pi}\sin\beta t\left(K_1 + \frac{A^2}{2}K_3\right) \\ & - \frac{3U_\infty a^2 A^2}{2Y^4}\sin 2\omega t + \frac{\Gamma_0}{4\pi}AK_2\cos(\beta-\omega)t \\ & - \frac{\Gamma_0}{4\pi}AK_2\cos(\beta+\omega)t - \frac{\Gamma_0}{8\pi}A^2K_3\sin(\beta-2\omega)t \\ & - \frac{\Gamma_0}{8\pi}A^2K_3\sin(\beta+2\omega)t \end{aligned}\right\} \qquad (4.2.42)$$

where $K_1 = \dfrac{Y}{Y^2+C_0^2} - \dfrac{YC_0^2}{Y^2C_0^2+a^4} + \dfrac{1}{2Y}$

$$K_2 = \frac{Y^2-C_0^2}{Y^2+C_0^2} - \frac{Y^2-a^4/C_0^2}{\left(Y^2+a^4/C_0^2\right)^2} + \frac{1}{2Y^2}$$

$$K_3 = \frac{Y(Y^2-3C_0^2)}{(Y^2+C_0^2)^3} - \frac{Y(Y^2-3a^4/C_0^2)}{\left(Y^2+a^4/C_0^2\right)^2} + \frac{1}{2Y^3}$$

Replacing Y in equation (4.2.42) with -Y gives the velocity u' at

the fixed point P' - see sketch (4.5).

The predicted phase differences of the frequency components of u' at the fixed points P and P' are presented in Table 4.2.

180^{o} out of phase terms	In phase terms
ωt , βt , $(\beta - 2\omega)t$ and $(\beta + 2\omega)t$	$2\omega t$, $(\beta - \omega)t$, $(\beta + \omega)t$

TABLE 4.2

The predicted phase relationships of Table 4.2 are in agreement with the hotwire measurements of Davies (1975) (see his Fig 54, 55, 56 and 57) in the wake of an oscillating flat plate. Thus in addition to predicting terms with frequencies ω , β , $\omega + \beta$, $\omega - \beta$ etc which are observed in practice, the potential flow model also predict accurately the phase difference between the fluctuating velocities at two fixed points on either side of the oscillating cylinder.

4.2.2.4 Possible improvements to the potential flow model

a) Include the effects of the separated shear layers prior to their roll-up to form vortices.

b) Include flow separation in the description of the mean flow field around the cylinder .

c) In the calculations C_0 was assumed constant. This is, strictly, not true because the induced velocity of the rest of the field on the wake vortex at B , see sketch (4.4), is not zero. There should therefore be a contribution to C_p' due to the velocity of the vortex at B.

4.2.2.5 Conclusion

The potential flow model appears to be a very useful tool for studying

the fluctuating pressures on a bluff body. It shows that the fluctuating pressures are dependent on vortex strength, formation region length and local velocities. However the present model is very far from "correct" as a thorough understanding of both the vortex formation region and the vortex shedding process are required before one can correctly model vortex shedding potentially or otherwise.

4.3 THE LIFT-OSCILLATOR MODEL OF VORTEX-INDUCED VIBRATION.

4.3.1 Introduction

This is not an attempt to model the flow around bluff bodies. The underlying idea of the model is that the fluctuating lift on bluff bodies may be considered to arise from the action of something akin to an oscillator in the separated flow. The problem is then reduced to finding the equation of an oscillator which can generate the important characteristics of the lift on bluff bodies undergoing either forced or vortex-induced synchronised oscillation.

Of the large number of possible oscillator equations that can be used to describe lift characteristics the basic equation used by investigators, so far, is the Van der Pol equation. This equation was first used to model vortex-induced vibration by Hartlen & Currie (1970). What follows is an investigation into how well the Van der Pol oscillator as used by Hartlen & Currie predicts the lift characteristics of a square section cylinder in forced oscillation.

4.3.2 Equation for lift coefficient C_L

Using the dimensionless variables defined as

$$\left.\begin{aligned} X_r &= X/D \\ \tau &= t\left(K/M\right)^{1/2} = \omega_n t \\ \omega_0 &= f_s/f_N = S\left(\frac{U_\infty}{f_N d}\right) \end{aligned}\right\} \quad \cdots \quad (4.3.1)$$

Hartlen & Currie (1970) proposed the following equation for C_L:

$$\ddot{C}_L - \alpha\omega_o \dot{C}_L + \frac{\gamma}{\omega_o}\left(\dot{C}_L\right)^3 + \omega_o^2 C_L = b_4 \dot{X}_r \quad \text{- - - - - (4.3.2)}$$

The only criteria used to formulate equation (4.3.2) are:

(a) The damping term must be such that the oscillator is self-excited and self-limited. This is to account for the presence of a finite fluctuating lift coefficient, C_{L_o}, on a stationary bluff body. A stationary body corresponds in equation (4.3.2) to the case $\dot{X}_r = 0$.

(b) The frequency, ω_o, of the free oscillation occurring in equation (4.3.2) is chosen to obey the strouhal relation

$$f_s = S U_\infty / D$$

(c) Finally the choice of the forcing function is arbitrary. This implies that a forcing function that is proportional to acceleration or displacement could equally well have been used in equation (4.3.2).

It is important to note that other non-linear oscillators satisfying the preceeding criteria (a) to (c) could as well have been used to define C_L. The advantage of the Van der Pol Oscillator is that its solution is readily available - see for example Stoker (1950).

The solution of equation (4.3.2) depends on the three unknown parameters α, γ, and b_4.

Self-Excited Oscillation (Fluctuating Lift on a Stationary body)

For self-excited oscillations the forcing term $b_4 \dot{X}_r$ in equation (4.3.2) is zero.

Introducing new parameters defined as:

$$\left.\begin{aligned} t_1 &= \omega_o \tau \\ C_{L_1} &= \sqrt{\frac{3\gamma}{\alpha}}\, C_L \end{aligned}\right\} \quad \text{- - - - - - - - (4.3.3)}$$

Equation (4.3.2) with $b_4 \dot{X}_r = 0$ becomes

$$\ddot{C}_{L_1} - \alpha\left[\dot{C}_{L_1} - \tfrac{1}{3}\left(\dot{C}_{L_1}\right)^3\right] + C_{L_1} = 0 \quad \text{- - - - (4.3.4)}$$

The solution of equation (4.3.4), depends on the single parameter α and is discussed in Stoker (1950). For small α, i.e. $\alpha << 1.0$, the steady state free oscillation given by the solution of equation (4.3.2) is nearly simple harmonic - and can be approximated, see for example Stoker (1950), by:

$$C_{L_1} = 2 \cos t_1 \quad - - - - - - - - - - (4.3.5)$$

Substituting for C_{L_1} and t_1 using equation (4.3.3) we have:

$$C_L = \left(\frac{4\alpha}{3\gamma}\right)^{1/2} \cos \omega_0 \tau \quad - - - - - - - - (4.3.6)$$

The amplitude of the lift coefficient, C_{L_0}, on the stationary body is therefore given by

$$C_{L_0} = \left(\frac{4\alpha}{3\gamma}\right)^{1/2} \quad - - - - - - - - (4.3.7)$$

The fact that the fluctuating lifts observed experimentally on stationary bluff bodies are approximately simple harmonic ~~therefore~~ restricts the choice of α in equation (4.3.7) to small values much less than unity.

Cylinder forced externally

With the Hartlen & Currie (1970) definition that

$$\left.\begin{aligned} x_r &= -X_r \cos \omega\tau \\ B &= \frac{b_4 \omega}{\omega_0^2} \end{aligned}\right\} \quad \ldots\ldots \quad (4.3.8)$$

equation (4.3.2) becomes

$$\ddot{C}_L - \alpha\omega_0 \dot{C}_L + \frac{\gamma}{\omega_0}\left(\dot{C}_L\right)^3 + \omega_0^2 C_L = B\omega_0^2 \sin\omega\tau \quad - - - - - (4.3.9)$$

Van der Pol suggests a general solution for equation (4.3.9) of the form:

$$C_1 = b_1 \sin \omega\tau + b_2 \cos \omega\tau \quad - - - - - - - - (4.3.10)$$

in which b_1 and b_2 are slowly varying functions of time. That b_1 and b_2 are slowly varying functions of time is interpreted in Stoker (1950) as meaning that the quantities $\dot{b}_i$ and $\ddot{b}_i$ are small of first and second order respectively in α.

Substituting equation (4.3.10) in (4.3.9) and neglecting terms of higher order than unity in α, we have after separately equating coefficients of terms containing $\sin\omega\tau$ and $\cos\omega\tau$ that:

$$\left.\begin{aligned} -2\dot{b}_2 + b_1\left(\frac{\omega_o^2 - \omega^2}{\omega}\right) + \alpha_1 b_2\left[1 - \frac{b^2}{a_1^2}\right] &= \frac{B\omega_o^2}{\omega} \\ 2\dot{b}_1 + b_2\left(\frac{\omega_o^2 - \omega^2}{\omega}\right) - \alpha_1 b_1\left[1 - b^2/a_1^2\right] &= 0 \end{aligned}\right\} \quad 4\cdot3\cdot11$$

$$\left.\begin{aligned} \text{where} \quad b^2 &= b_1^2 + b_2^2 \\ \alpha_1 &= \alpha\omega_o \\ a_1^2 &= \frac{4\alpha\omega_o^2}{3\gamma\omega^2} \end{aligned}\right\} \quad (4.3.12)$$

Terms involving frequency $3\omega\tau$ have been neglected.

Synchronised or "lock-in" oscillation

This is the condition where the free oscillations of frequency ω_o are completely supressed by the forced oscillations of frequency ω. The solution of equation (4.3.9) therefore contains only the frequency component ω. This condition is expressed as:

$$\dot{b}_1 = \dot{b}_2 = 0$$

Equation (4.3.11) then becomes

$$\left.\begin{aligned} b_1 Z + \alpha_1 b_2\left[1 - b^2/a_1^2\right] &= B_1\omega_o \\ b_2 Z - \alpha_1 b_1\left[1 - b^2/a_1^2\right] &= 0 \end{aligned}\right\} \quad - - - (4.3.13)$$

from equation (4.3.13) we have

$$Z^2 + \alpha_1^2 \left[1 - \frac{b^2}{a_1^2}\right]^2 = \frac{B_1^2 \omega_0^2}{b^2} \qquad \text{(4.3.14)}$$

where
$$\left.\begin{aligned} Z &= \frac{\omega_0^2 - \omega^2}{\omega} \\ B_1 &= \frac{B\omega_0}{\omega} \end{aligned}\right\} \qquad \text{(4.3.15)}$$

The particular solution of equation (4.3.9) given by equations (4.3.13) to (4.3.15) represents the "lock-in" phenomenon where the natural vortex shedding frequency given by the Strouhal relation $S = \frac{f_0 D}{U_\infty}$ is completely suppressed or 'captured' by the body oscillation frequency, f .

For the synchronised or 'lock-in' case, the stability of equations (4.3.13) and (4.3.14) can be investigated by replacing b_1 and b_2 in equation (4.3.11) by $b_1 + \delta b_1$ and $b_2 + \delta b_2$ respectively. When $\dot{b}_1 = \dot{b}_2 = 0$ is substituted in the resulting equation, the stability conditions can be expressed as in Van der Pol (1927) as:

$$b^2/a_1^2 > \tfrac{1}{2} \qquad \text{(4.3.16)}$$

$$\alpha_1^2 \left[1 - b^2/a_1^2\right]\left[1 - \frac{3b^2}{a_1^2}\right] + Z^2 > 0 \qquad \text{(4.3.17)}$$

Equations (4.3.16) and (4.3.17) are discussed by Van der Pol (1927). They determine the extent of the synchronised or lock-in zone where only oscillations of the forcing angular frequency ω are present in the solution of equation (4.3.9). For moderately strong forcing, it is demonstrated in Fig. 2 of Van der Pol (1927) that the extent of the lock-in zone is defined solely by equation (4.3.16) as:

$$\frac{b^2}{a_1^2} = \frac{1}{2} \qquad \text{(4.3.18)}$$

Substituting equation (4.3.18) into equation (4.3.14) and assuming that:

$$Z = \frac{\omega_o^2 - \omega^2}{\omega} \approx 2(\omega_o - \omega)$$

and $\frac{1}{16}\alpha^2 << (\omega_o - \omega)^2$

gives

$$\frac{\omega_o - \omega}{\omega_o} = \pm \frac{B_1}{\sqrt{2}\, a_1} \quad ; \quad \omega = \omega_o \left[1 \pm \frac{B_1}{\sqrt{2}\, a_1} \right]$$

or that

$$\Delta\omega = \frac{2 B_1}{\sqrt{2}\, a_1} \qquad (4.3.19)$$

$\Delta\omega$ is the bandwidth, $\frac{\Delta f}{f_o}$, of the lock-in zone.

Thus from the experimental value of $\Delta\omega$ we have another equation, equation (4.3.19), for determining the unknown parameters α, γ, and b_4.

4.3.3 Model Predictions

Calculation of Parameters B, α, γ

The model parameters B, α and γ will be determined from experiments on a square section cylinder oscillating with amplitude to diameter ratio, A/D, of 0.1. The following observations can be made from the experiments:

a) Measurements show that at lock-in, the pressure distributions on side faces B & D of sketch (4.6) are, for A/D = 0.1, scaled versions of the pressure distribution on the same faces with model stationary. This is demonstrated in Fig. 4.5. At lock-in the lift coefficient on the oscillating model with A/D = 0.1 can therefore be assumed proportional to the fluctuating pressure on the center of the side face B, marked 1/B in sketch (4.6). The fluctuating pressure at hole 1/B will therefore be used in the model instead of the fluctuating lift.

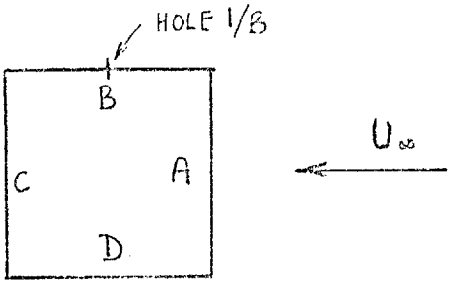

sketch (4.6)

b) The lock-in range for $A/D = 0.1$ was observed to lie between reduced windspeed, $\frac{U_\infty}{fd}$, of 7.0 and 9.0.

c) In most of the experiments U_∞ was kept constant while the frequency of body oscillation f was varied. Since U_∞ constant means a constant natural vortex shedding frequency f_0, the angular frequency ω_η used to non-dimensionalise t in equation (4.3.1) will be replaced by ω_0 in this analysis.

The preceeding observations can be expressed as:

a) $$C_{L_0} = \sqrt{2} \times 0.72 = 1.02 \quad \text{- - - - - - (4.3.20a)}$$

Since the rms value of the measured uncorrected fluctuating pressure coefficient at hole 1/B on a stationary model was 0.72.

b) At lock-in, $7.0 < \frac{U_\infty}{fd} < 9.0$

So that $7.0 \times 0.134 < f_0/f < 9.0 \times 0.134$

and

$$\frac{\Delta f}{f_0} = \Delta\omega = 0.24 \quad \text{- - - - - - (4.3.20b)}$$

To arrive at equation (4.3.20b) the uncorrected Strouhal number, $\frac{f_0 d}{U_\infty}$ of 0.134 measured on a stationary square section cylinder has been used. $\Delta\omega$ is the band-width of the lock-in zone.

c) $$\omega_0 = 1.0, \quad \omega = \frac{f}{f_0} \quad \text{- - - - - - (4.3.20c)}$$

At resonance $\omega = 1.0$, $Z = \frac{\omega_0^2 - \omega^2}{\omega} = 0$, equation (4.3.14) then becomes:

$$\alpha_1^2 \left[1 - \frac{b^2}{a_1^2}\right]^2 = \frac{B_1^2 \omega_0^2}{b^2} \quad \text{- - - - - - (4.3.21)}$$

To obtain a third equation for the three unknown parameters B, α and Y, the maximum fluctuating pressure coefficient measured in the lock-in range at hole 1/B for $A/D = 0.1$ will be substituted <u>arbitrarily</u> for b in equation (4.3.21). That is:

$$\left(b_{max}\right)_{\text{EXPERIMENT, } A/D = 0.1} = \left(b_{\omega=1}\right)_{\text{MODEL}}$$

It must however be pointed out that in the experiment, the maximum fluctuating pressure was observed at $\omega = \frac{f}{f_o} = 0.957$ rather than at $\omega = \frac{f}{f_o} = 1.0$ - See Fig. 4.7 .

With the measured values $C_{L_0} = 1.02$ and $b_{max} = 1.37$ and $\Delta\omega = 0.24$ equations (4.37) , (4.3.19) and (4.3.21) give:

$\alpha = 0.15$, $B = 0.17$, and $Y = 0.20$.

Calculation of the predicted amplitude and phase at lock-in

With the definition $b_1 = b\cos\phi_m$ and $b_2 = b\sin\phi_m$ equation (4.3.10) becomes

$$C_L = b\sin(\omega\tau + \phi_m) \quad - - - - (4.3.22)$$

where $\phi_m = \tan^{-1}(b_2/b_1)$ is the phase angle between the fluctuating lift output, C_L , and the forcing function, $B\omega_o^2\sin\omega\tau$. The interpretation of ϕ_m is discussed in section 4.3.4 .

The solution of equation (4.3.13) gives:

$$\left.\begin{aligned} b_1 &= \frac{Z}{Z^2 + A_1^2}\cdot\frac{B\omega_o^2}{\omega} \\ b_2 &= \frac{A_1}{Z^2 + A_1^2}\cdot\frac{B\omega_o^2}{\omega} \end{aligned}\right\} \quad - - - (4.3.23)$$

So that $\phi_m = \tan^{-1}(A_1/Z)$ (4.3.24)

where $A_1 = \alpha_1\left(1 - b^2/a_1^2\right)$

With the definition $y = b^2/a_1^2$, equation (4.3.14) can be written as

$$y\left[Z^2 + \alpha_1^2(1-y)^2\right] = \frac{B^2}{a_o} \quad - - - - (4.3.25)$$

By taking a value for ω in the lock-in range, Z was determined using equation (4.3.15). With Z known, y was obtained by solving equation (4.3.25) numerically. $A_1 = \alpha_1(1 - y)$ was next determined so that the phase

angle ϕ_m can be calculated from equation (4.3.24). Determination of b_1 and b_2 using equation (4.3.23) fixed the phase angle in the right quadrant. The model predictions are compared with experimental measurements on a square section cylinder in Fig 4.6 - where it is assumed that $\phi = \phi_m$. Since ϕ in Fig 4.6 is the phase angle between the fluctuating lift and the cylinder's displacement, equating ϕ to ϕ_m means that the forcing function is proportional to the cylinders displacement. Futher discussion about the interpretation of ϕ_m is presented below.

4.3.4 Determination of the lift phase angle ϕ from ϕ_m

ϕ_m has been defined in equation (4.3.22) as the phase angle by which the fluctuating lift leads the forcing function. Usually one is interested in the phase angle, ϕ, between the fluctuating lift and the cylinders displacement. To determine ϕ from ϕ_m, one must first specify the phase relationship between the forcing function and the displacement. Hartlen& Currie (1970) overcame this situation by assuming arbitrarily that the forcing function is proportional to the velocity. A rather more general approach is to redifine the cylinders displacement X_r as :

$$X_r = A \sin(\omega\tau - \theta) \quad \text{- - - - - - (4.3.26)}$$

so that the forcing function $B\omega_o \sin \omega\tau$ leads the cylinders displacement by the phase angle θ. ϕ is then given by:

$$\phi = \phi_m + \theta \quad \text{- - - - - - - - (4.3.27)}$$

θ, the unknown phase angle by which the forcing function leads the displacement, can now be chosen so that the predicted ϕ agrees as best as possible with experimental measurements.

For example when $\theta = 90^\circ$, $\phi = \phi_m + 90^\circ$ the forcing function is

in phase with the velocity. This is the case considered by Hartlen & Currie (1970) and is indicated by ϕ - curve 1 of Fig 4.6 .

When $\theta = 0^{\circ}$, $\phi = \phi_m$, the forcing function is in phase with the displacement. This is the case presented in Fig 4.6 as ϕ -curve 2 .

The good agreement between the measured ϕ and ϕ - curve 2 of Fig 4.6 demonstrates that Harlen & Currie's choice of forcing function, which they showed to be suitable for modelling ϕ on oscillating circular cylinders, is not suitable for modelling ϕ on oscillating square section cylinders. The difference between the ϕ values of square and circular cylinders may be due to the difference in afterbody shapes.

4.3.5 The Limits $\omega \longrightarrow 0$ and $\omega \longrightarrow \infty$

Since $\omega = f/f_o$, the limits $\omega \longrightarrow 0$ and $\omega \longrightarrow \infty$ may be viewed respectively as the case of periodic vortex shedding on a stationary body and the case of a body oscillating in still air.

One is no longer within the range of synchronisation or 'lock-in' and the previous solution given by equations (4.3.13) and (4.3.14) no longer apply. The general solution of equation (4.3.9) now consists of two frequencies f and f_o and is given by Van der Pol (1927) as:

$$C_L = b_f \sin(\omega_o \tau + \phi_1) + b_h \sin(\omega \tau + \phi_2) \quad - - - - (4.3.30)$$

b_f is the amplitude of the harmonic oscillation having the frequency, f_o , of the free oscillations.

b_h is the amplitude of the harmonic oscillation at the forcing frequency f .

From the equation (4.3.30) we have

$$\frac{\overline{C_L^2}}{a_0^2} = \frac{1}{2}\left(\frac{b_f^2}{a_0^2} + \frac{b_h^2}{a_0^2}\right) \quad - - - - - (4.3.31)$$

By substituting equation (4.3.30) in equation (4.3.9) and retaining only terms having the frequencies ω_0 and ω, it follows, after terms containing ϕ_1 and ϕ_2 have been eliminated from the resulting equations, that:

$$\alpha \omega_0^2 b_f \left[1 - \left(\frac{b_f}{a_0}\right)^2 - 2\left(\frac{b_h}{a_0}\right)^2\right] = 0 \quad \text{- - - - - (4.3.32)}$$

$$b_h^2 \left[Z^2 + \alpha^2 \omega_0^2 \left(1 - \left(\frac{b_h}{a_0}\right)^2 - 2\left(\frac{b_f}{a_0}\right)^2\right)^2\right] = \frac{B^2 \omega_0^4}{\omega^2} \quad \text{- - - (4.3.33)}$$

The parameters Z, a_1, and B are still as they have been defined.

When $b_f \neq 0$ equation (4.3.32) becomes

$$1 - \left(\frac{b_f}{a_0}\right)^2 - 2\left(\frac{b_h}{a_0}\right)^2 = 0 \qquad (4.3.34)$$

By substituting the value of b_f from equation (4.3.34) into equation (4.3.33) we have

$$Z^2 + \alpha^2 \omega_0^2 \left(1 - 3\left(\frac{b_h}{a_0}\right)^2\right)^2 = \frac{B^2 \omega_0^4}{b_h^2 \omega^2} \quad \text{- - - (4.3.35)}$$

Consider the limit $b_h \longrightarrow 0$

From equation (4.3.35) $Z^2 \longrightarrow \infty$

From equation (4.3.34) $\frac{b_f^2}{a_0^2} \longrightarrow 1.0$

So that in equation (4.3.31) $\frac{\overline{C_L^2}}{a_0^2} \longrightarrow \frac{1}{2}$

The fluctuating lift, C_L, predicted by equation (4.3.2) has amplitude tending to the free oscillation amplitude a_0, and is dominated by the component having the free oscillation frequency ω_0 as ω tends to either zero or infinity. This is shown diagramatically in Fig 3 of Van der Pol (1927).

4.3.6 Discussion of model predictions

Lock-in Range.

Fig 4.6 shows that within the 'lock-in' range, the predictions of C_L by the lift oscillator model of Hartlen & Currie (1970) are in good qualitative agreement with experimental measurements on a square section cylinder. Good qualitative agreement was obtained, see Fig 4.6, between the predicted and the measured ϕ by assuming that the forcing function is proportional to the cylinder's displacement, x_r (i.e. θ in equation (4.3.27) is equated to zero). When the forcing function is assumed to be proportional to the cylinder's velocity as in Hartlen & Currie (1970), the predicted phase angle ϕ is shown as ϕ -curve 2 in Fig 4.6. Thus within the lock-in range, the lift characteristics on a square section cylinder are better predicted with a forcing function that is proportional to the cylinder's displacement.

It is interesting to note that in Fig 4.6 the predicted maximum C_L is at $\frac{f}{f_o} = 0.978$ ($\frac{U_\infty}{fd} = 7.63$) instead of at resonance, $\frac{f}{f_o} = 1.0$, as one may at first expect. This shift in the position of maximum C_L away from resonance towards slightly lower values of $\frac{f}{f_o}$ (or higher $\frac{U_\infty}{fd}$) was also observed experimentally on the square section cylinder as shown in Fig 4.6.

The general features of Fig 4.6 are such that one cannot help but speculate about the possibilities of obtaining even better agreement between model and experiment by a different selection of the parameters B, α and γ of equation (4.3.9) together with a suitable choice of θ in equation (4.3.27) It is therefore concluded that in the lock-in range, the Van der Pol oscillator of Hartlen & Currie (1970) is capable of representing the lift characteristics of a square section cylinder in forced oscillation.

Limits $\frac{f}{f_o} \longrightarrow 0$ and $\frac{f}{f_o} \longrightarrow \infty$

According to the lift oscillator model the lift amplitude should tend to the stationary cylinder value, C_o, and should be dominated by the

stationary cylinder shedding frequency f_o as f/f_o tends to either zero or infinity. As f/f_o tends to zero (i.e. $\frac{U_\infty}{fd} \longrightarrow \infty$) the experimental characteristics of the fluctuating lift on a square section cylinder is seen at small amplitude of oscillation, see Fig 4.7 , to behave as predicted by the model. However as $\frac{f}{f_o} \longrightarrow \infty$ (i.e. $\frac{U_\infty}{fd} \longrightarrow 0$) experimental observations show that the body frequency f dominates and that the lift amplitude tends to the value that would exist when the cylinder is oscillating in still air. The Van der Pol oscillator of equation (4.3.9) cannot predict the characteristics of the lift on a square section cylinder in the limit $\frac{f}{f_o} \longrightarrow \infty$ or $\frac{U_\infty}{fd} \longrightarrow 0$.

4.3.7 Concluding Remarks

Other forms of the Van der Pol equation have been used by Landl (1975) and Skop & Griffin (1973) . Essentially these investigators added extra terms to the basic Hartlen & Currie equation in order to obtain good agreement between model and experimental measurement for the special case of a circular cylinder oscillating in the lock-in range. However the lift characteristics of bluff bodies depend on the nature of their afterbodies. Thus an oscillator which has been modelled specifically for a circular cylinder may not give good predictions of the lift characteristics for other bluff body shapes. It is for this reason that the equations of Landl (1975) and Skop & Griffin (1973) are not considered here.

Finally it is acknowledged that for a given set of experimental results, it is possible to find an oscillator which may predict lift characteristics better than equation (4.3.9). The problem is whether the parameters of such an oscillator can be linked with the characteristics of the flow field. Unless the parameters can be linked to the physics of the flow, it may be very difficult to apply an oscillator equation developed specifically for a particular test flow case to other flow situations. It is therefore suggested that the "correctness" of an oscillator equation should be judged not only

from how well it simulates a special test case but also from how well the parameters of the equation can be linked to the physics of the flow.

CHAPTER 5

5. FLOW VISUALISATION OF THE VORTEX SHEDDING PHENOMENON

5.1 INTRODUCTION

To complement measurements of pressures, lift phase angles, velocities etc., a film of the vortex shedding phenomenon was made. Flow visualisation was by a single stream of smoke introduced upstream of the model along the position of the stationary model stagnation streamline. The tunnel wind-speed was adjusted to produce a vortex shedding frequency , f_s , of 3.38 cps on the stationary model. (This value of f_s was chosen from consideration of the stability of the smoke stream). The films were taken at 32 frames/sec to give approximately 10 frames of pictures per vortex shedding cycle. By projecting the frames of the film one at a time, a study of the flow around the body during the process of vortex formation was conducted. The result of this study is presented in this chapter.

A detailed study of the entrainment process was not made because there was no way of discerning, in the near wake, the smoke particles from the opposing shear layers. Nevertheless the flow visualisation study is still very useful because one can observe the effects of body oscillation on vortex shedding and near wake flow configuration.

5.2 STATIONARY BODY ($f_s = 3.38$, $f_N = 0$)

5.2.1 Vortex shedding and flow configuration around the model.

The shear layers appear to swing generally towards the side where a vortex is forming (i.e. swing direction appears to be upwards when a vortex is forming in the upper shear layer and vice versa). The shear layers swing so vigorously that although there is no steady reattachment, the lower shear layer in Fig. (5.1) appears to touch the trailing corner, D , due to the induced field of the vortex forming in the upper shear layer. Similarly the formation of a vortex in the lower shear layer brings

the upper shear layer very close to the trailing corner C . It is as if a growing vortex pulls across the opposing shear layer. Thus the mechanism of vortex shedding appears to be that proposed by Gerrard (1966) where a fully grown vortex is said to draw the opposing shear layer across the wake to effect shedding. The flow patterns predicted by the numerical models of Abernathy & Kronauer (1962) and Clements (1973) also suggest a similar interaction between a fully grown vortex and the opposing shear layer.

The region between the shear layers and the side faces have traces of smoke indicating the secondary flows which exist on the side faces. This has also been shown by Mulhearn (1973).

The vortices are formed so close to the body that smoke sweeps continuously over the back face of he mode. Thus there is no 'dead-air' behind the model.

5.2.2 Wake flow configuration.

Fig. (5.7) shows the wake flow pattern. The smoke is so diffused that for nearly all the time one cannot discern distinct vortices. The wake, however, still looks 'snaky' or wavy suggesting the presence of a turbulent vortex street.

5.3 SYNCHRONISED OSCILLATIONS ($f_N = f_S = 3.38$, A/D = 0.25)

5.3.1 Vortex shedding and flow configuration around the model.

The observed flow pattern is sketched in Fig. (5.2) at every one-eight of a cycle interval as the body moves from the extreme top to the bottom extremity of its motion.

Fig. 5.2 (a) , $t = 0$. A vortex, V_1 , can be seen forming in the lower shear layer. The upper shear layer on the other hand appears to be attached to the back face near the trailing corner C .

Fig. 5.2 (b) , $t = T/8$. The vortex V_1 has grown bigger. A new vortex V_2 is now forming in the upper shear layer.

Fig. 5.2 (c), $t = T/4$. The body has now reached the centerline position The lower shear layer seems to have reattached to the side face DA at the position S. Vortex V_1 looks fully grown and seems to be 'pushed' downstream by the growing vortex V_2.

Figs. 5.2 (d) & (e), $t = 3T/8$ and $T/2$. As the body moves from the centerline position to the extreme bottom position, vortex V_1 drifts further downstream while vortex V_2 grows. The reattachment position S of Fig. 5.2 (c) moves nearer to the trailing corner, D, until at the position in Fig. 5.2 (e) the flow appears to reattach to the back face very near corner D. The growing vortex V_2 will be shed somewhere around the centerline position as the body moves upward.

Although it is difficult to discern the exact instant of vortex shedding, it is apparent that the bottom vortex V_1 is shed somewhere between positions (b) and (d) of Fig. 5.2. Generally a vortex is shed from a shear layer when the body is around the centerline position and is moving towards the shear layer in question.

Because of the growing vortices V_1 and V_2 in Figs. 5.2 (a) and (e) the shear layers appear to swing in the direction of the body's motion as the body starts to move away from the extremities of the motion. In contrast for a circular cylinder, Griffin & Ramberg (1974) reports that as the cylinder moves downward the shear layers appear to move upward while as the cylinder begins its upward motion, the shear layers appear to move downwards. The relevance of this observation to vortex induced vibrations is discussed in section 5.6.2.2.

5.3.2 Wake flow configuration.

Fig. 5.8 shows the wake flow pattern. In contrast to the stationary cylinder wake of Fig. 5.7 where no distinct vortex is visible, about four vortices can now be discerned in the wake. The vortices appear to arrange themselves in the wake on a single straight line and they are joined together by shear layer bridges labelled S_1 and S_2

in Fig 5.2 (e) . Because of the very small lateral separation between the vortices the apparent vortex spacing ratios appear to tend to zero.

5.4 $f_N/f_S = 2.0$ A/D = 0.25

5.4.1 Vortex shedding and flow configuration around the model.

The observed flow pattern is sketched in Fig. 5.3 at every one-sixth of a cycle interval as the body moves from the extreme top to the bottom extremity of its motion.

Fig. 5.3 (a) , $t = 0$. The fully formed vortex vortex V_1 appears to be drawing across the shear layer joining the lower vortex V_2 to the body. The flow has reattached to the upper side face.

Fig. 5.3 (b) , $t = T/6$. A vortex V_3 is now forming in the lower shear layer. A large separation bubble has formed on the upper side face BC .

Fig. 5.3 (c) , $t = T/3$. The bubble on face BC has grown bigger and has moved nearer corner C . The reverse flow due to the bubble gives the impression that a vortex is forming on the side face. The lower shear layer has reattached to side face DA. The vortex V_3 has grown bigger and has displaced vortex V_1 further downstream.

Fig. 5.3 (d) , $t = T/2$. The fully grown vortex V_3 has displaced vortex V_1 downstream. The upper shear layer no longer looks attached to the upper side face. The lower shear layer is on the other hand still attached to the lower side face.

The overall impression created is that vortices are shed at each extremity of the motion at the body frequency, f_N , from the shear layer nearer the extremity. The vortices seem to form at the back face of the model.

In Figs. 5.3 (a) and (d) the vortices V_1 and V_2 can be seen interacting with the shear layers opposite to them. This leads to the suggestion that vortices are shed by interaction of the opposing shear layers just as for the cases $f_N/f_S = 0$ (stationary) and

f_N/f_S = 1.0 already discussed. Wilkinson (1974) suggests that a vortex is shed not by interaction of the opposing shear layers but "by reason of its shear layer being drawn into the side face of the cylinder". This point is discussed in section 5.6.2.2 .

5.4.2 Wake flow configuration.

Fig. 5.9 shows the wake flow pattern. Unlike the case f_N/f_S = 1.0 (Fig.5.8) the vortices are 'packed' close to the back face. The shear layer bridges between consecutive vortices marked S_1 and S_2 in Fig. 5.2 (e) seems to have been rotated in Fig. 5.3(d) and Fig. 5.9 almost through 90° . Thus the few vortices visible in the wake appear to have a spacing ratio of about unity. As the smoke probe is fixed, the movement of the stagnation line as the body oscillates may have caused the smokelessness of the vortex centers in Fig. 5.9.

5.5 f_N/f_S = 0.5 , A/D = 0.25 (QUASI-STEADY OSCILLATIONS?)

5.5.1 Vortex shedding and flow configuration around the model.

The flow pattern observed during half a cycle of the body motion is sketched in Fig. 5.4 .

As the body moves downwards, the lower shear layer first reattaches to the side face roughly at $t = T/6$ - see Fig. 5.4 (c) . For the remainder of the downward journey, the lower shear layer continues to remain close to the side face. For $\frac{T}{2} < t < T$ the body moves upwards and the shear layers' position for a given $t = T'$ can be obtained by lateral inversion of the sketch for $t = T' - T/2$ in Fig. 5.4 . In general, therefore, the shear layer seem to reattach on the side of the body towards which the motion is directed. This may be due largely to the effects of changing incidence.

Although the vortices are no longer shed at the body's frequency they still seem to form close to the back face of the model.

5.5.2 Wake flow configuration.

Fig. 5.10 shows the wake flow pattern and as in the stationary body's case the near wake appears wavy. It is impossible, due to the diffusion of the smoke, to discern distinct vortices.

5.6 DISCUSSION OF FLOW VISUALISATION. RESULTS

5.6.1 Preliminary considerations.

Before starting a detailed discussion of the flow visualisation results, some of the factors which can, for an oscillating body, affect the position of the shear layers relative to the body are first considered Some of these factors are:

(a) The effects of oscillating the flow separation positions.

(b) The effects of changing incidence.

(c) The effects of the fluctuating pressures due to the acceleration of the body - i.e. "virtual mass" pressures.

5.6.1.1 The effects of oscillating the flow separation positions.

It is not clear if the oscillation of the flow separation points will cause the shear layers to lie asymmetrical relative to the body. It is pointed out by Davies (1975) that this effect can, by modifying flow separation velocity cause a modification of the vorticity shed by the body into the wake. This modification of the shed vorticity may in turn alter the equilibrium position of a fully grown vortex. Thus oscillating the flow separation points may cause the flow pattern around the body particularly in the vortex formation region to depart from that around a stationary body.

Wilkinson (1974) discusses another effect of oscillating the flow separation points. He suggests that perturbing the shear layer separation position can, according to the work of Rosenhead in 1932, cause premature roll-up of the shear layers. For the moment however the main interest is in those factors which can cause 'quantifyable' asymmetry in the configuration of the shear layers. The effects of oscillating the separation

positions on vortex formation will not be pursued further here but further discussion can be found in the works of Davies (1975) and Wilkinson (1974).

5.6.1.2 The effects of changing incidence.

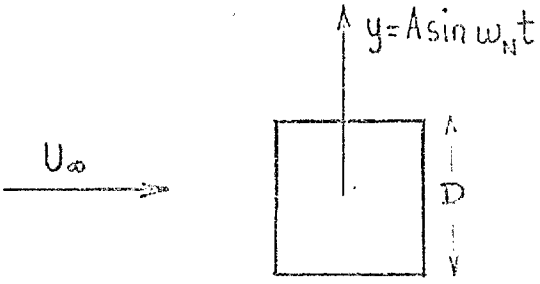

For a body performing simple harmonic motion normal to a free stream U_∞ as in the sketch, the instantaneous angle of incidence, θ, of the free stream relative to the body is given by:

$$\theta = \tan^{-1}\left(\frac{A\omega_N \cos \omega_N t}{U_\infty}\right)$$

The peak incidence θ_{MAX} is:

$$\theta_{MAX} = \tan^{-1}\left(\frac{A\omega_N}{U_\infty}\right) = \tan^{-1}\left(\frac{f_N D}{U_\infty} \cdot 2\pi A/D\right)$$

The values of θ_{MAX} are listed in table 5.1

f_N/f_S	$\frac{U_\infty}{f_N D}$	θ_{MAX} IN DEGREES	
		A/D = 0.10	A/D = 0.25
2.0	4.2	8.51	20.51
1.0	7.41	4.85	11.95
0.5	15	2.40	5.98

TABLE 5.1

If it is assumed that the flow has had sufficient time to adjust to the changing incidence, the changes in the flow pattern would be similar to those on a body performing galloping oscillations. The resulting flow pattern would be as sketched in Fig. 5.5 for θ_{MAX} sufficient to cause flow reattachment. As the body pulled out from the extreminties of the motion, the shear layers would swing against the direction of the body's motion - see Fig. 5.5.

Flow patterns similar to those in Fig. 5.5 have been observed by Parkinson (1971) around a galloping square section cylinder. In galloping instability, f_S/f_N is usually so large that the flow has time to adjust to the changing incidence so that the problem can be analysed

quasi-statically. It is very unlikely that the quasi-steady analysis will be applicable without some modifications in the present case where f_N and f_S are of the same order of magnitude. However it is to be expected that the changing incidence which causes the shear layers to be asymmetrical at high f_S/f_N will still cause asymmetry in the shear layers configuration at low f_S/f_N. That the quasi-steady analysis may not hold at low f_S/f_N is meant to imply that the magnitude of the shear layer asymmetry and the induced fluid dynamic forces may be different from that predicted by the quasi-steady theory alone.

5.6.1.3 The effects of the fluctuating pressures due to body acceleration ('virtual mass' pressures).

An oscillating body will experience fluctuating pressures due to the acceleration imparted to the fluid surrounding the body.

Very crudely as the body oscillates, the surrounding fluid may be considered to perform simple harmonic motion and so exert a reaction on the body equal but opposite to the force it experiences due to the body. Thus on the upper side face of an oscillating square section cylinder, the acceleration pressures would be minimum when the body is fully up, zero when the body is at the centerline and maximum when the body is fully down. The pressures on the lower side face would be exactly out of phase with those on the upper side face.

In separated flow the effects of the above acceleration pressures on shear layers configuration would be as sketched in Fig. 5.6 . As the body moves downwards the shear layers would swing upwards while as the body moves upwards the shear layers would swing downwards.

Although some acceleration pressures can be expected on an oscillating body at all f_N/f_S, they are likely to be important (or even dominant) at high f_N/f_S. Under dynamic conditions the acceleration or inertia effect of this section should by introducing a phase lag in the shear layer response, cause the shear layers configuration to depart

from that produced by purely changing the incidence as discussed in section 5.6.1.2 .

5.6.2 General Discussion.

The flow visualisation was conducted primarily to determine the effects of body oscillations on

a) The flow pattern around the body.

b) The vortex formation process.

c) The wake flow configuration.

The observations are important as they help in providing a physical explanation for some of the pressure measurement results to be presented in latter chapters. For the moment this section will be restricted in scope as much as possible to just a discussion of the observed flow configurations. In latter chapters the relevance of these flow configurations to the measured pressures will be discussed.

5.6.2.1 The flow pattern around the body.

a) Oscillating Model; A/D = 0.25 ; f_N/f_S = 2.0 , 1.0 and 0.5.

In Figs. 5.2 to 5.4 comparison of the shear layer configurations at the extremities of the motion with corresponding parts of Fig. 5.6 suggests strong acceleration or 'virtual mass' effects. For the case f_N/f_S = 2.0 - Fig. 5.3, this is to be expected because it was pointed out in section 5.6.1.3 that acceleration effects are likely to be important at high values of f_N/f_S . For the case f_N/f_S = 1.0 , Fig. 5.2 , this result may not be due to acceleration effects alone because the growing vortices V_1 and V_2 of Fig. 5.2 (a) and (e) may have 'pulled across' their opposing shear layers. The case f_N/f_S = 0.5 , Fig. 5.4 , is surprising because acceleration or inertia effects were expected to be small at such low values of f_N/f_S .

As the body passes the centerline position on its way down, the lower shear layer in Figs. 5.2 and 5.4 tend to reattach to the side face. This from the discussion of section 5.6.1.2 and Fig. 5.5 (c)

suggests that the body may be responding to the instantaneous flow incidence. For f_N/f_S = 1.0 - (Fig. 5.2) and f_N/f_S = 0.5 (Fig. 5.4) Table 5.1 shows that the instantaneous angles of incidence for A/D = 0.25 are approximately 12° and 6° respectively as the body passes the centerline of the motion. Since for a stationary square section cylinder flow reattachment first occurs at an incidence of 13.5°, the results suggest that under dynamic conditions reattachment may occur earlier.

The case f_N/f_S = 2.0 is more complex for Fig. 5.3 (c) suggests the possibility of simultaneous reattachment in the upper and lower shear layers as the body passes the centerline of the motion.

Generally it seems that both the acceleration and changing incidence effects contribute to the observed flow configuration. It is difficult to separate the individual effects because one must also consider the natural tendency (even when body oscillations are absent) of the shear layers to move in the direction of a growing vortex. Furthermore on a stationary body, f_N/f_S = 0, there may be intermittent reattachment in the shear layers. It is therefore possible, particularly for the case f_N/f_S = 0.5, that random reattachment of the shear layers may already be affecting the observed flow configuration.

b) f_N/f_S = 0, Stationary Model. No steady reattachment was observed. It was pointed out in section 5.2.1 that the shear layers appear to swing towards the direction of a growing vortex. These swings create the impression that the shear layers are flapping about the body.

5.6.2.2 Vortex Formation Process.

Formation region length.

For the cases f_N/f_S = 0, 1.0 and 0.5 the vortices form so close to the back face of the model that fluid can be seen sweeping continuously across the back face. For the flow case f_N/f_S = 2.0, the vortices form even closer to the model - one has the impression that the vortices are actually shed from the back face of the model.

So far in this chapter, the changes in the magnitudes of the formation region length due to body oscillations have not been quantified. Instead the vortices have been said to form close to the back face of the model. This is not meant to imply that under all circumstances body oscillations do not affect the size of the formation region. In the case $f_N/f_S = 2.0$ the vortices seemed to be shed from the back face of the model suggesting a marked reduction of the formation region length from the stationary cylinder value.

Davies (1975) has shown that synchronised oscillations, $f_N/f_S \approx 1.0$, produces marked reductions in the formation region lengths of a flat plate and a D-shaped cylinder. For a circular cylinder in the Reynolds number range $120 < Re < 350$ Griffin (1971) has shown that synchronised oscillations can, in some cases, reduce the size of the formation region to as little as 50% of the stationary cylinder value. In contrast for a square section cylinder it seems that the vortices, in the stationary body case, already form close to the model and synchronised oscillations do not produce marked reductions in the formation region length.

Mechanism and Phase Angle of Vortex Shedding.

For all the flow cases visualised, the shear layers, see Fig.5.1 to 5.4 , seem to interact in a manner suggesting that the mechanism of vortex shedding is that suggested by Gerrard (1966). According to Gerrard a vortex grows until it is strong enough to draw the opposing shear layer across the wake in order to effect shedding.

$f_N/f_S = 2.0$

Vortex shedding for the case $f_N/f_S = 2.0$ is further discussed in the recent work by Wilkinson (1974). Wilkinson describes this flow case as the side vortex regime. The following extracts from Wilkinson sets out his views on the mechanism of vortex shedding.

a) "The most striking aspect of the process was the manner in which each vortex was shed. This was a direct result of the

supplying shear layer being drawn onto the side face of the cylinder, thus cutting off the supply of vorticity to the forming eddy and forcing it to be shed. This happened as the body passed through the extreme position of the motion on the side of the shear layer in question."

b) "The shed vortices were stronger during the side vortex regime because whilst one eddy was forming on the rear face prior to being shed, the other shear layer had all its vorticity entrained in the side forming vortex, and thus there is no annihilation of vorticity on the rear face by entrainment of opposite signed vorticity. The shedding in this regime was a consequence of the shear layer supplying the next vortex being pulled onto the side face."

The present results agree with Wilkinson's only to the extent that the shear layers reattach to the side faces and that a vortex is shed from a shear layer when the body passes through the extreme position of the motion on the side of the shear layer in question. Fig. 5.3 (a) and (d) definitely show that there is some interaction between a formed vortex and the opposing shear layer. It is true that the large bubble in Fig. 5.3 (c) give the impression that the vortices start their growth on the side faces but that does not preclude the interaction of the shear layers as in Fig. 5.3 (a) and (d) at the instant of vortex shedding. It appears that the mechanism of vortex shedding, at least for $f_N/f_S = 2.0$, is still the same as for a stationary body i.e. interaction of the shear layers leading to cancellation of vorticity. It is of course possible that as $f_N/f_S \longrightarrow \infty$, the shear layers may interact less and 'shedding' may then be more as a result of single shear layer instability.

Contrary to the views of Wilkinson, no evidence from flow visualisation suggests that the vortices are stronger at $f_N/f_S = 2.0$ than at $f_N/f_S = 1.0$. Measurements both by Wilkinson and the author

show that the base pressure is higher (less negative) at $f_N/f_S = 2.0$ than at $f_N/f_S = 1.0$. This means that at $f_N/f_S = 2.0$, less vorticity per second is shed into the wake than at $f_N/f_S = 1.0$. Flow visualisation reveals that vortices are shed in the two flow cases at the body frequency, f_N. One therefore expects non-dimensional vortex strength, $\frac{\Gamma}{U_\infty D}$, at $f_N/f_S = 2.0$ to be considerably less than at $f_N/f_S = 1.0$ because a lesser vorticity producing vortices at twice the frequency suggests more than 50% reduction in vortex strength.

$f_N/f_S = 1.0$ It was reported in section 5.3.1 that a vortex is shed from a shear layer when the body is around the centerline on its way to the extremity of the motion on the side of the shear layer in question. As a result of the shedding the shear layers appear to swing downwards when the body commences its downwards journey and upwards as the body commences its upwards journey.

In contrast to the above observations, for a circular cylinder externally vibrated at $f_N/f_S = 0.85$ and A/D = 0.25 ('A' is half amplitude and not peak-to-peak amplitude). Griffin & Ramberg (1974) reported from flow visualisation that:

a) A vortex is shed from a shear layer as the body passes the centerline of the motion on its way FROM the extremity of the motion on the side of the shear layer in question (exactly 180° out of phase with present observations on a square section cylinder).

b) As the cylinder moves downwards the shear layers appear to move upwards and vice versa (also 180° out of phase with the shear layer motion reported here for a square section cylinder)

Now it is generally accepted that the shed vortices are responsible for most of the fluctuating forces observed on long bluff cylinders. Bearing in mind that phase angle can be critically dependent on f_N/f_S the above observation implies that for a square section cylinder oscillating

at approximately $f_N/f_S = 1.0$ and $A/D = 0.25$, the phase angle between lift and displacement may differ by as much as 180^o from corresponding value on a circular cylinder. Furthermore for a bluff cylinder in a uniform crossflow, whether or not an imposed transient oscillation is damped out by the vortices depends on the resulting phase angle between the lift and displacement. The flow visualisation result therefore suggests that significant differences exist between the susceptibilities of a circular cylinder and a square cylinder to vortex induced vibrations.

5.6.2.3 The Wake Flow Configuration.

Figs. 5.7 to 5.10 show the wake flow pattern at a Reynolds Number of 5200 both for the stationary model and for the model oscillating at $f_N/f_S = 1.0$, 2.0 and 0.5. The amplitude to diameter ratio, A/D, is 0.25 in all cases of body oscillation. Comparison of Fig. 5.7, 5.8 and 5.9 show that oscillation at $f_N/f_S = 1.0$ and 2.0 improves the clarity of the wake vortices. However the diffusion of the separated shear layers and the rapid dissipation of the vortices with downstream distance suggests that the vortices in Fig. 5.7 to 5.9 contain turbulent fluid.

Wilkinson (1974) injected smoke into the flow at seventeen discrete points along the span of a square section cylinder and photographed the resulting flow pattern. For the stationary cylinder he reported that the smoke was dispersed evenly along the span in a very short distance of about one diameter downstream of the body. By contrast he reported that for $f_N/f_S = 0.95$ to 2.0 the smoke does not disperse fully along the span until a distance of about 3 to 4 diameters downstream of the cylinder. Although he conducted his flow visualisation at a Reynolds Number of 1.31×10^4, he went on to suggest that the vortices in the cases $f_N/f_S = 1.0$ and 2.0 are formed from laminar fluid. The implification of this suggestion is that body oscillation has extended the

stable regime of vortex shedding from an upper Reynolds Number limit of 150 (see Roshko (1953)) to a Reynolds Number of 1.31×10^4. Griffin & Votaw (1972) among others have reported that synchronised body oscillations can extend the stable regime of vortex shedding from a circular cylinder to a Reynolds Number of 350. Nowhere in the literature has the stable regime of vortex shedding been reported to extend beyond 400. It seems odd that laminar vortices can be shed, as reported by Wilkinson, from a square section at a Reynolds Number of 1.31×10^4.

That the wake vortices are clearer in Figs. 5.8 and 5.9 than in Fig. 5.7 at best suggest that turbulence levels are lower in the shear layers at $f_N/f_S = 1.0$ and 2.0 than at $f_N/f_S = 0$ (this may be due to the greatly reduced spanwise flows at $f_N/f_S = 1.0$ and 2.0 reported by Wilkinson). The diffusion of the separated shear layers and the rapid dissipation of the vortices with downstream distance are evidence that even at Reynolds Number as low as 5200, the vortices at $f_N/f_S = 1.0$ and 2.0 contain turbulent fluid.

5.7 CONCLUSIONS

5.7.1 Flow Configuration around the body.

Observations of the flow configuration around the body suggest that at $f_N/f_S = 2.0$, 1.0 and 0.5 both acceleration ("virtual mass") and changing incidence (galloping?) forces affect the position of the shear layers relative to the body. The periodic reatachment of the shear layers to the side faces which are most noticeable at $f_N/f_S = 1.0$ and 2.0 are probably caused mainly by a nonlinear combination of the two effects.

5.7.2 Vortex Formation Process

a) Oscillations at $f_N/f_S = 2.0$, 1.0 and 0.5 do not appear to affect the mechanism of vortex shedding. It seems, in all the flow cases visualised, that vortices are shed by interaction between the opposing

shear layers. This supports the vortex shedding mechanism proposed by Gerrard (1966).

b) It was reported by Griffin (1971) that body oscillations at $f_N/f_S \approx 1.0$ markedly reduced the vortex formation region length from the stationary cylinder value. Davies (1975) similarly reported that body oscillations at approximately $f_N/f_S = 1.0$ produced large reductions in the vortex formation region lengths of a flat plate and a D-shaped cylinder. By contrast the present results indicate that for a stationary square section cylinder, the vortices are already forming so close to the body that body oscillation at $f_N/f_S = 1.0$ does not spectacularly change the vortex formation region length from the stationary cylinder value.

c) For $f_N/f_S = 1.0$ the observed vortex shedding phenomenon on a square section cylinder is compared with the observations of Griffin & Ramberg (1974) on a vibrating circular cylinder. It appears that the phase angle between fluctuating lift and displacement could differ by as much as 180° for the two bodies. This suggests that the responses to vortex shedding of the cylinders are significantly different when both are spring mounted under identical conditions of damping, f_N/f_S, etc. This is because the vortices which tend to promote instability in one case will tend to damp out instability in the other.

5.7.3 Wake Flow Pattern

a) At $f_N/f_S = 1.0$ the few wake vortices visible appear collinear - suggesting a very small spacing ratio. By contrast at $f_N/f_S = 2.0$ the spacing ratio appears very close to unity.

At $f_N/f_S = 0.5$ the wake structure looks very much like that of a stationary body. No distinct vortices could be discerned in the wake.

b) The vortices in the wake were observed to be more distinct at $f_N/f_S = 1.0$ and 2.0 than at $f_N/f_S = 0$ (stationary model) and 0.5.

CHAPTER 6

6. STATIONARY CYLINDER : RESULTS AND DISCUSSION.

6.1 NOTATION

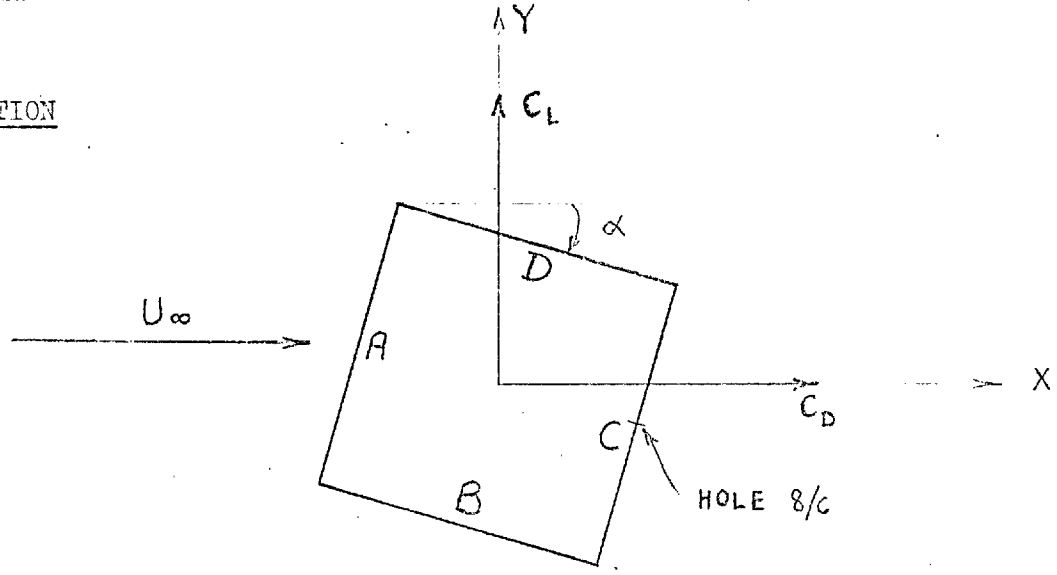

Sketch (6.1)

C_p - mean pressure coefficient.

α - angle of incidence.

$\overline{C}_{PA}$, $\overline{C}_{PB}$, $\overline{C}_{PC}$ and $\overline{C}_{PD}$ - these are the average mean pressure coefficients on faces A, B, C and D respectively -see sketch (6.1).

C_{pb} - the average value of C_p on the base. This is the same as $\overline{C}_{PC}$

$(C_p)_{B/C}$ - the value of C_p at the center of face C. This will sometimes be called the base pressure.

C_L and C_D are the sectional lift and drag coefficients.

Of the thirty mean pressure tappings distributed around the mid-section of the model as in Fig. 2.3, only three are positioned on each of the side faces B and D. Detailed measurements of C_p on the faces B and D were therefore obtained at each α by rotating the model through 90°. This rotation changes the configuration of the end plates relative to the wind direction from the one shown in sketch (6.2A) to that in sketch (6.2B). To minimise confusion all the results presented on faces B and D of the plots of C_p distribution, see Fig 6.2 to 6.8, are for the end configuration shown in sketch (6.2B). The results presented on faces A and C of Fig 6.2 to 6.8 correspond to the end configuration shown in sketch (6.2A),

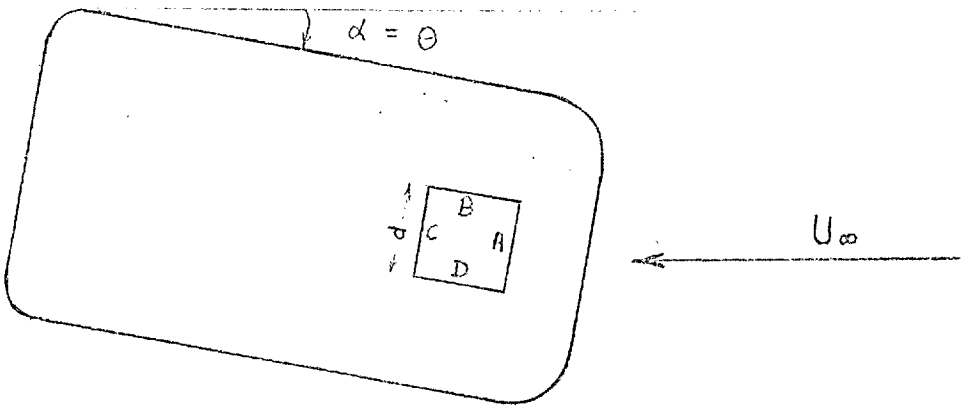

$\alpha = \theta$ where $0^\circ \leq \theta \leq 45^\circ$

Sketch (6.2A)

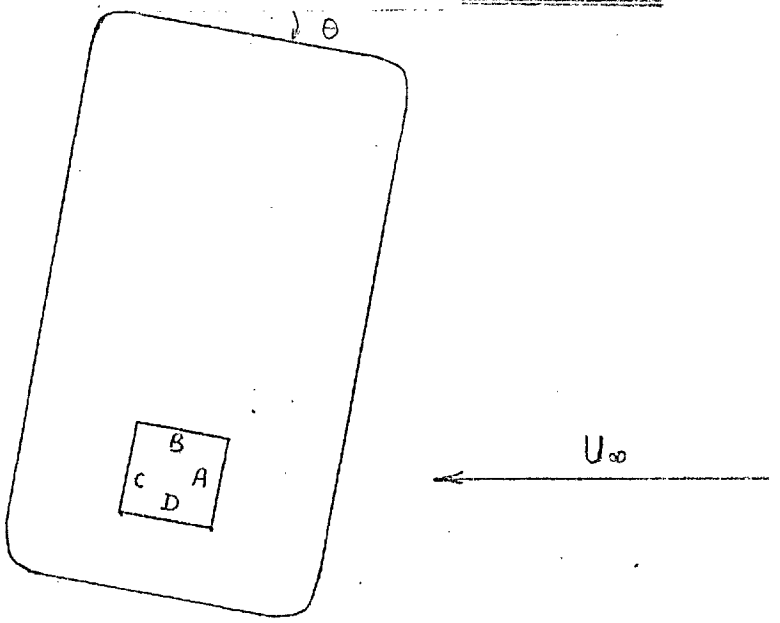

$\alpha = (\theta + 90)^\circ$ where $0^\circ \leq \theta \leq 45^\circ$

Sketch (6.2B)

6.2 FLOW NORMAL TO THE CYLINDER ($\alpha = 0^\circ$)

6.2.1 Mean pressure distribution including the effects of end plates and Reynolds number.

The mean pressure distribution was measured at several values of Reynolds number, R_e, in the range $4 \times 10^4 \leq R_e \leq 12 \times 10^4$. At each value

of R_e , the model was tested with and without one of the five sets of end plates referred to simply as NO.1 , NO.2 , NO.3 , NO.4 and NO.5 end plates. Some of the interesting points observed are:

Point 1. The effect of end plates on the C_p at mid-section is small. For example the average value of C_{pb} observed with the five sets of end plates is -1.43 as compared to the value of -1.40 observed without end plates - see Fig 6.14 . When end plates are used, the C_p distribution was also found to be unchanged, within the accuracy of measurement, when the model was rotated through 90^o thus changing the end configuration from that in sketch (6.2A) to that in sketch (6.2B). It can however be seen in Fig 6.10 that the $-C_{pb}$ (and hence C_D) measured with end plates are consistently higher than those measured without using end plates. This indicates that the effects of end plates, even though small, are genuine.

At $R_e = 4.74 \times 10^4$ the observed C_{pb} of -1.43 , see Fig 6.15 , is in good agreement both with the EDSU (1971) value of -1.42 and the value of -1.39 reported by Bearman & Trueman (1971) at $2 \times 10^4 < R_e < 7 \times 10^4$ By contrast the present value of C_{pb} is surprisingly lower (i.e. more negative) than the values of -1.27 and -1.26 measured respectively by Pocha (1971) at $R_e = 9 \times 10^4$ and Lee (1974) at $R_e = 1.75 \times 10^5$ even though C_{pb} was observed in the present study, see Fig 6.10, to decrease with increasing R_e . This could be due to the influence of aspect ratio. Bearman & Trueman, Pocha and Lee tested, without using end plates, cylinders of aspect ratios 17.0 , 8.7 and 9.3 respectively. In the present work the aspect ratio is 18.0 and 17.0 respectively without and with end plates (the end plates are fitted 17 diameters apart). It is reported in EDSU (1971) that C_D (and therefore $-C_{pb}$) decreases with decreasing aspect ratio particularly when the aspect ratio is lower than 20.

The above results show that care must be taken to isolate the effects

of aspect ratio in experiments, like those of Lee (1975/1976) and McLaren et al (1969), where aspect ratios are varied over a wide range. For example Lee (1975/1976) tested, without using end plates, square cylinders with aspect ratios of 9.27 , 10 , 24.4 and 30 . The results of this section show that even without considering other factors (like changes in blockage, and the variations in the distance between the turbulence grid and the model), the changes in $-C_{pb}$, see Fig 1.10C, that were attributed by Lee to the influence of turbulent length scale, could be accounted for by changes in aspect ratio. Clearly the conclusions arrived at in Lee (1975/1976) and other similar works, should be re-examined.

Point 2. The C_p on the base (i.e. face C), contrary to EDSU (1971), is not uniform but, in agreement with Bearman & Trueman (1971), is a minimum at the centre tapping and a maximum at approximately 0.1 diameters from each edge of the base - see Fig 6.2 and 6.11 . The measurements of Pocha (1971) and Lee (1974) also indicate minimum base pressure at the centre tapping.

Non-uniformity of base pressure is consistent with flow visualisation which shows, see Chapter 5 , that the flow sweeps continuously over the base.

Point 3. As R_e increases in the range $4 \times 10^4 < R_e \leq 1.2 \times 10^5$, C_D and $-C_{pb}$ can be seen in Fig 6.10 to rise. This is in agreement with Bearman & Trueman (1971) who reported that sharp edged rectangular cylinders with side ratios d/h (d is section width normal to the stream) in the range 0.5 to 1.0 are not free from Reynolds number effects. The present results do not agree with EDSU (1971) where force coefficients are reported to be independent of Reynolds number when $10^4 < R_e < 10^6$.

Since the free stream turbulence intensity is less than 0.04% the Reynolds number effects reported here could be caused by the upstream movement of the transition in the separated shear layers. Earlier

transition could, by causing increased shear layers' entrainment, increase $-C_{pb}$ and C_D. At higher Reynolds number transition could occur just downstream of the separation points so that further increases in R_e would have little effect on C_D and $-C_{pb}$. This could explain why C_D and $-C_{pb}$ (Fig 6.10) level off at high Reynolds number.

Point 4. Measurements of the spanwise distribution of base pressure with and without end plates show, see Fig 6.9 , that over at least the mid 60% of the span, the base pressure, measured along the center-line of the base, is within 3% of the value at mid-span . The values of spanwise base pressure can be seen in Fig 6.9 to be always slightly higher without than with end plates. This supports the remark made under point 1 that the effects of end plates are genuine.

6.2.2 The effects of the end clearance holes.

As reported in section 2.4.3 and Fig 2.6, the models that were oscillated were mounted externally on the arms of the oscillating mechanism through two circular slots (or clearance holes), each of diameter 6.5", on the wind tunnel's side walls. The large clearance holes allow the models to move freely during oscillation. Although each model mounted through the clearance holes was fitted with the NO.2 set of end plates to reduce spanwise flow, it was still thought worthwhile to investigate the effects of the clearance holes on the pressure measurements.

Fig 6.12 shows that the values of $(C_p)_{B/C}$ measured, when R_e is below 4×10^4 , on the model mounted with the clearance holes merge smoothly with those observed at higher R_e on models that are fitted with end plates but are mounted without the clearance holes. This shows that the clearance holes do not affect mean pressure measurement at center-span when R_e is below 4×10^4 .

By comparing the two results presented for the NO.2 end plates it can be seen in Fig 6.9 that when R_e is as high as 4.74×10^4 , the end clearance holes reduce the extent of the span over which the base pressure is uniform

from approximately the mid 60% of the span to the mid 40% . Most of the tests on the models mounted through the clearance holes was conducted at R_e of about 1.1×10^4 . Measurements at $R_e = 1.1 \times 10^4$ show, see chapter 7 Fig 7.1 , that the base pressure is uniform over at least the mid 80% of the span.

6.3 FLOW AT INCIDENCE TO THE CYLINDER

6.3.1 Mean pressure distribution including the effects of end plates.

The pressure distribution around the mid-section was measured at $R_e = 4.74 \times 10^4$ with the model set at 10 angles of incidence namely 5° , 10° , 13.5° , 15° , 20° , 25° , 30° , 35° , 40° and 45° . In addition measurements were also made at several other values of R_e in the range $2.3 \times 10^4 < R_e < 10.54 \times 10^4$ when $\alpha = 13.5^\circ$. Some of the results obtained are presented in Fig 6.3 to 6.8.

Some of the interesting points about the results are:

Point A1 At small values of α , particularly $\alpha = 5^\circ$ (Fig 6.3), there is some scatter in the C_p observed on faces B , C and D . This is mainly due to measurement difficulties. Despite the use of long small bore plastic tubings, difficulties were experienced in damping out the fluctuating component of surface pressure. From time to time the surface pressures in the separated flow region of the model were seen on the multitube manometers to surge in unison.

Point A2 On face A , the stagnation position (i.e. position at which $C_p = 1.0$) can be seen to move from the centre of the face to the leading edge A/B as α increases from 0° to 45° . Other workers , see for example Pocha (1971), have also reported similar findings.

Point A3 At $\alpha = 5^\circ$, 10° and 13.5° (Figs 6.3 and 6.4) there is, towards the rear of face B , a pressure recovery that is most marked at $\alpha = 13.5^\circ$ and least marked at $\alpha = 10^\circ$. The pressure recovery indicates, see Pocha (1971), the passage of the separated shear layer close

to the trailing edge B/C - see sketch 6.1 .

As α increases from 13.5° to 45° it can be seen in Fig 6.4 to 6.8 that the position of maximum C_p on face B moves from the trailing to the leading edge of the face. It was reported in section 1.4.1.1 that for smooth flow, the shear layer first reattaches steadily to corner B/C when α is approximately 13.5 . It is a widely held view, see for example Pocha (1971) and Roberston (1976), that this reattachment occurs in the region of maximum C_p . Thus the movement of the position of maximum C_p indicates that as α increases beyond 13.5° , the reattachment position on face B moves nearer edge A/B thus decreasing the size of the separation bubble on that face. This upstream movement of the reattachment position as α increases from 13.5° to 45° can be seen in Fig 6.13 to produce large reductions in the average suction, $-\bar{C}_{pB}$, on the reattachment face.

Point A4 Model set at $\alpha = \theta^{\circ}$, where $0^{\circ} \leq \theta \leq 45^{\circ}$ so that the end plates are as in sketch (6.2A)

Although C_p was measured on all faces, only the results shown on faces A and C of Fig 6.2 to 6.8 correspond to the present situation.

The C_p on the rear faces C and D were observed to be more negative with than without end plates particularly at high values of α (see the results presented on face C of Figs 6.3(b) , 6.4 , 6.6 , 6.7(b) and 6.8) . This point is also demonstrated in Fig 6.14 where C_{pb} is plotted against α . These results demonstrate the effectiveness of end plates. In addition, at each α , the C_p observed at each tapping was, within the accuracy of measurement, the same regardless of the end plates used - see face C of Figs 6.2 to 6.8 and also the C_{pb} versus α curve presented in Fig 6.14 . This shows that under the present condition (i.e. $\alpha = \theta^{\circ}$ where $0^{\circ} \leq \theta \leq 45^{\circ}$), the smallest pair of end plates, the NO.1 end plates is sufficient.

Point A5 Model and end-plates rotated through 90° so that the end plates are as in sketch (6.2B) [i.e. $\alpha = (90 + \theta)^\circ$ where $0^\circ \leq \theta \leq 45^\circ$]

As reported in section 6.1 , because of the distribution of the pressure tappings, a detailed distribution of C_p on faces B and D could only be obtained by rotating the model through 90° . Although C_p was measured on all faces after the 90° rotation , only the results for faces B and D are shown in Fig 6.2 to 6.8 .

When θ is between 13.5° and 45°, the values of C_p on the rear faces C and D were found to be very sensitive to the type of end plates used. For example it can be seen on Face D of Figs 6.4 , 6.6 , 6.7(b) and 6.8 , that the C_p's measured with the NO.1 end plates are much higher (less negative) than those measured without using end plates particularly at $\alpha = 45^\circ$ (Fig 6.8) - see also the $\bar{C}_{PD}$ versus α curve presented in Fig 6.14 . By contrast it can be seen in the same Figures that the C_p's measured on face D with the NO.3 end plates are more negative than those measured with the NO.2 end plates which are in turn more negative than those measured without end plates. The results for the NO.1 end plates indicate that end plates will have negative effects (i.e. decrease base suction) if they are not wide enough.

Although not shown in Fig 6.4 to 6.8 , it was also found that the C_p distributions observed, when $\alpha = (90 + \theta)^\circ$, with the NO.3 end plates were, within the accuracy of measurement, the same as those measured when, as already reported under point A4 , all end plates are set at $\alpha = \theta$. This shows that the NO.3 end plates are large enough when $\alpha = (90 + \theta)^\circ$. This is the reason why the curves of C_p distribution have been drawn through the points for the NO.3 end plates on face D of Fig 6.2 to 6.8 .

Point A6 It was reported in section 6.2 than an increase in Reynolds number could cause earlier transition. Earlier transition could, at low angles of incidence, cause earlier reattachment. To find out whether higher Reynolds number causes earlier reattachment, the C_p distribution on the reattachment face was measured at several values of Reynolds number, R_e, in the range $4.27 \times 10^4 \leq R_e \leq 10.54 \times 10^4$ when $\alpha = 13.5^\circ$. [It has already been reported in section 1.4.1.1 that in smooth flow, steady flow reattachment first occurs at $\alpha = 13.5^\circ$]. The results obtained at $R_e = 4.27 \times 10^4$ and 10.54×10^4 are presented in Fig 6.11.B.

There is an overall trend towards higher values of C_p as R_e increases such that the pressure recovery towards the rear of face B becomes less marked at higher values of R_e - see Fig 6.11B. It can be seen in Fig 6.11B that the increase in R_e does not make the pressure recovery begin nearer to the upstream edge A/B. This suggests that in the small range of R_e investigated, an increase in R_e does not cause earlier reattachment.

6.3.2 Variation of C_{PA}, C_{PB}, C_{PC}, C_{PD}, C_D and C_L with α.

$$\left.\begin{aligned} C_D &= (\bar{C}_{PB} - \bar{C}_{PD})\sin\alpha + (\bar{C}_{PA} - \bar{C}_{PC})\cos\alpha \\ C_L &= (\bar{C}_{PB} - \bar{C}_{PD})\cos\alpha + (\bar{C}_{PC} - \bar{C}_{PA})\sin\alpha \end{aligned}\right\} \quad (6.1)$$

See section 6.1 for notations.

Fig 6.13 shows the values of $\bar{C}_{PA}$, $\bar{C}_{PB}$, $\bar{C}_{PC}$ and $\bar{C}_{PD}$ that were estimated from the plots of C_p distribution. The values of C_D and C_L that were estimated from Fig 6.13 using equation (6.1) are presented in Figs 6.16 and 6.17.

In the range $0^\circ < \alpha \leq 13.5^\circ$ $-\bar{C}_{PB}$ can be seen in Fig 6.13 to be greater than $-\bar{C}_{PD}$. This has already been attributed in section 1.4.1.1 to asymetry in the shear layers configuration. The shear layer separating from edge A/B is closer to side face B than the opposing shear layer is to side face D. This is why C_L decreases, see Fig 6.17, as α increases

from 0° to 13.5° .

Beyond $\alpha = 13.5^{\circ}$ $\bar{C}_{PB}$ can be seen in Fig 6.13 to rise sharply with increasing α . This behaviour of $\bar{C}_{PB}$ is responsible for the rise in C_L (Fig 6.17) as α increases from 13.5° to 45° . The rise in $\bar{C}_{PB}$ is, see sections 1.4.1.1 and 6.3.1 , due to the movement of the reattachment position from the trailing to the leading edge of face B as α increases from 13.5° to 45° .

C_D and $-C_{pb}$ can be seen in Figs 6.15 and 6.16 to follow broadly the same trend. However unlike $-C_{pb}$ which is maximum at $\alpha = 0^{\circ}$, C_D is maximum at $\alpha = 45^{\circ}$. This is because C_D was calculated using the cylinder diameter, d , rather than the frontal width, $d(\sin\alpha + \cos\alpha)$, as reference length. The fall in C_D and $-C_{pb}$ (Figs 6,15 and 6.16) as α increases from 0° to 13.5° has already been attributed in section 1.4.1.1 to increases in the vortex formation region length l_f . The increase of C_D and $-C_{pb}$ as α increases from 13.5° to 45° has also been attributed in section 1.4.1.1 to decreases in l_f . The changes in l_f as α increases from 0° to 45° can be seen in the flow visualisation of Pocha (1971).

The present values of C_{pb} , C_L and C_D are compared in Figs 6.15 to 6.17 with those Parkinson & Brooks (1961), EDSU(1971), Pocha (1971) and Lee (1974). The author has corrected the results of Parkinson & Brooks (1961) for wind tunnel blockage effects using Maskell (1963). Lee's (1974) results, which were originally corrected for blockage effects by the method of Allen & Vincenti, were also recorrected by Maskell (1963). The present values of C_D and $-C_{pb}$ are, see Fig 6.15 and 6.16 , generally higher, particularly at large α , than those reported by these other workers. For example at $\alpha = 45^{\circ}$, the present value of C_D is 2.42 compared to the values of 2.21 and 2.18 reported respectively by EDSU(1971) and Lee (1974). This is thought to be because the present results were obtained using suitable end plates.

The effects of end plates on C_{pb} and $\bar{C}_{PD}$ are shown in Fig 6.14 . A

discussion of the effects of end plates can be found under points A4 and A5 of section 6.3.1 .

6.4 FLUCTUATING PRESSURE MEASUREMENT

The $C_{p_{rms}}$ distributions that were measured at $\alpha = 0^\circ$, 10° , 13.5° , 15° and 45° without using end plates are presented in Fig 6.18 to 6.21 along with those of Vickery (1966), Pocha (1971), Lee (1974) and Wilkinson (1974). To conform with the present results, the author has corrected the results of Lee and Wilkinson for blockage using Maskell's (1963). Although some measurements were made, see Figs 6.22 and 6.23 , using end plates, the effects of end plates on $C_{p_{rms}}$ were not investigated.

The distribution of $C_{p_{rms}}$ at various values of α will now be discussed.

A. $\alpha = 0^\circ$

On faces A and C , the present results can be seen to be in good quantitative agreement with those of Lee (1974). On each of these faces, $C_{p_{rms}}$ falls with distance from the edges to a minimum at the centre - see Fig 6.19. A similar trend was also observed by Pocha (1971) and Wilkinson (1974). The position of minimum $C_{p_{rms}}$ on face A corresponds to the stagnation position.

There is some discrepancy between the present results and those of Lee (1974) around the center of the side faces B and D . Lee's results, see Figs 1.9 and 6.19 , indicate a very large drop in $C_{p_{rms}}$ close to the center of the side faces. By contrast the present results and those of other workers indicate, see Fig 6.19 , only a small variation of $C_{p_{rms}}$. Both the present and Lee's results, particularly Lee's, indicate that the variation of mean pressures on the side faces are small - see Fig 6.2 . The $C_{p_{rms}}$ results of Lee (1974) therefore may be suspect because experience, see for example Pocha (1971), has shown that large variations in $C_{p_{rms}}$ are usually accompanied by large non-uniformity in mean pressures.

Generally the present values of C_{prms} are lower than those of Vickery (1966) and Pocha (1971) but higher than those of Wilkinson (1974) - see Fig 6.19 . The average values of C_{prms} in the separated flow region (faces B , C and D) are also much higher than on the front face A where flow is attached.

Fig 6.23 shows the effects of Reynolds number, R_e , on $(C_{prms})_{B/B}$ and $(C_{prms})_{B/C}$ which are respectively the fluctuating pressures at the centers of the side and back faces of the model. $(C_{prms})_{B/C}$ increases with R_e up to R_e of about 6×10^4 and then remains practically constant. This is similar to the behaviour of C_D and $-C_{pb}$ presented in Fig 6.10 . By contrast $(C_{prms})_{B/B}$ is , see Fig 6.23 , unaffected by R_e . The values of C_{prms} on all of the base and on the parts of the side faces that are very close to the trailing corners behave like $(C_{prms})_{B/C}$ as R_e increases.

It can be seen in Fig 6.23 that the C_{prms} measured with the $\frac{1}{2}$" Setra pressure transducer are generally slightly higher than those measured with the B & K $\frac{1}{4}$" microphone. This is as it should be. Because of changes in dynamic sensitivity factors at low frequencies, the B & K $\frac{1}{4}$" microphone is expected, see section 3.3.2 , to yield values of C_{prms} that are 3% too low.

The results for the NO.2 end plates in Fig 6.23 also show that mounting the model through end clearance holes as in Fig 2.6 (also see section 2.4.3) does not affect C_{prms} at center-span when Reynolds number is low.

B. $\alpha = 10^\circ$, 13.5° , 15° and 45°

The results obtained are presented in Figs 6.20 and 6.21 . Only two workers, Pocha (1971) and Lee (1974), are known to have publised measurements of C_{prms} distribution on a square section cylinder at incidence. Because of the different values of α investigated comparison between these works and the present one is only possible at $\alpha = 15^\circ$ and 45° . The

agreement between the present results and those of Lee (1974) can be seen, at $\alpha = 15^{\circ}$ and 45°, to be generally good on face D and very good on faces A, B, and C - see Fig 6.21. Pocha (1971) results are generally slightly higher than the present ones but the trends indicated by the two sets of results are, see Fig 6.21, the same.

Some interesting aspects of the C_{prms} distribution are:

Point (a) On face A, the position of minimum C_{prms} can be seen in Figs 6.20 and 6.21 to move from the center of the face to the leading edge. A/B as α increases from 0° to 45°. This movement corresponds to the movement of the stagnation position from the center of face A to the leading edge as α increases from 0° to 45° - see point A2 of section 6.3.1.

Point (b) At $\alpha = 13.5^{\circ}$ and 15°, the C_{prms} distribution on face B has a minimum near the trailing edge B/C - see Fig 6.20 and 6.21. This minimum is well defined at $\alpha = 15^{\circ}$ and is located, see Fig 6.21, at approximately 0.3 diameter from edge B/C. At $\alpha = 45^{\circ}$ the position of this minimum is, see Fig 6.21, at the leading edge of face B.

Pocha (1971) has reported for a square section cylinder that the position of the above minimum is the same as the flow reattachment position. The position of maximum mean pressure, C_p, on face B has also been linked when $13.5^{\circ} < \alpha < 45^{\circ}$ to the flow reattachment position - see under point A3 of section 6.31. One thus expects the position of maximum C_p to coincide with that of minimum C_{prms}. By comparing Figs 6.20 and 6.21 respectively to Figs 6.4 and 6.5 it can be seen that at $\alpha = 13.5^{\circ}$ and 15°, particularly $\alpha = 15^{\circ}$, that the position of minimum C_{prms} on face B is upstream that of maximum C_p. It would thus seem that flow reattachment occur upstream of the position of maximum mean pressure - at least when α is close to 13.5°

Point (c) It was expected, as in Pocha (1971) and section 1.4.1.2B, that the behaviour of $(C_{prms})_{B/C}$ and $(C_{prms})_{B/D}$ (see Footnotes (6.1) for definition)

as α increases will be similar to that of $-C_{pb}$. Surprisingly $(C_{prms})_{8/c}$ is maximum, see Fig 6.22, somewhere around $\alpha = 5^{\circ}$ unlike $-C_{pb}$ which, see Fig 6.15, is maximum at $\alpha = 0^{\circ}$. Furthermore in the range $15^{\circ} < \alpha < 45^{\circ}$ $(C_{prms})_{8/c}$ remains practically constant whereas $-C_{pb}$ increases with α.

The present results also show, see Fig 6.22, that $(C_{prms})_{8/B}$ (see Footnotes (6.1) for definition) is maximum around $\alpha = 5^{\circ}$ instead of at $\alpha = 0^{\circ}$ as indicated by the results of Pocha (1971). This is in accordance with Rockwell (1976) who measured pressures at two tappings on face B and reported that C_{prms} is maximum at each tapping when $\alpha = 5^{\circ}$.

6.5 CORRELATION OF FLUCTUATING PRESSURES

6.5.1 Spanwise Correlation

Measurements of spanwise correlation at $\alpha = 0^{\circ}$ are presented in Fig 6.24. As in Vickery (1966) the present results can be seen, particularly at large spanwise separation, to lie within a broad band.

As the separation increases from 0 to 4d the correlation decreases rapidly from 1.0 to 0.5 - see Fig 6.24. Beyond a separation of 4d the correlation falls steadily to zero at a separation of 11.5 d. In direct contrast Wilkinson (1974) measurements indicate, see Fig 6.24, that the correlation decreases very rapidly from 1.0 at zero separation to 0.5 at a separation of only 2.1d and then falls to 0 at a separation of only 7 d. The present results agree very closely, see Fig 6.24, with those of Vickery (1966), Pocha (1971) and Lee (1974). The spanwise correlation length indicated by the present results is 5.6 diameters.

6.5.2 Chordwise Correlation at $\alpha = 0^{\circ}$

Some measurements of chordwise correlation on a side face at center-span

---

Footnotes (6.1) As in Fig 6.22 C_{prms} at the centers of faces B, C and D are denoted respectively by $(C_{prms})_{8/B}$, $(C_{prms})_{8/c}$ and $(C_{prms})_{8/D}$,

with $\alpha = 0^{\circ}$ are presented in Fig 6.25 . The correlation is seen to be higher than 0.92 over the mid 75% of the side face. Because of the high chordwise correlation there is practically no difference between the sectional R.M.S lift coefficients, C_{Lrms} , of 1.21 and 1.23 estimated respectively with and without consideration of chordwise correlation. These values of C_{Lrms} are close to the results of other workers. The values of C_{Lrms} measured by Vickery (1966), Pocha (1971), Lee (1974) and Wilkinson (1974) have already been reported, see section 1.4.1.2, to lie between 1.2 and 1.4 .

6.6 SPECTRAL MEASUREMENT

6.6.1 Shedding Frequency Measurement

6.6.1.1 Description of Spectra

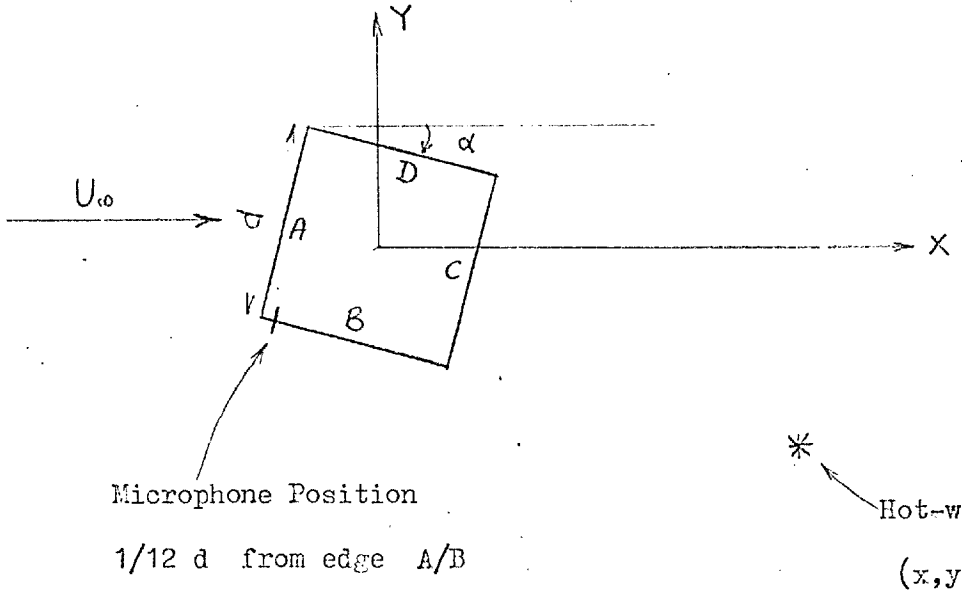

Sketch (6.3)

A selection of the power spectra of pressure and velocity fluctuations, that were computed as described in section 3.6.1.1, is presented in Figs 6.28 and 6.29 . Measurements were made at selected values of α in the range $0 \leq \alpha \leq 45^{\circ}$. The positions of the pressure transducer and hot-wire are indicated in sketch (6.3). All tests were conducted at a Reynolds number of 4.74×10^4 .

As expected there is on each plot shown in Figs 6.28 and 6.29 , a dominant peak centered on the vortex shedding frequency, f_s . This peak can be seen to be fairly broad-band - an indication that the shedding frequency in fact varies around f_s . Due to mains and electronic noise, there are also sharp line-like peaks at 50 cycles and its harmonics. At $\alpha = 0^\circ$ 5° and 10° small peaks can also be discerned at $2f_s$ and $3f_s$.

Surprisingly there are, at $\alpha = 5^\circ$ and 10° , broad-band peaks centered at approximately $f_{s/2}$ in both the spectra of velocity and pressure - see in particular the plots of Figs 6.28 and 6.29 that correspond to $\alpha = 10^\circ$. These low frequency peaks could be caused by oscillation of the vortex formation position. At $\alpha = 40^\circ$ and 45° there are also very broad-band peaks at approximately $f_{s/4}$ in the spectra of pressure but not in those of velocity - see Figs 6.28.

6.6.1.2 Variation of Strouhal Number, S , with α

$$S = \frac{f_s d}{U_\infty}$$

Because the Reynolds number is fixed, the movement of the dominant peaks in Figs 6.28 and 6.29 indicate the variation of S with α . Thus S can be seen in Fig 6.28 , despite the small scale, to be maximum and minimum at $\alpha = 13.5^\circ$ and 45° respectively.

The Strouhal number calculated from spectral analysis (i.e. from the frequency of the dominant spectral peaks) are presented in Fig 6.26 together with the S obtained by 'peak-count' on a storage oscilloscope. Also shown in Fig 6.26 are the results of Bearman & Trueman (1971), Pocha (1971) and Lee (1974) together with the values of S estimated from the spectral plots in the unpublished work of Rockwell (1976). Bearman & Trueman (1971) measured f_s using a wave analyser whereas Pocha (1971) obtained f_s by 'peak-count' on an oscilloscope. Lee (1974) did not state how he determined S .

Despite the scatter Fig 6.27 indicate that at $\alpha = 0^\circ$ there is a trend towards lower values of S for higher values of Reynolds number. For this

reason comparison between the present values of S and those of other workers will be limited only to qualitative trends.

All measurements indicate, see Fig 6.26, that S is maximum when α is approximately 13.5° and that for $13.5^\circ < \alpha < 45^\circ$ S decreases with increasing α. Discrepancies exist when α is between 0° and 13.5°. The measurements of Lee and Pocha and the values of S obtained in the present study by 'peak-count' indicate that S increase with increasing when $0 < \alpha < 13.5^\circ$. [This suggests that Lee's results were obtained by 'peak-count' !]. The S obtained in the present study by spectral analysis decreases slightly at first with increasing α when $0 < \alpha < 10^\circ$ before rising very sharply to a maximum at $\alpha = 13.5^\circ$ - see Fig 6.26. Rockwell's (1976) S (also obtained from spectral analysis) also decreases slightly with increasing α when α is between 0° and 8° before rising sharply to a maximum at $\alpha \approx 13.5^\circ$.

Consideration will now be given to two reasons why when α is between 0° and 13.5°, the trend indicated by the 'peak-count' values of S could be different from that of the spectral analysis. Firstly the 'peak-count' results could be inaccurate partly because a significant amount of energy is present, see $\alpha = 5^\circ$ and 10° of Figs 6.28 and 6.29, at other frequencies apart from f_s and also because of the variation in the shedding frequency shown by the spectral broadening around f_s. Variation of shedding frequency will particularly affect the 'peak-count' results because only about 20 cycles (or even less) of the vortex shedding signal are usually averaged at a time when f_s is counted on oscilloscope. By contrast the present spectral analysis method involved the processing of over 7000 cycles of the vortex shedding signal. Secondly, and perhaps more important, the 'peak-count' results indicate the average shedding frequency whereas the spectral analysis results indicate the dominant shedding frequency Even neglecting inaccuracies in measurement, the dominant vortex shedding frequency, f_s, could be different from the average vortex shedding frequency if,

as spectral analysis suggests, the spectral peak is not symmetrical about f_s.

6.6.2 The spectral distribution of sectional fluctuating pressures

6.6.2.1 Description of Spectra

The digital analysis required for the determination of spectra has been outlined in section 3.6.1 .

At $\alpha = 0^\circ$ the spectra of fluctuating pressure were measured around the mid-section of the model at the seven positions shown in Fig 6.31 . The resulting spectral plots are presented in Fig 6.30 (a) to (g) . On each plot f_s , $2f_s$ and $3f_s$ correspond to Frequency (log) 1.65 , 1.95 and 2.13 respectively. f_s denotes the vortex shedding frequency.

At the center of the front face (Hole 8/A) , the pressure fluctuations are so small that the pressure spectrum (Fig 6.30 (a)) is dominated by line-like peaks at 50 cycles and its harmonics. These peaks are caused by mains hums and electronic noise. The vortex shedding activities can still however be discerned in the background of Fig 6.30 (a) in the form of a broad-band peak at $2f_s$.

Fig 6.30 (c) to (e) show that on the side face (Holes 6/B , 8/B and 6/B) most of the pressure energy is centered on the shedding frequency f_s , and that there is also a small amount of energy at $2f_s$. The same is also true on the parts of the front and back faces, particularly the former, that are near the corners - see Fig 6.30 (a) and (f) .

There are, surprisingly, fairly prominent spectral peaks at $3f_s$ on the side and back faces near to the trailing corners - see Fig 6.30 (e) and (c) . This phenomenon has not been previously reported in the literature.

The pressure spectrum at the center of the back face (Fig 6.30 (g)) has a dominant peak at $2f_s$ and no peak at f_s . There is a large amount of energy at the low frequency end of the spectrum which is due to the pressure fluctuations caused by turbulence in the wake.

6.6.2.2 Estimation of the mean square pressure in the spectral peaks

Due to normalisation, the total area under each spectral plot is unity .

The power centered on a peak frequency f_p , was estimated from the product of P_1 and Δf_p where P_1 and Δf_p are respectively the power at f_p and the bandwidth of the half-power points .

The results obtained in this way are presented in Fig 6.31 . Fig 6.31 shows very clearly the redistribution of spectral energy on the side face. For example near the trailing edge of the side face (Hole 6/D) the percentage of the total pressure energy at f_s , $2f_s$, and $3f_s$ are 66.9% 6.9% and 3.9% respectively. By contrast at the center of the side face (Hole 8/B) the percentage of energy at f_s and $2f_s$ are 82.2% and 1.6% respectively and there is no discernable peak at $3f_s$. This redistribution of spectral energy is largely responsible for the reduction observed, see Fig 6.25 , in the chordwise correlation of pressure fluctuations at large separations. Previous workers, see for example Wilkinson (1974), have attributed reductions in chordwise pressure fluctuations to both turbulence and to differences in phase angles at the vortex shedding frequency.

Fig 6.31 shows, as reported earlier, that the spectral peaks at $3f_s$ are prominent only near the trailing corners - Holes 6/D and 6/C .

6.6.3 Variation of the phase angle at the shedding frequency around the mid-section

The measurement procedure is described in section 3.5.1.2 (e) . The measured phase angles are presented in Fig 6.32 .

It can be seen in Fig 6.32 that the phase differences measured over the mid 83% of the top and bottom side faces are respectively only 13.9° and 14.7° . This shows that changes in phase angle do not contribute much to the decreases shown, see Fig 6.25, in the chordwise pressure correlation at large separations. Two points that are situated one diameter apart on the upper and lower side faces can be seen in Fig 6.32 to have a phase difference of 180° . By contrast points 6 and 3 that are located one diameter apart on the front and back faces respectively can be seen to have only a phase difference of 6.5° .

On the whole the phase angle around the section does not vary in any consistent way with downstream distance. For example on the side faces the phase angle increases, see Fig 6.32, with downstream distance. By contrast around the lower corners A/D and D/C of Fig 6.32 the phase angle can be seen to decrease with increasing downstream distance.

Chaplin (1970) has reported from measurement of correlation time delay that the phase angle on the side face of a square section decreases with increasing downstream distance. He suggested that this can be explained in terms of velocity fluctuations in the shear layers passing downstream at the flow separation velocity $K U_\infty$. According to this hypothesis the phase angle near the leading edge of the side face should lead that near the trailing edge by about 29° . This hypothesis is not borne out by the present results. On the side faces, the phase angle near the leading edge can be seen in Fig 6.32 to lag that near the trailing edge by approximately 14° . The present results thus suggest an influence (produced by the forming vortex?) that is convected upstream.

6.6.4. Longitudinal vortex spacing a/d

The measurement procedure has been described in section 3.5.1.2 . The results obtained at $\alpha = 0^\circ$, 10° , 13.5°, 20° and 45° are presented in Fig 6.33 together with the results of Chaplin (1970) at $\alpha = 0^\circ$, 15° , 30° and 45° . The locations of the reference microphone and the moving hot-wire are also indicated in Fig 6.33 .

Some of the interesting points are:

1) The values of a/d measured at $\alpha = 0^\circ$ with the wake hot-wire at vertical heights (Y/d) of 3.0 , 3.7 and 5.0 are practically the same - see Fig 6.33 (a) . This is in contrast to Simmons (1974A) who reported that on a D -shaped body, a/d is dependent on Y/d when Y/d is between 0.5 and 3.0 . Simmons used two hot-wires that were mounted together a fixed distance apart in a holder that was transversed in the flow. In the present study the phase angle of a single moving

hot-wire was, see section 3.5.1.2 , compared to that of a fixed microphone that was connected to the side face of the model.

Observations at $R_e = 10^4$ and 4.74×10^4 can also be seen to yield the same value of a/d at $\alpha = 0^\circ$.

2) Despite the difference in experimental methods the a/d of 6.58 and 6.88 that were measured at $\alpha = 0$ and 45° respectively are, see Fig 6.33 (a) , close to the values of 6.54 and 7.26 reported by the Chaplin (1970) . Chaplin used two hot-wires, one fixed and the other traversed up and downstream.

3) In the present study a/d appears to be inversely proportional to the Strouhal number S . This is demonstrated in Fig 6.33 (b) where the product of S and a/d is shown at each α to be practically constant at 0.85 when the U_∞ used to form S is uncorrected for wind tunnel blockage effects. When S is corrected for blockage effects $S.(a/d)$ is, see Fig 6.33 (b) , practically constant at 0.81 .

$S.(a/d)$ is the convection velocity of the vortices.

6.7 CALCULATION OF $\frac{\Gamma_o}{\pi U_\infty d}$, ϵ AND b/a FROM THE MEASURED VALUES OF C_D , S , C_{pb} AND a/d

$\frac{\Gamma_o}{\pi U_\infty d}$ — the non-dimensional strength of each vortex in the wake.

b — lateral spacing between the rows of vortices .

b/a — vortex spacing ratio .

ϵ — the circulation defect ratio i.e. the fraction of the vorticity in the shear layers that is present in the discrete vortices of the wake.

The circulation K_v discharged into the wake per second by each shear layer can be shown, see for example Roshko (1954A) to be:

$$K_v = \frac{1}{2} U_s^2 \qquad \text{- - - - - - - - - - (6.2)}$$

where U_s is the separation velocity.

Measurements, see for example Fage & Johansen (1927) and Simmons (1974B) have shown that U_s is related to the free stream velocity, U_∞, and the base pressure coefficient, C_{pb}, by:

$$\left(\frac{U_s}{U_\infty}\right)^2 = \left(1 - C_{Pb}\right) \qquad \text{- - - - - - - - - - - (6.3)}$$

From equations (6.2) and (6.3) the non-dimensional vorticity, $\frac{K_V}{f_s . \pi U_\infty d}$, that is shed by each shear layer per cycle of vortex shedding is:

$$\frac{K_V}{f_s . \pi U_\infty d} = \frac{1 - C_{Pb}}{2\pi S} \qquad \text{- - - - - - - - (6.4)}$$

$$\text{so that} \quad \epsilon = \left(\frac{\Gamma_o}{\pi U_\infty d}\right)\left(\frac{1 - C_{Pb}}{2\pi S}\right)^{-1} \qquad \text{- - - - - - (6.5)}$$

When the wake of a bluff body is idealized as a double row of staggered point potential vortices, the associated drag can be expressed, see for example Bearman & Trueman (1971), in the form:

$$C_D . S = \frac{4}{\pi}\left(1 - \frac{U_s}{U_\infty}\right)\left(\frac{U_s}{U_\infty}\right)^2 \left[\coth^2\left(\frac{\pi b}{a}\right) + \left(\frac{U_\infty}{U_s} - 2\right)\frac{\pi b}{a}\coth\left(\frac{\pi b}{a}\right)\right] \qquad \text{- - - (6.6)}$$

$$\text{where} \quad \frac{U_s}{U_\infty} = 1 - S . a/d \qquad \text{- - - - - - - - - (6.7)}$$

The non-dimensional strength of each potential vortex in the vortex street is (see Milne-Thomson (1965) :

$$\frac{\Gamma_o}{\pi U_\infty d} = \frac{2 U_s a}{\pi U_\infty d}\coth\left(\frac{\pi b}{a}\right) \qquad \text{- - - - - - (6.8)}$$

Fig 6.34 shows the values of $C_D . S$ obtained from equation (6.6) against b/a using the values of $\frac{U_s}{U_\infty}$ (i.e $1 - S\,a/d$) indicated by Fig 6.33 (b) .

The predictions of b/a (and hence $\frac{\Gamma_o}{\pi U_\infty d}$, b/d and ϵ) were

obtained from Fig 6.34 by using the measured values of C_D , S and a/d . When C_D and S were corrected for wind tunnel blockage effects, $C_D.S$ was so small at $\alpha = 10^\circ$ that no value of b/a could be obtained from the corresponding $\frac{U_s}{U_\infty} = 0.19$ curve of Fig 6.34 . It was therefore decided to use uncorrected values of C_{pb} , C_D and S and obtain values of b/a from the corresponding curve (i.e. $\frac{U_s}{U_\infty} = 0.15$) in Fig 6.34. The results obtained in this way are presented in Fig 6.35 .

Fig 6.35 shows that:

(i) The predicted values of the circulation defect ratio , ϵ , are 0.54 when $0^\circ \leq \alpha \leq 10^\circ$ and 0.59 when $13.5^\circ \leq \alpha \leq 45^\circ$. These values of ϵ are within the range $0.403 \leq \epsilon \leq 0.66$ said, see Berger & Wille (1972), to have been observed on bluff bodies by various workers. The predicted values of b/a (and hence $\frac{\Gamma_o}{\pi U_\infty d}$ and b/d) thus seem reasonable.

(ii) The curves of $-C_{pb}$ (Fig 6.15) and $\frac{\Gamma_o}{\pi U_\infty d}$ Fig 6.35) follow the same trend except that $-C_{pb}$ is maximum at $\alpha = 0^\circ$ whereas $\frac{\Gamma_o}{\pi U_\infty d}$ is maximum at $\alpha = 45^\circ$. It was reported in Chapter 1 that the overall level of surface fluctuating pressures, C_{prms} , around a section, particularly in the separated flow region, follow the trend in $-C_{pb}$ when α is in the range $0 < \alpha < 45^\circ$. Within this range of α , changes in $-C_{pb}$ (and hence C_D) have been attributed, see Chapter 1 , to opposite changes in the vortex formation region length l_f . The predicted $\frac{\Gamma_o}{\pi U_\infty d}$ thus support the notion that decreases in l_f are accompanied by increases in $\frac{\Gamma_o}{\pi U_\infty d}$, $-C_{pb}$, C_D and C_{prms} and vice versa.

(iii) As α increases from 0° to 10° the predicted lateral spacing of the vortex street, b/d (Fig 6.35) , increases whereas the measured drag coefficient, C_D (Fig 6.16) , decreases. Beyond $\alpha = 13.5^\circ$, b/d (Fig 6.35) remains virtually constant whilst C_D (Fig 6.16) increases with α . Assuming that the wake width is proportional to b/d , these

results suggest that changes in C_D are not accompanied by corresponding changes in wake width. This does not agree with Lee (1974). Lee suggested that as α increases from 0° to 13.5°, decreases in C_D are accompanied by decreases in wake width which in turn produce increases S It has already been demonstrated in section 6.6.1.2 that because the waveform of the vortex shedding signal is complex, S would incorrectly appear to increase as α increases from 0° to 10° if the 'peak-count' method is used to determine the shedding frequency.

Griffin & Ramberg (1975) have also reported that for a vibrating circular cylinder C_D, calculated from the vortex street drag formula, increases as b/d decreases.

6.8 PHOTOGRAPHS OF PRESSURE TRANSDUCER SIGNALS AT 0° INCIDENCE

The photographs of the simultaneous signals of surface pressure fluctuations indicated by two pressure transducers placed along the center-line of the side faces are presented in Fig 6.36 . The cross-correlation coefficient, R_{P12}, between the two pressure signals are indicated underneath each picture together with the values of f_s and R_e.

Some points to note in Fig 6.36 are:

(i) The amplitudes of pressure fluctuations are highly modulated. This can be seen in Fig 6.36 (a) , (c) and (d) where the horizontal or time scales are compressed to emphasize the amplitude modulations. Previous workers on stationary circular and square cylinders have reported similar findings. This phenomenon could be caused by variations in the strength of the vortices.

(ii) The shedding frequency at a given windspeed is not constant. This is demonstrated in the upper trace of Fig 6.36 (b) where there are slightly more shedding cycles to the left than to the right of the center-line. The broadening of the spectral peaks at f_s has already been attributed, see section 6.6.1.1, to variations in shedding

frequency.

(iii) The correlation between the upper and lower traces of Fig 6.36 (a) can be seen to be excellent but there is, see Fig 6.36 (b), a phase shift of 180° . As an indication of the very high degree of correlation, the amplitude modulation can be seen in Fig 6.36 (a) to occur simultaneously in both the upper and lower traces. Measurement also indicate that R_{P12} is -0.97 .

Fig. 6.36 (b) support the earlier finding, see section 6.6.3, that two points located one diameter apart on the upper and lower side face have a phase difference of 180° .

(iv) When the pressure transducers are separated on the top side face by a spanwise distance of 2.5 diameters, the correlation is, see Fig 6.36 (c) , still good although occasionally the amplitude modulations do not appear simultaneously in both pressure traces. The phase angle (not shown) between the two pressure signals was observed to vary.

At a spanwise separation of 9.5 diameters the pressure can be seen in Fig 6.36 (d) to be poorly correlated. The amplitude modulations are no longer correlated. The phase difference between the two pressure signals is random. For example the phase difference can be seen to change from approximately 180° at one instant (Fig 6.36 (e)) to 0° at another instant (Fig 6.36 (f)) .

The above results are consistent with measurement of spanwise correlation of fluctuating pressures, $R_{(P,Z)}$, shown in Fig 6.24 . The variation in phase angle reported above is largely responsible for the scatter observed, see Fig 6.24 , in the data of $R_{(P,Z)}$ when the spanwise separation is large.

6.9 FURTHER DISCUSSION

THE FLOW AROUND THE CYLINDER

Bearman & Trueman (1971) investigated the flow around rectangular

cylinders with values of d/h (where d is section depth and h is section width normal to the wind direction) ranging from 0.2 to 1.205. They explained the decreased base suction (and hence decreased drag) which they measured for higher values of d/h, when $d/h > 0.6$, by suggesting that the vortices are forced to form further downstream because of the influence of the trailing corners. For the section with $d/h = 0.62$, they demonstrated that increasing the incidence from 0° produced the same effect as increasing d/h - i.e. decrease base suction. They argued that this is to be expected because flow visualisation shows, when $d/h = 0.6$, that the shear layers pass close to the trailing corners as the vortices form very close to the base. Therefore, the trailing edge corner (when the model is set at incidence) and the downstream corners (when $\alpha = 0$ and d/h increases beyond 0.62) would produce the same effect - in this case force vortices to form further downstream. For a square section cylinder ($d/h = 1.0$) at $\alpha = 0^\circ$, flow visualisation, see for example chapter 5 and Pocha (1971), shows that the vortices form close to the base with the separated shear layers passing close to the trailing corners. It is therefore to be expected that setting the section at incidence will produce the same effects (on C_D and $-C_{pb}$) as increasing d/h when $\alpha = 0^\circ$ provided flow does not reattach (see footnotes (6.2)). By comparing the present results (Figs 6.15 and 6.16) to Figs 1.1A and 1.1B it can be seen that this is the case. It thus appears that for a square section cylinder, it is the trailing corner that forces the vortices to form further downstream (as observed by for example Pocha (1971) when α increases from 0° to 13.5° thereby decreasing C_D and $-C_{pb}$.

Footnotes (6.2) In smooth flow, flow reattachment occur on rectangular cylinders that are set at $\alpha = 0^\circ$ when $d/h > 2.5$, see Parkinson (1971), and on square section cylinders when $\alpha \approx 13.5^\circ$.

Up to reattachment (see footnotes (6.2)) the S versus α curve of the square section cylinder, Fig (6.26), can be seen to similar to the S versus d/h , Fig (1.1A), curve of rectangular cylinders. In both figures S decreases before reattachment and rises very sharply at reattachment. This further suggests that the same mechanism, the influence of the trailing corners, governs the flow in both cases. Some workers, see for example Pocha (1971) and Lee (1974), have reported (incorrectly - see section 6.6.1.2) that S increases steadily with α when $0^\circ < \alpha < 13.5^\circ$ thus masking, at least to some extent, the flow mechanism involved. A factor that could contribute to the initial decrease in S as α increases from 0° is , see Bearman & Trueman (1971), increased diffusion. The shear layers could be more diffused and thicker at small α because the distance from the separation points to the position of vortex formation is (see Pocha (1971)) longer at small α ($\alpha < 13.5^\circ$) than at $\alpha = 0^\circ$ Another factor that could contribute to this initial decrease in S is the divergence of the shear layers. As α increases from 0° the frontal width , $d(\cos\alpha + \sin\alpha)$, (see sketch 6.4) , increases. Thus if there is to be no flow reattachment, the shear layers would diverge if they are to completely clear the corners of the body.

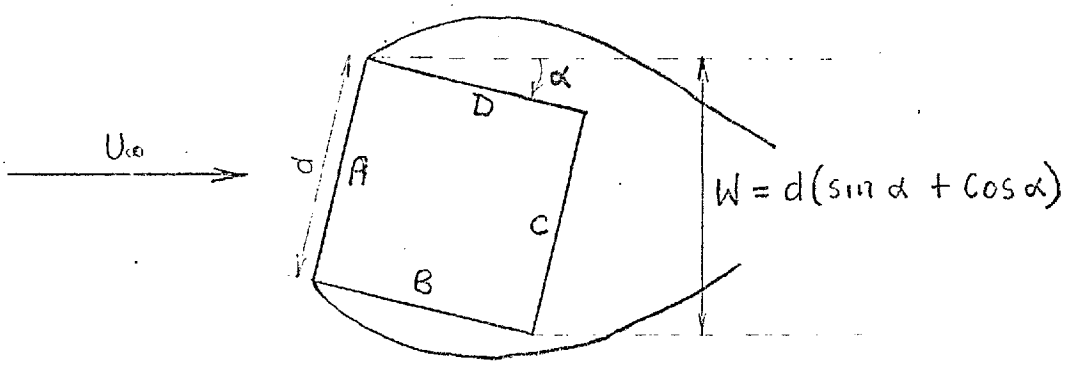

Sketch (6.4)

When $\alpha = 45^{\circ}$ flow visualisation, see for example Pocha (1971), show that the vortices form very close to the trailing corner D/C . Thus it is to be expected that as α decreases from 45° , the trailing corner would interfere with the shear layer and so force vortices to form further downstream thereby decreasing $-C_{pb}$ and C_D . Results obtained on a square section cylinder when $13.5^{\circ} < \alpha < 45^{\circ}$ appear to demonstrate this effect. Beyond $\alpha = 13.5^{\circ}$ $-C_{pb}$ and C_D can be seen in Figs 6.15 and 6.16 to decrease with increasing α .

After flow reattachment ($\alpha > 13.5^{\circ}$) the frontal width , $d(\cos\alpha + \sin\alpha)$, is also the lateral distance between the shear layers at separation. Thus as α increases from 13.5° , $d(\cos\alpha + \sin\alpha)$ also increases causing the shear layers to diverge . This could cause the decrease in S , see Fig 6.26 , as α increases from 13.5° to 45° .

CHAPTER 7

OSCILLATING MODEL : RESULTS AND DISCUSSION.

7.1 POWER SPECTRA OF PRESSURE AND VELOCITY FLUCTUATIONS.

7.1.1 Description of Power Spectra.

Power spectra of pressure and velocity fluctuations were computed digitally (as described in sections 2.5 and 3.6) for A/D = 0.05 , 0.10 and 0.25 with $\frac{U_\infty}{f_N d}$ ranging from 3.0 to 15.0 . A selection of the results obtained is presented in Figs 7.40 to 7.43 .

In the following discussion, f_N and f_s denote respectively the body oscillation frequency and the natural vortex shedding frequency. The uncorrected Strouhal number, S or $\frac{f_s d}{U_\infty}$, is taken as 0.134 so that $f_s / f_N = 0.134 \left(\frac{U_\infty}{f_N d}\right)$. Thus resonance (i.e. $f_N = f_s$) occurs at $\frac{U_\infty}{f_N d} = \frac{1}{0.134}$ or 7.46 . This resonant value of $\frac{U_\infty}{f_N d}$ will be denoted by $\left(\frac{U_\infty}{f_N d}\right)_R$.

As in the stationary model flow case, the spectra measured during model oscillation have sharp line-like peaks at 50 cyles (Frequency (log)$\approx$1.70) and its harmonics. These peaks are caused by mains and electronic noise.

The characteristics of the spectra measured at the different values of A/D will now be described.

A/D = 0.05 and 0.10

The spectra measured at A/D = 0.05 and 0.10 can be classed into two regimes of $\frac{U_\infty}{f_N d}$ namely the 'lock-in' regime and the 'off-look' regime. In the lock-in regime vortices are shed at the body's frequency so that the spectral plots are dominated by peaks at f_N and its harmonics - see Fig 7.40(f) to (i) and Fig 7.41(c) & (d) . These harmonics are, at A/D = 0.10 , particularly prominent in the spectra of velocity fluctuations at $\frac{U_\infty}{f_N d}$ of about 7.8 , see Fig 7.41 (d) , which, see sections 7.3 and 7.4 , is the value of $\frac{U_\infty}{f_N d}$ at which lift pressure fluctuations and spanwise correlations are maximum.

Compared to both the body displacement pressure spectrum (Fig 7.40(a)) and the line-like peaks at 50 cycles, the dominant peaks in the spectra are, see Fig 7.40(f) to (i) and Fig 7.41(c) & (d), broad band. This shows that there is still some variation in vortex shedding frequency during 'lock-in'.

In the off-lock regimes, the spectra of pressure and velocity fluctuations have peaks at two basic frequencies namely the body frequency, f_N, and another frequency, f_{so}, which is close to f_s particularly when $\frac{U_\infty}{f_N d}$ is far above $\left(\frac{U_\infty}{f_N d}\right)_R$. There are also peaks in the spectra at combinations and harmonics of these basic frequencies particularly the difference, $f_N - f_{so}$, and the sum $f_N + f_{so}$. The complexity of the spectra can be seen in Fig 7.40 (c), (d), (e), (j), (k) and (l) and also in Fig 7.41 (a), (b), (e) and (f). Davies (1975) has also observed similar peaks in the spectra of velocity fluctuations measured downstream of three oscillating cylinders namely a D-shaped cylinder, a flat plate and a triangular cylinder. It is interesting to note that the results of workers like Otsuki et al (1974) and Protos et al (1968), who measured total fluctuating lift, indicate peaks only at f_N and f_{so}. This is because some of the frequency components of pressure fluctuations will be in phase across the wake and so cannot contribute to total fluctuating lift.

The potential flow model presented in Chapter 4, also predicts peaks at f_N, f_{so}, $f_N + f_{so}$, $f_N - f_{so}$, in the off-locked flow case. This model also predicts across-the-wake phase relations between the frequency components of velocity fluctuations that agree with those measured by Davies (1975).

A/D = 0.25

Power spectra of pressure and velocity fluctuations at A/D = 0.25 are presented in Fig 7.42 and 7.43 respectively.

When $\frac{U_\infty}{f_N d}$ is between 5.37 and 7.18, there is a very pronounced

peak in each spectral plot at f_N - see plots (a) to (c) of Fig 7.42 and 7.43 . This peak is surrounded by very small peaks which are particularly noticeable in the spectra of velocity fluctuations at $\frac{U_\infty}{f_N d}$ = 5.70 and 6.50 - see plots (a) and (b) of Fig 7.43. These small peaks were not present at A/D = 0.05 and 0.10 .

Between $\frac{U_\infty}{f_N d}$ of 7.18 and 9.0 the dominant peak is again at f_N but there is a prominent low frequency peak in the spectra - see plots (c) to (f) of Figs 7.42 and 7.43 . This low frequency peak may not be the difference frequency, $f_{so} - f_N$, because there is no other distinct peak near f_N that can be taken as f_{so} . Furthermore flow visualisation at $\frac{U_\infty}{f_N d} \approx 7.5$ shows, see Chapter 5 , that vortices are shed at the body frequency f_N .

At $\frac{U_\infty}{f_N d}$ = 10.00 and 12.67 there is, apart from the dominant peak at f_N , a peak just below $2f_N$ (see Fig 7.42 (g) and (h)) which, judging from the flow visualisation of Chapter 5, is caused by vortex shedding. However unlike the previously described A/D = 0.05 and 0.10 flow cases, ther appears to be no prominent peaks at $f_{so} - f_N$, and $f_N + f_{so}$.

7.1.2 Variation of the shedding frequency, f_{so} , with $\frac{U_\infty}{f_N d}$

For A/D = 0.05 and 0.10 , the variations of f_{so} with $\frac{U_\infty}{f_N d}$ are presented in Fig 7.39 . Also shown on the same figure are the variations of f_s/f_N with $\frac{U_\infty}{f_N d}$ when S = 0.134 and 0.130 .

When $\frac{U_\infty}{f_N d}$ is much higher than the resonant windspeed $\left(\frac{U_\infty}{f_N d}\right)_R$, f_{so}/f_N can be seen in fig 7.39 to be equal to f_s/f_N if is S= 0.130 . This would seem to suggest that S should be more nearly 0.130 instead of the value of 0.134 chosen. Some difficulty was experienced in choosing S because some of the tests were conducted by keeping f_N constant and varying U_∞ . S has been shown in Chapter 6 to be weakly dependent on U_∞ (i.e. Reynolds number).

At $A/D = 0.10$, f_{so}/f_N can be seen to be lower than f_s/f_N at low values of $\frac{U_\infty}{f_N d}$. This finding is in agreement with those of Otsuki et al (1974) . The lock-in regime (the range of $\frac{U_\infty}{f_N d}$ in which $f_{so}/f_N = 1.0$) can be seen in Fig 7.39 to be wider at $A/D = 0.10$, where lock-in starts and ends approximately at $\frac{U_\infty}{f_N d}$ of 7.0 and 8.8 respectively, than at $A/D = 0.05$ where the boundaries of the lock-in are given by $\frac{U_\infty}{f_N d}$ of 7.0 and 8.0 . An increase of the lock-in zone with cylinders amplitude is consistent with the findings of previous workers on various bluff body shapes like square section cylinders (see for example Otsuki et al (1974)), circular cylinders (see for example Koopman (1967)), and triangular cylinders (see for example Protos et al (1968)).

7.2 MEAN PRESSURE MEASUREMENTS

7.2.1 Spanwise distribution of base pressure

Measurements of the spanwise distribution of base pressure are presented in Figs 7.1 A & B . The oscillating model measurements were made at $A/D = 0.10$ and three values of $\frac{U_\infty}{f_N d}$ namely 4.34 , 7.0 and 17.9 that corresponds respectively to Reynolds number, R_e , of 1.11×10^4, 1.86×10^4 and 4.74×10^4 . The stationary model measurements were made at $R_e = 1.09 \times 10^4$ and 4.74×10^4 .

Some of the interesting points indicated by Figs 7.1 A and B are :

(a) When R_e is fixed, both the shape of the spanwise base pressure distribution and the extent of the span over which the base pressure is uniform are unaffected by oscillation. This is shown by curves (1) and (3) of Fig 7.1 A and the two curves in Fig 7.1 B .

(b) The extent of the central span over which the base pressure, C_{PB} , is uniform is higher at lower values of R_e . For example C_{PB} can be seen in Figs 7.1 A and B to be uniform over approximately the mid 80% and 40% of the span respectively at $R_e = 1.09 \times 10^4$

and 4.74×10^4 . The decrease in the spanwise uniformity of base pressure at high R_e is caused, at least in part, by the clearance holes on the wind tunnel side walls. (As reported in section 2.4.3 , the models that were oscillated were mounted externally through circular slots, or clearance holes, on the wind tunnel side walls). Results obtained on the stationary model at $R_e = 4.74 \times 10^4$ indicate, see section 6.2.2, that these clearance holes reduce the extent of the span over which the base pressure is uniform.

(c) The results obtained at $R_e = 1.09 \times 10^4$, 1.11×10^4 and 1.86×10^4 (i.e. Fig 7.1A) are particularly interesting because the tests values of windspeed and body oscillation frequency, f_N , were chosen such that wake synchronisation occurred either around $f_N = 8.6$ (i.e. $R_e \approx 1.1 \times 10^4$) or around $f_N = 14.9$ (i.e. $R_e \approx 1.9 \times 10^4$) . Since it was reported under point (a) above that oscillation did not alter the extent of the span over which the base pressure is uniform, the results of Fig 7.1A, particularly curves ① & ② , indicate that the base pressure is uniform over most of the span during lock-in.

7.2.2 Measurements of mean pressure at centre-span.

7.2.2.1 Variation of base pressure with $\frac{U_\infty}{f_N d}$.

Fig 7.2 shows the variation of $(C_p)_{s/c}$, the base pressure coefficient at the centre tapping with $\frac{U_\infty}{f_N d}$ at $A/D = 0.10$ and 0 ($A/D = 0$ indicates that model is stationary).

During an experiment both A/D and f_N were held constant whilst the tunnel windspeed, U_∞ , was changed to vary $\frac{U_\infty}{f_N d}$. Increases in $\frac{U_\infty}{f_N d}$ therefore corresponds to increases in Reynolds number. The increase of base suction with $\frac{U_\infty}{f_N d}$ shown by the stationary model results of Fig 7.2 demonstrates an influence of R_e . This influence of R_e has already been discussed in section 6.2.1 .

For A/D = 0.10 , Fig 7.2 shows that with increasing $\frac{U_\infty}{f_N d}$, the base suction, $-(C_p)_{B/C}$, rises very rapidly from 0.42 at $\frac{U_\infty}{f_N d} = 3.6$ to a local maximum of 1.58 at $\frac{U_\infty}{f_N d} = 7.3$ (this maximum value of $-(C_p)_{B/C}$ is, see Fig 7.2, just under the stationary cylinder value) and then falls equally rapidly to a local minimum of 1.28 at $\frac{U_\infty}{f_N d} = 8.43$ before rising steadily towards the stationary cylinder value. Thus for an oscillating square section cylinder, $-(C_p)_{B/C}$, is always less than the stationary cylinder value and maximum base suction occurs during lock-in when $\frac{U_\infty}{f_N d}$ is below the resonant value $\left(\frac{U_\infty}{f_N d}\right)_R$. The measurements of Davies (1975) on an oscillating triangular cylinder with vertex pointing downstream, indicate a similar trend. By contrast the results of Davies (1975) for a flat plate and D-shaped cylinder indicate, during lock-in, that $-(C_p)_{B/C}$ is far higher than the stationary cylinder value and also that $-(C_p)_{B/C}$ is maximum when $\frac{U_\infty}{f_N d}$ is above $\left(\frac{U_\infty}{f_N d}\right)_R$. The face presented to the flow (i.e. the forebody) of each of the above cylinders is flat. The dissimilarity in the behaviour of base suction therefore demonstrate the influence of the afterbody.

7.2.2.2 <u>The distribution of mean pressure around the mid-section.</u>

Figs 7.3 A, B, and C show the distributions of C_p around the mid-section at A/D = 0.10 and $\frac{U_\infty}{f_N d} = 5.3$, 7.53 , 7.90 , 8.46 and 11.91 . The stationary model results presented in Figs 7.3 A , B and C are respectively for $\frac{U_\infty}{f_N d} = 5.3$, 7.53 and 11.91 . The results for A/D = 0.25 and $\frac{U_\infty}{f_N d} = 6.51$, 7.03 , 7.18 , 7.54 , 7.81 and 8.51 are presented in Fig 7.4 together with the corresponding stationary cylinder results. The values of the sectional drag coefficient, C_D , and the average mean pressure coefficient on the base, C_{pb} ,are indicated on each figure.

For $A/D = 0.10$ (Figs 7.3 A, B and C) the shape of the base pressure distribution is not very much changed by oscillation. This means that changes in $-(C_p)_{s/c}$ (the base pressure at the centre tapping) indicate corresponding changes in $-C_{pb}$ and hence C_D . Thus Fig 7.2 indicates that during lock-in C_D at $A/D = 0.10$ has a maximum value, which is less than the stationary cylinder value, at $\frac{U_\infty}{f_N d} = 7.3$ and a minimum value at $\frac{U_\infty}{f_N d} = 8.43$. This agrees qualitatively with the results of Wilkinson (1974) who measured C_D on a square section cylinder oscillating at A/D of 0.022 to 0.134 . Wilkinson's results indicate that with decreasing $\frac{U_\infty}{f_N d}$, C_D decreases from approximately the stationary cylinder value at a very high value of $\frac{U_\infty}{f_N d}$ to a local minimum at $\frac{U_\infty}{f_N d} \approx 8.70$ (i.e. $f_N/f_s = 0.85$) and then rises until a maximum value equal to the stationary cylinder value is attained at $\frac{U_\infty}{f_N d} = 6.72$ and then falls off.

For $A/D = 0.25$, Fig 7.4 shows that C_D is again less than the stationary cylinder when $\frac{U_\infty}{f_N d}$ is at and around resonance. Results for $\frac{U_\infty}{f_N d} = 6,51$, 7.03 and 7.18 , can be seen in Fig 7.4 to indicate practically the same values of mean pressures whereas those for $\frac{U_\infty}{f_N d} = 7.54$, 7.81 and 8.51 indicate that the suctions on the and back faces decrease with increasing $\frac{U_\infty}{f_N d}$. This is unlike the $A/D = 0.10$ flow case for which base pressures are highly sensitive to $\frac{U_\infty}{f_N d}$ throughout lock-in (see Fig 7.2) and for which, in addition, there are well-defined maximum and minimum in the base suction at $\frac{U_\infty}{f_N d}$ of 7.3 and 8.43 respectively.

It is interesting to use Figs 7.3 and 7.4 to deduce the behaviour of $\frac{1 - C_{pb}}{2\pi S}$ during lock-in. As shown in chapter 6 , $\frac{1 - C_{pb}}{2\pi S}$ is equal to the non-dimensional vorticity that is shed by each shear layer per cycle of vortex shedding. The variation of $\frac{1 - C_{pb}}{2\pi S}$ with $\frac{U_\infty}{f_N d}$ could thus give some information about the likely trend in $\frac{\Gamma_o}{\pi U_\infty d}$, the non-dimensional strength of each vortex in the

wake. Values of $\frac{1 - C_{pb}}{2\pi S}$ calculated from the lock-in base pressure distributions at $A/D = 0.10$ and 0.25 are compared with the stationary cylinder values in Table 1 where it can be seen that the oscillating model values of $\frac{1 - C_{pb}}{2\pi S}$ are less than the stationary cylinder values. Assuming that the value of the circulation defect ratio, $\frac{\Gamma_o}{\pi U_\infty d}\left(\frac{1 - C_{pb}}{2\pi S}\right)^{-1}$, during wake synchronisation is, as indicated by the results of Davies (1975) for a D-shaped cylinder, very close to the stationary cylinder value, Table 1 suggests that the value of the non-dimensional vortex strength during wake synchronisation is less than the stationary cylinder value.

It is interesting to compare the mean pressure distribution observed on the oscillating square section cylinder during lock-in with that on a stationary cylinder placed normal to a turbulent free stream. Compared to the stationary cylinder smooth flow case, it can be seen in Fig 7.3B that, at $A/D = 0.10$ and $\frac{U_\infty}{f_N d} = 7.53$, 7.90 and 8.46, the side face suction is more pronounced around the centre but less pronounced towards the rear so that the lower base suction on the osoillating model is accompanied by a more marked pressure recovery towards the rear of the side face. A similar effect is demonstrated more markedly at $A/D = 0.25$ and $\frac{U_\infty}{f_N d} = 6.51$, 7.03, 7.18, 7.54, 7.81 and 8.51 by Fig 7.4 . A similar finding was also reported by Wilkinson (1974) for a square section cylinder undergoing synchronised oscillation at $A/D = 0.134$. The above is similar to the finding of Lee (1974) whose measurements on a stationary square section cylinder at 0^o incidence indicate that free stream turbulence increase the suction around the centre of the side faces whilst decreasing the suction both at the rear of the side faces and on the base. Now previous workers, see for example Mulhearn (1973), have reported that free stream turbulence brings the separated shear layers closer to the stationary square section cylinder when the angle of incidence is small. The above similarity in

mean pressure distribution therefore suggests that in the mean, the shear layers are closer to the body during lock-in than when the model is stationary.

The above result suggests a way of explaining the overall behaviour of C_D and $-C_{pb}$ during lock-in. It was reported in chapter 6 that for the stationary square section cylinder, the shear layers pass very close to the trailing edge corners - so close that when the section is put at incidence, the influence of the trailing edge corners on the shear layers force vortices to form further downstream thus decreasing $-C_{pb}$ and C_D. Thus when the shear layers on the oscillating model come closer to the body during lock-in as suggested by the mean pressure distribution, the shear layers would, assuming that there is no steady flow reattachment, be deflected by the trailing edge corners. This deflection would decrease the base suction (and hence the drag) by increasing the base cavity volume and/or by increasing the distance to vortex formation. The values attained by $-C_{pb}$ and C_D during lock-in would thus be generally less than the stationary cylinder values.

According to the above discussion, the mean flow pattern would be as in sketch (7.1)

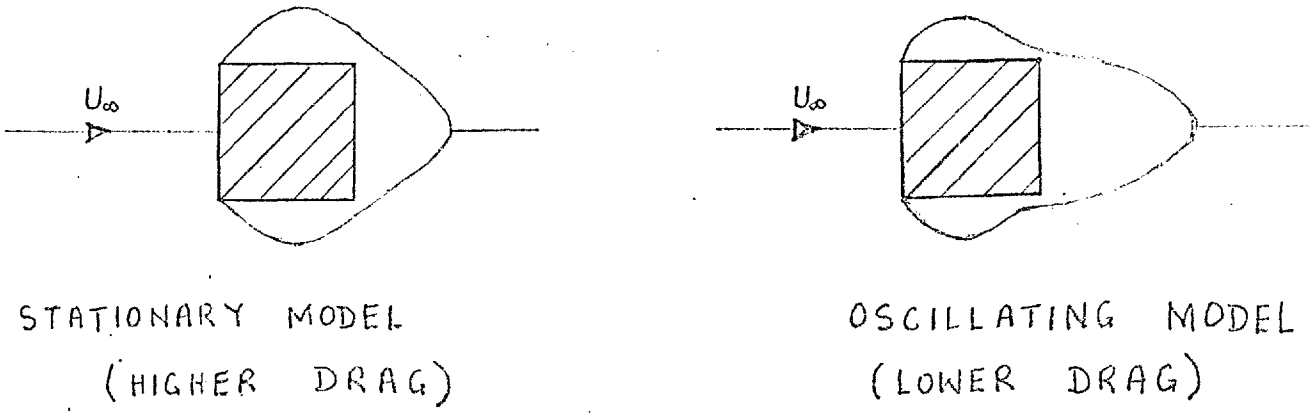

Sketch (7.1).

7.3 FLUCTUATING PRESSURE MEASUREMENTS.

7.3.1 Notations.

$(C_{Prms})_s$ - the RMS pressure coefficient on the stationary model.

$(C_{Prms})_a$ - the RMS pressure coefficient produced by the air in the tubing connecting the model surface to the transducer's diaphragm.

$(C_{Prms})_v$ and $(C_{Prms})_f$ are the RMS pressure coefficients on the model during oscillation in still ($U_\infty = 0$) and flowing fluid respectively.

C_{Lrms} and C_{Drms} - denote the sectional values of RMS lift and drag coefficients respectively. The subscripts f, s, a and v have the same meanings as for C_{Prms} above. For example $(C_{Lrms})_f$ indicate the sectional RMS lift coefficient on the model during oscillation in flowing fluid.

7.3.2 Correction of RMS pressures for the acceleration effects produced by the column of air in the tubing connecting the model surface to the transducer's diaphragm.

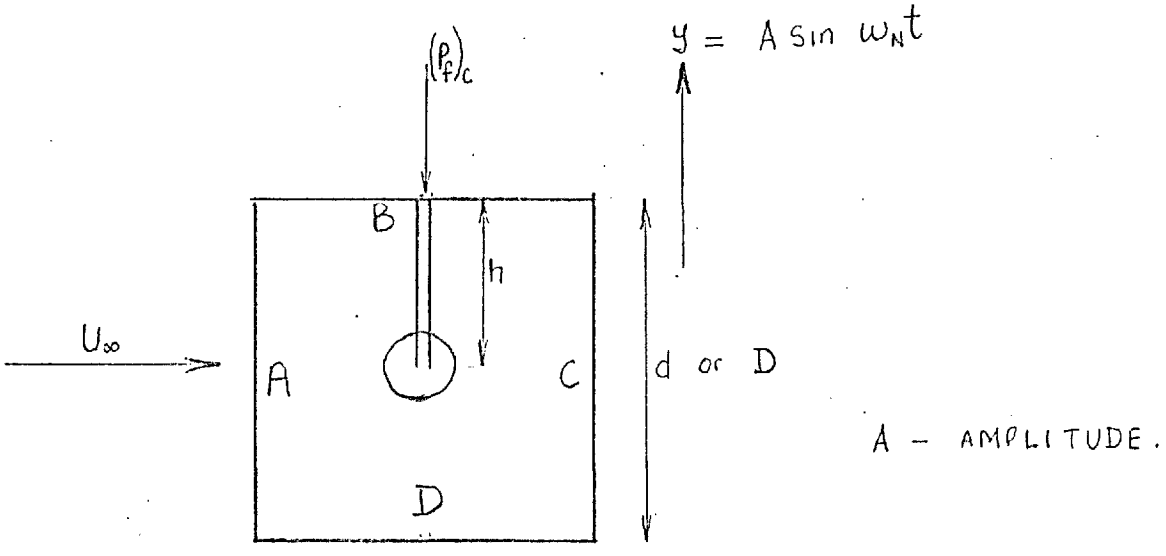

Sketch (7.2)

Because it was not possible to mount the pressure transducer flush

with the model surface, fluctuating pressure will be generated within the pressure tube connecting the model surface to the transducer diaphragm due to the acceleration of the model. Assuming that the air column within the pressure tube oscillates with the model as a solid body, the fluctuating pressure, P_a , generated at the transducer's diaphragm by the acceleration of the air column within the pressure tube is given, see sketch (7.2), by :

$$P_a = \rho \ddot{y} h \qquad \text{(7.1)}$$

where $\ddot{y}$ is the acceleration of the model and h is the vertical height of the air column - see sketch (7.2).

For $y = A \sin \omega_N t$, $\ddot{y} = -A \omega_N^2 \sin \omega_N t$

so that

$$P_a = -\rho h A \omega_N^2 \sin \omega_N t \qquad \text{(7.2)}$$

The <u>lift</u> fluctuations produced by P_a is thus in phase with the cylinder's displacement.

Expressed as a pressure coefficient

$$\left(C_{Prms}\right)_a = \frac{(P_{rms})_a}{\frac{1}{2}\rho U_\infty^2} = \sqrt{2} \cdot 4\pi^2 \cdot \frac{h}{D} \frac{A}{D} \left(\frac{f_N d}{U_\infty}\right)^2 \qquad \text{(7.3)}$$

Denoting the pressure measured by the transducer by P_f ,

$$\overrightarrow{(P_F)_c} = \overrightarrow{P_f} - \overrightarrow{P_a} \qquad \text{(7.4)}$$

where $(P_f)_c$ is the pressure generated on the model surface by the flow. The arrows in equation (7.4) indicate that the quantities are vectors in the phase plane (i.e. they have magnitude as well as

phase angles).

P_a will therefore generally affect the magnitude as well as the phase angle ϕ of $(P_f)_c$. Both the rms values of P_f and the phase angle ϕ will thus generally require correction.

The pressure spectra presented in Figs 7.40 to 7.43 show that P_f is generally a multi-frequency force especially when the wake frequency is not synchronised or 'locked' to the body frequency. Thus to determine $(P_f)_c$ and ϕ_c (the subscript c indicates corrected quantities) from measurements of P_f and ϕ in flowing fluid one must also measure the component of P_f at the body frequency, f_N , and the phase angle between this component and the body's displacement. This is obviously very time-consuming especially when, as in the present work, numerous measurements of P_f and ϕ are involved.

When the model is oscillating in still air ($U_\infty = 0$) most of the power of P_f is concentrated at f_N when A/D is small. P_f has also the same phase relationship with the cylinder's displacement as P_a . $(P_f)_c$ can thus be obtained by substracting P_a from P_f algebraically. Typically P_a is about 40% of P_f (see Fig 7.21) so that the correction involved is large. These corrections were not applied to the results obtained at A/D = 0.05 and 0.10 because both $(C_{Prms})_f$ and $(C_{Prms})_V$ are plotted on the same graph and it was not thought prudent to correct the RMS pressure coefficients measured during oscillation in still air, i.e. $(C_{Prms})_V$, without correcting the ones measured during oscillation in flowing fluid - i.e $(C_{Prms})_f$.

Consider the flow cases A/D = 0.05 and 0.10 . The correction to $(C_{Prms})_f$ is significant only at low values of $\frac{U_\infty}{f_N d}$ (values below lock-in) where $(C_{Prms})_a$ is large. From measurements of $(C_{Prms})_f$ and ϕ on the side faces during lock-

in, it was estimated that the correction to $(C_{prms})_f$ and ϕ is very small (about 2%). Therefore ϕ will require correction only in the off-locked flow cases whereas $(C_{prms})_f$ will require correction only at low values of $\frac{U_\infty}{f_N d}$ (i.e. below lock-in).

The situation at A/D = 0.25 is different. $(C_{prms})_a$ is a substantial fraction of $(C_{prms})_f$ at all values of $\frac{U_\infty}{f_N d}$ in the range of measurement i.e. $\frac{U_\infty}{f_N d} \lesssim 12.0$. The corrections to $(C_{prms})_f$ and ϕ will therefore be generally appreciable. Estimates of the corrected values of $(C_{prms})_f$, $(C_{prms})_V$ and ϕ are indicated respectively in Figs 7.21 and 7.44. To obtain these estimates all the power of $(C_{prms})_f$ was assumed to be concentrated at f_N. This assumption is, judging from the spectra of pressure fluctuations (see Fig 7.42), quite reasonable.

7.3.3 Fluctuating pressure measurements: results and some discussion.

7.3.3.1 Variation of $(C_{prms})_f$ at each tapping around the mid-section

Measurements of fluctuating pressures at the centre section of the model at A/D = 0 (stationary model), 0.05, 0.10 and 0.25 and $\frac{U_\infty}{f_N d}$ in the range $4.0 < \frac{U_\infty}{f_N d} \lesssim 12.0$ are presented in Figs 7.5 to 7.22. Measurements at A/D = 0 and 0.10 were made at sixteen tappings distributed around the mid-section whilst those at A/D = 0.05 and 0.25 were made principally at one tapping positioned at the centre of the top side face. The values of $(C_{prms})_V$, the RMS pressure coefficient on the model during oscillation in still air, are indicated on each figure.

Consider first the behaviour of $(C_{prms})_f$ at low values of $\frac{U_\infty}{f_N d}$ (i.e. $\frac{U_\infty}{f_N d} \lesssim 5.5$). $(C_{prms})_f$ and $(C_{prms})_V$ are generally, fairly close to each other and follow the same trend - see Figs 7.5 to 7.22. The higher the value of A/D, the closer the values of $(C_{prms})_f$ and $(C_{prms})_V$ - compare Figs 7.5, 7.20 and 7.21. This behaviour of $(C_{prms})_f$ demonstrates that inertia effects are

significant at low values of $\frac{U_\infty}{f_N d}$.

There are, however, departures from the above general trend. There is, on the back face - see Figs 7.12 to 7.15 , a small peak in $(C_{prms})_f$ at $\frac{U_\infty}{f_N d} \approx 5.1$ but for lower values of $\frac{U_\infty}{f_N d}$ $\left(\frac{U_\infty}{f_N d} < 4.5\right)$ $(C_{prms})_f$ is close to and follows the trend in $(C_{prms})_v$. There is also a peak at $\frac{U_\infty}{f_N d} = 4.7$ in the $(C_{prms})_f$ measured at tappings 2/D (Fig 7.8) and 6/D (Fig 7.7) which are the tappings on the side face next to the trailing corner. For tapping 2/D (this is the tapping nearest the trailing corner), this peak is, see Fig 7.8, even more pronounced than the peak near resonance. It is as if there are two flow natural frequencies: one near $f_N = f_s$ and the other near $2f_N = f_s$.

Consider next the behaviour of $(C_{prms})_f$ in the range $6.2 \lesssim \frac{U_\infty}{f_N d} \lesssim 8.8$ when $A/D = 0.10$. The lock-in range, which for $A/D = 0.10$ lies between $\frac{U_\infty}{f_N d}$ of 7.0 and 8.75 , is included in this range. There is a peak in $(C_{prms})_f$ at a value of $\frac{U_\infty}{f_N d}$ that will be denoted by $\left(\frac{U_\infty}{f_N d}\right)_{max}$. At each tapping around the mid-section, the value of $(C_{prms})_f$ at $\left(\frac{U_\infty}{f_N d}\right)_{max}$ is see Figs 7.5 to 7.19 , higher than the stationary cylinder value, $(C_{prms})_s$. On the side faces, $(C_{prms})_f$ is, at $\left(\frac{U_\infty}{f_N d}\right)_{max}$, about 130% of $(C_{prms})_s$ except at the tapping nearest the trailing corner (Fig 7.8) where $(C_{prms})_f$ attains a level as high as 150% of $(C_{prms})_s$. Away from $\left(\frac{U_\infty}{f_N d}\right)_{max}$, $(C_{prms})_f$ falls to two minima at $\frac{U_\infty}{f_N d} \approx 8.75$ and 6.2 which are most marked at the tappings on the side faces - see Figs 7.5 to 7.12 . The above variations in $(C_{prms})_f$ are similar to that of $-(C_p)_{8/c}$ (Fig 7.2), the base suction at the centre tapping, except that $-(C_p)_{8/c}$ has a peak at $\frac{U_\infty}{f_N d} = 7.30$ and only one local minimum at $\frac{U_\infty}{f_N d} \approx 8.4$ — see Fig 7.2.

The above measurements suggest that during lock-in, maximum sectional

RMS lift coefficient, $(C_{Lrms})_{max}$, occurs at $\frac{U_\infty}{f_N d} \approx 7.8$ (i.e. above resonance) whereas maximum sectional RMS drag coefficient, $(C_{Drms})_{max}$, occurs between $\frac{U_\infty}{f_N d}$ of about 7.1 and 7.3 (below resonance). At A/D = 0.10, maximum sectional mean drag coefficient, $(C_D)_{max}$, occurs, see section 7.2, at $\frac{U_\infty}{f_N d} = 7.3$. The position of $(C_D)_{max}$ therefore seemsto agree closely with that of $(C_{Drms})_{max}$ but is different from that of $(C_{Lrms})_{max}$. Wilkinson (1974) has also reported that $(C_{Lrms})_{max}$ and $(C_D)_{max}$ do not occur at the same value of $\frac{U_\infty}{f_N d}$. Wilkinson did not report measurements of drag RMS pressures but he reported that $(C_{Lrms})_{max}$ appeared to occur at the value of $\frac{U_\infty}{f_N d}$ for which the sectional mean drag is minimum.

Except at A/D = 0.25, $(C_{Prms})_f$ approaches $(C_{Prms})_s$ assymptotically at high values of $\frac{U_\infty}{f_N d}$ ($\frac{U_\infty}{f_N d} > 8.75$). At A/D = 0.25, $(C_{Prms})_f$ falls rapidly with $\frac{U_\infty}{f_N d}$ up to the maximum value of $\frac{U_\infty}{f_N d}$ investigated - see Fig 7.21 and 7.22.

Measurements of $(C_{Prms})_f$ at the centre of the side face at A/D = 0.05, 0.10 and 0.25 are compared with the stationary cylinder value in Fig 7.22. These results show, see Fig 7.22, that at a given value of $\frac{U_\infty}{f_N d}$, $(C_{Prms})_f$, generally does not follow any consistent trend with A/D except in the range $7.1 < \frac{U_\infty}{f_N d} \lesssim 8.3$ where $(C_{Prms})_f$ increases with A/D. It can also be seen in Fig 7.22 that during lock-in $(C_{Prms})_f$ has a maximum at approximately $\frac{U_\infty}{f_N d} = 7.8$, regardless of the value of A/D. This maximum value of $(C_{Prms})_f$ is not very sensitive to A/D - see curve (3) of Fig 7.32.

7.3.3.2 <u>The distribution of $(C_{Prms})_f$ around the mid-section.</u>

The distributions $(C_{Prms})_f$ around the mid-section at A/D = 0.10 and $\frac{U_\infty}{f_N d}$ = 4.8, 6.25, 7.0, 7.5, 7.8, 8.75 and 12.0 are presented in Figs 7.24 to 7.30. For comparison purposes,

the stationary model results (A/D = 0) are presented in Fig 7.23 . All values of $(C_{Prms})_f$ are taken from Fig 7.5 to 7.19 .

There is not much change in the C_{Prms} distribution on the front and back faces during oscillation. On each of these faces, $(C_{Prms})_f$ generally falls with distance from the edges to a minimum at the centre - a trend similar to that on the stationary model. During lock-in, $(C_{Prms})_f$ rises markedly at the edges thus making the minimum at the centres of the side and back faces more pronounced - see Figs 7.26 to 7.28 .

The distribution of $(C_{Prms})_f$ on the side faces differ at high and low values of $\frac{U_\infty}{f_N d}$. At high values of $\frac{U_\infty}{f_N d}$ ($\frac{U_\infty}{f_N d} > 6.75$) , particularly during lock-in, oscillation changes the level of $(C_{Prms})_f$ but the shape of the distribution is close to that on the stationary model - compare Figs 7.26 to 7.29 with 7.23 . By contrast for low values of $\frac{U_\infty}{f_N d}$, see $\frac{U_\infty}{f_N d} = 4.8$ (Fig 7.24) and $\frac{U_\infty}{f_N d} = 6.25$ (Fig 7.25) , $(C_{Prms})_f$ rises very sharply towards the trailing edge of the side face thus changing the shape of the distribution totally from that on the stationary model.

The distributions of $(C_{Prms})_f$ on the side face at $\frac{U_\infty}{f_N d} = 7.85$ and A/D = 0 , 0.10 and 0.25 are presented in Fig 7.31. For the stationary cylinder (A/D = 0) , it can be seen that the shape of the distribution in Fig 7.31 differs slightly from the one in Fig 7.23 . This is because more data points are available for Fig 7.31 . The results for A/D = 0.10 again demonstrate that synchronised oscillation at this amplitude changes the level but not the shape of the $(C_{Prms})_f$ distribution. By contrast the results for A/D = 0.25 indicate that synchronised oscillation at high amplitude changes both the level and the shape of the distribution.

7.3.3.3 Comparison between the present results and Wilkinson's (1974)

Only Wilkinson (1974) is known to have published measurements of surface RMS pressures on an oscillating square section cylinder. His values of $(C_{Prms})_f$ are generally very much higher than the present ones. This can be seen by comparing the present variation of $(C_{Prms})_f$ at the centre of the side face, Fig 7.22 , with that of Wilkinson (Fig 1.17B) . To illustrate this further, the peak values of $(C_{Prms})_f / (C_{Prms})_S$ during lock-in are plotted in Fig 7.32 together with the values of $(C_{Prms})_f / (C_{Prms})_S$ and $(C_{Prms})_V / (C_{Prms})_S$ attained at $\frac{U_\infty}{f_N d} = 4.5$. At lock-in the present peak values of $(C_{Prms})_f / (C_{Prms})_S$ are very much lower than those of Wilkinson - compare curves (2) and (3) of Fig 7.32 . For example at A/D = 0.10 the present results (curve (3) of Fig 7.32) indicate a peak value of 1.35 whereas Wilkinson results (Curve (2) of Fig 7.32) indicate a peak value of 2.2 . The discrepancy between the values of $(C_{Prms})_f / (C_{Prms})_S$ is even larger at $\frac{U_\infty}{f_N d} = 4.5$. For example Wilkinson result (Curve (1) of Fig 7.32) indicate a value of 2.3 at A/D = 0.10 whereas the present results (Curve 4 of Fig 7.32) indicate only 0.96 . It is to be noted that Wilkinson reported a $(C_{Prms})_f$ of 0.65 which is comparable with the present value of 0.71 . It is thus fair to compare the two results in this way.

Another point of disagreement between the present results and Wilkinson's is the following : Wilkinson's results show, see Fig 1.17B, that $(C_{Prms})_f$ is always higher than $(C_{Prms})_S$ and that $(C_{Prms})_f$ inoreases with A/D in the range of his experiment (his measurements were made between $\frac{U_\infty}{f_N d}$ of about 3.8 and 14.9 and his maximum value of A/D was 0.134) . The present results (Fig 7.22) show that $(C_{Prms})_f$ generally does not follow a consistent trend with A/D except in the narrow range $7.1 \lesssim \frac{U_\infty}{f_N d} \lesssim 8.3$ where $(C_{Prms})_f$ increases with A/D . Furthermore it was observed

in the present study that $\left(C_{prms}\right)_f$ can, under certain circumstances, fall to a value as low as $\frac{1}{3}\left(C_{prms}\right)_s$ particularly at around $\frac{U_\infty}{f_N d} = 6.15$ - see for example Fig 7.5 .

Wilkinson's work has already been reviewed in section 1.4.2.2 . It was noted in this review that he used such a long length of tubing between the pressure tappings and the transducer that his dynamic calibration indicated, see Fig 1.12, resonance and phase shift in his frequency range of interest. It was also remarked that 'flappings' of the tubing during oscillation will create spurious pressure signals particularly at high values of f_N/f_s (i.e. low values of $\frac{U_\infty}{f_N d}$) . Because of these sources of inaccuracy it was concluded in the review that Wilkinson results can at best indicate only broad qualitative trends The interested reader is referred to section 1.4.2.2 where a more detailed discussion of Wilkinson work is presented.

7.4 CORRELATION OF FLUCTUATING PRESSURES.

7.4.1 Spanwise Correlation, $R_{(P,Z)}$

Measurements of $R_{(P,Z)}$ were made along the centreline of the top side face at $A/D = 0.05$, 0.10 and 0.25 and $5.0 < \frac{U_\infty}{f_N d} < 12.0$. The results obtained at spanwise separations, Z , of 2.5 , 6.0 , 9.5 and 13.25 body diameters are presented in Figs 7.33 and 7.34 . The spanwise distribution of $R_{(P,Z)}$ indicated by these figures at several values of $\frac{U_\infty}{f_N d}$ are presented in Figs 7.35 and 7.36 .

It can be seen in Figs 7.33 and 7.34 that at $A/D = 0.10$, $R_{(P,Z)}$ is, at high values of $\frac{U_\infty}{f_N d}$, higher at $f_N = 8.6$ cps than at $f_N = 13.9$ cps . This means that under the present test condition, $R_{(P,Z)}$ is lower at higher values of R_e . This may not however be a genuine Reynolds number effect because it was reported in section 7.2 that the spanwise uniformity of mean base pressure is less at higher values of R_e . This behaviour was attributed, at least in part, to the

existence of clearance holes on the wind tunnel side walls.

The results of Figs 7.33 and 7.34 indicate that the values of $R_{(P,Z)}$ are higher during oscillation than when the model is stationary. These figures also show that $R_{(P,Z)}$ generally increases with A/D within the range of $\frac{U_\infty}{f_N d}$ investigated.

The behaviour of $R_{(P,Z)}$ at A/D = 0.05 and 0.10 is, during lock-in, broadly similar to that of $(C_{Prms})_f$. Take for example the flow case A/D = 0.10 for which lock-in starts and ends at approximately $\frac{U_\infty}{f_N d}$ of 7.0 and 8.75 respectively. As $\frac{U_\infty}{f_N d}$ increases from about 6.2 , $R_{(P,Z)}$ rises very rapidly, particularly at large spanwise separations, to a broad maximum centered at approximately $\frac{U_\infty}{f_N d} = 7.8$ see Figs 7.33 and 7.34 . This maximum value of $R_{(P,Z)}$ is very close to unity even when the spanwise separation , Z , is as large as 13.25 body diameters - see Fig 7.34 . $R_{(P,Z)}$ maintains this maximum value up to about $\frac{U_\infty}{f_N d} = 8.3$ and then falls very rapidly as $\frac{U_\infty}{f_N d}$ increases to about 8.75 which is the end of the lock-in range. This is similar to the behaviour of the $(C_{Prms})_f$ measured at the centre of the side face, see Fig 7.5 , except that the peak in $(C_{Prms})_f$ at $\frac{U_\infty}{f_N d} \approx 7.8$ is sharper. The measurements of Wilkinson (1974) also indicate that during lock-in, the position of maximum $R_{(P,Z)}$ agrees closely with that of maximum $(C_{Prms})_f$ - where $(C_{Prms})_f$ is measured at the centre of the side face.

The plots of $R_{(P,Z)}$ against spanwise separation, Z , again show, see Fig 7.35 and 7.36, that $R_{(P,Z)}$ on the oscillating model is higher than that on the stationary model. Curves (1) of Figs 7.35 (A/D = 0.10) and 7.36 (A/D = 0.25) also further demonstrate the excellent spanwise correlation that exists within lock-in range - especially in the central part of the range where lift RMS pressures are maximum.

7.4.2 Chordwise Correlation including estimates of the peak values of sectional RMS lift coefficient during lock-in.

Measurements of chordwise correlation at $A/D = 0.10$ and $\frac{U_\infty}{f_N d} = 7.85$ are compared in Fig 7.37 with the stationary cylinder results. Other values of chordwise correlations measured at $A/D = 0.10$ and 0.25 are presented in Table 4 .

The results indicate that oscillation generally decreases chordwise correlation. This is demonstrated in Fig 7.37 where the fall in chordwise correlation towards the trailing edge of the side face can be seen to be more marked during lock-in than when the model is stationary. Table 4 also show that there is generally a decrease in chordwise correlation at $A/D = 0.10$ and 0.25 especially near the trailing edges of the side faces - see in particular cases (2) and (4) of Table 4 .

The sectional lift coefficient, $(C_{Lrms})_f$, was calculated at $A/D = 0.10$ and $\frac{U_\infty}{f_N d} = 7.85$ by using the distributions of $(C_{Prms})_f$ and the chordwise correlation presented in Figs 7.31 and 7.37 respectively. The value of $(C_{Lrms})_f$ calculated without taking chordwise correlation into consideration was found to be 5% higher than the value obtained by the method of section 3.6.3 which takes chordwise correlation into account. This flat rate value of 5% was used to estimate the values of $(C_{Lrms})_f$ at $A/D = 0.05$ and 0.25 when $\frac{U_\infty}{f_N d} = 7.85$ (the few measurements made, see Table 4 , indicate that there is little difference between the chordwise correlations at $A/D = 0.10$ and 0.25 when $\frac{U_\infty}{f_N d}$ is about 7.85). For $A/D = 0.25$, $(C_{Lrms})_f$ was calculated from the distribution of $(C_{Prms})_f$ presented in Fig 7.31 whereas it was assumed, at $A/D = 0.05$, that the distribution of $(C_{Prms})_f$ on the side face during lock-in is, as suggested by the results obtained at $A/D = 0.10$, similar to that on the stationary model. The values of $(C_{Lrms})_f$ obtained at $\frac{U_\infty}{f_N d} = 7.85$ are called the peak

values (or the maximum value) because this is the value of $\frac{U_o}{f_N d}$ at which the lift RMS surface pressures are maximum during lock-in. The peak values of $(C_{Lrms})_f$ obtained in the present study are 1.51, 1.65 and 1.95 at A/D = 0.05 , 0.10 and 0.25 respectively whereas the stationary cylinder value of $(C_{Lrms})_f$ is 1.33 . These values of $(C_{Lrms})_f$ are not corrected for wind tunnel blockage effects. They are however corrected for the acceleration effects of the column of air in the tubing connecting the model surface to the transducer's diaphragm. The corrections applied to $(C_{Lrms})_f$ are 2.6% , 2.9% and 3% at A/D = 0.05 , 0.10 and 0.25 respectively.

The above peak values of sectional $(C_{Lrms})_f$ are compared in Fig 7.38 with those of Wilkinson (1974) and the values estimated from the total force measurements of Otsuki et al (1974) and Nakamura & Mizota (1975). For all workers except Wilkinson (1974), the ordinate of Fig 7.38 is $\overrightarrow{(C_{Lrms})_f} - \overrightarrow{(C_{Lrms})_V}$ which is the difference when $(C_{Lrms})_V$ is substracted vectorially (i.e. phase angles taken into account) from $(C_{Lrms})_f$. In Wilkinson's case, $(C_{Lrms})_f$ has been plotted because his measurement indicate that $(C_{Lrms})_V$ is very much smaller than $(C_{Lrms})_f$. $\overrightarrow{(C_{Lrms})_f} - \overrightarrow{(C_{Lrms})_V}$ is plotted because as reported in section 1.4.2.2 , both Nakamura & Mizota (1975) and Otsuki et al (1974) measured $L_{in(t)}$ which is the component of the total force $L(t) - V(t)$ at the body's frequency where $L(t)$ and $V(t)$ denote the total fluctuating lift on the square section cylinder when oscillated respectively in flowing fluid and still air. Since the present results and Wilkinson's (1974) indicate very high spanwise correlation during lock-in particularly at high values of A/D , the peak value of the average RMS lift coefficients calculated from the results of Otsuki et al (1974) and Nakamura & Mizota (1975) will be very close to the peak sectional C_{Lrms} particularly at high values

of A/D . Thus if agreement between the measurements is good, the results of Otsuki et al and Nakamura & Mizota should approach the present results and Wilkinson's at high values of A/D . The present results can be seen in Fig 7.38 to indicate this trend. By contrast the results of Otsuki et al and Nakamura & Mizota can be seen in Fig 7.38 to diverge away from those of Wilkinson at high values of A/D . Thus the present values of $(C_{Lrms})_f$ appear to be in good agreement with those of Otsuki et al and Nakamura & Mizota by contrast to Wilkinson's values which appear to be much too high.

7.5 THE PHASE ANGLE, ϕ , BETWEEN THE FLUCTUATING LIFT AND CYLINDER'S DISPLACEMENT

7.5.1 Present Results.

The phase angle, ϕ, by which the lift fluctuation, measured at the centre of the side face, leads cylinder's displacement was computed digitally (as described in section 3.6.1) at A/D = 0.05 , 0.10 and 0.25 . The resulting variations of ϕ with $\frac{U_\infty}{f_N d}$ are presented in Fig 7.44 .

For each value of A/D , very large variation can be observed, see Fig 7.44 , in ϕ just above the resonance windspeed, $\left(\frac{U_\infty}{f_N d}\right)_R$. ϕ = 0 can also be seen to occur <u>above</u> resonance at value of $\frac{U_\infty}{f_N d}$, $\left(\frac{U_\infty}{f_N d}\right)_{\phi=0}$; that increases with A/D . For example $\left(\frac{U_\infty}{f_N d}\right)_{\phi=0}$ is (see Fig 7.44) 7.93 , 8.43 and 10.13 at A/D of 0.05 , 0.10 and 0.25 respectively. Beyond $\left(\frac{U_\infty}{f_N d}\right)_{\phi=0}$, ϕ rises very sharply with $\frac{U_\infty}{f_N d}$ up to a maximum value of between 45° and 60° and then decreases. For A/D = 0.05 and 0.10 , this maximum value of ϕ occurs very close to the end of the lock-in range. Below $\left(\frac{U_\infty}{f_N d}\right)_{\phi=0}$, ϕ falls very sharply to a minimum value of between -98° and -105° . Again for A/D = 0.05 and 0.10 , the position of this minimum is very close to the low $\frac{U_\infty}{f_N d}$ end of the lock-in range. Below

the position of this minimum, ϕ rises rapidly with decreasing $\frac{U_\infty}{f_N d}$ when $A/D = 0.05$ and 0.10 whereas for $A/D = 0.25$, ϕ remains virtually constant at this minimum value over a range of windspeed before increasing very rapidly with decreasing $\frac{U_\infty}{f_N d}$.

Generally it is interesting to note that ϕ does not follow a consistent trend with A/D except in the range $7.13 < \frac{U_\infty}{f_N d} < 8.6$ where ϕ decreases with increasing A/D.

The large variations in ϕ during lock-in indicate that the flow configuration is highly sensitive to $\frac{U_\infty}{f_N d}$. In particular the behaviour of ϕ indicate that the vortices, which are largely responsible for the fluctuating lift on the cylinder, are being shed at different stages during the cylinder's motion for different values of $\frac{U_\infty}{f_N d}$.

It is interesting to compare the present results with the flow visualisation results presented in Chapter 5. It was reported in chapter 5 that for $A/D = 0.25$ and $f_s/f_N \approx 1.0$, vortices are shed from the lower shear layer when the body is moving downwards and is around the centreline of its motion. The phase angle measurement indicate, see Fig 7.44, that ϕ is approximately -90° when $A/D = 0.25$ and $f_s/f_N \approx 1.0$ (note $f_s/f_N = 0.134 \frac{U_\infty}{f_N d}$) - i.e. that the lift is maximum as the body passes the centreline on its downwards journey. These results suggest the oscillating square section cylinder experiences maximum fluctuating lift during lock-in when a vortex shed from the lower shear layer. (One could also have deduced this from the notion that a shed vortex induces an equal but opposite circulation on the body). Thus generally during lock-in, a negative ϕ appears to suggest that vortices are shed from a shear layer when the body is moving towards the shear layer in question whereas a positive ϕ suggests the reverse.

7.5.2 Comparison between the present values of ϕ and those of previous workers.

Only three workers (Wilkinson (1974), Otsuki et al (1974) and Nakamura & Mizota (1975)) are known to have published measurements of ϕ on square section cylinders oscillating at and around resonance. These works have been reviewed in section 1.4.2.2 . The results of Wilkinson will be considered first because the range and scope of his measurements are similar to the present ones.

WILKINSON (1974).

As in the present study, Wilkinson measured the phase angle, ϕ , by which the lift fluctuation measured at the centre of the top side face leads the cylinder's displacement. He reported that below $f_N/f_s = 0.8$ (i.e. above $\frac{U_\infty}{f_N d} \approx 9.33$) ϕ is about 120° and that above $f_N/f_s = 0.9$ (i.e. below $\frac{U_\infty}{f_N d} \approx 8.29$) ϕ is about -120° . In other words there is a large change in ϕ during lock-in Wilkinson also reported that his results at small values of A/D indicate that as $\frac{U_\infty}{f_N d}$ is increased from about 8.29 to 9.33 , ϕ decreases from -120° through -180° to -240° (or 120°) whilst his high A/D results indicate that ϕ increases from -120° through 0° to 120° . He also reported that increasing A/D increases ϕ in any particular situation and accordingly his results indicate that the value of $\frac{U_\infty}{f_N d}$ at which $\phi = 0$, $\left(\frac{U_\infty}{f_N d}\right)_{\phi=0}$, decreases very rapidly with increasing A/D .

The only point of agreement between the present results and Wilkinson's is that there is a large change in ϕ during lock-in. The present results (Fig 7.44) indicate that the direction of the change in ϕ as $\frac{U_\infty}{f_N d}$ increases is through 0° regardless of the value of A/D. In addition the present values of ϕ generally do not follow a consistent trend with A/D except between $\frac{U_\infty}{f_N d}$ of 7.12 and 8.6 where ϕ decreases with increasing A/D . The values of $\left(\frac{U_\infty}{f_N d}\right)_{\phi=0}$

were also found in the present study to increase with increasing A/D .

An examination of the measurement technique used by Wilkinson reveals why his results are likely to be highly inaccurate. Wilkinson assumed that all the power of the fluctuating pressure, measured at the centre of the side face, is concentrated at the body frequency f_N all through the range $6.2 < \frac{U_\infty}{f_N d} < 12.4$ where his ϕ measurements are made. He then measured the normalised cross-correlation, ρ , between the fluctuating pressure and the acceleration of the body and went on to calculate ϕ from the relationship $\rho = \cos\phi$. Wilkinson assumption does not hold in practice because the 'lock-in' range is much narrower than the range $6.2 < \frac{U_\infty}{f_N d} < 12.4$ even at his maximum value of A/D , A/D = 0.134 . The spectra of fluctuating pressure will, as reported in 7.1 , have power at f_N , f_{so} , f_N+f_{so} $f_N- f_{so}$, etc when $\frac{U_\infty}{f_N d}$ is outside the lock-in range. Even during lock-in, the spectral peak centered on f_N is, because of the variation in vortex shedding frequency, comparatively broad-band, see Fig 7.40 for which A/D = 0.10 , thus indicating that the power is distributed around f_N instead of being concentrated at f_N as assumed by Wilkinson. Other major sources of error in Wilkinson's case are the substantial amount of turbulence in the free stream and the fact that he, as reported in section 1.4.2.2 , connected the pressure transducer to the model surface with pressure tubing that was so long that it suffered from resonance and phase lag in his frequency range of interest. One therefore cannot put much trust in Wilkinson's results.

B. OTSUKI ET AL (1974) AND NAKAMURA & MIZOTA (1975).

As reported in section 1.4.2.2 Otsuki et al (1974) and Nakamura & Mizota (1975) measured the phase angle ϕ_m between $L_m(t)$ and the cylinder's displacement where $L_m(t)$ is the component of the total force $L(t) - V(t)$ at the body's frequency. $L(t)$ and $V(t)$ denote

the total fluctuating lift on the body during oscillation in flowing and still fluid respectively. Since ϕ is the phase angle between $L(t)$ and the cylinder's displacement, ϕ_m will generally be different from ϕ particularly at low values of $\frac{U_\infty}{f_N d}$ (or high values of f_N/f_s) where $V(t)$ can be large. Because Otsuki et al and Nakamura & Mizota did not report values of $V(t)$, ϕ was deduce from their values of ϕ_m by using the values of $V(t)$ estimated from the still-air results of the present study. The resulting values of ϕ are compared with the present ones in Fig 7.45 A & B.

It is interesting to note however that $\phi = \phi_m$ at the lock-in value of $\frac{U_\infty}{f_N d}$ where $\phi = 0$ - i.e. at $\left(\frac{U_\infty}{f_N d}\right)_{\phi=0}$. This is because measurements indicate that $V(t)$ is in phase with the cylinders displacement and also that $L(t)$ is greater than $V(t)$. The zero crossings (i.e. the values of A/D and $\frac{U_\infty}{f_N d}$ at which $\phi = \phi_m = 0$) of Otsuki et al and Nakamura & Mizota can thus be compared directly both with the present results and Wilkinson (1974). This comparison is made in Fig 7.46.

Starting with Fig 7.46, it was argued in section 1.4.2.2 that the zero crossings measured on a cylinder undergoing forced oscillation should indicate the steady state value of A/D that will be attained at a given value of $\frac{U_\infty}{f_N d}$ (or f_s/f_N) by the undamped spring-mounted cylinder when undergoing self-excited oscillation. Any plausible values of A/D and f_s/f_N that are obtained from zero crossings in forced oscillation experiments should then at least indicate the same trend as the steady-state values measured on the lightly-damped, or preferably undamped, cylinder during free oscillation. This is the reason why the free oscillation results of Otsuki et al (1974) and Nakamura & Mizota (1975) are also presented in Fig 7.46. From the above arguments Fig 7.46 demonstrate that the zero crossings

obtained from the present results are plausible because they follow very closely the trends indicated by the free and the forced oscillation results of Otsuki et al (1974) and Nakamura & Mizota (1975) . Wilkinson's (1974) results can be seen in Fig 7.46 to follow a totally different trend and are, as already noted, therefore highly suspect.

The above discussion is for $\left(\frac{U_\infty}{f_N d}\right)_{\phi=0}$, the value of $\frac{U_\infty}{f_N d}$ at which $\phi = \phi_m = 0$. At other values of $\frac{U_\infty}{f_N d}$, it can be seen in Fig 7.45 A, where ϕ is plotted against $\frac{U_\infty}{f_N d}$ at $A/D = 0.05$ and 0.10 , that the present results are very similar to those of Nakamura & Mizota (1975) but the results of the latter appear shifted to the right on the $\frac{U_\infty}{f_N d}$ axis. This shift is less when is plotted against f_s/f_N (i.e. $S \times \frac{U_\infty}{f_N d}$) , see Fig 7.45B, because Nakamura & Mizota reported S to be 0.125 whereas in the present study S is taken as 0.134 . When Nakamura & Mizota's value of S is assumed to be 0.118 (i.e. assuming an error of 6% in S which is possible when, as in the present situation, f_s and U_∞ are fairly low), their results can be brought even closer to the present results - see Fig 7.45B. The shift between the two sets of results presented in Fig 7.45 A & B may thus be caused, at least in part, by difficulties in measuring S . It must also be noted that Nakamura & Mizota values of ϕ indicate the phase angle by which the total fluctuating lift leads the cylinder's displacement whereas the present values indicate the phase angle by which the fluctuating lift at the centre of the side face leads the cylinder's displacement. There will generally be a chordwise (see for example section 6.6.3) and spanwise variation of phase angle, the latter being most likely to occur when the spanwise correlation is not unity over the whole span. The value of ϕ obtained from total force measurement may thus differ from the one obtained from one-point surface fluctuating pressure especially away from the central portion

of the lock-in range. Strictly therefore comparison between the values of ϕ obtained from total force measurement and the ones obtained from one-point surface pressure measurement should be limited to qualitative trends. In this respect the agreement between the present results and those of Nakamura & Mizota is, see Figs 7.45 A & B , excellent.

By comparing Fig 7.44 to Fig 1.14B it can also be seen that there is good qualitative agreement between the present values of ϕ and those of Otsuki et al (1974) who like Nakamura & Mizota above obtained phase angle from total lift force measurement.

7.6 MEASUREMENT OF LONGITUDINAL VORTEX SPACING AND CALCULATION OF NON-DIMENSIONAL VORTEX STRENGTH.

The longitudinal vortex spacing, a/d , (and hence vortex convection velocity, $S.a/d$) was measured digitally, as described in Chapter 3, by computing the phase angle $\phi_{\omega}(f_s)$ at the vortex shedding frequency between the signal of a reference pressure transducer connected to the top side face of the model and that of a single hot-wire traversed up and downstream in the wake. The average value of a/d (and hence $S.a/d$ or $\frac{U_c}{U_\infty}$) calculated from the slope of the best fit straight line to the plot of $\phi_{\omega}(f_s)$ against the downstream displacement, $\frac{X}{d}$, of the hot-wire is presented in Table 2. Fig 7.47 shows the variations of $\frac{U_c}{U_\infty}$ with x/d where $\frac{U_c}{U_\infty}$ is calculated from the change in $\phi_{\omega}(f_s)$ during a step change of typically one cylinder diameter in x/d .

There is a large amount of scatter in the data for the variation of $\frac{U_c}{U_\infty}$ with x/d (Fig 7.47) particularly at A/D = 0.10 . This scatter may be caused more by inaccuracies in measuring the reduced windspeed, $\frac{U_\infty}{f_N d}$, rather than by inaccuracies in measuring $\phi_{\omega}(f_s)$. For example at $\frac{U_\infty}{f_N d}$ = 7.91 and

$A/D = 0.10$, where the scatter in Fig 7.47 seems most pronounced, the coherence at the vortex shedding frequency between the hot-wire and the pressure transducer signals varied between 0.985 and 0.998 (i.e. practically unity) in the range of measurement. Under this condition, the digital analysis should, see for example Davies (1975), produce very reliable estimates of $\phi_w(f_s)$. On the other hand $\phi_w(f_s)$ was found to be very sensitive to $\frac{U_\infty}{f_N d}$ especially at low values of A/D . For example at a downstream distance of 12.0 diameters, a change of 75° was observed in $\phi_w(f_s)$ when $\frac{U_\infty}{f_N d}$ was increased from 7.21 to 7.91 at $A/D = 0.10$. Thus an error of 1% in $\frac{U_\infty}{f_N d}$ at $A/D = 0.10$ could produce a 7.7° error in $\phi_w(f_s)$ leading to about 15% error in the instantaneous values of a/d and $\frac{U_c}{U_\infty}$. Because of the large amount of scatter in the data for $A/D = 0.10$, see Fig 7.47, not much confidence can be placed on the values of $\frac{U_c}{U_\infty}$ obtained at this amplitude. It was therefore decided not to calculate other characteristics of the vortex street in the $A/D = 0.10$ flow case.

Concentrating therefore on the results for $A/D = 0.25$, it can be seen in Table 2 that during lock-in, the average value of the longitudinal vortex spacing, a/d , decreases from the stationary cylinder value when the body frequency f_N is increased above the natural vortex shedding frequency f_s . The trend in a/d is, see Table 2 , reversed when f_N is decreased below f_s . As a result of this behaviour, the vortex convection velocity, $\frac{U_c}{U_\infty}$ (or $S \cdot a/d$), can be seen in Table 2 and Fig 7.47 to maintain the stationary cylinder value. Similar findings have also been reported for circular cylinders by workers like Griffin & Votaw (1972).

For $A/D = 0.25$, calculation of vortex spacing ratio, b/a , was made during lock-in, by using the measured values of C_D (Fig 7.4) and $\frac{U_c}{U_\infty}$ (Table 2) in the potential vortex wake drag formula of

equation (6.6) - (see section 6.7). These values of b/a were then used, as described in section 6.7, to calculate the non-dimensional vortex strength $\left(\frac{\Gamma_o}{\pi U_\infty d}\right)$, the circulation defect ratio (ϵ), and the lateral vortex spacing (b/d). The results are presented in Table 3.

Before discussing Table 3, it is useful to comment on how well the trends predicted by the potential vortex wake drag formula compare with real flow situation. Comparison can only be made for the circular cylinder because this is the bluff-body shape for which there is sufficient data. As previously reported the measurements of Griffin & Votaw (1972) indicate during lock-in that the vortex convection velocity, $\frac{U_c}{U_\infty}$, maintains the stationary cylinder value. The mean drag measurements of Tanida et al (1974) show that C_D is higher during lock-in than when the model is stationary. Thus at resonance the product $C_D \cdot S$ will be higher for the oscillating circular cylinder than for the stationary one. This, according to the potential wake drag formula, means that relative to the stationary cylinder values, the vortex spacing ratio (b/a) and the lateral vortex spacing (b/d) are decreased whereas the non-dimensional vortex strength, $\frac{\Gamma_o}{\pi U_\infty d}$, is increased. These theoretical predictions are in agreement with the flow visualisations of Koopman (1967) and Griffin & Votaw (1972) where wake synchronisation is shown to decrease b/d. Griffin & Ramberg (1975) also reported that they observed in their earlier work (Griffin & Ramberg (1974), where a mathematical model for the vortex street was matched with the RMS and mean velocity profiles measured behind an oscillating circular cylinder) that, during lock-in, $\frac{\Gamma_o}{\pi U_\infty d}$ and b/d were respectively increased and decreased from the stationary cylinder values. These results suggest that the potential vortex wake drag formula is capable of indicating the correct trends.

Returning to Table 3 it can be seen that the predicted values of

non-dimensional vortex strength, $\frac{\Gamma_o}{\pi U_\infty d}$, are lower during lock-in than when the model is stationary. As reported in section 7.2.2.2, the measured values of the non-dimensional circulation shed by each shear layer per cycle of vortex shedding, $\frac{1 - C_{pb}}{2\pi S}$, is, see Table 1, also lower during lock-in than when the model is stationary - in fact it can be seen in Table 3 that $\frac{1 - C_{pb}}{2\pi S}$ follows the same trend as $\frac{\Gamma_o}{\pi U_\infty d}$. This adds credibility to the trend indicated by the predicted values of $\frac{\Gamma_o}{\pi U_\infty d}$.

The above finding is interesting because it suggests, contrary to Wilkinson (1974), that the increase reported, see section 7.3, in sectional RMS pressures during lock-in is not caused by increased vortex strength. To account for his unusually high values of $(C_{p_{rms}})_f$ during lock-in, Wilkinson suggested that the non-dimensional strength of the vortices are higher than the stationary cylinder values even though his mean pressure measurements indicate the opposite.

7.7 PRESSURE AND DISPLACEMENT TRANSDUCER SIGNALS DURING BODY OSCILLATION

The photographs of the simultaneous outputs of pressure and displacement transducers during body oscillation at $A/D = 0.10$ and 0.25 are presented in Figs 7.48 and 7.49 respectively. To complement these photographs pen-recordings of the waveform of the pressure transducer output at $A/D = 0.0$ (stationary model) and 0.10 are presented in Figs 7.50 and 7.51.

Some points of interest are:

(1) The amplitudes of pressure fluctuations are less modulated during wake synchronisation, or 'lock-in', than when the body is stationary. Comparing the pressure transducer output during 'lock-in' (see the lower traces of Figs 7.48, 7.49(b), and 7.49(d)) to the output when the model is stationary (see Figs 6.36 (a), (c) and (d)) illustrates this point.

(ii) Outside the synchronisation range, the waveform of the pressure fluctuation can be seen in Figs 7.51 (b), (d) and (e) to be very complex. It is particularly interesting to note the existence of beats in Fig 7.51 (d) at $\frac{U_\infty}{f_N d} = 9.0$ where the vortex shedding frequency, f_{so}, is slightly higher than the body frequency, f_N. These findings are consistent with spectral analysis which shows, see section 7.1, that there are generally peaks at f_N, f_{so}, $f_N + f_{so}$, $f_{so} - f_N$, etc when $\frac{U_\infty}{f_N d}$ is outside the lock-in range.

(iii) There is a variation in vortex shedding frequency during lock-in even when $\frac{U_\infty}{f_N d}$ (or windspeed) is maintained at practically the resonant value. Counting the shedding frequencies in the lower traces of Figs 7.48 (a) (A/D = 0.10) and Fig 7.49 (b) (A/D = 0.25) demonstrates this. This finding is consistent with spectral analysis which shows during lock-in, see section 7.1, that the spectral peaks at f_N are less highly tuned than the line-like 50HZ peak. These results are surprising because it was thought that synchronised oscillation would force vortices to shed precisely at the body frequency.

(iv) Fig 7.48(C) explains why the spanwise correlation can be so high during lock-in. This figure shows that at $\frac{U_\infty}{f_N d} = 7.78$ and A/D = 0.10, there is no phase difference between the signals of the two pressure transducers placed 9.5 body diameters apart along the centreline of the top side face. Thus even though the shedding frequency may vary (see point (iii) above) it appears that vortices are shed simultaneously all along the span.

By contrast to the above finding it can be seen in Fig 7.50 that at $\frac{U_\infty}{f_N d} = 9.0$ and A/D = 0.10, there is a variation in beat frequency on each trace and in addition the

beating does not always occur simultaneously in the outputs of the two pressure transducers (the transducers are placed 9.5 body diameters apart on the centreline of the top side face). This indicates that there is some variation in shedding frequency at each section and also that vortices are not always shed simultaneously along the span. This explains why the spanwise correlation falls as indicated in Figs 7.33 and 7.34 when is above the lock-in values.

(v) The phase angles, ϕ , indicated by the photographs agree closely with the results obtained, see Fig 7.44, from digital analysis. For example Figs 7.49 (a), (c) and (e) indicate that at $A/D = 0.25$, ϕ is approximately -108° , -90° and 0° at $\frac{U_\infty}{f_N d} = 6.14$, 7.52 and 10.0 respectively (Note that the pressure trace is not inverted in Fig 7.49 (e)). These values of ϕ are close to the measured values of -98° ,-90° and -5° - see $A/D = 0.25$ Fig 7.44 .

(vi) The pen-recorder traces of Fig 7.51 illustrate the behaviour of the lift RMS pressures at $A/D = 0.10$. The windspeed and the amplification are the same for each trace in Fig 7.51 . Thus the relative amplitudes of the traces indicate the relative values of $(C_{Prms})_f$. The variation of $(C_{Prms})_f$ at the centre of the side face (where the traces in Fig 7.51 are recorded) with $\frac{U_\infty}{f_N d}$ is presented in Fig 7.5 .

Figs 7.51 (b) and (d) demonstrate why the RMS lift fluctuations on the model oscillating at $A/D = 0.10$ are, at $\frac{U_\infty}{f_N d} = 6.26$ and 9.0 , lower than the stationary cylinder value. It can be seen in these figures that the amplitudes of the lift fluctuations are, during oscillation, more highly modulated, particularly at $\frac{U_\infty}{f_N d} = 6.26$, than when the model is stationary - Compare Figs 7.51 (b) and (d) to Fig 7.51 (a).

By comparing traces (c) and (a) of Fig 7.51 it can be seen that the value of $(C_{p_{rms}})_f$ is high during lock-in because there is less modulation in the pressure signal. It is particularly interesting to observe that the overall level of the pressure signal at $\frac{U_\infty}{f_N d} = 7.81$ (Fig 7.51 (c)) (where the lift $(C_{p_{rms}})_f$ is, as reported in section 7.3, maximum during lock-in) is not higher than the peak level attained from time to time, see Fig 7.51 (a), on the stationary model. Thus synchronised oscillations increases the lift $(C_{p_{rms}})_f$ by regularising the level of the amplitude of pressure fluctuations to approximately the peak level that occurs on the stationary model.

The above results explain why the maximum value attained by the lift $(C_{p_{rms}})_f$ during lock-in tends, as shown by curve (3) of Fig 7.32, to level off at high values of A/D. For assuming that the contribution of inertia and other non-vortex-induced effects are small, the maximum value attained by the lift during lock-in would level off at high values of A/D because once an initial value of A/D has made the lift RMS pressure signal fairly regular, further increases in A/D would produce little increase in $(C_{p_{rms}})_f$.

The results of this section are also compatible with those of section 7.6 which indicate that the lock-in values of non-dimensional vortex strength, $\frac{\Gamma_o}{\pi U_\infty d}$, are not higher than the stationary cylinder value. The results presented in section 6.8 indicate that in the stationary model case, vortices are not usually shed simultaneously along the span. There will, at a given instant, be spanwise flow across a section if a vortex is fully formed at this section whilst the vortices of adjacent sections are not yet fully formed. This spanwise flow will decrease the amplitude of fluctuating pressure (at the section

with the fully formed vortex) below the level that would occur when the vortices of this section and those of adjacent sections are formed simultaneously. Thus even when $\frac{\Gamma_o}{\pi U_\infty d}$ has the same constant value all along the span, the amplitude of the stationary model surface fluctuating lift pressure signal will be modulated with peak amplitude occuring at a section when vortices of this section and those of adjacent sections are shed simultaneously. Now for lock-in oscillation at A/D = 0.10 and $\frac{U_\infty}{f_N d}$ = 7.8 , vortices are, as reported under point (iv) of this section, shed simultaneously all along the span. The amplitude of surface fluctuating pressure will be less modulated and may , neglecting other effects (like inertia for example) and assuming that both the vortex formation region length and $\frac{\Gamma_o}{\pi U_\infty d}$ are little affected by oscillation, have a level that is close to the peak value observed on the stationary model. Thus the lock-in RMS pressure coefficient can be higher than the stationary cylinder value even when the lock-in value of $\frac{\Gamma_o}{\pi U_\infty d}$ is slightly lower than the stationary cylinder value.

Keefe (1961) reported a substantial increase in the RMS lift coefficient of a stationary cylinder when two circular disks are placed in close proximity on either side of the transducer. He reported that when this increase occured, the amplitude of the fluctuating lift signal had less modulation and that there was no noticeable increase in the RMS drag coefficient. He then went on to suggest that the proximity of the disks made the flow between them more two dimensional so that the lift is accordingly well correlated spanwise between the disks in contrast to the limited spanwise correlation in the absence of the disks. Keefe's observations and suggestion appear to fit exactly with what happens on the oscillating square section cylinder during wake synchronisation. For the square section cylinder the lift

RMS pressure is maximum during lock-in at the $\frac{U_\infty}{f_N d}$ where, as reported in section 7.4 , the lift is well correlated over the whole span. Where this maximum occur, the lift amplitude modulation is, as reported under points (i) and (vi) of this section, less. Maximum lift fluctuation on the oscillating square section cylinder is, as reported in section 7.3 , also not accompanied by maximum drag fluctuation. Thus it appears that for the square section cylinder, the primary effect of synchronised oscillation is to correlate the lift along the span thus making the flow more two-dimensional.

7.8 FURTHER DISCUSSION

7.8.1 The flow around the square section cylinder during wake synchronisation or 'lock-in'

To explain the overall behaviour of $-C_{Pb}$ and C_D during lock-in, it was suggested in section 7.2 that oscillation brings the shear layers closer to the body thus causing them to be deflected by the trailing edge corners. If this is the flow mechanism that operates, the values attained by $-C_{pb}$ and C_D during lock-in should be very sensitive to the 'effective' position of the trailing edge corners. The position of the trailing edge corners varies during body oscillation but it seems reasonable to assume that it is the position (of the corners) at the time vortices are fully formed and are about to be shed that will be crucial. For example if the body is away from the centreline around the time a vortex is about the shed, one would expect the trailing corners to interfere with one of the shear layers and so force vortices to shed further downstream thus lowering $-C_{pb}$ and C_D . The further away the body is from the centreline, the bigger the interference and the smaller should be the values of $-C_{pb}$ and C_D . Thus from knowledge of the position of the body at the time vortices are shed, one should be able to deduce the trend in $-C_{pb}$ and C_D .

The relationship between the phase angle, ϕ, and the position of the body when vortices are about to be shed was discussed in section 7.5 where it was argued that the fluctuating lift is maximum when a vortex is shed from the lower shear layer. Assuming this is the case, one can determine the position of the body when vortices are about to be shed from the values of ϕ presented in Fig 7.44. Putting the arguments together: one should, during lock-in, be able to deduce the trend in $-C_{pb}$ (and hence C_D) as $\frac{U_\infty}{f_N d}$ changes from the variation of ϕ with $\frac{U_\infty}{f_N d}$.

Consider then the situation at A/D = 0.10. The lock-in range lies, see Fig 7.39, between $\frac{U_\infty}{f_N d}$ of 7.0 and 8.75. During lock-in ϕ (Fig 7.44) rises from -97° at $\frac{U_\infty}{f_N d}$ = 7.0 to -90°, 0° and 50° at $\frac{U_\infty}{f_N d}$ = 7.2, 8.4 and 8.75 respectively. From the arguments, see section 7.5, that fluctuating lift is maximum when a vortex is shed from the lower layer, ϕ = 0 or 180° indicate that vortices are shed when the body is at the extreme ends of its travel whereas $\phi = \pm 90^\circ$ indicate that vortices are shed as the body passes the centreline. From the arguments of the preceeding paragraph, the further away the body is from the centreline at the time of vortex shedding, the smaller should be the value of $-C_{pb}$. Thus one would, from the changes in ϕ, expect $-C_{pb}$ to increase from its value at $\frac{U_\infty}{f_N d}$ = 7.0 to a maximum at $\frac{U_\infty}{f_N d} \approx 7.2$ (where $\phi = -90^\circ$) and then decrease to a minimum at $\frac{U_\infty}{f_N d}$ = 8.4 (where $\phi = 0^\circ$). From $\frac{U_\infty}{f_N d}$ of 8.4 to 8.75, $-C_{pb}$ should again increase with $\frac{U_\infty}{f_N d}$ because ϕ increases from 0°. The base pressure measured during lock-in can be seen in Fig 7.2 to follow exactly this trend. This appears to suggest that the basis of the argument is correct and that it is the position of the trailing edge corners at the time vortices are shed that determine the base suction and drag during lock-in.

At $A/D = 0.25$, the behaviour of $-C_{pb}$ during lock-in also follows broadly the trend expected from the above line of reasoning. The measured values of $-C_{pb}$ can be seen in Fig 7.4 to be constant in the range $5.61 < \frac{U_\infty}{f_N d} < 7.18$ where ϕ, see Fig 7.44, is constant at -98°. As $\frac{U_\infty}{f_N d}$ increases from 7.18 to 8.51, ϕ (Fig 7.44) rises to -90° at $\frac{U_\infty}{f_N d} \approx 7.4$ and thence to -47° at $\frac{U_\infty}{f_N d} = 8.51$. The mean pressure measurement (Fig 7.4) suggest that $-C_{pb}$ decreases continuously with increasing $\frac{U_\infty}{f_N d}$ when $\frac{U_\infty}{f_N d} > 7.18$ instead of rising first to a maximum at $\frac{U_\infty}{f_N d} = 7.4$, where $\phi = -90^\circ$, before decreasing. Thus the behaviour of $-C_{pb}$ between $\frac{U_\infty}{f_N d}$ of 7.18 and 7.40 apparently seem to contradict the ideas of the preceeding paragraph. This contradiction may however not be real because the contribution of other factors (like inertia and changing incidence effects for example) to RMS lift are likely to be appreciable when A/D is as high as 0.25. So that the resultant value of ϕ may differ, at least a little, from -90° when the contribution of the vortices to RMS lift has a phase angle of -90°. In other words it is possible that at $A/D = 0.25$, ϕ may have a value of say -98° when the vortices are shed as the body passes through the centreline. When this is the case $-C_{pb}$ would be maximum when $\phi = -98^\circ$ and decrease as ϕ moves away from -98° - a trend similar to one actually observed.

It thus seems, at least when A/D is small, that the afterbody of the oscillating square section cylinder behaves, during lock-in, like trailing edge spoilers. Bearman & Trueman (1971) have demonstrated that $-C_{pb}$ decreases when small spoilers are attached, normal to the section, at the trailing edge corners of a stationary rectangular cylinder with $d/h = 0.62$ (d is section depth and h is section width normal to the wind direction). Their measurements show that

the higher the spoilers the smaller the value of $-C_{pb}$. For the oscillating square section cylinder, the trailing edge corners appear to behave like the spoilers. The farther away the trailing corners are, at the time of vortex shedding, from their mean positions the smaller the value $-C_{pb}$ appears to take.

7.8.2 Application of the results obtained during forced vibration to the problem of flow-induced vibration.

Consider the cylinder as a rigid body of mass M , oscillating on spring of stiffness K in opposition to a damping force of coefficient C .

The equation of motion is:

$$M\ddot{y} + C\dot{y} + Ky = L(t) \quad \text{- - - - - - - (7.1)}$$

$L(t)$ is the periodic fluid forcing given by $L_o \sin(\omega_N t + \phi)$ where ϕ is the phase angle between the fluctuating lift and the cylinder's displacement $y = A \sin \omega_N t$.

Writing $L(t)$ in terms of components that are parallel to the cylinder displacement (y) and velocity $(\dot{y})$ gives

$$L(t) = \frac{L_o \cos\phi}{A} y + \frac{L_o \sin\phi}{A\omega_N} \dot{y} \quad \text{- - - -(7.2)}$$

Equation (7.1) can then be written as

$$M\ddot{y} + (C - C_a)\dot{y} + (K - K_a)y = 0 \quad \text{- - - -(7.3)}$$

where $$C_a = \frac{L_o \sin\phi}{A\omega_N} \; , \; K_a = \frac{L_o \cos\phi}{A} \quad \text{- - - (7.4)}$$

L_o can be written as

$$L_o = \tfrac{1}{2} \rho U_\infty^2 \, dL \sqrt{2} \left(C_{L\,rms}\right)_{AV}$$

where d and L are the cylinder diameter and span respectively. $(C_{Lrms})_{AV}$ is the average RMS lift coefficient.

C_a can then be written as

$$C_a = (C_{Lrms})_{AV} \sin\phi \left(\frac{U_\infty}{f_N d}\right)^2 \cdot \left(\frac{A}{D}\right)^{-1} \left(\frac{\rho f_N d^2 L}{2\sqrt{2}\,\pi}\right) \quad ---(7.5)$$

From equation (7.3) the undamped natural frequency of the combined system, ω_0, is $\sqrt{\frac{K - K_a}{M}}$ instead of the value $\sqrt{\frac{K}{M}}$ that exists in the absence of aerodynamic forcing.

Consider first the component $K_a y$ of the exciting force. Usually the exciting force is, see Sachs (1972), considerably smaller than the inertia or stiffness forces. Walshe (1972) also remarked that the fact that wind-excited oscillation of structures, are usually observed to take place at a frequency close to a natural frequency indates that K_a is small compared to K. Thus any oscillation resulting from the component, $K_a y$, of the exciting force will usually be small and insignificant.

Consider next the component $C_a \dot{y}$ of the exciting force. Consider the following cases: $(C - C_a) > 0$ and $(C - C_a) \leq 0$.

When $(C - C_a) > 0$ in equation (7.3), any transient oscillation will be damped out. The case $C_a < 0$ is particularly interesting because it indicates that instability cannot exist no matter how small the structural damping, C, is made. From equation (7.4) $C_a < 0$ means that $180^\circ < \phi < 360^\circ$ or $-180^\circ < \phi < 0^\circ$. Applying this finding to the oscillating square section cylinder, it can be seen in Fig 7.44 that ϕ lies between 0° and -180° when $\frac{U_\infty}{f_N d} < \left(\frac{U_\infty}{f_N d}\right)_R$ or $f_s/f_N < 1.0$. The phase angle measurement (Fig 7.44) therefore indicate that significant self-excited lateral oscillation of a spring-mounted square section cylinder cannot occur when f_s/f_N is below unity. This finding is, as reported in

sections 1.4.2.1 and 1.4.2.2, consistent with experimental observations.

When $(C - C_a) < 0$ oscillation will grow in amplitude until, barring structural failure, a steady state amplitude is reached where $(C - C_a) = 0$. When $C = 0$ (no structural damping), steady state amplitude will be reached when $C_a = 0$. From equation 7.4 $C_a = 0$ means $\phi = 0^\circ$ or 180°, For the oscillating square section cylinder ϕ (Fig 7.44) is always less than 180°. Thus at a given value of $\frac{U_\infty}{f_N d}$, the steady state amplitude, $\left(\frac{A}{D}\right)_{\phi=0}$ that would occur on the undamped square section cylinder during self-excited oscillation is given by the value of A/D at which $\phi = 0$. The values of $\left(\frac{A}{D}\right)_{\phi=0}$ deduced from the present values of ϕ are shown in Fig 7.46 to be in good qualitative agreement with steady state amplitude measured by Otsuki et al (1974) and Nakamura & Mizota (1975) during self-excited oscillation.. A discussion of Fig 7.46 has already been presented in section 7.5.2 .

When $C - C_a < 0$ and $C > 0$ (i.e. there is structural damping), steady state amplitude will be attained when $C - C_a = 0$ i.e. $C = C_a = \frac{L_o \sin\phi}{A\,\omega_N}$. Thus measurements of ϕ and L_o during forced oscillation can give the steady state amplitude that will occur on the spring-mounted model during self-excited oscillation when the damping parameter, C , is specified. An interesting point worth noticing in Fig 7.44 is this: it can be seen that for values of A/D that are very close the value at the $\frac{U_\infty}{f_N d}$ where ϕ (and hence C_a) equals zero, ϕ (and hence C_a) increases from zero as A/D decreases from $\left(\frac{A}{D}\right)_{\phi=0}$ .. Since a positive value of C_a is required to balance the damping force, this shows, at least for small damping, that the amplitude of damped free oscillation will be less than the undamped one. This is consistent with experimental observations of workers like Parkinson & Brooks (1961) who reported that structural damping decreases the steady state

amplitude of self-excited oscillation. It is interesting to note that if in every situation ϕ increases with A/D as reported by Wilkinson (1974), the undamped self-excited oscillation amplitude will be less than the damped one - i.e. damping will increase rather than decrease the amplitude of self-excited oscillation. This behaviour is, of course, unrealistic.

Consider the situation in which f_N and A/D are fixed while U_∞ is varied to obtain the variations in ϕ and $(C_{p\,rms})_f$ presented in Figs 7.44 and 7.22 respectively. Take in particular the case A/D = 0.10 . The behaviour of ϕ (Fig 7.44) at A/D = 0.10 and $(C_{p\,rms})_f$ (Fig 7.22 or 7.5) suggests that C_a (see equation (7.5)) rises very sharply from 0 at $\frac{U_\infty}{f_N d} = 8.4$ where $\phi = 0$ to a maximum at $\frac{U_\infty}{f_N d} \approx 8.7$ where ϕ is maximum. Beyond $\frac{U_\infty}{f_N d} = 8.7$ the very sharp initial fall in ϕ (Fig 7.44) suggest that C_a at first falls before rising at high values of $\frac{U_\infty}{f_N d}$ because of the influence, see equation (7.5) , of the $\left(\frac{U_\infty}{f_N d}\right)^2$ term in the expression for C_a . Thus the resulting trend in C_a will be as shown in sketch (7.3).

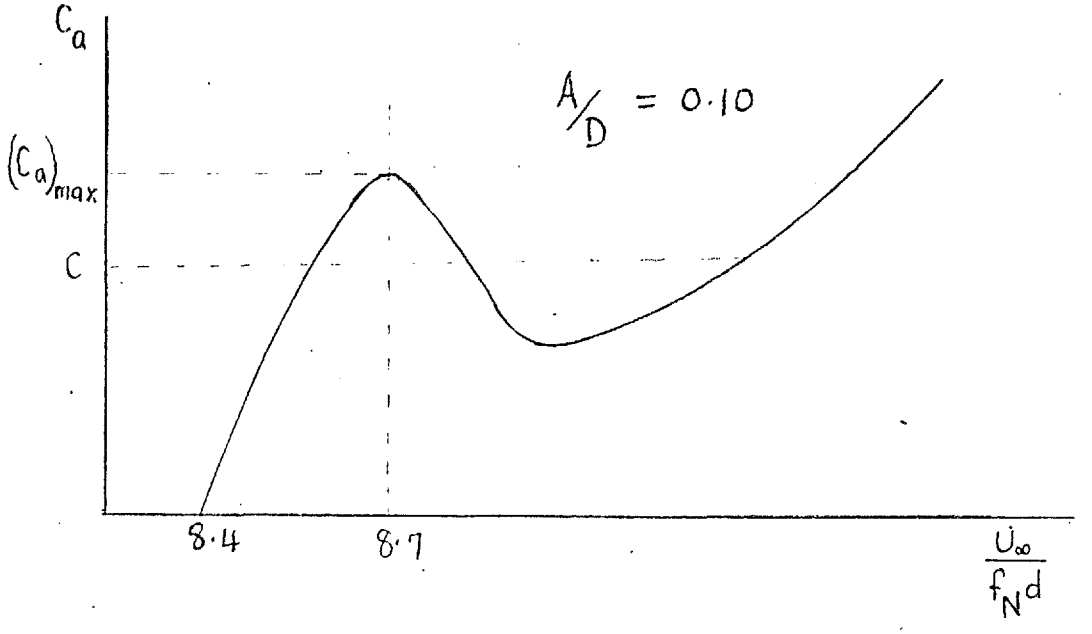

Sketch (7.3)

If during self-excited oscillation, the damping parameter of the system is say C , where C is , as shown in sketch (7.3), less than $(C_a)_{max}$, the steady state amplitude of self-excited oscillation will be less than A/D = 0.10 when $C > C_a$ and greater than A/D = 0.10 where $C < C_a$. The resulting response pattern can therefore be similar to the one presented in sketch (7.4). A response pattern of the type shown

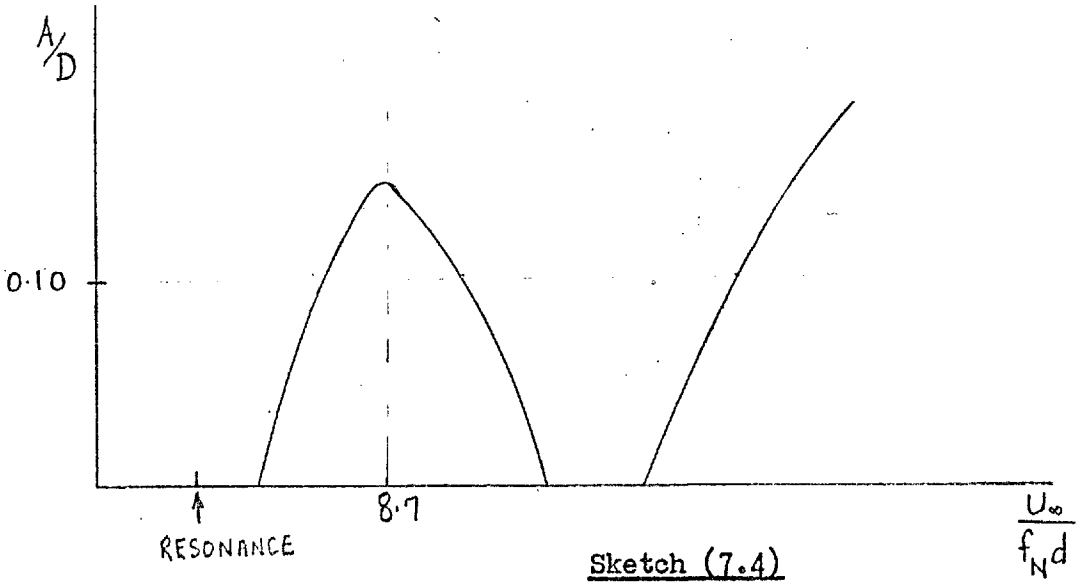

Sketch (7.4)

in sketch (7.4) is consistent with the stability diagram presented by Scruton, see for example Scruton & Rogers (1971), for a square section cylinder.

The discussion of this section demonstrates that the characteristics of the body-wake interaction observed on a square section cylinder during self-excited oscillation can be deduced from results obtained in forced vibration experiments. Forced-vibration experiments can in addition, indicate the aero-elastic behaviour of the cylinder when there is no structural damping - something that is impossible to obtain from free-oscillation experiments.

CHAPTER 8

8.0 CONCLUSIONS

8.1 FLOW VISUALISATION

a) For the stationary model at 0° incidence, vortices are seen to form very close to the back face. No change was discerned in the vortex formation region length during synchronised oscillation.

b) For all the flow cases visualised (i.e. $f_N/f_s = 0$, 0.5 , 1.0 and 2.0) , the opposing shear layers are seen to interact in a manner that suggests that the vortex shedding mechanism is similar to the one proposed by Gerrard (1966) .

c) The wake vortices were seen more distinctly at $f_N/f_s = 1.0$ and 2.0 than at $f_N/f_s = 0$ (model stationary) and $f_N/f_s = 0.50$. The wake vortices seen at $f_N/f_s = 1.0$ appear collinear whereas those seen at $f_N/f_s = 2.0$ appear packed close together with a spacing ratio of about unity.

d) Observations of the near-wake flow configuration at $f_N/f_s = 2.0$, 1.0 and 0.5 suggest that both inertia and changing incidence effects affect the position of the shear layers relative to the body. For $f_N/f_s = 1.0$ and 0.5 , flow reattachment was seen to occur earlier than indicated by quasi-steady considerations.

8.2 MATHEMATICAL MODELS OF VORTEX-INDUCED LIFT FORCES

a) Consideration was given to the Von Karman-type potential flow wake model proposed first by Ruedy (1935) where the fluctuating lift experienced by the body is equated to the rate of flow of Y-momentum out of a large control volume surrounding the body. It is noted that this is incorrect because no consideration is given to the rate of change of momentum in the vortex formation region of the body.

b) The potential flow model proposed by McGregor (1957) is improved by including a bound vortex to represent the effect of the wake vortex

street. This improved model is applied to both the stationary and oscillating body flow cases. For the stationary model, the improved model appears to predict reasonable values of non-dimensional vortex strength, $\frac{\Gamma_o}{\pi U_\infty d}$, when realistic values of surface fluctuating pressures and vortex formation region length (C_o) are used. With realistic values of $\frac{\Gamma_o}{\pi U_\infty d}$ and C_o, the sectional fluctuating pressures predicted by the improved model are better than McGregor's (1957).

During body oscillation, the present potential flow model is shown to be useful for studying both the surface fluctuating pressures and the harmonic contents of velocity fluctuations.

c) The Van der Pol oscillator model proposed by Hartlen & Currie (1970) has been used to model the lift characteristics of a forced square section cylinder. When the parameters of the oscillator are selected carefully, it is shown that the model can predict good lock-in values of fluctuating lift. The predicted lock-in values of lift phase angle was made to agree fairly well with the square section cylinder values by assuming that the forcing function of the oscillator is proportional to the cylinder's displacement. (Hartlen & Currie (1970) assumed that the forcing function is proportional to cylinder's velocity).

8.3 STATIONARY MODEL : RESULTS AND DISCUSSION

a) Even though the aspect ratio of the square section cylinder is as high as 18.0, the base suction $-C_{pb}$ (and hence the sectional drag coefficient, C_D) was found to change, particularly at high angles of incidence, when end plates were fitted. End plates were found to have a detrimental effect (i.e. decrease base suction) if they were not wide enough laterally. By contrast large end plates were found, at high angles of incidence, to produce up to 12% increase in base suction. With large end plates, the values of $-C_{pb}$ observed at high

angles of incidence were found to be higher than previously reported values.

b) Even without end plates, the values of $-C_{pb}$ and C_D observed in the present study are higher than those reported by Pocha (1971) and Lee (1974) who used cylinders of smaller aspect ratios. This, it was noted, indicates the need to isolate the influence of aspect ratio in experiments such as those of Lee (1975/1976) and Mclaren et al (1969) where aspect ratio is varied over a wide range.

c) For flow normal to the cylinder and Reynolds number in the range $2 \times 10^4 < Re < 12 \times 10^4$, an influence of Reynolds number was detected on $-C_{pb}$, C_D and the fluctuating pressure coefficients measured on the back face and around the trailing corners of the side faces.

d) The sectional distributions of surface fluctuating pressure coefficients measured at several angles of incidence are generally - in good agreement with Lee's (1974), higher than Wilkinson's (1974) and lower than both Vickery's (1966) and Pocha's (1971).

e) At 0° incidence, the spanwise correlation length of fluctuating lift was found to be 5.6 body diameters. This result is in agreement with Vickery (1966), Pocha (1971), Lee (1974) but not Wilkinson (1974).

At 0° incidence, the sectional RMS lift coefficients estimated with and without consideration of chordwise correlation are 1.21 and 1.23 respectively. These values are within the range of results observed by previous workers.

f) The strouhal number, S, was calculated both from spectral analysis (i.e. the dominant shedding frequency) and from 'peak-count' (i.e. the average shedding frequency) on a storage oscilloscope. The spectral analysis results indicate that S decreases with increasing α up to $\alpha \approx 10^\circ$ and then rises very sharply to a maximum at $\alpha = 13.5^\circ$. By contrast the 'peak-count' results appear to suggest, as reported by Pocha (1971) and Lee (1974), that as α

increases from 0°, S increases steadily to a maximum at $\alpha = 13.5$.

Measurement of the longitudinal vortex spacing, a/d, indicates that the convection velocity, $S \cdot \frac{a}{d}$, does not vary with incidence Using the measured values of C_D, S, C_{pb} and a/d in the potential vortex street wake drag formula, $\frac{\Gamma_o}{\pi U_\infty d}$, ϵ, b/a and b/d were calculated. The calculated values of $\frac{\Gamma_o}{\pi U_\infty d}$ follow the qualitative trend in $-C_{pb}$ as α increases from 0° to 45°. The calculated values of b/d increase as α increases from 0° to 10° but remain virtually constant beyond $\alpha = 13.5^\circ$. It is noted that the calculated trend in b/d and the above observation that S (measured from spectral analysis) decreases as α increases from 0° do not support the notion (see for example Lee (1974)) that decreases in C_D as α increases from 0° are accompanied by decreases in wake width which in turn produce increases in S.

g) At $\alpha = 0^\circ$, the spectra of surface fluctuating pressures were measured at several locations around the mid-section of the cylinder. The results indicate the usual dominant peaks at f_s (on the side faces and the parts of the front and back faces that are near the corners) and, at the centre of the back face, at $2f_s$. Fairly prominent peaks were also observed at $3f_s$ on the side and back faces near to the trailing corners - a phenomenon apparently unreported in the literature.

The phase angles at f_s were measured at several positions around the mid-section for $\alpha = 0^\circ$. Over the mid 83% of the side face, only a phase difference of approximately 14° was observed with the phase angle at the leading edge lagging that near the trailing edge. This finding, it was noted, is contrary to the notion, see for example Chaplin (1971), that the variation of phase angle on the side face is caused by a disturbance that is convected downstream at the flow separation velocity.

h) It is shown that the amplitudes of the signals of lift fluctuating pressures are randomly modulated. For two positions that are many cylinder diameters apart along the centreline of the side face, it is shown that the amplitude modulation is poorly correlated It was also noted that there is a variation in shedding frequency and that vortices are not usually shed simultaneously along the whole span.

i) Following the work of Bearman & Trueman (1971), the variations of C_D , $-C_{pb}$ and S with α were explained from consideration of the influence of the afterbody.

8.4 OSCILLATING MODEL : RESULTS AND DISCUSSION

a) It is shown - that at A/D = 0.10 and 0.25 , C_D and $-C_{pb}$ are always less than the stationary cylinder values and also that during wake synchronisation at A/D = 0.10 , $-C_{pb}$ (and hence C_D) has a resonant response pattern broadly similar to that of a non-linear oscillator but with maximum $-C_{pb}$ occuring below the resonant windspeed The overall trend in $-C_{pb}$ during lock-in is explained from consideration of the influence of the trailing edge corners.

b) For low values of $\frac{U_\infty}{f_N d}$, the fluctuating pressure coefficient, $(C_{prms})_f$, tends to the value attained during oscillation in still air whereas for high values of $\frac{U_\infty}{f_N d}$, $(C_{prms})_f$ tends towards the stationary cylinder value. During lock-in, $(C_{prms})_f$ generally has a resonant response pattern similar to that of a non-linear oscillator with the lift pressure fluctuation attaining a maximum above the resonant windspeed whilst the drag pressure fluctuation, by contrast, generally attains a maximum below resonance at a value of $\frac{U_\infty}{f_N d}$ that is very close to that of maximum mean base suction. These maximum values of $(C_{prms})_f$ are higher than the corresponding stationary cylinder values.

c) When no correction is applied for wind tunnel blockage effects,

the maximum values attained by the sectional RMS lift coefficients (i.e. $(C_{Lrms})_f$) are estimated to be 1.51 , 1.65 and 1.95 at A/D = 0.05 , 0.10 and 0.25 respectively compared to the stationary cylinder value of 1.33 . It is shown that these maximum values of $(C_{Lrms})_f$ are compatible with the total RMS lift coefficients measured by Otsuki et al (1974) and Nakamura & Mizota (1975) .

d) For A/D = 0.25 , the vortex convection velocity (i.e. $S \cdot \frac{9}{d}$) was, during lock-in, found to maintain the stationary cylinder value.

Both the measurement of $\frac{1 - C_{Pb}}{2\pi S}$ (the non-dimensional vorticity shed by each shear layer into the wake per cycle of vortex shedding) and the calculation $\frac{\Gamma_o}{\pi U_\infty d}$ (using the potential vortex wake drag formula) suggest that the lock-in values of non-dimensional vortex strength are less than the stationary cylinder value.

e) The spanwise correlation of lift fluctuations, $R_{(P,Z)}$, is improved during oscillation especially at lock-in. For A/D = 0.05 and 0.10 , the lock-in value of $R_{(P,Z)}$ has a resonant response pattern with maximum $R_{(P,Z)}$ occuring at about $\frac{U_\infty}{f_N d} = 7.8$ which is also the $\frac{U_\infty}{f_N d}$ at which the lock-in values of RMS lift pressure fluctuations are maximum. This maximum value of $R_{(P,Z)}$ is shown to be practically unity over the whole span.

During oscillation, a reduction was generally observed in the chordwise correlation of fluctuating pressures especially near the trailing edges of the side faces.

f) During lock-in, variations of up to 160° were observed in ϕ (in the present work ϕ is the phase angle by which the fluctuating lift pressure at the centre of the side face leads the cylinder's displacement). Results at A/D = 0.05 , 0.10 and 0.25 indicate that $\left(\frac{U_\infty}{f_N d}\right)_{\phi=0}$ (the value of $\frac{U_\infty}{f_N d}$ at which $\phi = 0$) increases with A/D . This, it was noted, indicates that the steady-state amplitude attained by an undamped spring-mounted cylinder during

free oscillation increases with $\frac{U_\infty}{f_N d}$ - a trend compatible with the free oscillation results of previous workers. The present values of ϕ are also shown to suggest, as observed experimentally by previous workers, firstly that the square section cylinder cannot undergo significant self-excited oscillation when $\frac{U_\infty}{f_N d}$ is below resonance and secondly that structural damping will reduce the amplitude of self-excited oscillation.

It is shown that the present values of ϕ are in good qualitative agreement with the values deduced from the total force measurements of Otsuki et al (1974) and Nakamura & Mizota (1975) - particularly the former (the ϕ values of these other workers indicate the phase angle by which the <u>total</u> fluctuating lift leads the cylinder's displacement).

g) The present values of $(C_{prms})_f$ and ϕ are compared with those of Wilkinson (1974) - the only other worker known to have conducted such measurements on forced square section cylinders. The lack of agreement between the two investigations is attributed, at least in part, to instrumentation problems on Wilkinson's part.

Wilkinson's (1974) results are also shown to be incompatible firstly with the total force measurements of Otsuki et al (1974) and Nakamura & Mizota (1975) and secondly with experimental observations on square section cylinders undergoing self-excited oscillation.

h) Outside the lock-in range, the waveform of the lift pressure fluctuation is, in agreement with spectral analysis, shown to be complex with beats occuring when the vortex shedding frequency is slightly higher than the body oscillation frequency. Using these beats, it is shown that there is a spanwise as well as timewise variation in vortex shedding frequency.

During lock-in, the amplitude of the signal of surface lift pressure fluctuation is shown to be less modulated. At $\frac{U_\infty}{f_N d} = 7.8$

(the lock-in value of $\frac{U_\infty}{f_N d}$ at which both the lift fluctuating pressure and spanwise correlation are maximum), it is shown firstly that vortices are shed simultaneously all along the span and secondly that the amplitude of the lift pressure fluctuation is approximately constant at the peak level that occurs on the stationary model. From these findings and from the trends indicated both by the measured pressures and the calculated values of $\frac{\Gamma_0}{\pi U_\infty d}$, it is suggested that the primary effect of synchronised oscillation is to correlate the lift along the span thus making the flow more two dimensional.

i) By combining the measured values of $\oint$ and C_{pb} with flow visualisation results, it was deduced that there is an inverse relation between the base suction and the lateral displacement of the oscillating body away from the centreline at the time a vortex is about to be shed. This finding is likened to the effect of trailing edge spoilers on the base suction of certain stationary rectangular cylinders.

REFERENCES

Abernathy, F.H. and Kronauer, R.E.	1962	"The formation of vortex streets", J. Fluid Mech., 13 , 1 - 20 .
Bearman, P.W.	1965	"Investigation of the flow behind a two-dimensional model with a blunt trailing edge fitted with splitter plates ", J. Fluid Mech., 21 , 241 - 255 .
Bearman, P.W.	1972	"Some measurements of the distortion of turbulence approaching a two-dimensional bluff body", J. Fluid Mech., 53 , 451 - 467 .
Bearman, P.W. and Trueman, D.M.	1971	"An Investigation of the Flow around Rectangular Cylinders ", I.C. Aero Report 71 - 15 June 1971
Belvins, R.D. and Burton, T.E.	1976	"Fluid Forces Induced by vortex shedding," Trans. ASME, J. Fluids Engineering 98 , Series 1 No. 1 , 19 - 26 .
Berger, E. and Wille, R.	1972	"Periodic Flow Phenomena" Ann. Rev. Fluid Mech., 4 , 313 - 340.
Birkhoff, G. and Zarantanello, E.H.	1957	"Jets, Wakes and Cavities" Academic Press, Page 280 .
Bishop, R.E.D. and Hassan, A.Y.	1964A	"The lift and drag forces on a circular cylinder in a flowing fluid", Proc. Roy. Soc. Lond. A, 277 , 32 - 50.
Bishop, R.E.D. and Hassan, A.Y.	1964B	"The lift and drag forces on a circular cylinder oscillating in a flowing fluid" Proc. Roy. Soc. Lond. A, 277 , 51 - 75.

Bloor, M.S. and Gerrard, J.H.	1966	"Measurements on turbulent vortices in a cylinder wake", Proc. Roy. Soc. Lond. A, 294 , 319 - 342.
Bradshaw, P.	1972	"The Imperial College Aero Dept. digital magtape data-logging system", I,C. Aero TN 72 - 101 ,
Chaplin, J.R.	1970	"Flow Induced Forces and Wake Dynamics of Cylindrical Bodies", Ph. D Thesis, Dept. of Civil Engineering University of Bristol, England.
Chaplin, J.R. and Shaw, T.L.	1971	"Flow-induced dynamic pressures on square section cylinders", Proc. I.A.H.R. Congress, Paris 1971 .
Chen, Y.N.	1972	"Fluctuating Lift Forces of the Karman Vortex Streets on Single Circular Cylinders and in Tube Bundles. Part 2 - Lift Forces on Single Cylinders", Trans. ASME, J. Engineering for Industry 96 , Series B , 613 - 622 .
Clements, R.R.	1973	"An inviscid model of two-dimensional vortex shedding", J. Fluid. Mech., 57 , 321 - 336 .
Clements, M.P.M. and Unwin, G.P.	1973	"Calibration of the 3'x 3' low speed wind tunnel of Imperial College", Dept. of Aeronautics, 3rd Year Report, June 1973 .
Cowdrey, C.F. and Lawes, J.A.	1959	"Force measurements on square and dodecagonial sectional cylinders at high Reynolds numbers", NPL Aero Rep. 351 .

Davenport, A.G.	1975	"Perspectives on the full-scale measurements of wind effects ", J. Industrial Aerodynamics, 1 , 23 - 54 .
Davies, M.E.	1974	"Spectral Analysis Programs Powspec and Cophase ", I.C. Aero TN 74 - 103, Imperial College Aeronautics Department.
Davies, M.E.	1975	"Wakes of oscillating bluff bodies" Ph. D Thesis, Dept. of Aeronautics, Imperial College, London University.
Doebelin, E.O.	1966	"Measurement Systems : Application and design ", McGraw-Hill Book Company, Page 401 .
Eaton, K.J.	1977	"Proceedings of the Fourth International Conference on Wind Effects on Buildings and Structures" Cambridge University Press.
Engineering Sciences Data Unit	1971	Data Sheet 71016 .
Fackrell, J.E.	1973	"The Aerodynamics of an Isolated wheel Rotating in contact with the ground ", Ph. D Thesis, Dept of Aeronautics, Imperial College, London University.
Fage, A, and Johansen, F.C.	1927	"On the flow of air behind an inclined flat plate of infinite span", R & M 1104 .

Feng, C.C. 1968 "The measurement of vortex induced effects in flow past stationary and oscillating circular and D-section cylinders", M.A.Sc. Thesis, Univ. of British Columbia, Dept. of Mech. Eng. October.

Gerrard, J.H. 1961 "An experimental investigation of the oscillating lift and drag of a circular cylinder shedding turbulent vortices", J.Fluid Mech., 11 , 244 - 456 .

Gerrard, J.H. 1965 "A disturbance-sensitive Reynolds number range of the flow past a circular cylinder", J. Fluid Mech., 22 , 187 - 196 .

Gerrard, J.H. 1966 "The mechanics of the formation region of vortices behind bluff bodies", F. Fluid Mech., 25 , 401 - 413 .

Griffin, O.M. 1971 "The Unsteady Wake of an Oscillating Cylinder at Low Reynolds Number", Trans. ASME, J. Appl. Mech., 38, 729- 738 .

Griffin, O.M. and Ramberg, S.E. 1974 "The vortex-street wakes of vibrating cylinders ", J. Fluid Mech., 66 , 553 - 576 .

Griffin, O.M. and Ramberg, S.E. 1975 "On vortex strength and drag in bluff-body wakes", J. Fluid Mech., 69 , 721 - 728 .

Griffin, O.M. and Votaw, C.W.	1972	"The vortex street in the wake of a vibrating cylinder", J. Fluid Mech., 51 , 31 - 48 .
Hartlen, R.T. and Currie, I.G.	1970	"Lift-oscillator model of vortex-induced vibration", Proc. of the American Soc. of Civil Engrs., Jnl. of the Engineering Mechanics Division, 96 , 577 - 591.
Keefe, R.T.	1961	"An investigation of the fluctuating forces acting on a stationary circular cylinder in a subsonic stream and of the associated sound field", UTIA Report No. 76 .
Koopman, G.H.	1967	"The vortex wakes of vibrating cylinders at low Reynolds numbers", J. Fluid Mech., 28 , 501 - 512 .
Landl, R.	1975	"A mathematical model for vortex-excited vibrating of bluff bodies", Journal of Sound and Vibrations, 42 219 - 234 .
Laneville, A. Gartshore, I.S. and Parkinson, G.V.	1975	"An explanation of some effects of turbulence on bluff bodies", Int. Conf. Wind Effects on Buildings & Structures, Heathrow, London.
Lee, B.E.	1974	"The surface pressure field experienced by a two-dimensional square prism", C.E.R.L. Note No RD/L/N/17/74 .

Lee, B.E. 1975/1976 "Some effects of turbulence scale on the mean forces on a bluff body" Journal of Industrial Aerodynamics, 1 , 361 - 370 .

Mair, W.A. and Maull, D.J. 1971 "Bluff bodies and vortex shedding a report on Euromech 17 ", J. Fluid Mech., 45 , 209 - 224 .

Maskell, E.C. 1963 "A theory of the blockage effects on bluff bodies and stalled wings in a closed wind tunnel", A.R.C. R and M No 3400 .

McGregor, D.M. 1957 "An Experimental Investigation of the Oscillating Pressures on a Circular Cylinder in a Fluid Stream", UTIA Technical Note No. 14 .

Mclaren, F.G. Sherratt, A.F.C. and Morton, A.S. 1969 "Effect of Free Stream Turbulence on the Drag Coefficient of Bluff Sharp-edged Cylinders ", Nature, 224 , 908 - 909 .

Milne-Thomson, L.M. 1968 "Theoretical Hydrodynamics", 5th ed., MacMillan,

Morkovin, M.V. 1964 "Flow around a circular cylinder. A kaleidescope of challenging fluid phenomena ", Symposium on Fully Separate flows, American Soc. Mech. Engrs.

Mulhearn, P.J. 1973 "Stagnation and Reattachment Lines on a Cylinder of Square Cross-section in Smooth and Turbulent Flows", Nature Physical Science, 241 , 165 - 167 .

Nakamura, Y. and Mizota, T. 1975 "Unsteady lifts and wakes of oscillating rectangular prisms", Journal of the Eng. Mech. Division, ASCE, NO EM6, Proc. Paper 11813 , 855 - 871 .

Naudascher, E. 1974 "Flow-induced structural vibrations", Proc. of the IUTAM/IAHR Symposium Karlsruhe (Germany) 1972 Published by: Springer-Verlag.

Novak, M. and Tanaka, H 1975 "Pressure correlations on a vibrating cylinder", Int. Conf. Wind Effects on Buildings and Structures, Heathrow,London

Otsuki, Y., Washizu, K, Tomizawa, H and Ohya, A. 1974 "A note on the aeroelastic instability of a prismatic bar with square section". Journal of Sound and Vibration, 34 , 233 - 248.

Parkinson, G.V. 1971 "Wind-induced instability of structures", Phil. Trans. Roy. Soc. London A , 269 , 395 - 409 .

Parkinson, G.V.	1972	"Mathematical models of flow-induced vibrations of bluff bodies" Proc. of IUTAM. IAHR Symp, on Flow-induced structural vibrations, Karlsruhe, Germany.
Parkinson, G.V. and Brooks, N.P.H.	1961	"On the Aeroelastic Instability of Bluff Cylinders", Trans. ASME, J. Appl. Mech., 28 , 252 - 258 .
Parkinson, G.V., Feng, C.C. and Ferguson, N.	1968	"Mechanisms of vortex-excited oscillation of bluff cylinders", Proc. Symp. on wind effects on buildings and structures, Loughborough, England.
Parkinson, G.V. and Smith, J.D.	1962	"An Aeroelastic Oscillator with Two Stable Limit Cycles", Trans. ASME, J. Appl. Mech., 29 , 444 - 445 .
Parkinson, G.V. and Smith, J.D.	1964	"The square prism as an aeroelastic non-linear oscillator", Quart. Journ. Mech. and Applied Math. Vol 17 , 225 - 239 .
Pocha, J.J.	1971	"On unsteady flow past cylinders of square cross-section", Ph. D. Thesis, Dept. of Aeronautics Queen Mary College, London University.
Prendergast, V.	1958	"Measurements of two-point correlations of the surface pressure on a circular cylinder", UTIA Technical Note 23 .

Protos, A.
Goldschmidt, V.W. and Toebes, G.H. 1968 "Hydroelastic forces on bluff cylinders", Trans. A.S.M.E., J. of Basic Engineering Paper No. 68 -FE-12, 378 - 386, September

Robertson, J.M. 1975 "Pressure field at reattachment of separated flows", Paper No. IV-26-1 , Second U.S. National Conference on Wind Engineering Research, Colorado State University Fort Collins, Colorado.

Rockwell, D.O. 1976 "Organized fluctuations due to flow past a square cross section cylinder", Unpublished report, Institute of Hydromechanics, University of Karlsruhe, Karlsruhe, West Germany.

Rosenhead, L. 1953 "Vortex systems in Wakes", Advances in Applied Mechanics III Academic Press.

Roshko, A, 1953 "On the development of turbulent wakes from vortex streets", N.A.C.A. Tech. Note 2913, Washington D.C.

Roshko, A. 1954A "On the Drag and Shedding Frequency of Two-Dimensional Bluff Bodies", NACA TN 3169.

Roshko, A. 1954B "A New Hodograph for Free-Streamline Theory", NACA TN 3168 .

Ruedy, R. 1935 "Vibration of power lines in a steady wind", Canadian Journ. of Research, 13, 82 - 92 .

Sachs, P. 1972 "Wind Forces in Engineering", Pergamon Press, P. 135 .

Scruton, C. and Rogers, E.W.E. 1971 "Steady and unsteady wind loading of buildings and structures", Phil. Trans. Roy. Soc. London A, 269 353 - 383 .

Simmons, J.E.L. 1974A "Phase-angle measurements between hot-wire signals in the turbulent wake of a two-dimensional bluff body", J. Fluid Mech., 64 , 599 - 609 .

Simmons, J.E.L. 1974B "The relationship between the base pressure on a bluff body and the velocity at separation", The Aeronautical Journal, Vol 78, 330 - 331 .

Skop, R.A. and Griffin, O.M. 1973 "A model for the vortex-excited resonant response of bluff cylinders", J. of Sound and Vibration, 27 , 225- 233.

Stansby, P.K. 1976 "The locking-on of vortex shedding due to the cross-stream vibration of circular cylinders in uniform and shear flows", J. Fluid Mech., 74 , 641 - 665.

Stoker, J.J. 1950 "Non-linear Vibrations", Interscience Publishers.

Tanida, Y. Okajima, A. and Watanabe, Y.	1973	"Stability of a circular cylinder oscillating in uniform flow or in a wake", J. Fluid Mech., 61 , 769 - 784 .
Thom, A.	1931	"Experiments on cylinders oscillating in a stream of water", Phil. Mag (7), 12 , 490 - 503 .
Van der Pol, B.	1927	"Forced Oscillations in a System with Non-linear Resistance", Phil. Mag (7), 3 , 65 - 80 .
Vickery, B.J.	1966	"Fluctuating lift and drag on a long cylinder of square cross-section in a smooth and in a turbulent stream" J. Fluid Mech., 25 , 481 - 494 .
Walshe, D.E.J.	1972	"Wind-excited oscillations of structures", Her Majesty's Stationery Office, London.
Wilkinson, R.H.	1974	"On the vortex-induced loading on long bluff cylinders ", Ph. D. Thesis, Faculty of Engineering, University of Bristol, Bristol, England

$\frac{U_\infty}{f_N d}$	$\frac{(1 - C_{pb})}{2\pi S}$		
	OSCILLATING MODEL $A/D = 0.10$	STATIONARY MODEL $S = 0.134$	STATIONARY MODEL $S = 0.130$
7.53	2.91	2.98	3.07
7.90	2.90	2.98	3.07
8.46	3.04	2.98	3.07

CALCULATED FROM FIG. 7.3 (b).

$\frac{U_\infty}{f_N d}$	$\frac{(1 - C_{pb})}{2\pi S}$		
	OSCILLATING MODEL $A/D = 0.25$	STATIONARY MODEL $S = 0.134$	STATIONARY MODEL $S = 0.130$
6.51	2.57	3.09	3.18
7.03	2.78	3.09	3.18
7.18	2.84	3.09	3.18
7.54	2.87	3.09	3.18
7.81	2.83	3.09	3.18
8.51	2.67	3.09	3.18

CALCULATED FROM FIG. 7.4

TABLE I. THE BEHAVIOUR OF $\frac{1 - C_{pb}}{2\pi S}$ DURING 'LOCK-IN'.

* Refer to Chapter 7.

AMPLITUDE TO DIAMETER RATIO A/D	REDUCED WINDSPEED $\frac{U_\infty}{f_N d}$	$\frac{f_N}{f_S}$	LONGITUDINAL VORTEX SPACING a/d	CONVECTION VELOCITY $\frac{U_c}{U_\infty} = S \cdot \frac{a}{d}$	
0.10	7.21	1.04	6.82	0.95	0.97
0.10	7.55	0.99	7.38	0.98	
0.10	7.91	0.94	7.64	0.97	
0.25	7.19	1.04	6.45	0.90	0.90
0.25	7.63	0.98	6.87	0.90	
0.25	7.79	0.96	6.85	0.92	
0	7.54		6.71	0.89	

TABLE 2 MEASUREMENTS OF LONGITUDINAL VORTEX SPACING, a/d, DURING WAKE SYNCHRONISATION OR 'LOCK-IN'.

× Refer to Chapter 7.

$\frac{f_N}{f_S}$	$\frac{A}{D}$	$\frac{U_\infty}{f_N d}$	MEASURED $C_D \cdot S$	$\frac{b}{a}$	$\frac{a}{d}$ OR $\left(\frac{1}{S} \cdot \frac{U_c}{U_\infty}\right)$	b/d	$\frac{\Gamma_0}{\pi U_\infty d}$	$\frac{1-C_{pb}}{2\pi S}$	ϵ
	0	7.54	0.314	0.074	6.79	0.50	1.90	3.09	0.61
1.15	0.25	6.51	0.343	0.069	5.86	0.41	1.74	2.57	0.68
1.06	0.25	7.03	0.317	0.073	6.33	0.46	1.78	2.78	0.64
1.04	0.25	7.18	0.311	0.075	6.46	0.48	1.79	2.84	0.63
0.99	0.25	7.54	0.284	0.080	6.79	0.54	1.76	2.87	0.61
0.96	0.25	7.81	0.261	0.085	7.03	0.60	1.71	2.83	0.60
0.88	0.25	8.51	0.207	0.106	7.66	0.81	1.52	2.67	0.57

$$\epsilon = \left(\frac{\Gamma_0}{\pi U_\infty d}\right)\left(\frac{1-C_{pb}}{2\pi S}\right)^{-1} \quad ; \quad \frac{\Gamma_0}{\pi U_\infty d} = \frac{2U_s a}{\pi U_\infty d}\operatorname{Coth}\left(\frac{\pi b}{a}\right).$$

C_D AND C_{pb} WERE OBTAINED FROM FIG. 7.4.

AT LOCK-IN, $S = \left(\frac{U_\infty}{f_N d}\right)^{-1}$.

b/a WAS CALCULATED FROM THE EQUATION-

$$C_D \cdot S = \frac{4}{\pi}\left(1-\frac{U_s}{U_\infty}\right)\left(\frac{U_s}{U_\infty}\right)^2\left[\operatorname{Coth}^2\left(\frac{\pi b}{a}\right) + \left(\frac{U_\infty}{U_s}-2\right)\frac{\pi b}{a}\operatorname{coth}\left(\frac{\pi b}{a}\right)\right]$$

TABLE 3. PREDICTIONS OF THE VORTEX STREET DRAG FORMULA DURING WAKE SYNCHRONISATION OR 'LOCK-IN', $\frac{U_c}{U_\infty} = 0.90$.

* Refer to Chapter 7.

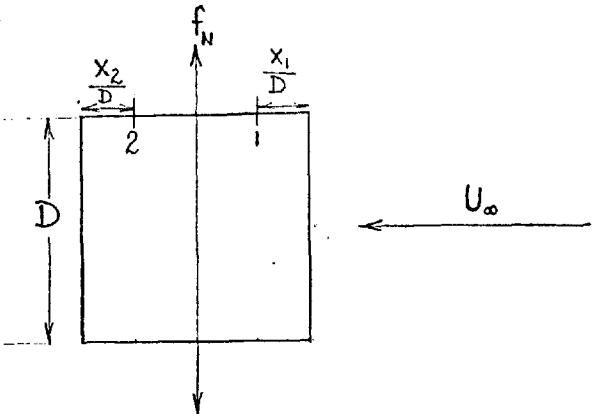

CASE 1 : $\frac{X_2}{D} = \frac{X_1}{D} = 0.25$

A/D	$\frac{U_\infty}{f_N d}$	R_{P12}
0	–	1.02
0.10	5.20	0.77
0.10	6.16	0.82
0.10	7.14	0.98
0.10	7.22	0.96
0.10	7.85	1.00
0.10	8.17	0.97
0.10	13.02	0.98

CASE 2 ; $\frac{X_2}{D} = \frac{X_1}{D} = 0.125$

A/D	$\frac{U_\infty}{f_N d}$	R_{P12}
0	–	0.93
0.10	4.71	- 0.24
0.10	6.22	0.63
0.10	7.82	0.70
0.10	8.72	0.68
0.10	11.94	0.78

CASE 3 ; $\frac{X_2}{D} = 0.5, \frac{X_1}{D} = 0.125$

A/D	$\frac{U_\infty}{f_N d}$	R_{P12}
0	–	0.99
0.10	7.85	1.03
0.25	7.17	1.02
0.25	7.77	1.01

CASE 4; $\frac{X_2}{D} = 0.125, \frac{X_1}{D} = 0.5$

A/D	$\frac{U_\infty}{f_N d}$	R_{P12}
0	–	0.98
0.10	7.85	0.72
0.25	7.17	0.82
0.25	7.85	0.79

TABLE 4 : MEASUREMENTS OF CHORDWISE CORRELATION

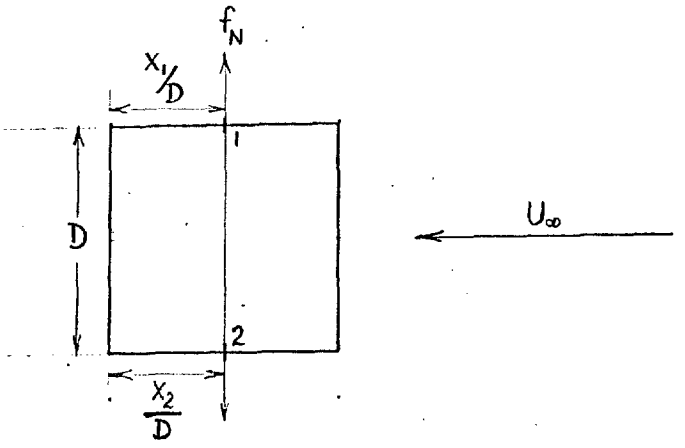

CASE 5 ; $\frac{X_1}{D} = \frac{X_2}{D} = 0.5$		
A/D	$\frac{U_\infty}{f_N d}$	R_{P12}
0	-	- 0.96
0.10	4.71	- 0.89
0.10	6.21	- 0.82
0.10	7.80	- 0.99
0.10	8.72	- 0.93
0.10	9.30	- 0.86
0.10	11.94	- 0.91

TABLE 4 (CONTD.). MEASUREMENTS OF CHORDWISE CORRELATION.

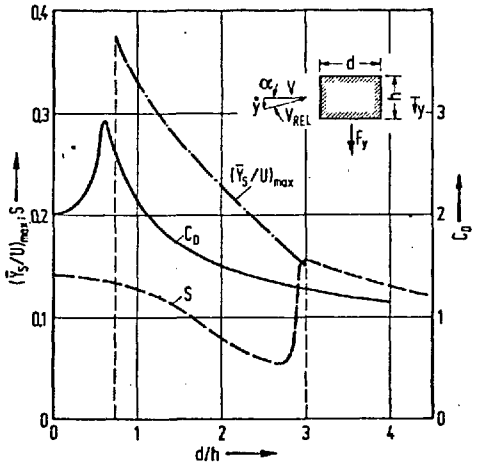

FIG.1.1A Effects of rectangular section afterbody length (FROM PARKINSON (1972))

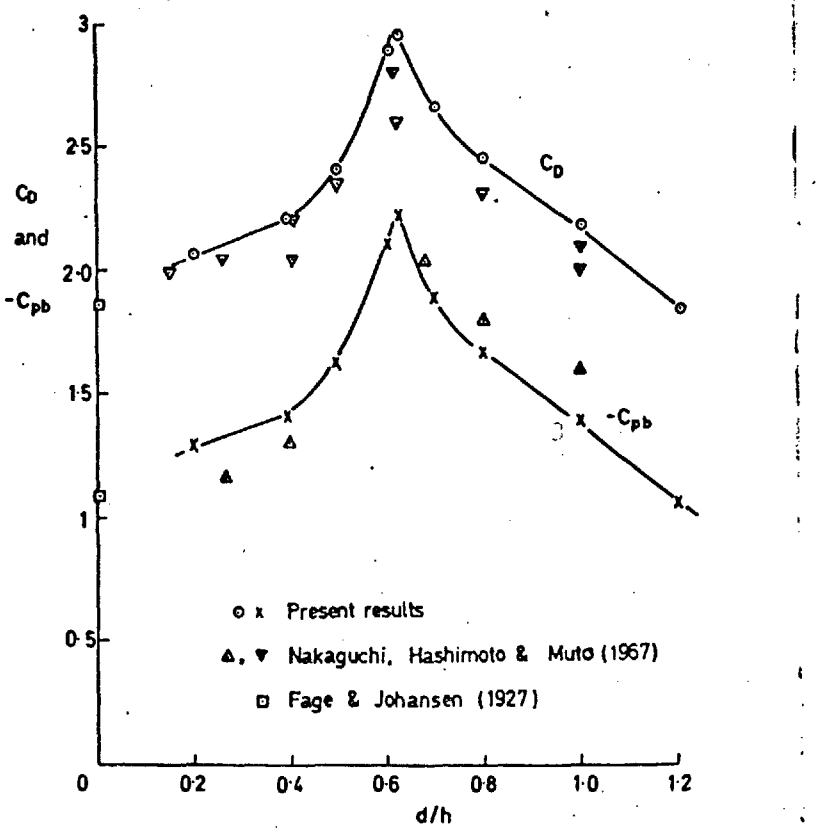

Figure 1.1B Drag coefficient and base pressure coefficient measurements on rectangular sections, $Re = 2 \times 10^4 - 7 \times 10^4$

FROM BEARMAN & TRUEMAN (1971)

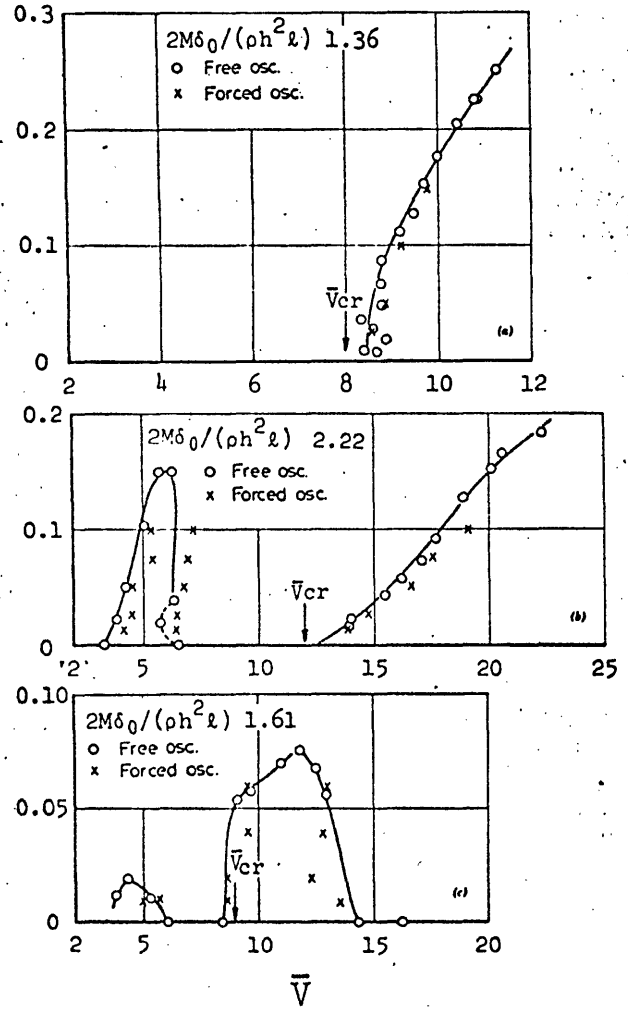

FIG. 1.2 A —Steady-State Amplitude Versus Reduced Wind Velocity in Free Oscillation Experiment: (*a*) Model 1:1; (*b*) Model 1:2; (*c*) Model 1:4

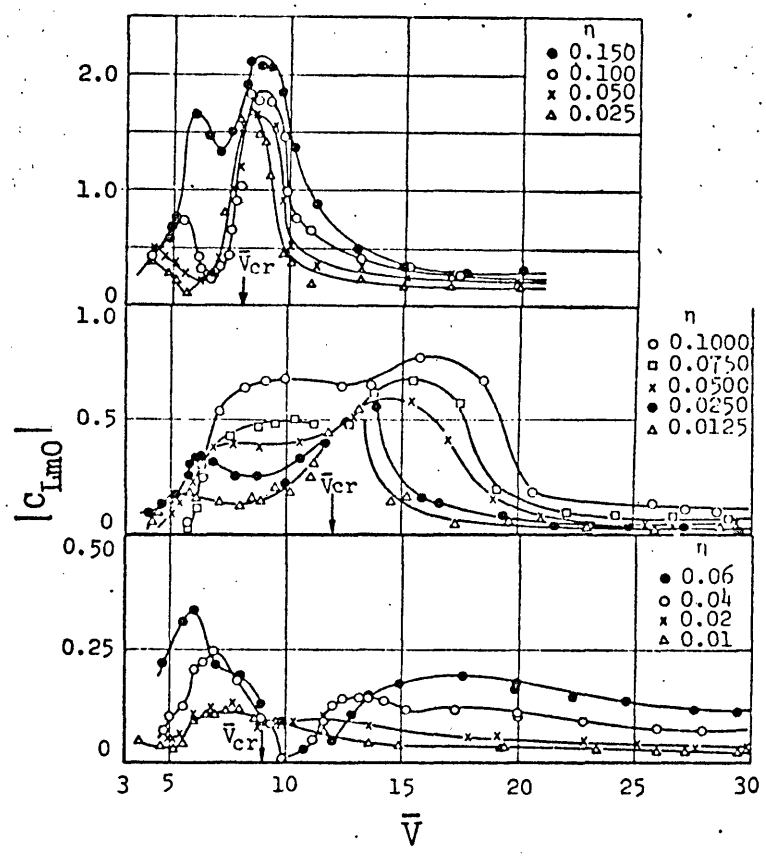

FIG. 1.2 B —Amplitude of Frequency Response Component of Unsteady Lift Force Coefficient Versus Reduced Wind Velocity: (*a*) Model 1:1; (*b*) Model 1:2; (*c*) Model 1:4

[$\bar{V} = \frac{U_\infty}{f_N D}$; $\eta = A/D$. FIGS. 1.2 A&B ARE REPRODUCED FROM NAKAMURA & MIZOTA (1975).]

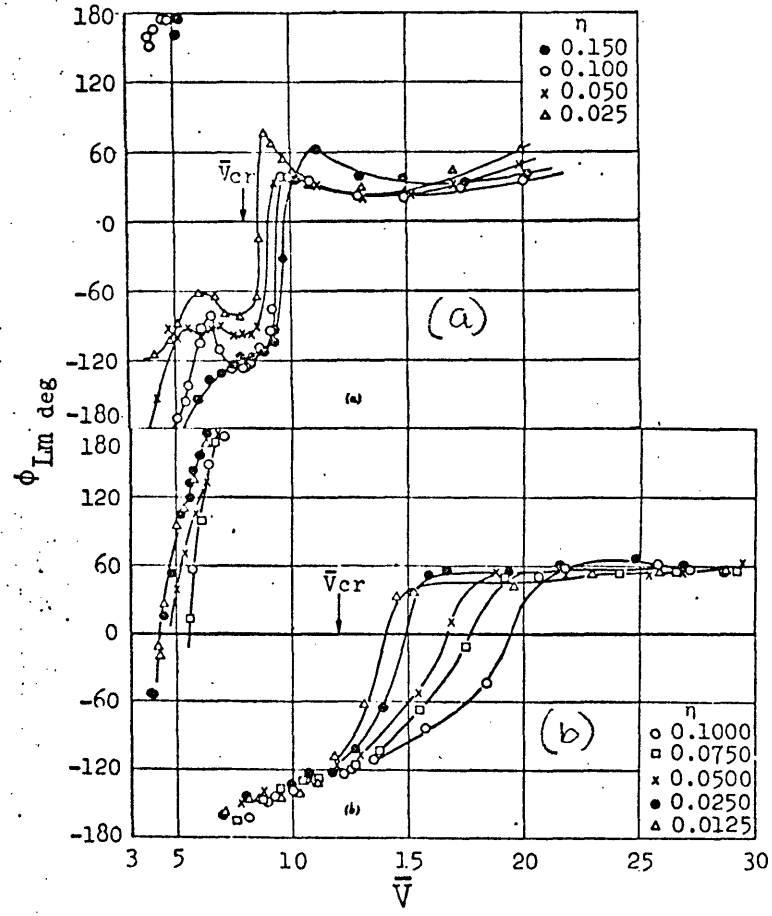

FIG. 1·3 A —Phase Angle of Frequency Response Component of Unsteady Lift Force Coefficient Versus Reduced Wind Velocity: (a) Model 1:1; (b) Model 1:2; (c) Model 1:4

[ALL FIGURES REPRODUCED FROM NAKAMURA & MIZOTA (1975)]

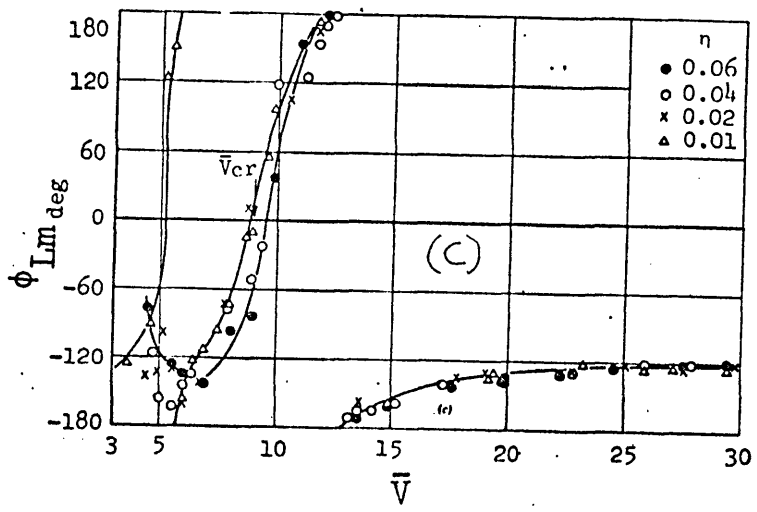

FIG. 1·3 A —Continued

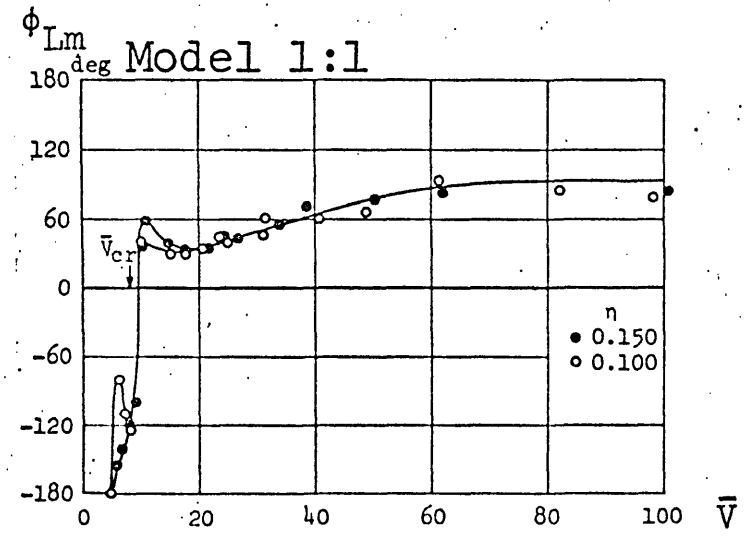

FIG. 1·3 B —Phase Angle Plot at High Reduced Wind Velocities

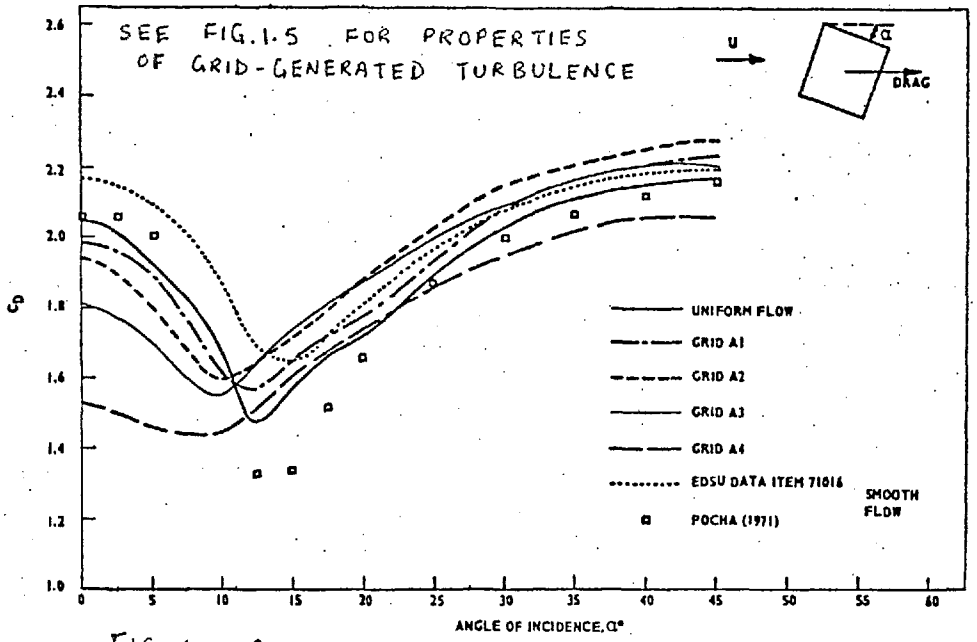

FIG. 1.4 A VARIATION OF MEAN DRAG COEFFICIENT WITH FLOW DIRECTION

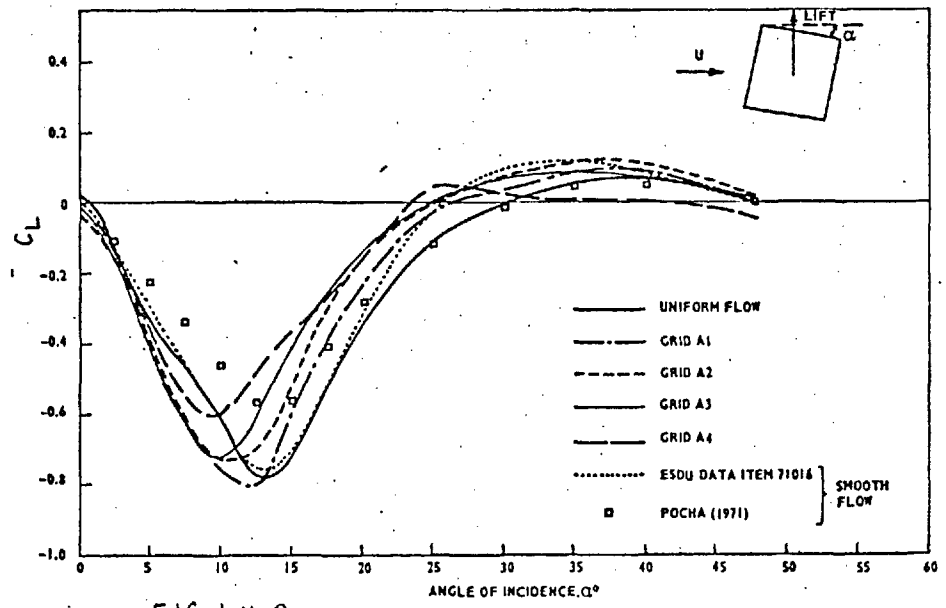

FIG. 1.4 B VARIATION OF MEAN LIFT COEFFICIENT WITH FLOW DIRECTION

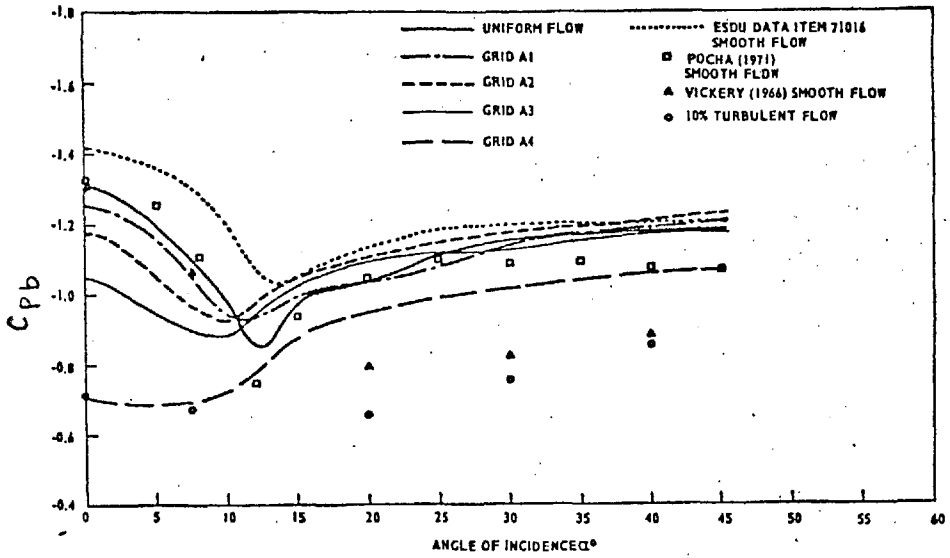

FIG. 1.4 C VARIATION OF BASE PRESSURE COEFFICIENT WITH FLOW DIRECTION

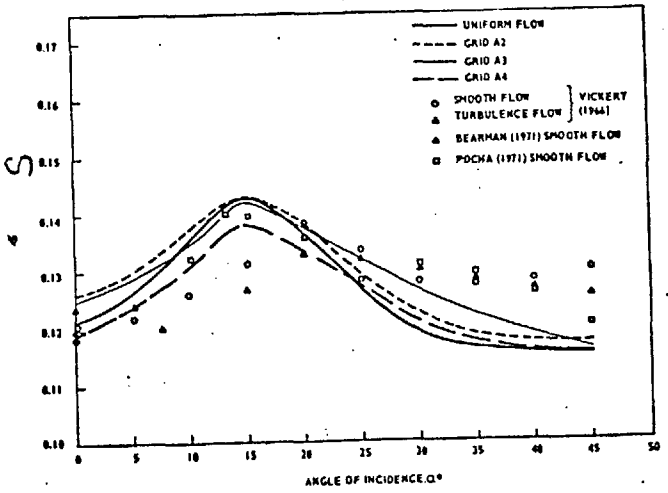

FIG. 1.4 D VARIATION OF STROUHAL NUMBER WITH FLOW DIRECTION

ALL FIGURES ARE REPRODUCED FROM LEE (1974).

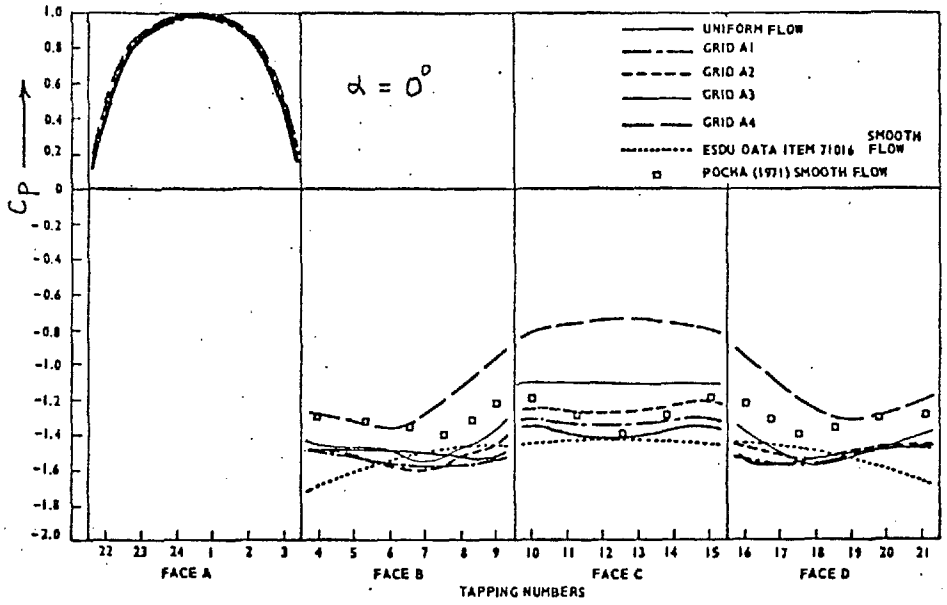

Grid number	$\frac{(\overline{u^2})^{\frac{1}{2}}}{U}$ %	L_1 (m)	L_2 (m)	$\frac{L_2}{D}$	Upstream distance (m)	Bar size (mm)	Mesh size (m)
Uniform flow	0·5						
A1	4·4	0·063	0·160	0·97	6·9	50·8	0·31
A2	6·5	0·072	0·188	1·14	6·9	88·9	0·51
A3	8·0	0·049	0·120	0·73	3·65	50·8	0·31
A4	12·5	0·046	0·155	0·94	3·65	88·9	0·51

. Properties of grid-generated turbulence

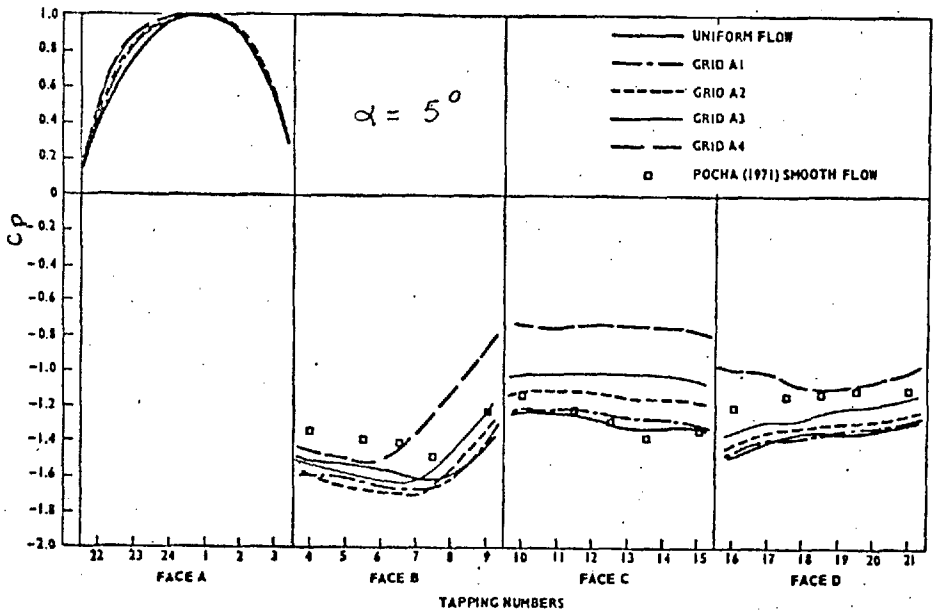

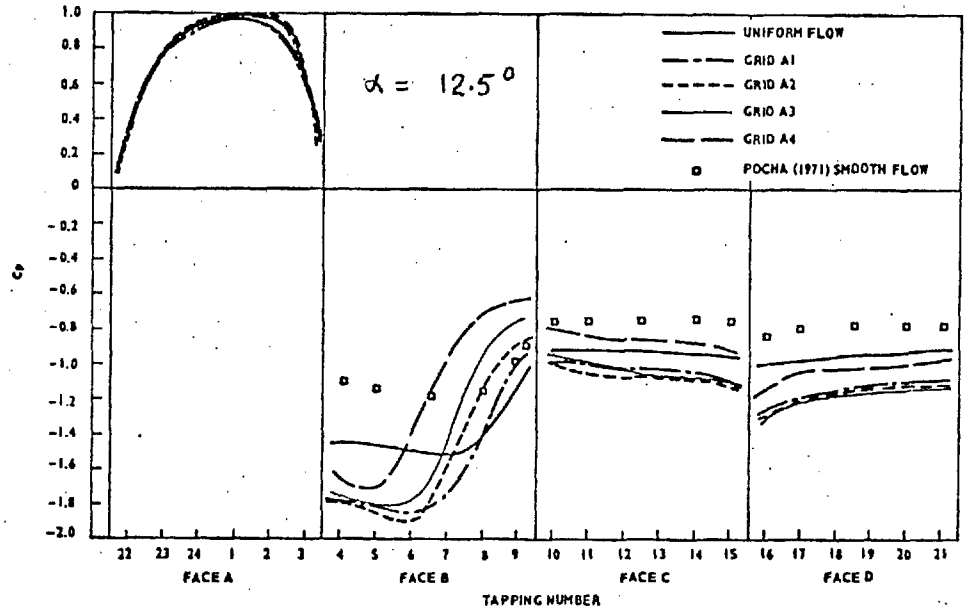

FIG. 1·5 MEAN PRESSURE DISTRIBUTION ON A SQUARE SECTION CYLINDER AT INCIDENCE α.
[REPRODUCED FROM LEE (1974)]

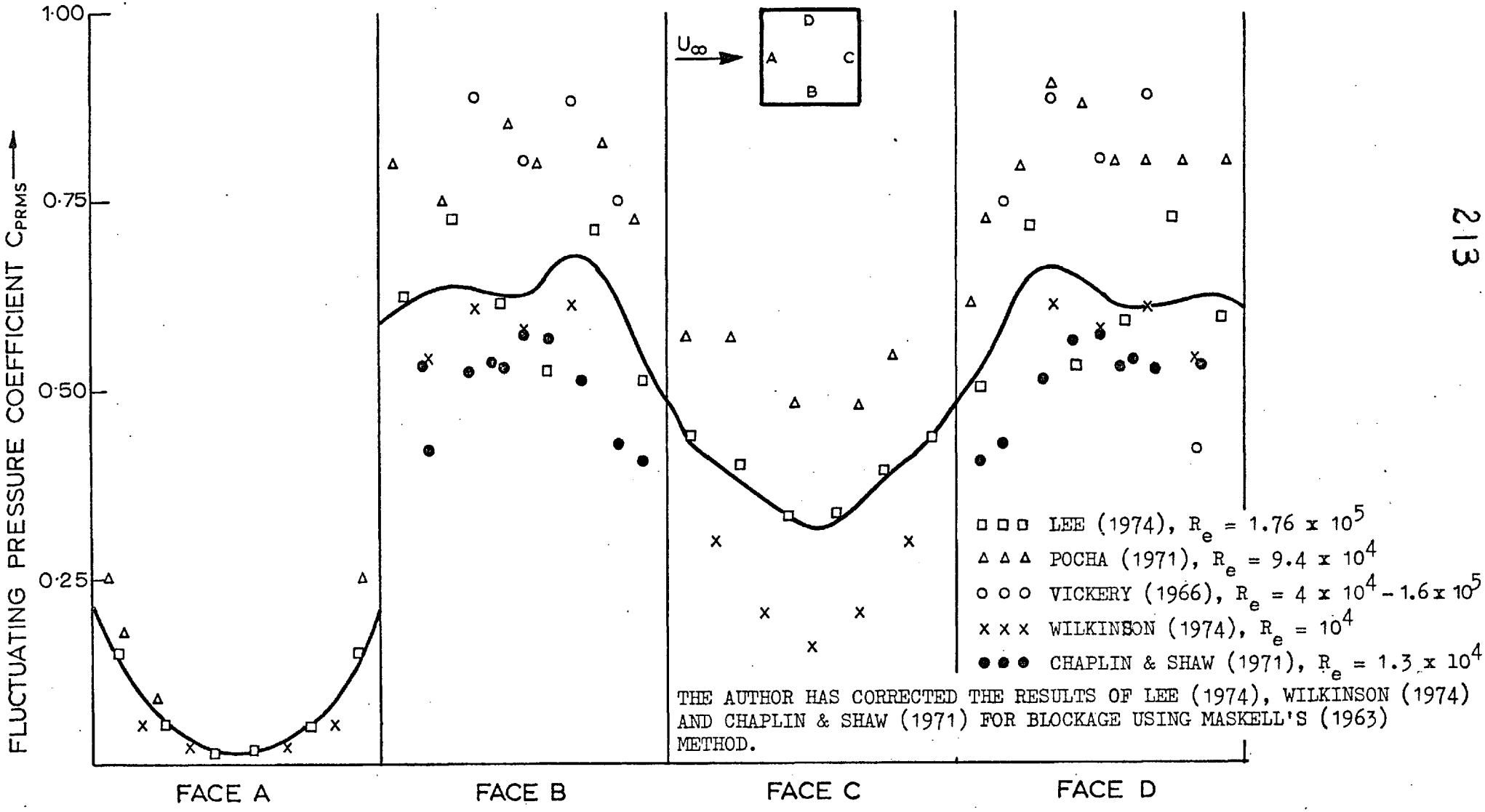

Fig. 1·6 a Distribution of C_{PRMS} on a stationary square section cylinder in smooth flow at 0° incidence

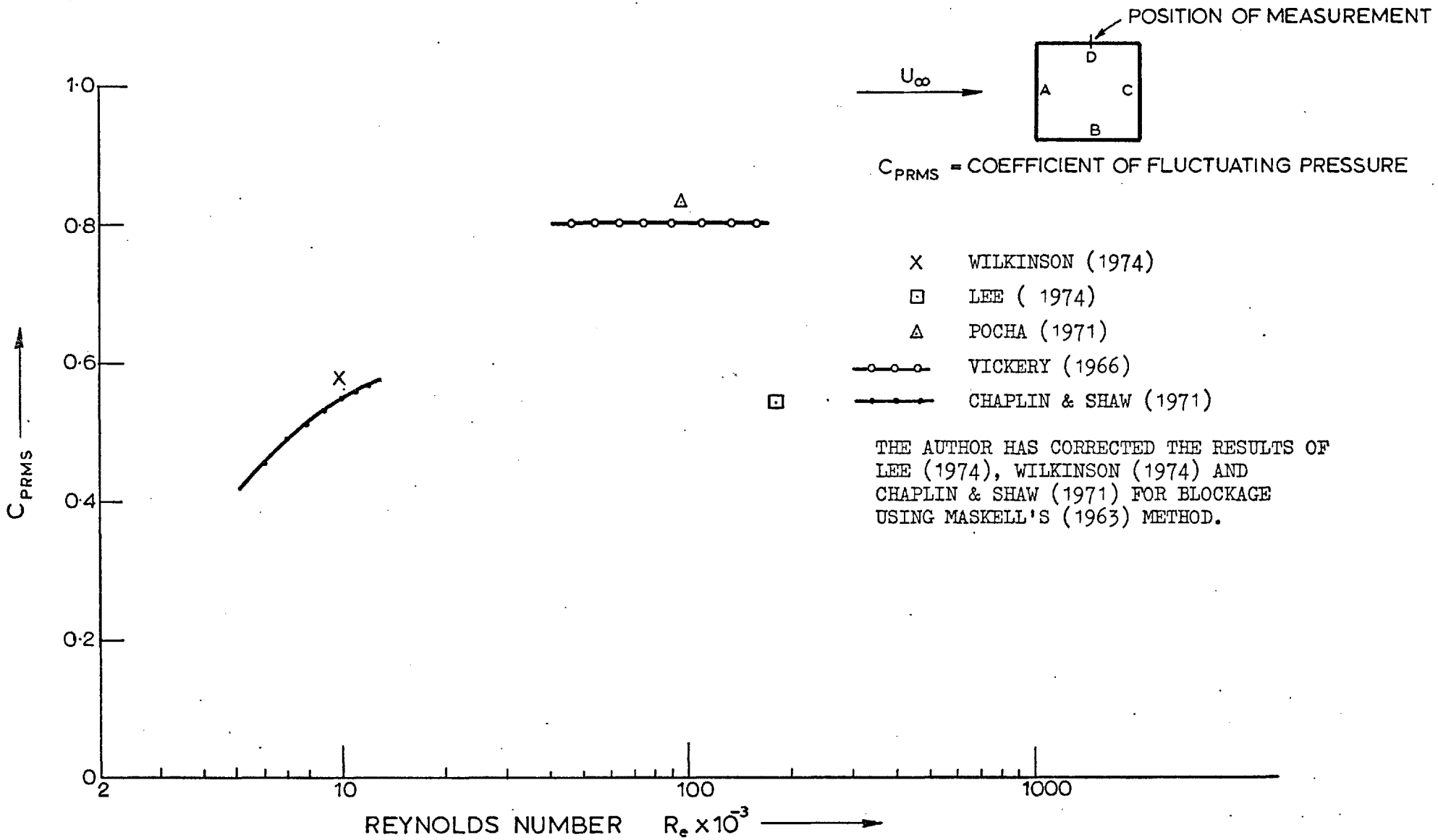

Fig. 1·6 b C_{PRMS} *at the centre of the side face versus Reynolds number*

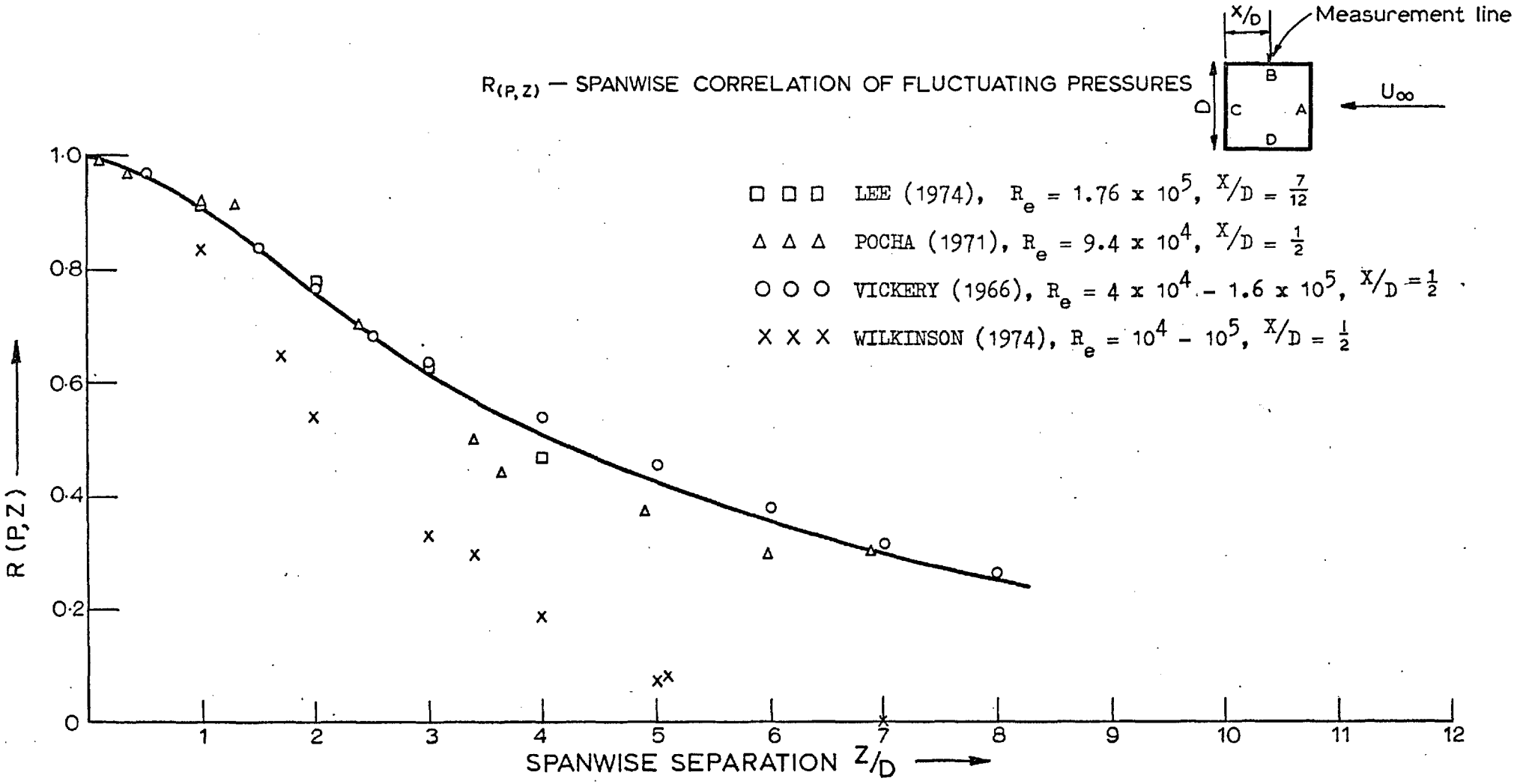

Fig. 1·7 $R_{(PZ)}$ of face B of a stationary square section cylinder in smooth flow at 0° incidence

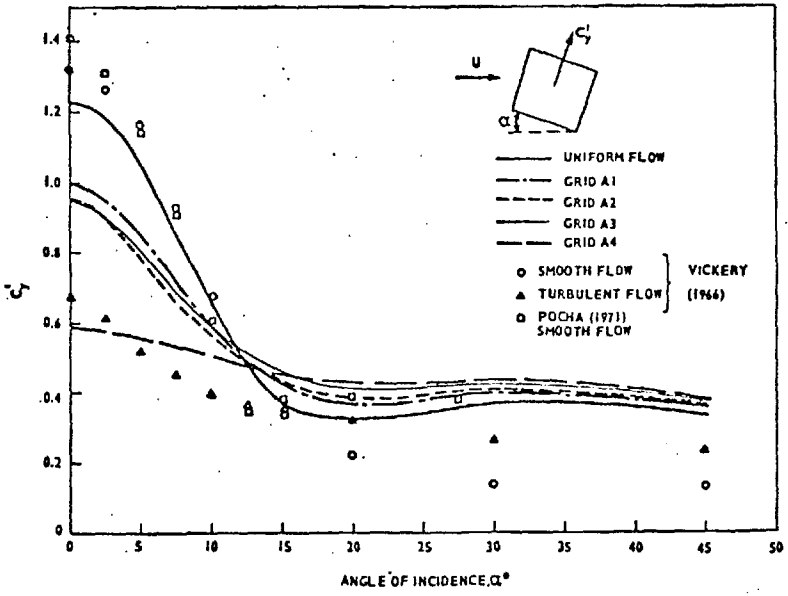

FIG. 1.8 A VARIATION OF C_y' WITH FLOW DIRECTION

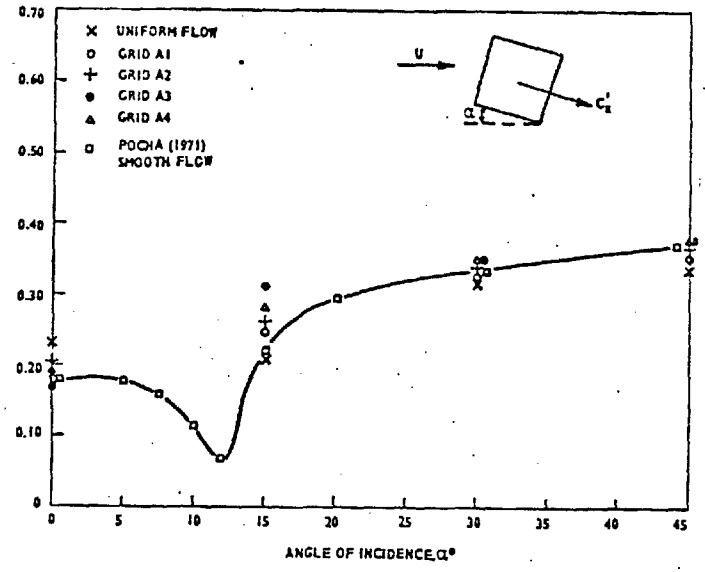

FIG. 1.8 B VARIATION OF C_L' WITH FLOW DIRECTION

ALL FIGURES REPRODUCED FROM LEE (1974). SEE FIG. 1.5 FOR PROPERTIES OF GRID-GENERATED TURBULENCE.

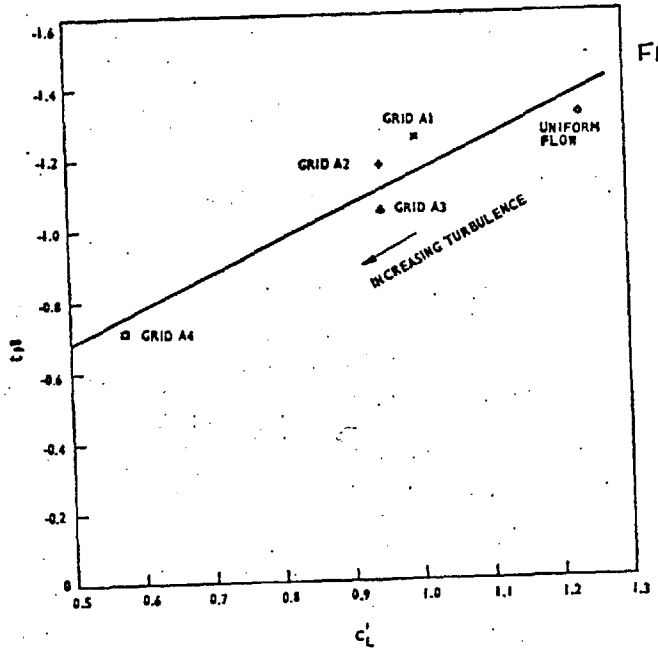

FIG. 1.8 C RELATIONSHIP BETWEEN BASE PRESSURE COEFFICIENT AND FLUCTUATING LIFT COEFFICIENT AT $\alpha = 0°$

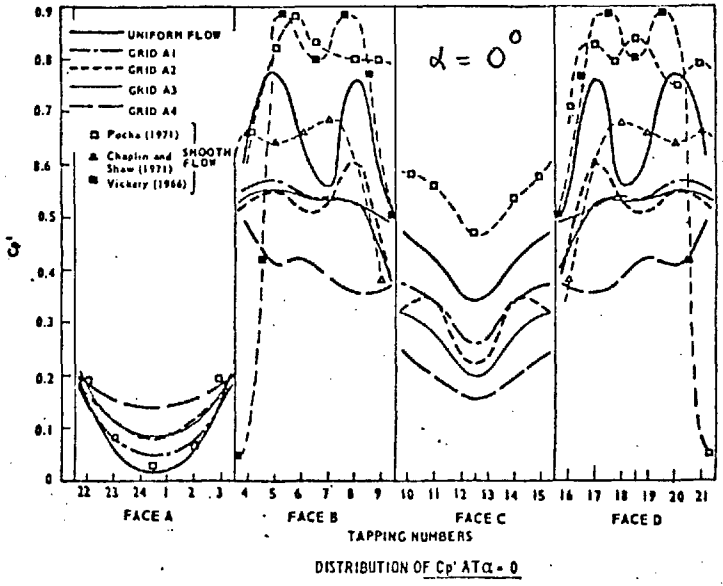

DISTRIBUTION OF Cp' AT α = 0

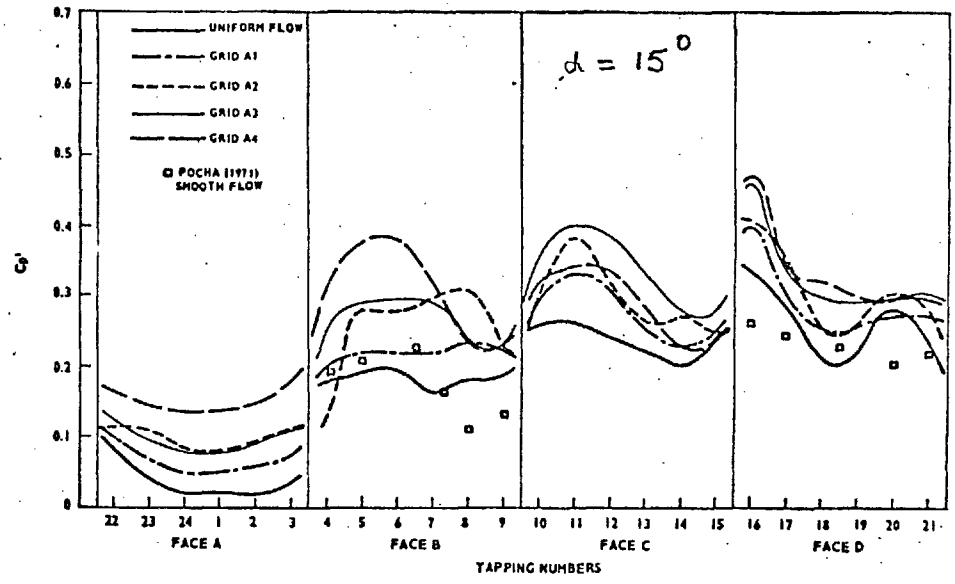

DISTRIBUTION OF Cp' AT α = 15°

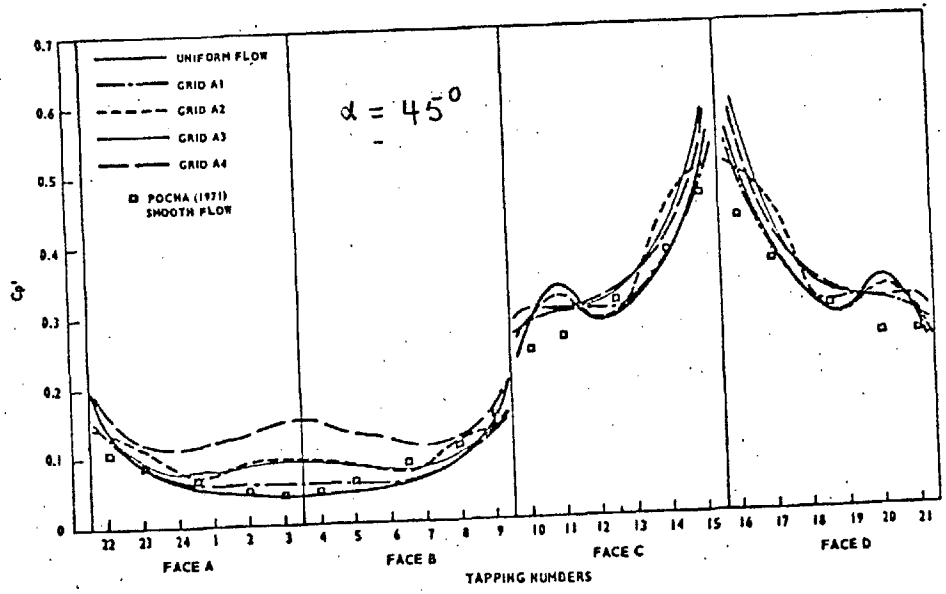

DISTRIBUTION OF Cp' AT α = 45°

SEE FIG. 1.5 FOR PROPERTIES OF GRID - GENERATED TURBULENCE.

FIG. 1.9 DISTRIBUTION OF FLUCTUATING PRESSURES AROUND A SQUARE SECTION CYLINDER AT INCIDENCE α (REPRODUCED FROM LEE (1974))

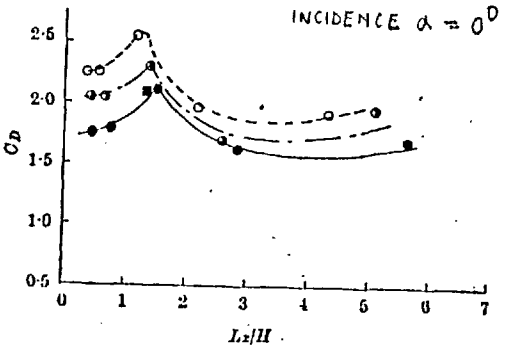

FIG. 1.10 A Drag coefficient versus L_x/H, $\alpha = 0$. Turbulence intensity: ○, 3·4 per cent; ◑, 0·7 per cent; ●, 0·8 per cent. ◧, Vickery[8].

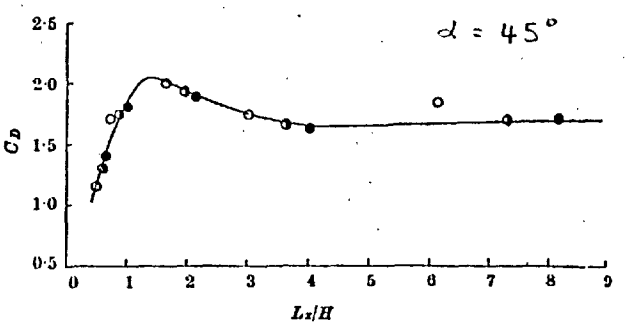

FIG. 1.10 B Drag coefficient versus L_x/H, $\alpha = 45°$. Symbols as in Fig. 1.

FIGS 1.10 A & B ARE REPRODUCED FROM MCLAREN (1969)

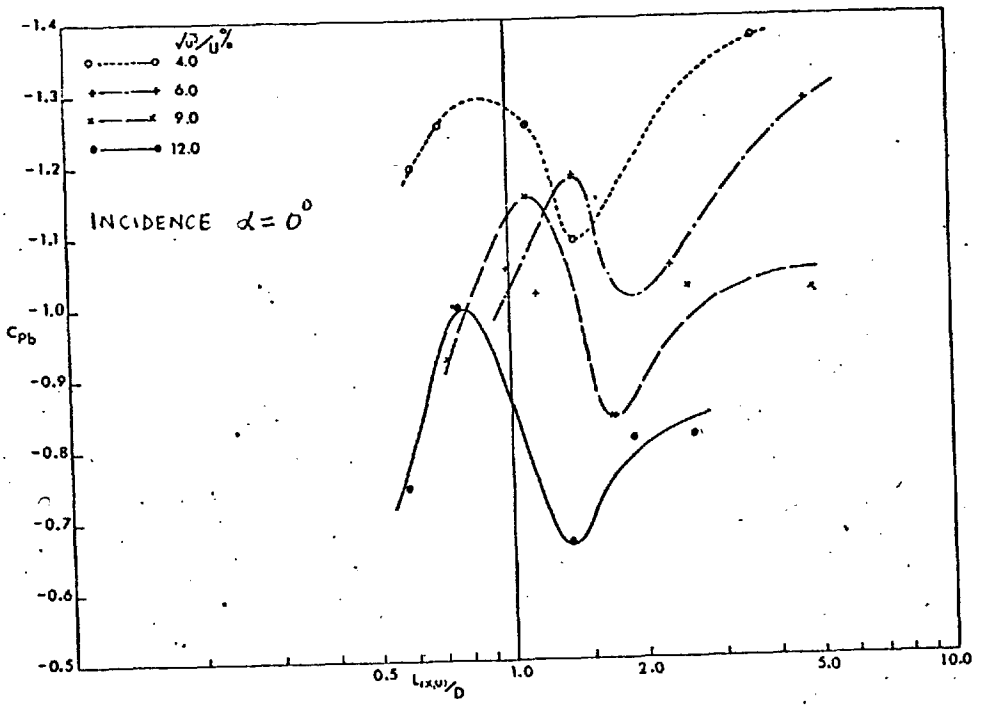

FIG. 1.10 C Variation of base pressure with longitudinal turbulence scale.

FIG. 1.10 C IS REPRODUCED FROM LEE (1975/1976)

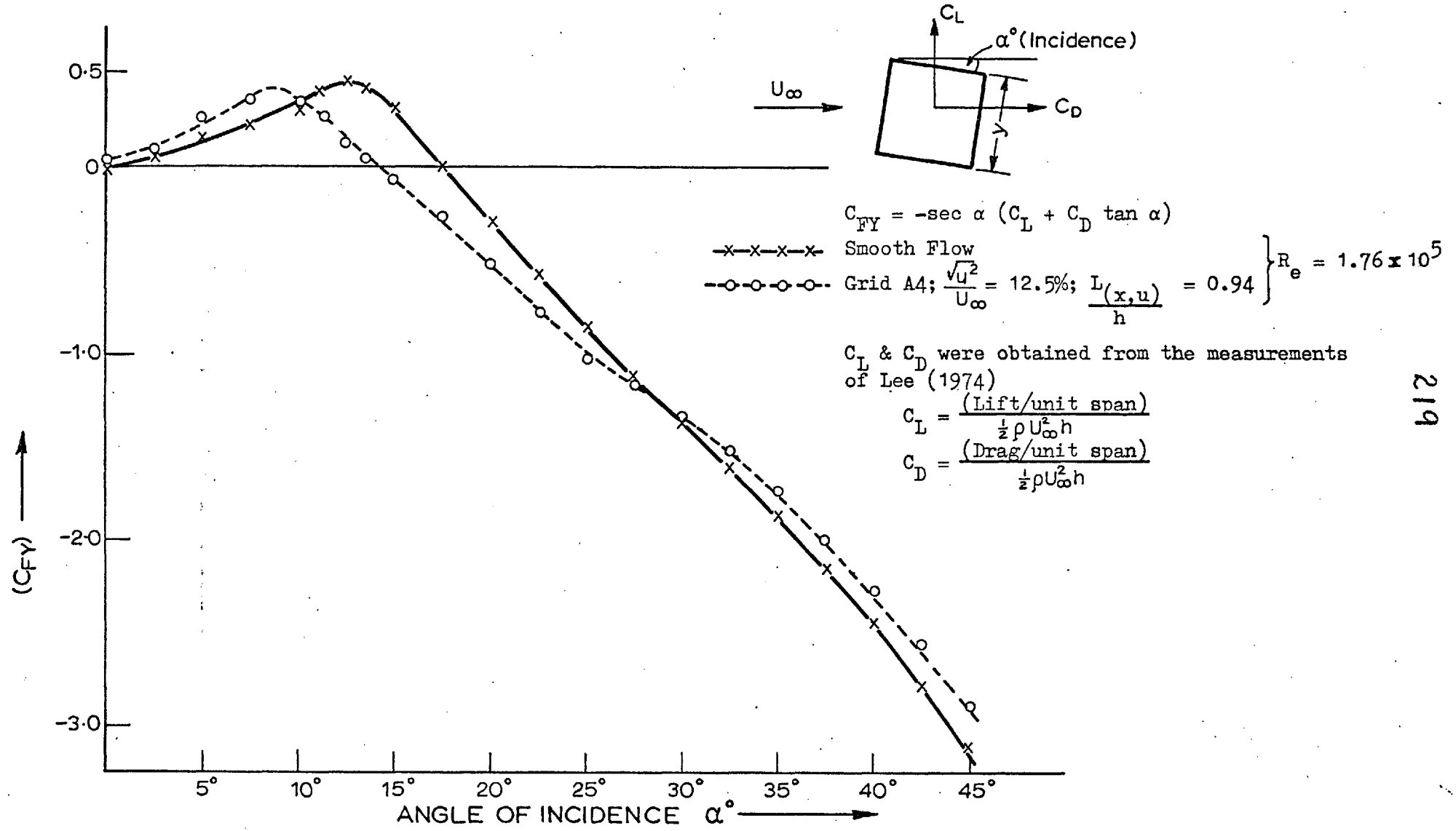

Fig.1·11 Variation of C_{FY} with incidence α

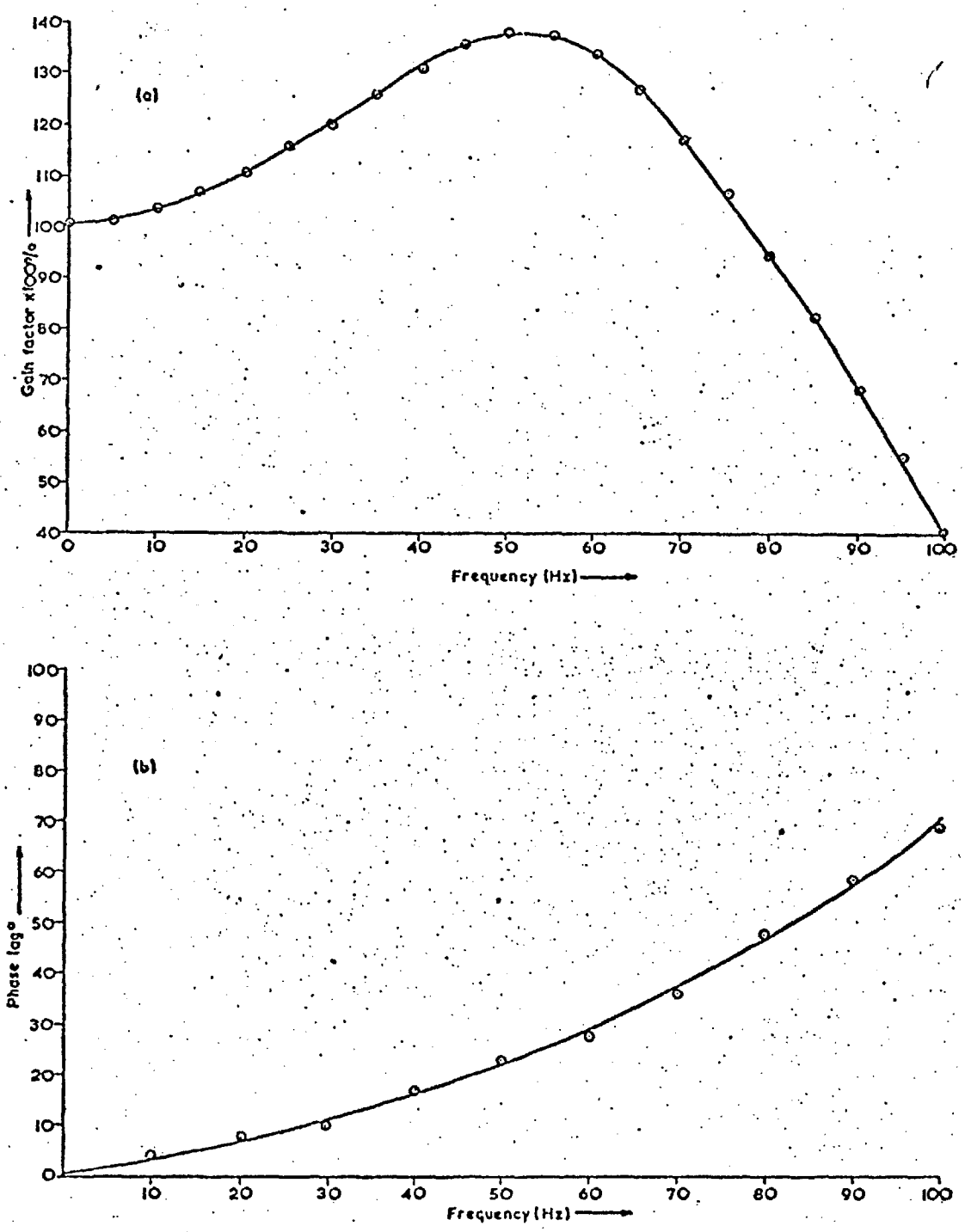

FIG. 1.12 DYNAMIC CALIBRATION CURVES OF PRESSURE TRANSDUCER

[REPRODUCED FROM WILKINSON (1974)]

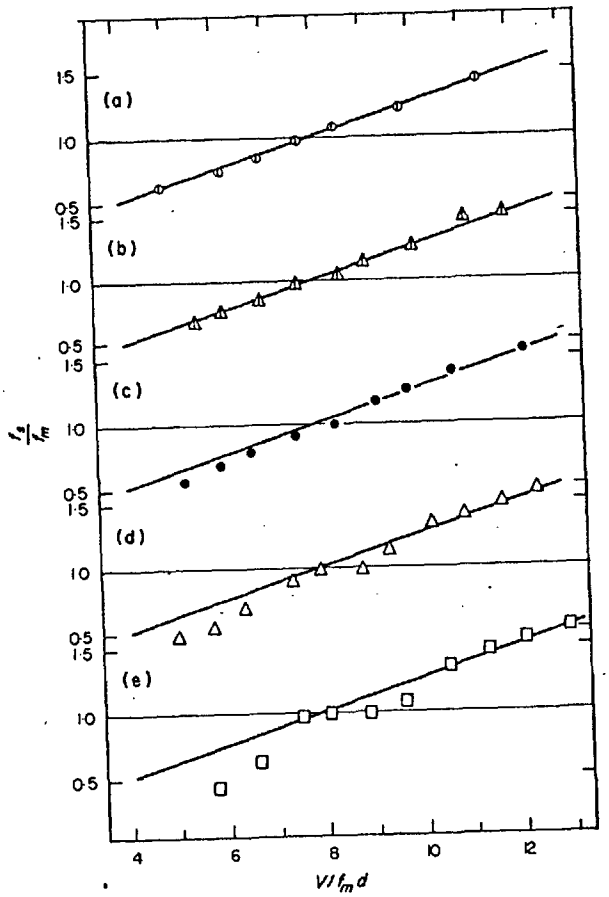

FIG 1.13 A f_s/f_m *vs.* $V/f_m d$. (a) $h_0 = 2$ mm; (b) $h_0 = 5$ mm; (c) $h_0 = 10$ mm; (d) $h_0 = 15$ mm; (e) $h_0 = 20$ mm.

h_0 - OSCILLATION AMPLITUDE; d - CYLINDER DIAMETER = 150 mm.

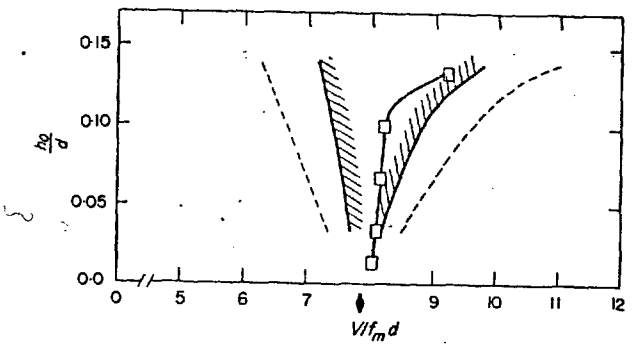

FIG. 1.13 B . Locking-in region.

f_{OL} - OSCILLATION FREQUENCY

f_S - VORTEX SHEDDING FREQUENCY

ALL FIGURES ARE REPRODUCED FROM OTSUKI ET AL. (1974).

ALL FIGURES ARE REPRODUCED FROM Y. OTSUKI *ET AL.* (1974)

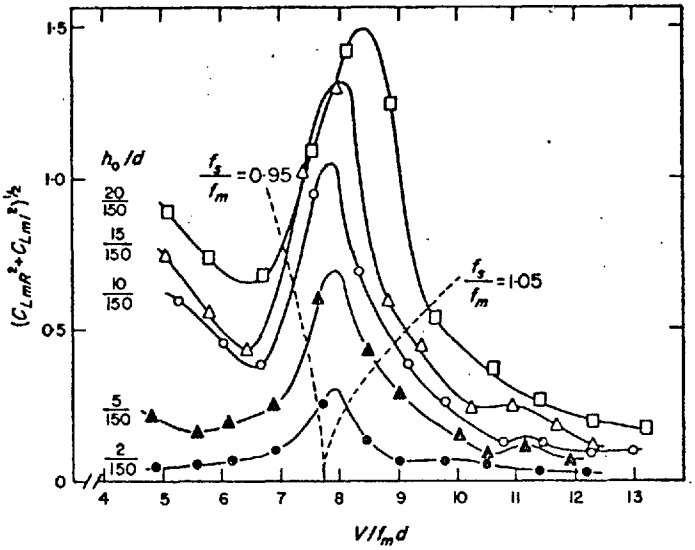

FIG. 1·14 A . $(C_{LmR}^2 + C_{LmI}^2)^{1/2}$ *vs.* $V/f_m d$. h_0(mm): ●, 2; ▲, 5; ○, 10; △, 15; □, 20.

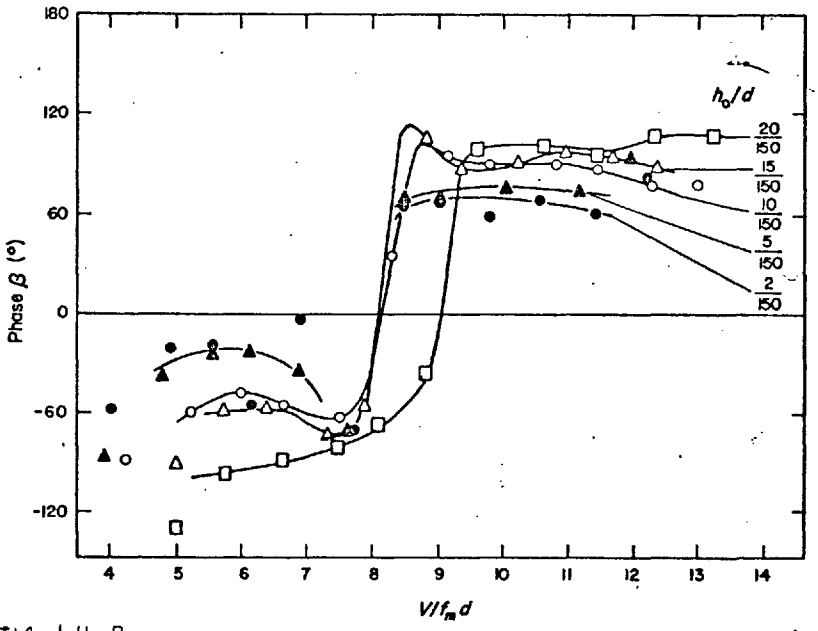

FIG. 1·14 B . β *vs.* $V/f_m d$. h_0(mm): ●, 2; ▲, 5; ○, 10; △, 15; □, 20.

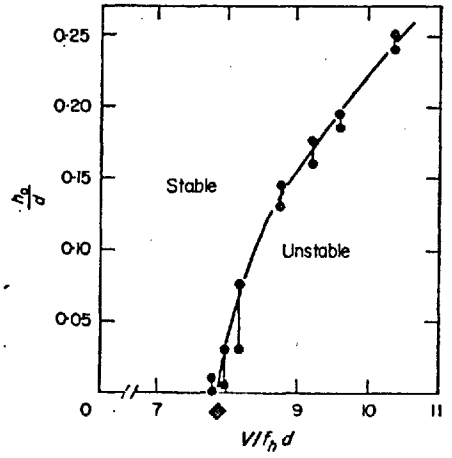

FIG. 1·14 C Aeroelastic instability in heaving mode. ◆, Resonance speed. (STEADY-STATE AMPLITUDE DURING FREE OSCILLATION)

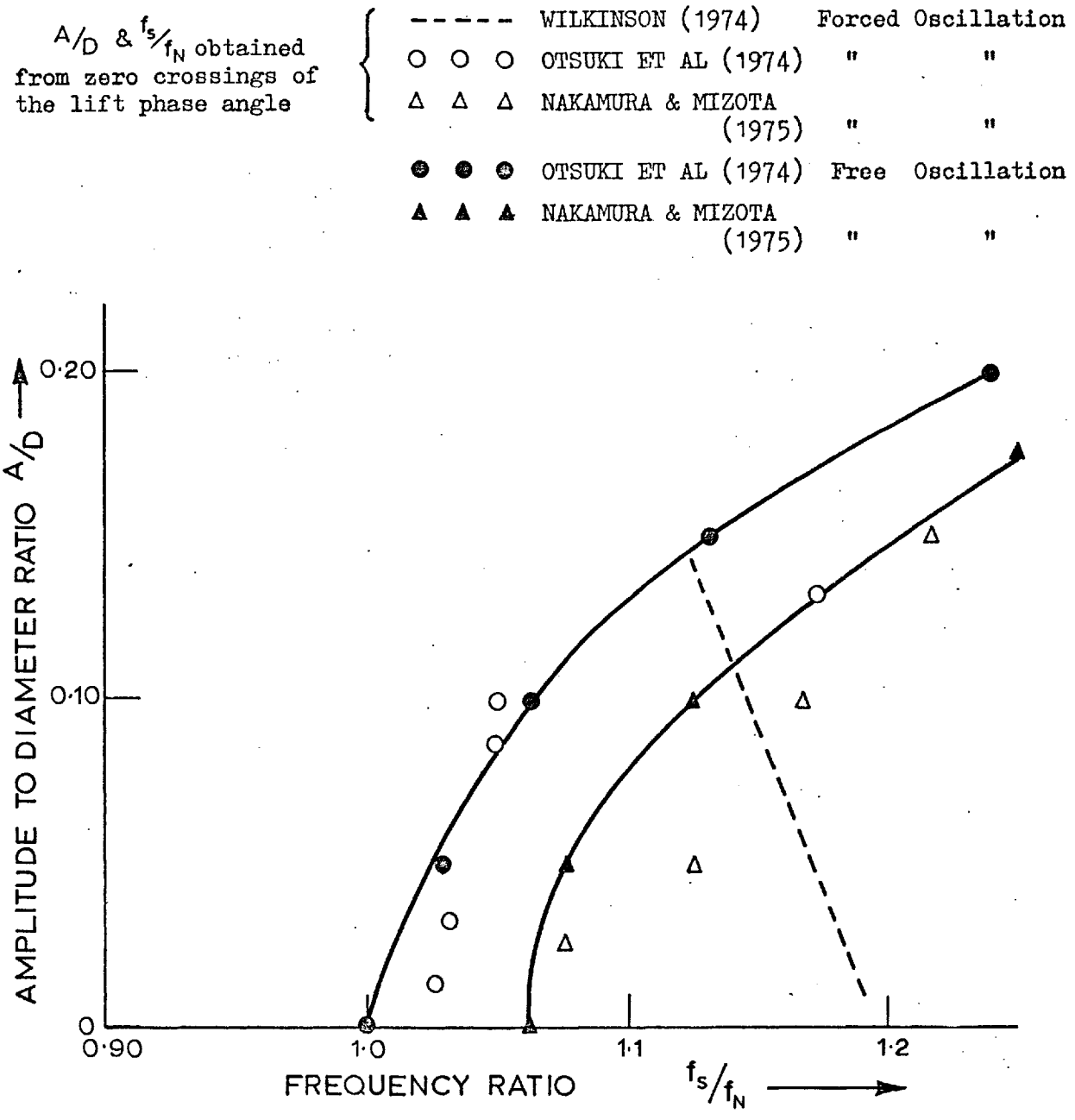

Fig. 1·15 Zero crossings of the lift phase angle, ϕ

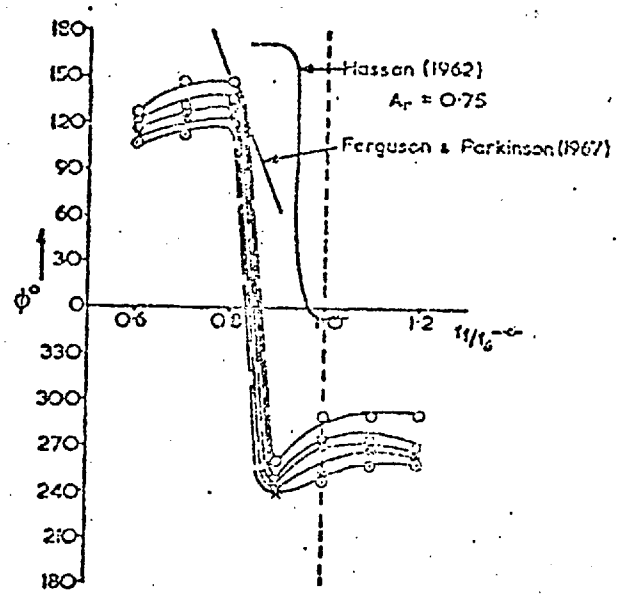

FIG. 1.16A PHASE ANGLE BETWEEN SURFACE PRESSURE AND ACCELERATION (DEDUCED FROM NORMALISED CROSS CORRELATION COEFFICIENT)

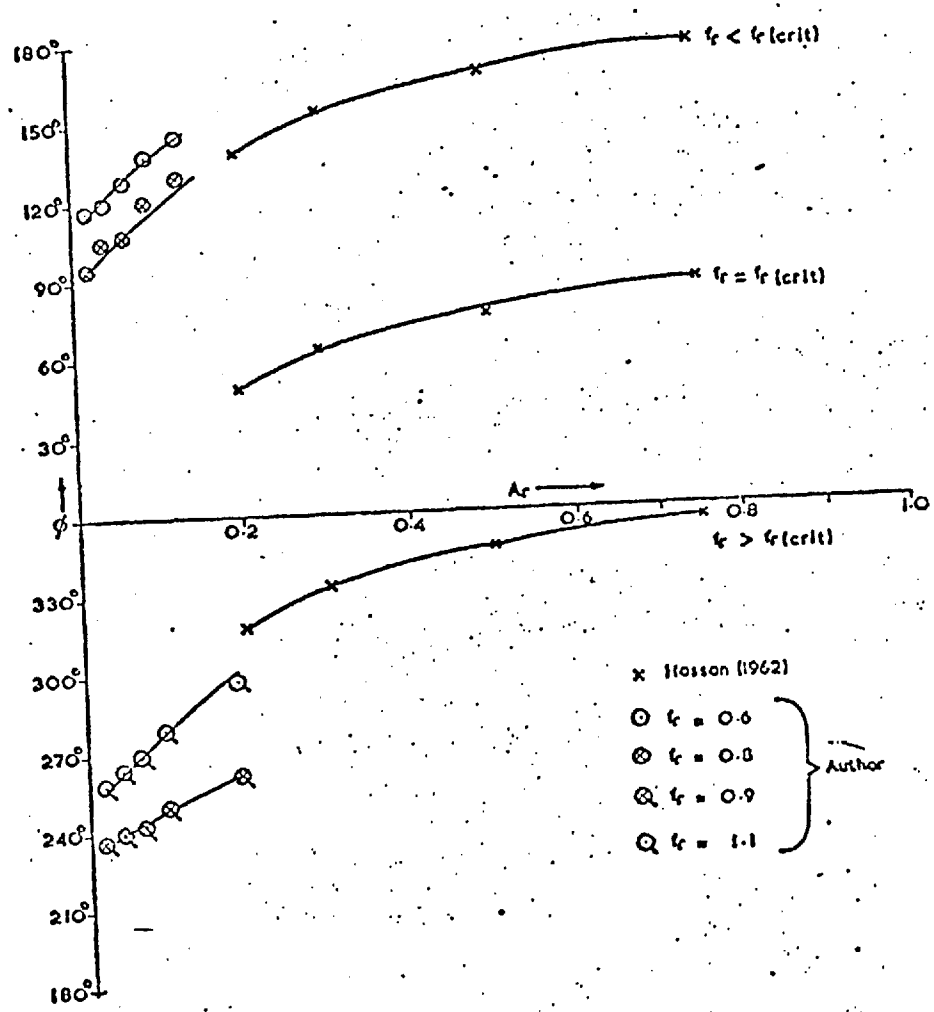

FIG. 1.16 B PHASE ANGLE CHANGE DURING LOCKING-ON

ALL FIGURES ARE REPRODUCED FROM WILKINSON (1974).

ALL FIGURES ARE REPRODUCED FROM WILKINSON (1974)

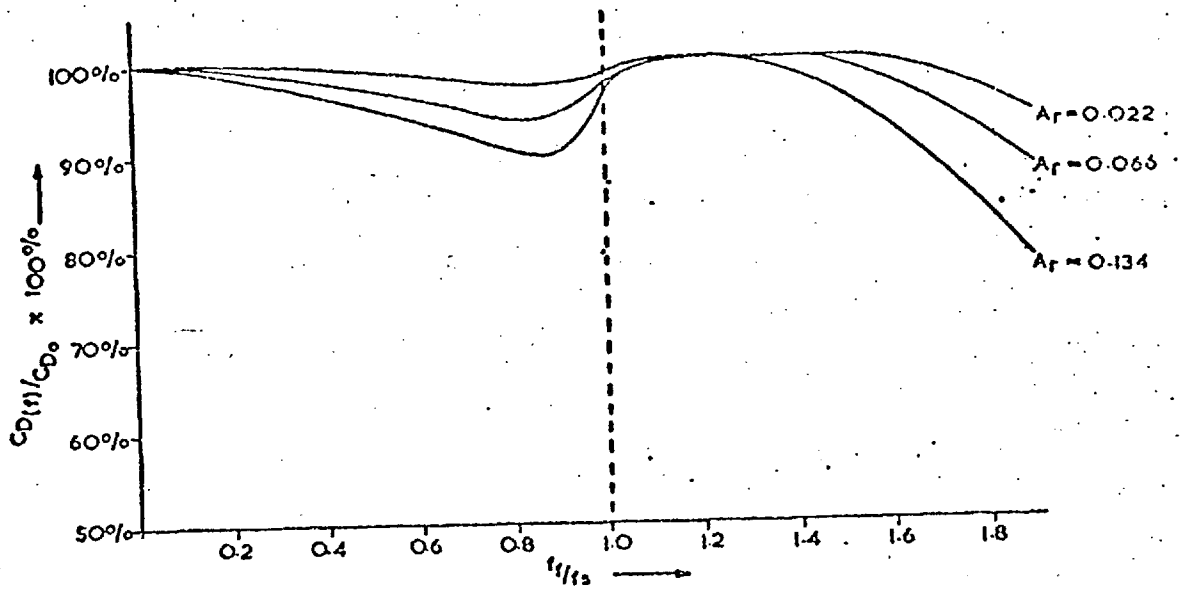

FIG 1·17 A (b) MEAN DRAG COEFFICIENT DURING VIBRATION TESTS AS PERCENTAGE OF VALUE ON STATIONARY MODEL

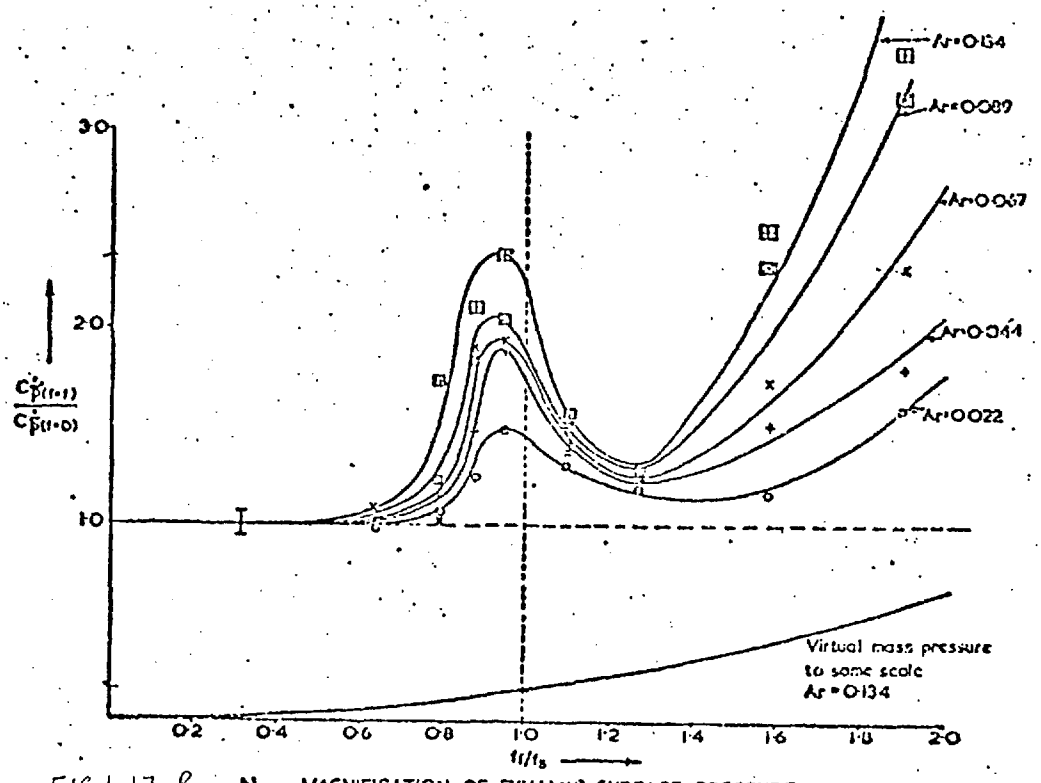

FIG 1·17 B b) MAGNIFICATION OF DYNAMIC SURFACE PRESSURE AT CENTRE, SIDE FACE WITH OSCILLATION

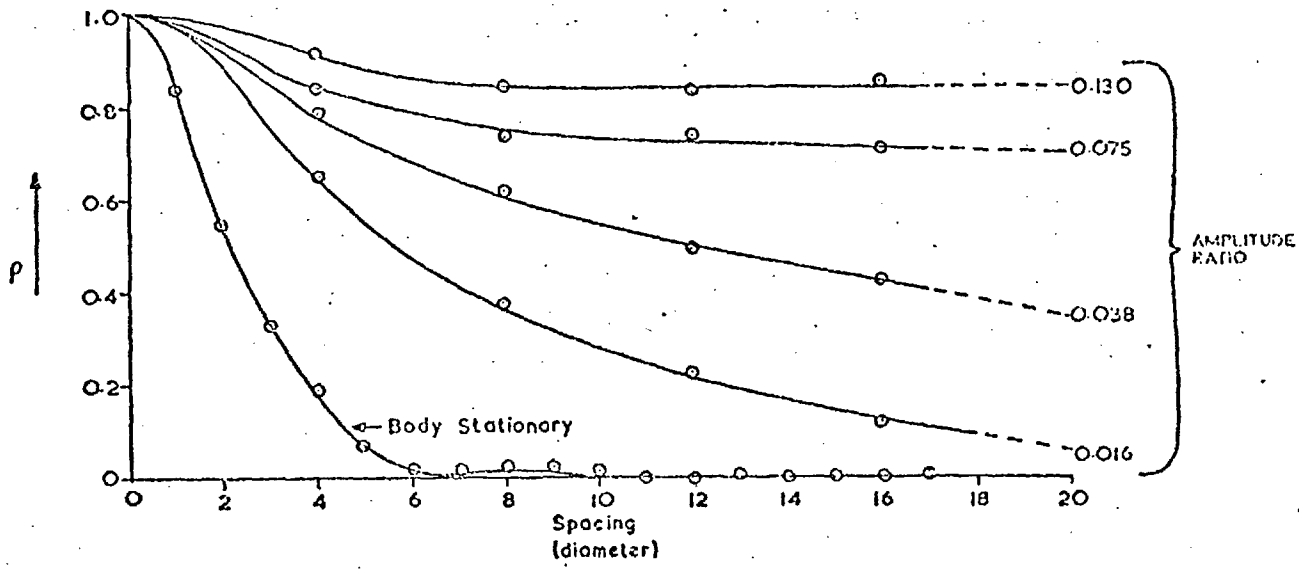

FIG. 1.18 A (a) EFFECT OF VIBRATION ON SPANWISE PRESSURE CORRELATIONS

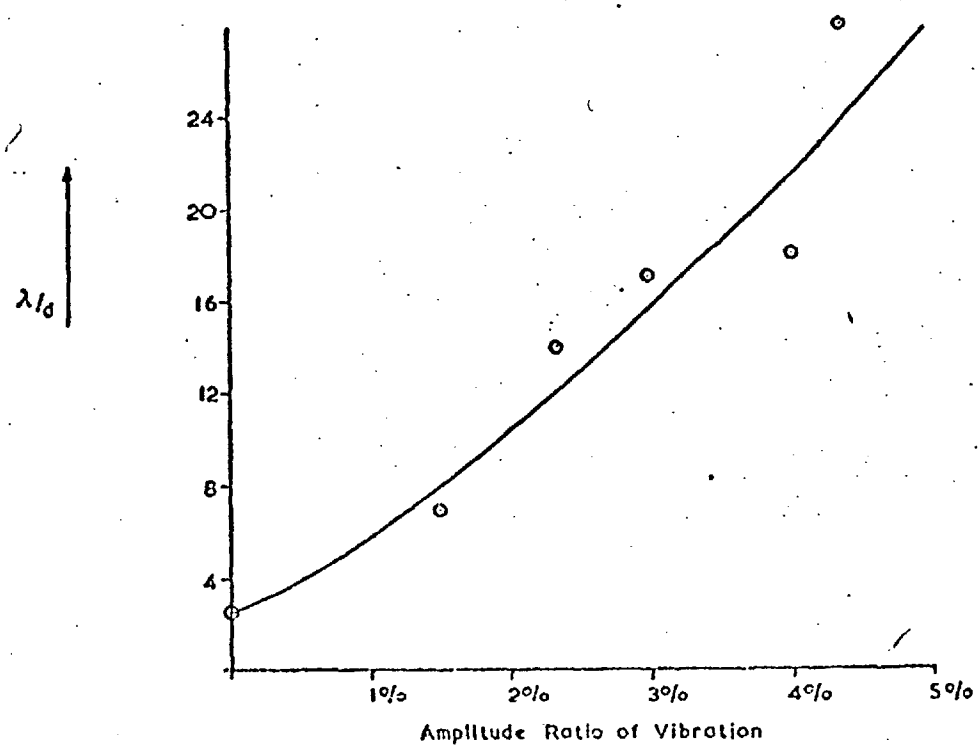

FIG 1.18 B (b) ESTIMATE OF INCREASE OF PRESSURE CORRELATION LENGTH DUE TO VIBRATION

ALL FIGURES ARE REPRODUCED FROM WILKINSON (1974)

ALL FIGURES ARE REPRODUCED FROM WILKINSON (1974)

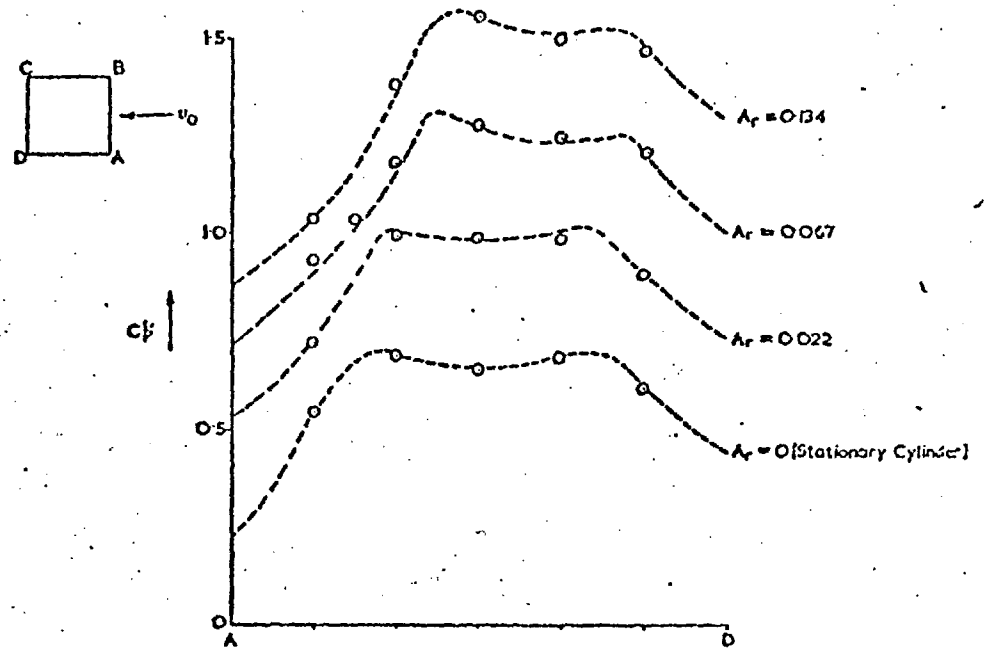

FIG. 1.19A a) DISTRIBUTION OF DYNAMIC PRESSURE ON SIDE FACE OF VIBRATING CYLINDER AT MAXIMUM AMPLIFICATION ($f_{/f_s}$=0·9)

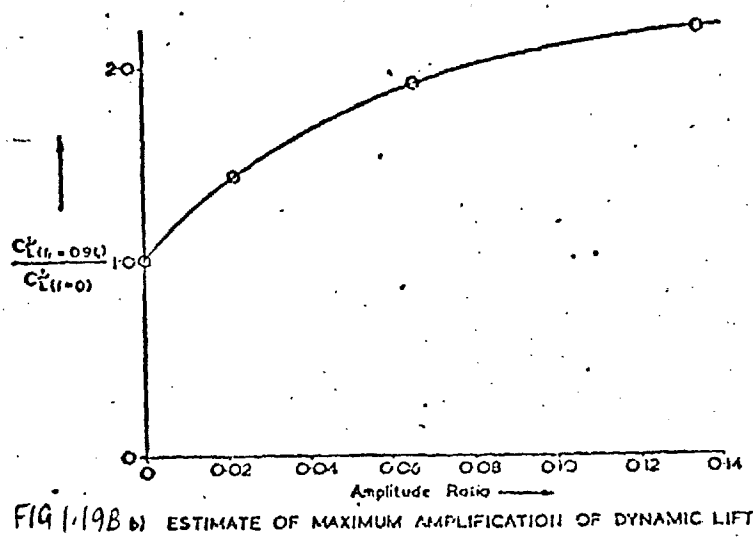

FIG 1.19B b) ESTIMATE OF MAXIMUM AMPLIFICATION OF DYNAMIC LIFT FORCE ($f_{/f_s}$=0·9)

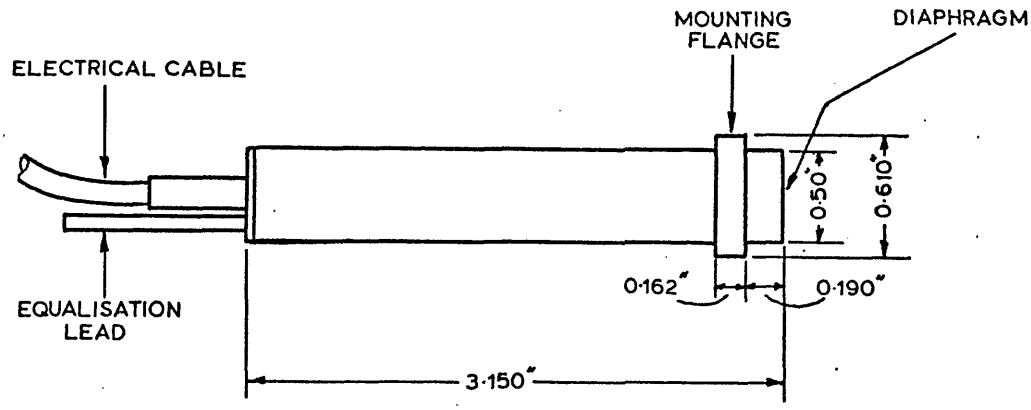

Fig. 2·1 (a)

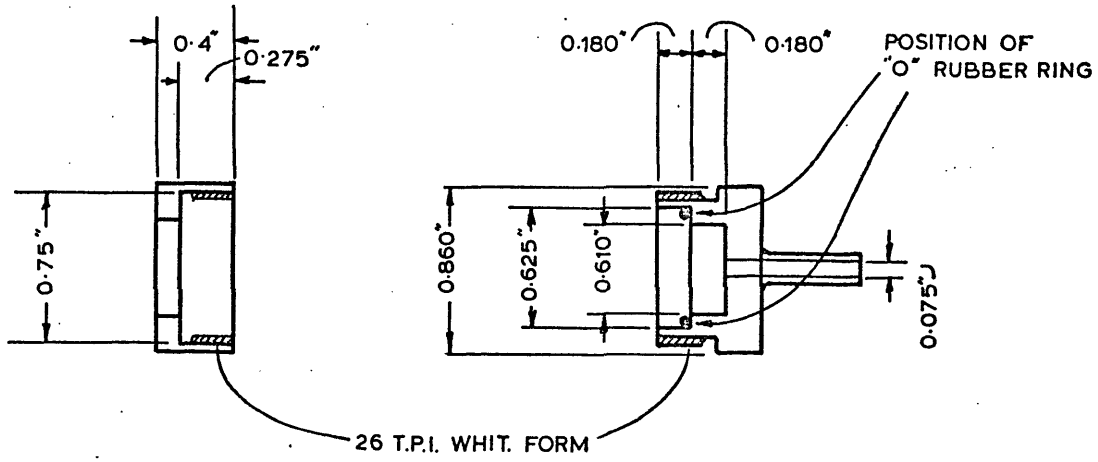

Fig. 2·1 (b)

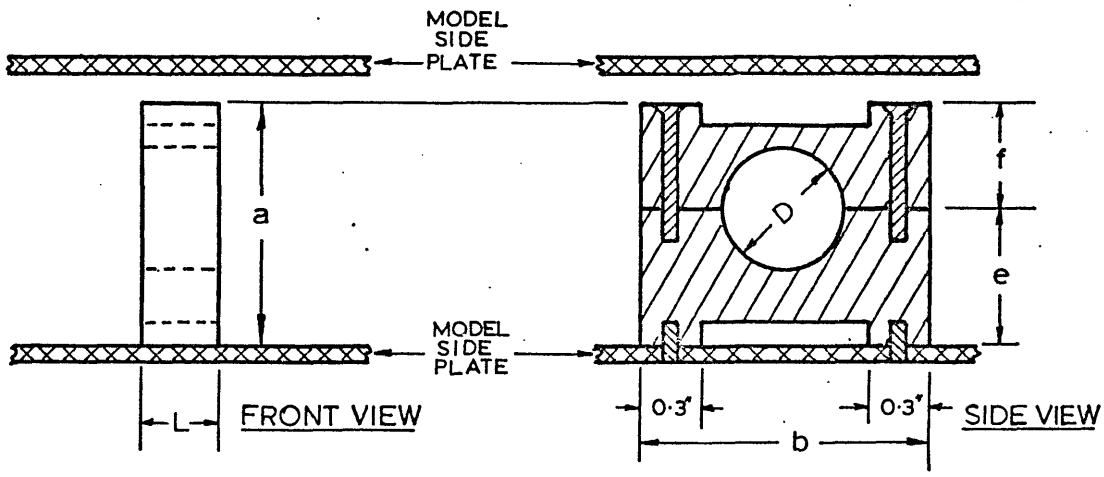

THE DIMENSIONS OF THE HOLDERS ARE GIVEN ON THE NEXT PAGE

Fig. 2·1 (c)

Fig. 2·1 The $\frac{1}{2}$" Setra pressure transducer and associated mounting procedure

HOLDER A			HOLDER B		
L	=	0.4"	L	=	0.4"
D	≒	0.9"	D	≒	0.5"
b	=	1.5"	b	=	1.5"
e	=	$\frac{7}{8}$"	e	=	$\frac{7}{8}$"
f	=	0.6"	f	=	0.4"

EXACT VALUES OF D WERE CHOSEN SO THAT HOLDERS A & B PROVIDE TIGHT-FITS WITH THE CAP AND THE TAIL OF THE $\frac{1}{2}$" SETRA MICROPHONE RESPECTIVELY.

HOLDERS ARE MADE FROM ELECTRICALLY INSULATING MATERIAL.

Fig. 2.1(C) CONTINUED.

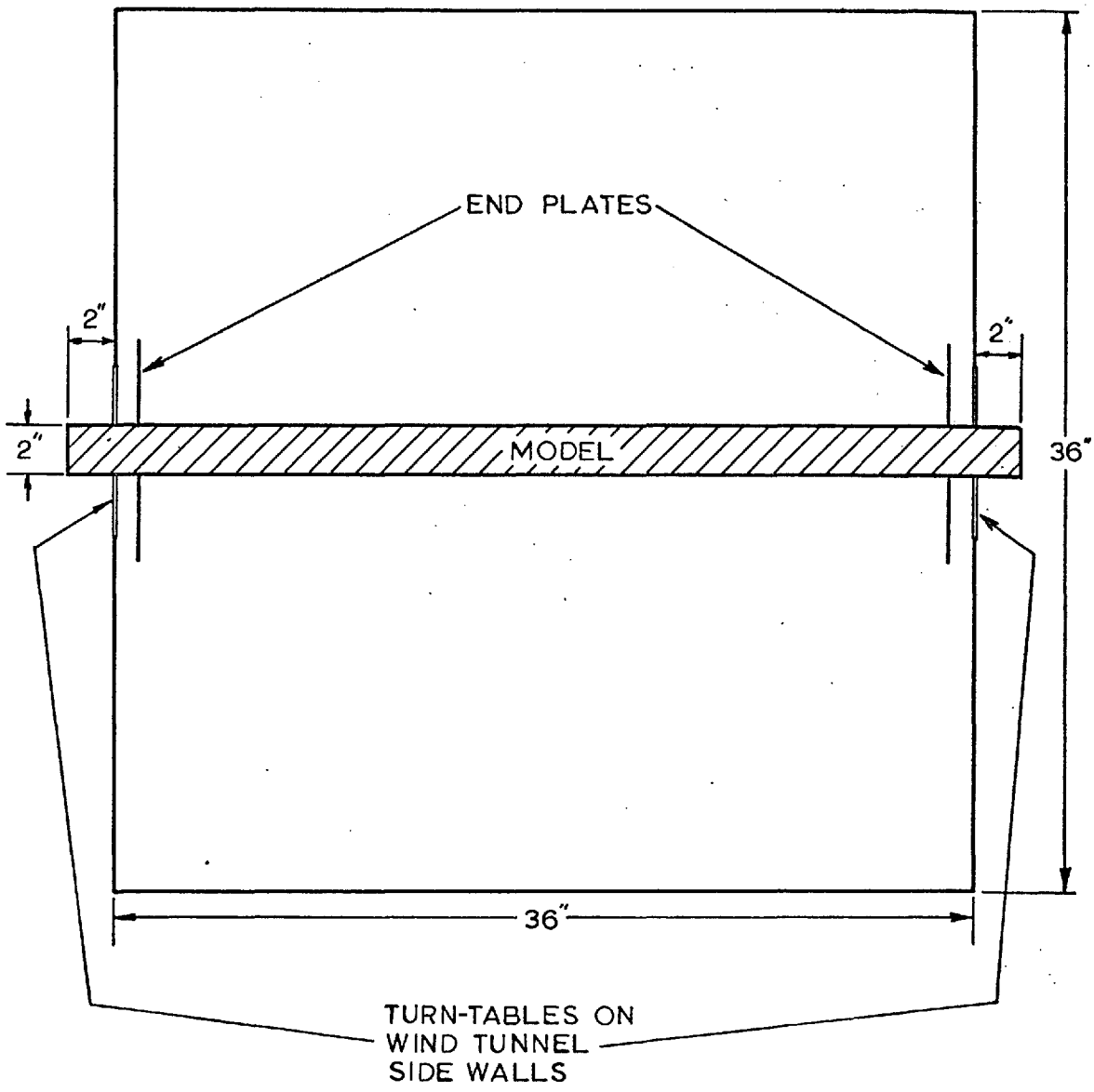

Fig. 2·2 Stationary model mounting procedure

Fig. 2·3 Location of type (B) pressure tappings on the stationary model

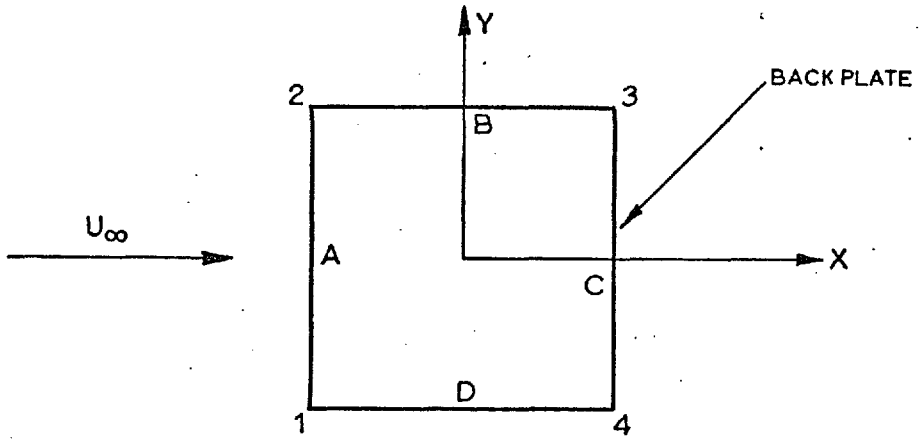

MODEL MID-SECTION

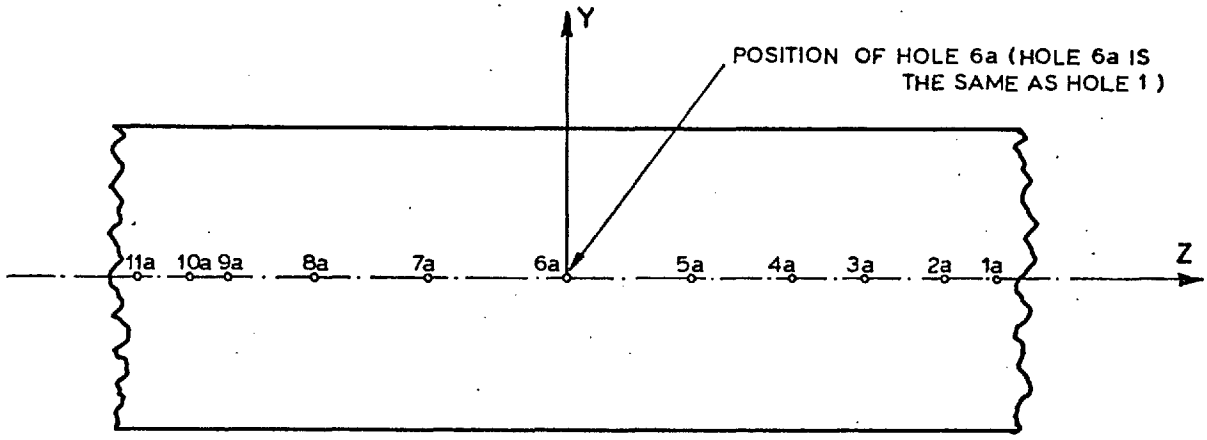

MODEL BACK PLATE

CO-ORDINATES OF PRESSURE TAPPINGS AT MODEL MID-SECTION

HOLE NO.	X & Y CO-ORDINATES	HOLE NO.	X & Y CO-ORDINATES	HOLE NO.	X & Y CO-ORDINATES	HOLE NO.	X & Y CO-ORDINATES
1	(1", 0)	9	(-1", $\frac{13}{16}$")	17	(-1", $-\frac{9}{16}$")	25	(1", $-\frac{11}{16}$")
2	(1", $\frac{1}{2}$")	10	(-1", $\frac{11}{16}$")	18	(-1", $-\frac{11}{16}$")	26	(1", $-\frac{1}{2}$")
3	(1", $\frac{11}{16}$")	11	(-1", $\frac{9}{16}$")	19	(-1", $-\frac{13}{16}$")	27	(1", $-\frac{1}{4}$")
4	(1", $\frac{13}{16}$")	12	(-1", $\frac{7}{16}$")	20	(-1", $-\frac{15}{16}$")	28	(1", $\frac{1}{4}$")
5	(1", $\frac{15}{16}$")	13	(-1", $\frac{3}{16}$")	21	($-\frac{7}{8}$", - 1")	29	($\frac{3}{8}$", - 1")
6	($-\frac{1}{2}$", 1")	14	(-1", 0)	22	($-\frac{1}{2}$", - 1")	30	($\frac{3}{8}$", 1")
7	($-\frac{7}{8}$", 1")	15	(-1", $-\frac{3}{16}$")	23	(1", $-\frac{15}{16}$")		
8	(-1", $\frac{15}{16}$")	16	(-1", $-\frac{7}{16}$")	24	(1", $-\frac{13}{16}$")		

Z— CO-ORDINATES OF SPANWISE PRESSURE TAPPINGS ON MODEL BACK FACE. ALL TAPPINGS ARE LOCATED ALONG Y = 0, X = 1"

1a Z = 15"; 2a Z = 13"; 3a Z = 11"; 4a Z = 8"; 5a Z = 4"; 6a Z = 0

7a Z = - 4"; 8a Z = - 8"; 9a Z = -11"; 10a Z = -13"; 11a Z = -15"

Fig. 2·4 Details of a type (B) pressure tapping

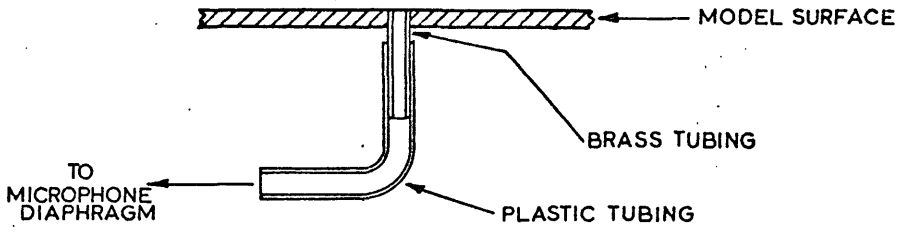

I.D. OF BRASS TUBING = $\frac{1}{16}$"

O.D. OF BRASS TUBING = $\frac{3}{32}$"

Maximum allowable length of brass and plastic tubing between model surface and microphone diaphragm is $2\frac{3}{4}$"

CO-ORDINATES OF TYPE (B) PRESSURE TAPPINGS ON THE STATIONARY MODEL (AXES ARE AS DEFINED IN FIG.3)

HOLE NO.	X, Y & Z CO-ORDINATES	HOLE NO.	X, Y & Z CO-ORDINATES
1	($\frac{5}{6}$", 1", $2\frac{1}{2}$")	6	($\frac{5}{6}$", 1", $2\frac{1}{2}$")
2	($\frac{3}{6}$", 1", $2\frac{1}{2}$")	7	($-\frac{1}{3}$", 1", $2\frac{5}{16}$")
3	($\frac{1}{6}$", 1", $2\frac{1}{2}$")	8	(0 , 1", $2\frac{5}{6}$")
4	($-\frac{1}{6}$", 1", $2\frac{1}{2}$")	9	($\frac{1}{3}$", 1", $2\frac{5}{6}$")
5	($-\frac{3}{6}$", 1", $2\frac{1}{2}$")		

Z POSITIVE IS TOWARDS THE INSTRUMENTS' END OF THE MODEL.

Fig. 2·5 Details of end plates

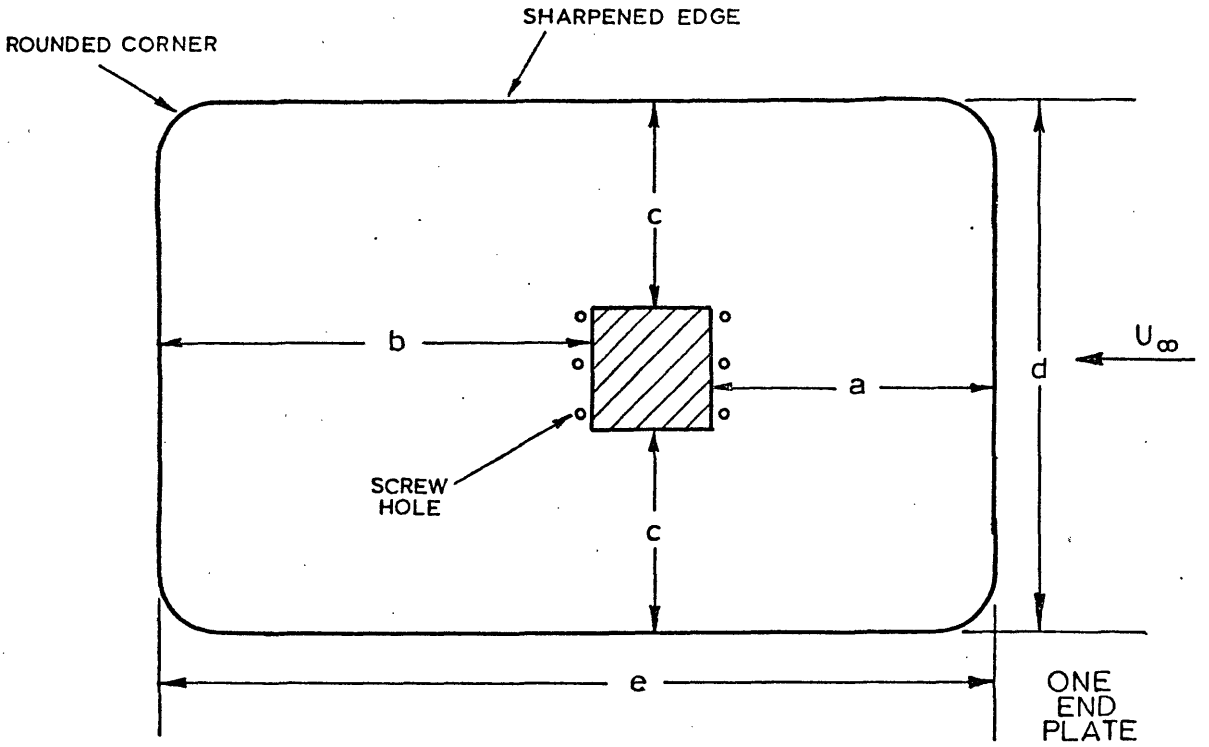

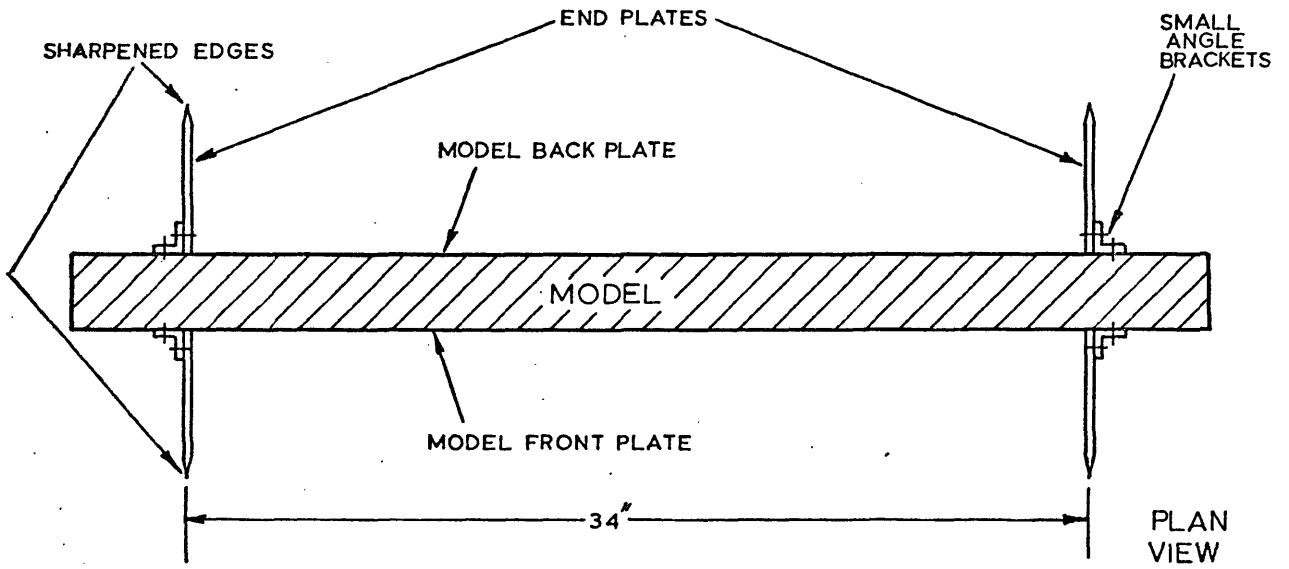

DIMENSION OF END PLATES

TYPE OF END PLATE	D I M E N S I O N				
	a	b	c	d	e
No. 1	1"	6"	3½"	9"	9"
No. 2	4"	6"	3½"	9"	12"
No. 3	4"	8"	6"	14"	14"
No. 4	4"	6"	6"	14"	12"
No. 5	4"	8"	3½"	9"	14"

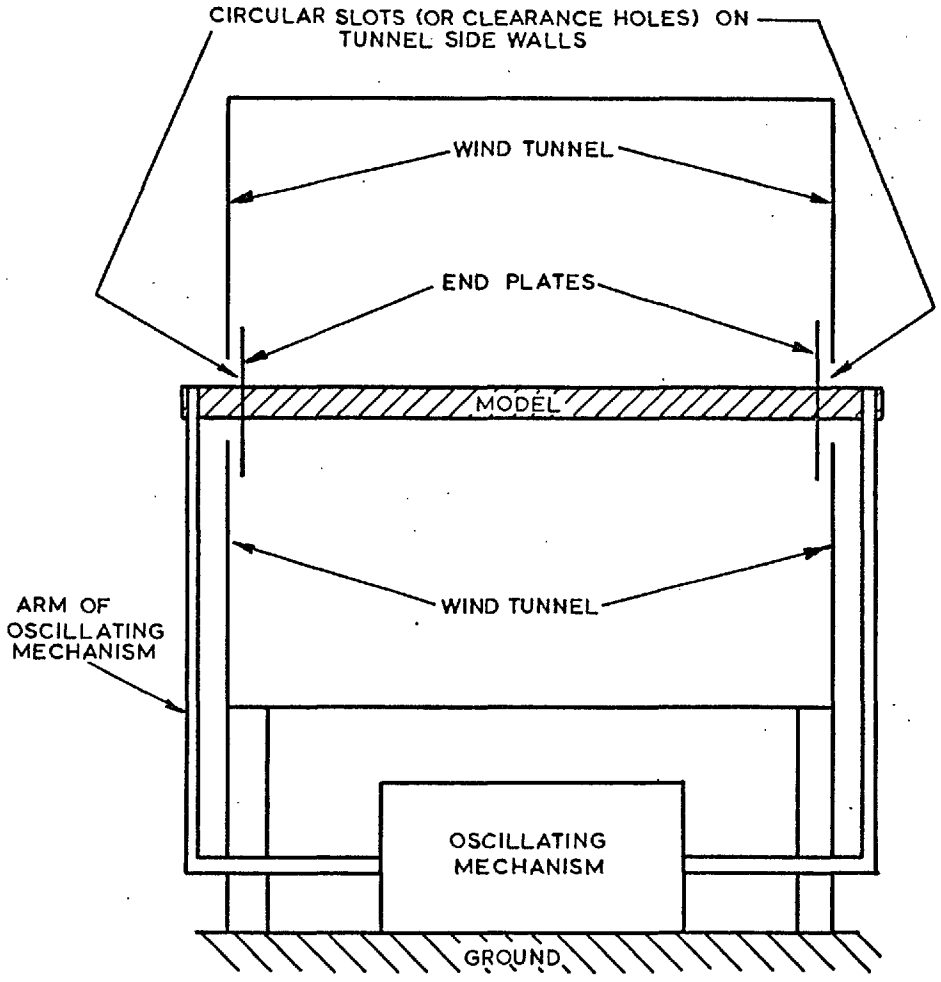

Fig. 2·6 Oscillating model mounting procedure

Fig. 2·7 Location of pressure tappings on the oscillating models

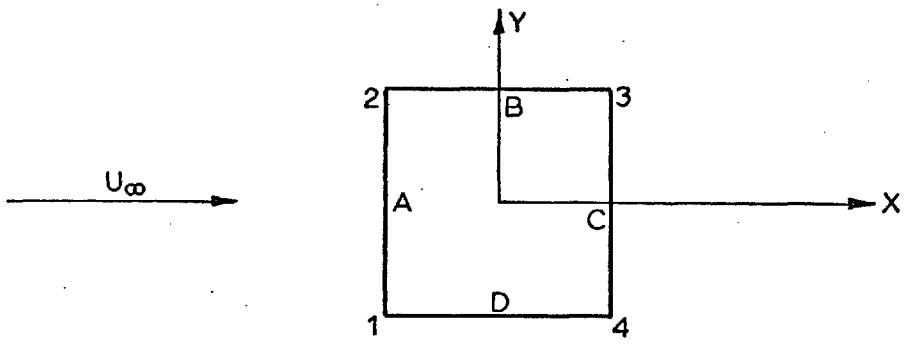

OSCILLATING MODEL 1

ALL TAPPINGS ARE POSITIONED SPANWISE ALONG THE CENTRELINE OF FACE (Y = 0, X = 1" FOR ALL TAPPINGS)

HOLE NO.	1	2	3	4	5	6
Z - CO-ORDINATES	16"	8"	0	-4"	-12"	-14"

Z = 0 CORRESPONDS TO THE MODEL CENTER SECTION

OSCILLATING MODEL 2

ALL TAPPINGS ARE POSITIONED AROUND THE MODEL CENTER SECTION (Z = 0)

HOLE NO.	1	2	3	4	5	6	7	8
X - CO-ORDINATE	0	$-\frac{27}{32}$"	-1"	-1"	$-\frac{5}{32}$"	$\frac{1}{2}$"	1"	1"
Y - CO-ORDINATE	1"	1"	$\frac{5}{32}$"	$-\frac{1}{2}$"	-1"	-1"	0	$\frac{25}{32}$"

OSCILLATING MODEL 3

A) THIRTEEN PRESSURE TAPPINGS ARE POSITIONED AROUND THE MID-SECTION OF THE MODEL (Z = 0) AS BELOW

HOLE NO.	1	2	3	4	5	6	7	8	9	10	11	12	13
X - CO-ORDINATE	$\frac{3}{4}$"	$\frac{1}{2}$"	0	$-\frac{1}{2}$"	$-\frac{3}{4}$"	-1"	-1"	-1"	0	$\frac{3}{4}$"	1"	1"	1"
Y - CO-ORDINATE	1"	1"	1"	1"	1"	$\frac{1}{4}$"	0	$-\frac{3}{4}$"	-1"	-1"	$-\frac{1}{4}$"	0	$\frac{1}{4}$"

B) THIRTEEN ADDITIONAL PRESSURE TAPPINGS ARE POSITIONED SPANWISE ON THE CENTERLINE OF SIDE-FACE B (X = 0, Y = 1")

HOLE NO.	1	2	3	4	5	6	7	8	9	10	11	12	13
Z - CO-ORDINATES	$16\frac{1}{2}$"	15"	$12\frac{1}{2}$"	10"	6"	2"	0	-3"	-6"	-9"	$-11\frac{1}{2}$"	-14"	$-16\frac{1}{2}$"

HOLE 3 IN Ⓐ IS THE SAME AS HOLE 7 IN Ⓑ

Z POSITIVE IS TOWARDS THE INSTRUMENTS' END OF THE MODEL.

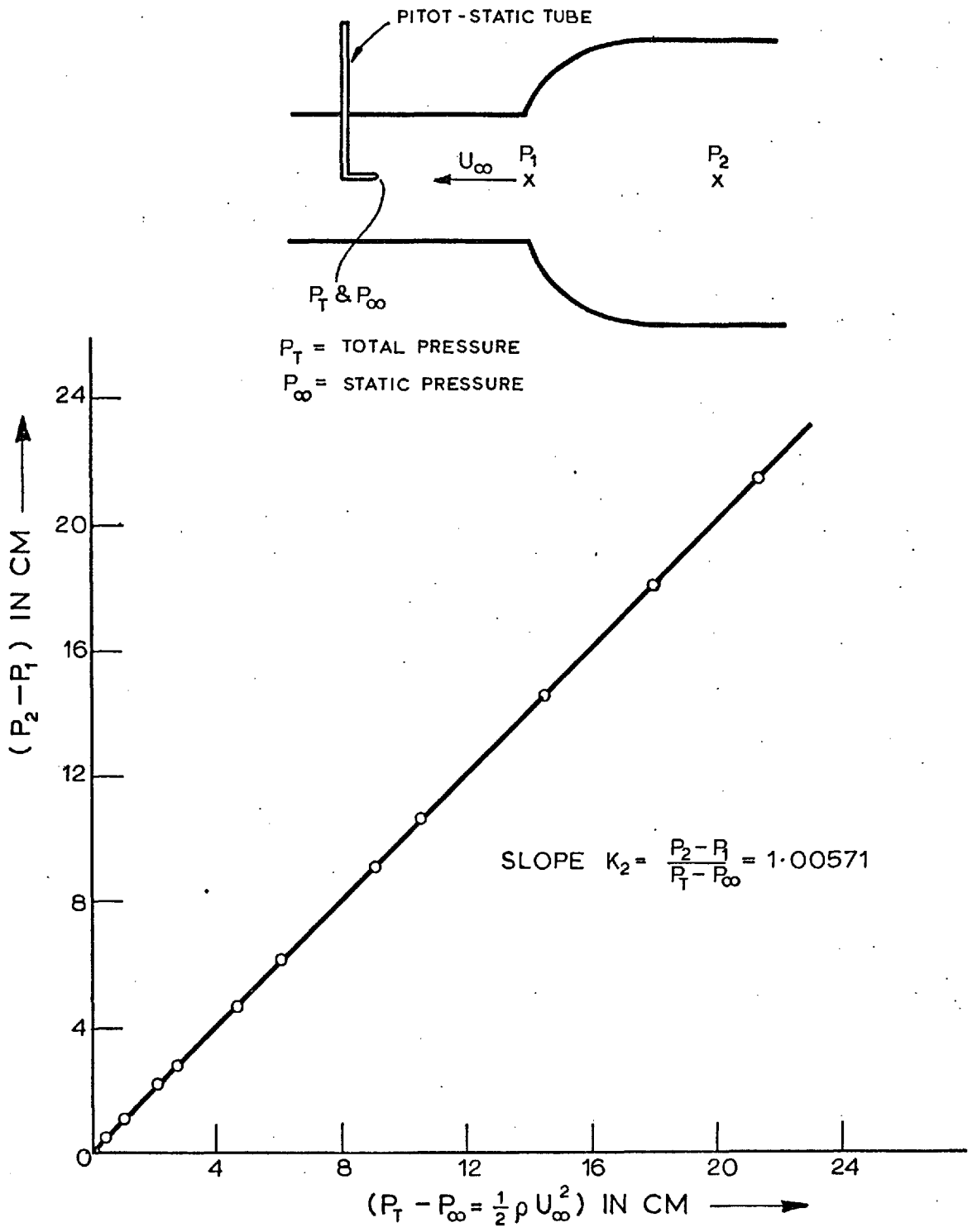

(ALL PRESSURES WERE MEASURED WITH AN INCLINED ALCOHOL MULTI-TUBE MANOMETER)

Fig. 31 Wind tunnel calibration

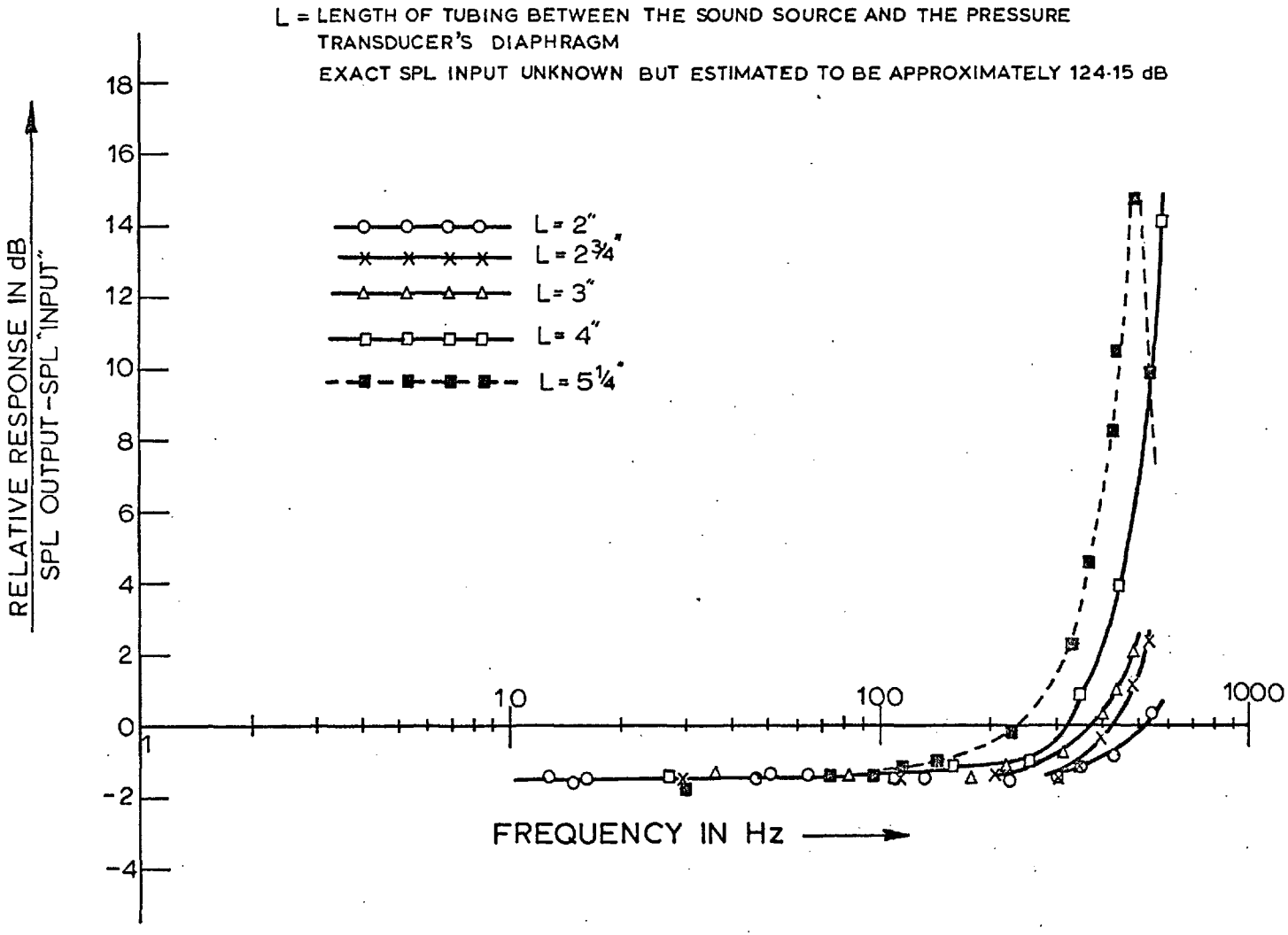

Fig. 3·2 Frequency response of the $\frac{1}{2}$" Setra pressure transducer Model 237

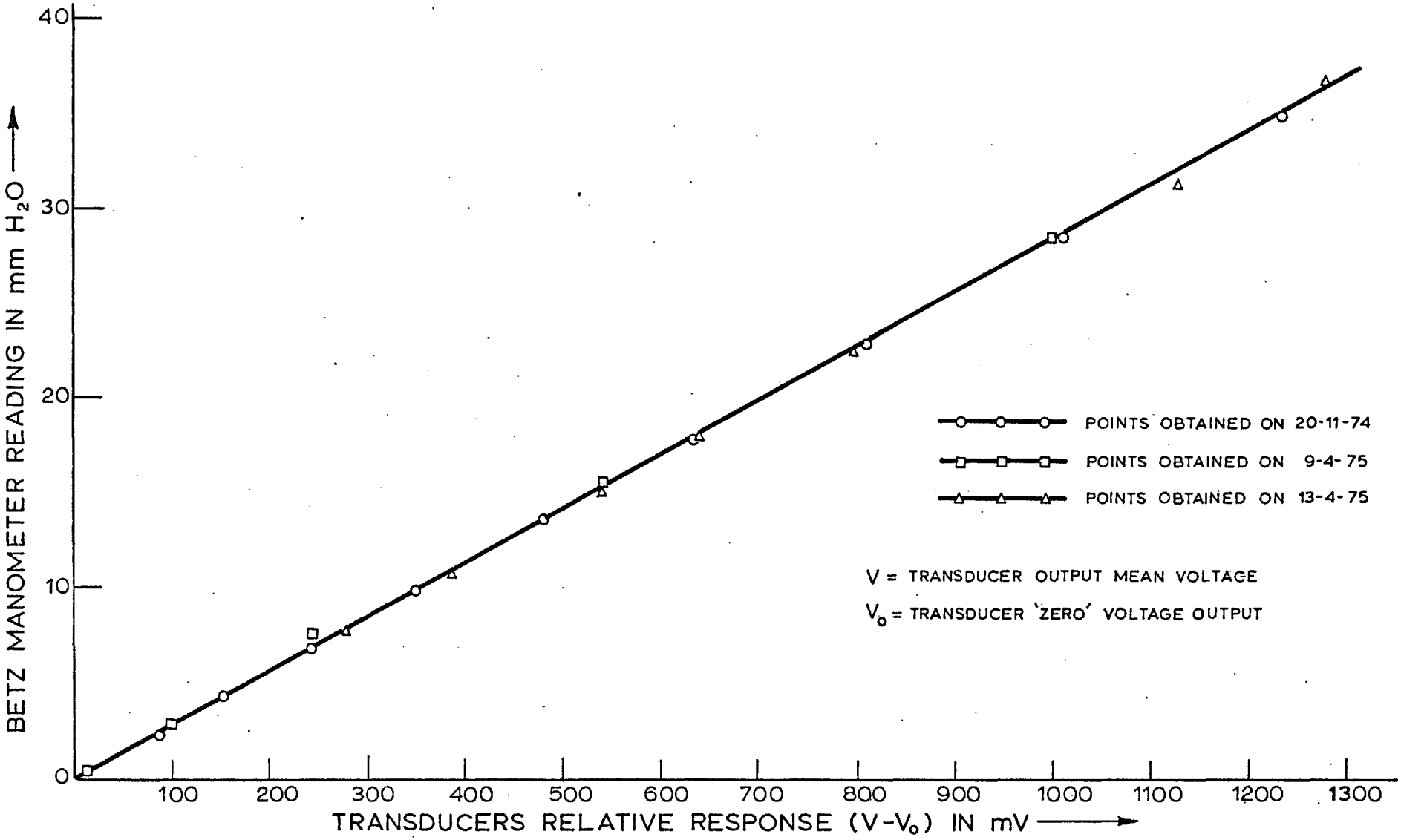

Fig. 3.3 Static calibration of the $\frac{1}{2}$" Setra pressure transducer Model 237

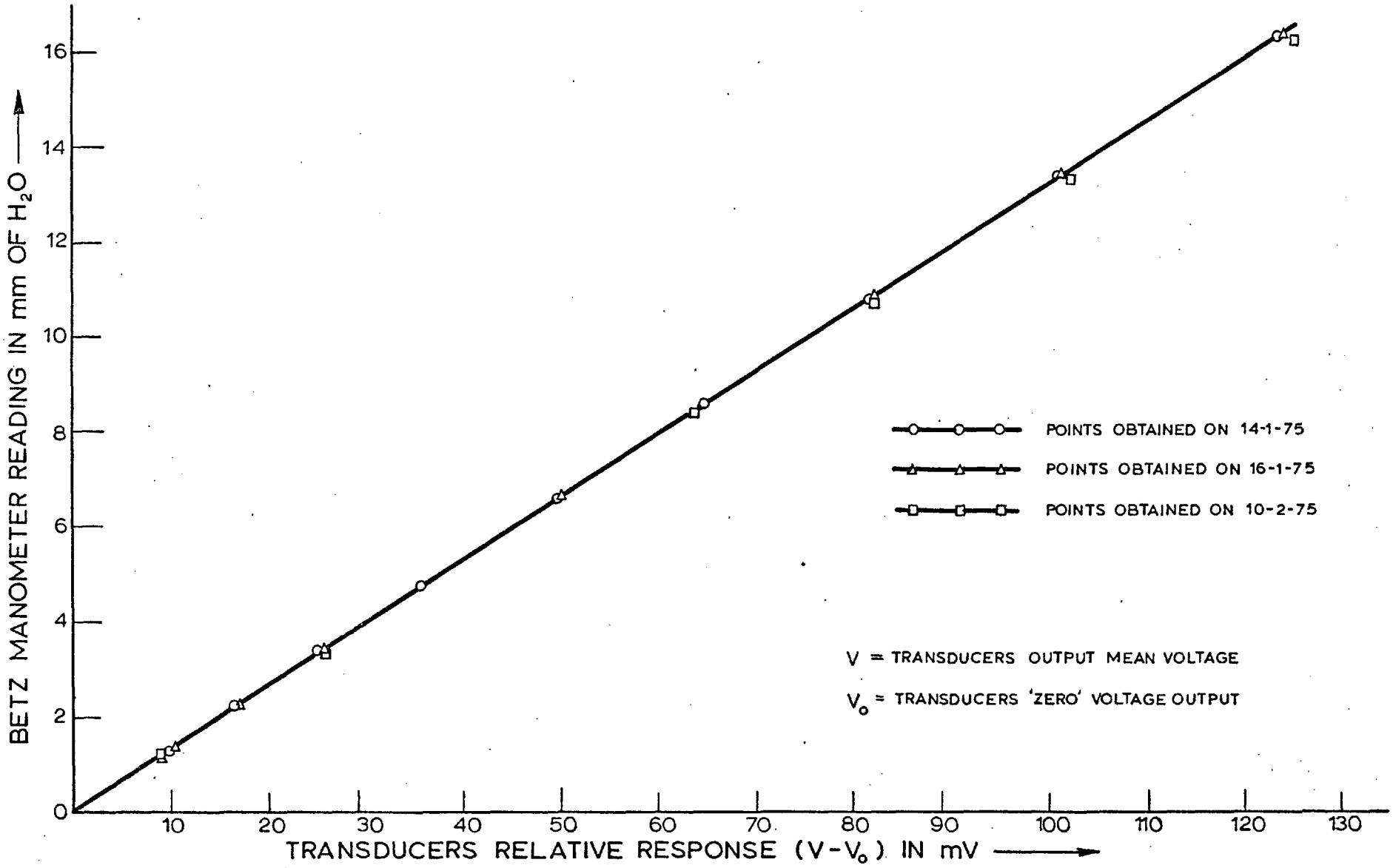

Fig. 3·4 Static calibration of the $\frac{1}{4}$" B & K microphone system

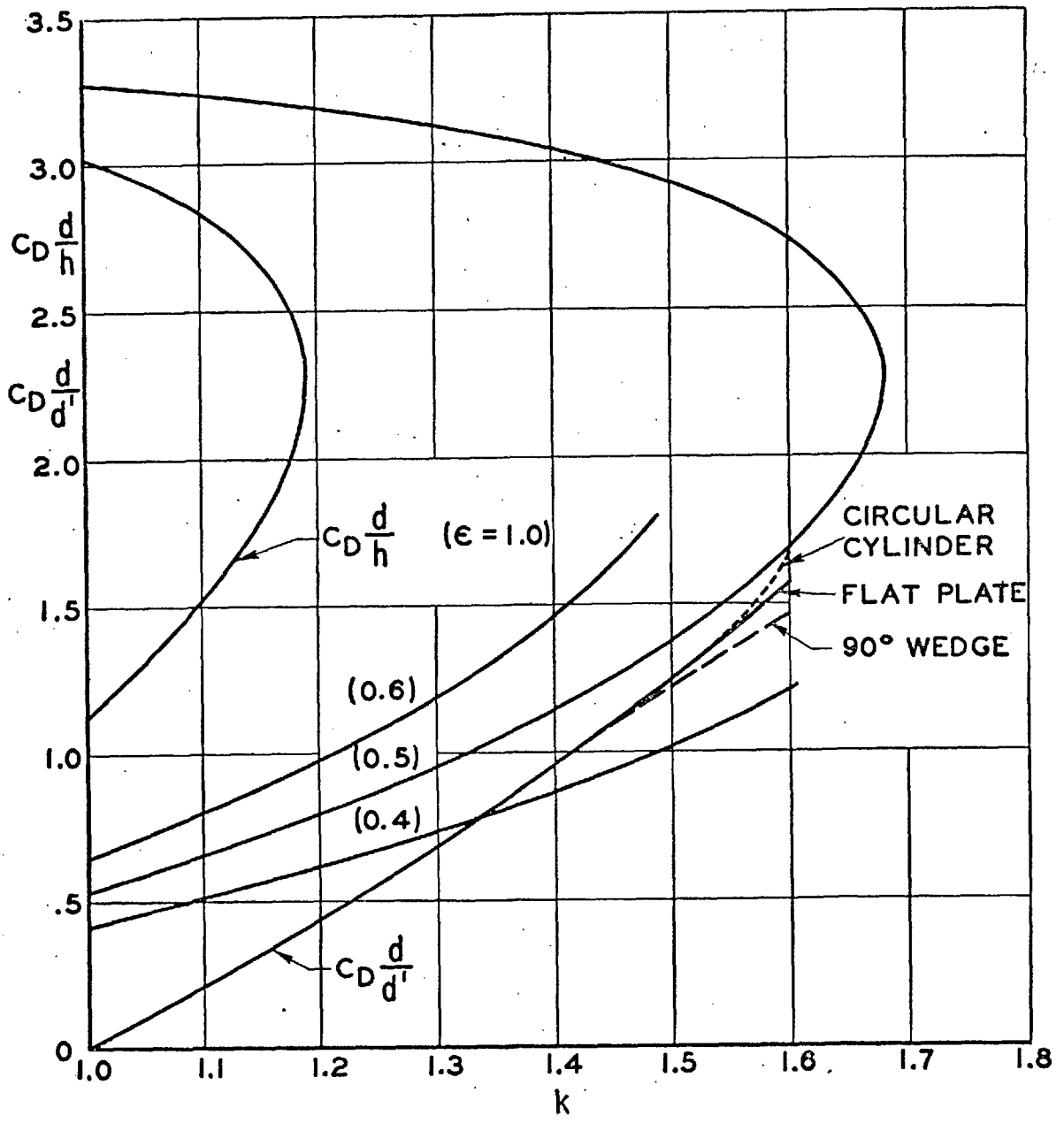

FIG. 4.1 Wake solutions.

REPRODUCED FROM ROSHKO (1954 A), NACA 3169.

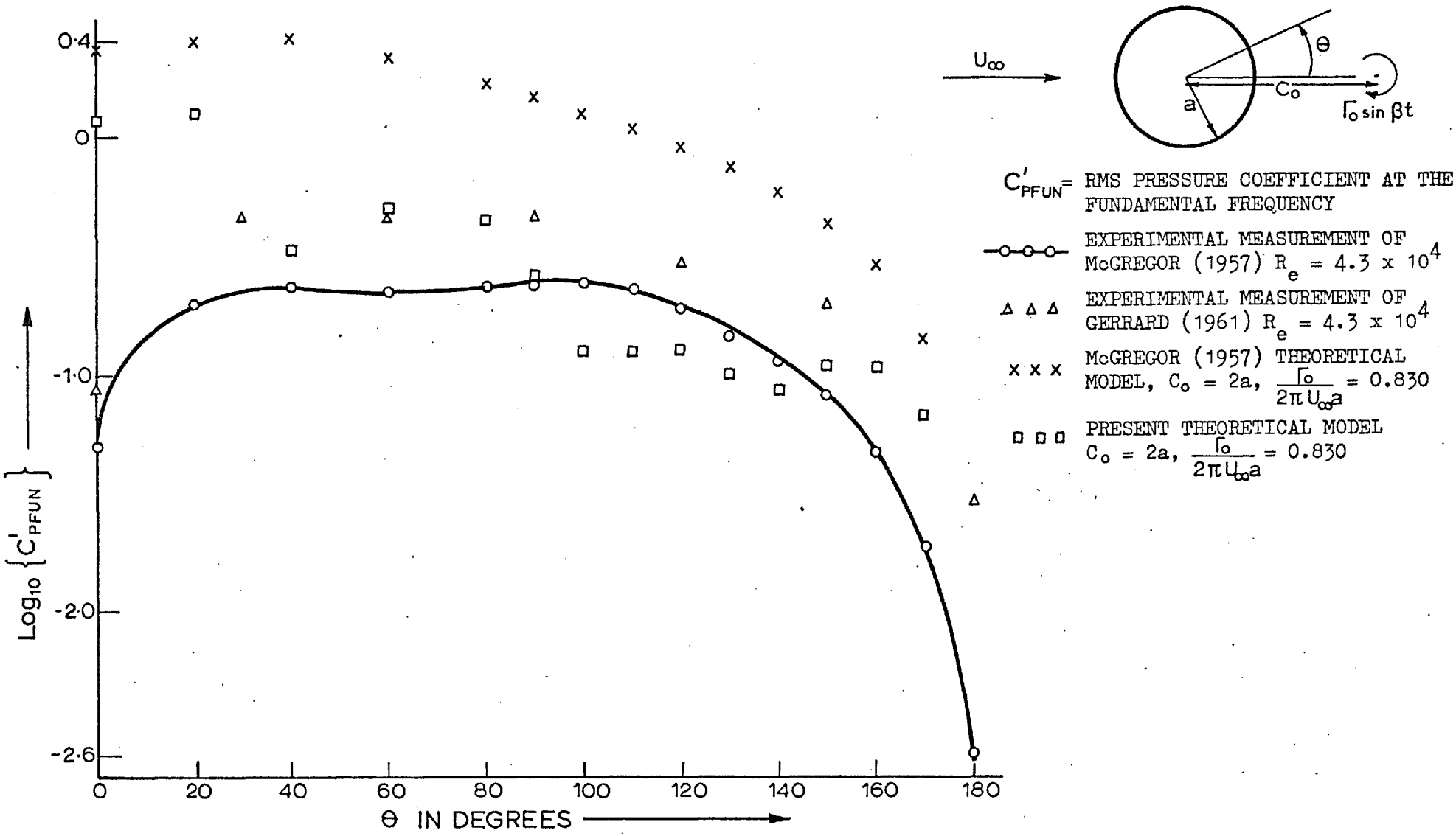

Fig. 4·2 Comparison of theoretical and experimental values of C'_{PFUN} for a stationary circular cylinder

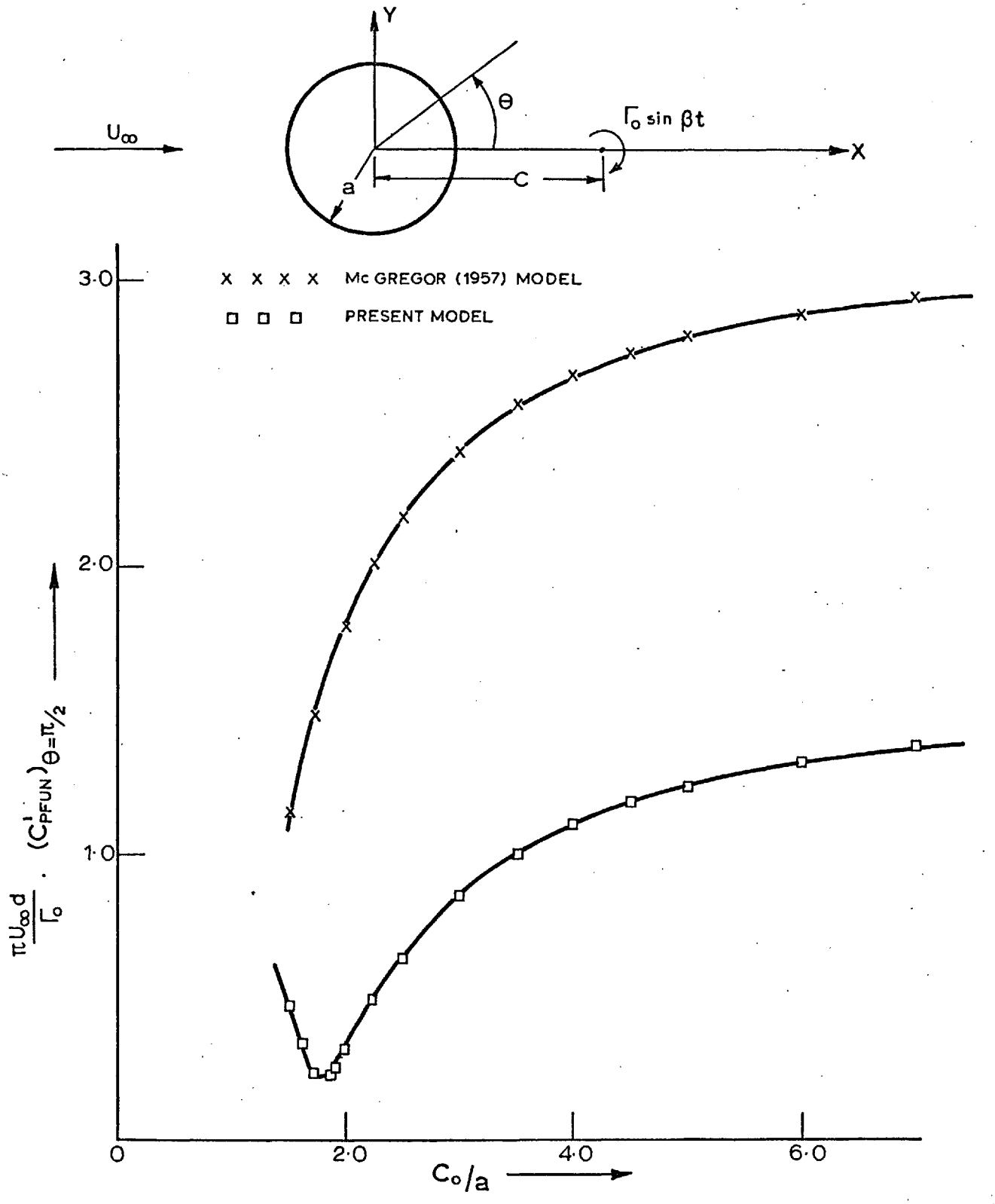

$(C'_{PFUN})_{\theta=\frac{\pi}{2}}$ – RMS PRESSURE COEFFICIENT AT THE FUNDAMENTAL FREQUENCY AT $\theta = \pi/2$

$\frac{\Gamma_o}{\pi U_\infty d}$ – NON-DIMENSIONAL VORTEX STRENGTH (d=2a)

Fig. 4·3 Potential flow model – variation of $\left(\frac{\Gamma_o}{\pi U_\infty d}\right)^{-1} (C'_{PFUN})_{\theta=\frac{\pi}{2}}$ *with* $\frac{C_o}{a}$

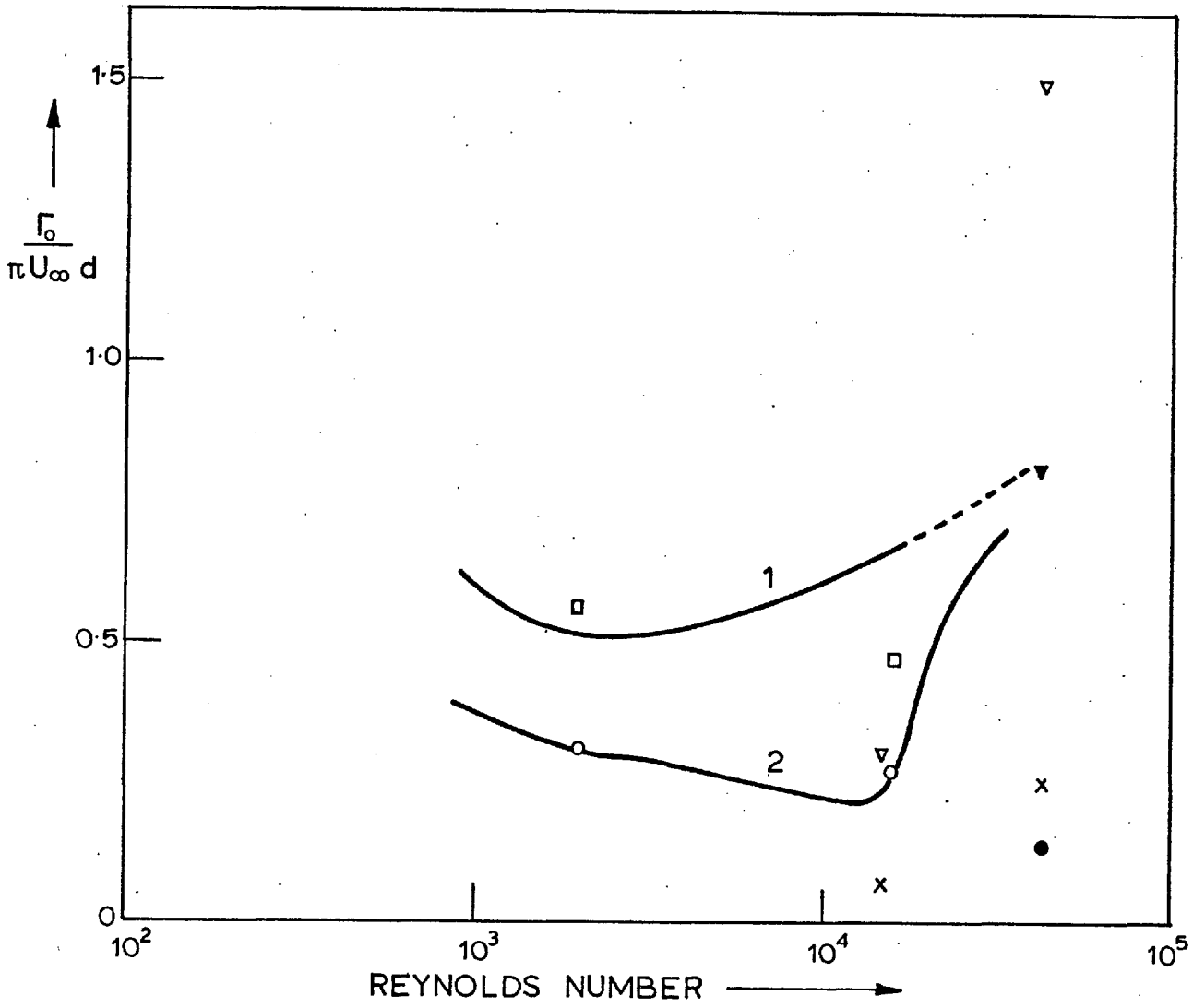

Fig. 4·4 Non-dimensional vortex strength as a function of Reynolds number

o BLOOR & GERRARD (1967) measurement $^x/_d$ = 10.0

□ " " " " $^x/_d$ = 6.0

Curve 1 ROSHKO'S (1954A) method using his observation of K

Curve 2 ROSHKO'S (1954A) method using Bloor & Gerrard (1967) value of K

● McGREGOR'S (1957) model using his value of $(C_{PFUN})_{\theta=\frac{\pi}{2}}$

x McGREGOR'S (1957) model using Gerrard (1961) value of $(C_{PFUN})_{\theta=\frac{\pi}{2}}$

▼ Present model using McGregor's (1957) value of $(C_{PFUN})_{\theta=\frac{\pi}{2}}$

▽ Present model using Gerrard (1961) value of $(C_{PFUN})_{\theta=\frac{\pi}{2}}$

Curves 1 and 2 are taken from Bloor & Gerrard (1967).

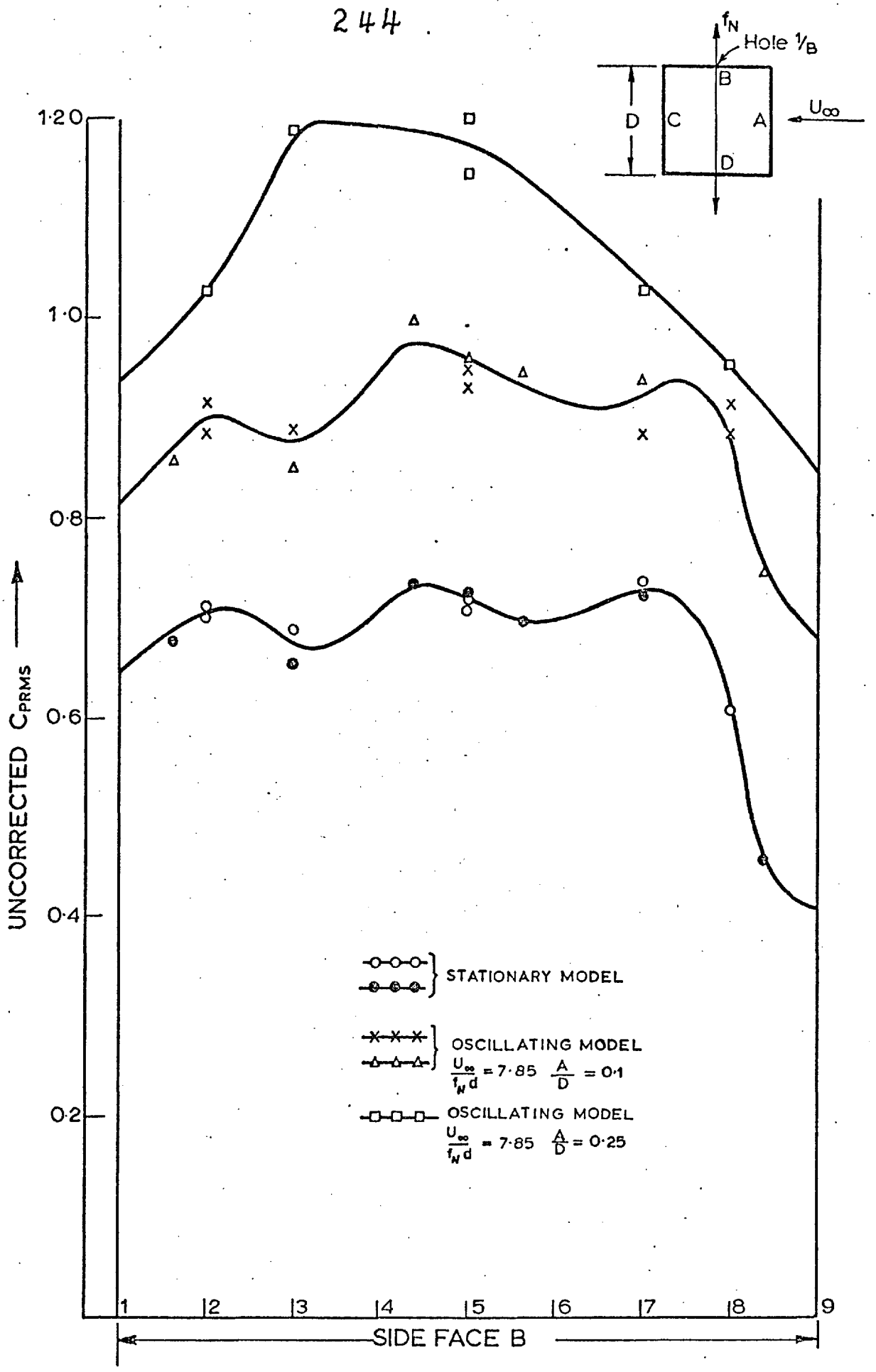

Fig.4·5 Effects of model oscillation on the fluctuating pressures of side face B

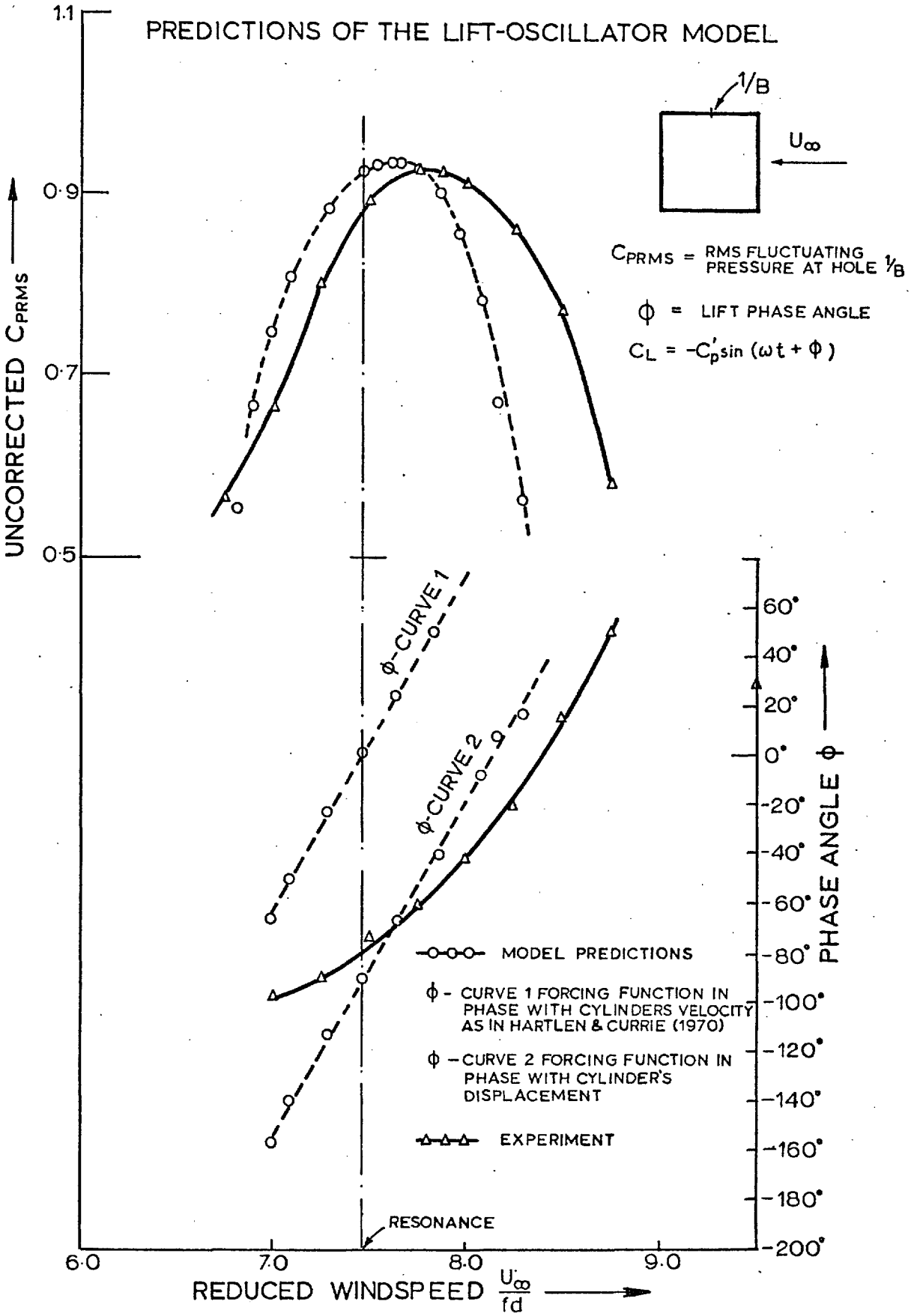

Fig. 4·6 Comparison of theoretical and experimental values of C_{PRMS} and ϕ for synchronised oscillations

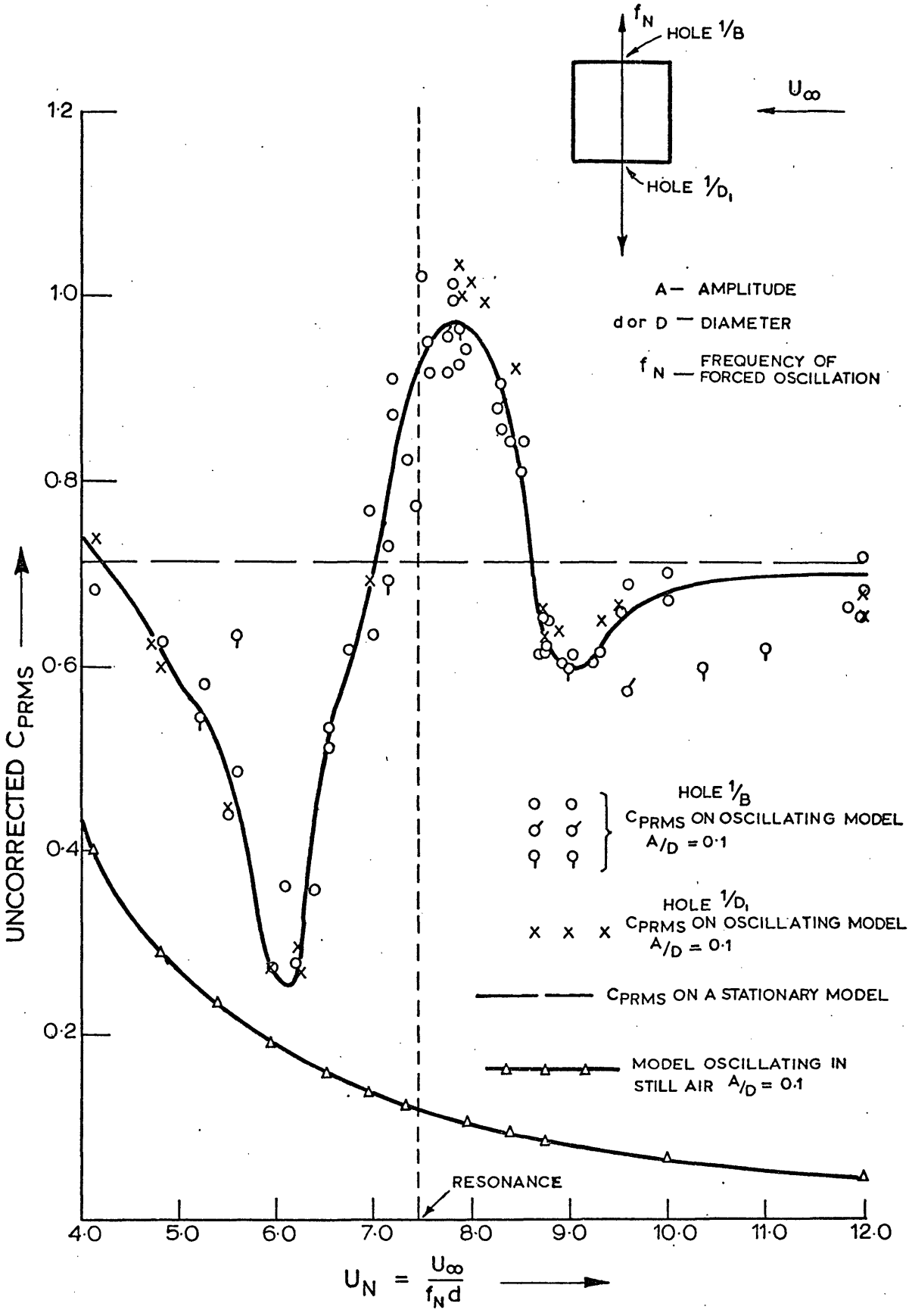

Fig. 4·7 Variation of C_{PRMS} with $\frac{U_\infty}{f_N d}$, $\frac{A}{D} = 0·1$

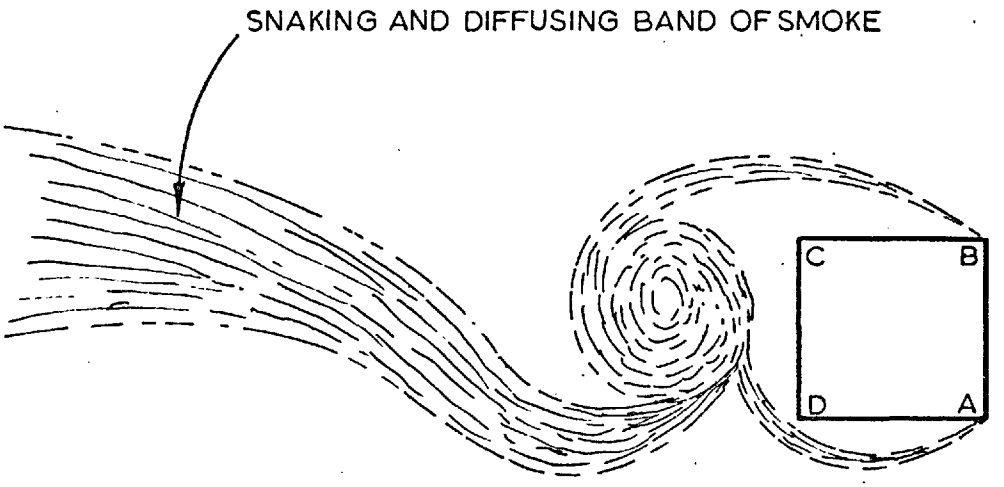

f_s = 3·38 c.p.s.

Fig. 5·1 Wake of a stationary square section

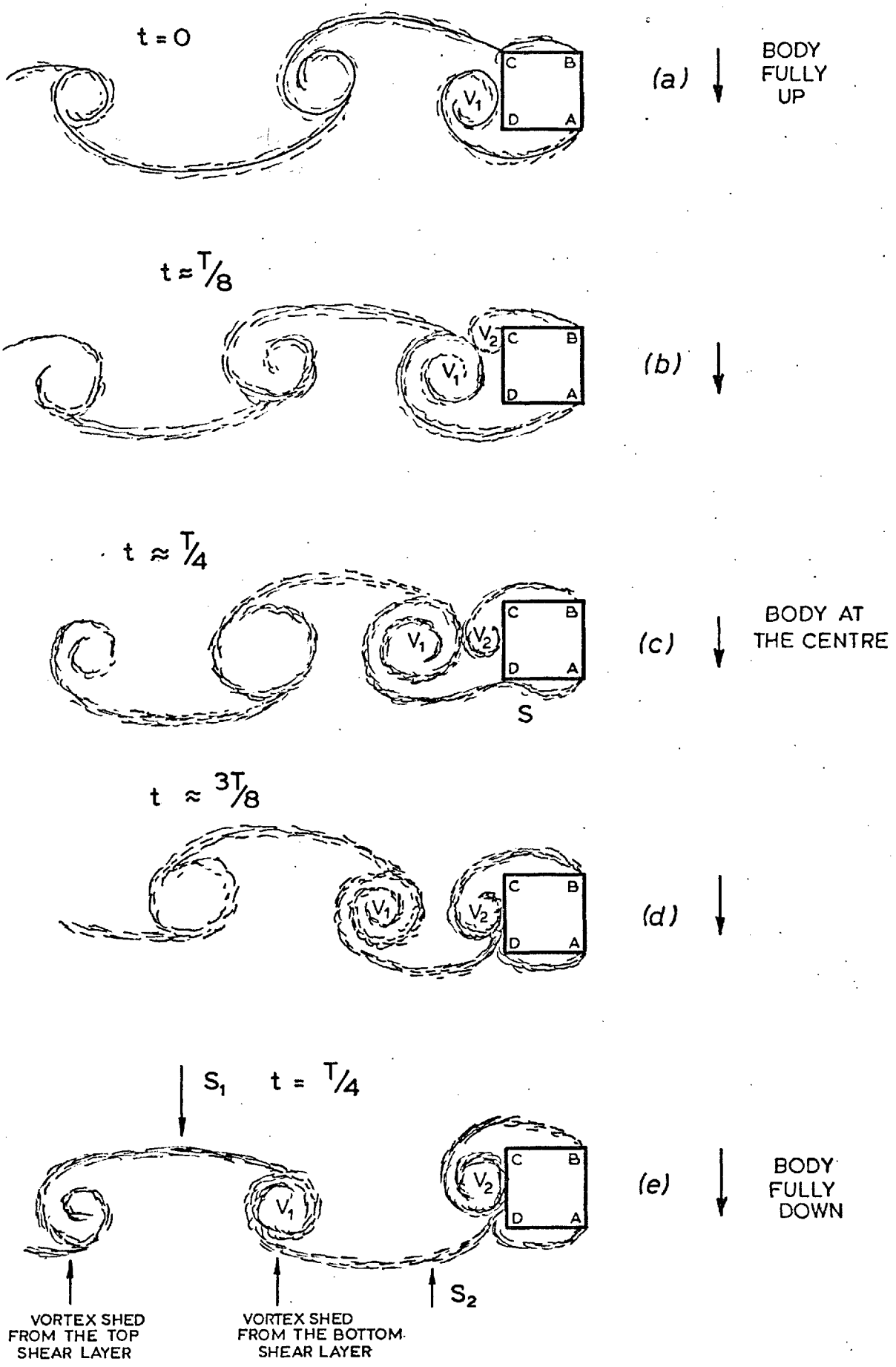

Fig. 5·2 Effects of oscillation on flow configuration (body is moving downwards)

$A/D = 0·25 \quad f_n/f_s = 1·0$

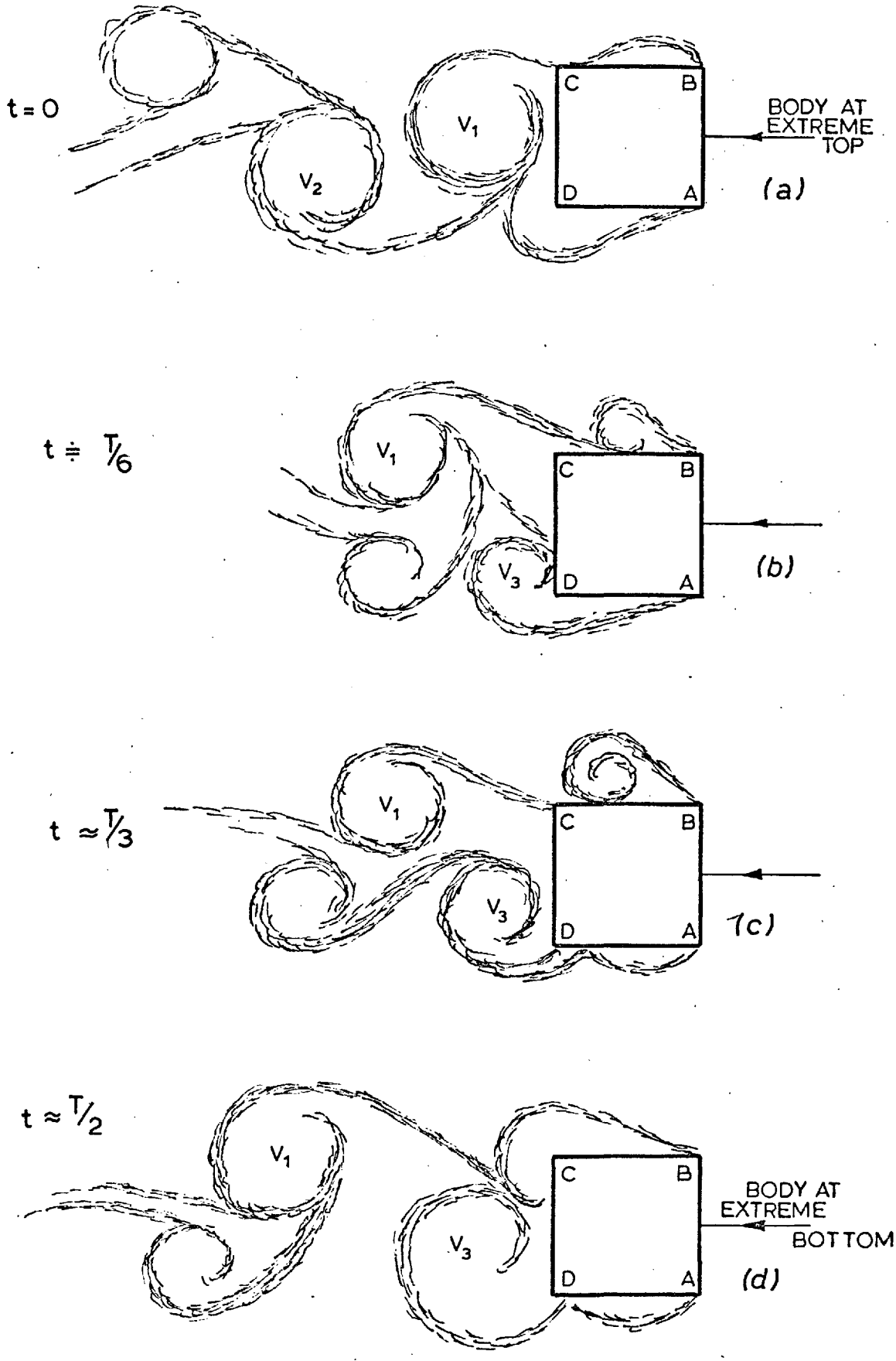

T = PERIOD OF BODY MOTION, BODY IS MOVING DOWNWARDS

Fig. 5·3 Effects of body oscillation on flow configuration

$f_n/f_s = 2{\cdot}0$, $A/D = 0{\cdot}25$

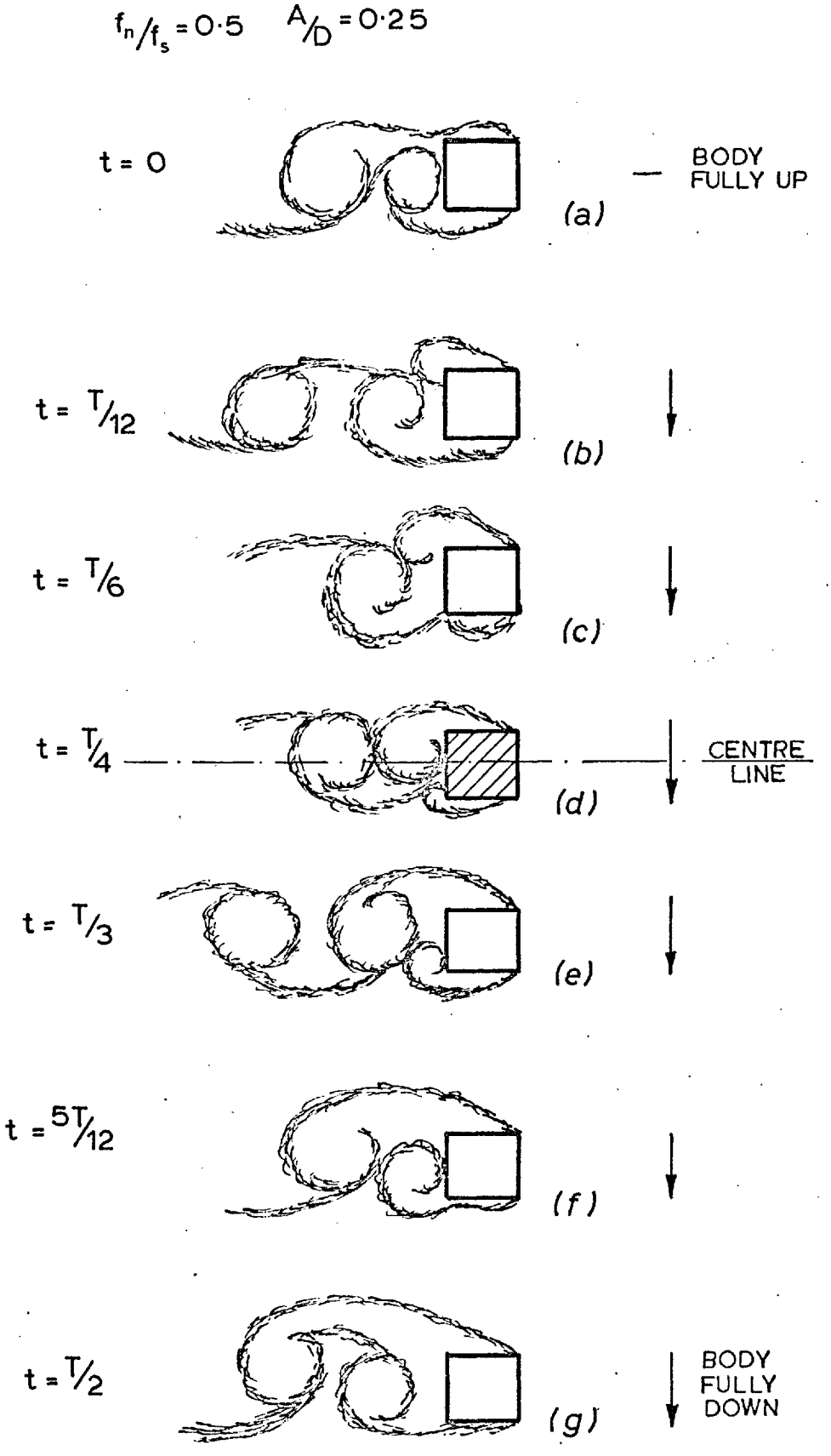

Fig. 5·4 Effects of oscillation on flow configuration

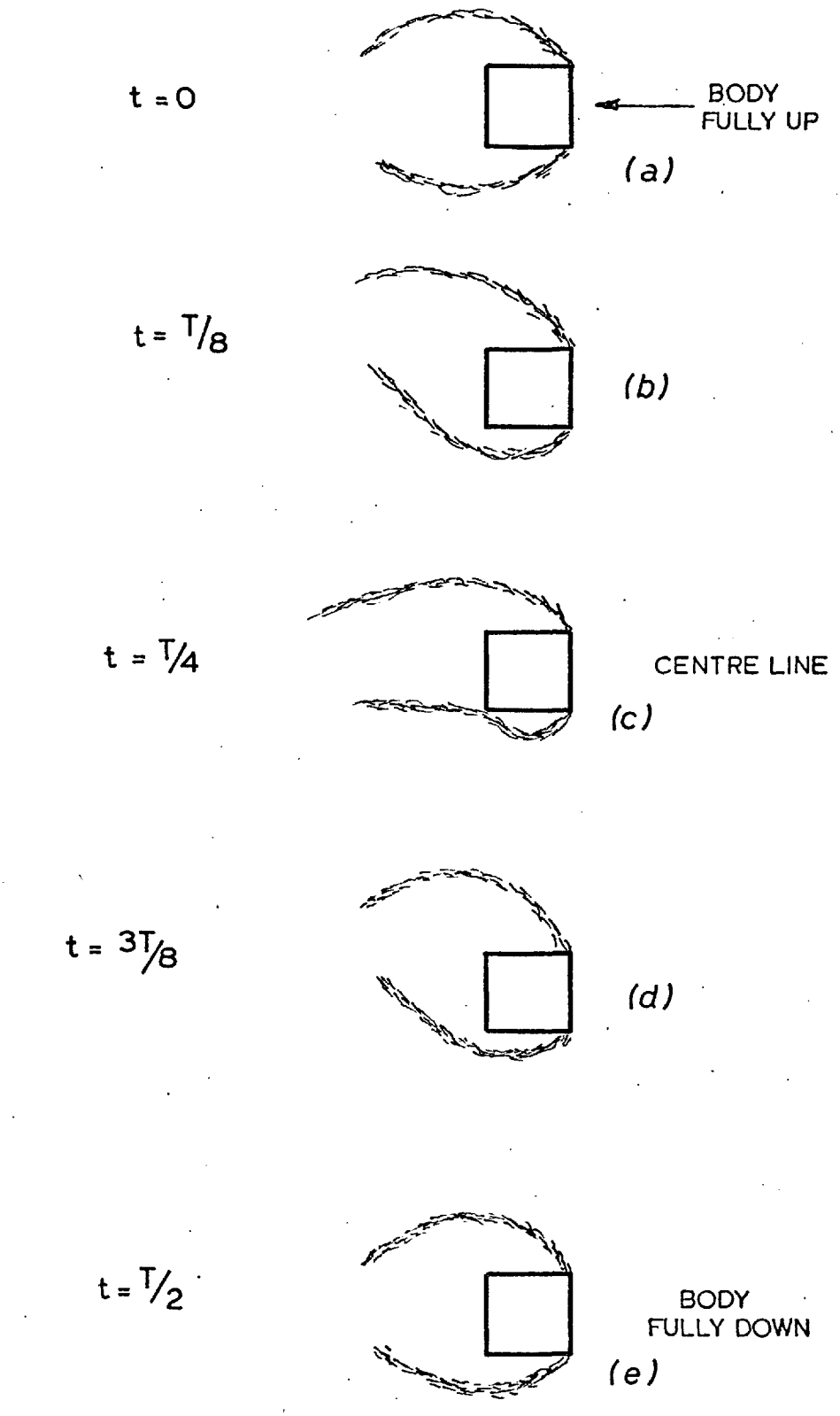

Fig. 5·5 Expected effects of instantaneous incidence on shear layers configuration

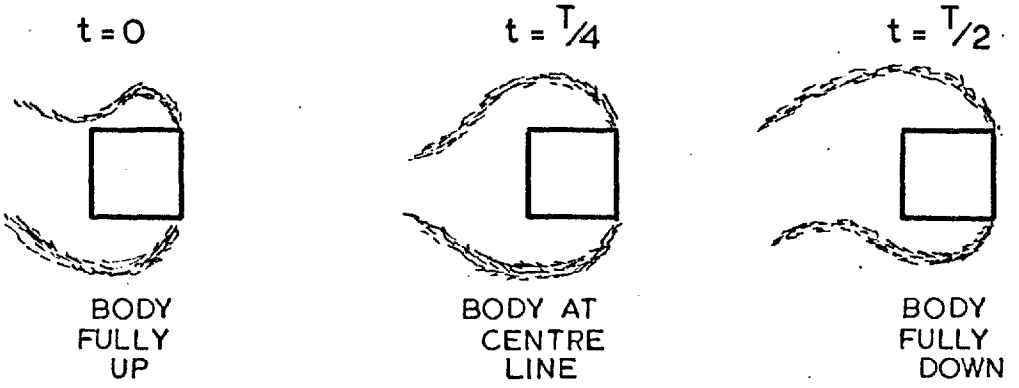

Fig. 5.6 Expected effects of body acceleration on shear layers configuration

FLOW AROUND A STATIONARY SQUARE SECTION CYLINDER; $R_e = 5.2 \times 10^3$

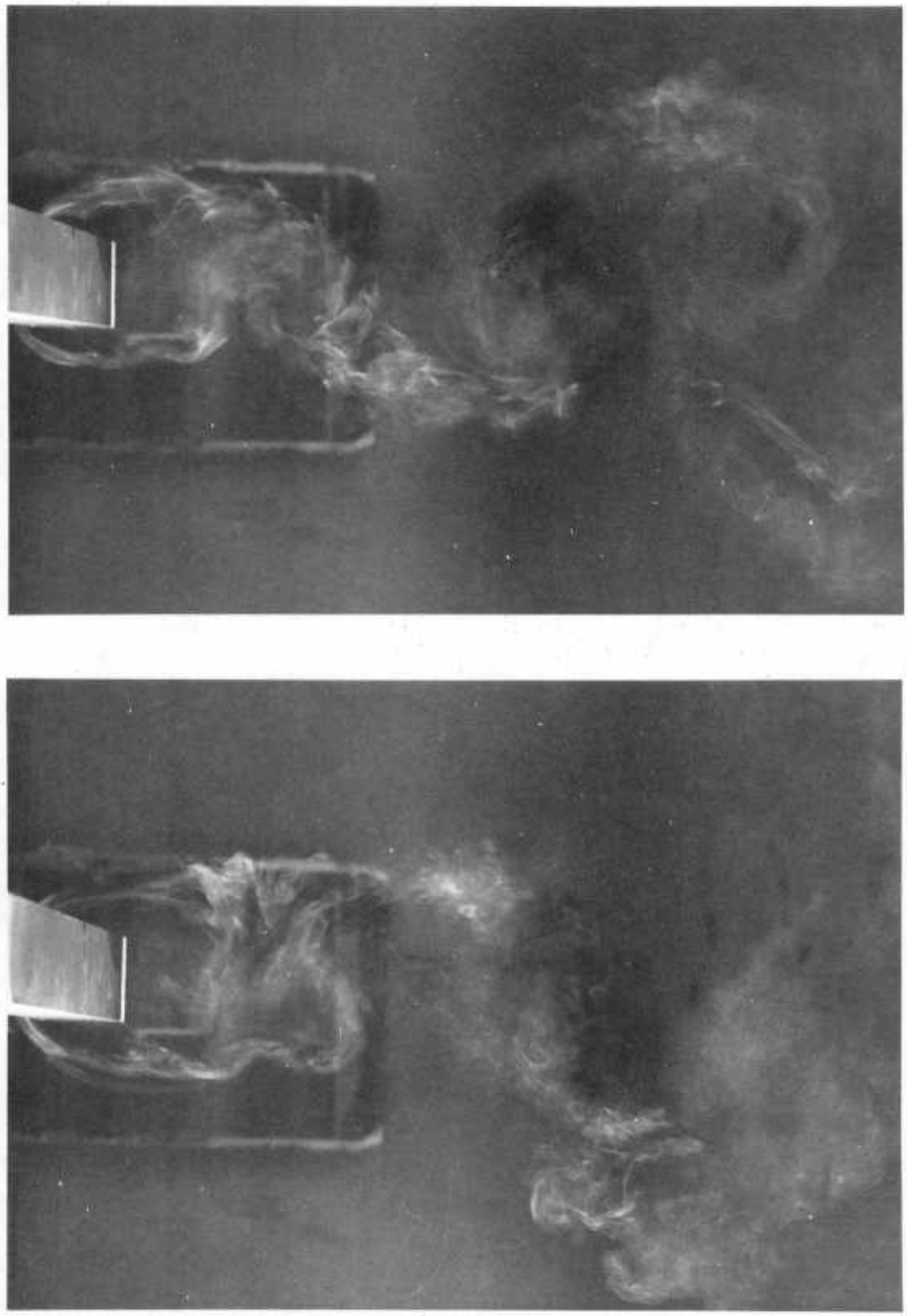

FIG. 5·7

FLOW AROUND AN OSCILLATING SQUARE SECTION CYLINDER; $R_e = 5{\cdot}2 \times 10^3$; $A/D = 0{\cdot}25$

$f_N/f_s \doteqdot 1{\cdot}0$

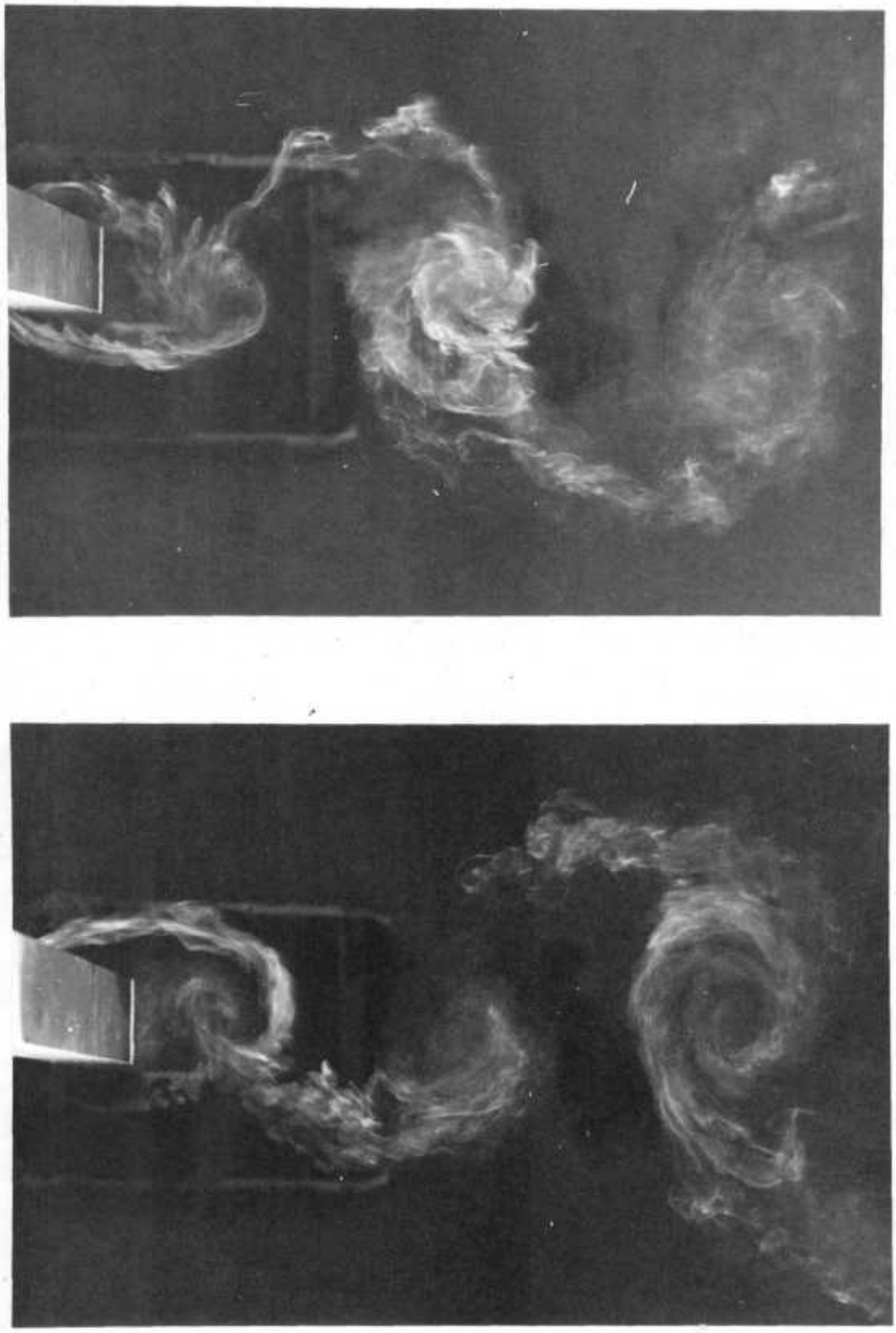

FIG. 5·8

FLOW AROUND AN OSCILLATING SQUARE SECTION CYLINDER; $R_e = 5{\cdot}2 \times 10^3$; $A/D = 0{\cdot}25$

$f_N \doteqdot 2 f_S$

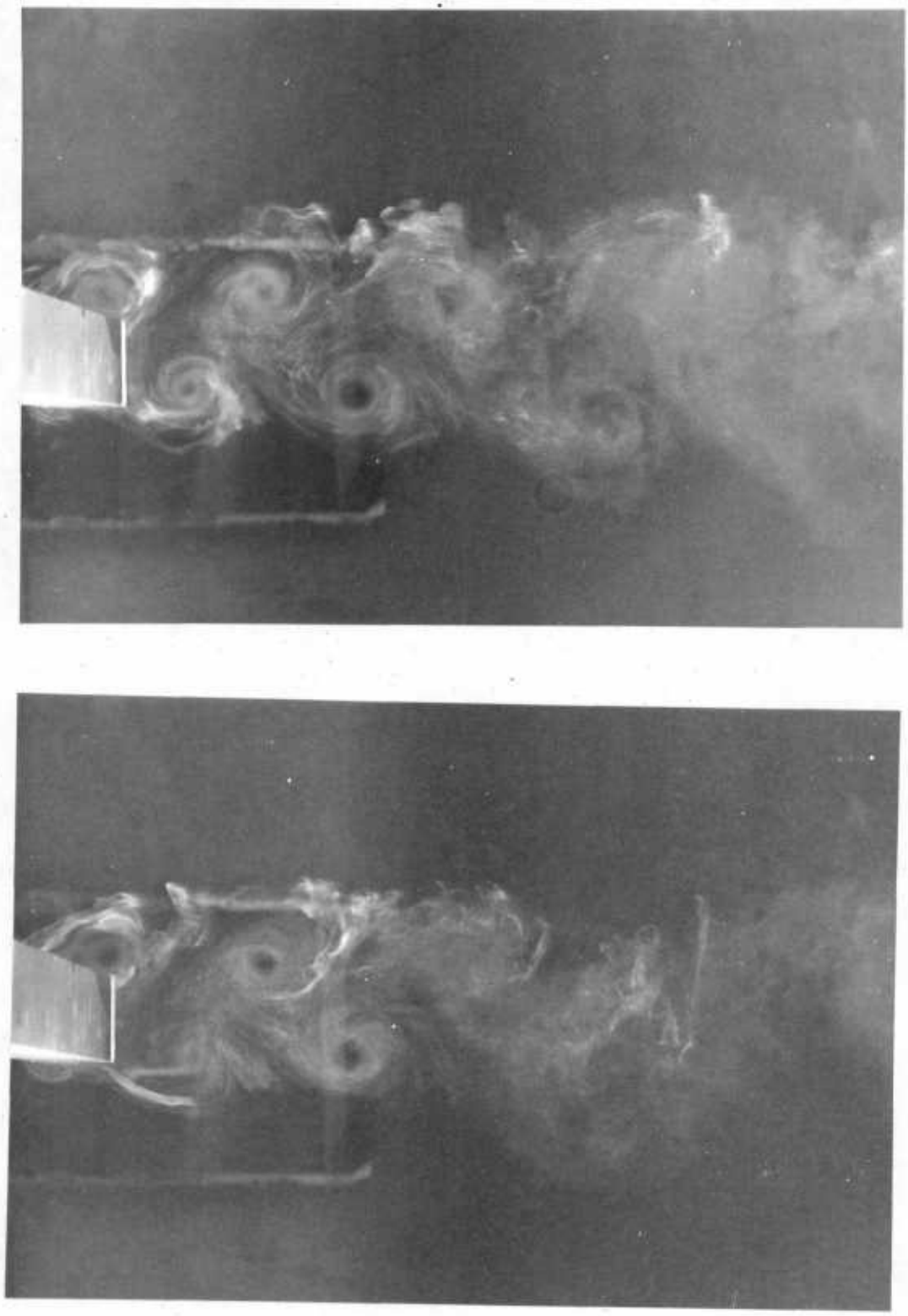

FIG. 5.9

FLOW AROUND AN OSCILLATING SQUARE SECTION CYLINDER; $R_e = 5.2 \times 10^3$; $A/D = 0.25$

$f_N \doteqdot 0.5\, f_S$

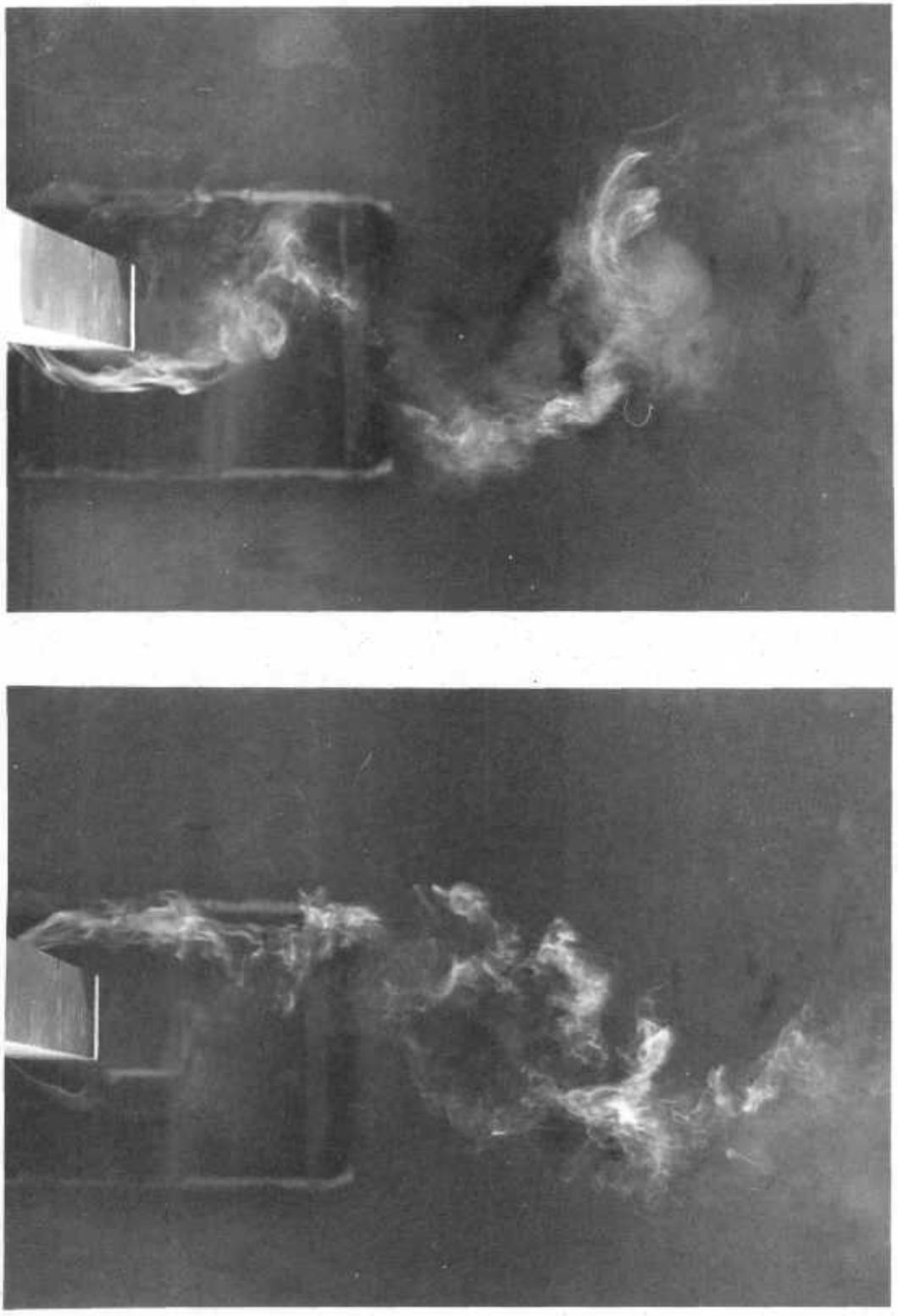

FIG. 5.10

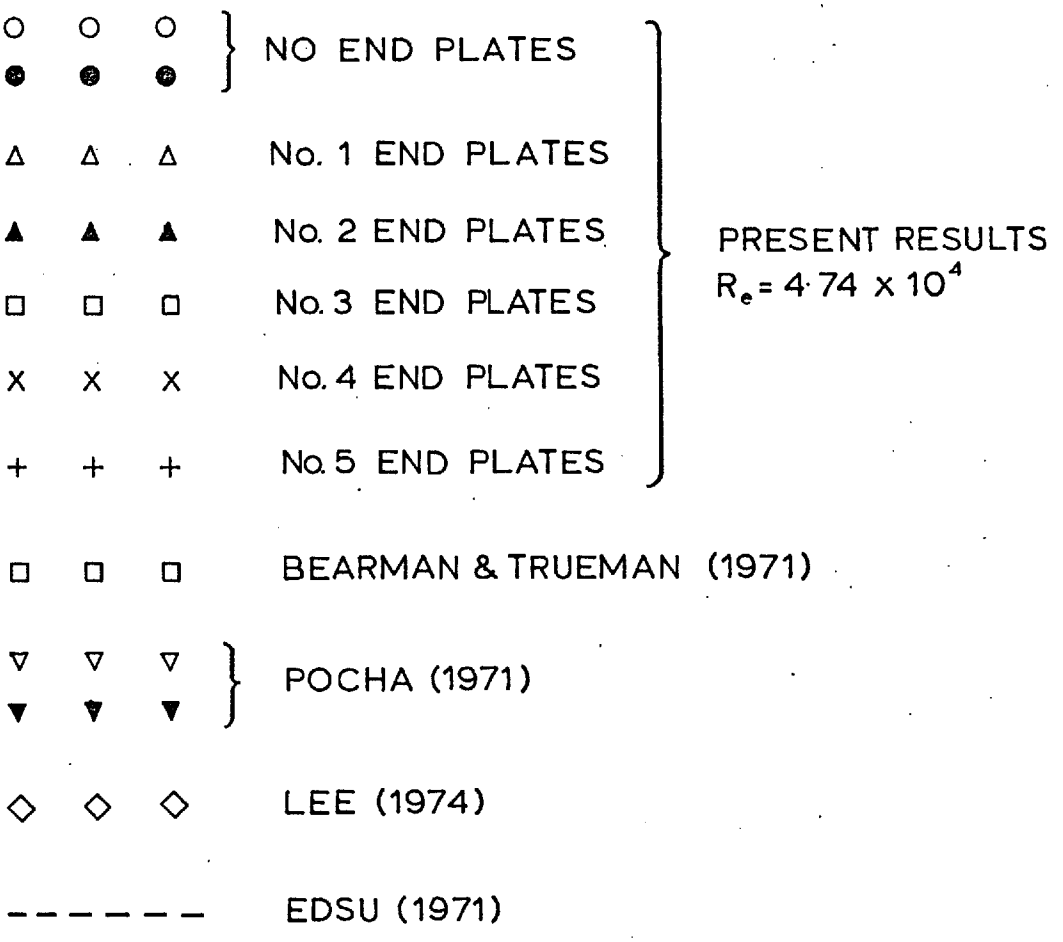

Fig. 6·1 Notation for Figs. 6·2 to 6·8

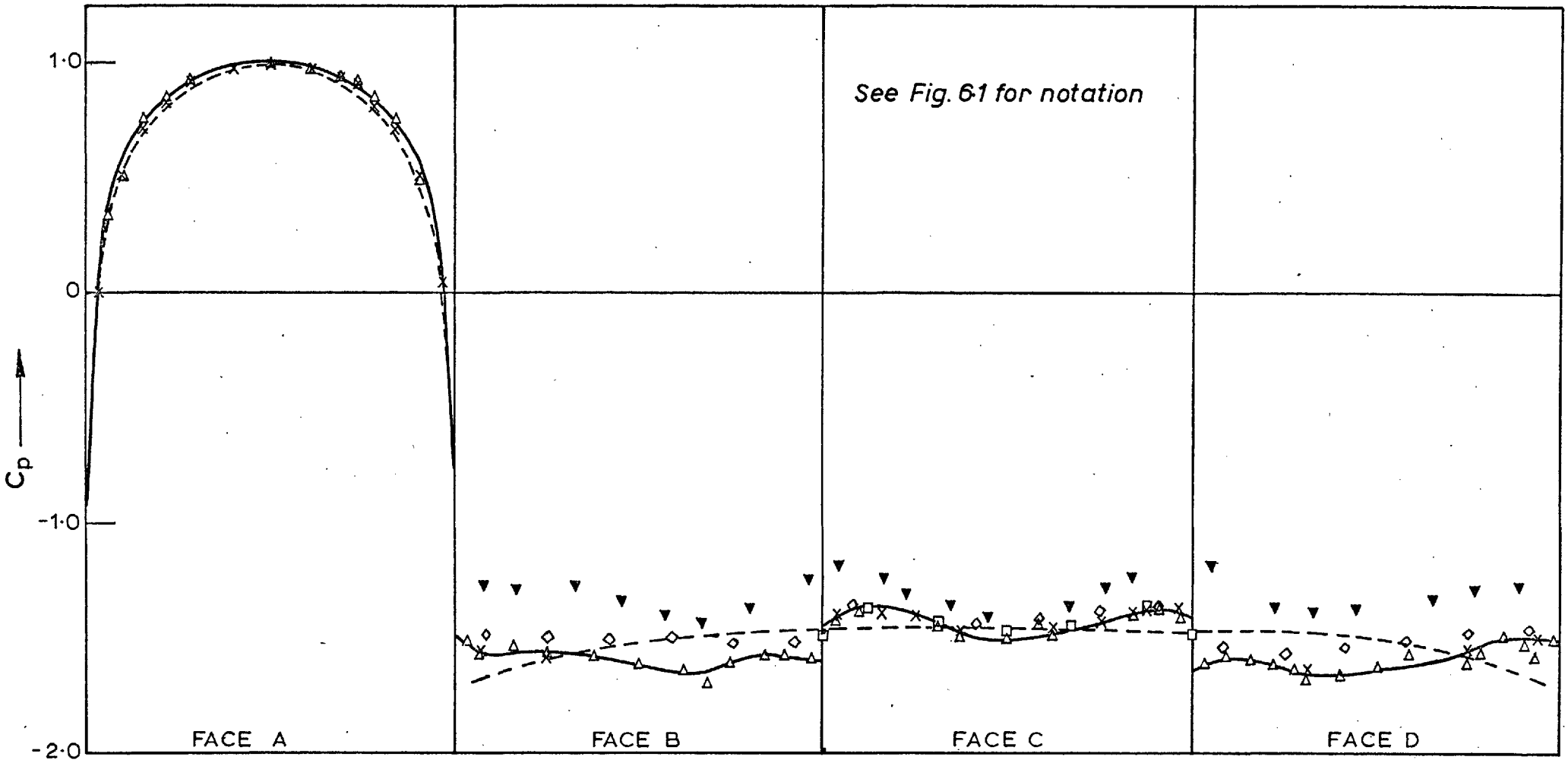

Fig. 6·2 Mean pressure distribution on a square section cylinder at 0° incidence

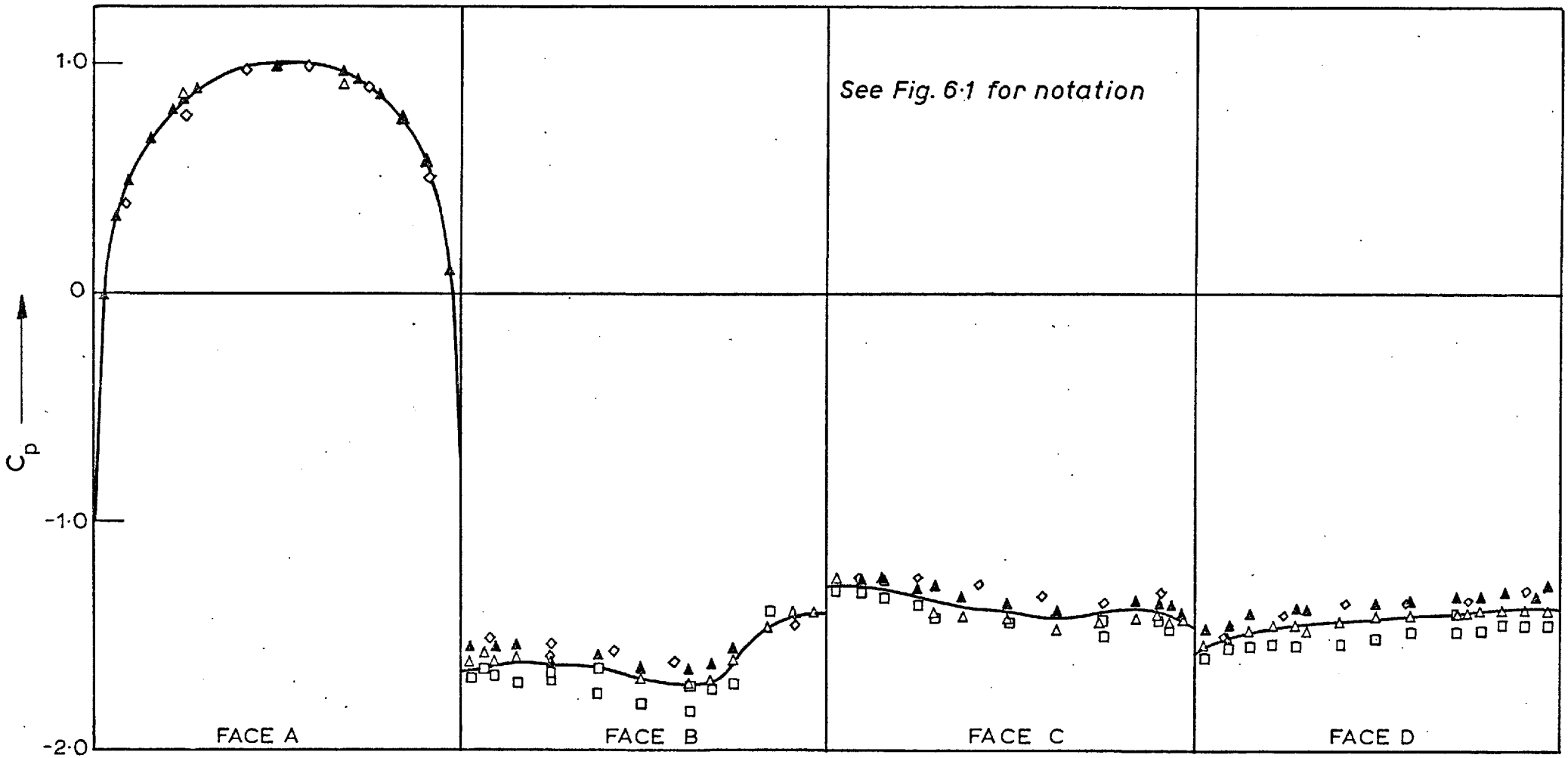

Fig. 6·3 (a) Mean pressure distribution on a square section cylinder at 5° incidence

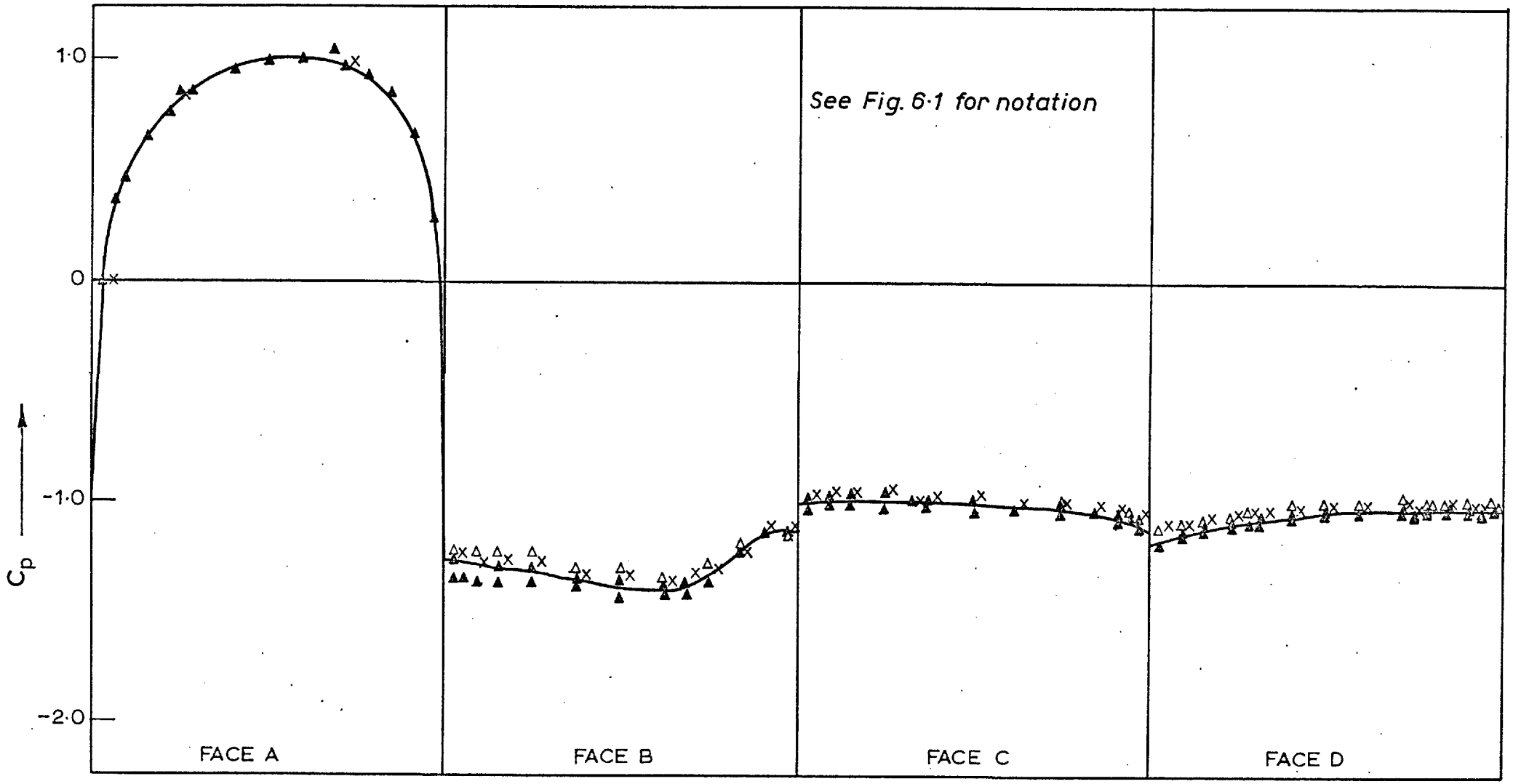

Fig. 6·3 (b) Mean pressure distribution on a square section cylinder at 10° incidence

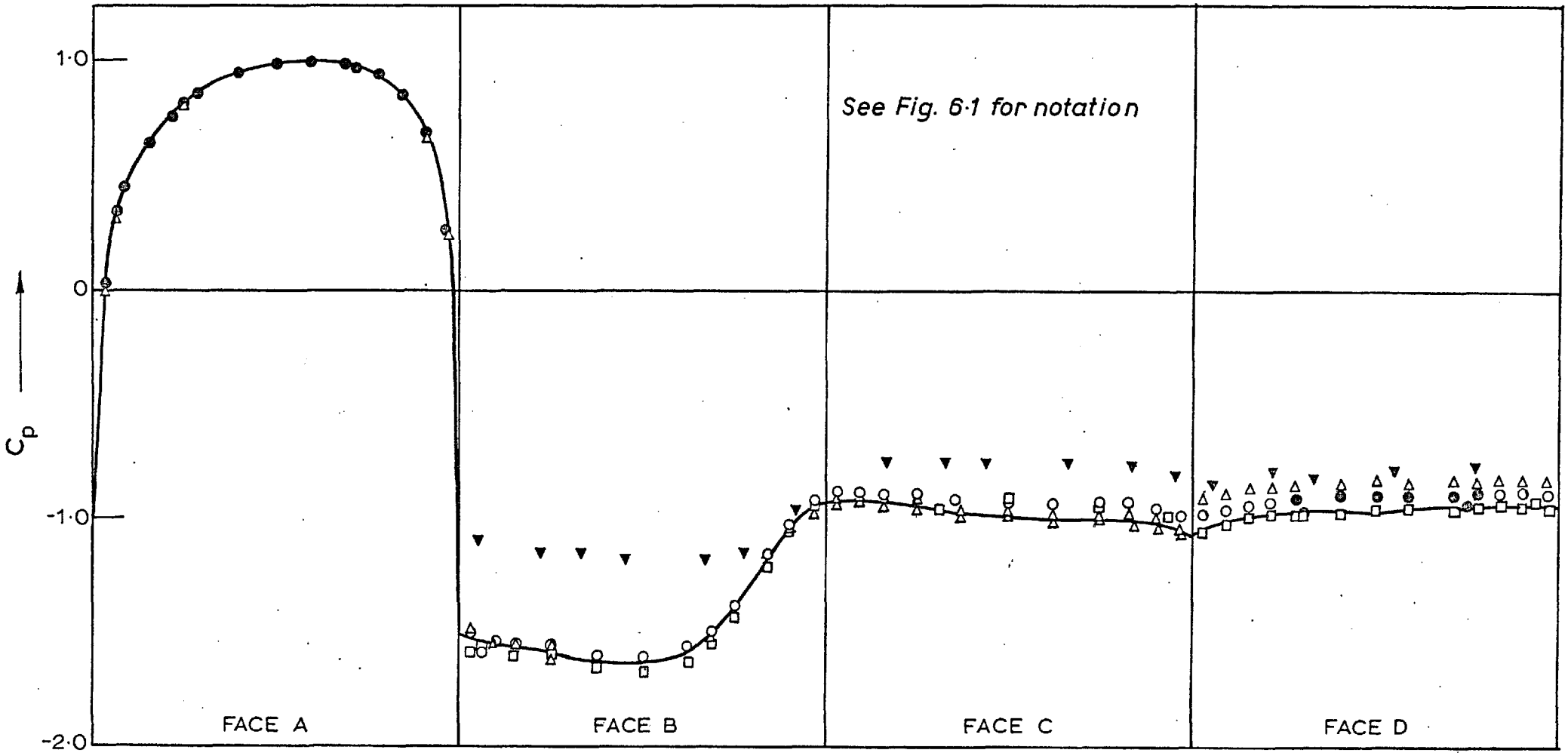

Fig. 6·4 Mean pressure distribution on a square section cylinder at 13·5° incidence

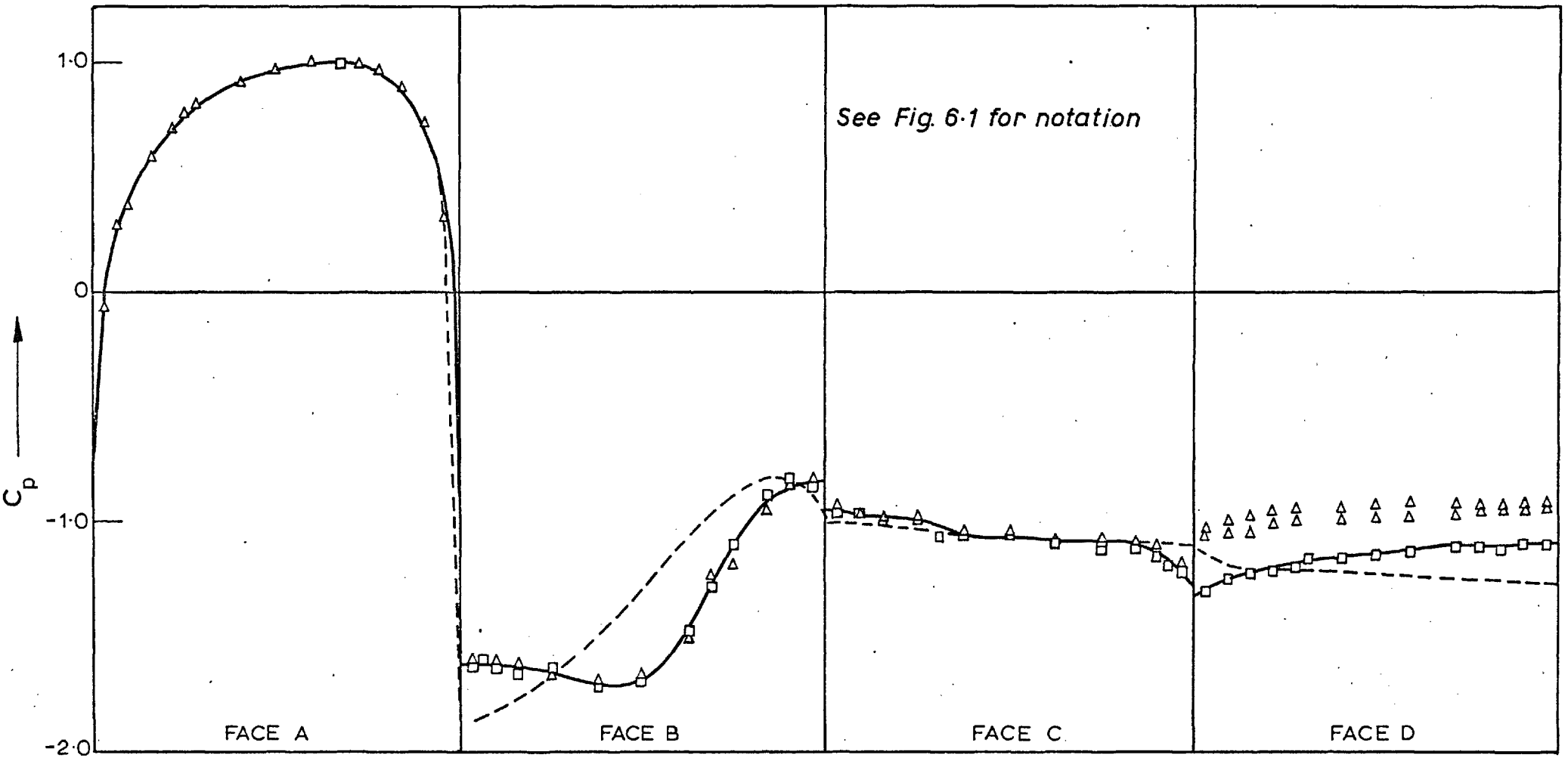

Fig. 6·5 Mean pressure distribution on a square section cylinder at 15° incidence

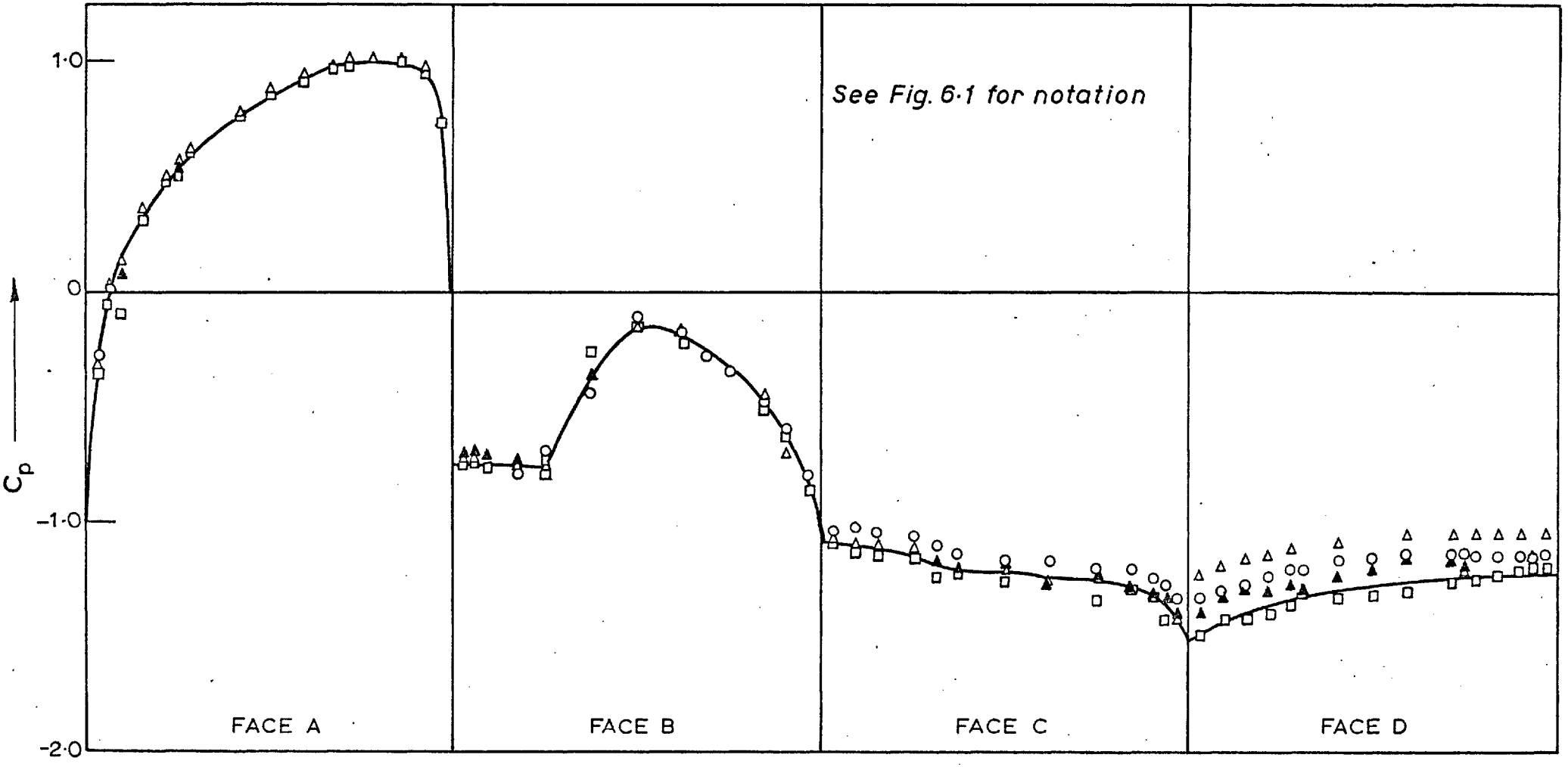

Fig. 6·6 Mean pressure distribution on a square section cylinder at 25° incidence

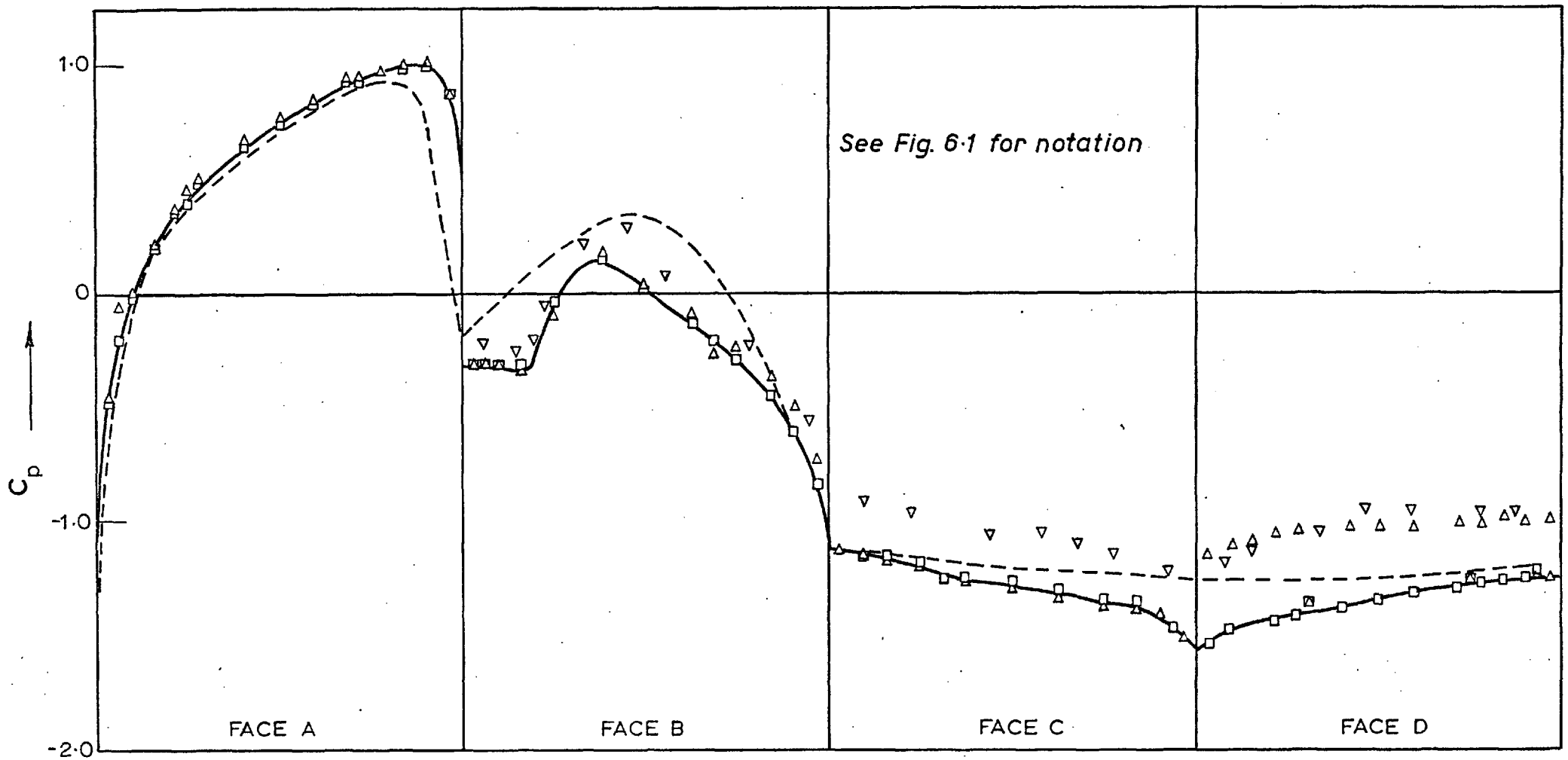

Fig. 6·7(a) Mean pressure distribution on a square section cylinder at 30° incidence

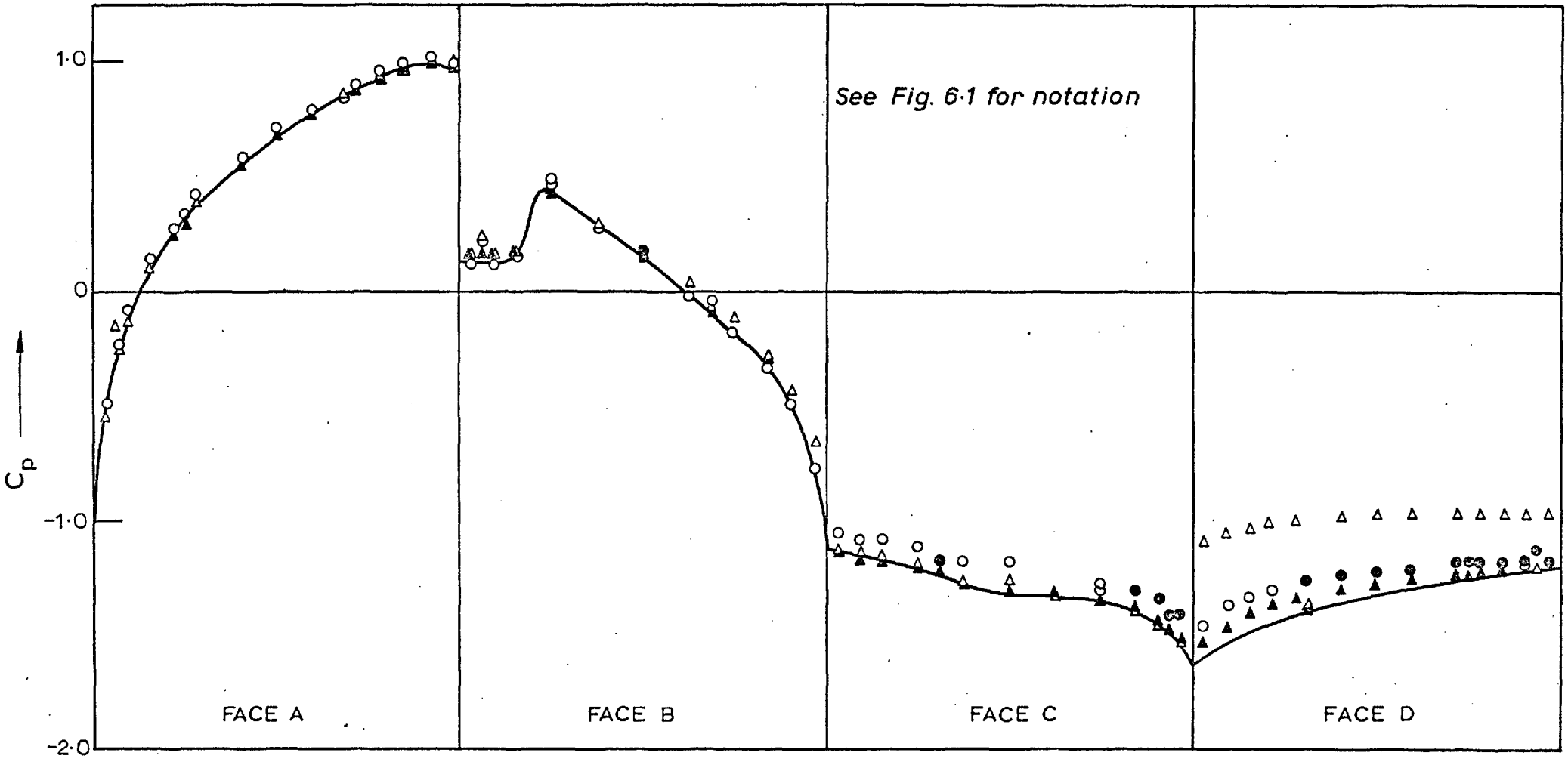

Fig. 6·7(b) Mean pressure distribution on a square section cylinder at 35° incidence

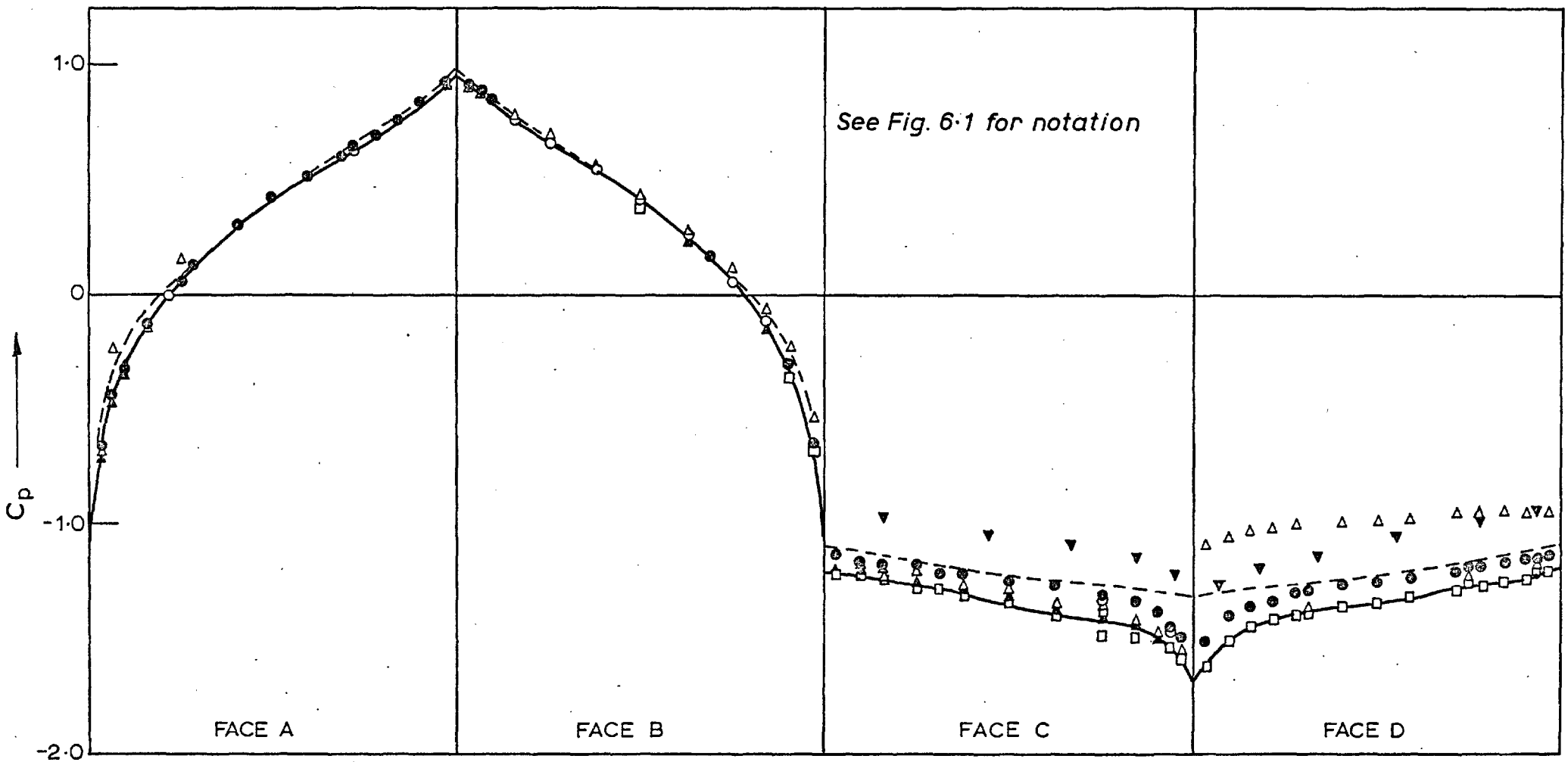

Fig. 6·8 Mean pressure distribution on a square section cylinder at 45° incidence

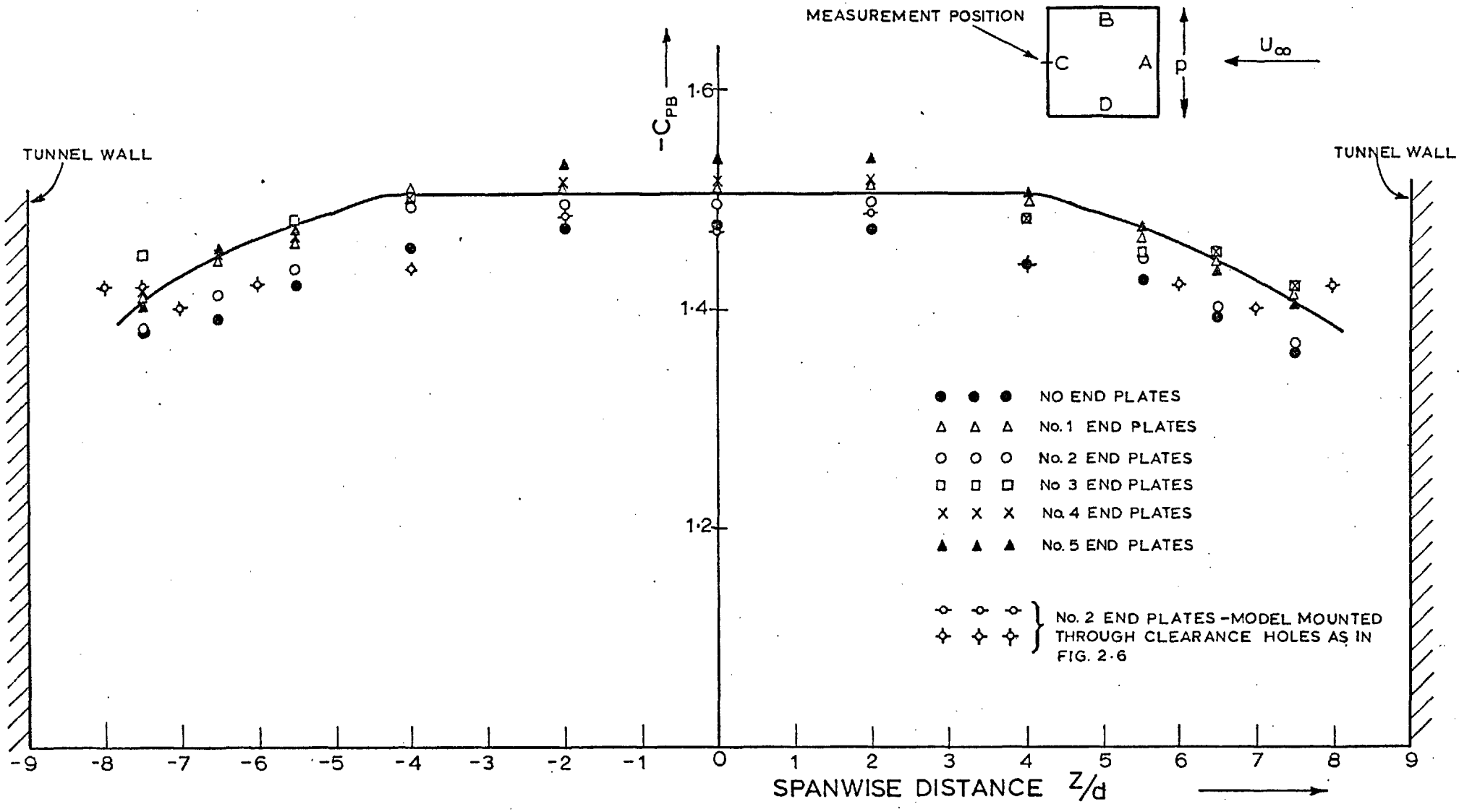

Fig. 6·9 Spanwise distribution of mean base pressure coefficient on the centre-line of Face C

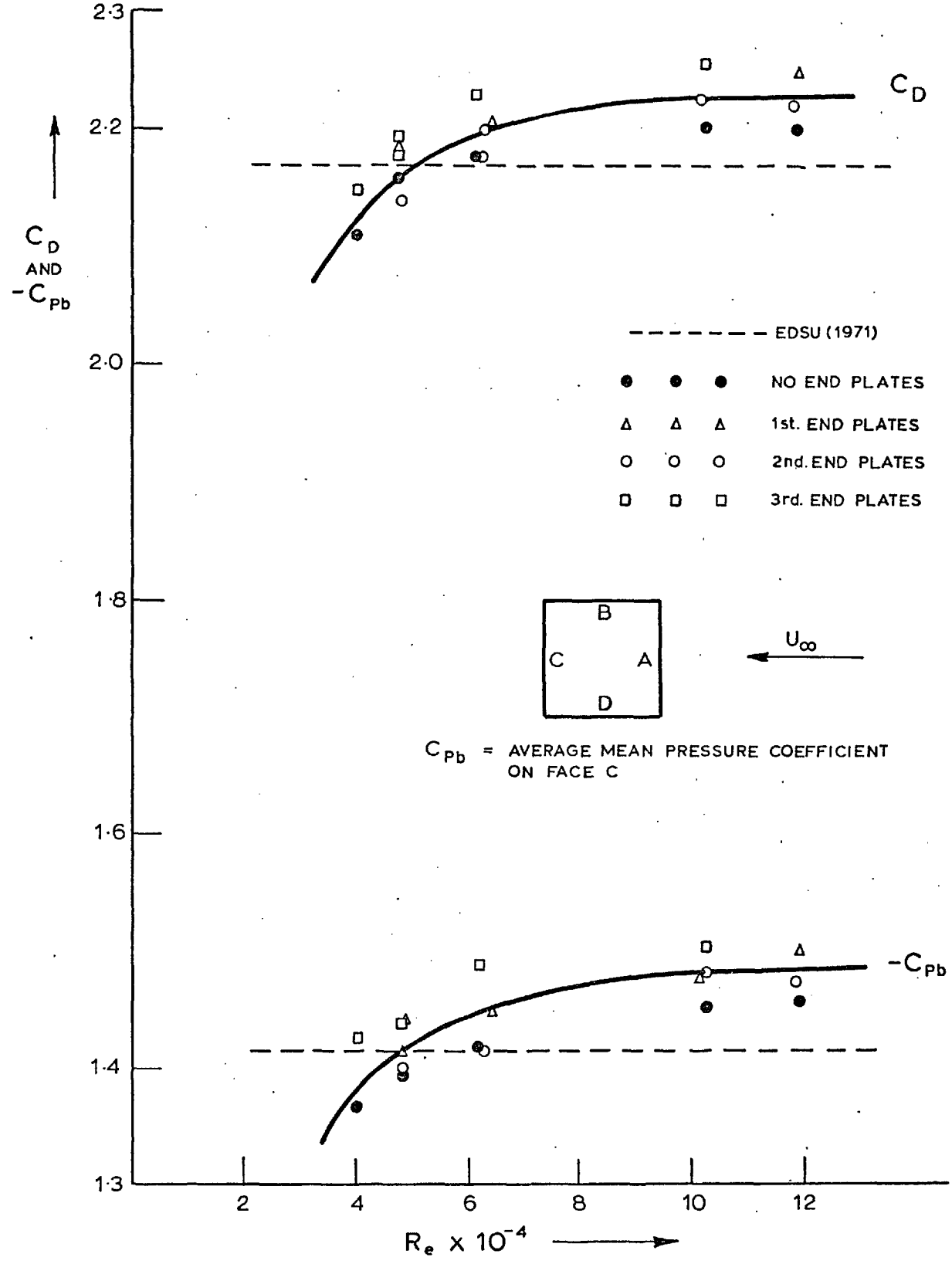

Fig. 6·10 Variation of drag and base pressure coefficients with Reynolds number at 0° incidence

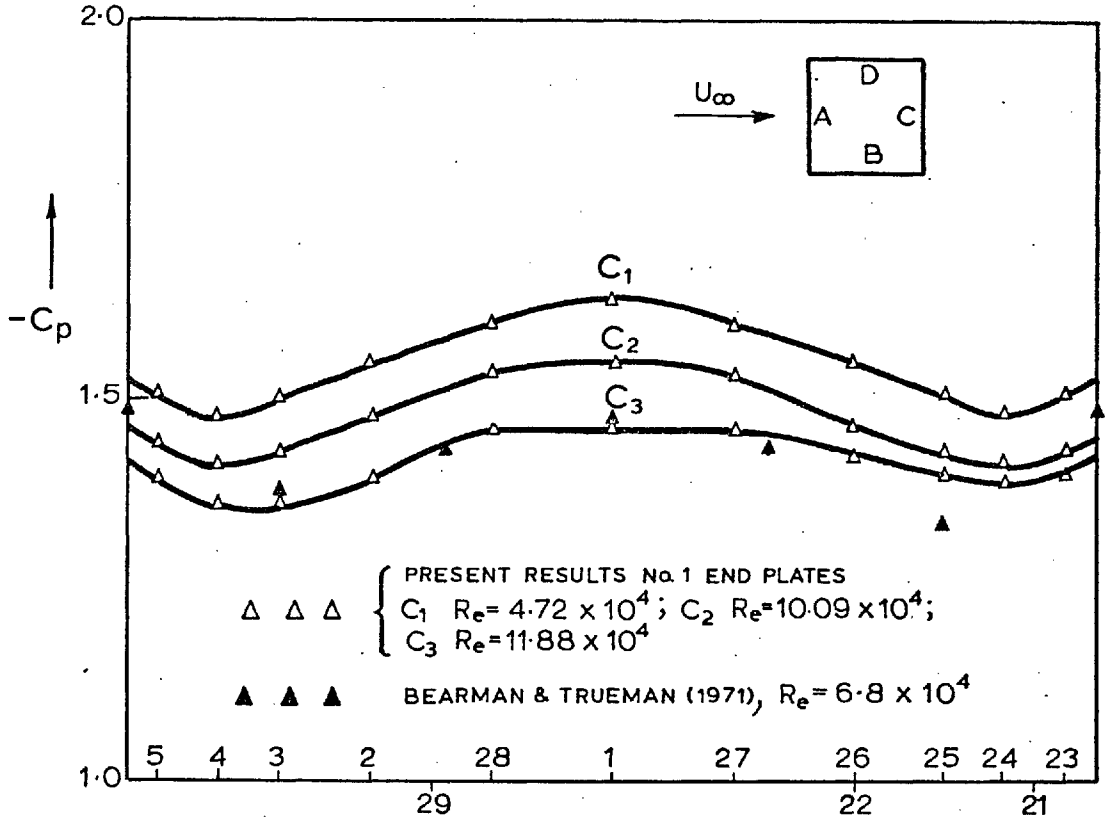

Fig. 6·11 (a) Mean pressure distribution on Face C at 0° incidence

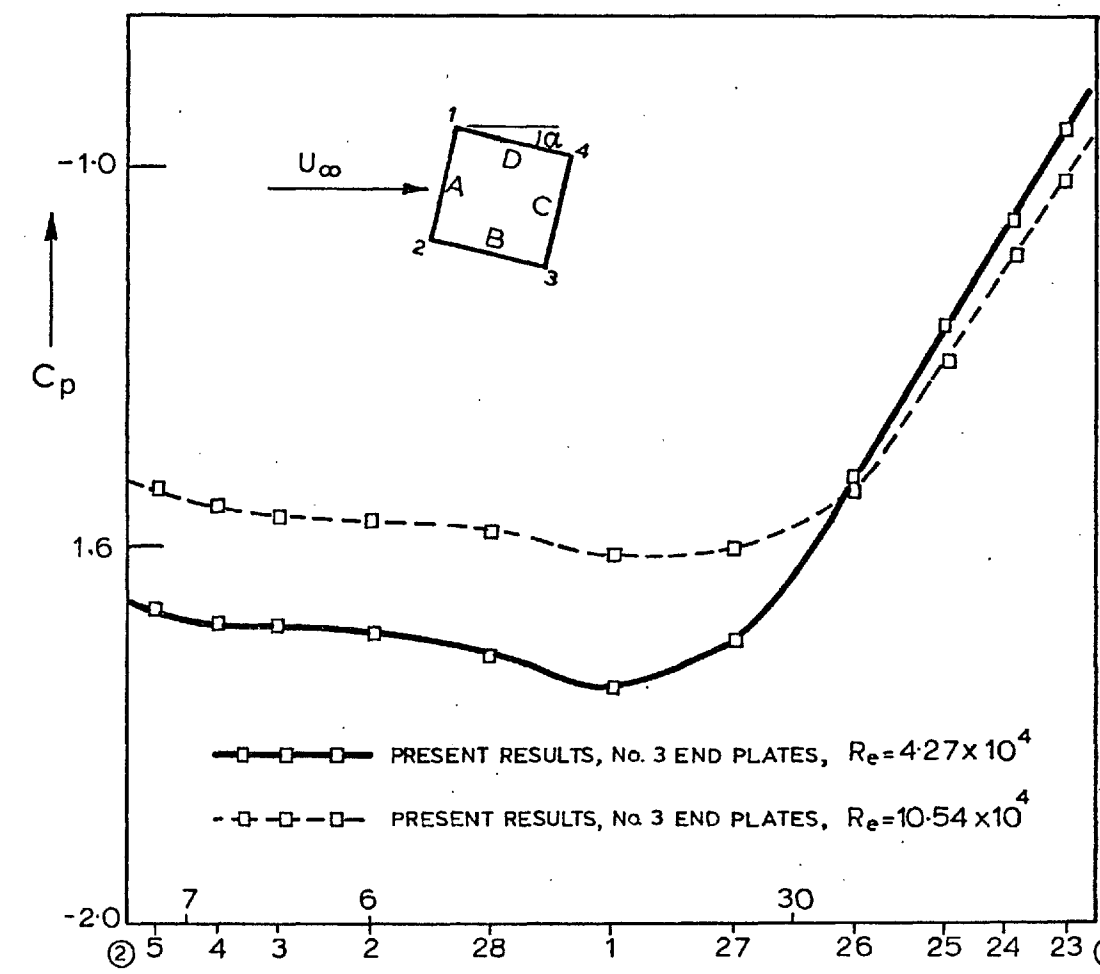

Fig. 6·11 (b) Mean pressure distribution on Face B at 13·5° inclination

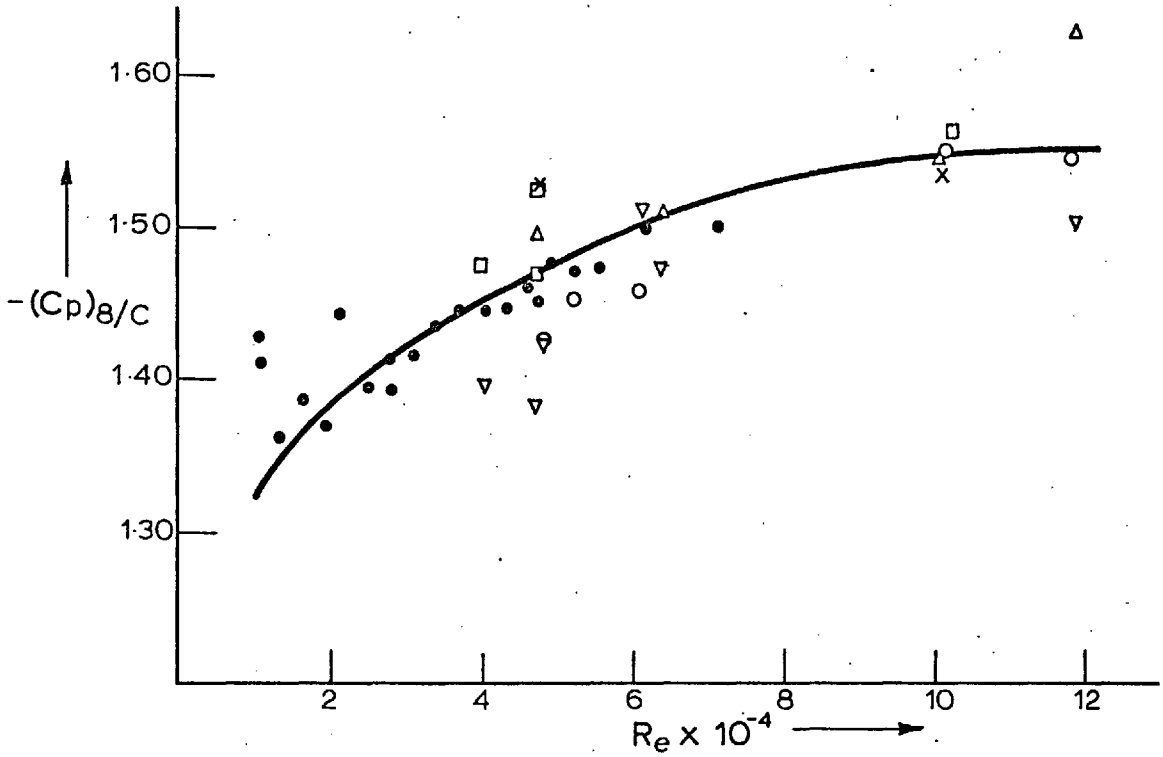

$(C_p)_{B/C}$ – MEAN PRESSURE COEFFICIENT AT THE CENTRE OF FACE C

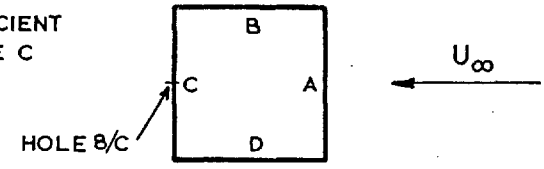

▽ ▽ ▽	NO END PLATES
△ △ △	No. 1 END PLATES
○ ○ ○	No. 2 END PLATES
□ □ □	No. 3 END PLATES
X X X	No. 4 END PLATES

} STATIONARY MODEL. MODEL BUILT INTO WIND TUNNEL SIDE WALLS

● ● ●	No. 2 END PLATES

} MODEL STATIONARY BUT MOUNTED THROUGH CLEARANCE HOLES AS IN Fig. 2·6

Fig. 6·12 Variation of $(C_p)_{B/C}$ with Reynolds number

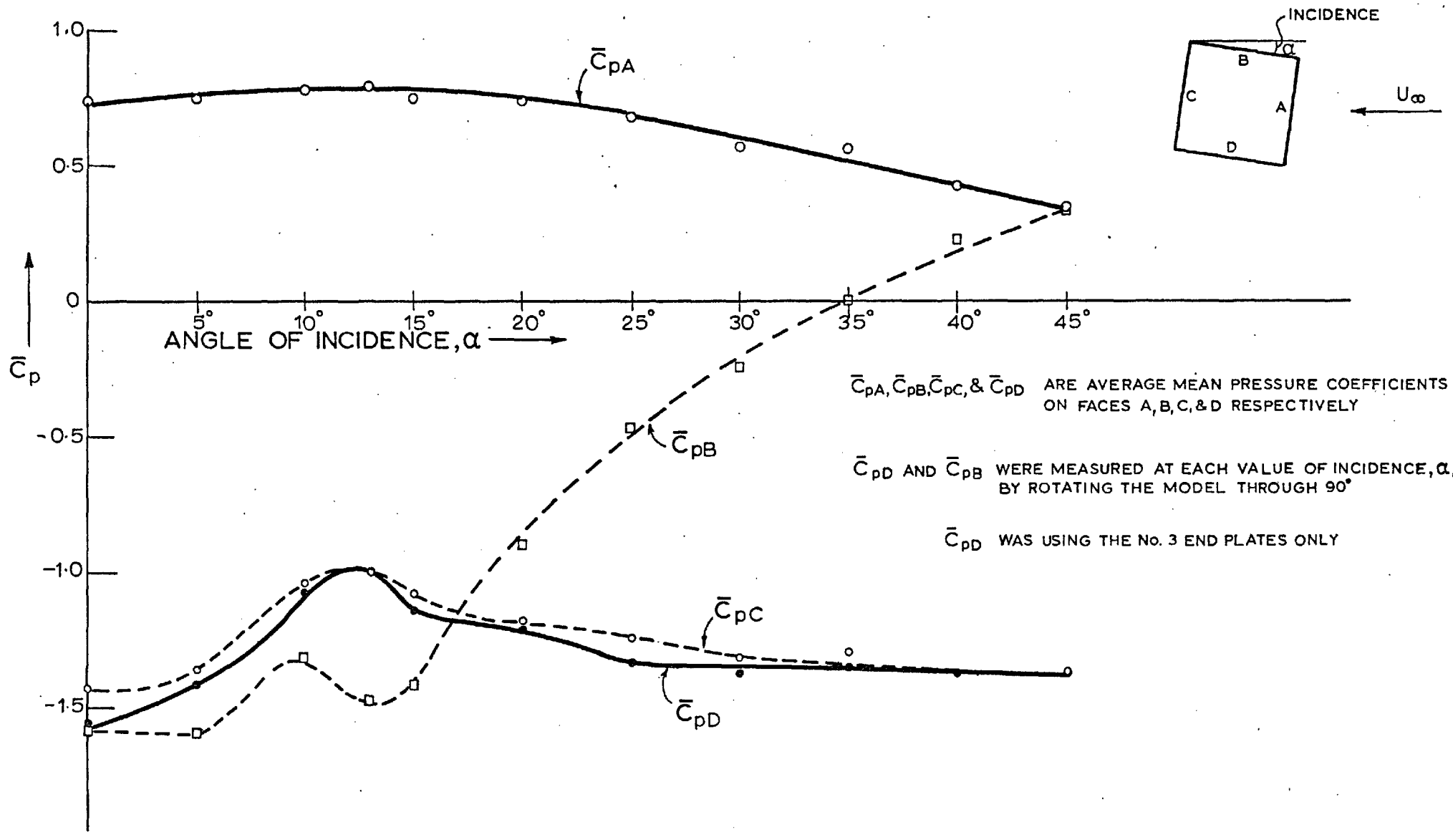

Fig. 6·13 Variation of $\bar{C}_{pA}$, $\bar{C}_{pB}$, $\bar{C}_{pC}$ & $\bar{C}_{pD}$ on a stationary square section cylinder with incidence

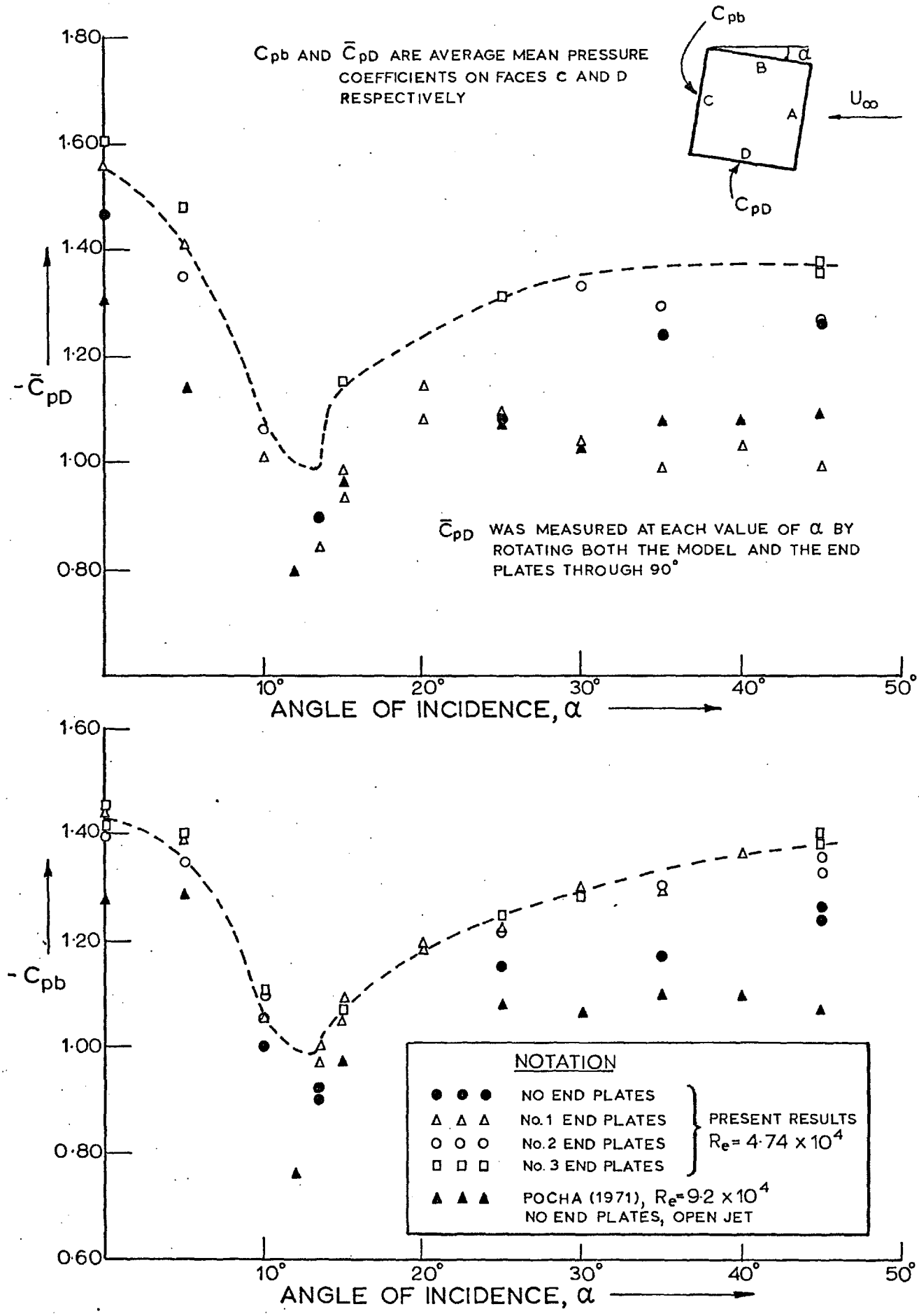

Fig. 6·14 Effects of end plates on C_{pb} and $\bar{C}_{pD}$

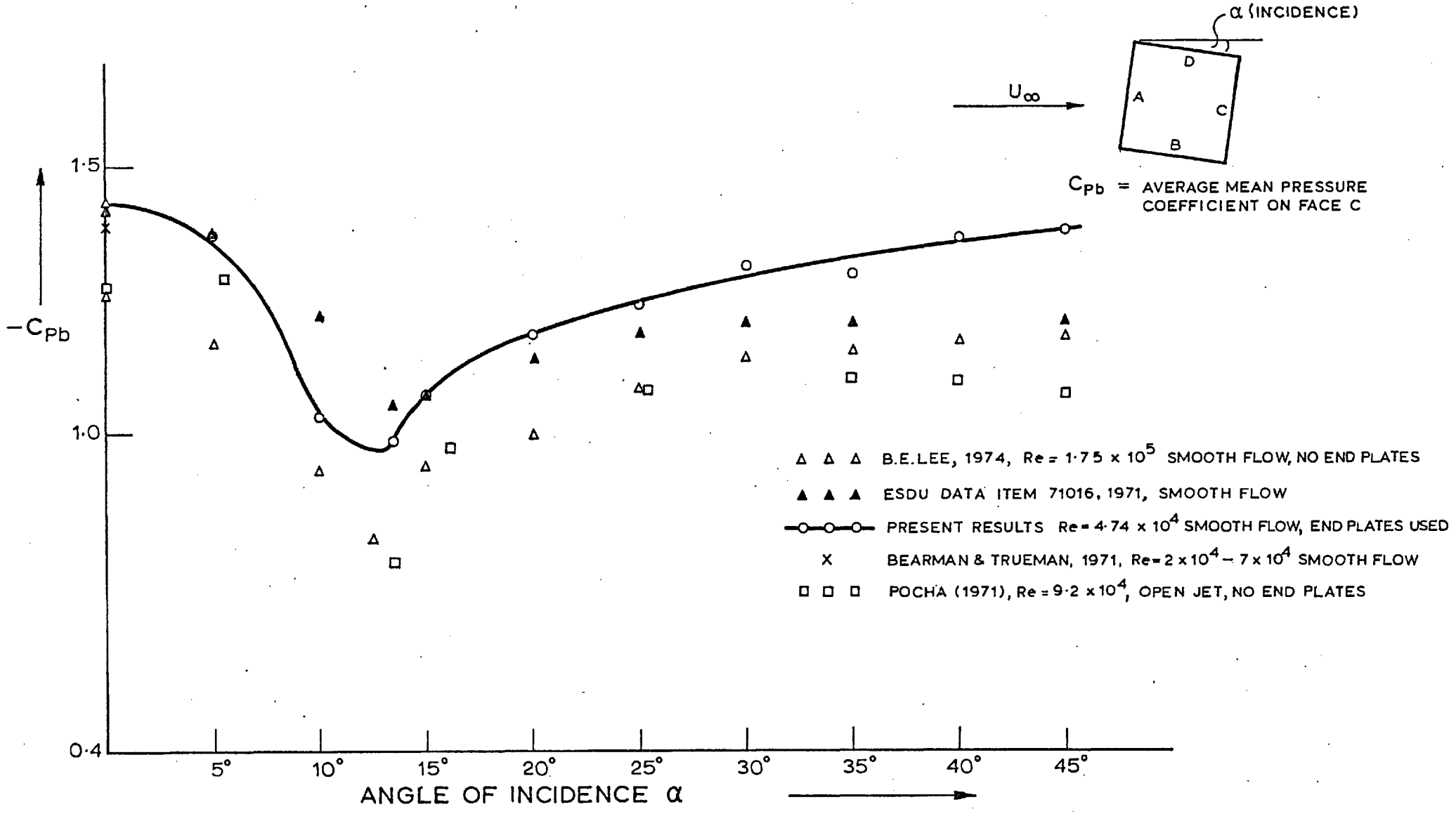

Fig. 6·15 Base pressure coefficient on a square section cylinder

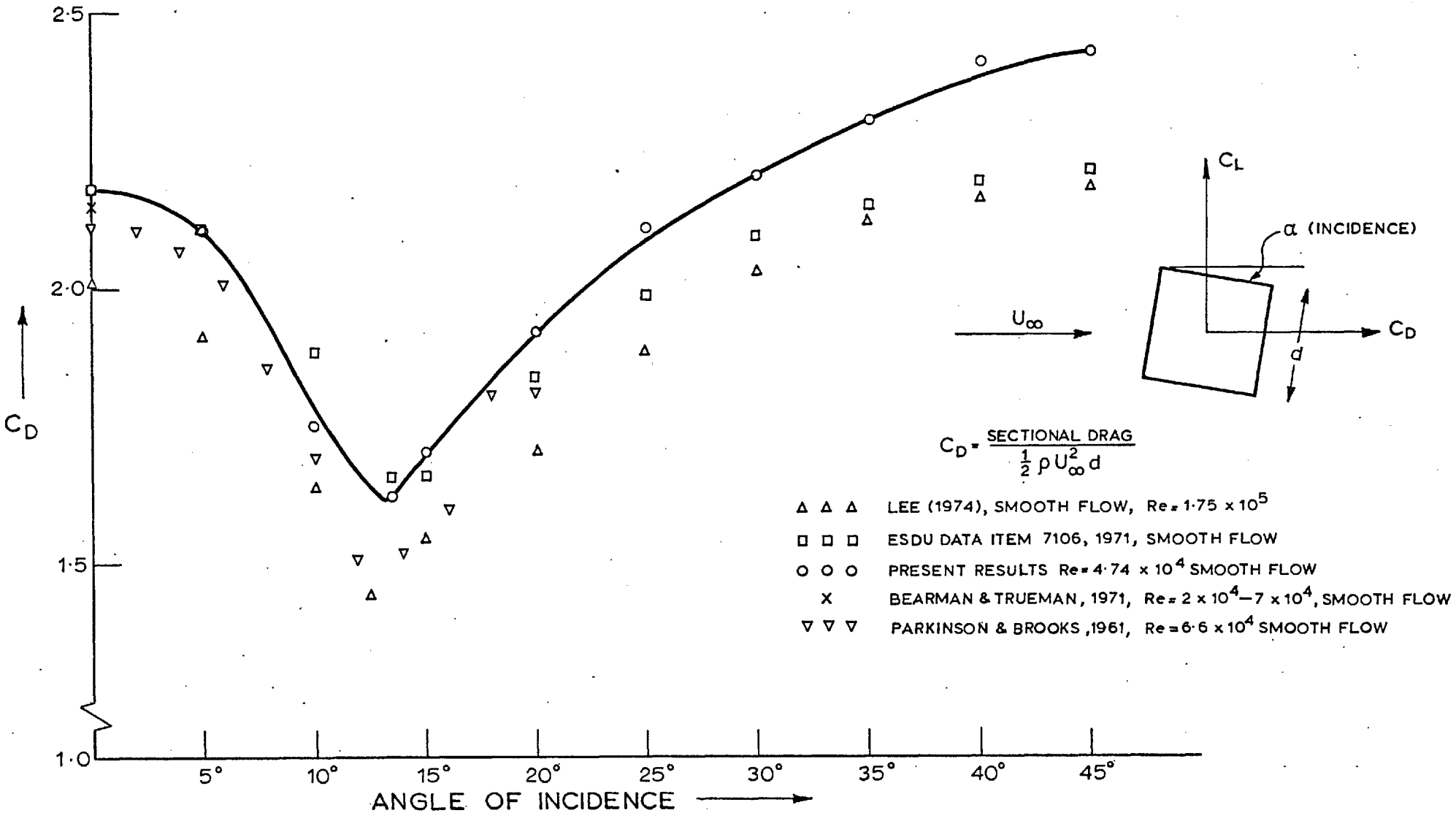

Fig. 6.16 Sectional drag coefficient of a square section cylinder

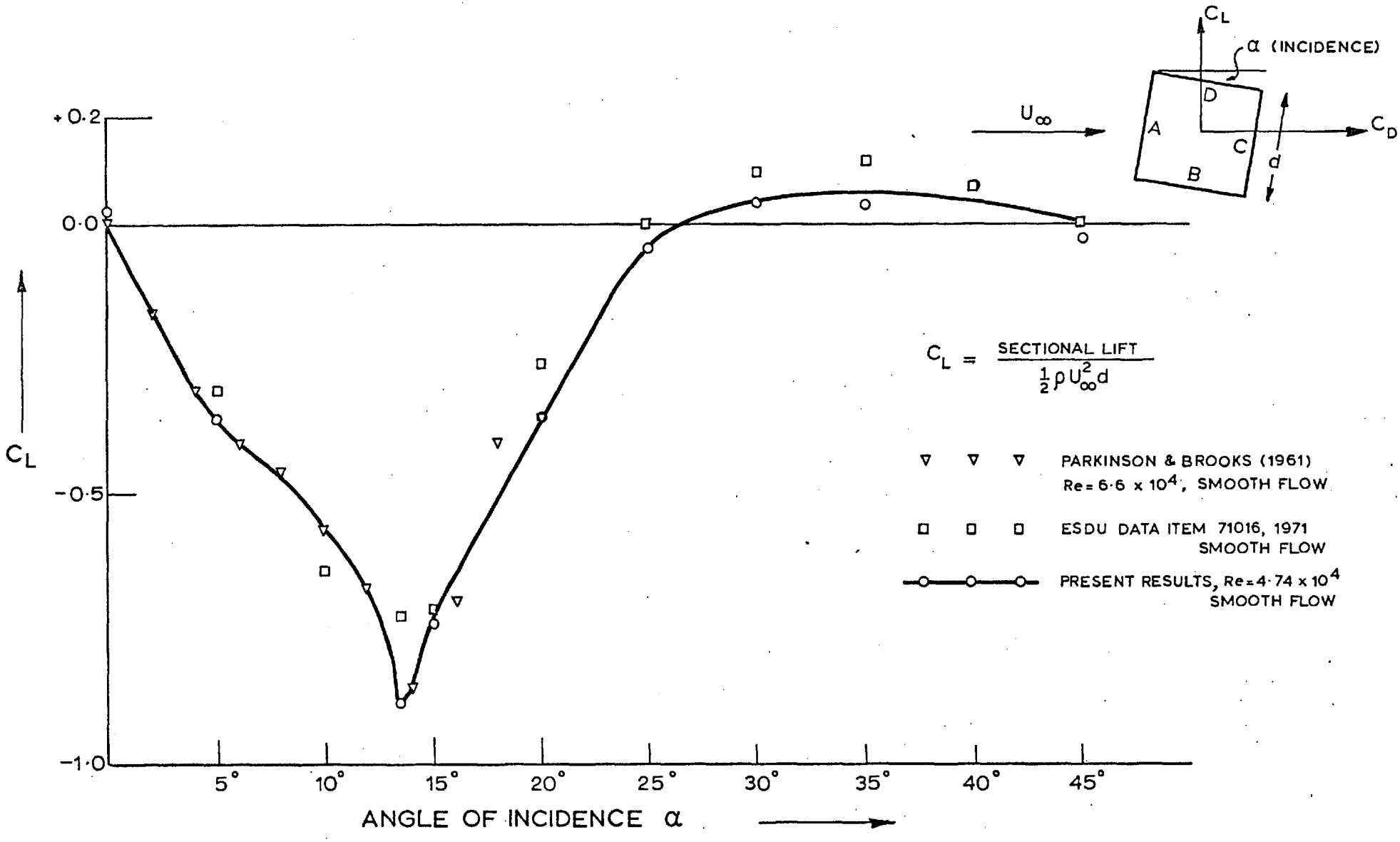

Fig. 6·17 Lift coefficient of a square section cylinder

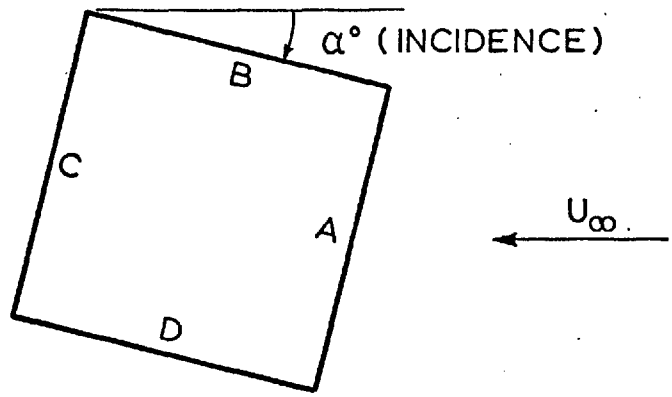

PRESENT RESULT, B & K $\frac{1}{4}$" MICROPHONE MODEL 4136, STATIONARY MODEL, $R_e = 6{\cdot}06 \times 10^4$ SMOOTH FLOW

B.E. LEE; 1974, $R_e = 1{\cdot}76 \times 10^5$, SMOOTH FLOW

J.J. POCHA; 1971, $R_e \approx 9{\cdot}2 \times 10^4$

B.J. VICKERY; 1966, $R_e = 4 \times 10^4 - 1{\cdot}6 \times 10^5$

R.H. WILKINSON; 1974, $R_e = 10^4 - 10^5$

B.E. Lee & R.H. Wilkinson measurements are corrected for blockage by the author using Maskell's method.

Fig. 6·18 Distribution of fluctuating pressures (C_{PRMS}) on a stationary model at α° incidence.

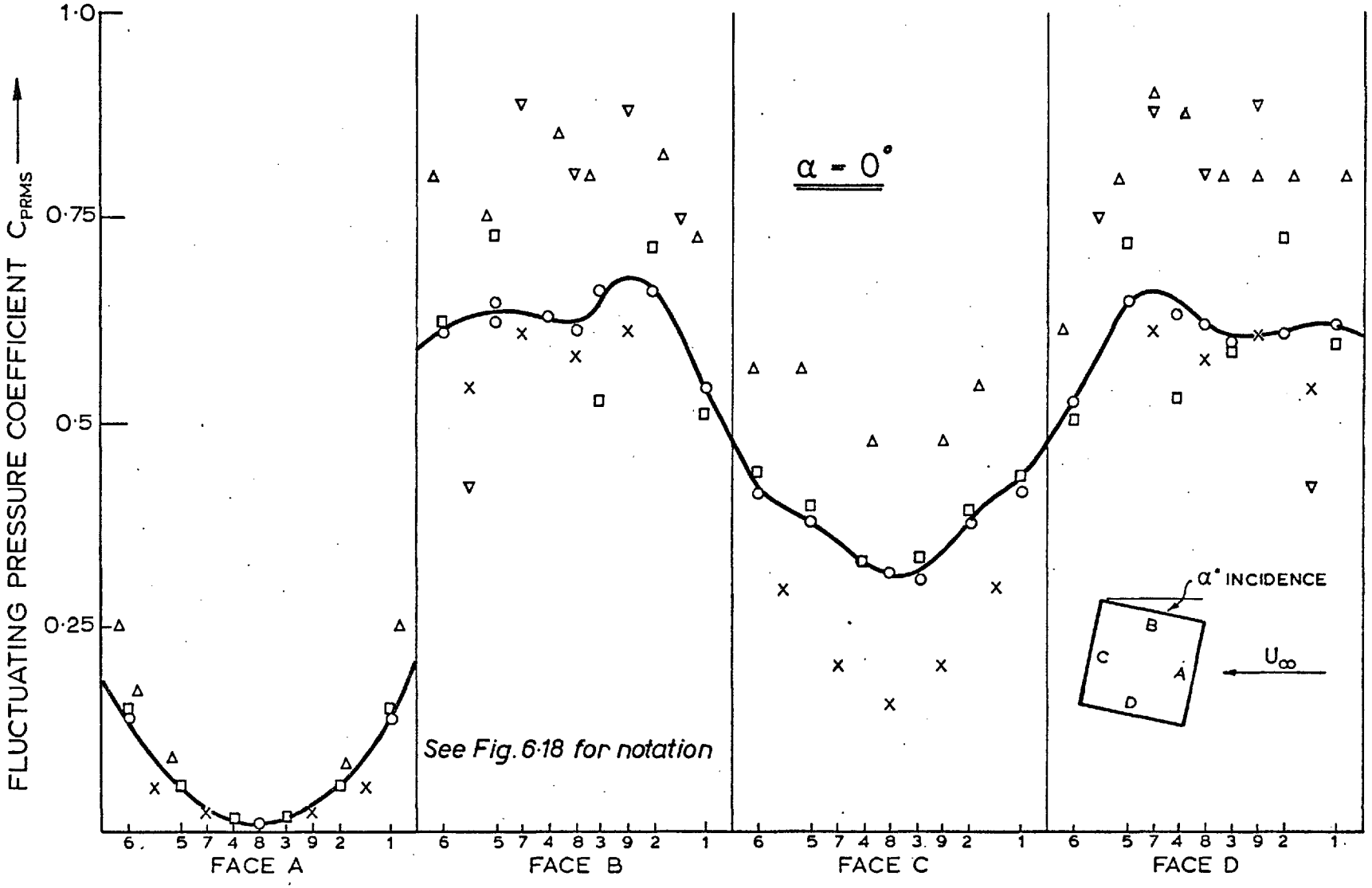

Fig. 6·19 Fluctuating pressure distribution on a stationary square section at 0° incidence

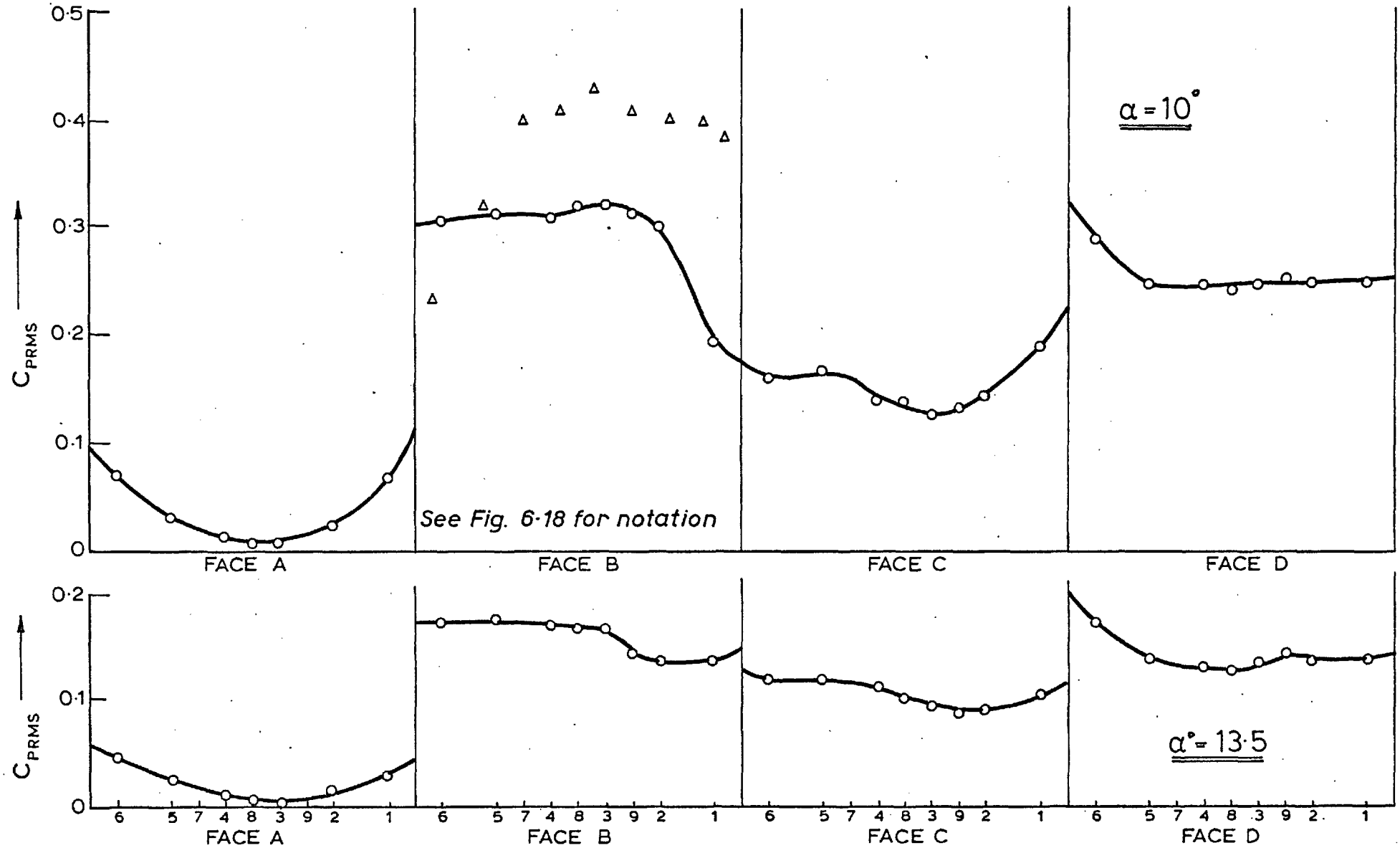

Fig. 6·20 Distribution of C_{PRMS} on a square section cylinder at α° incidence

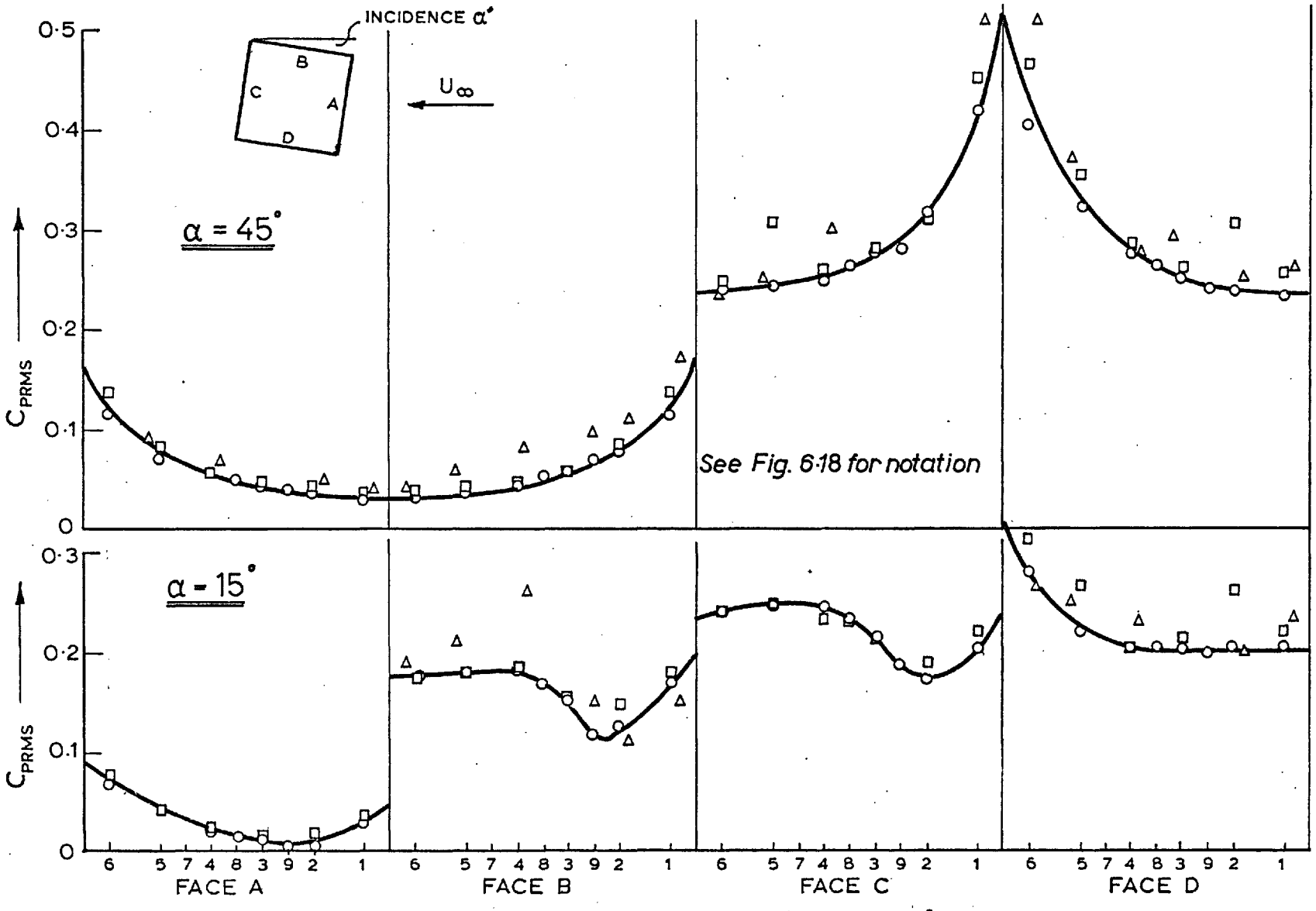

Fig. 6·21 Distribution of C_{PRMS} on a square section cylinder at α° incidence

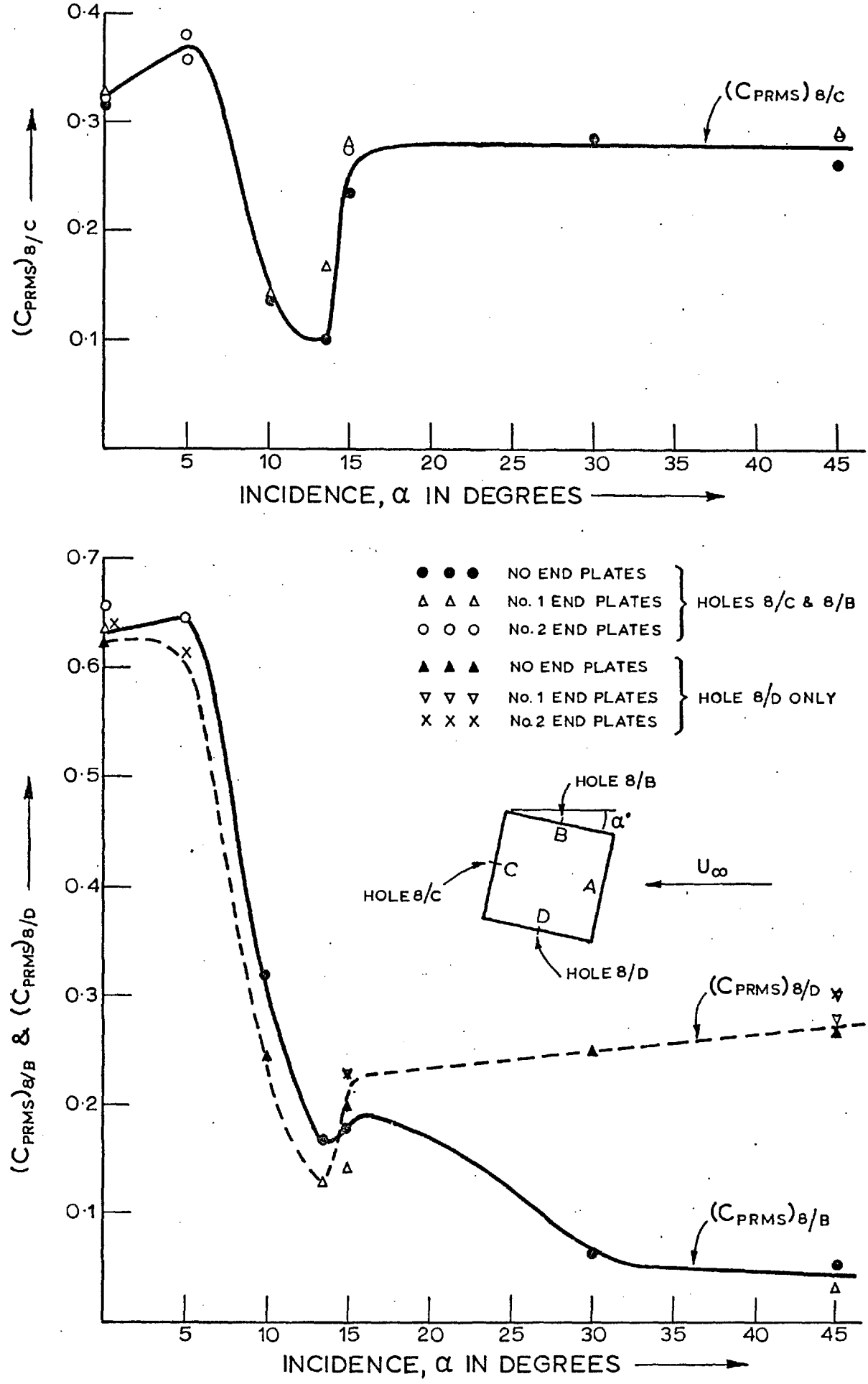

Fig. 6·22 Variation of C_{PRMS} at tappings 8/B, 8/C and 8/D with incidence α° on a stationary model

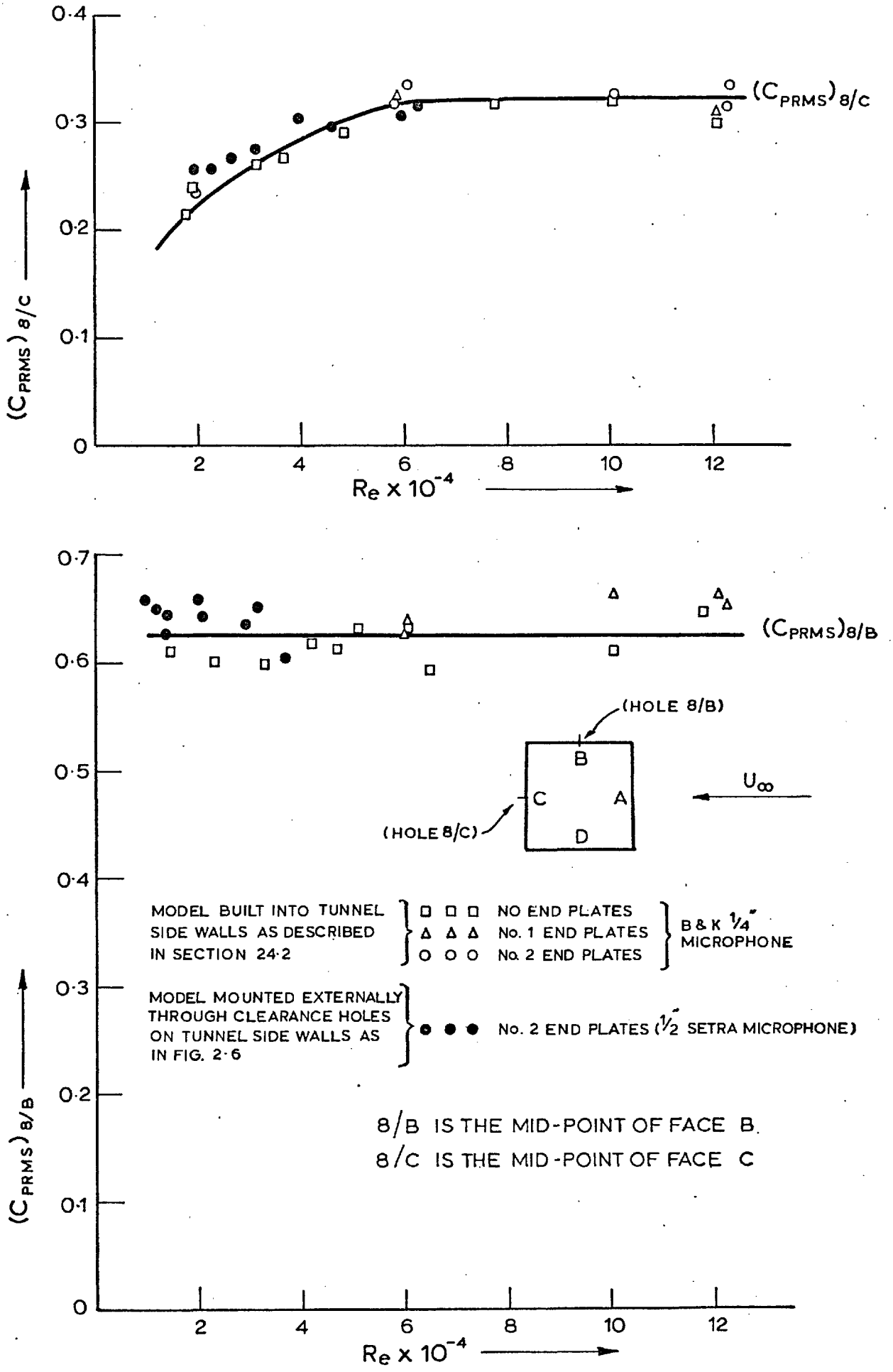

Fig. 6·23 Variation of fluctuating pressure at tappings 8/B and 8/C with Reynolds number at $\alpha = 0°$ on a stationary square section cylinder.

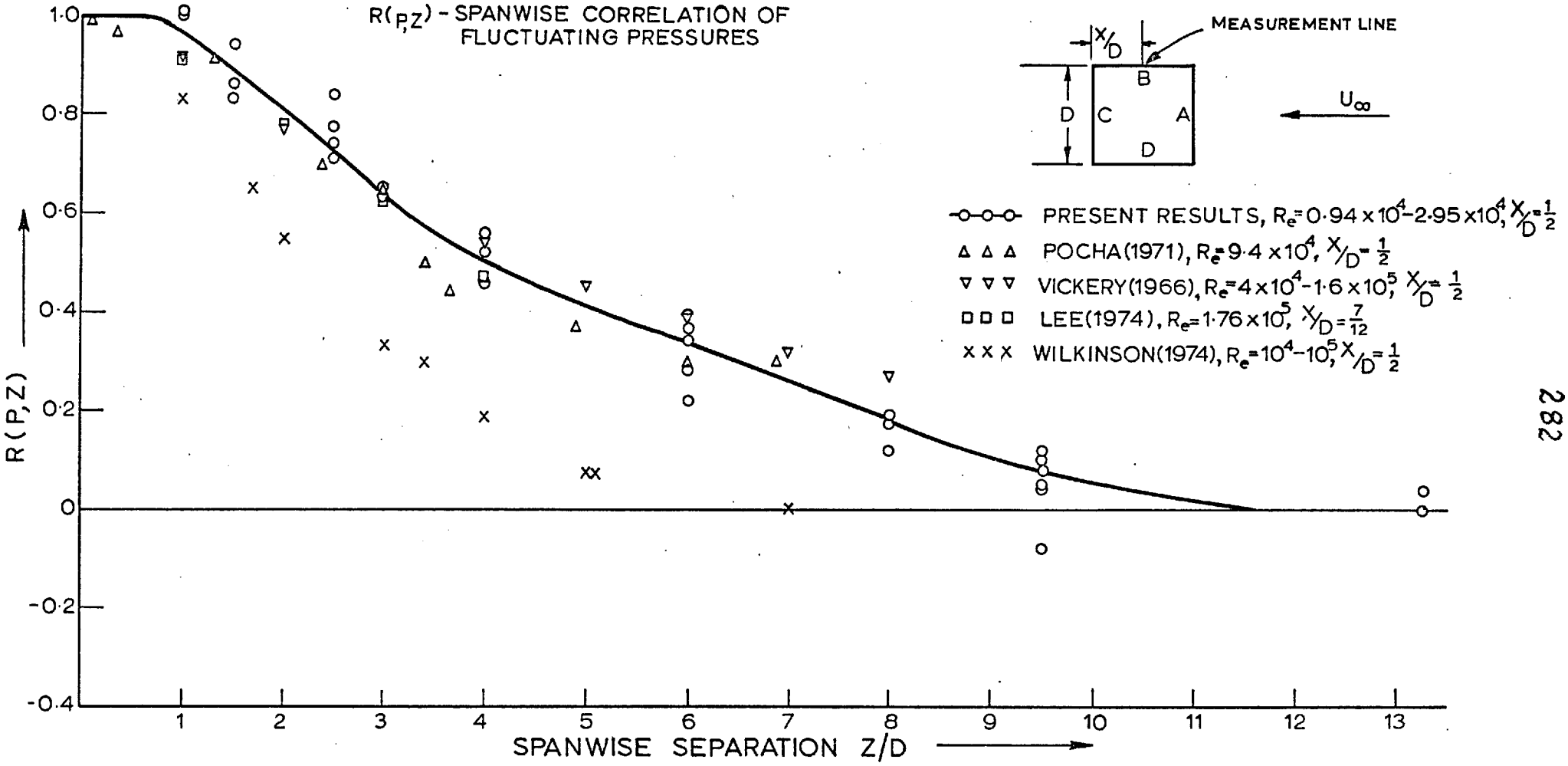

Fig. 6·24 Spanwise distribution of R(P,Z) on face B of a stationary square section cylinder at α=0°

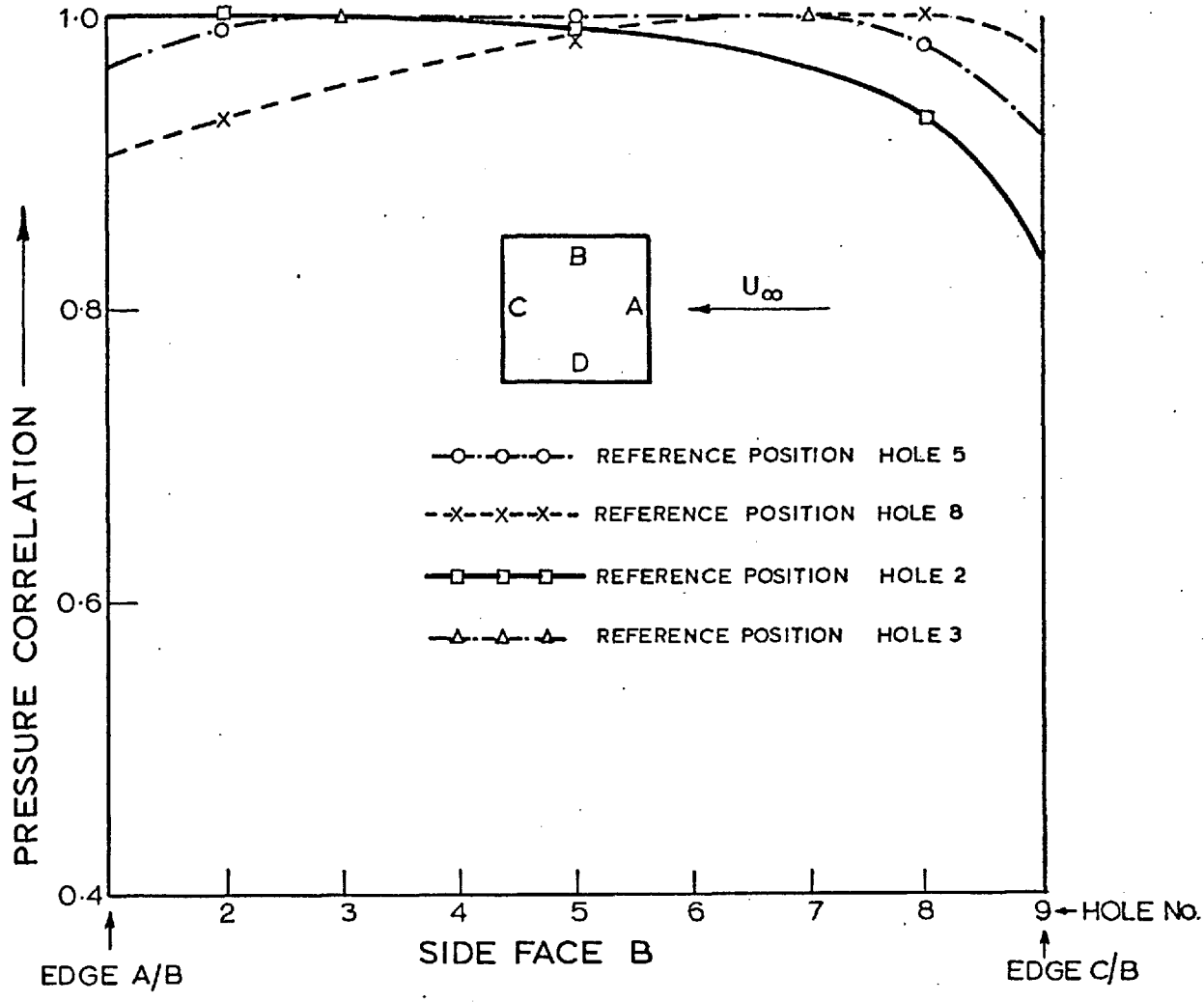

Fig. 6·25 Pressure correlation on side face B of a stationary square section cylinder

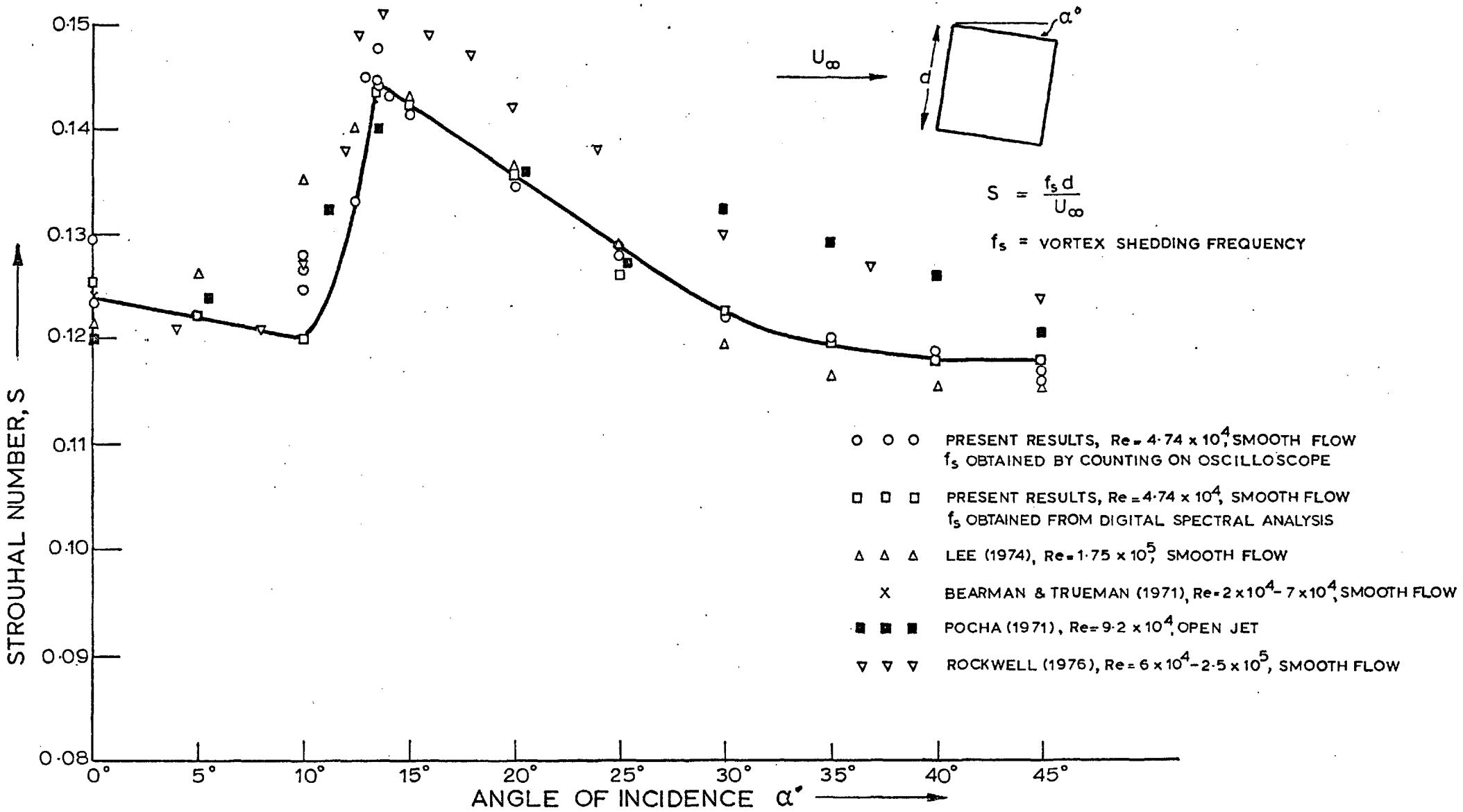

Fig 6.26 Variation of Strouhal number, S, with incidence, α.

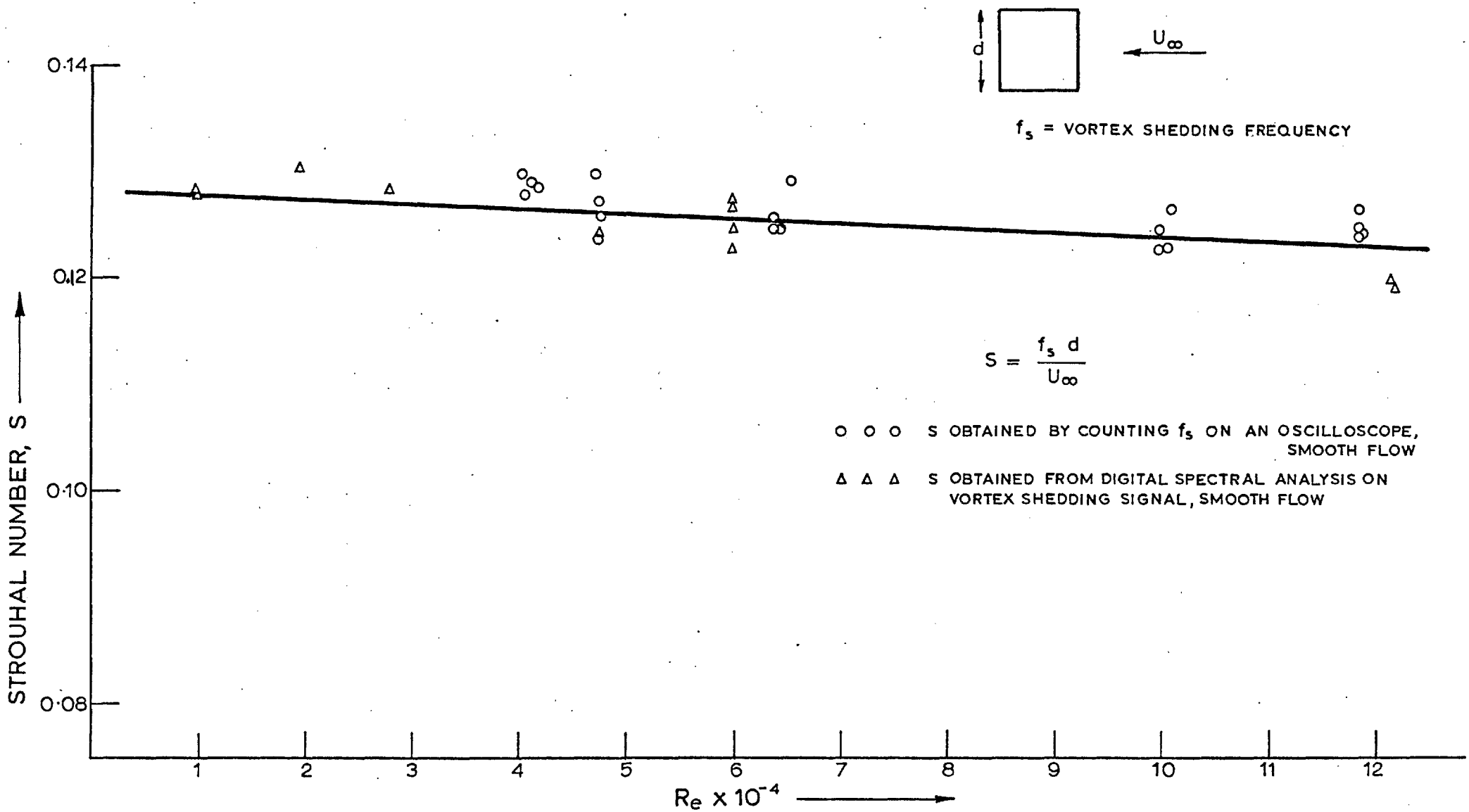

Fig. 6·27 Variation of Strouhal number S, with Reynolds number R_e, incidence $\alpha = 0°$

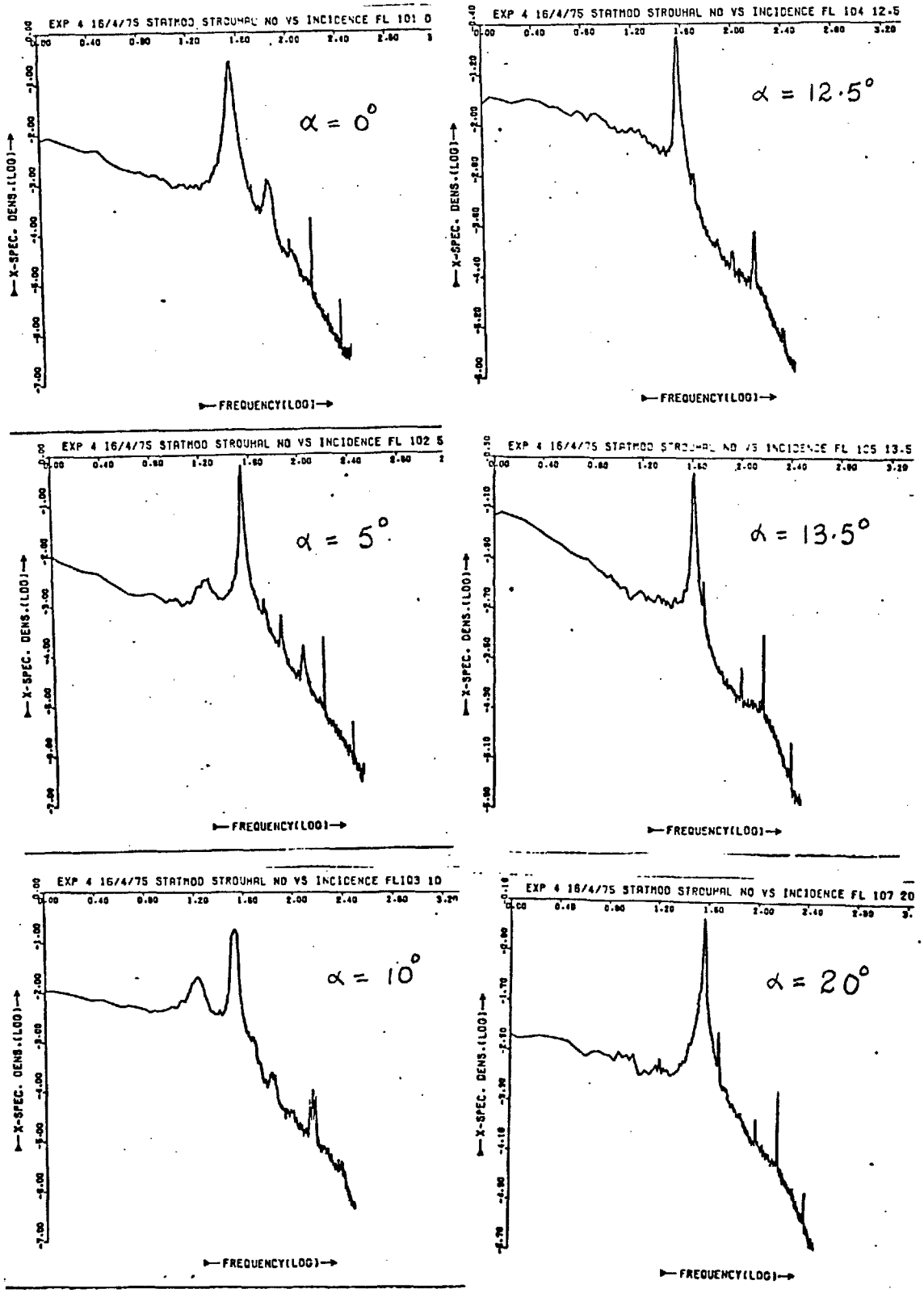

FIG. 6·28 (a) - SPECTRA OF PRESSURE FLUCTUATIONS AT SELECTED VALUES OF INCIDENCE, α.
(Pressure transducer positioned on the reattachment face at 1/12 d from the leading edge)

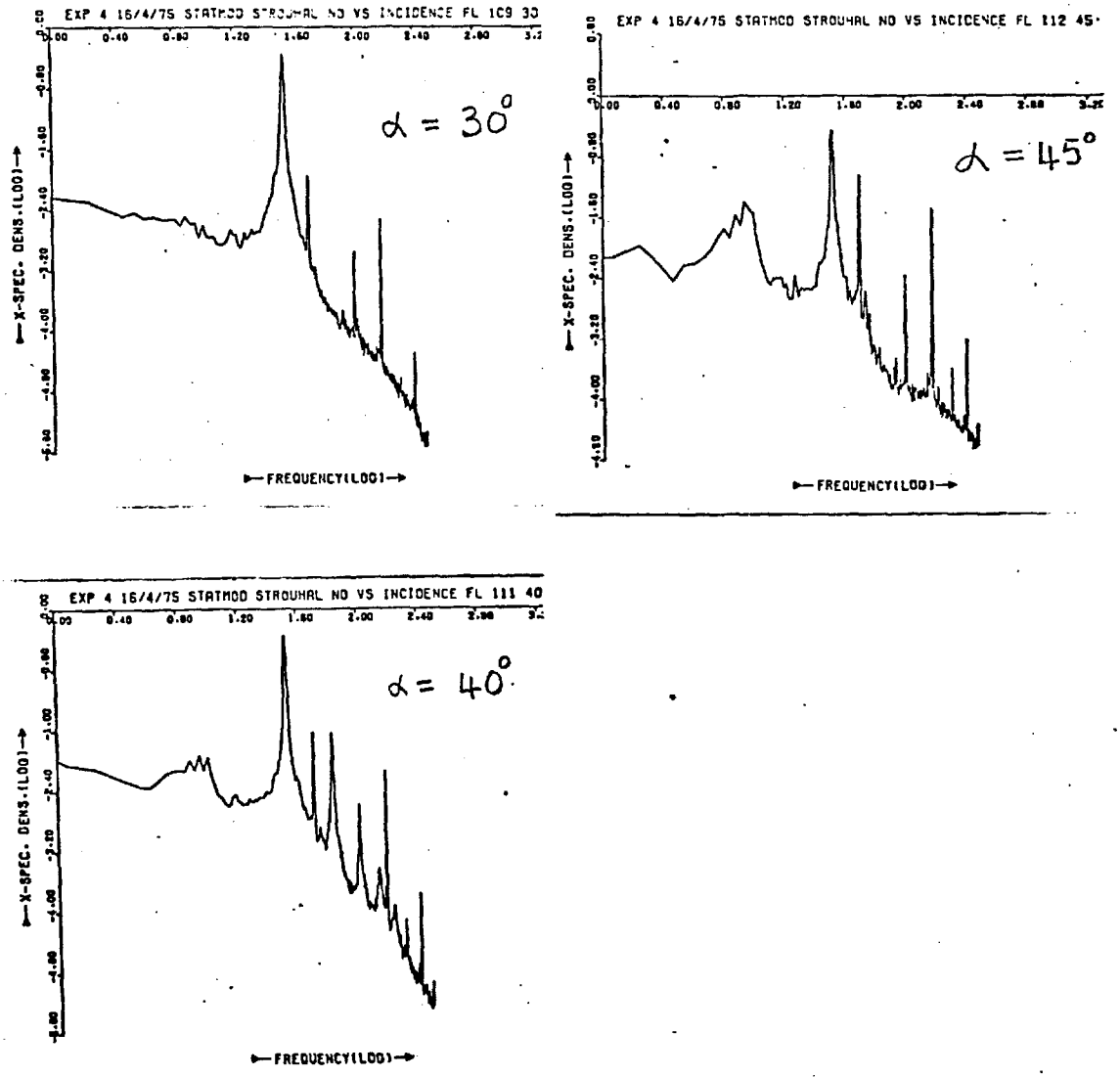

FIG. 6.28(b) SPECTRA OF PRESSURE FLUCTUATIONS AT SELECTED VALUES OF INCIDENCE, α.

(Pressure transducer positioned on the reattachment face at $\frac{1}{12}d$ from the leading edge.)

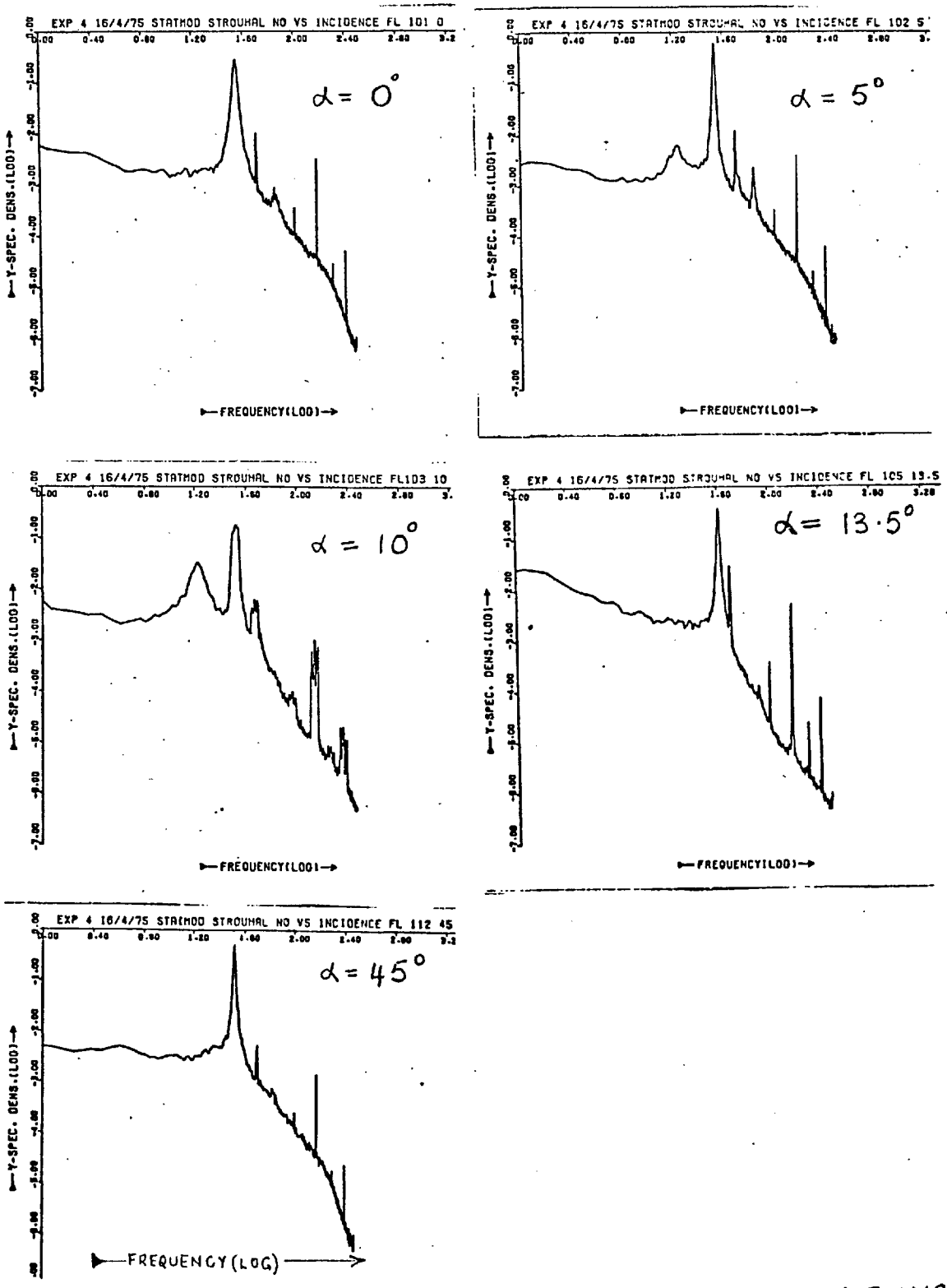

FIG. 6.29. SPECTRA OF VELOCITY FLUCTUATIONS AT SELECTED VALUES OF INCIDENCE, α.

[Hot-wire positioned in the wake at $(x, y) = (3.5d, -3d)$ i.e on the same side as the reattachment face]

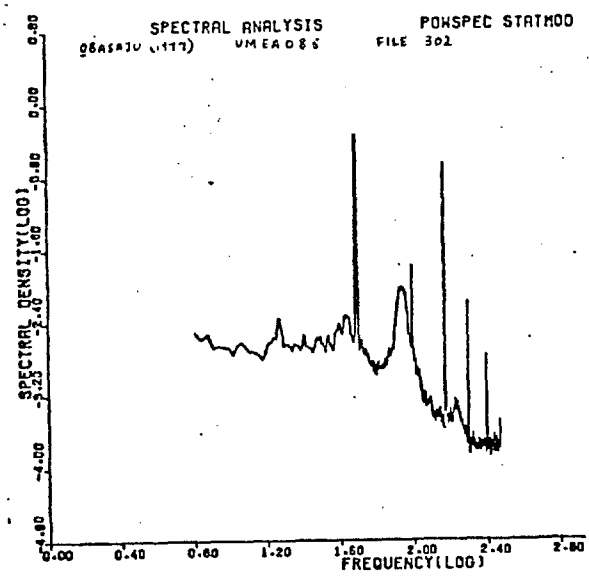

a) HOLE 8/A

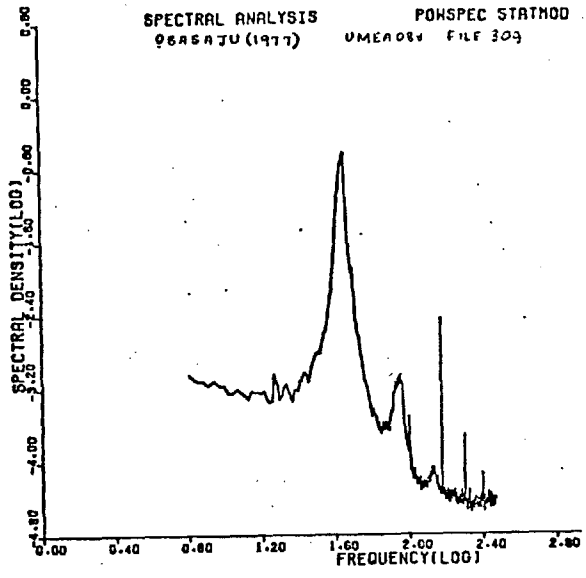

b) HOLE 6/A

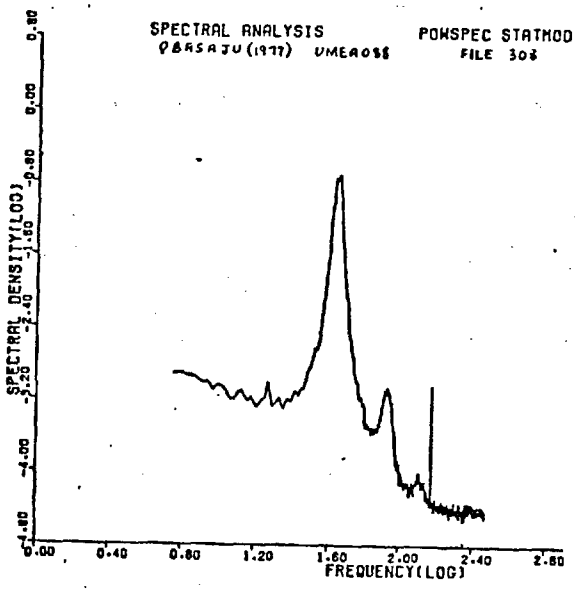

c) HOLE 6/B

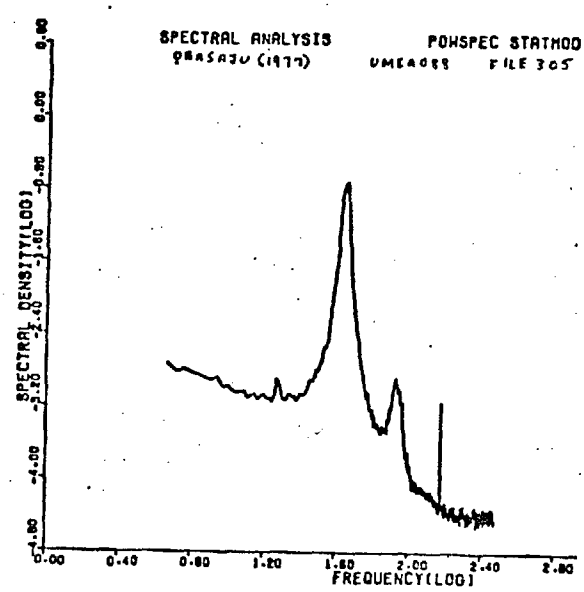

d) HOLE 8/B

FIG. 6.30 (a) SPECTRAL DISTRIBUTIONS OF PRESSURE FLUCTUATIONS AROUND THE MID-SECTION OF A SQUARE SECTION CYLINDER AT 0° INCIDENCE.

[SEE FIG. 6.31 FOR LOCATIONS OF HOLES]

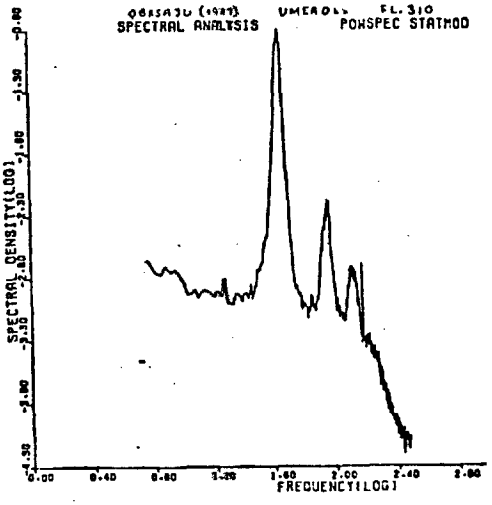

e) HOLE 6/D

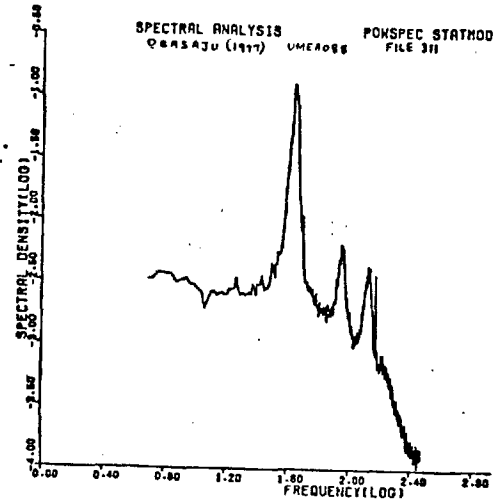

f) HOLE 6/C

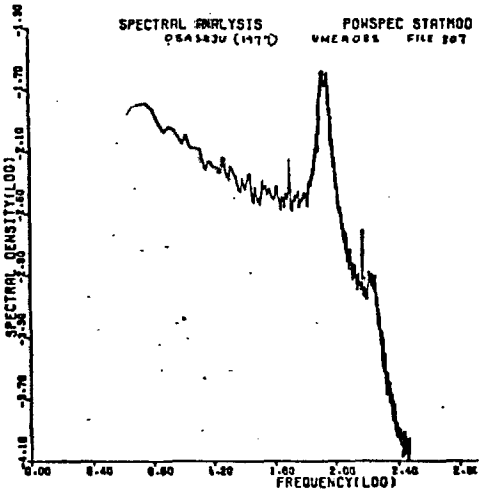

g) HOLE 8/C

FIG. 6.30(b) SPECTRAL DISTRIBUTIONS OF PRESSURE FLUCTUATIONS AROUND THE MID-SECTION OF A SQUARE SECTION CYLINDER AT 0° INCIDENCE.

(SEE FIG. 6.31 FOR LOCATIONS OF HOLES)

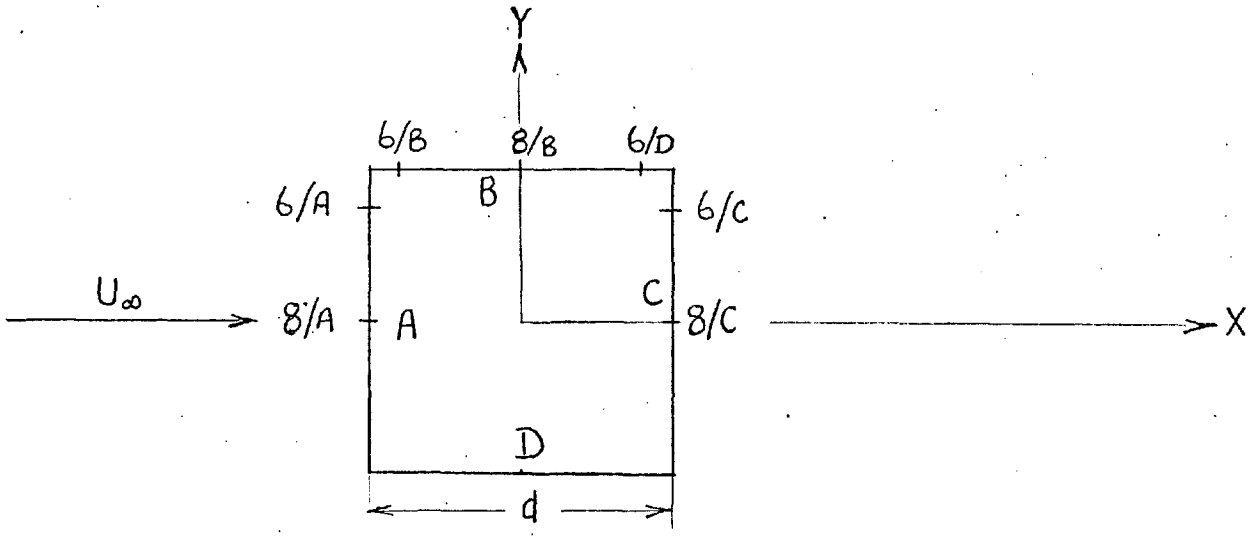

HOLE NO	$\frac{X}{d}$ AND $\frac{Y}{d}$ COORDINATES OF HOLE	C_{PRMS}	PEAK POWER FREQUENCY f_P	% OF PRESSURE ENERGY AT				$\frac{\Delta f}{f_P}$ %
				f_S	$2f_S$	$3f_S$	$4f_S$	
8/A	(-0.5, 0)	0.01	$2f_S$	-	11.3	-	Traces	14.3
6/A	(-0.5, 5/12)	0.14	f_S	74.5	0.8	Traces	-	7.1
6/B	(-5/12, 0.5)	0.62	f_S	78.6	1.5	Traces	-	9.1
8/B	(0, 0.5)	0.63	f_S	82.2	1.6	-	-	9.8
6/D	(5/12, 0.5)	0.54	f_S	66.9	6.9	3.9	-	9.4
6/C	(0.5, 5/12)	0.42	f_S	47.1	7.5	6.6	Traces	8.5
8/C	(0.5, 0)	0.32	$2f_S$	-	38.6	-	Traces	17.3

f_S - VORTEX SHEDDING FREQUENCY.

f_P - PEAK POWER FREQUENCY.

Δf - BANDWIDTH OF THE HALF PEAK POWER POINTS.

FIG. 6.31 SPECTRAL COMPOSITION OF FLUCTUATING PRESSURES AROUND THE MID-SECTION OF A SQUARE SECTION CYLINDER AT 0° INCIDENCE.

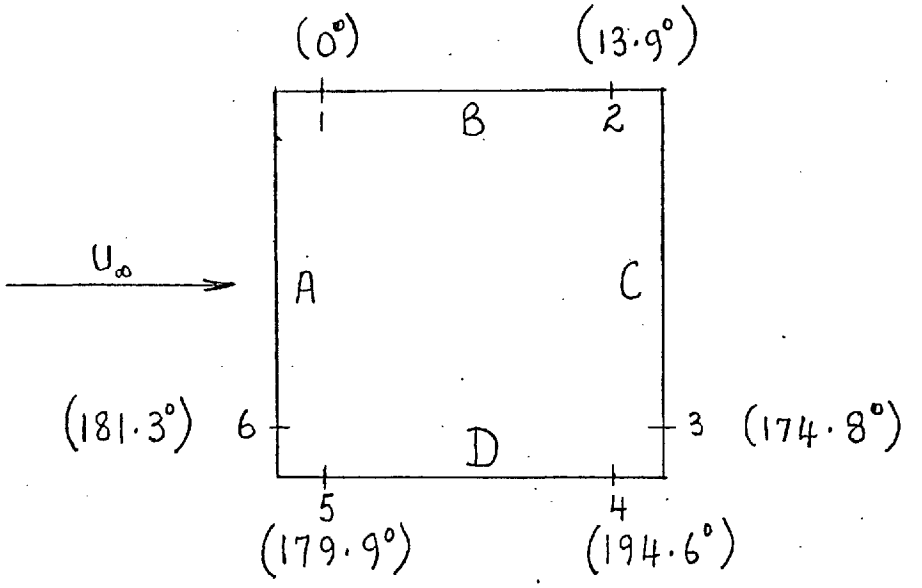

- HOLE 1 IS THE REFERENCE POSITION

- EACH HOLE IS $\frac{1}{12}$ TH OF A DIAMETER FROM THE CORNER NEAREST TO IT.

FIG. 6.32. VARIATION OF THE PHASE ANGLE AT THE SHEDDING FREQUENCY AROUND THE MID-SECTION OF A SQUARE SECTION CYLINDER AT 0° INCIDENCE.

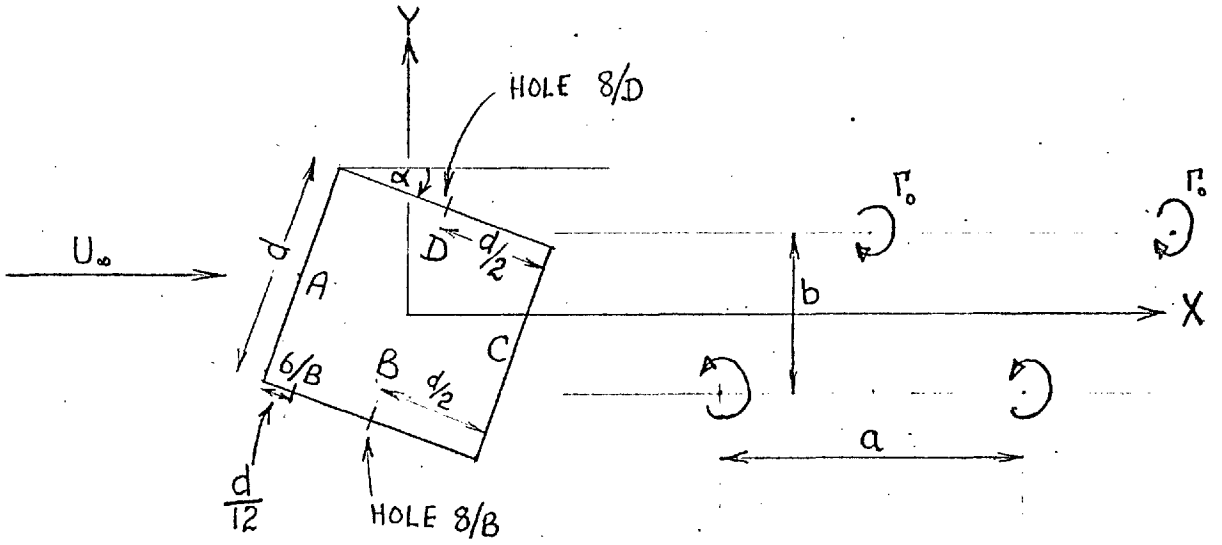

(ALL MEASUREMENTS OF a/d WERE MADE IN THE RANGE $4.5 \leq x/d \leq 11.5$)

INCIDENCE α°	REYNOLDS NUMBER R_e	REFERENCE MICROPHONE POSITION	HOT-WIRE Y/d	MEASURED a/d		CHAPLIN (1970) VALUE OF a/d	PRESENT VALUE OF S
0	10^4	8/B	-3.7	6.48	6.58	6.54	0.124
0	10^4	8/B	-5.9	6.71			
0	4.74×10^4	6/B	-3.0	6.55			
10	10^4	8/D	4.4	6.53			0.120
13.5	10^4	8/B	-3.7	5.63			0.144
15						5.77	
20	10^4	8/D	4.4	6.04			0.136
30						7.16	
45	10^4	8/D	4.4	6.88		7.26	0.118

FIG. 6.33 (a) MEASUREMENTS OF THE LONGITUDINAL VORTEX SPACING a/d.

INCIDENCE	MEASURED	UNCORRECTED VALUES OF			CORRECTED VALUES OF		
α°	a/d	S	$\frac{U_c}{U_\infty} = S \cdot a/d$		S	$\frac{U_c}{U_\infty} = S \cdot a/d$	
0	6.58	0.129	0.85		0.124	0.81	
10	6.53	0.126	0.82		0.120	0.78	
13.5	5.63	0.151	0.85	0.85	0.144	0.81	0.81
20	6.04	0.143	0.86		0.136	0.82	
45	6.88	0.124	0.85		0.118	0.81	

FIG 6.33 (b) CALCULATION OF THE VORTEX CONVECTION VELOCITY $\frac{U_c}{U_\infty}$

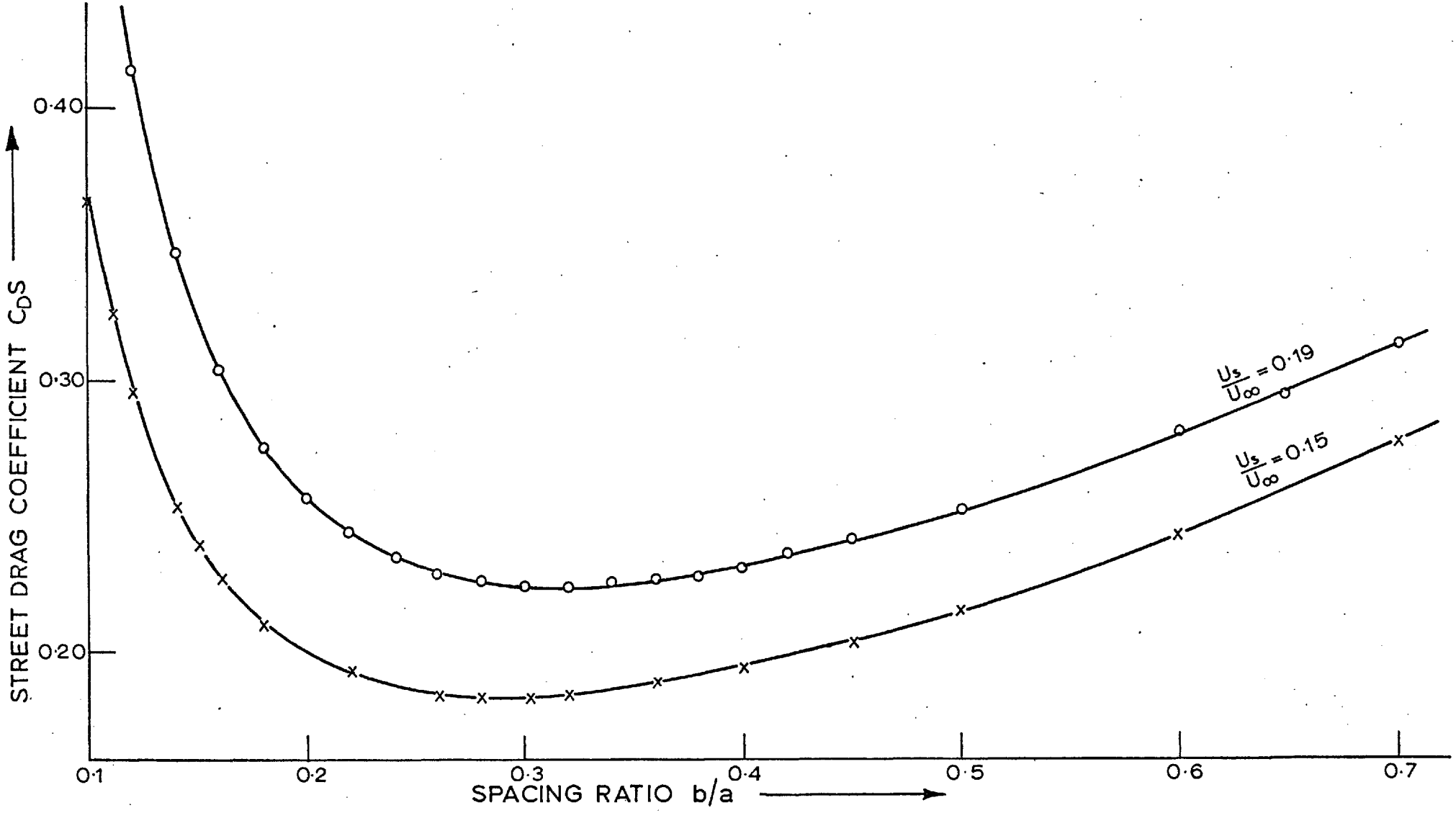

Fig. 6·34 VORTEX STREET DRAG COEFFICIENT VERSUS SPACING RATIO

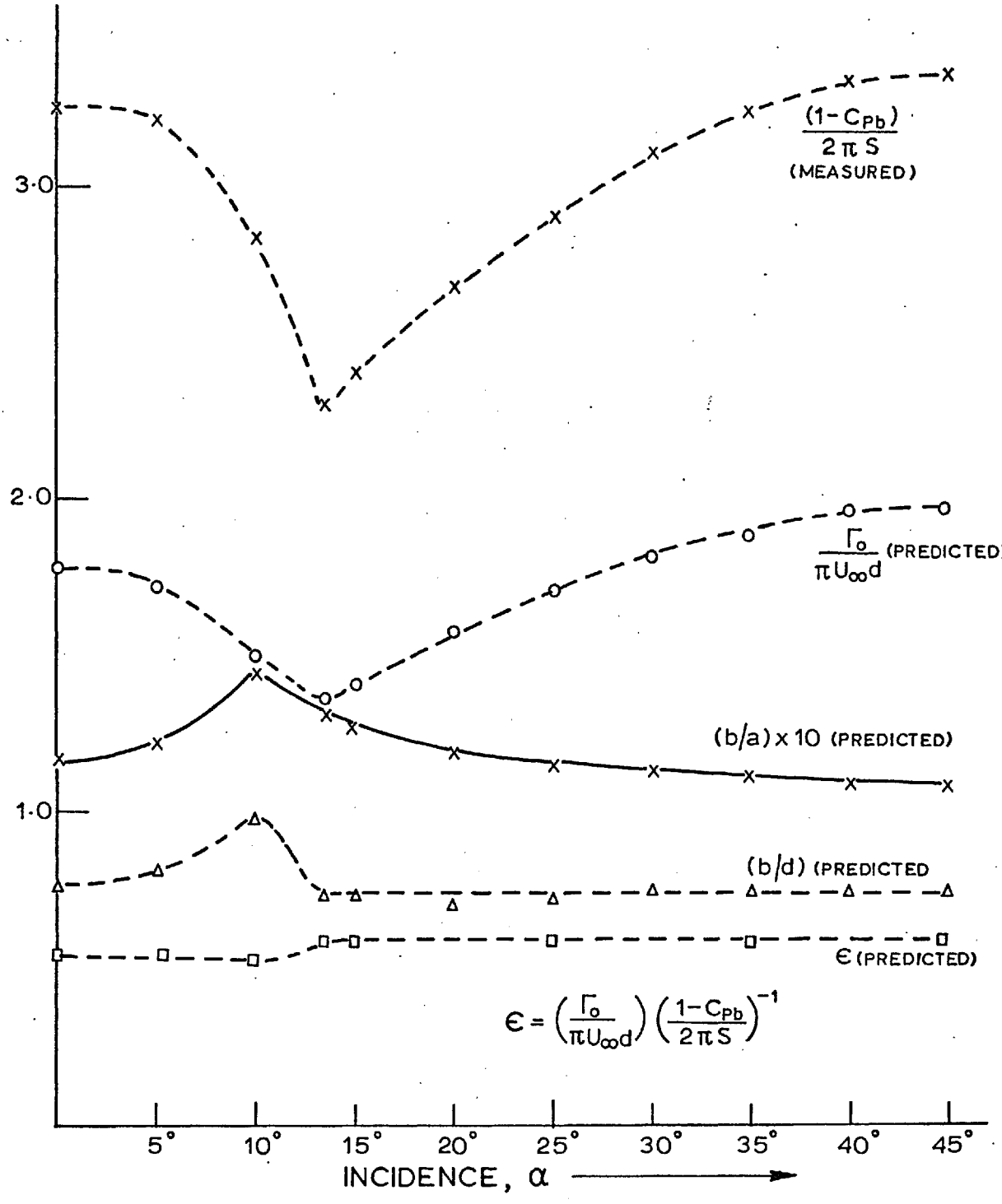

Fig. 6·35 PREDICTIONS OF THE VORTEX STREET DRAG FORMULA WHEN S, a/d = 0·85

Note: C_D, S and C_{Pb} are not corrected for wind tunnel blockage effects.

THE SIMULTANEOUS OUTPUT OF TWO PRESSURE TRANSDUCERS PLACED ALONG THE CENTRELINE OF THE SIDE FACES OF A STATIONARY SQUARE SECTION CYLINDER AT $\alpha = 0°$.

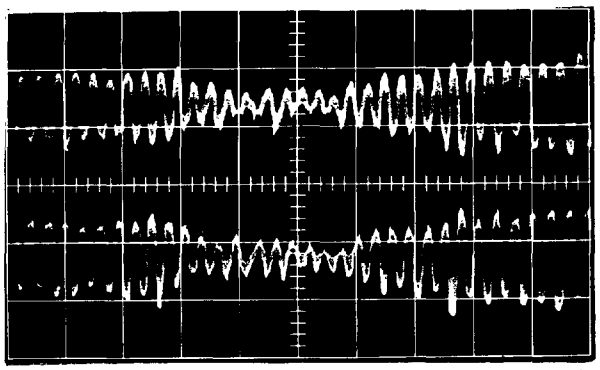

(a) $R_{P12} = -0.96$; $f_s = 8.31$; $R_e = 1.09 \times 10^4$

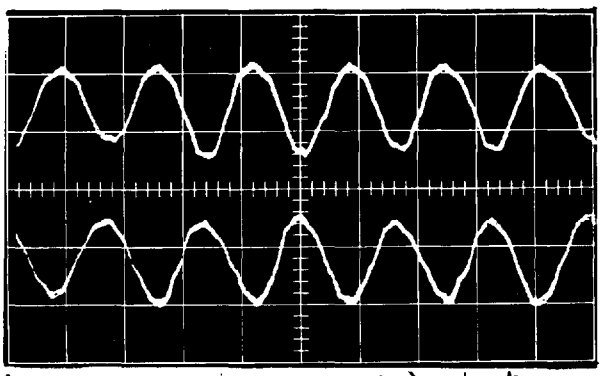

(b) Same signals as (a) but horizontal scale expanded.

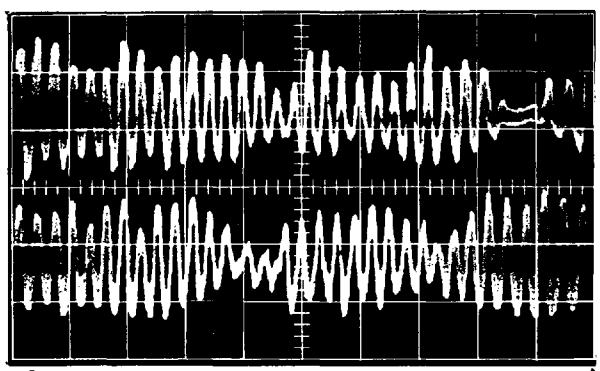

(c) $R_{P12} = 0.73$; $f_s = 7.55$; $R_e = 0.99 \times 10^4$
spanwise separation, $Z = 2.5\,d$

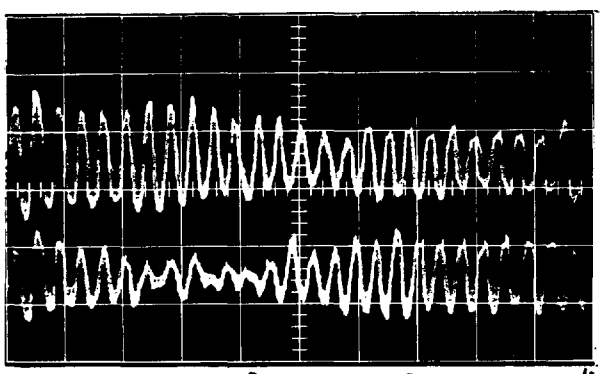

(d) $R_{P12} = 0.08$; $f_s = 7.55$; $R_e = 0.99 \times 10^4$
spanwise separation $Z = 9.5\,d$

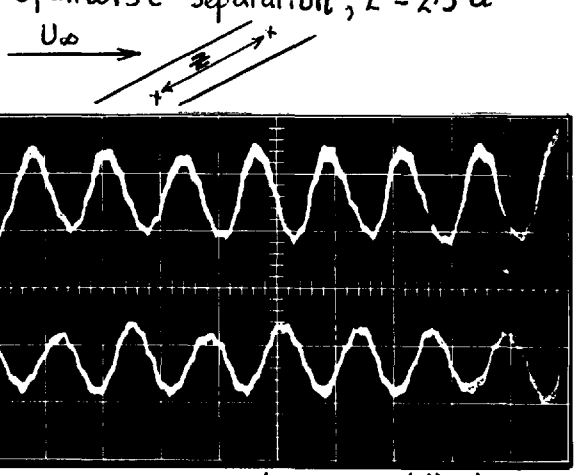

(e) Same signals as (d) but horizontal scale expanded.

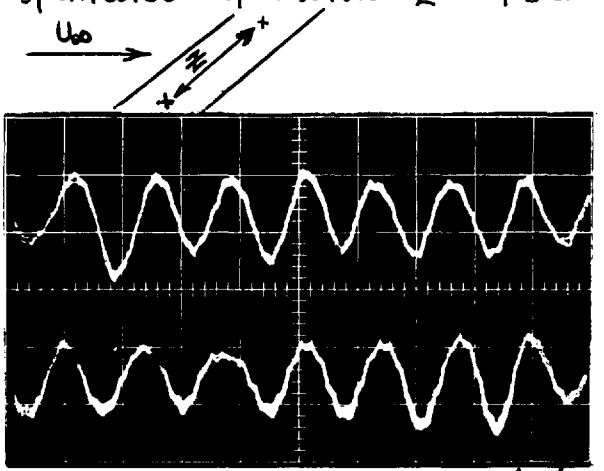

(f) Same signals as (d) but horizontal scale expanded.

FIG. 6.36

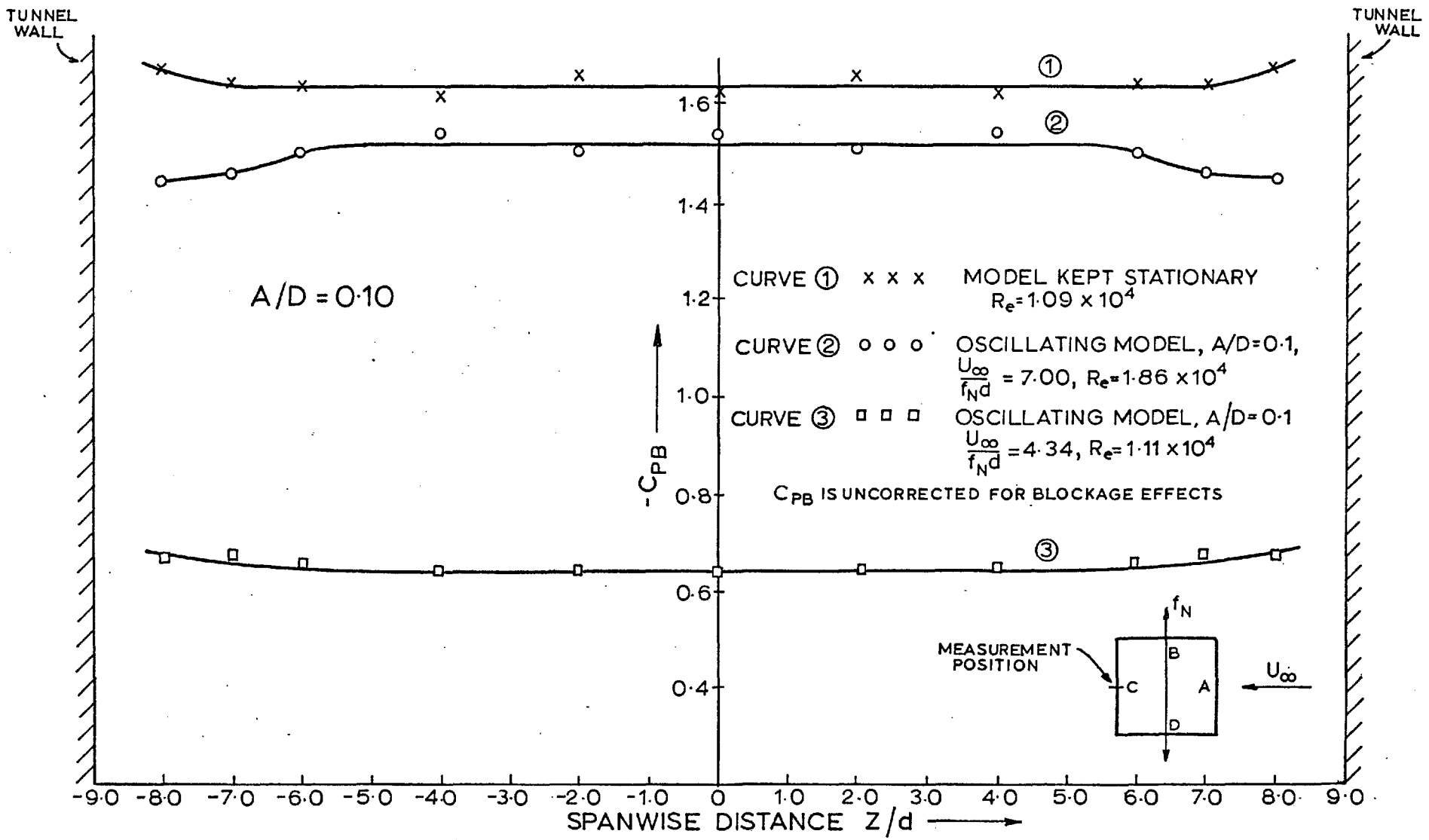

Fig 7·1a Effects of oscillation on the spanwise distribution of mean base pressure coefficient

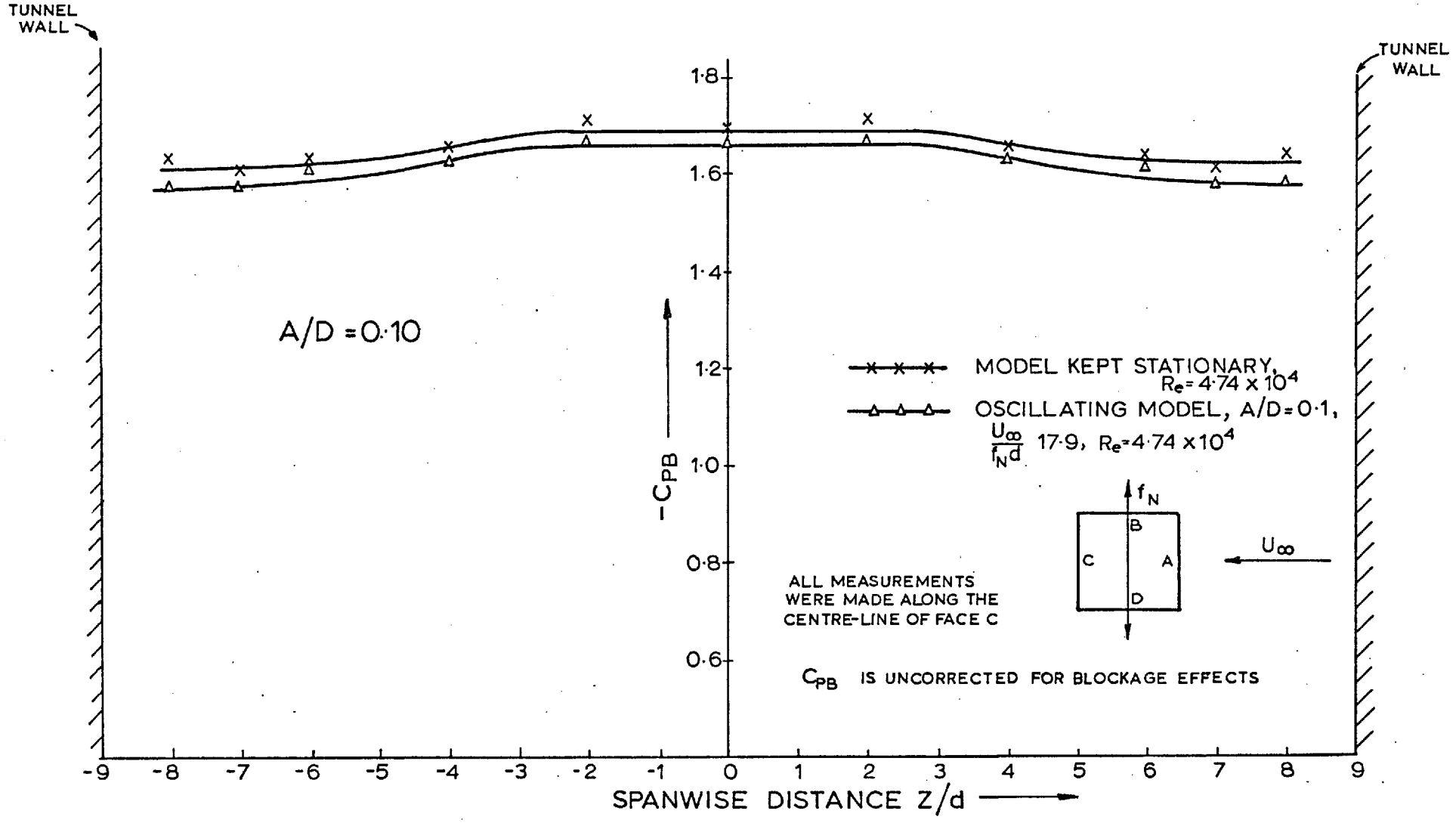

Fig 7·1b Effects of oscillation on the spanwise distribution of mean base pressure coefficient

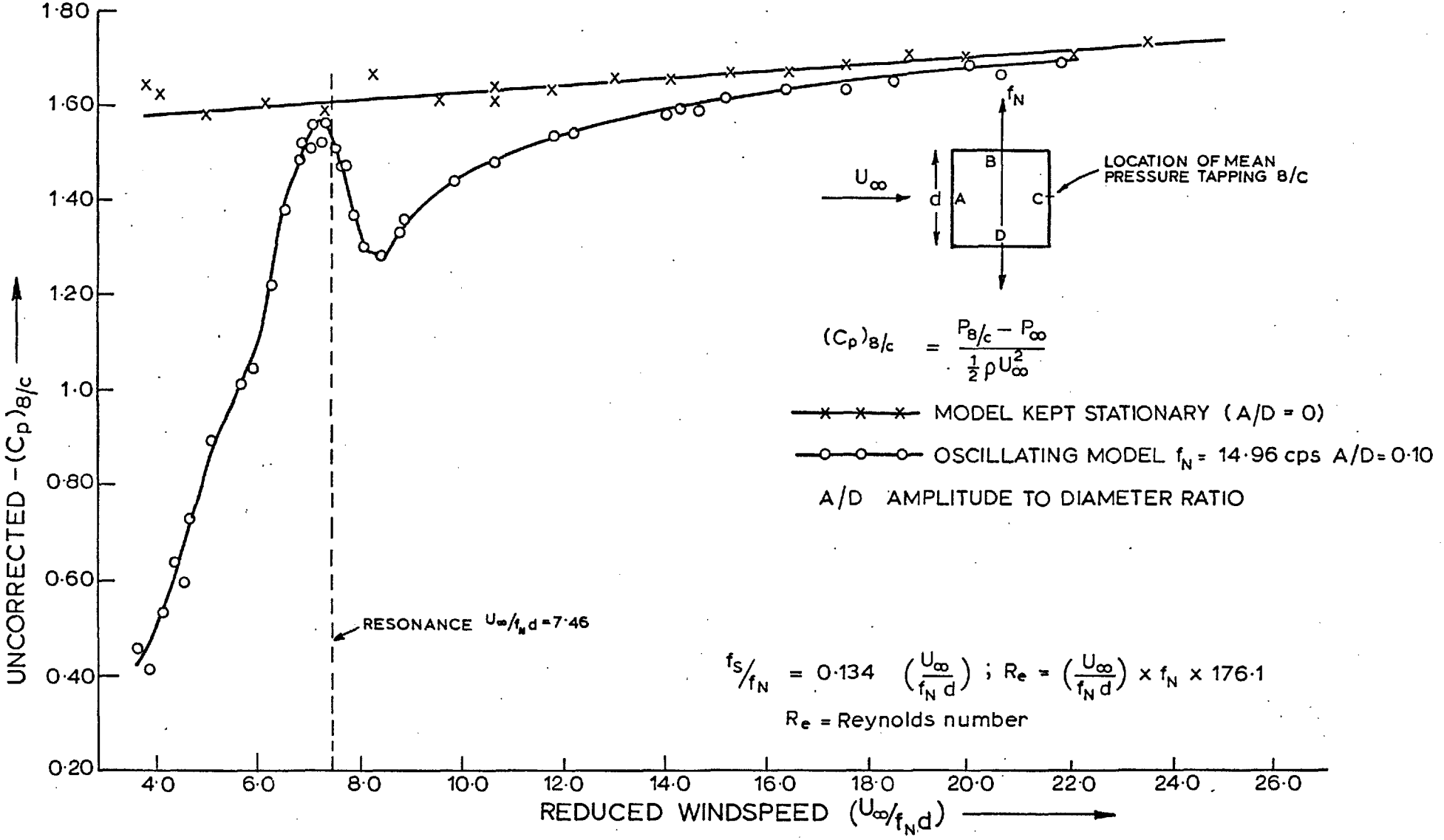

Fig 7·2 Effects of oscillation on mean base pressure coefficient

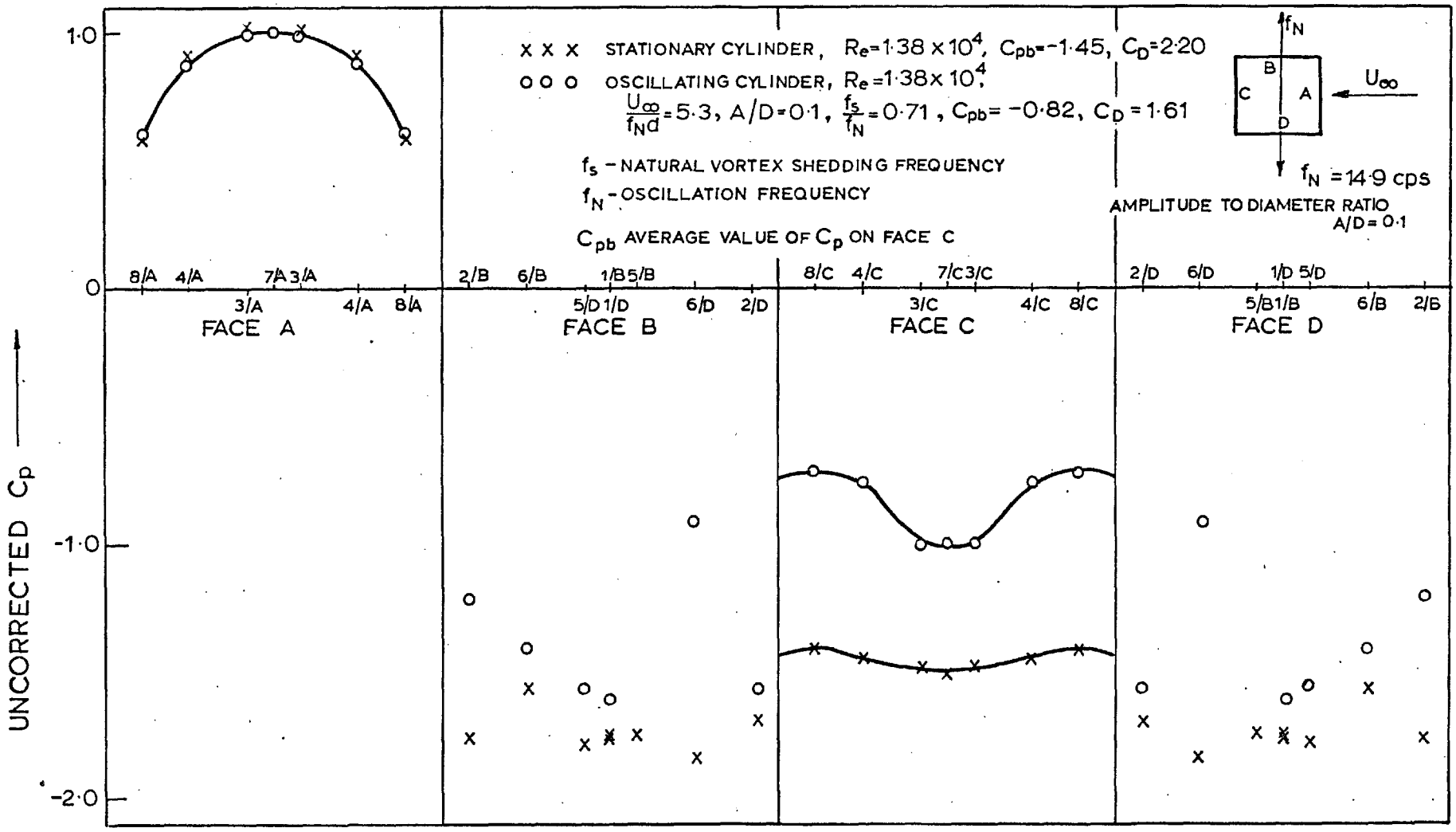

Fig 7·3a The effects of oscillation on mean pressure distribution

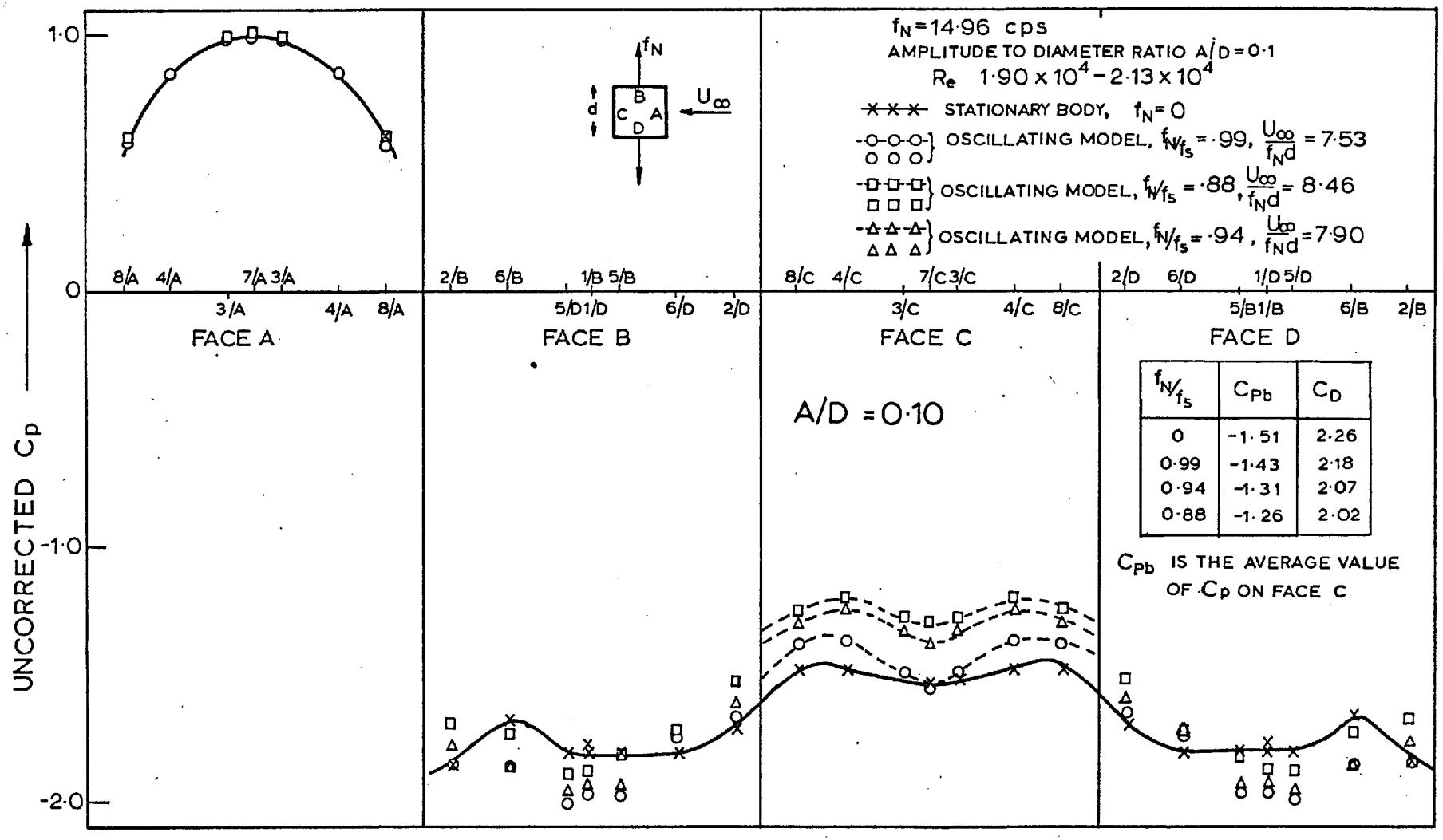

f_N/f_s	C_{Pb}	C_D
0	-1·51	2·26
0·99	-1·43	2·18
0·94	-1·31	2·07
0·88	-1·26	2·02

Fig 7·3b The effects of oscillation on mean pressure distribution

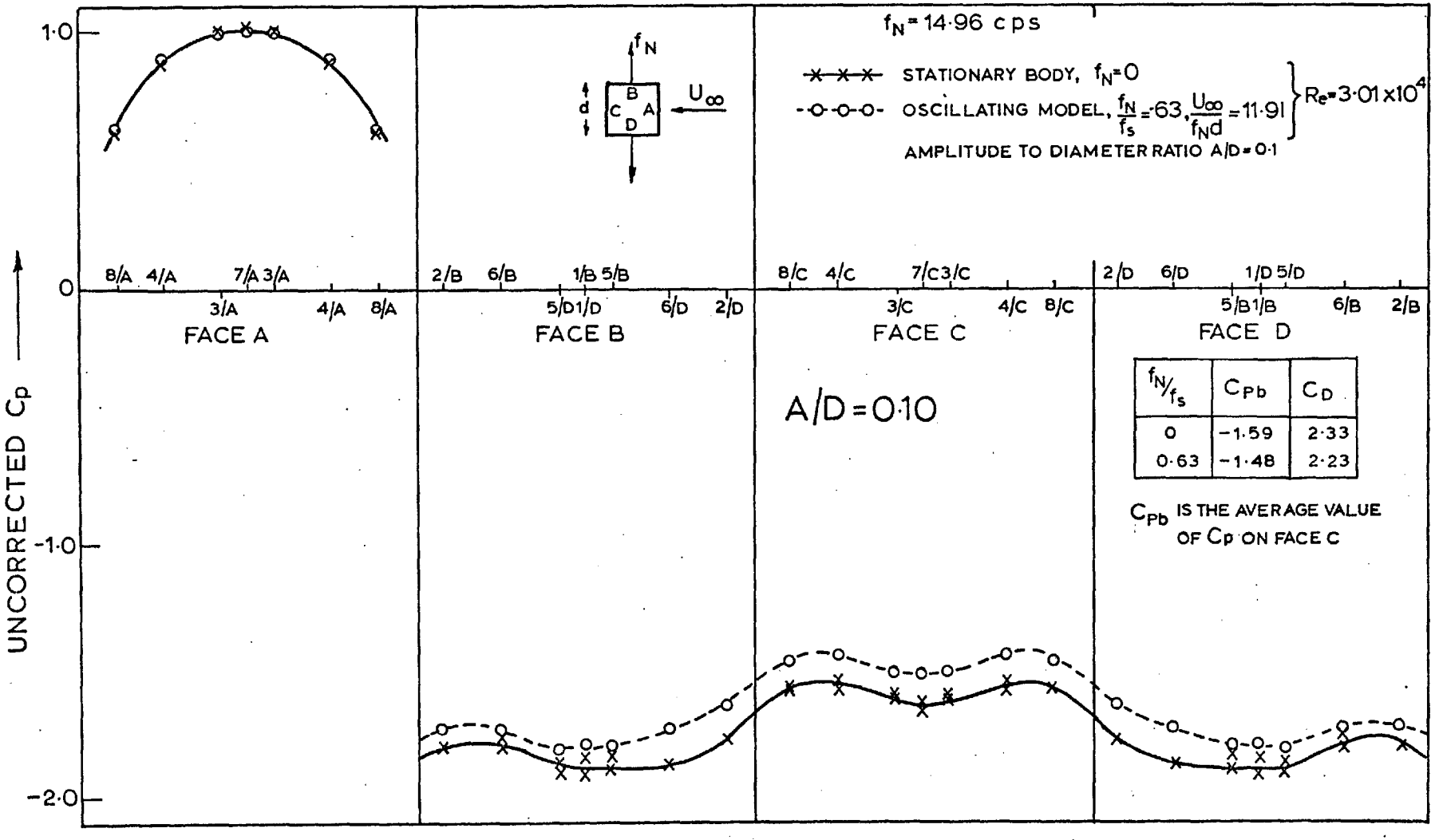

Fig 7·3c The effects of oscillation on mean pressure distribution

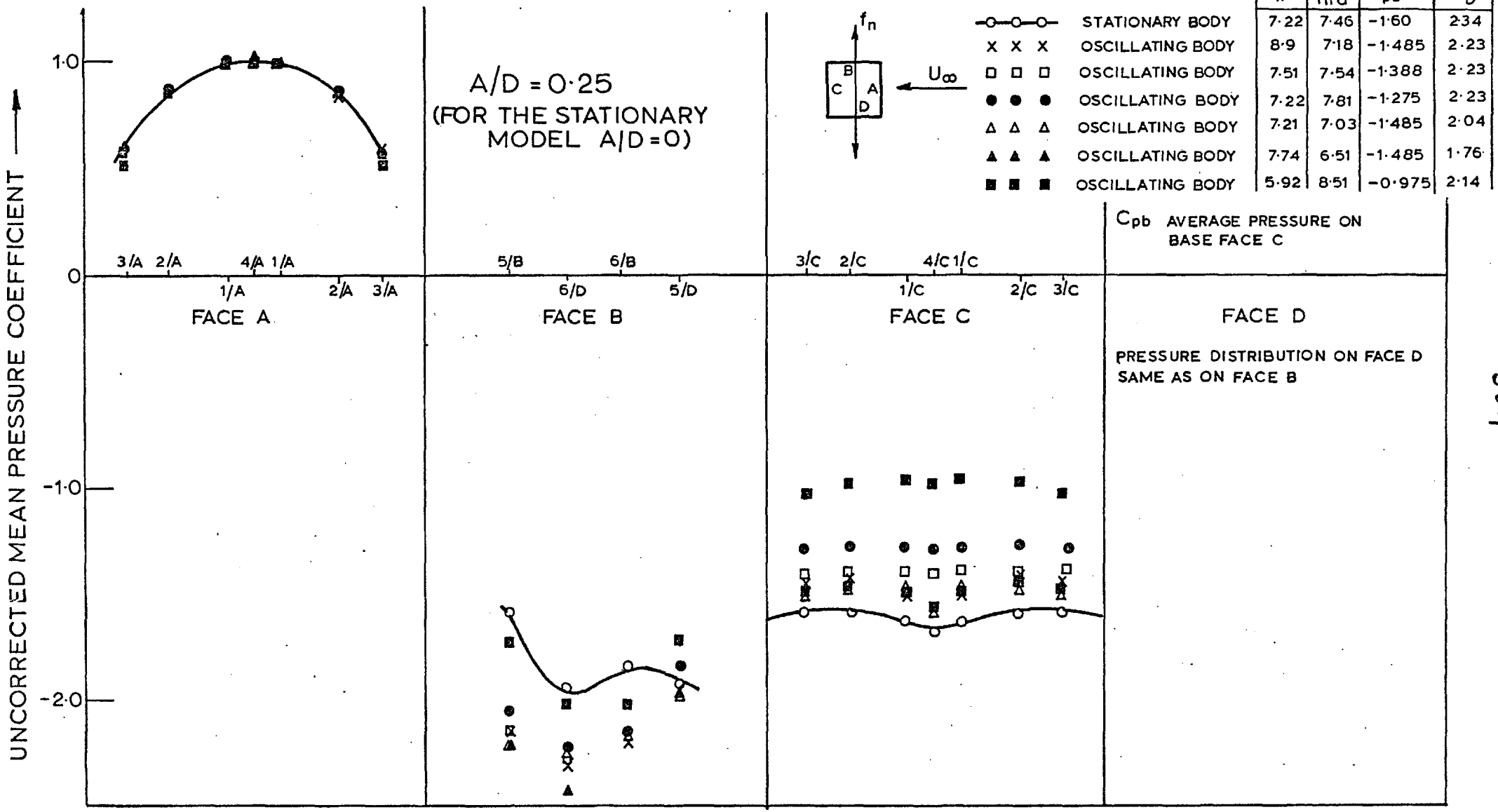

	f_n	$\frac{U_\infty}{f_n d}$	C_{pb}	C_D
STATIONARY BODY	7·22	7·46	-1·60	2·34
OSCILLATING BODY	8·9	7·18	-1·485	2·23
OSCILLATING BODY	7·51	7·54	-1·388	2·23
OSCILLATING BODY	7·22	7·81	-1·275	2·23
OSCILLATING BODY	7·21	7·03	-1·485	2·04
OSCILLATING BODY	7·74	6·51	-1·485	1·76
OSCILLATING BODY	5·92	8·51	-0·975	2·14

Fig 7·4 Mean pressure distribution on sides A, B, & C of an oscillating square section, incidence = 0°, amplitude = 0·5"

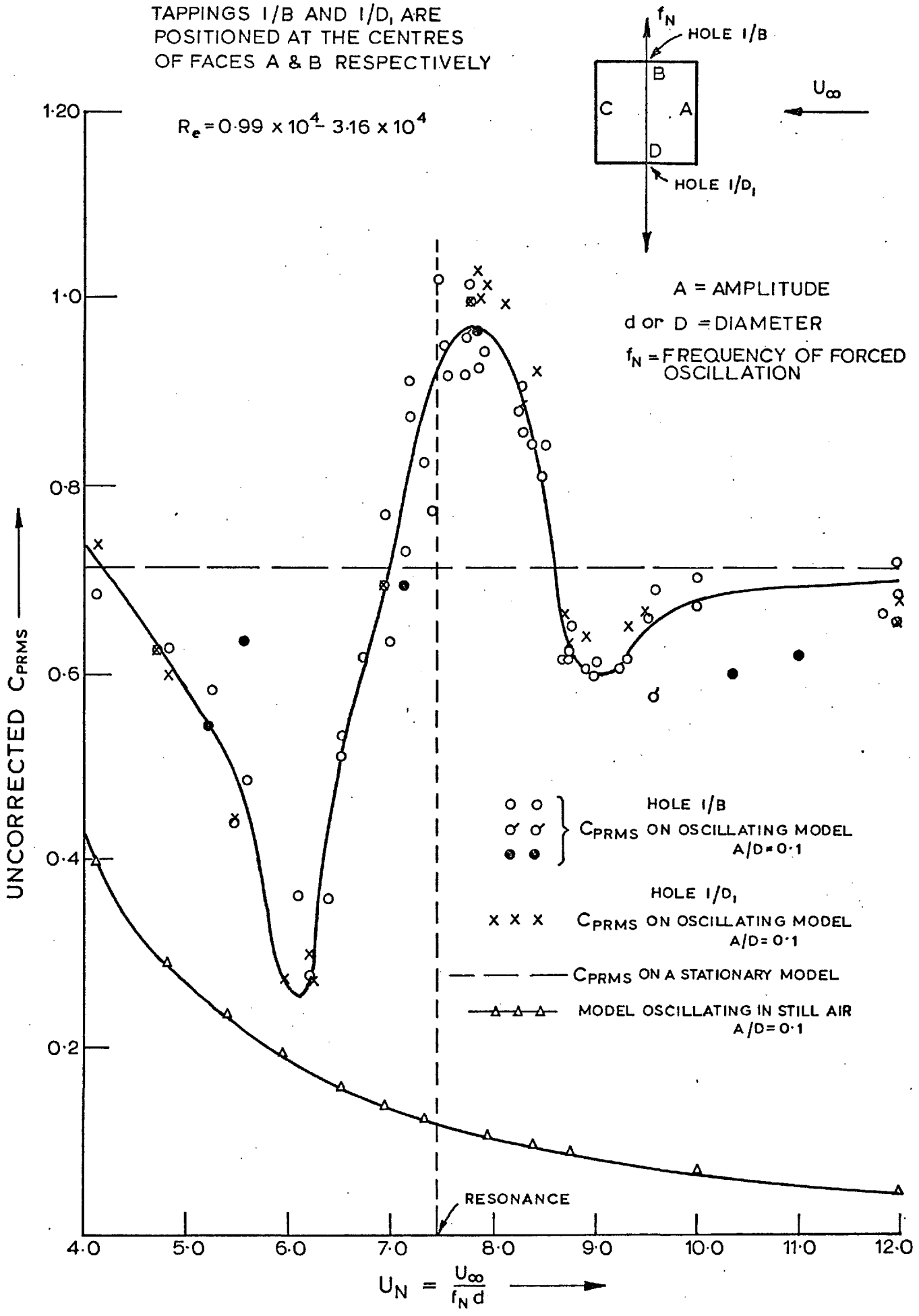

Fig. 7·5 Variation of C_{PRMS} with $\frac{U_\infty}{f_N d}$, A/D = 0·1

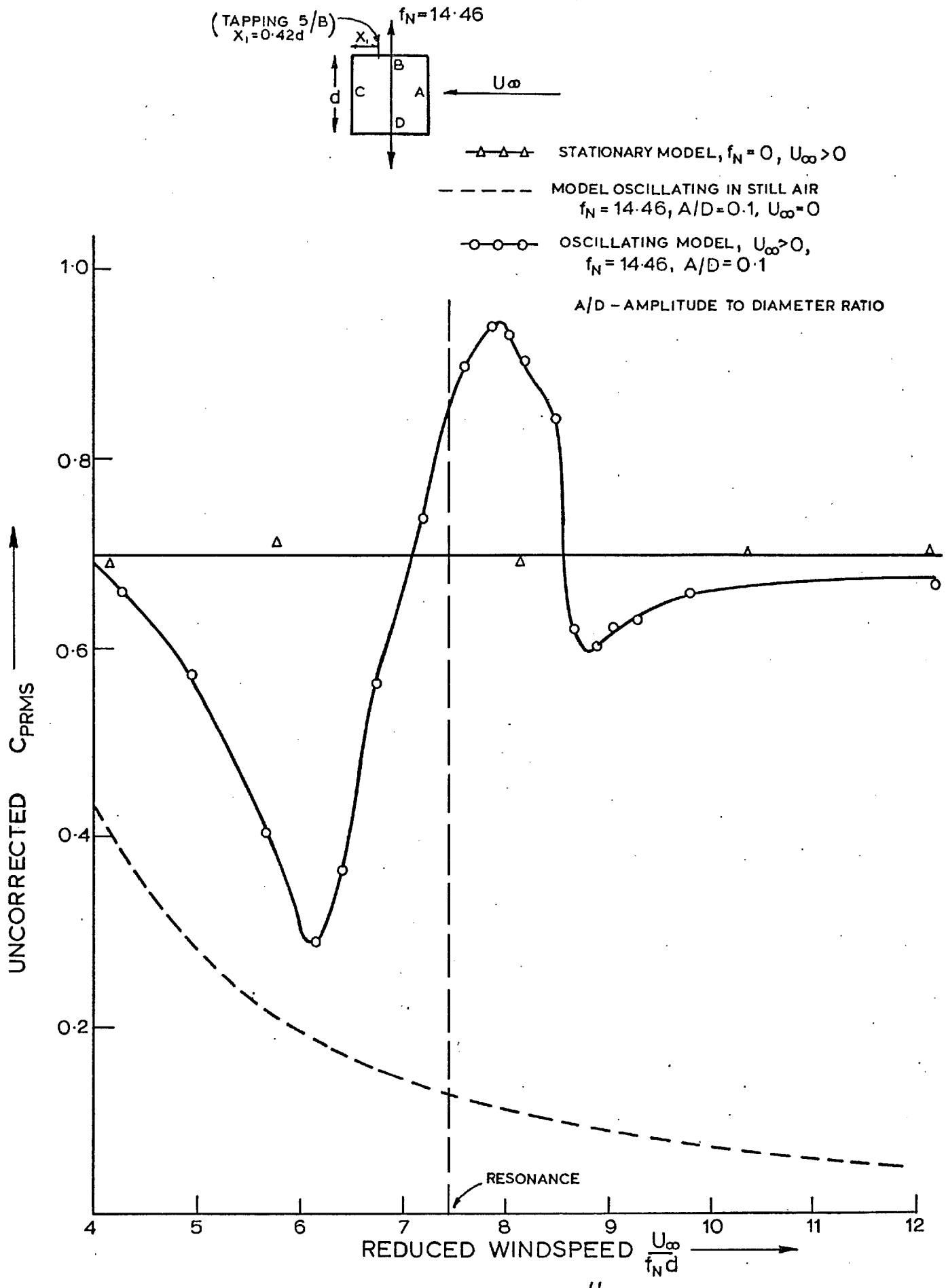

Fig 7·6 C_{PRMS} AT TAPPING 5/B VERSUS $\frac{U_\infty}{f_N d}$, A/D = 0·1

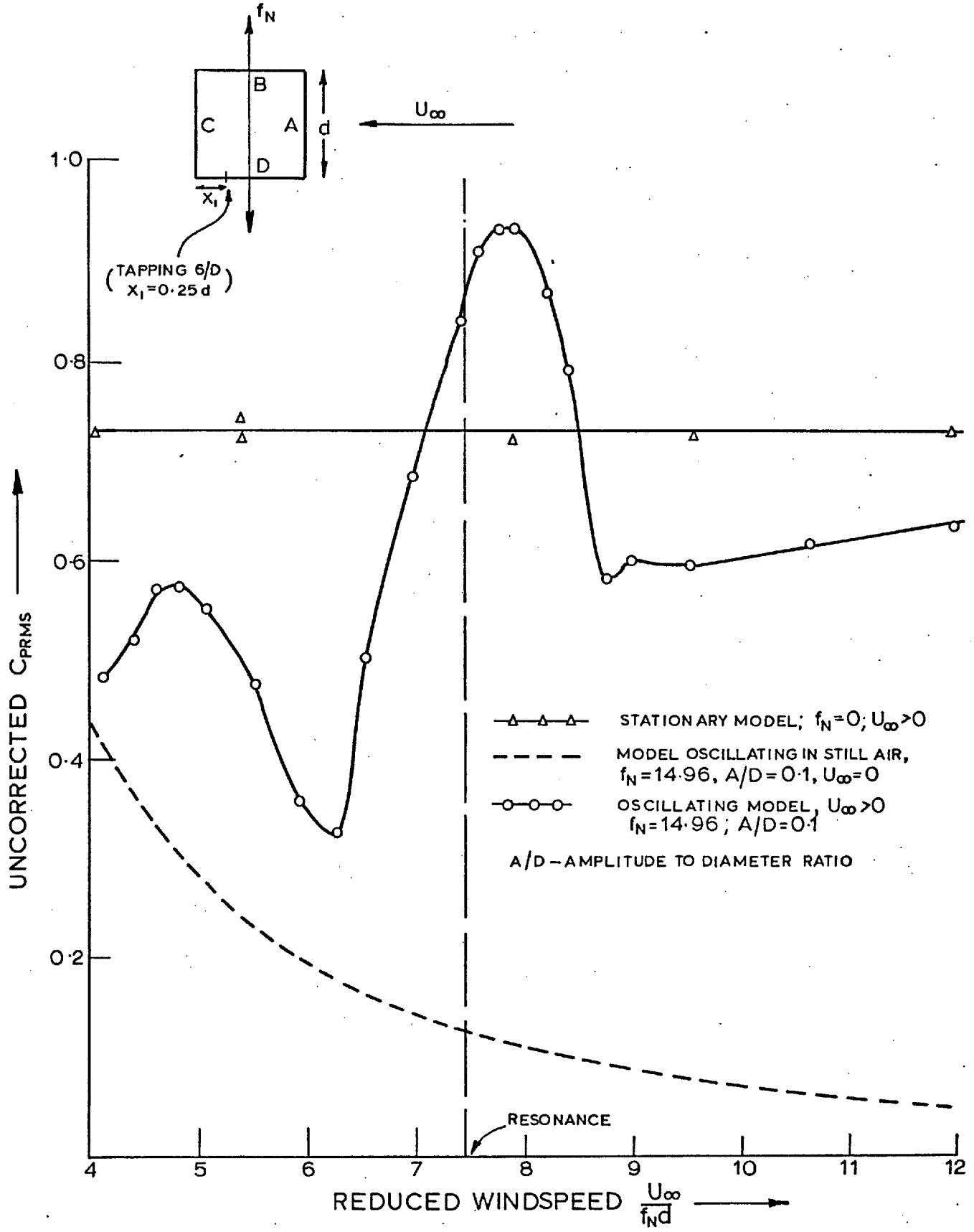

Fig 7·7 C_{PRMS} AT TAPPING 6/D VERSUS $\frac{U_\infty}{f_N d}$, A/D= 0·1

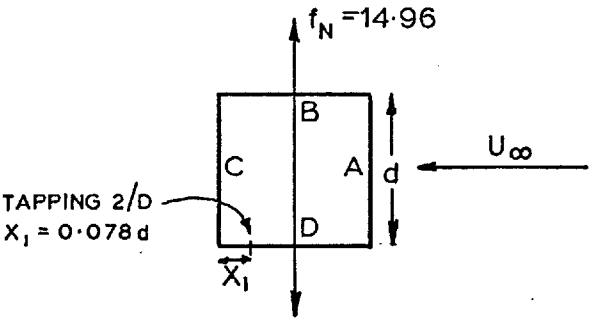

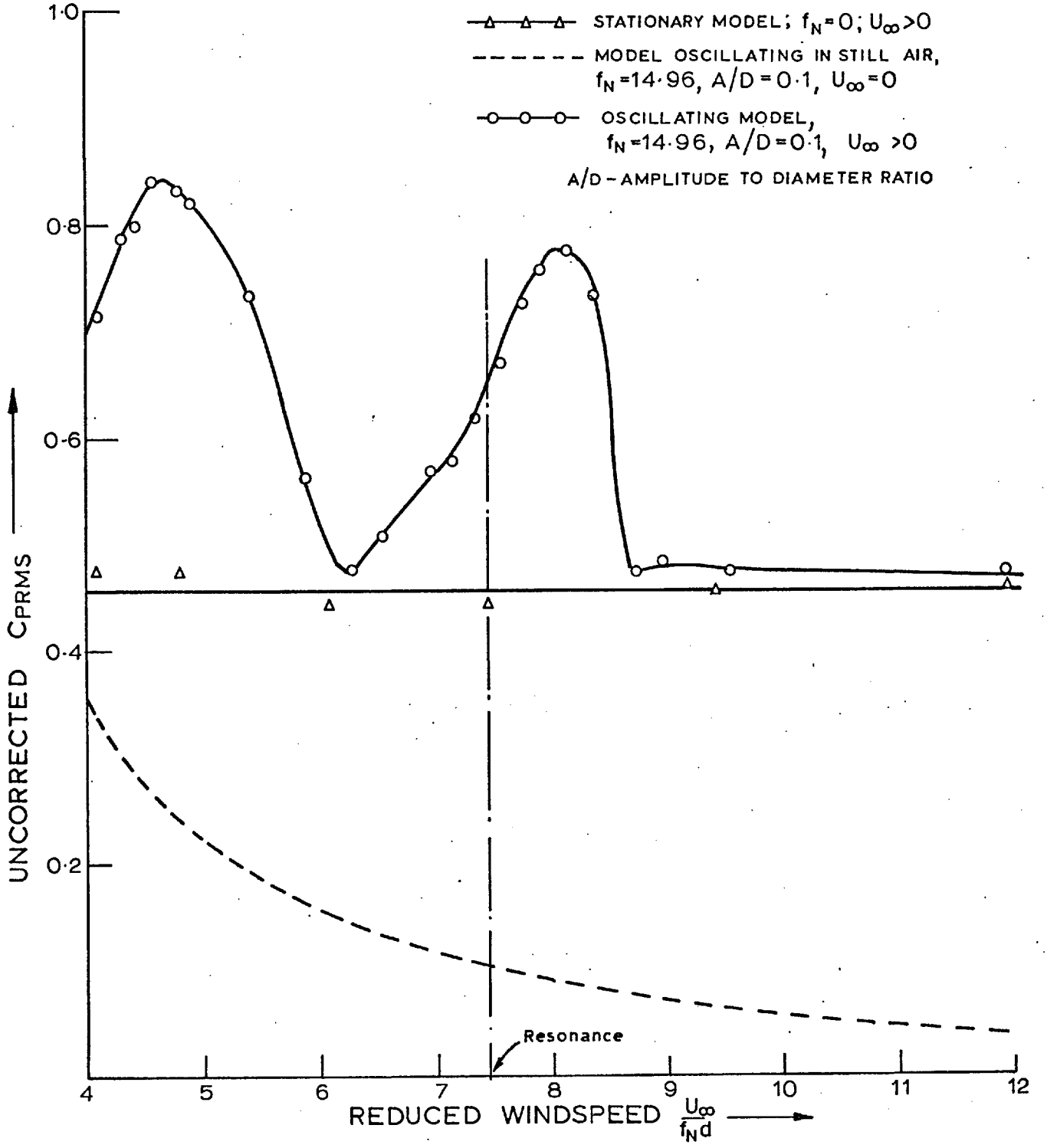

Fig 7·8 C_{PRMS} AT TAPPING 2/D VERSUS $\frac{U_\infty}{f_N d}$, A/D = 0·1

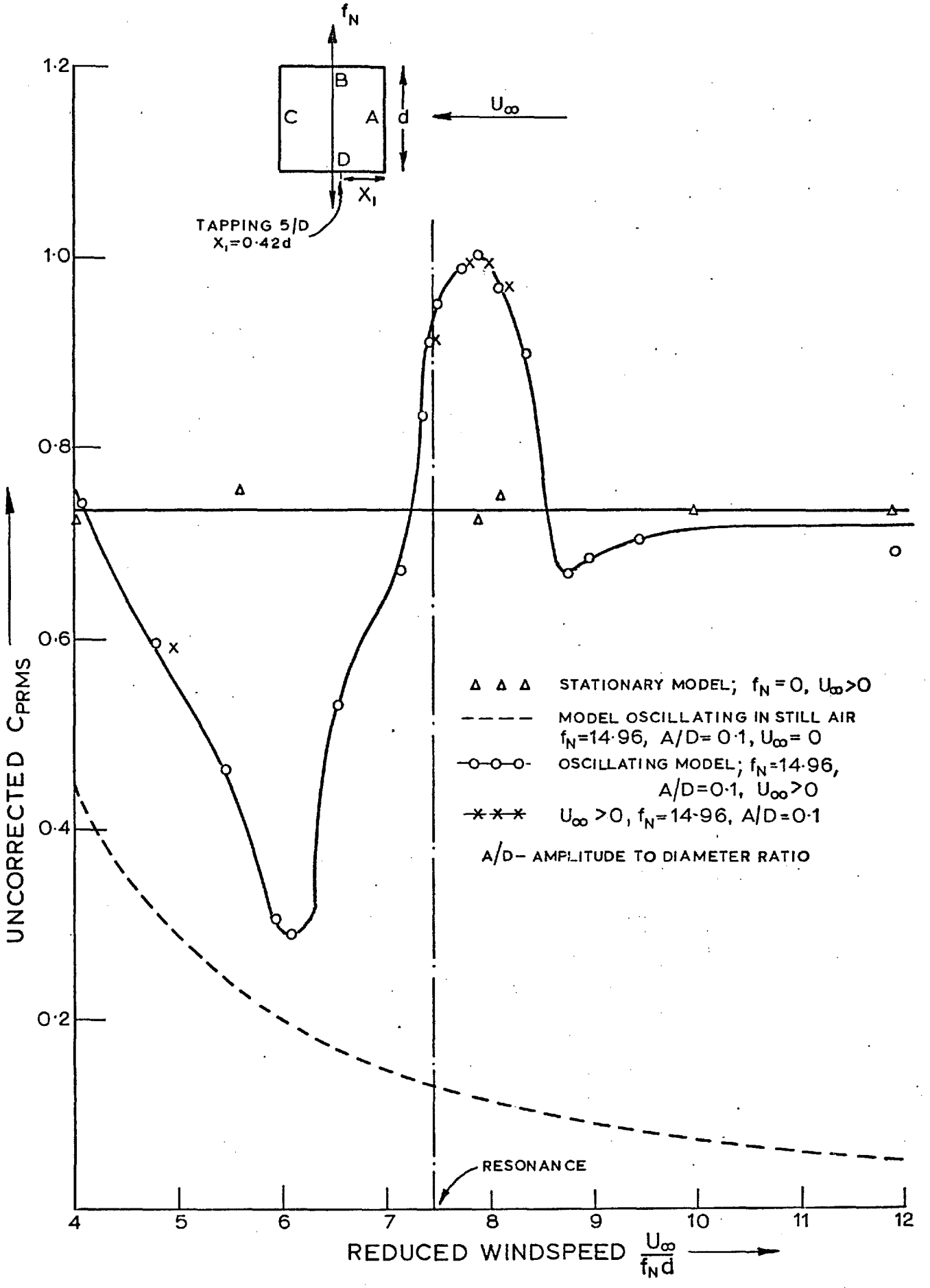

Fig 7·9 C_{PRMS} AT TAPPING 5/D VERSUS $\frac{U_\infty}{f_N d}$, A/D 0·1

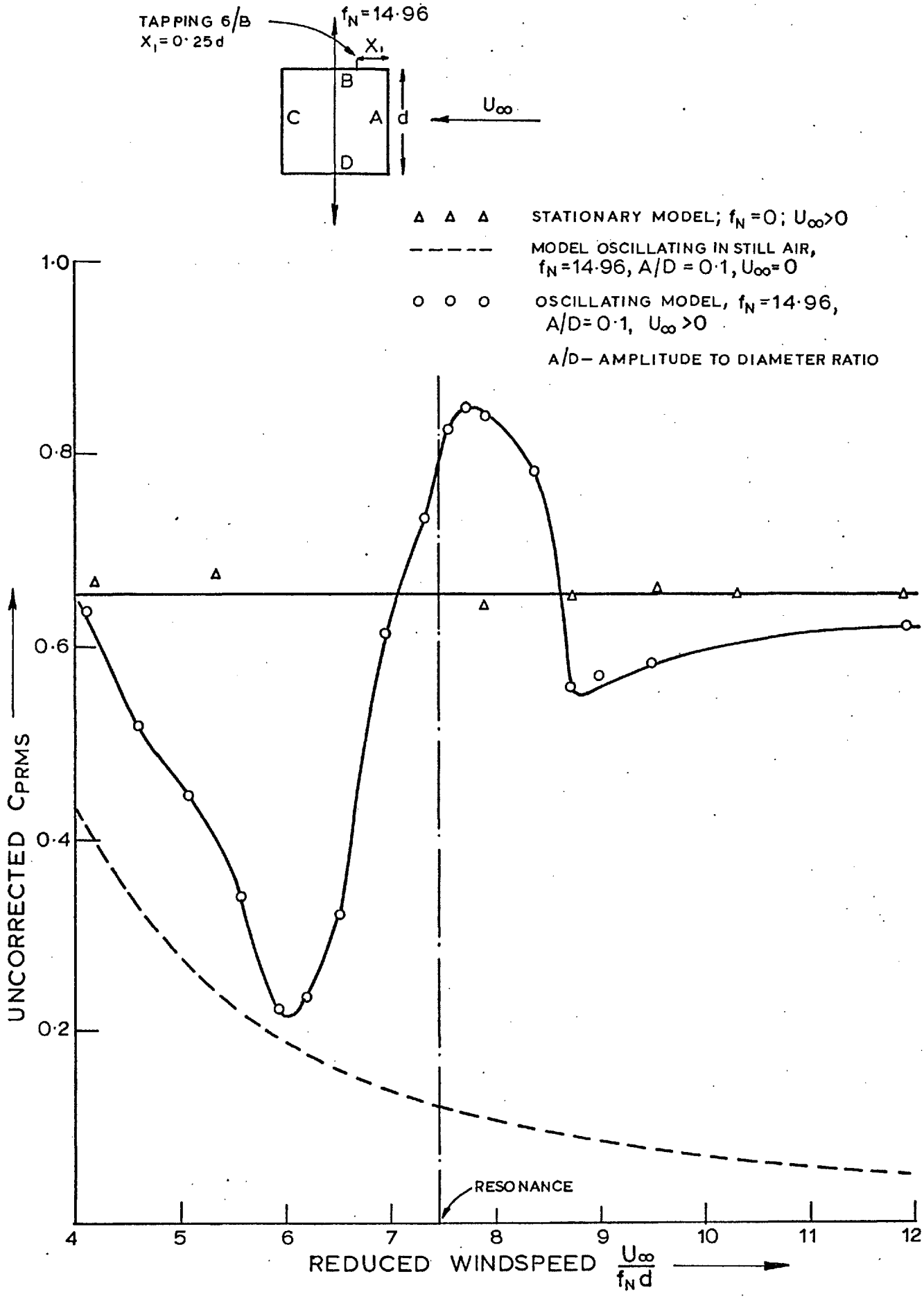

Fig 7·10 C_{PRMS} AT TAPPING 6/B VERSUS $\frac{U_\infty}{f_N d}$, A/D = 0·1

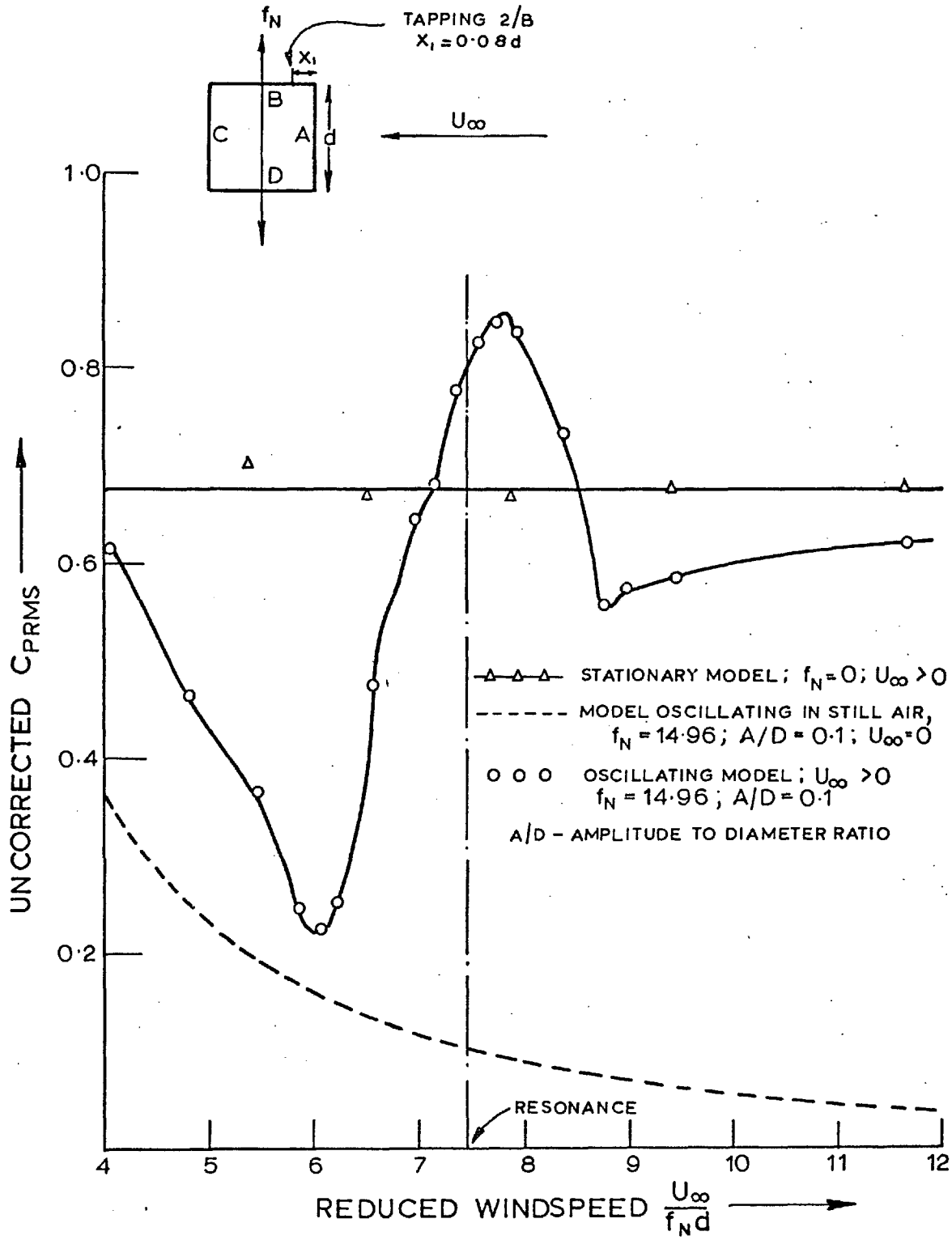

Fig 7·11 C_{PRMS} AT TAPPING 2/B VERSUS $\frac{U_\infty}{f_N d}$, $A/D = 0{\cdot}1$

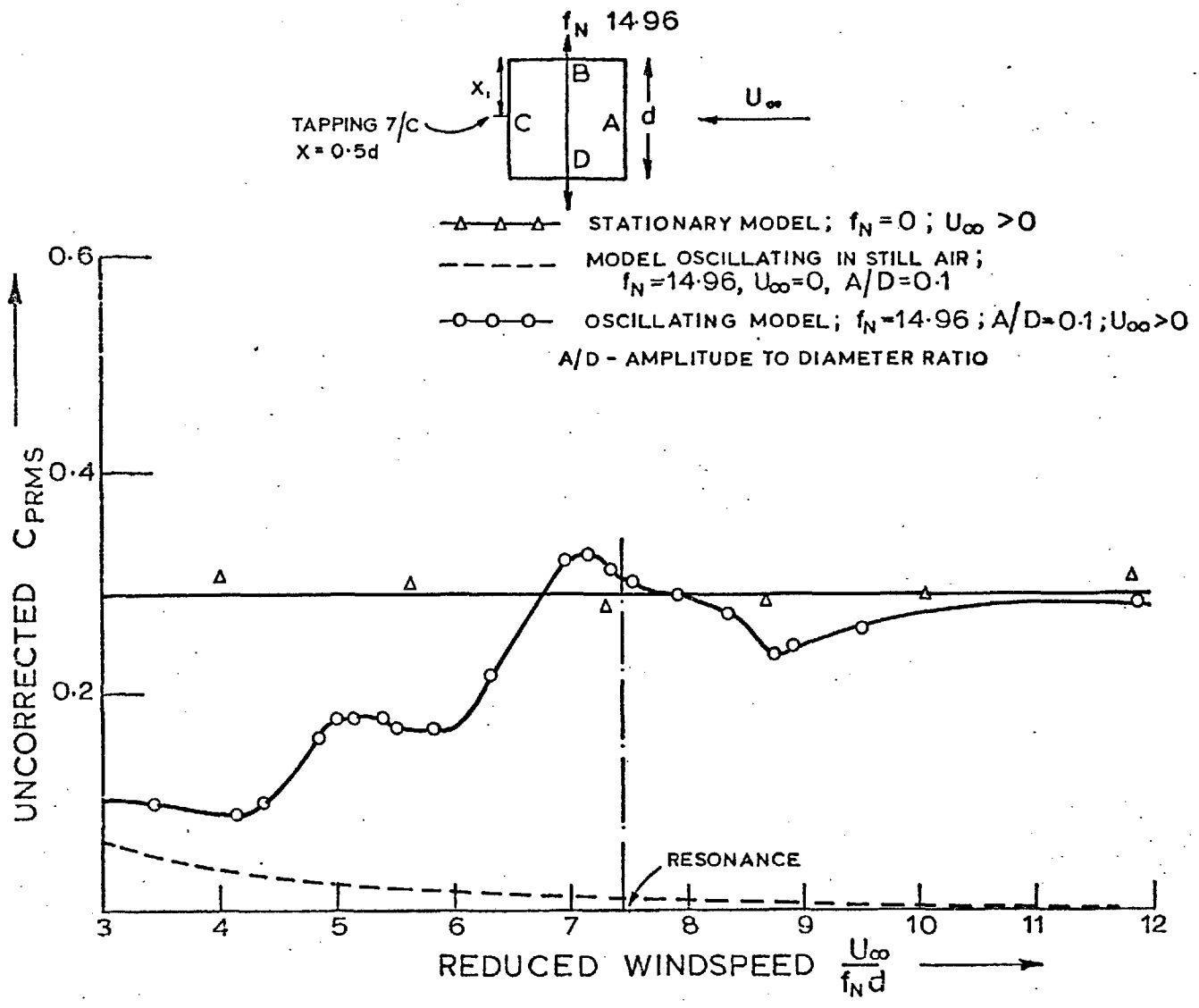

Fig 7·12 C_{PRMS} AT TAPPING 7/C VERSUS $\frac{U_\infty}{f_N d}$, A/D = 0·1

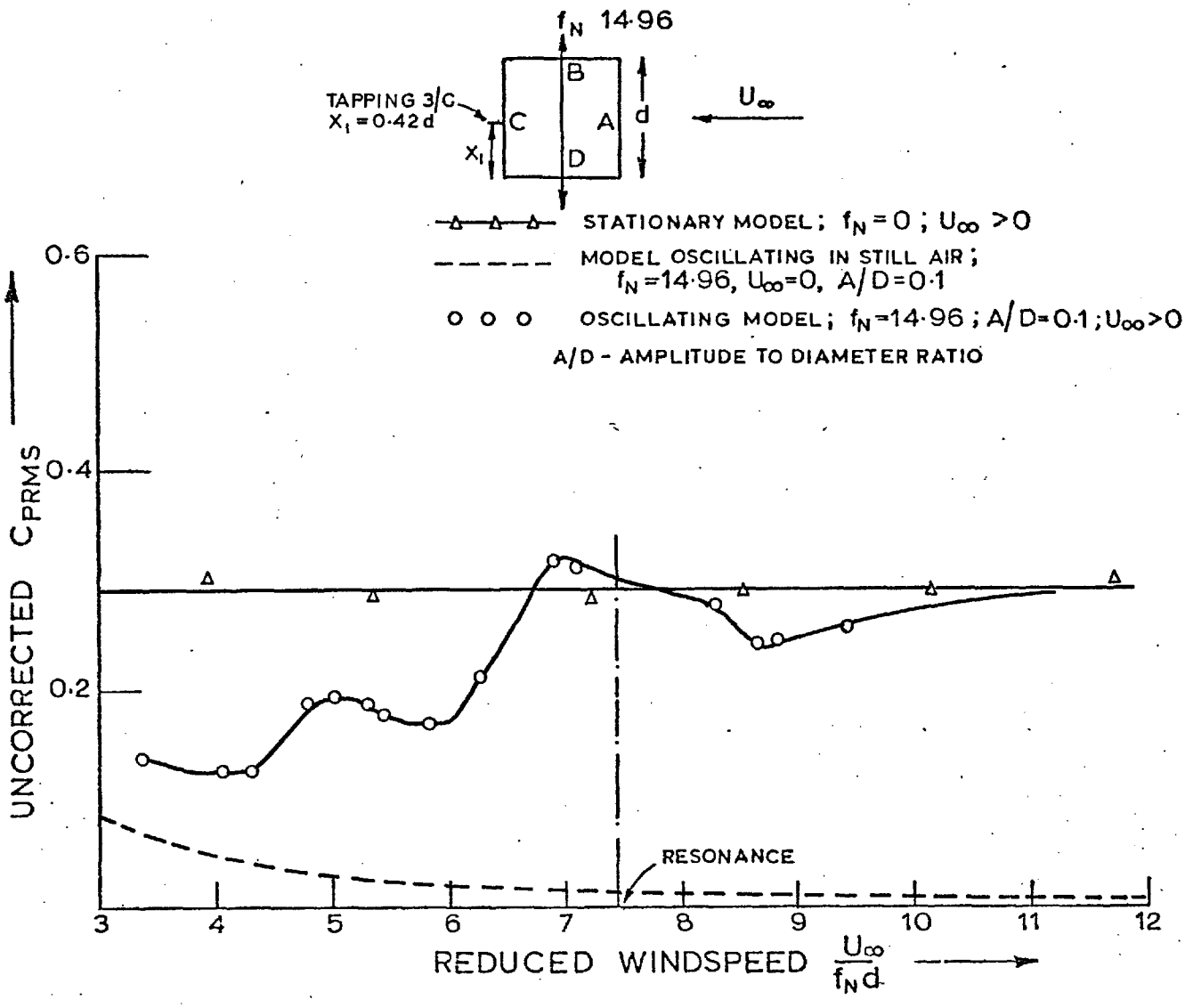

Fig 7·13 C_{PRMS} AT TAPPING 3/C VERSUS $\frac{U_\infty}{f_N d}$, $A/D = 0.1$

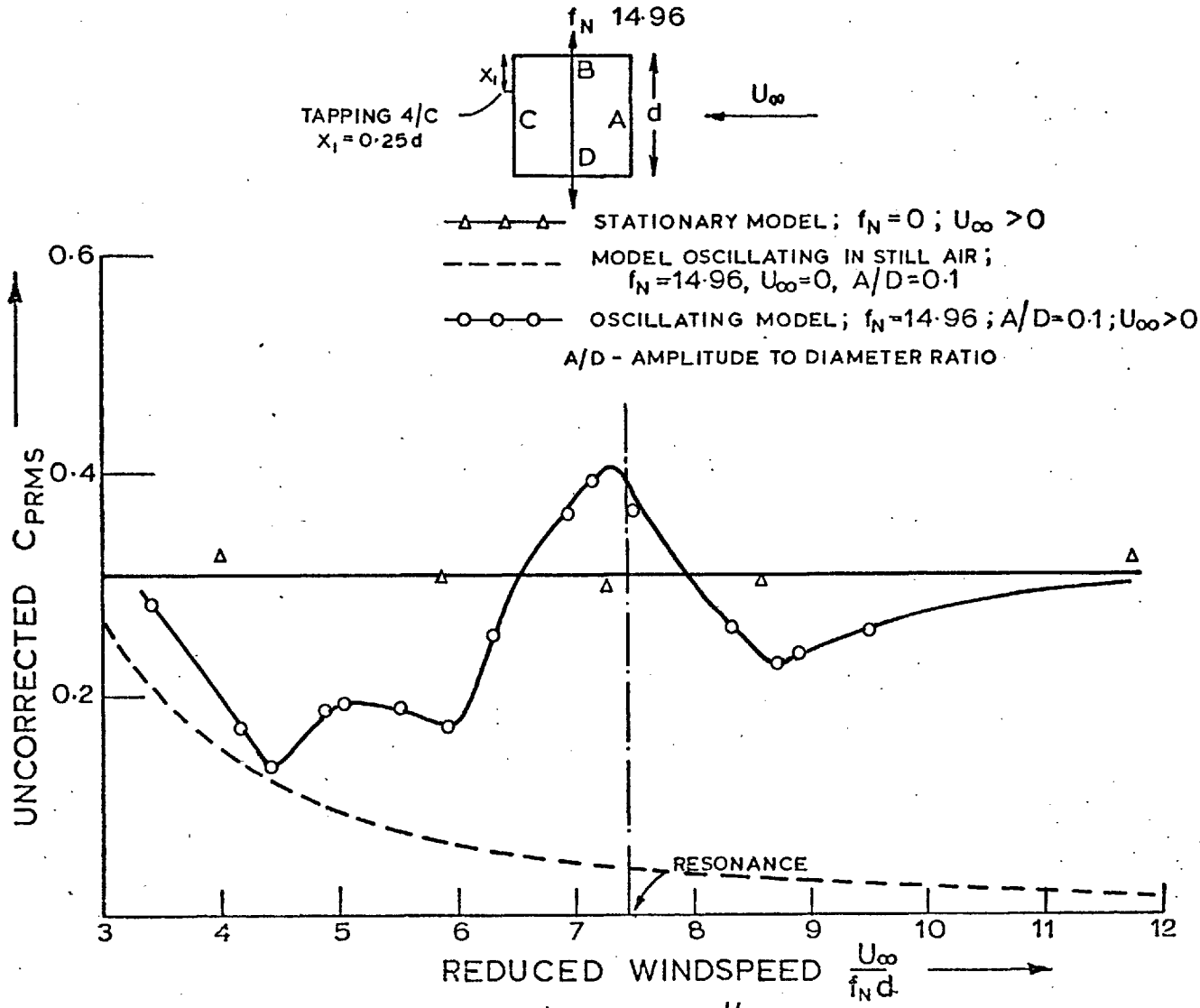

Fig 7·14 C_{PRMS} AT TAPPING 4/C VERSUS $\frac{U_\infty}{f_N d}$, A/D = 0·1

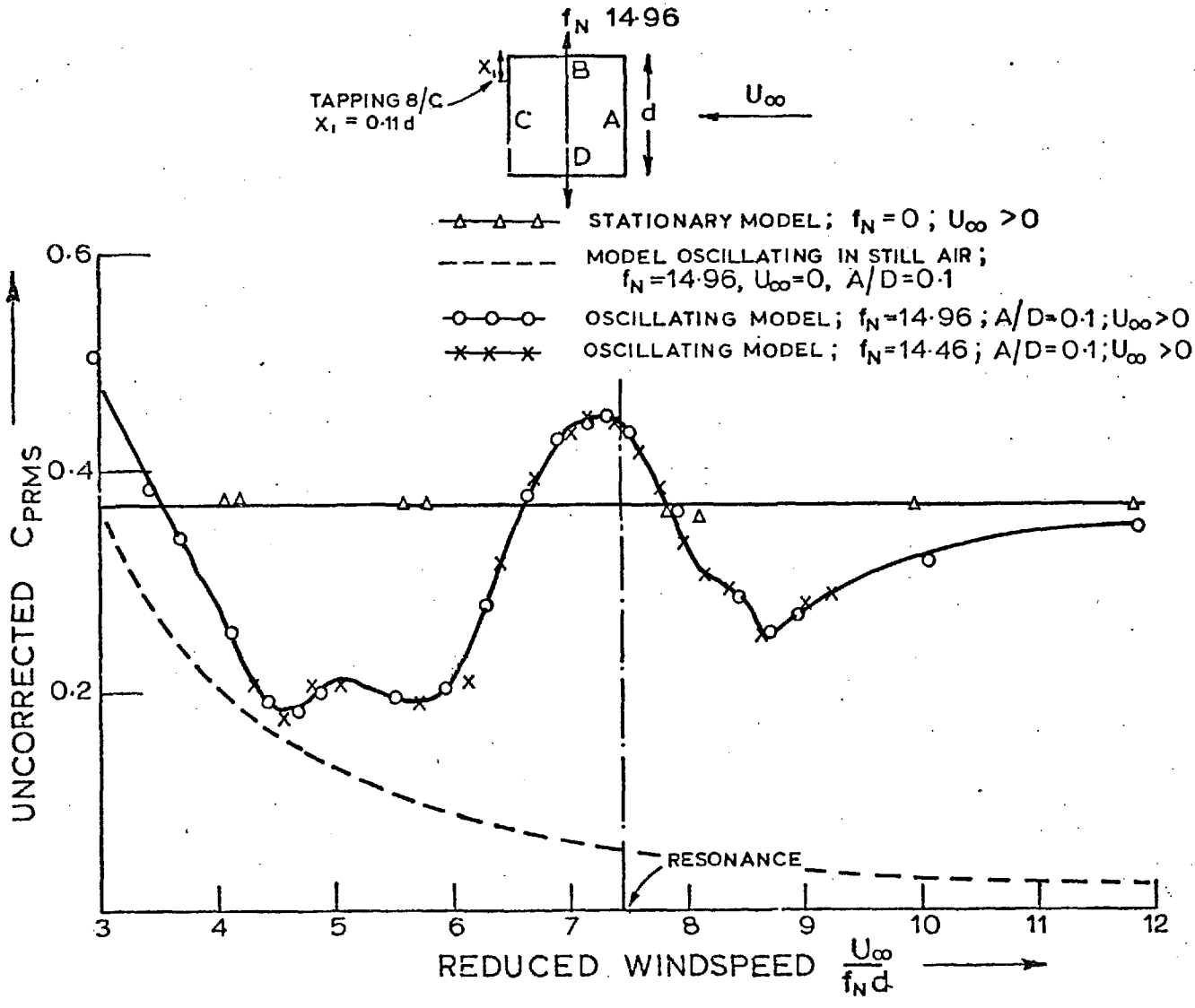

Fig 7·15 C_{PRMS} AT TAPPING 8/C VERSUS $\frac{U_\infty}{f_N d}$, A/D=0·1

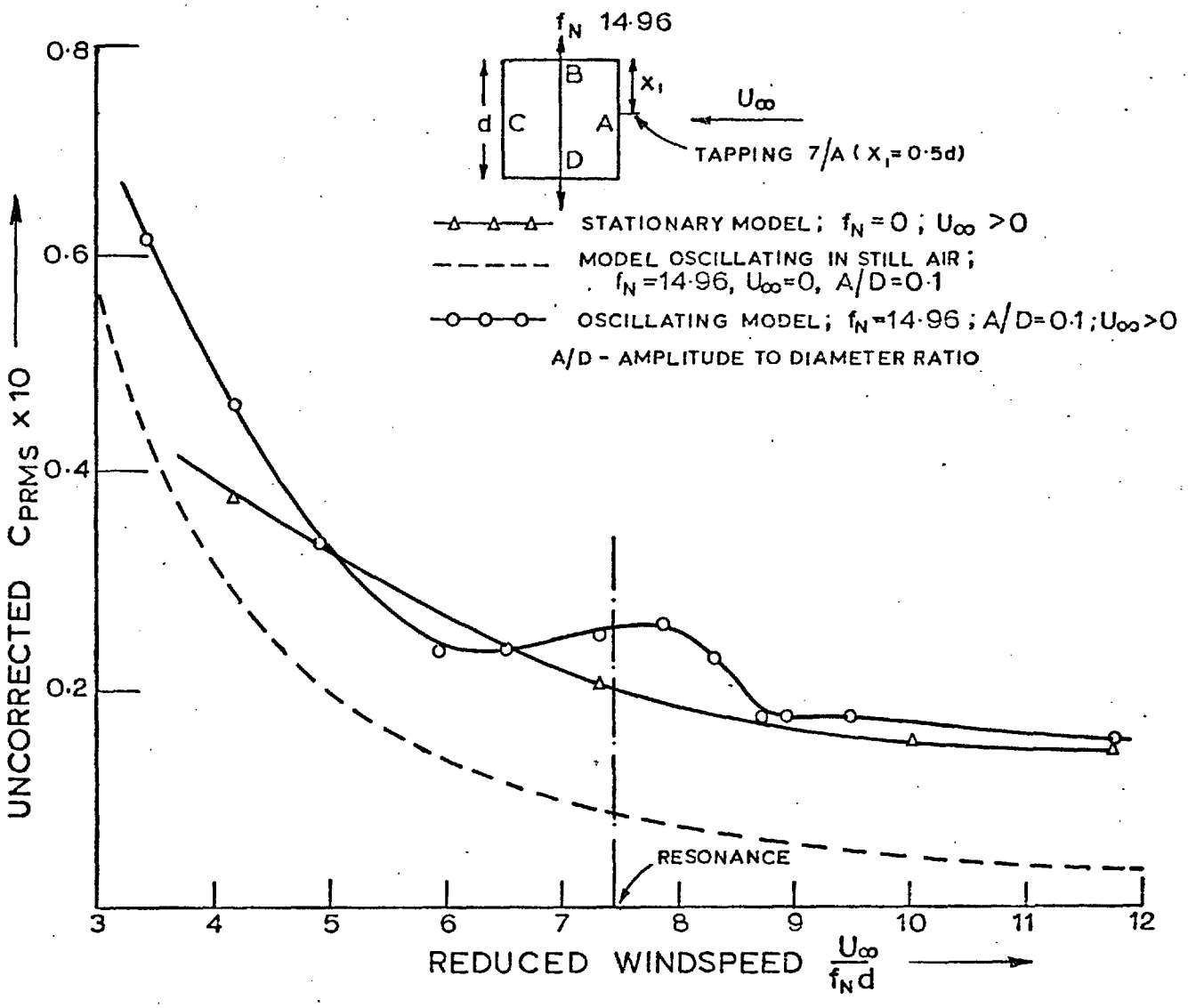

Fig 7·16 C_{PRMS} AT TAPPING 7/A VERSUS $\frac{U_\infty}{f_N d}$, A/D = 0·1

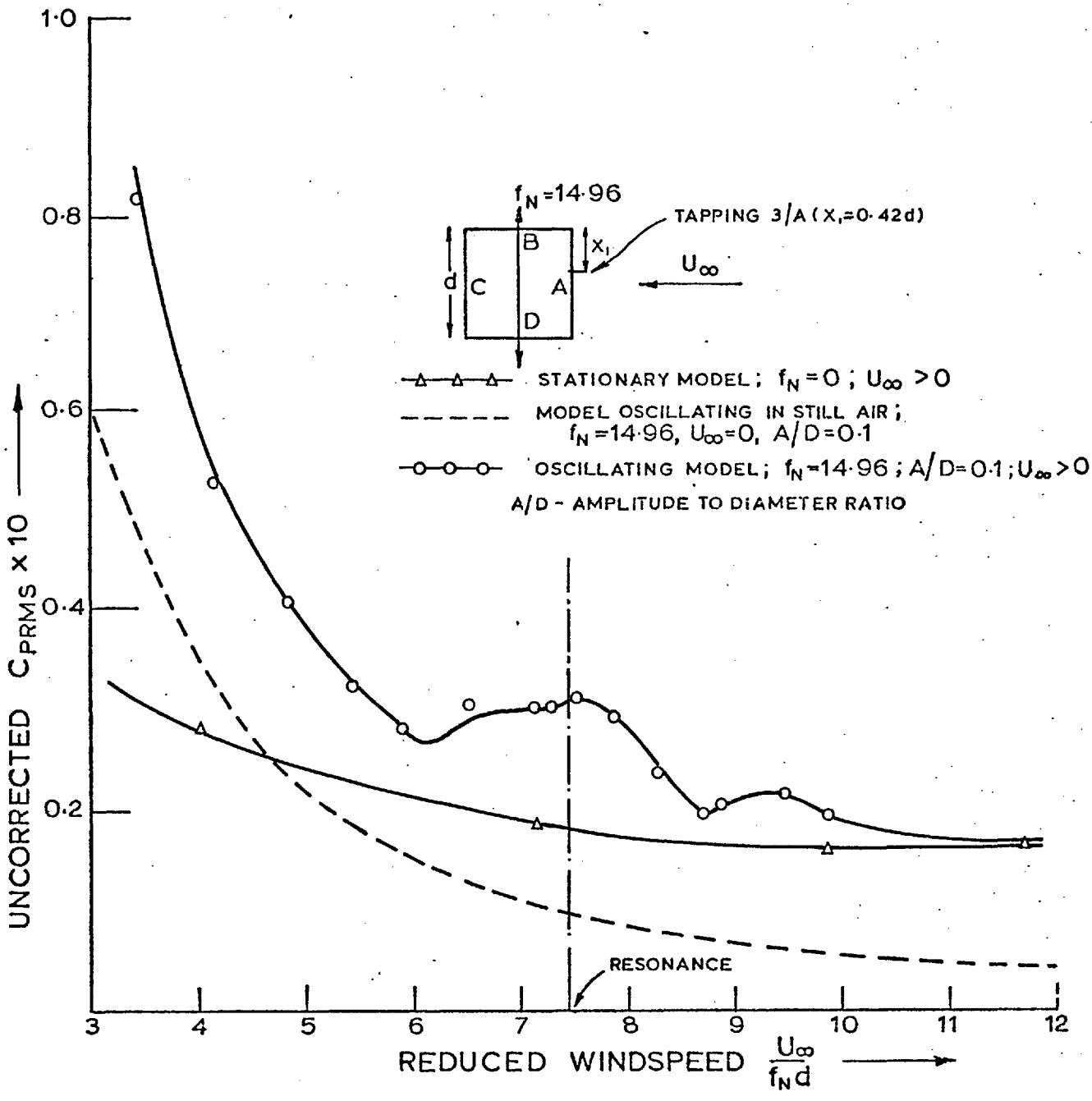

Fig 7·17 C_{PRMS} AT TAPPING 3/A VERSUS $\frac{U_\infty}{f_N d}$, A/D = 0·1

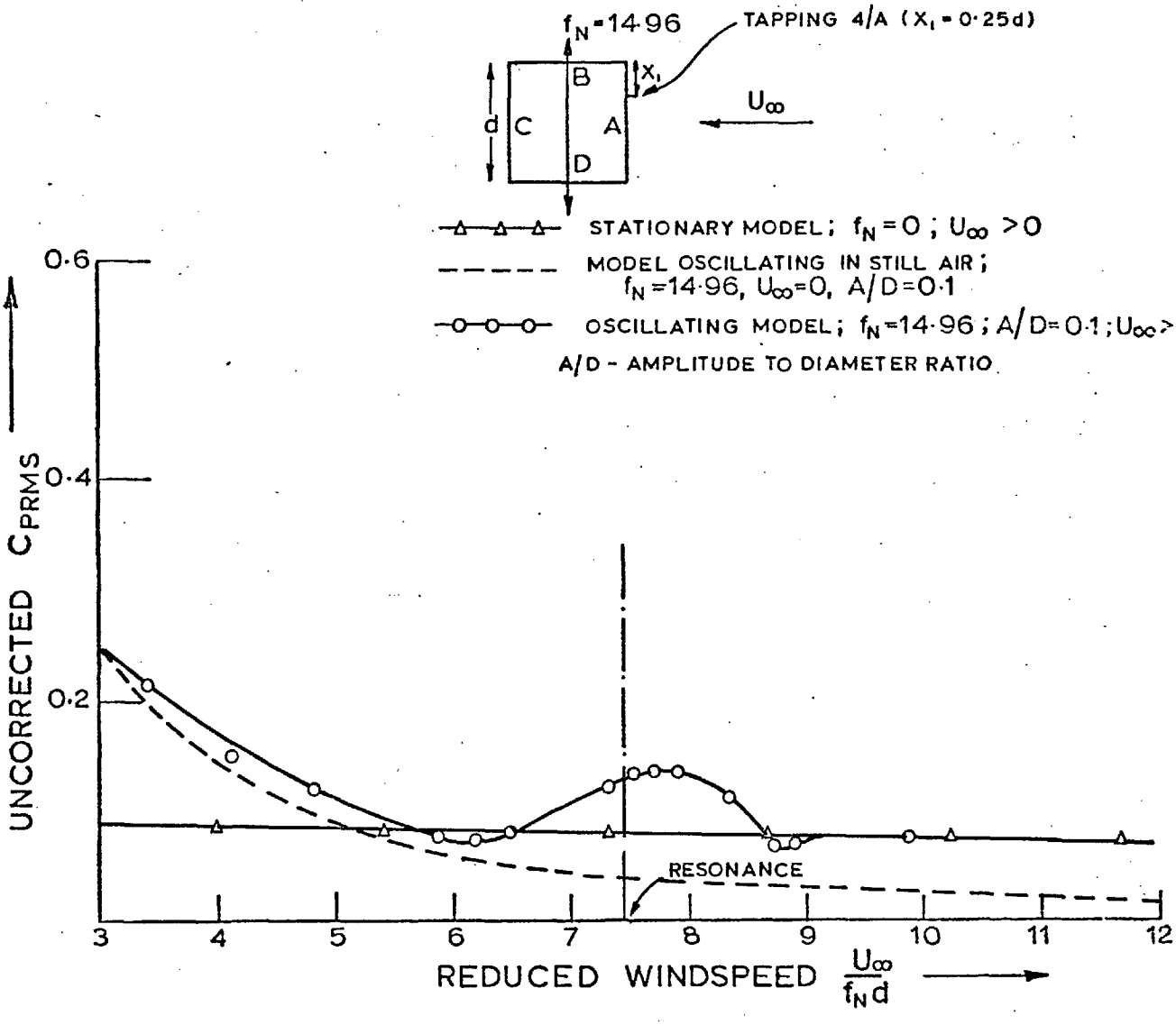

Fig 7·18 C_{PRMS} AT TAPPING 4/A VERSUS $\frac{U_\infty}{f_N d}$, A/D=0·1

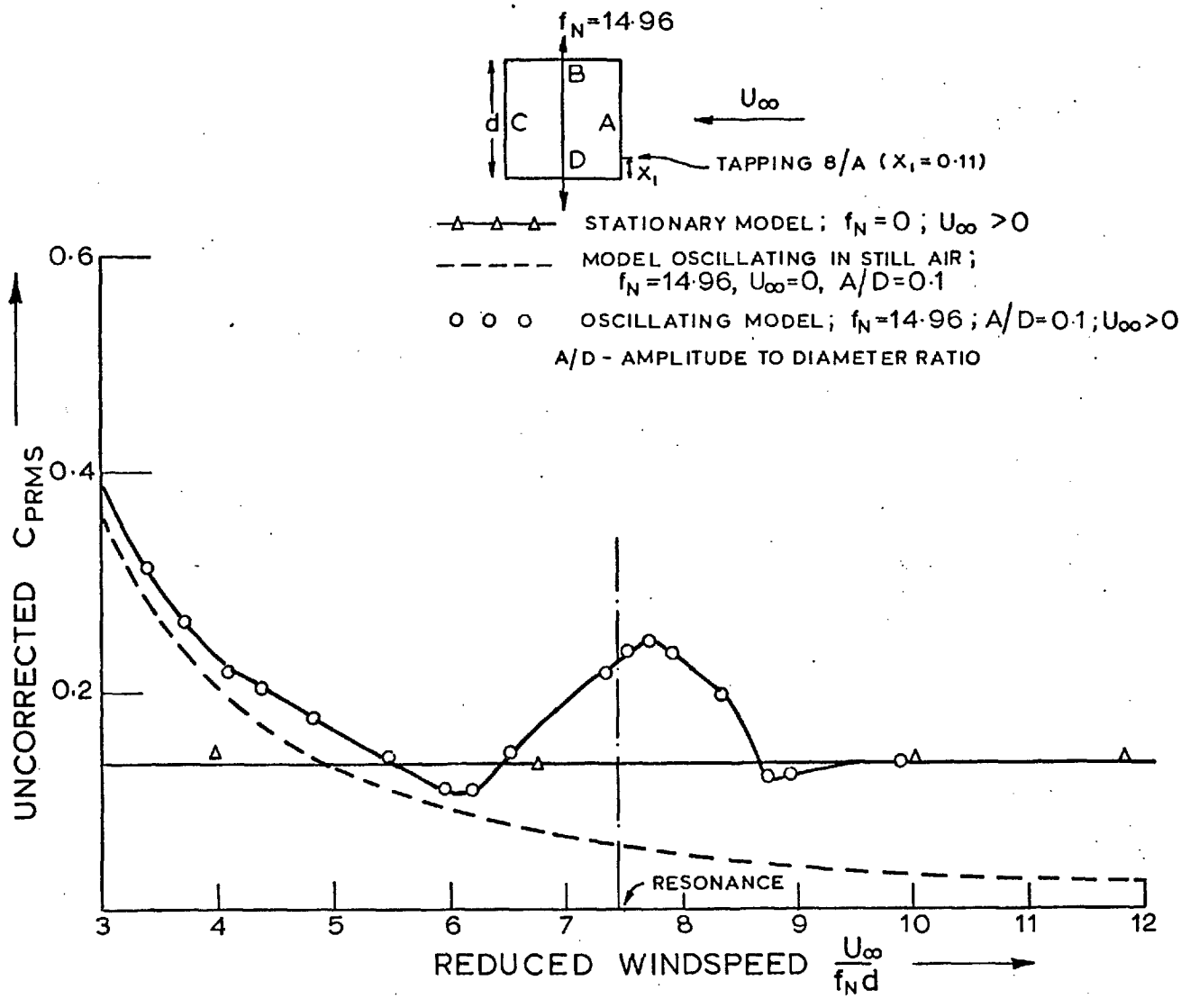

Fig 7·19 C_{PRMS} AT TAPPING 8/A VERSUS $\frac{U_\infty}{f_N d}$, A/D=0·1

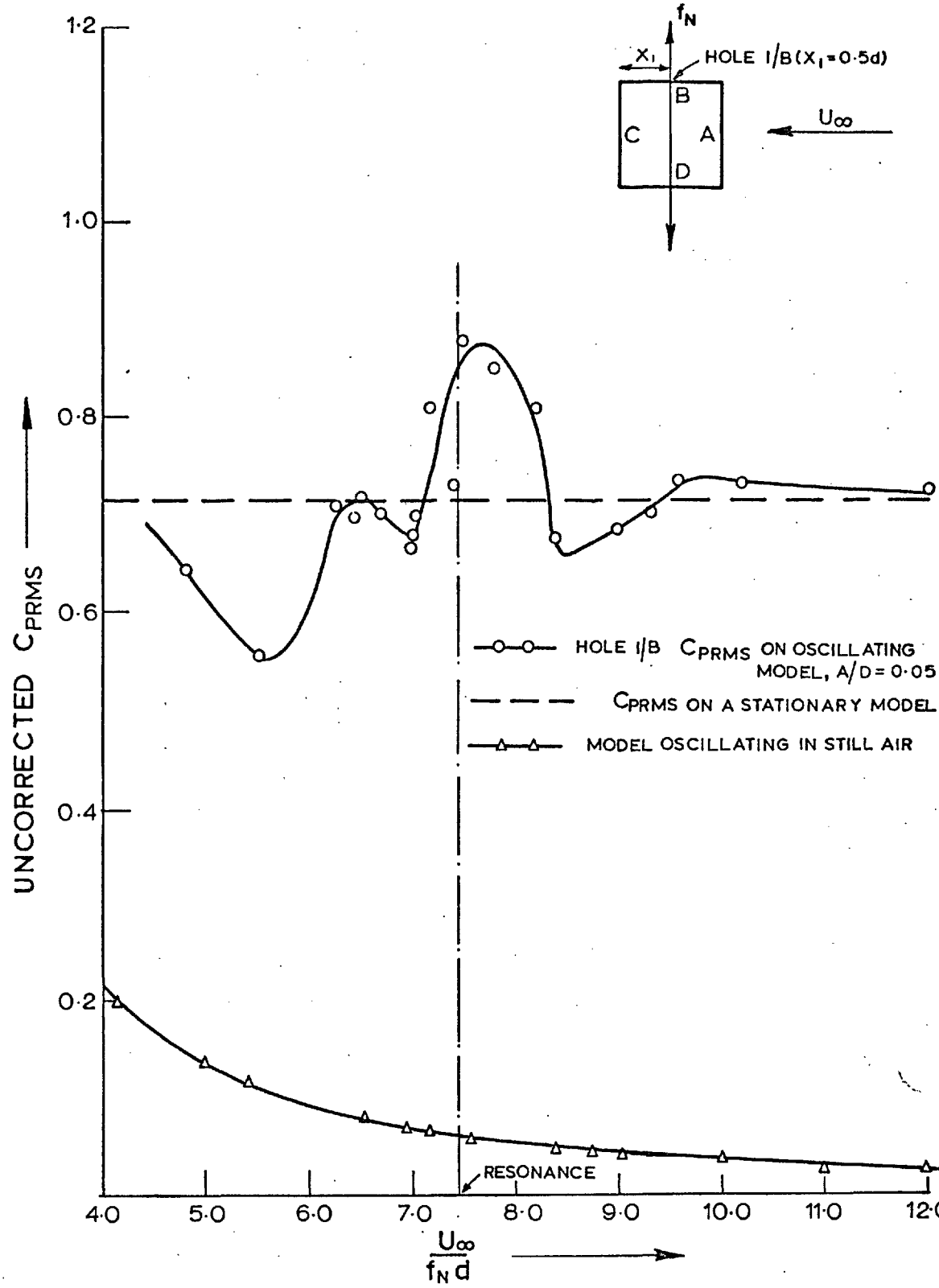

Fig 7·20 C_{PRMS} AT TAPPING 1/B VERSUS $\frac{U_\infty}{f_N d}$ A/D = 0·05

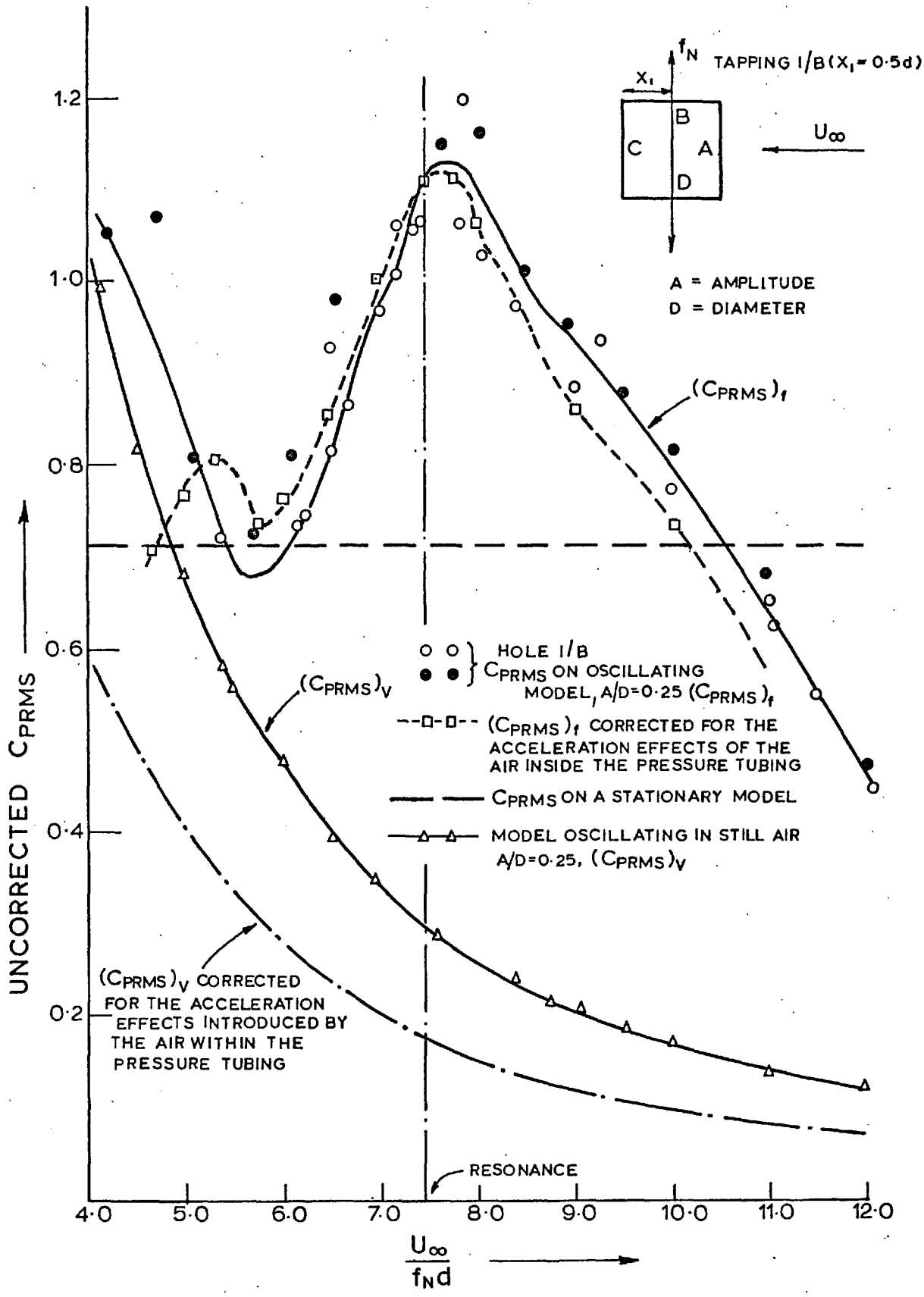

Fig 7·21 C_{PRMS} AT TAPPING I/B VERSUS $\frac{U_\infty}{f_N d}$, A/D = 0·25

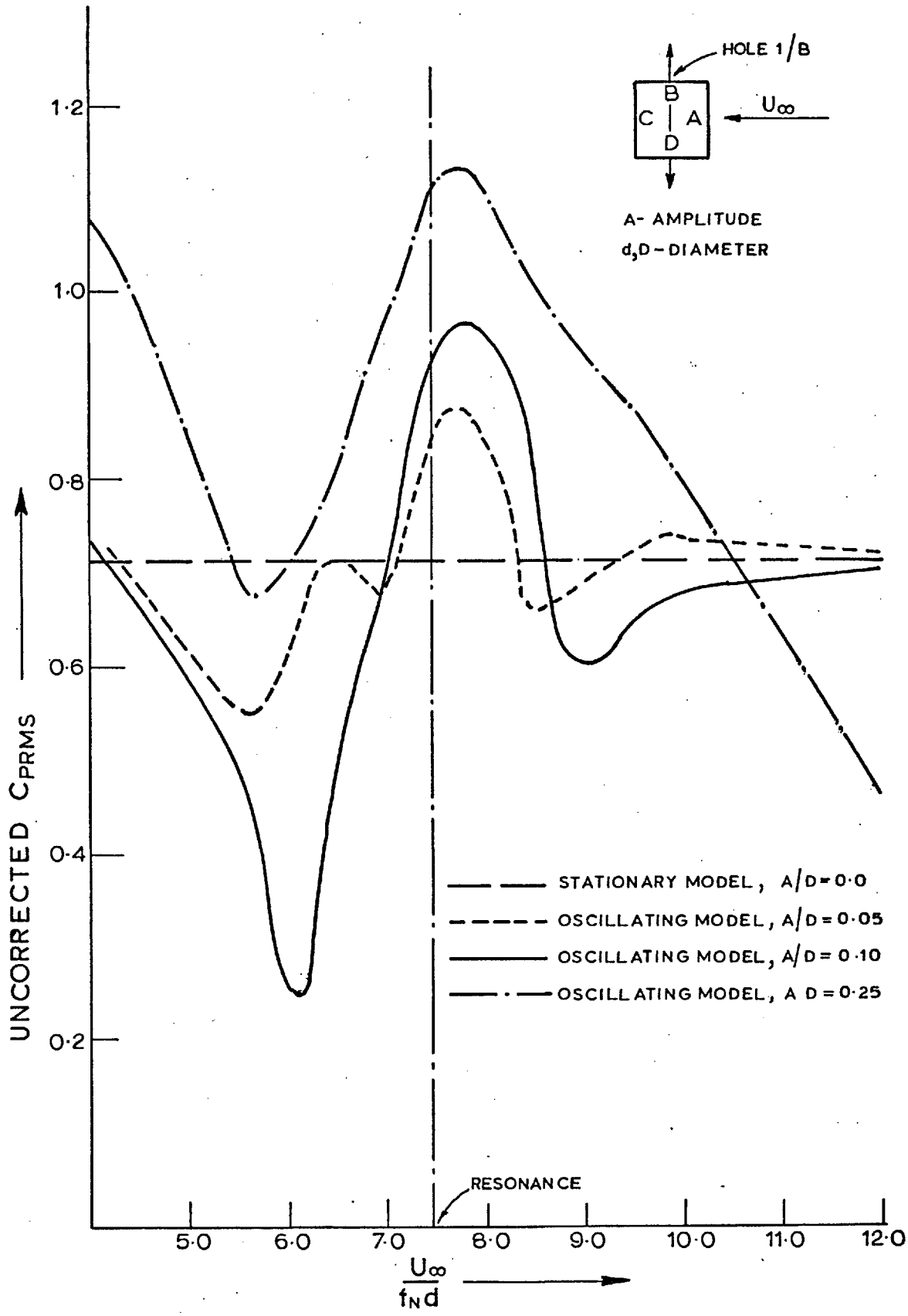

Fig 7·22 C_{PRMS} AT TAPPING 1/B VERSUS $\frac{U_\infty}{f_N d}$; A/D 0·0, 0·05, 0·10 & 0·25

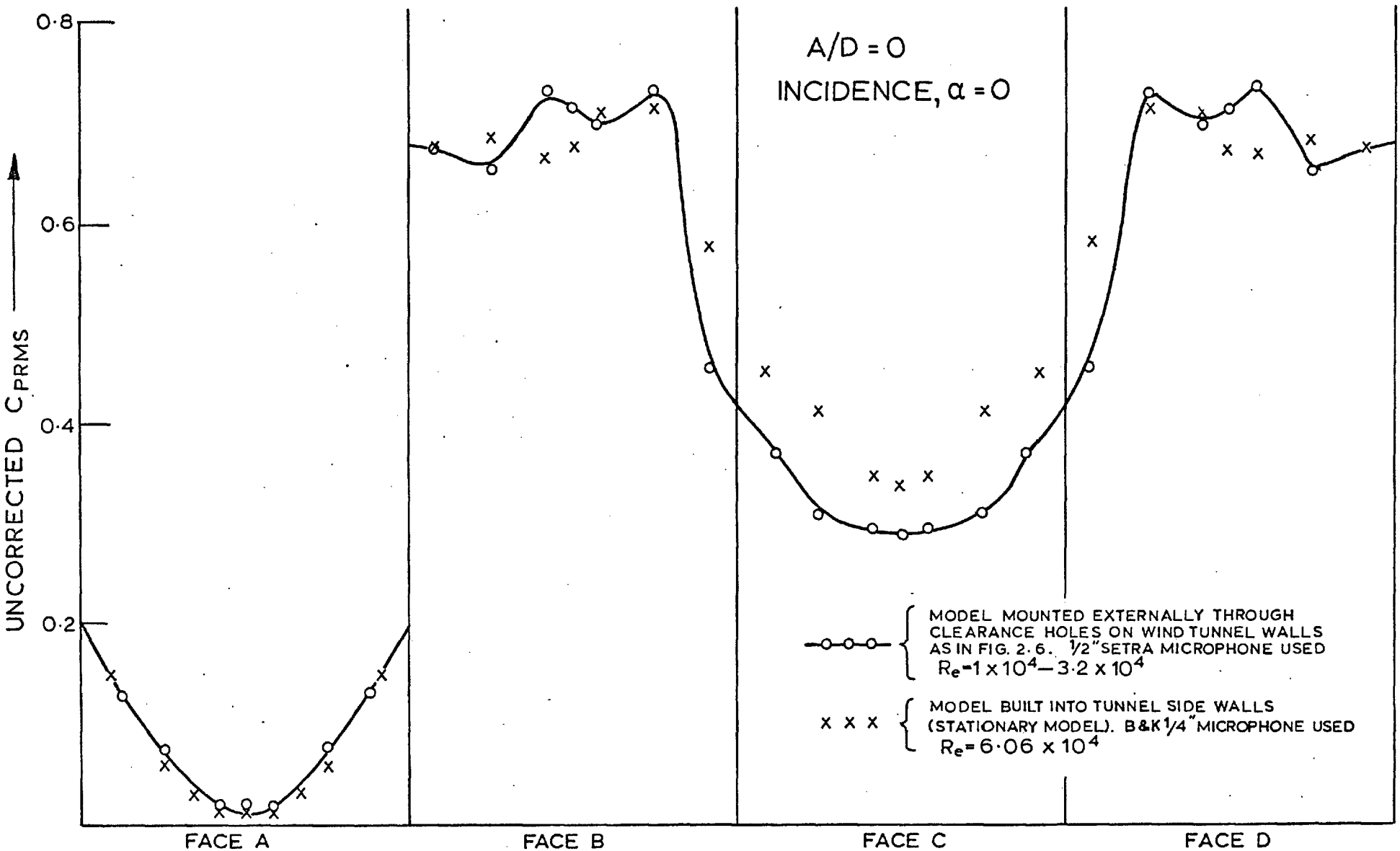

Fig 7·23 DISTRIBUTION OF C_{PRMS} AT THE CENTRE-SPAN OF THE "OSCILLATING MODEL"

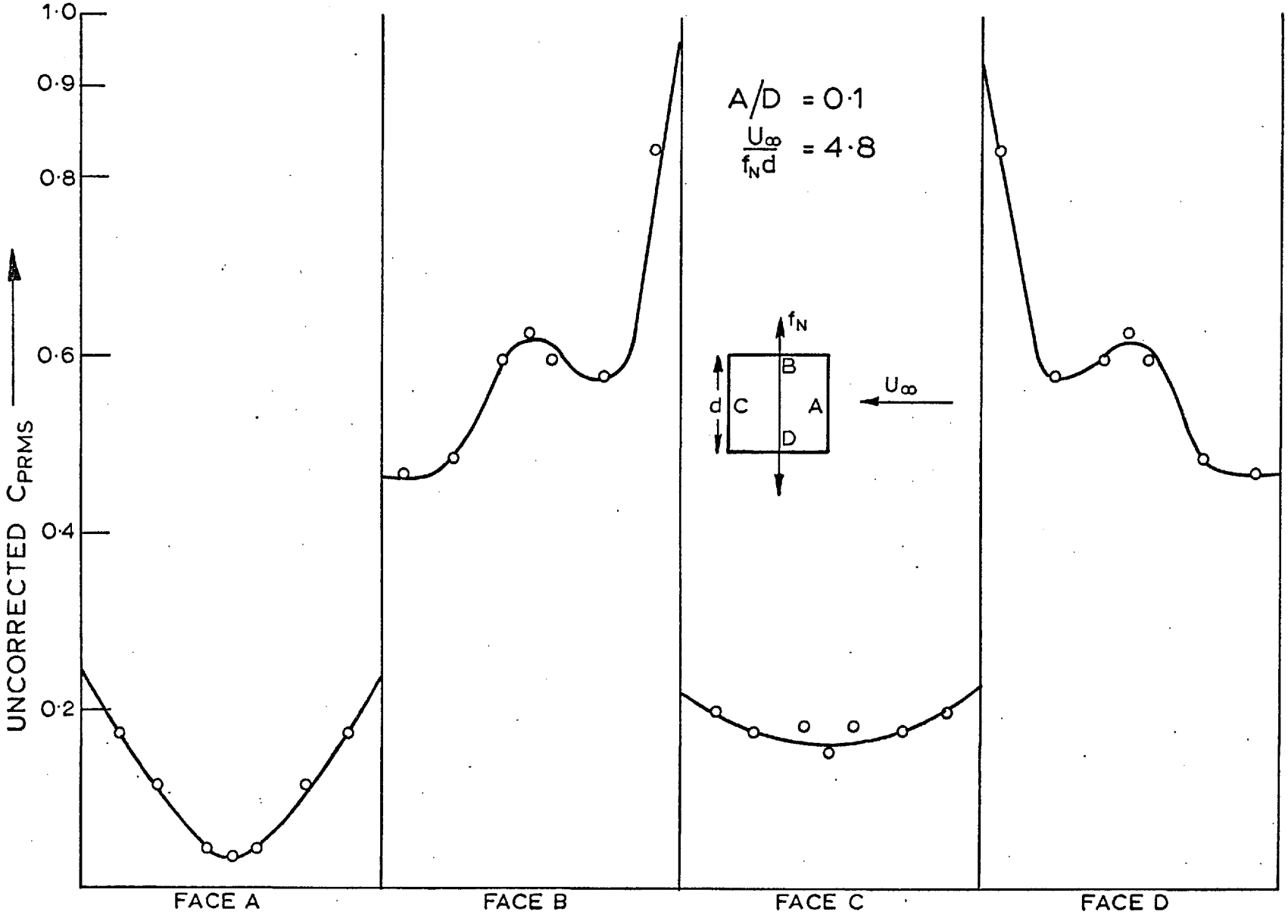

Fig 7·24 DISTRIBUTION OF C_{PRMS} AT CENTRE-SPAN DURING OSCILLATION

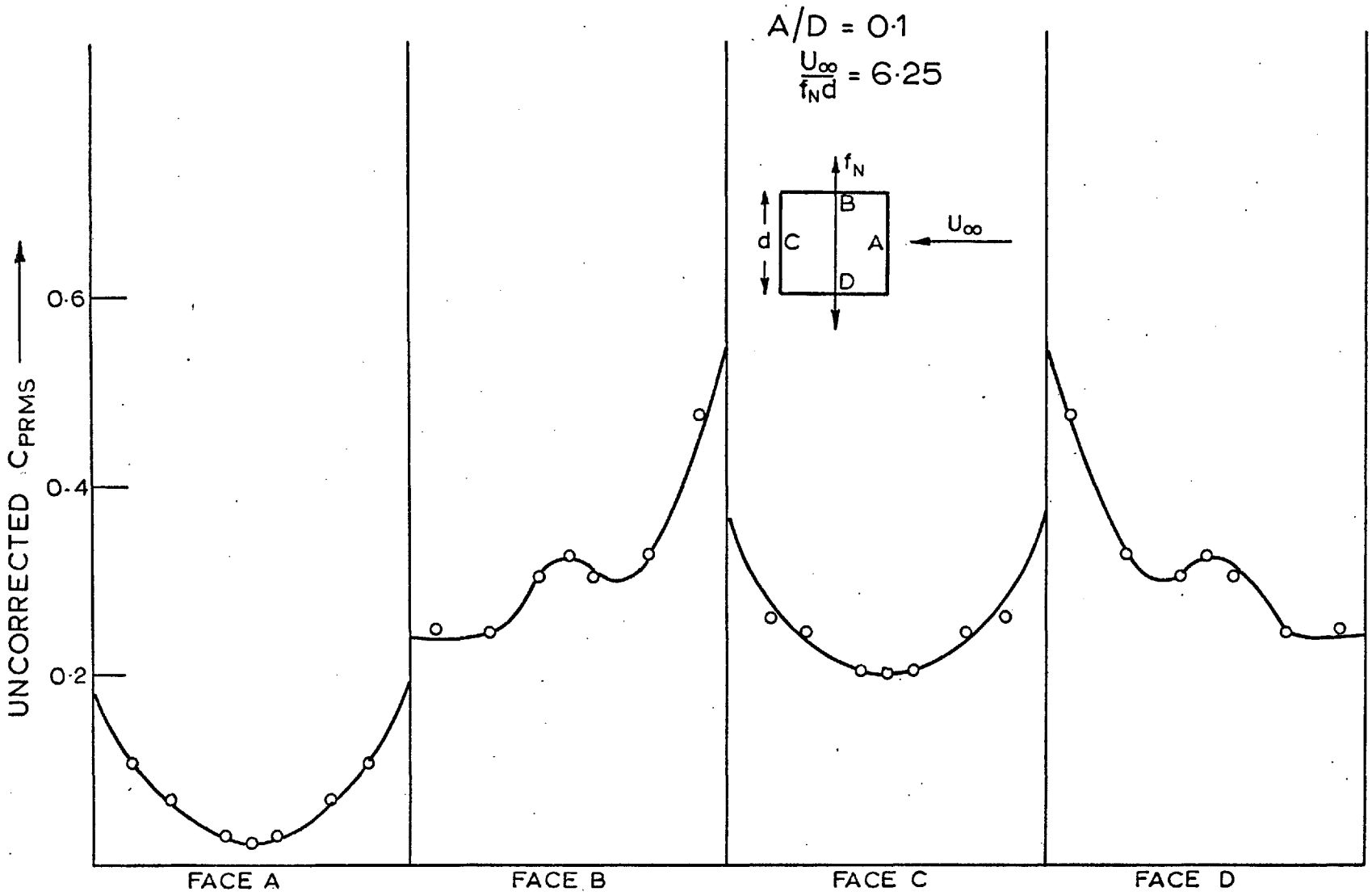

Fig 7·25 DISTRIBUTION OF C_{PRMS} AT CENTRE-SPAN DURING OSCILLATION

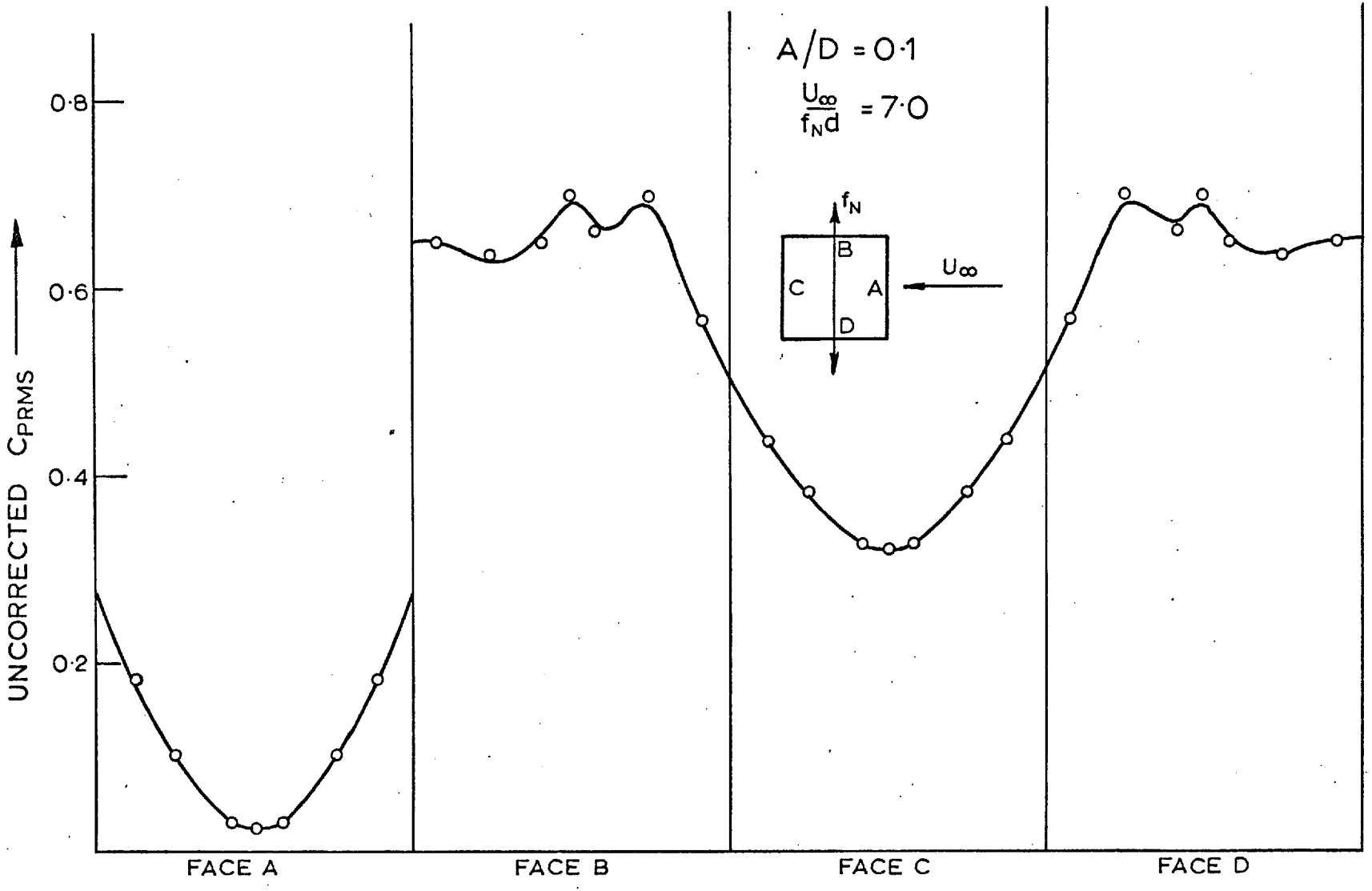

Fig 7·26 DISTRIBUTION OF C_{PRMS} AT CENTRE-SPAN DURING OSCILLATION

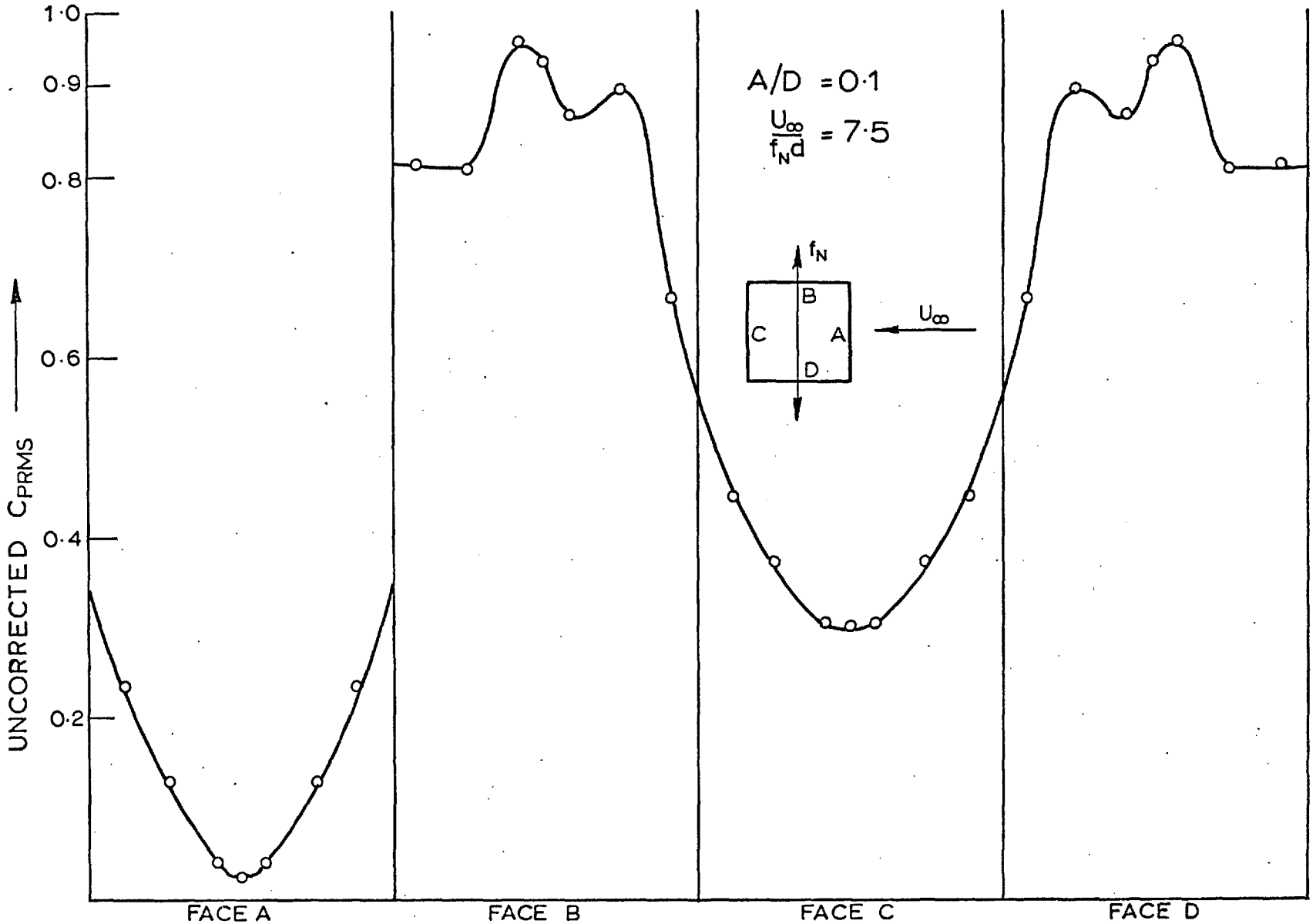

Fig 7·27 DISTRIBUTION OF C_{PRMS} AT CENTRE-SPAN DURING OSCILLATION

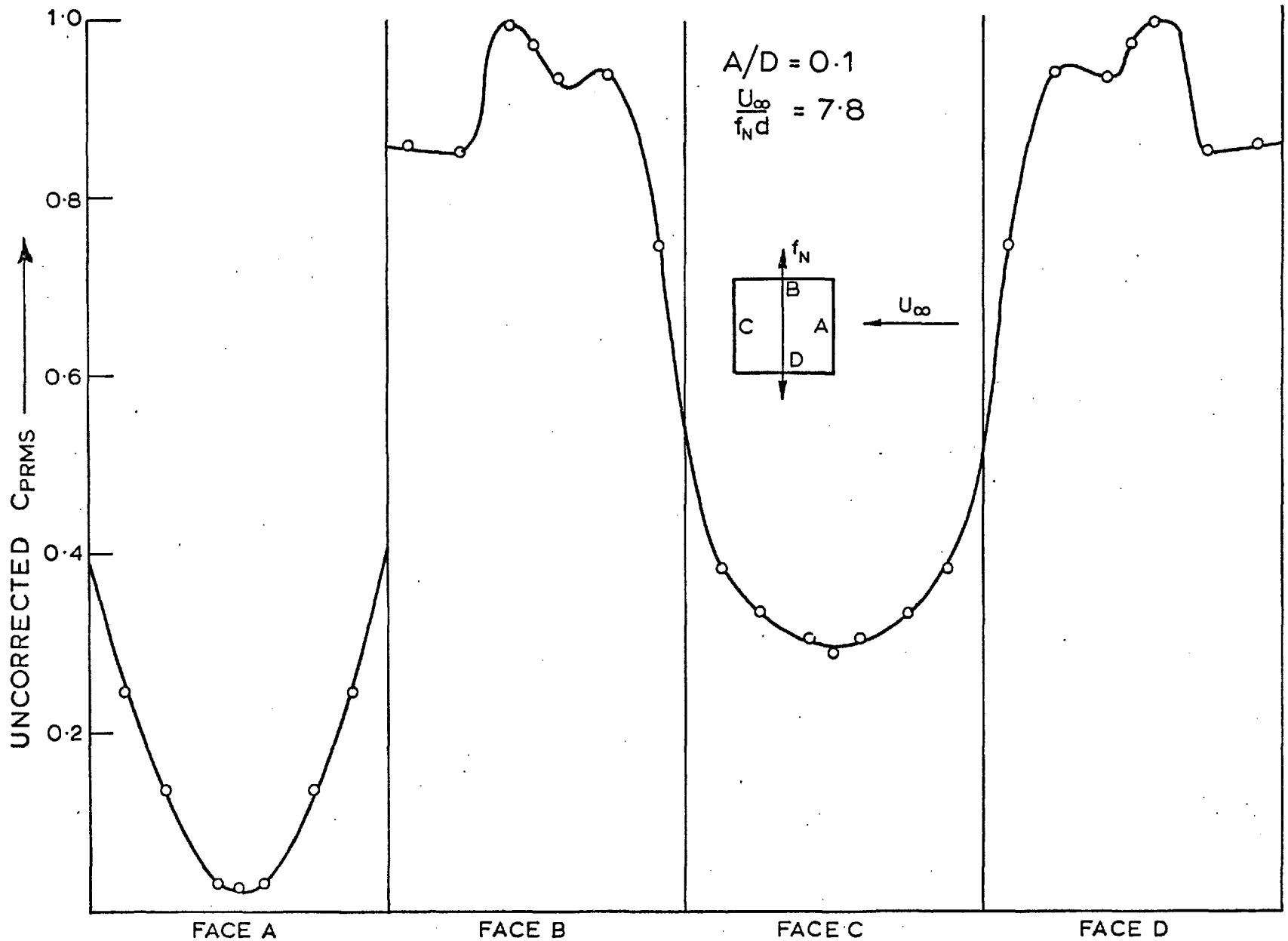

Fig 7·28 DISTRIBUTION OF C_{PRMS} AT CENTRE-SPAN DURING OSCILLATION

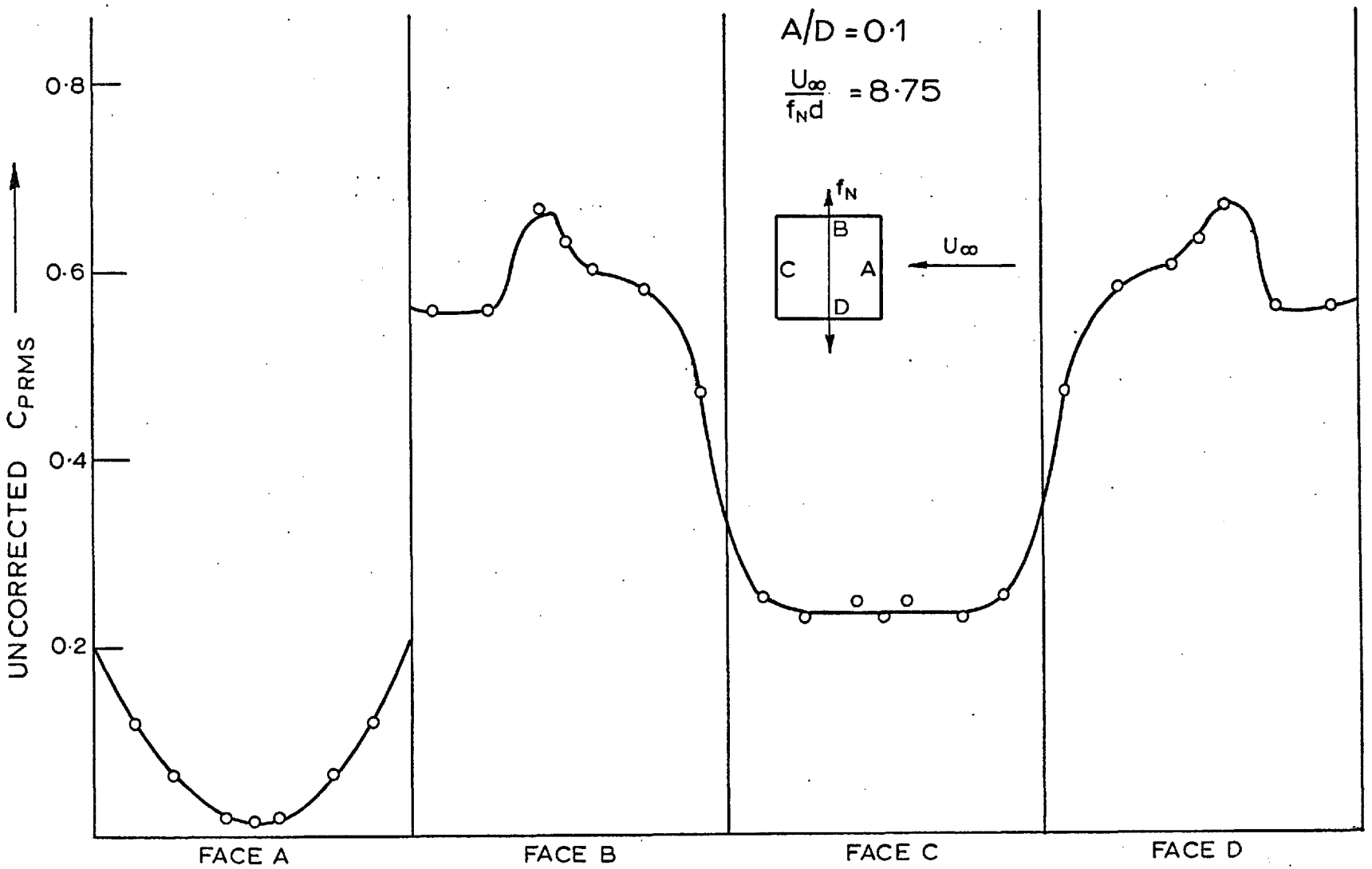

Fig 7·29 DISTRIBUTION OF C_{PRMS} AT CENTRE-SPAN DURING OSCILLATION

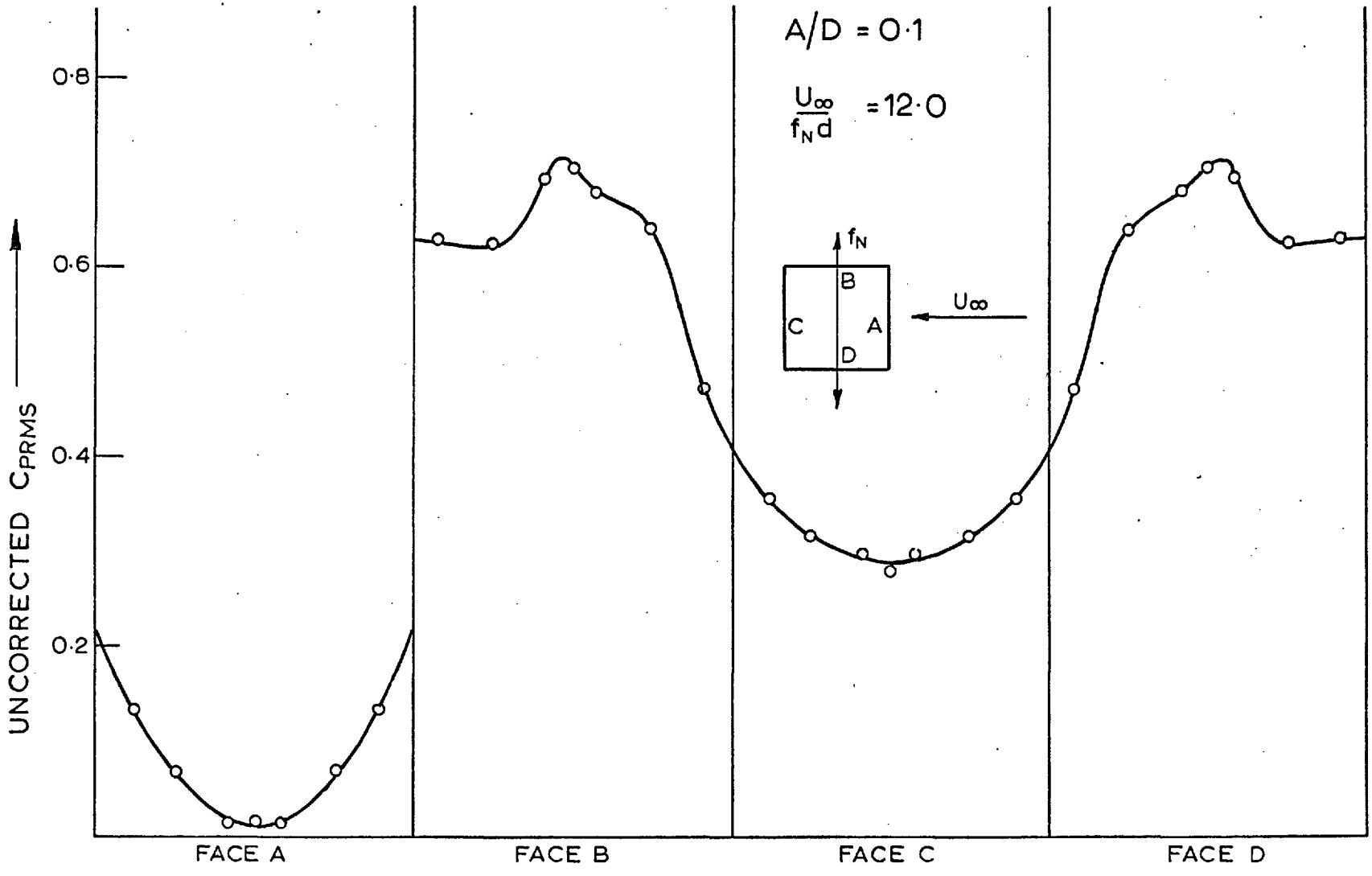

Fig 7·30 DISTRIBUTION OF C_{PRMS} AT CENTRE-SPAN DURING OSCILLATION

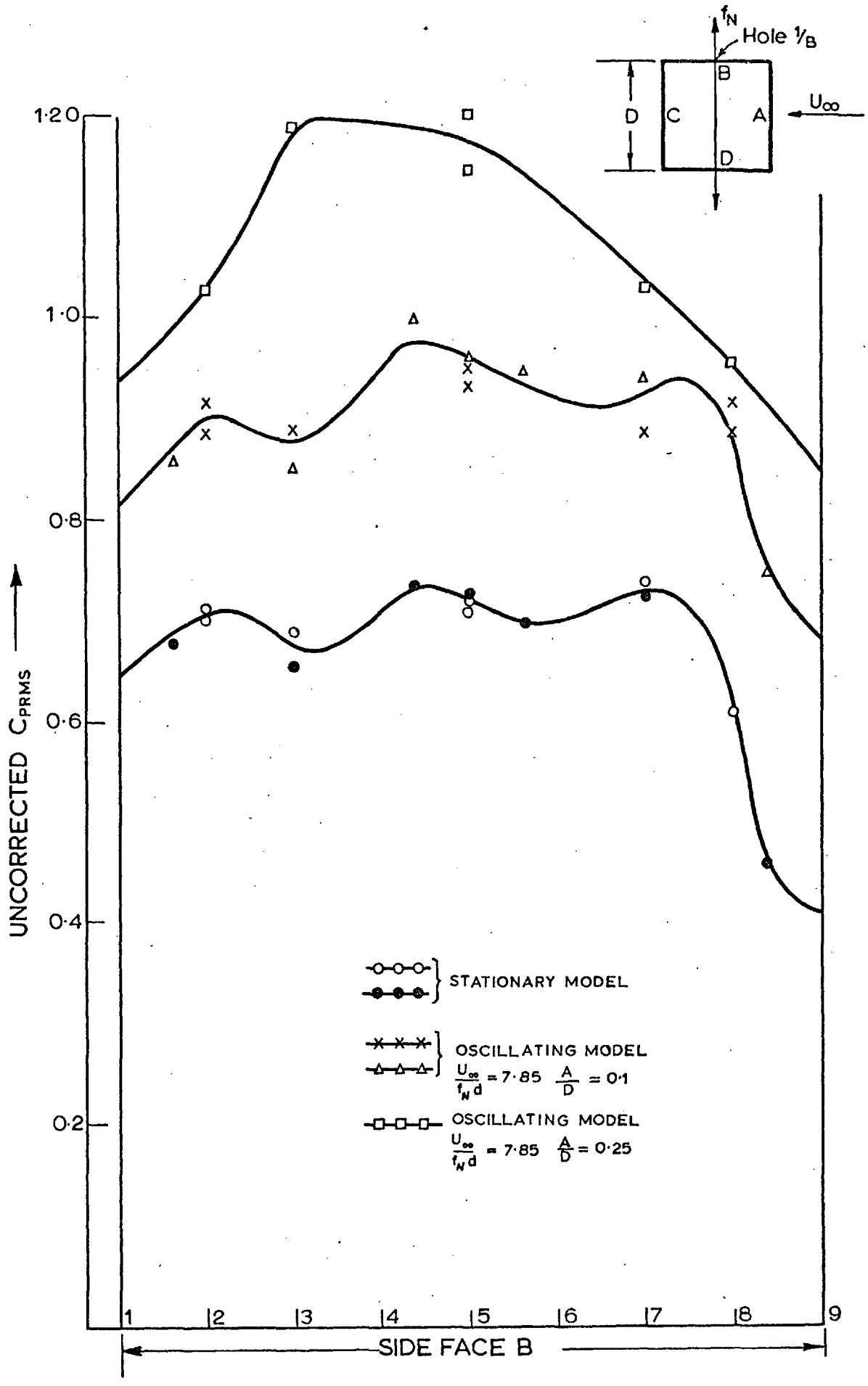

Fig.7·31 Effects of model oscillation on the fluctuating pressures of side face B

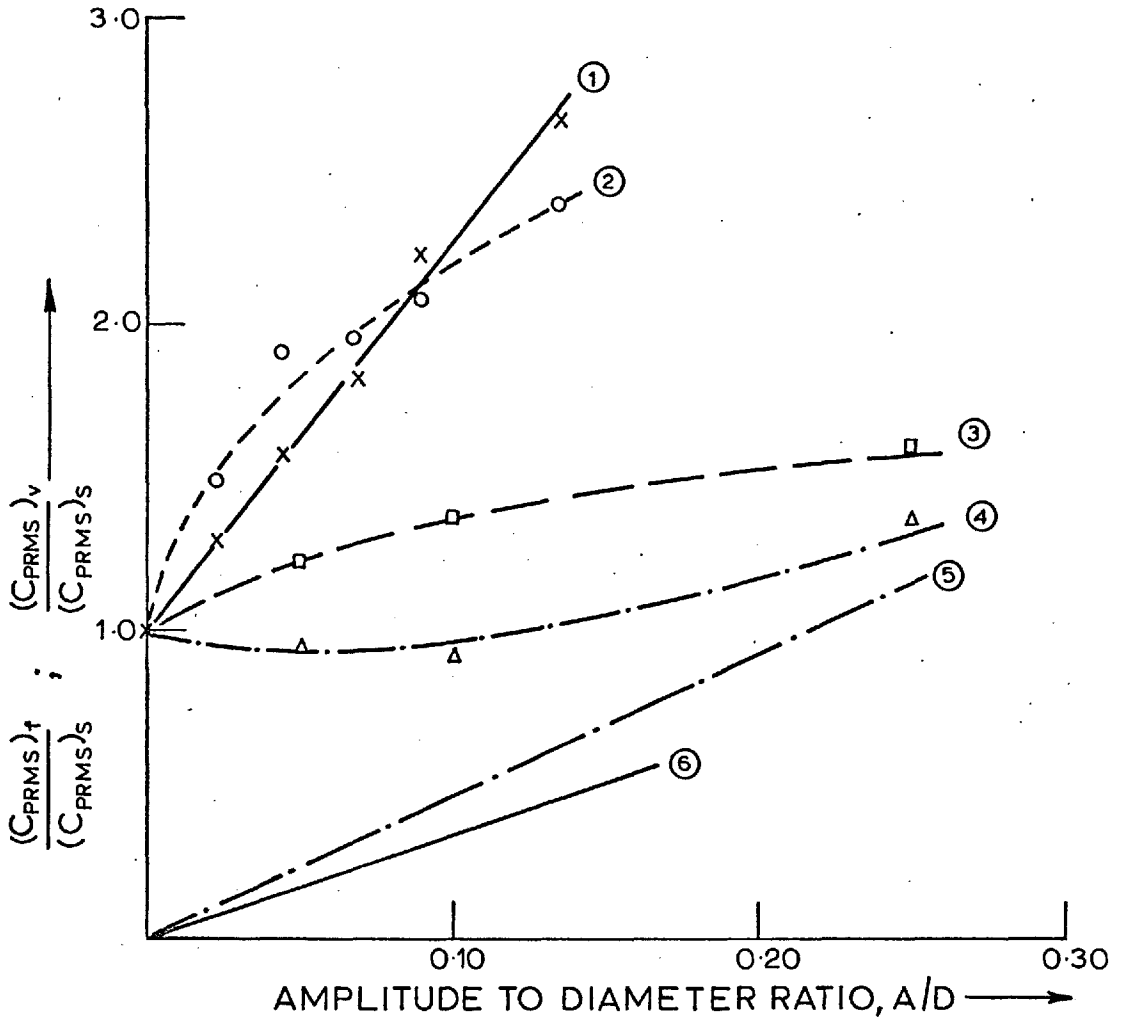

CURVE ①, WILKINSON (1974) ; $\frac{(C_{PRMS})_f}{(C_{PRMS})_S}$; $\frac{U_\infty}{f_N d} = 4{\cdot}5$ or $\frac{f_N}{f_S} = 1{\cdot}66$

CURVE ②; WILKINSON (1974)
CURVE ③; PRESENT RESULTS
} MAXIMUM VALUE OF $\frac{(C_{PRMS})_f}{(C_{PRMS})_S}$ DURING 'LOCK IN'

CURVE ④; PRESENT RESULTS ; $\frac{(C_{PRMS})_f}{(C_{PRMS})_S}$; $\frac{U_\infty}{f_N d} = 4{\cdot}5$ or $\frac{f_N}{f_S} = 1{\cdot}66$

CURVE ⑤; PRESENT RESULTS
CURVE ⑥; WILKINSON (1974)
} $\frac{(C_{PRMS})_v}{(C_{PRMS})_S}$, $\frac{f_N}{f_S} = 1{\cdot}66$

$(C_{PRMS})_f$ and $(C_{PRMS})_v$ DENOTE THE RMS PRESSURE COEFFICIENT ON THE MODEL WHEN OSCILLATED RESPECTIVELY IN FLOWING FLUID AND STILL AIR

$(C_{PRMS})_S$ — RMS PRESSURE COEFFICIENT ON THE STATIONARY MODEL IN FLOWING FLUID

f_N — FREQUENCY OF OSCILLATION

f_S — FREQUENCY OF VORTEX SHEDDING

Fig 7·32 MAGNIFICATION OF SURFACE DYNAMIC PRESSURE AT THE CENTRE OF THE SIDE FACE DURING OSCILLATION.

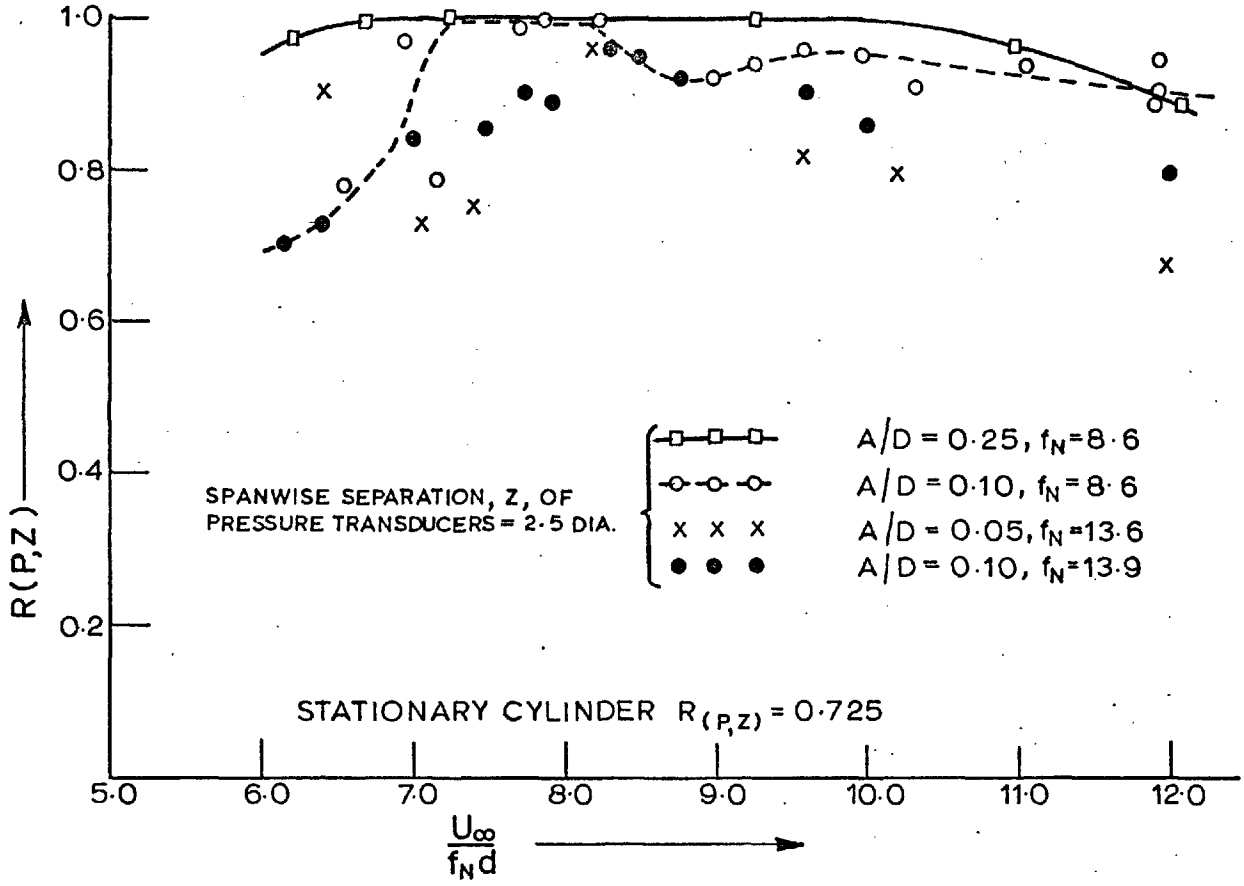

PRESSURE CORRELATION COEFFICIENT, $R(P,Z)$ vs $\frac{U_\infty}{f_N d}$; SEPARATION $Z = 2{\cdot}5D$

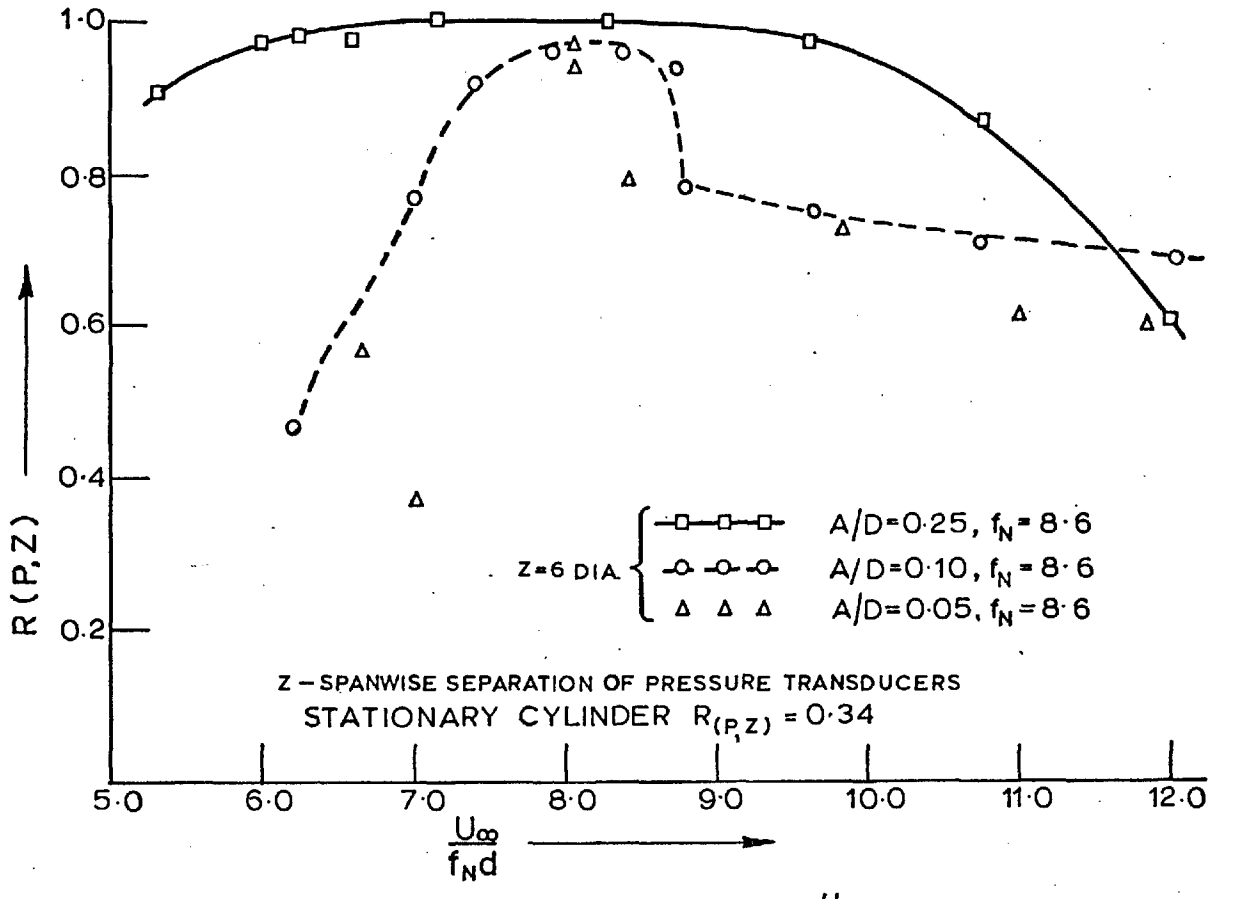

Fig 7·33 PRESSURE CORRELATION COEFFICIENT, $R(P,Z)$ vs $\frac{U_\infty}{f_N d}$; SEPARATION $Z = 6{\cdot}0D$

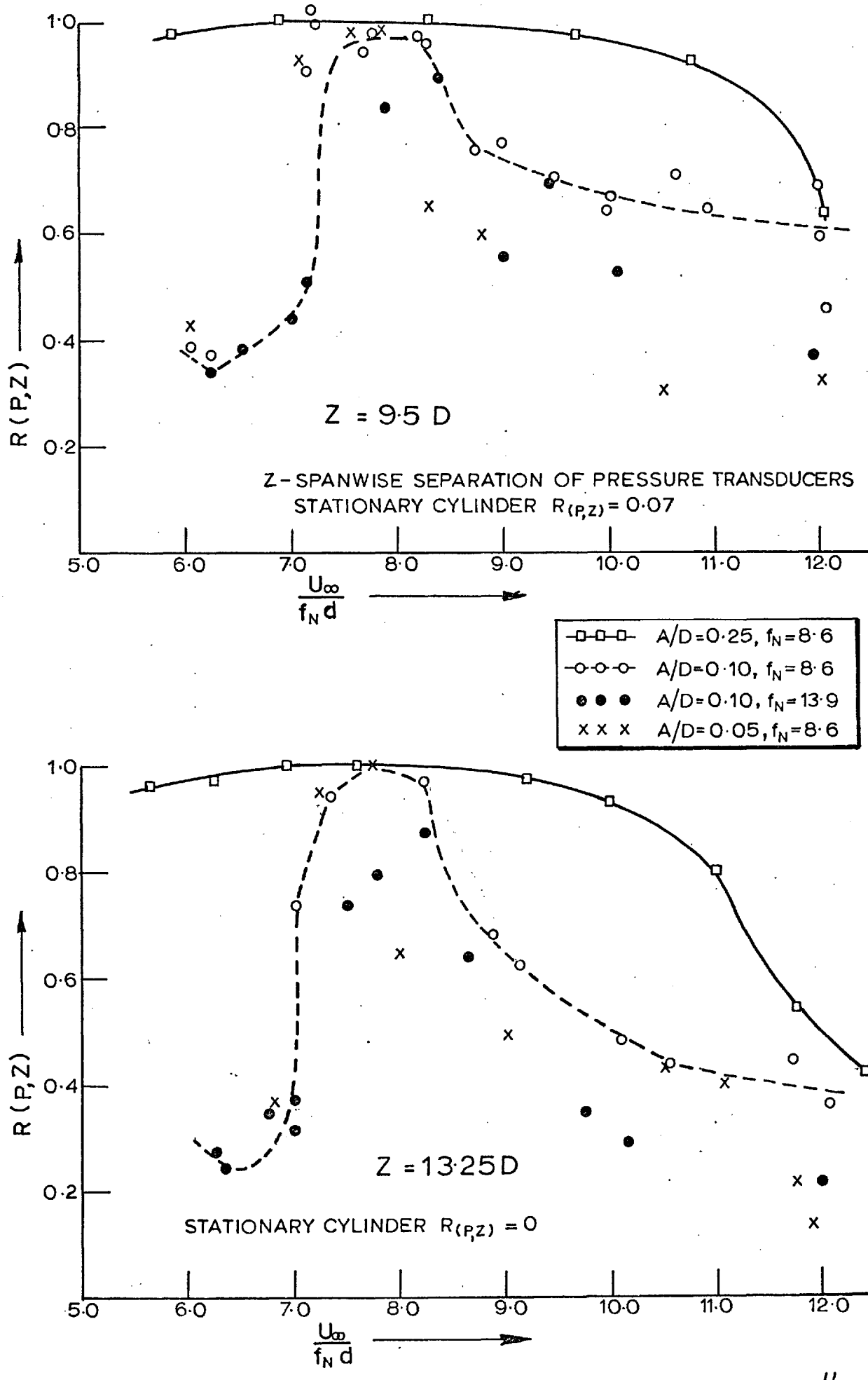

Fig. 7·34 PRESSURE CORRELATION COEFFICIENT, R(P,Z) vs $\frac{U_\infty}{f_N d}$

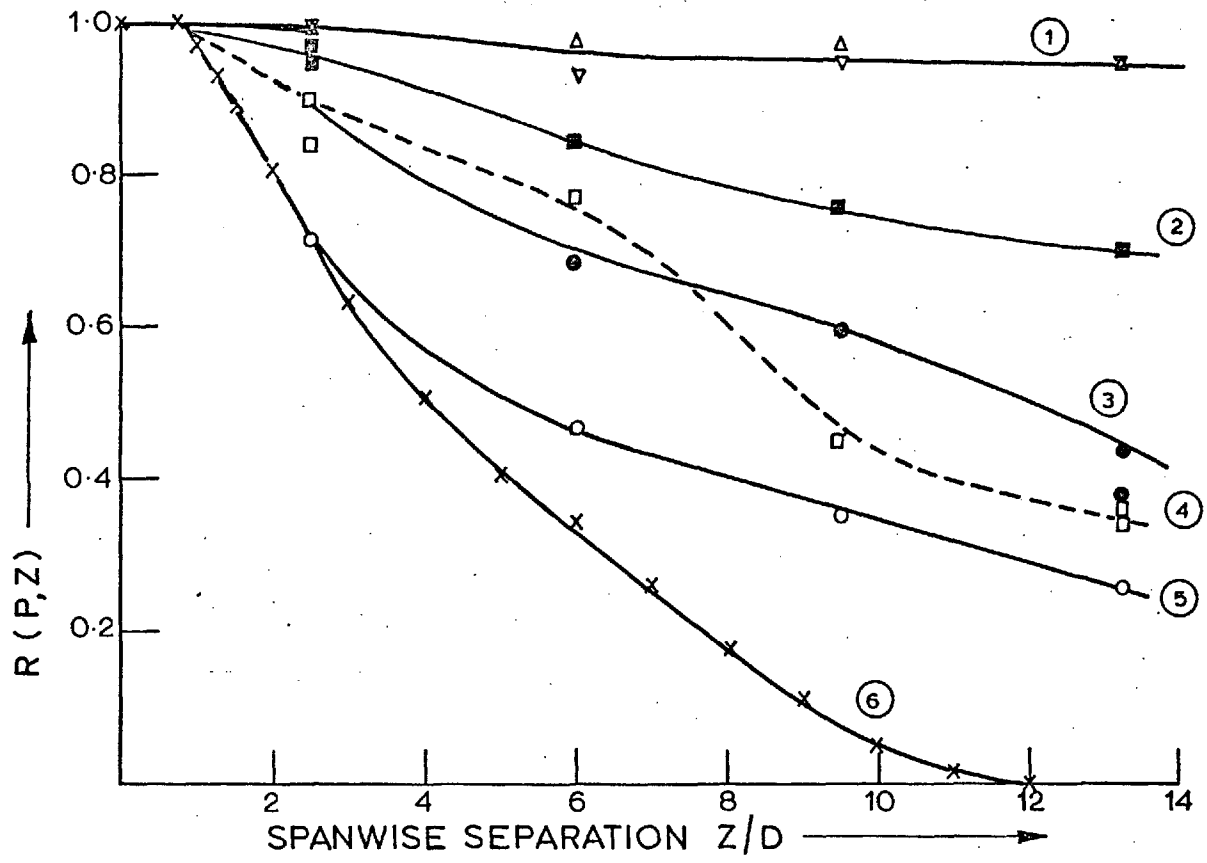

CURVE ① $\frac{U_\infty}{f_N d}$ = 7·5, 7·75 and 8·3 i.e. $\frac{f_s}{f_N}$ of 1·01, 1·04 and 1·11 respectively

CURVE ② $\frac{U_\infty}{f_N d}$ = 8·75 or $\frac{f_s}{f_N}$ = 1·17

CURVE ③ $\frac{U_\infty}{f_N d}$ = 12·0 or $\frac{f_s}{f_N}$ = 1·61

CURVE ④ $\frac{U_\infty}{f_N d}$ = 7·0 or $\frac{f_s}{f_N}$ = 0·94

CURVE ⑤ $\frac{U_\infty}{f_N}$ = 6·25 or $\frac{f_s}{f_N}$ = 0·84

} A/D = 0·10

CURVE ⑥ STATIONARY MODEL

Fig 7·35 THE EFFECTS OF OSCILLATION ON THE SPANWISE CORRELATION OF FLUCTUATING PRESSURES, A/D = 0·1

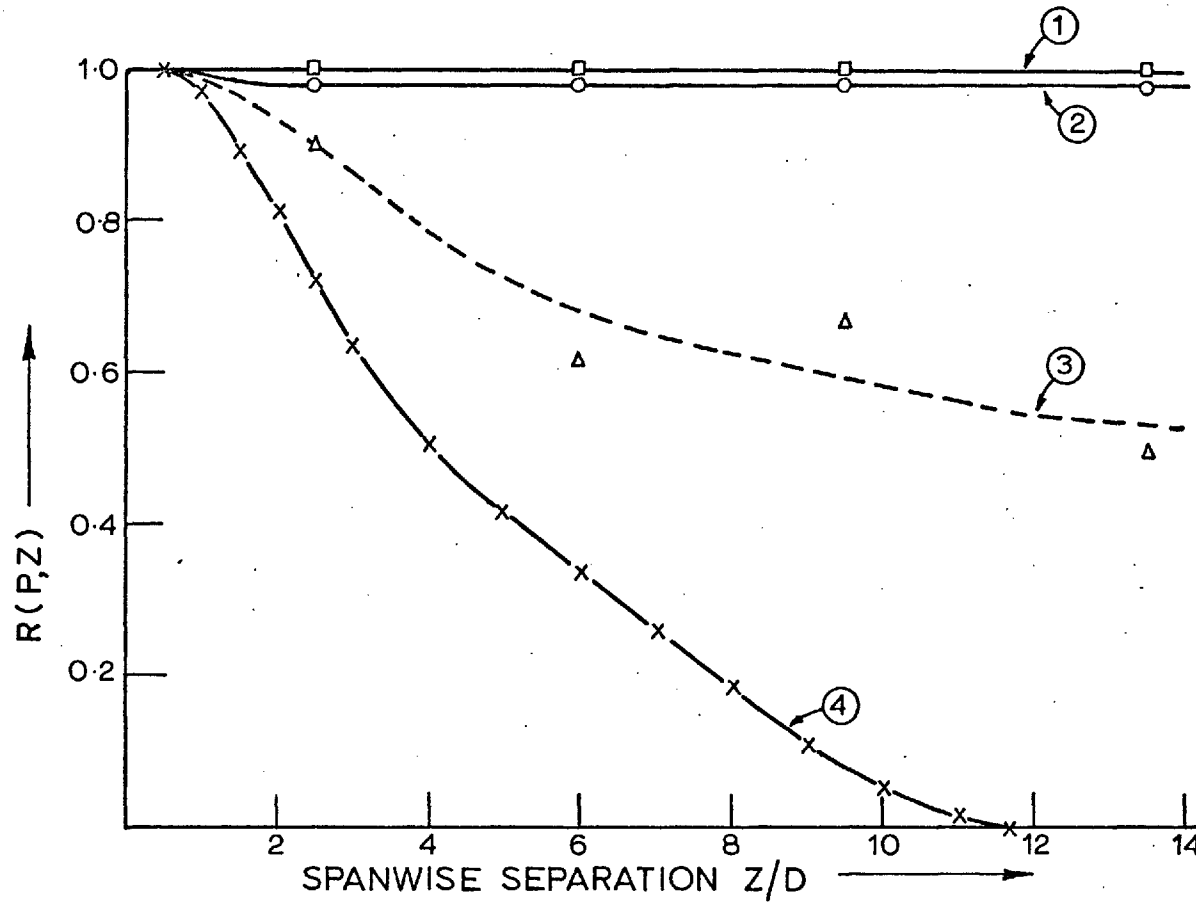

CURVE ① $6{\cdot}75 \lesssim \frac{U_\infty}{f_N d} \lesssim 9{\cdot}75$ or $0{\cdot}90 \lesssim \frac{f_s}{f_N} \lesssim 1{\cdot}31$

CURVE ② $\frac{U_\infty}{f_N d} = 6{\cdot}25$ or $\frac{f_s}{f_N} = 0{\cdot}84$

CURVE ③ $\frac{U_\infty}{f_N d} = 12{\cdot}0$ or $\frac{f_s}{f_N} = 1{\cdot}61$

} $A/D = 0{\cdot}25$

CURVE ④ STATIONARY MODEL, $f_N = 0$

Fig 7·36 THE EFFECTS OF OSCILLATION ON THE SPANWISE CORRELATION OF FLUCTUATING PRESSURES, $A/D = 0{\cdot}25$

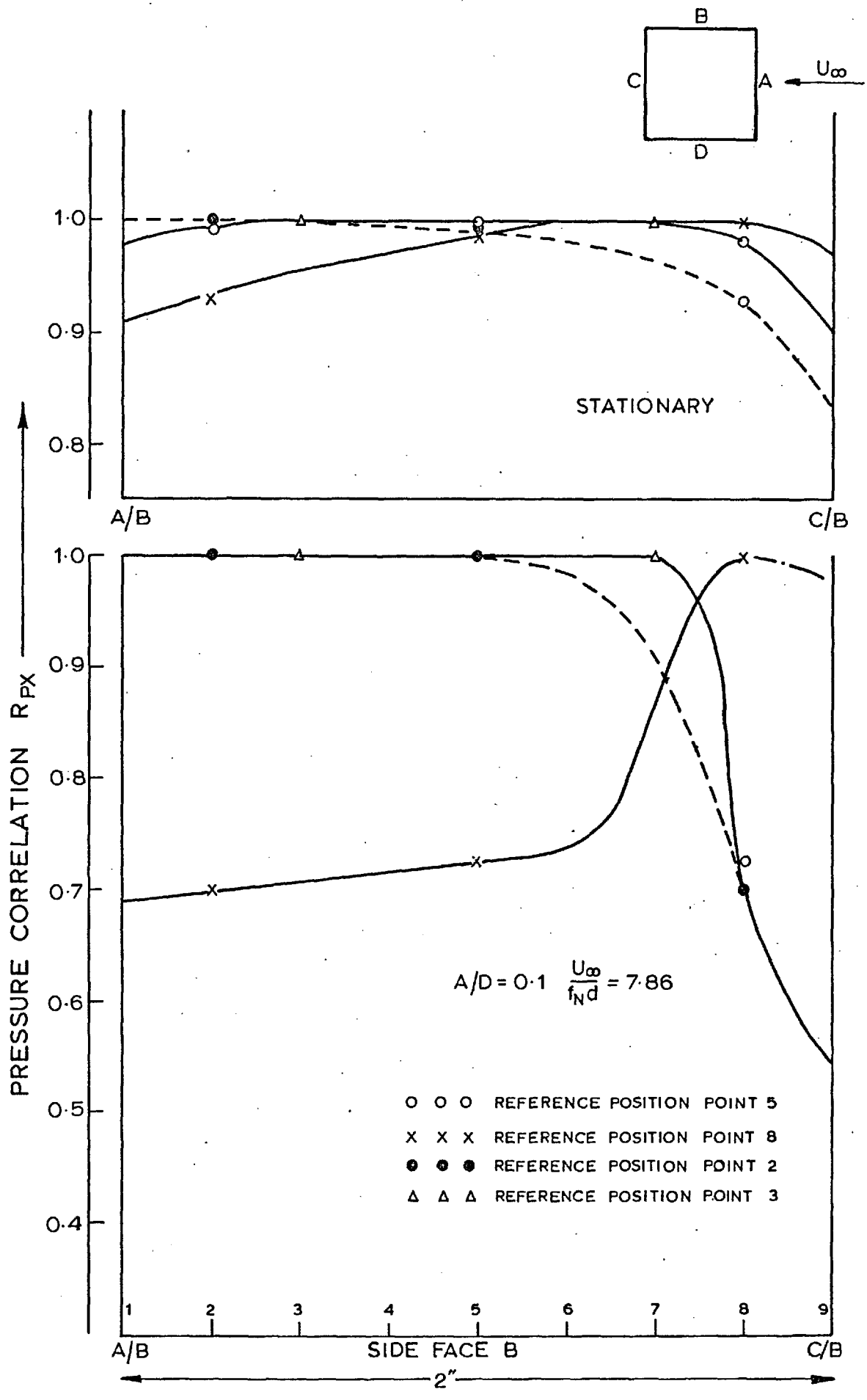

Fig 7·37 PRESSURE CORRELATION ON THE SIDE FACE B OF A SQUARE SECTION

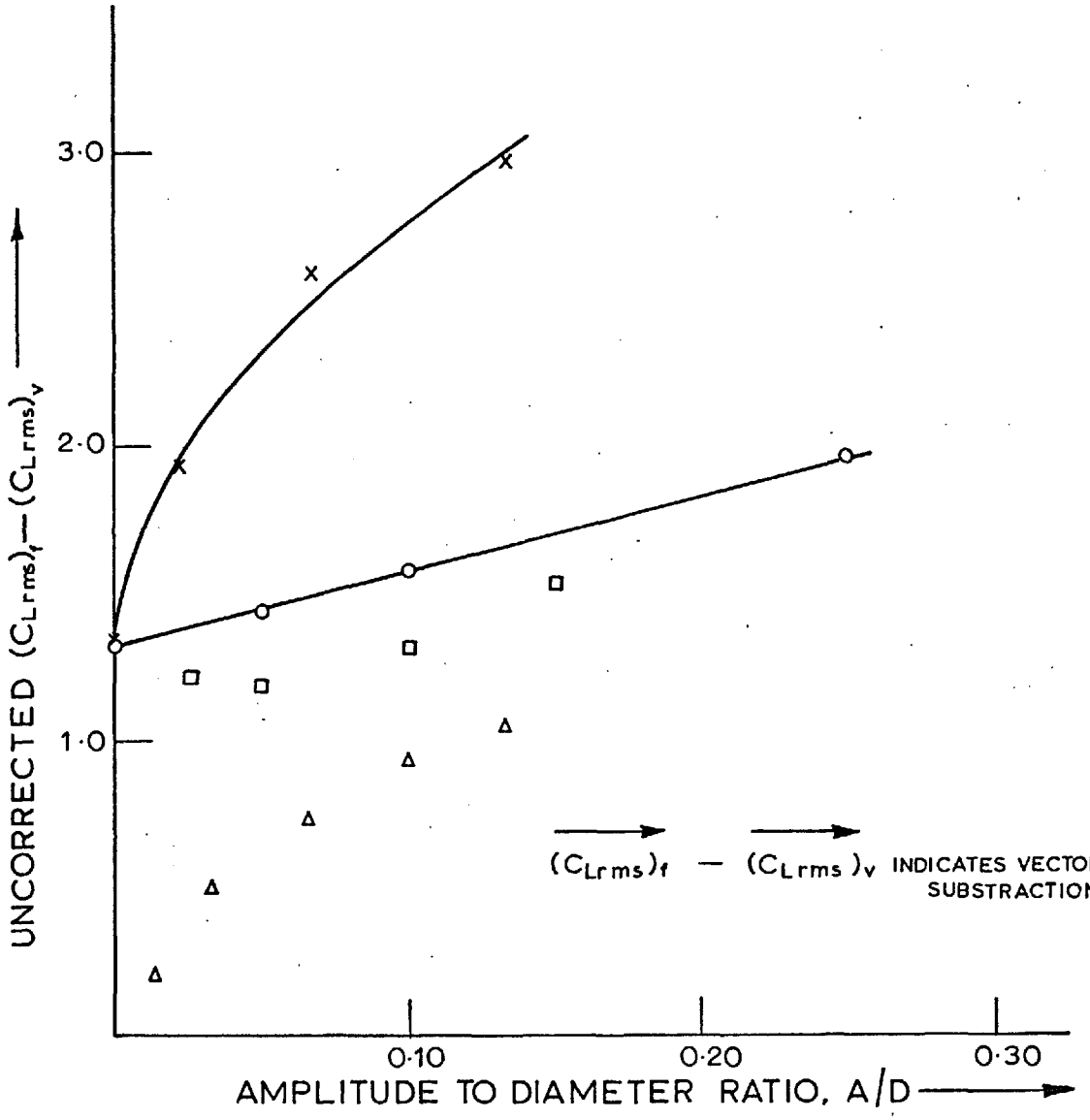

Fig 7·38 ESTIMATES OF THE MAXIMUM VALUES OF THE SECTIONAL FLUCTUATING LIFTS DURING 'LOCK-IN'

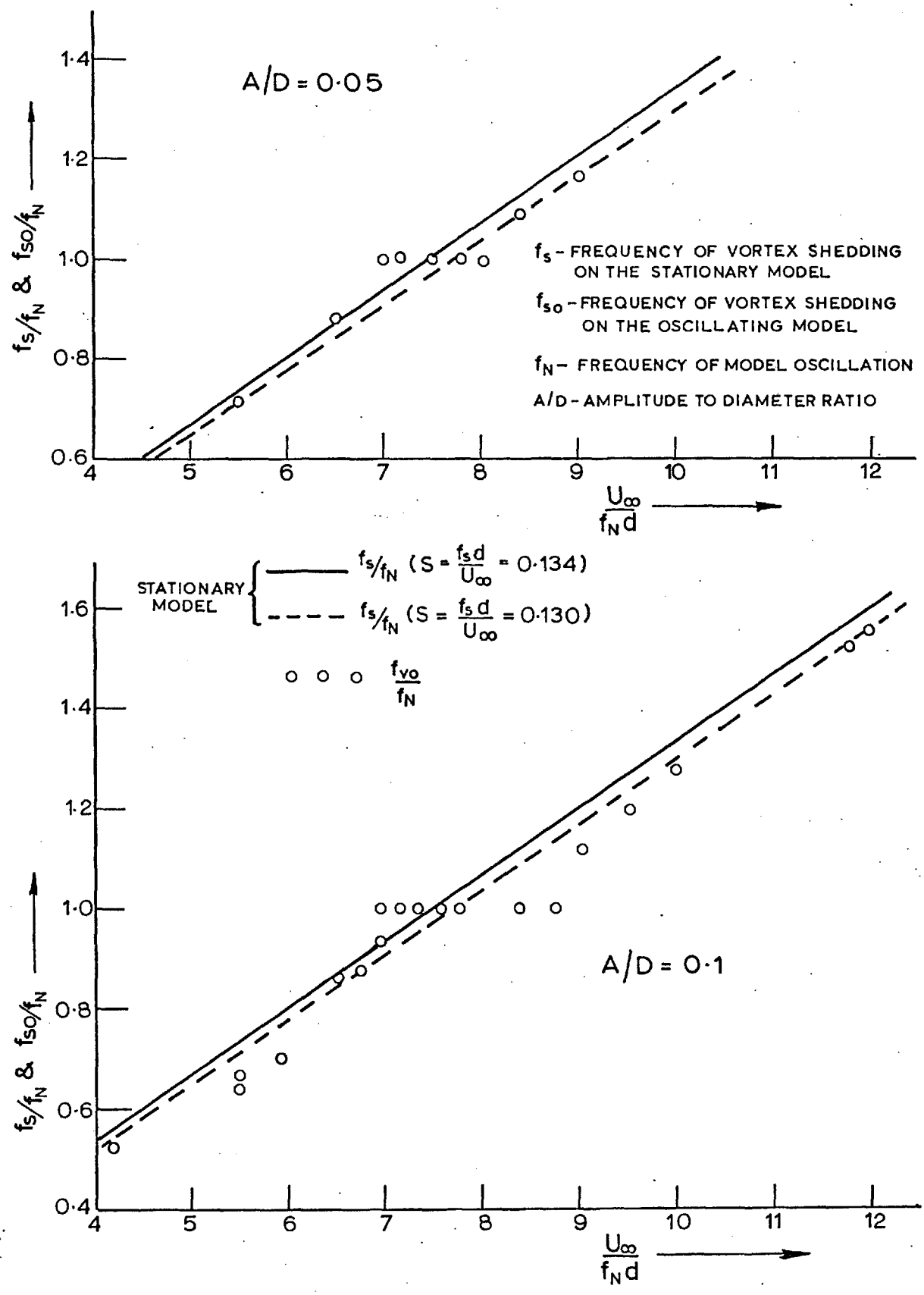

Fig 7·39 EFFECTS OF OSCILLATION ON VORTEX SHEDDING FREQUENCY

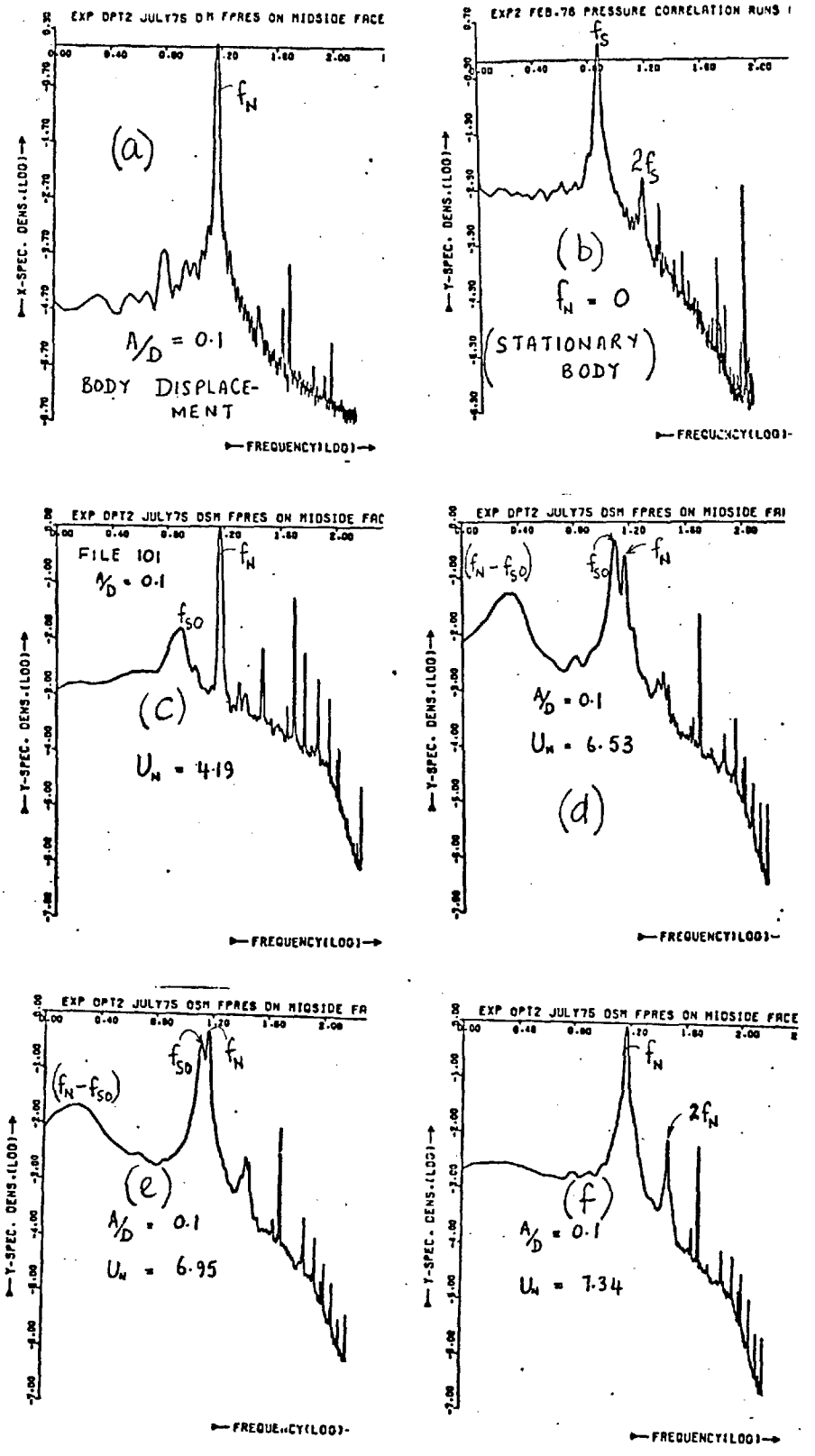

FIG. 7.40 (a) - (f) THE SPECTRA OF LIFT PRESSURE FLUCTATIONS MEASURED AT THE CENTRE OF THE TOP SIDE FACE OF A SQUARE SECTION CYLINDER OSCILLATING NORMAL TO A UNIFORM FREE STREAM.

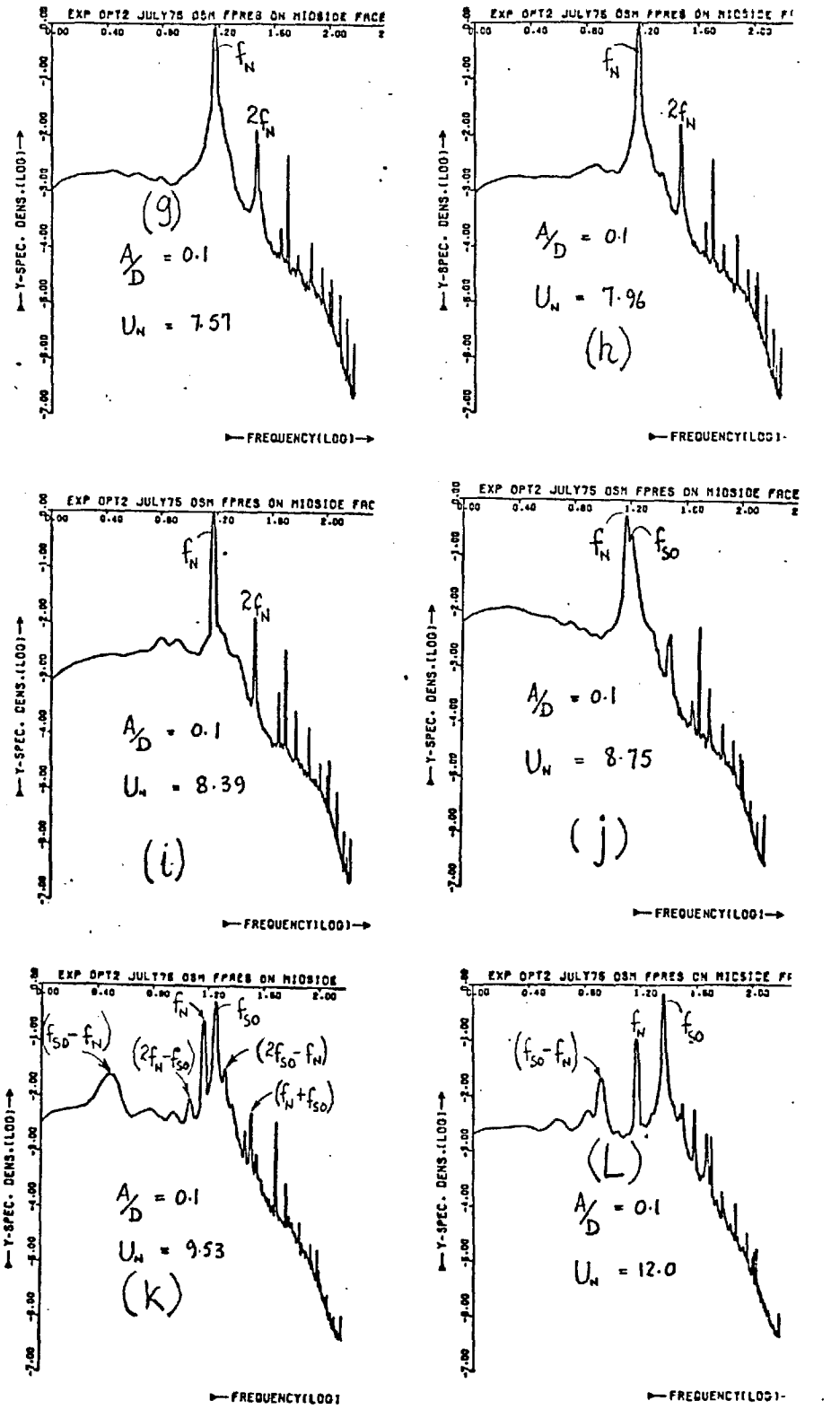

FIG. 7.40(g)-(L) THE SPECTRA OF LIFT PRESSURE FLUCTUATIONS MEASURED AT THE CENTRE OF THE TOP SIDE FACE OF A SQUARE SECTION CYLINDER OSCILLATING PERPENDICULAR TO A UNIFORM FREE STREAM.

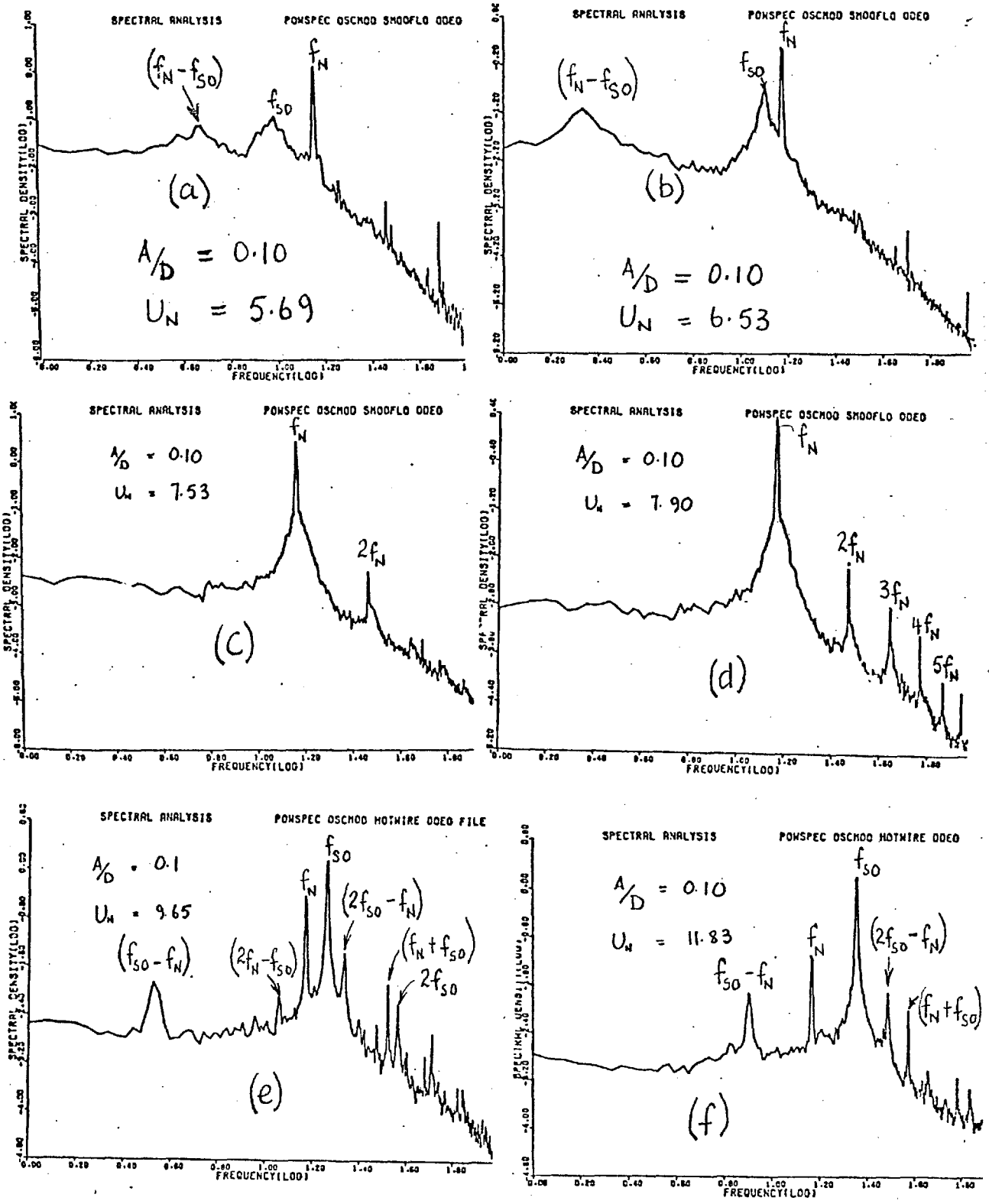

FIG. 7.41. SPECTRA OF VELOCITY FLUCTUATIONS MEASURED AT $(x, y) = (3.0d, 3.0d)$ DOWNSTREAM OF AN OSCILLATING SQUARE SECTION CYLINDER.

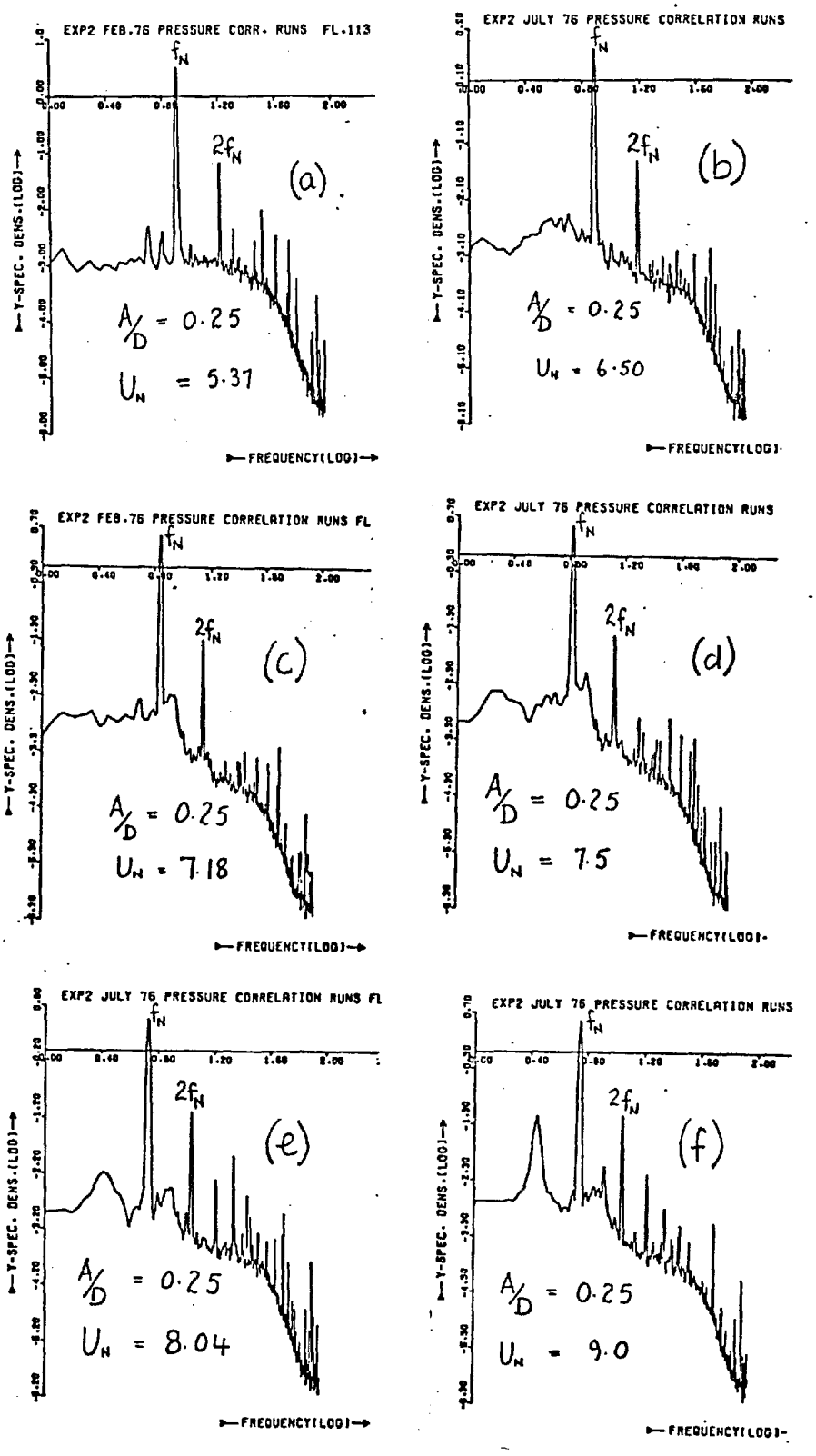

FIG. 7.42 (a) - (f). THE SPECTRA OF LIFT PRESSURE FLUCTUATIONS MEASURED AT THE CENTRE OF THE TOP SIDE FACE OF A SQUARE SECTION CYLINDER OSCILLATING NORMAL TO A UNIFORM FREE STREAM.

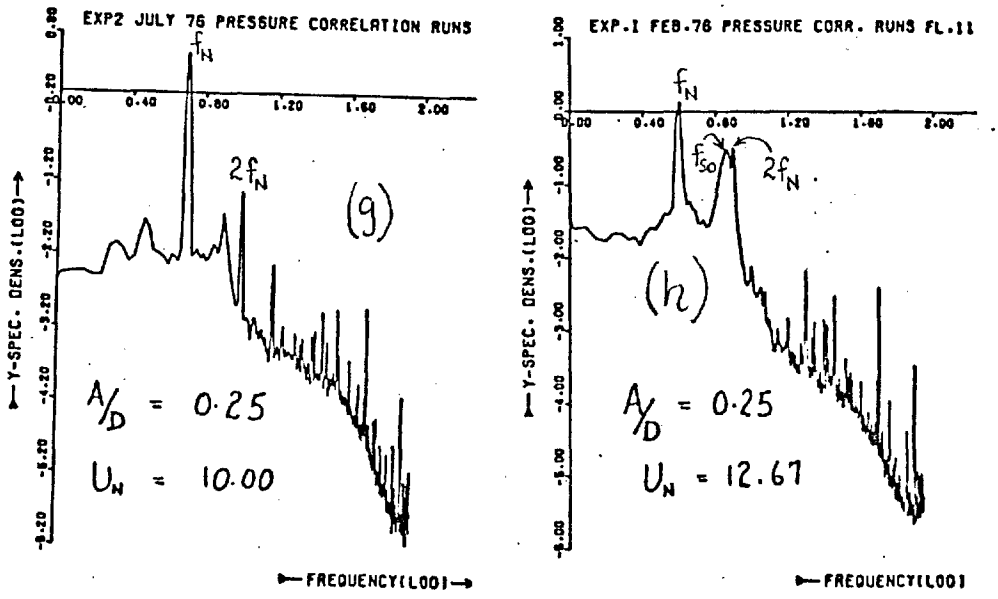

FIG. 7.42 (g) & (h). THE SPECTRA OF LIFT PRESSURE FLUCTUATIONS MEASURED AT THE TOP SIDE FACE OF A SQUARE SECTION CYLINDER OSCILLATING NORMAL TO A UNIFORM FREE STREAM.

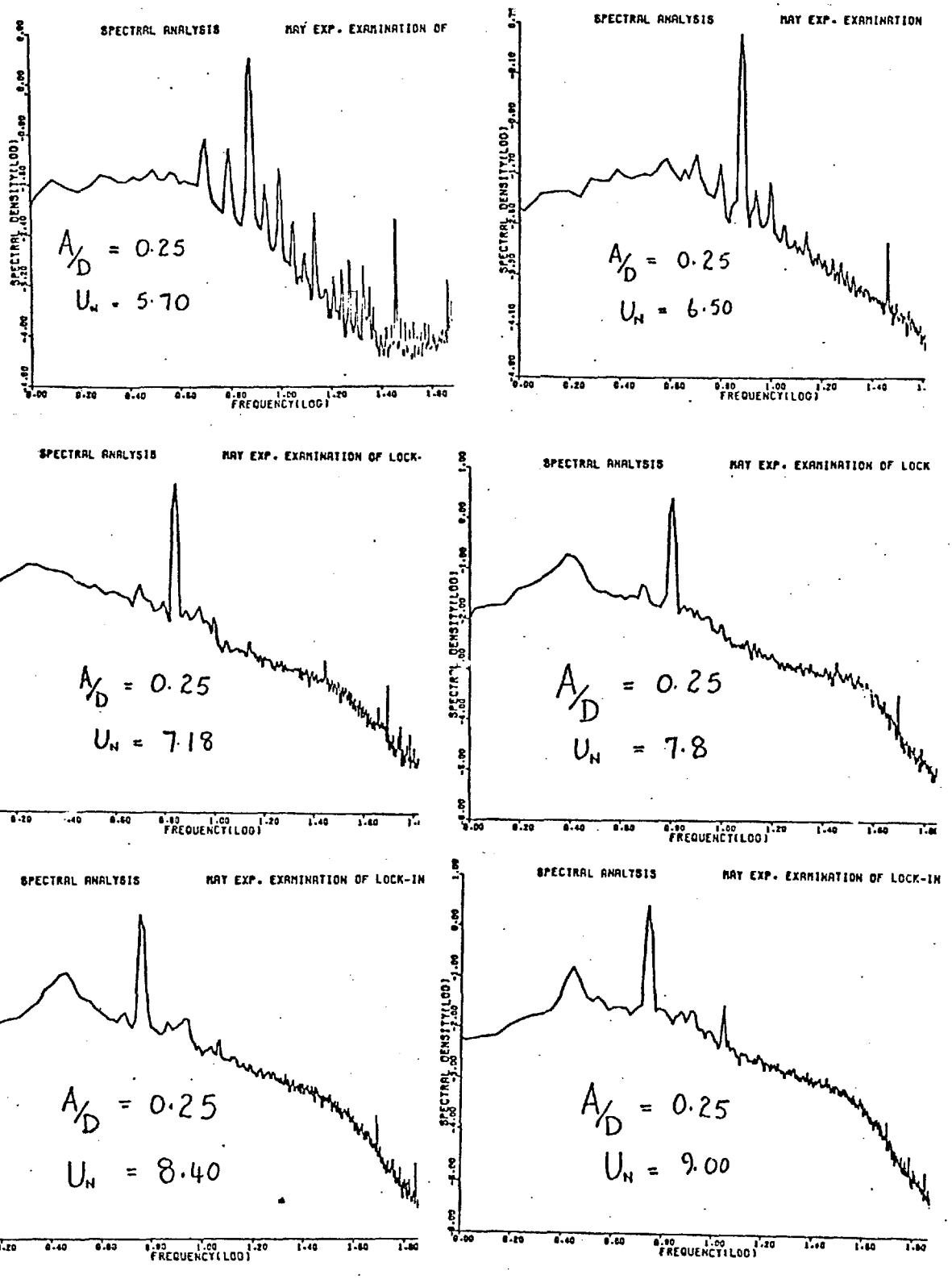

FIG. 7.43 SPECTRA OF VELOCITY FLUCTUATIONS MEASURED AT $(x, y) = (11.0d, 5.9d)$ DOWNSTREAM OF AN OSCILLATING SQUARE SECTION CYLINDER.

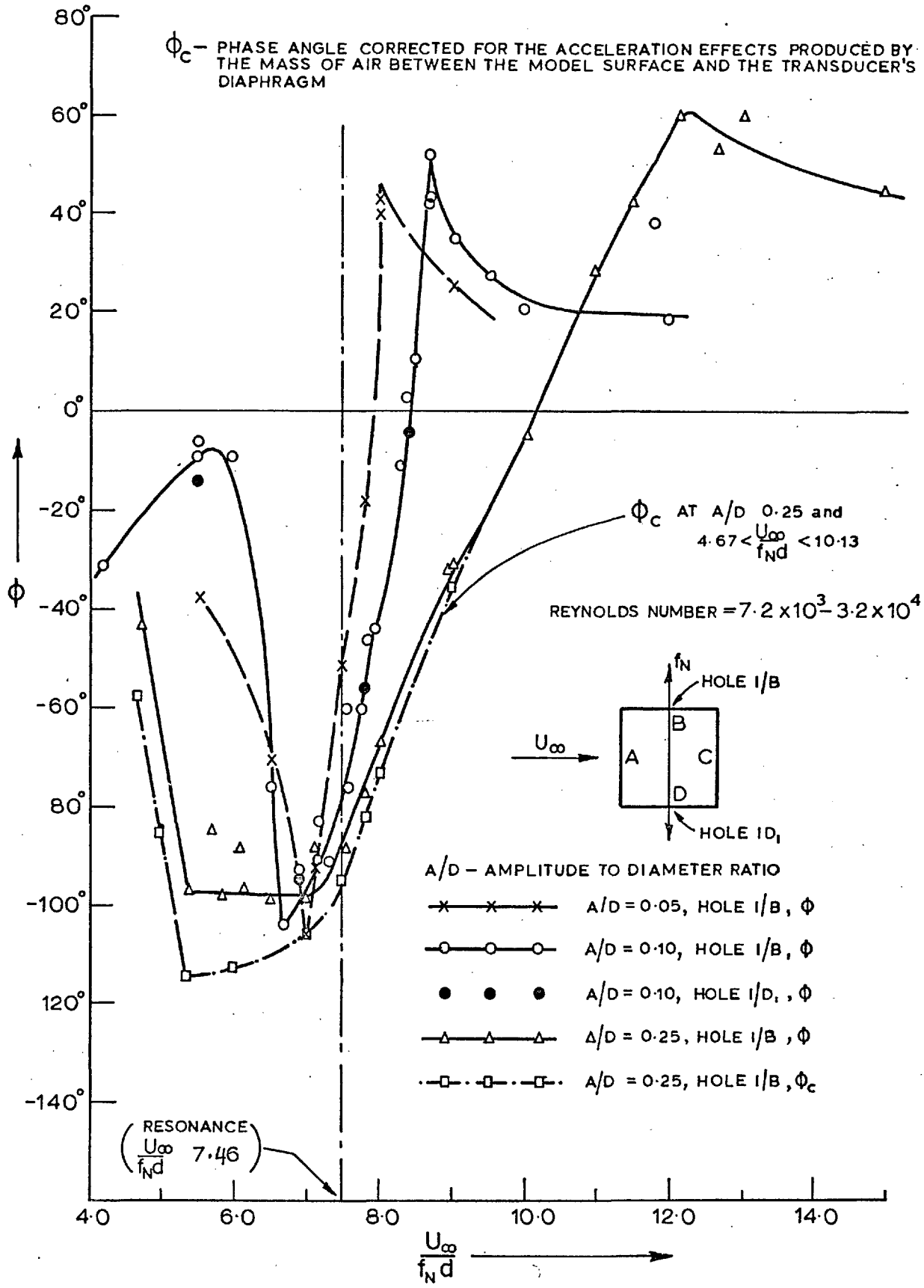

Fig 7·44 ϕ VERSUS $\frac{U_\infty}{f_N d}$ (WHERE ϕ IS THE PHASE ANGLE BETWEEN THE FLUCTUATING LIFT AND THE CYLINDER'S DISPLACEMENT)

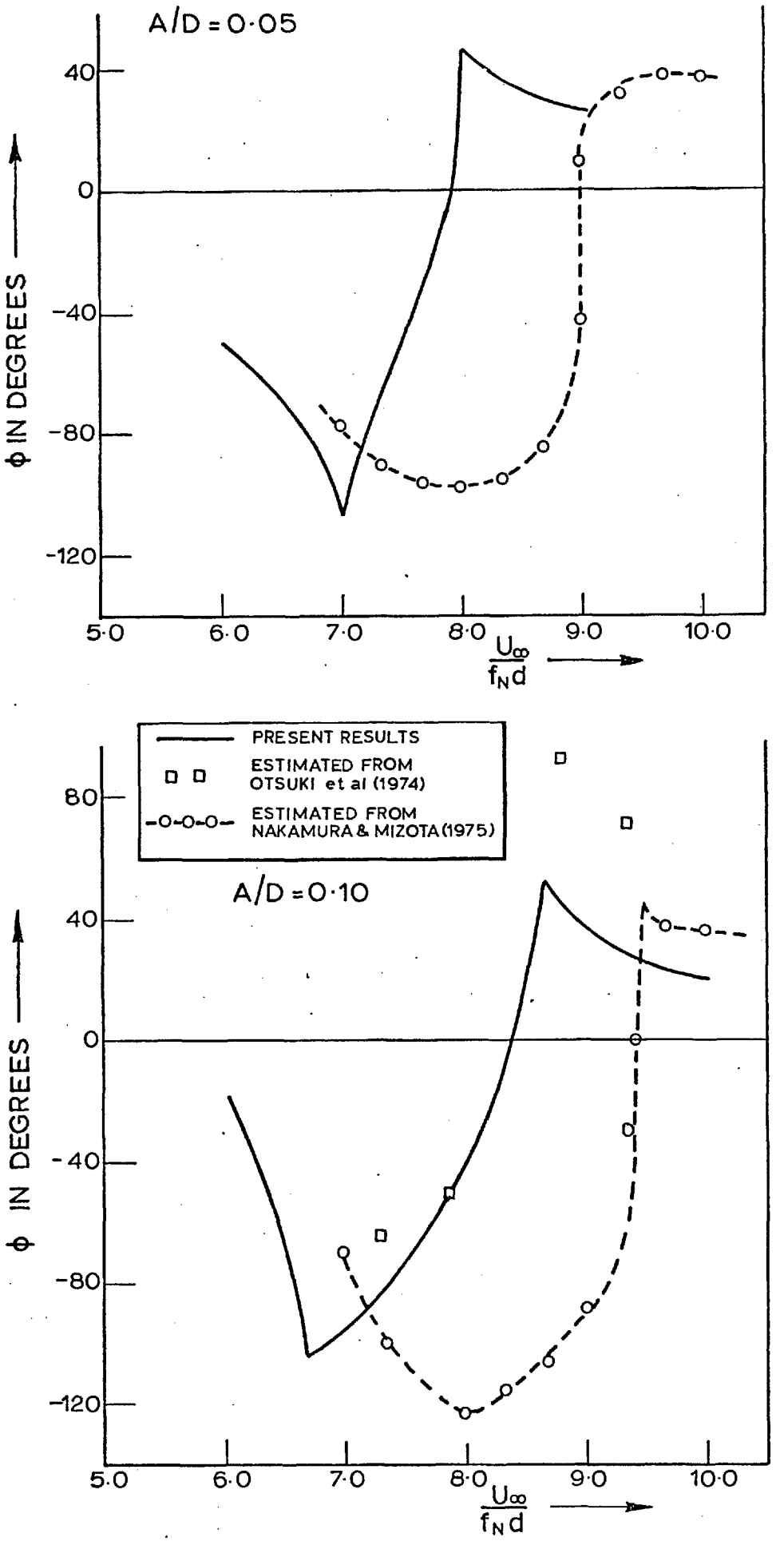

Fig. 7·45 (a) ϕ *versus* $\frac{U_\infty}{f_N d}$

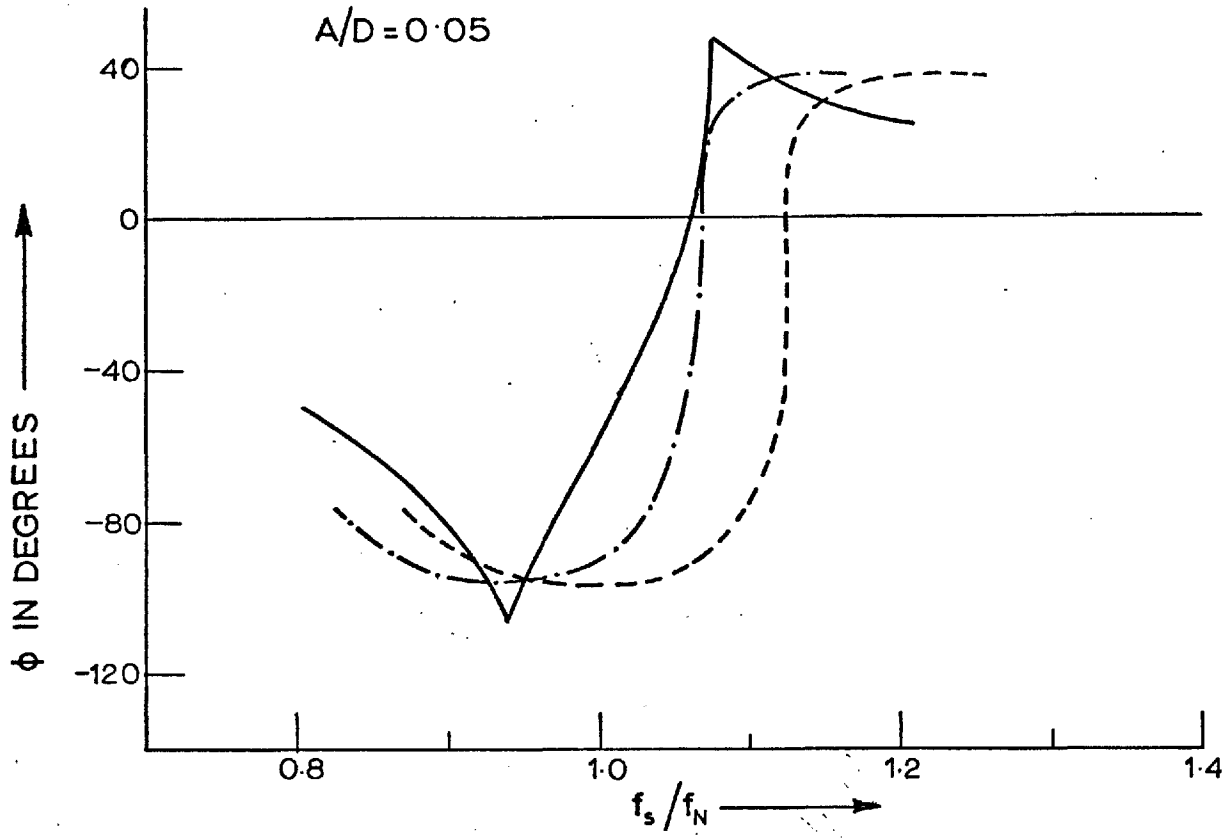

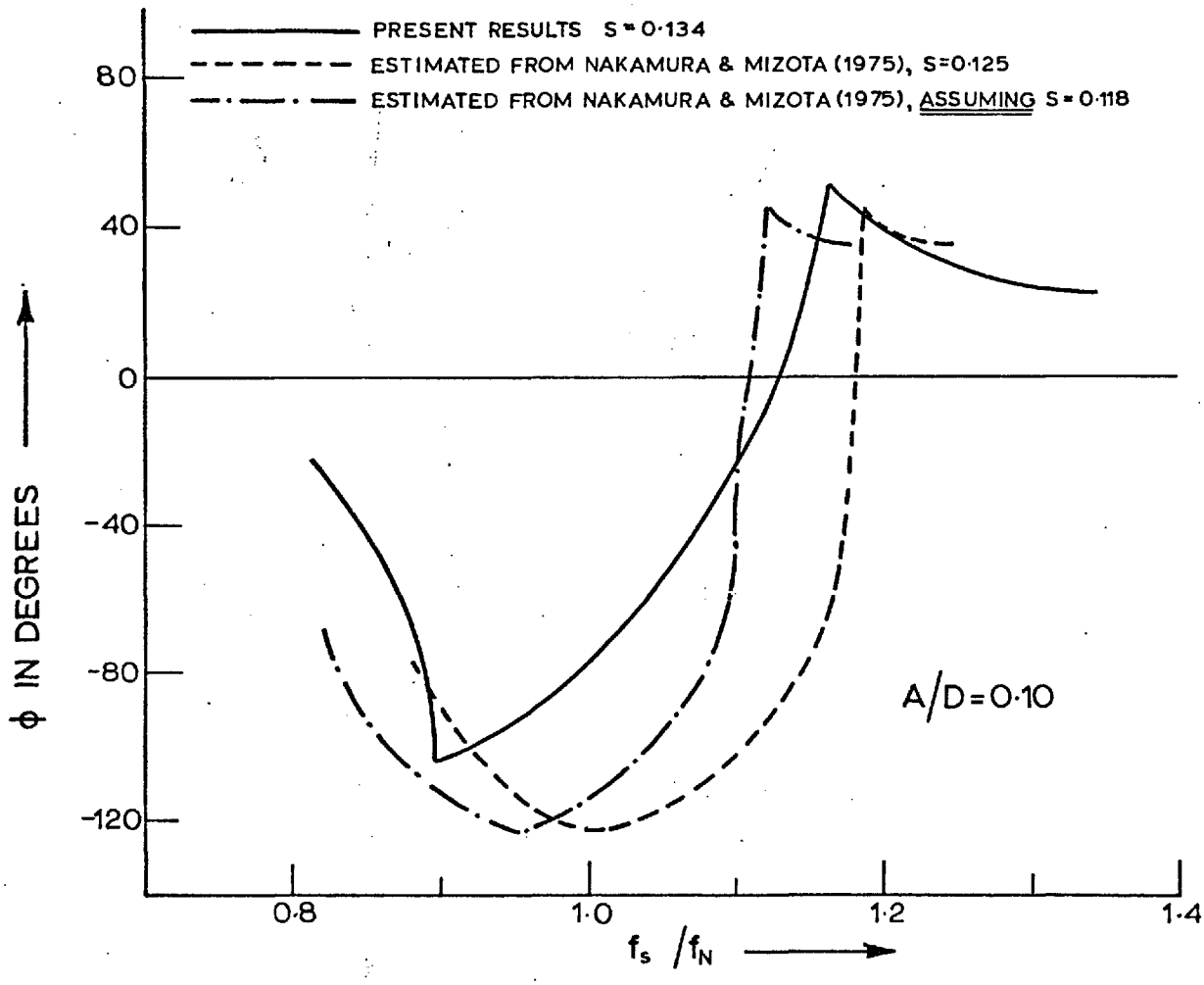

Fig. 7·45(b) ϕ *versus* f_s / f_N

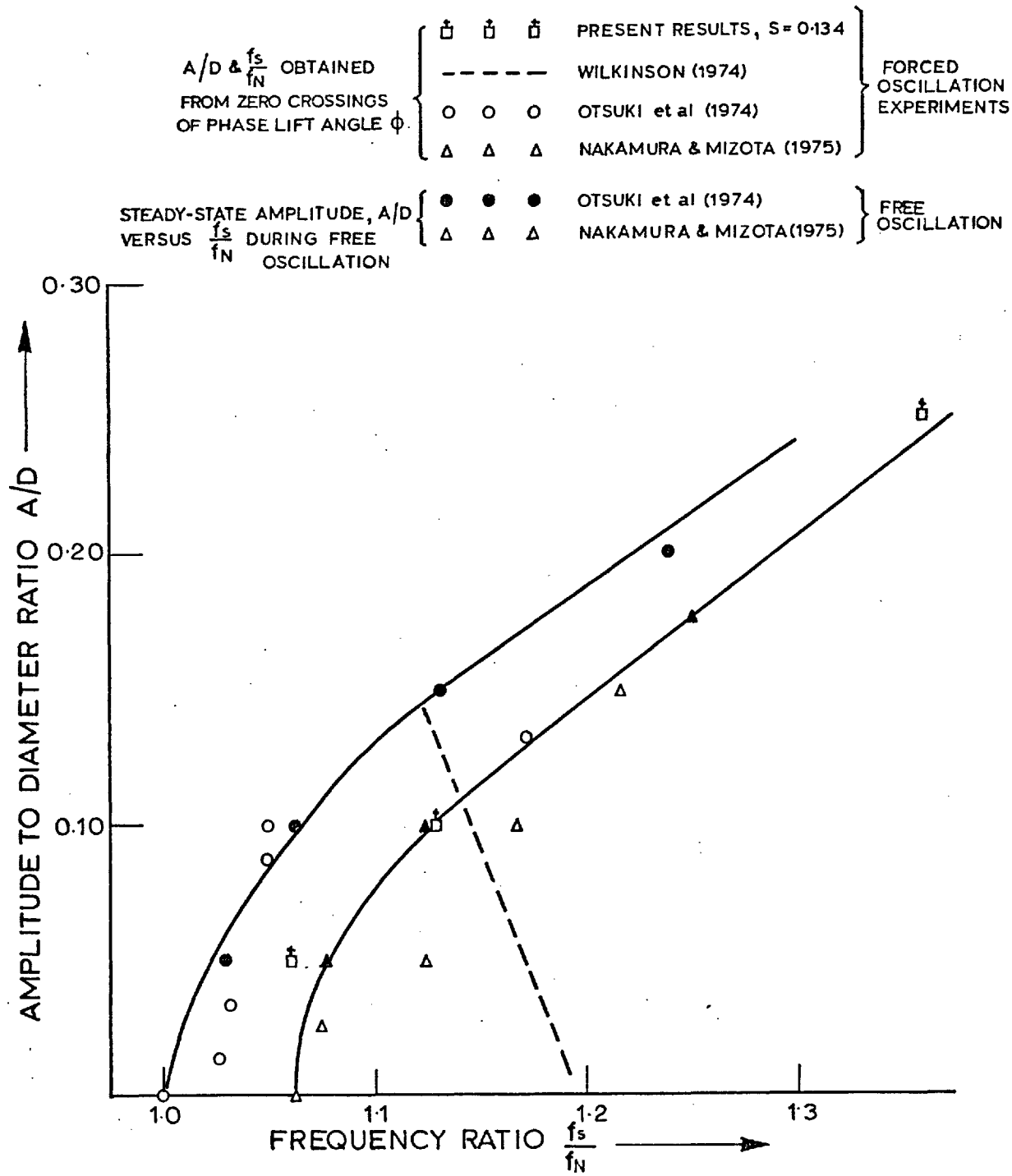

Fig 7·46 COMPARISON BETWEEN THE STEADY-STATE VALUES OF A/D MEASURED ON AN ELASTIC SQUARE SECTION CYLINDER DURING FREE OSCILLATION AND THE VALUES OF A/D INDICATED BY THE ZERO CROSSINGS OF THE LIFT PHASE ANGLE DURING FORCE OSCILLATION

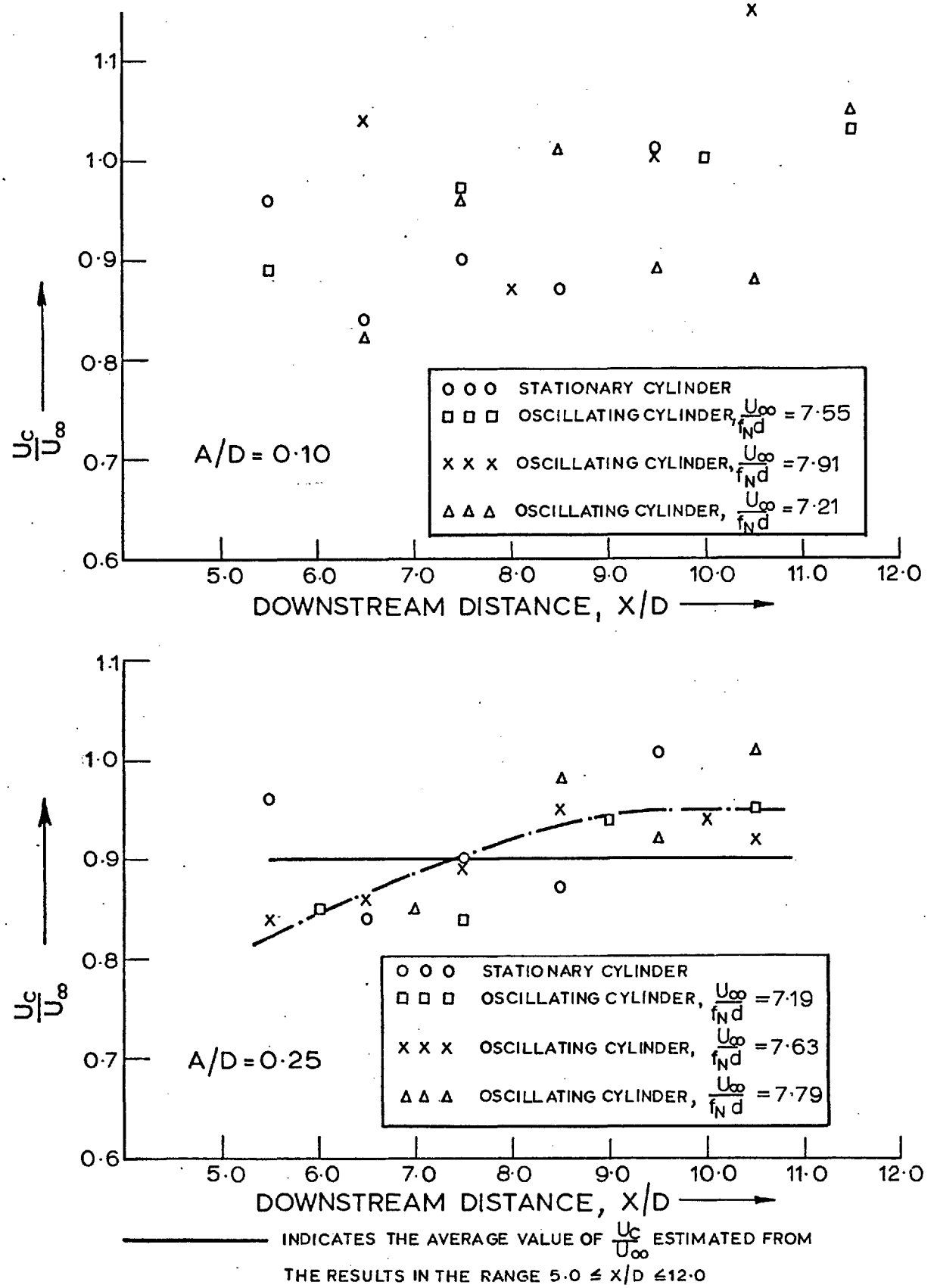

Fig 7·47 VORTEX CONVECTION VELOCITY IN THE WAKE OF A SQUARE SECTION CYLINDER.

THE SIMULTANEOUS OUTPUTS OF PRESSURE AND DISPLACEMENT TRANSDUCERS DURING WAKE SYNCHRONISATION OR 'LOCK-IN'. $A/D = 0.10$

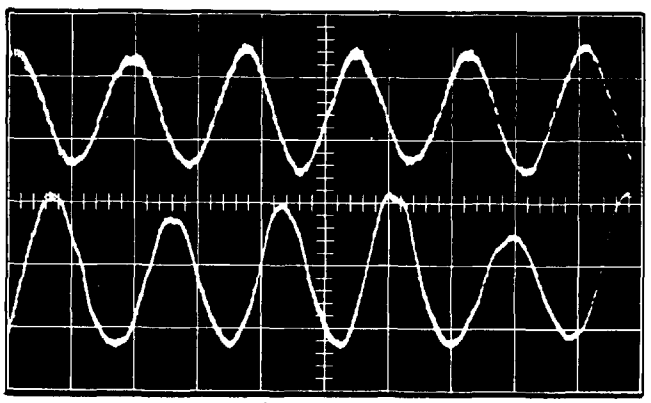

(a) $A/D = 0.10$; $\frac{U_\infty}{f_N d} = 7.54$; Pressure transducer positioned at the centre of the top side face.

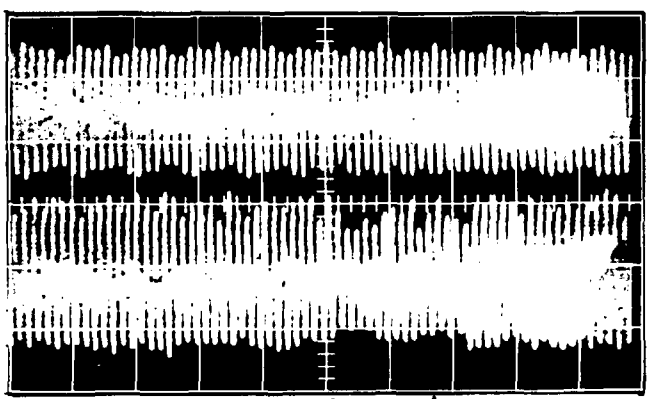

(b) Same as (a) but horizontal scale is contracted.

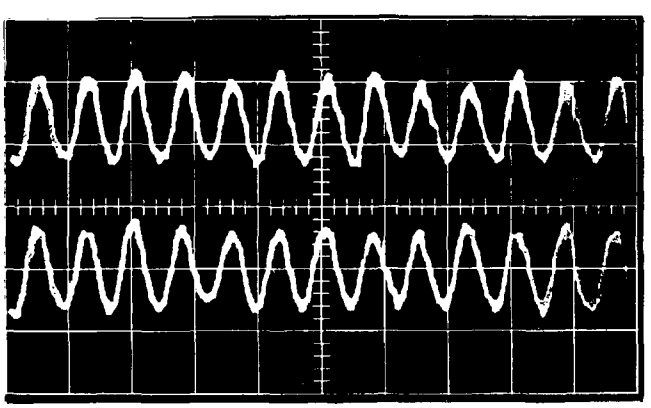

(c) $A/D = 0.10$; $Z = 9.5d$; $\frac{U_\infty}{f_N d} = 7.78$

Z - spanwise separation of Pressure transducers.

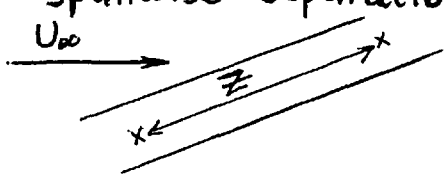

FIG 7.48

THE SIMULTANEOUS OUTPUTS OF PRESSURE AND DISPLACEMENT TRANSDUCERS DURING BODY OSCILLATION AT $A/D = 0.25$.

Upper trace - body displacement; Lower trace - fluctuating pressure at the centre of the top side face.

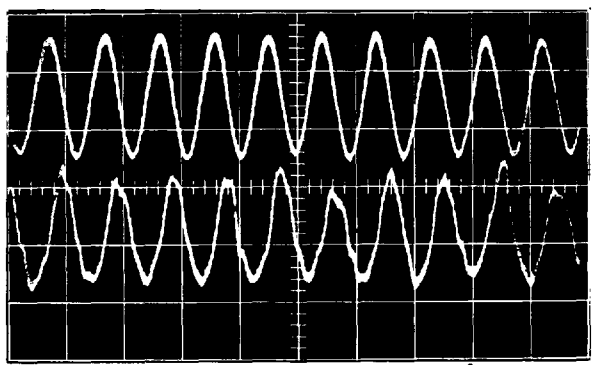

(a) $A/D = 0.25$, $\frac{U_\infty}{f_N d} = 6.14$, $\frac{f_s}{f_N} = 0.82$

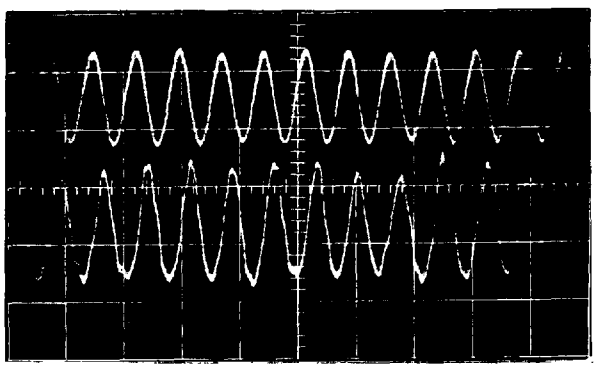

(b) $A/D = 0.25$, $\frac{U_\infty}{f_N d} = 7.52$, $\frac{f_s}{f_N} = 1.01$

Pressure signal (Lower trace) inverted in (a), (b) and (c).

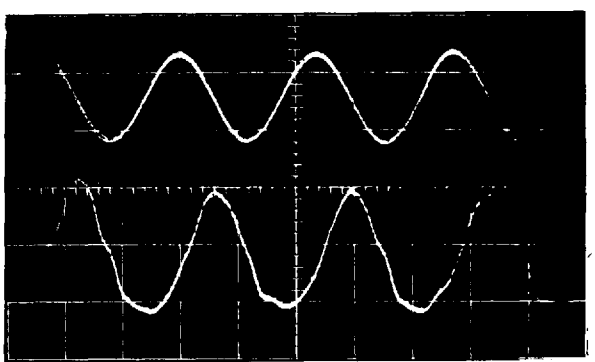

(c) Same signals as (b) but horizontal scale expanded.

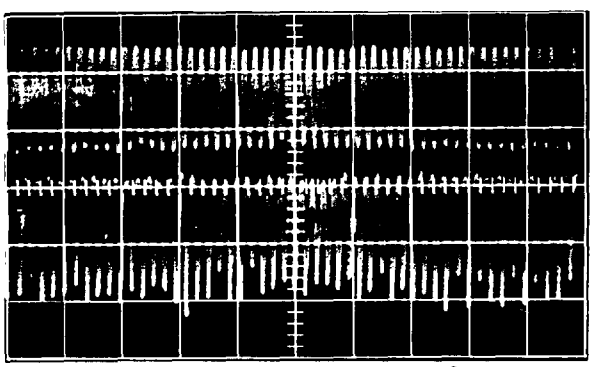

(d) $A/D = 0.25$, $\frac{U_\infty}{f_N d} = 7.80$, $\frac{f_s}{f_N} = 1.05$

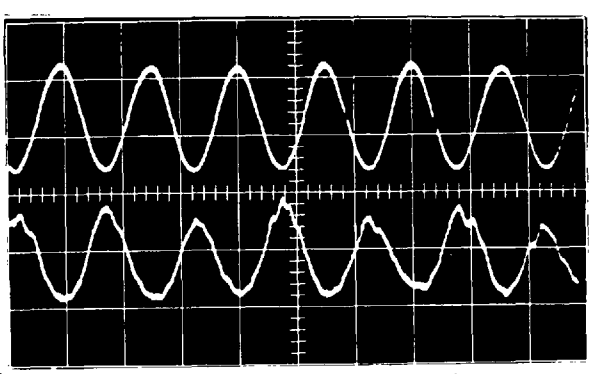

(e) $A/D = 0.25$, $\frac{U_\infty}{f_N d} = 10.00$, $\frac{f_s}{f_N} = 1.34$.

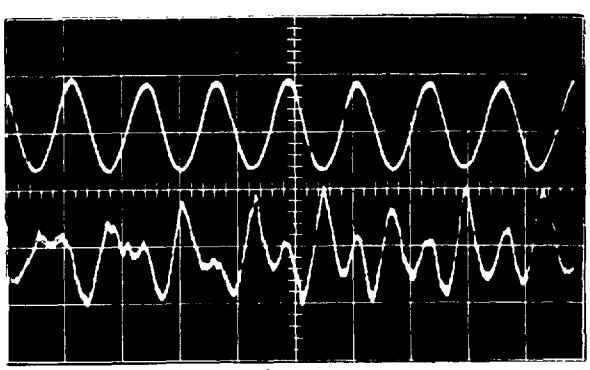

(f) $A/D = 0.25$, $\frac{U_\infty}{f_N d} = 12.67$, $\frac{f_s}{f_N} = 1.70$

FIG 7.49

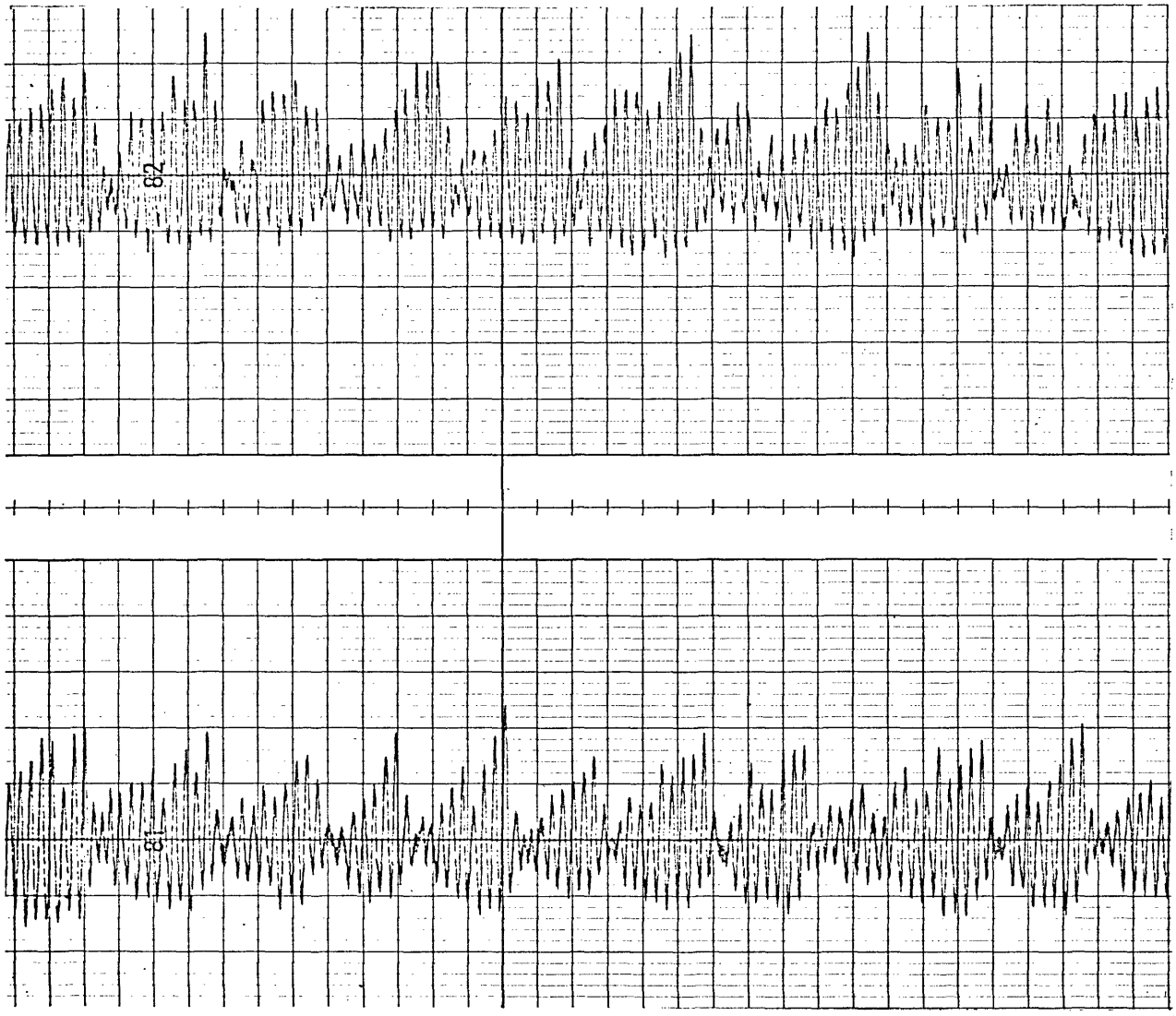

$$A/D = 0.10\ ; \quad \frac{U_\infty}{f_N d} = 9.0\ , \quad \frac{f_s}{f_N} = 1.21$$

THE SIMULTANEOUS PEN-RECORDING OF THE OUTPUTS OF TWO PRESSURE TRANSDUCERS THAT ARE POSITIONED 9.5 BODY DIAMETERS APART ALONG THE CENTRELINE OF THE TOP SIDE FACE.

FIG. 7.50